

Non-Proprietary

Severe Accident Analysis Report

APR1400-E-P-NR-14003-NP, Rev.0

Severe Accident Analysis Report

Revision 0

Non-Proprietary

December 2014

Copyright © 2014

**Korea Electric Power Corporation &
Korea Hydro & Nuclear Power Co., Ltd
All Rights Reserved**

REVISION HISTORY

Revision	Date	Page	Description
0	December 2014	All	First Issue

This document was prepared for the design certification application to the U.S. Nuclear Regulatory Commission and contains technological information that constitutes intellectual property.

Copying, using, or distributing the information in this document in whole or in part is permitted only by the U.S. Nuclear Regulatory Commission and its contractors for the purpose of reviewing design certification application materials. Other uses are strictly prohibited without the written permission of Korea Electric Power Corporation and Korea Hydro & Nuclear Power Co., Ltd.

ABSTRACT

This document provides the severe accident analysis for the Advanced Power Reactor 1400 (APR1400). The APR1400 is designed for the prevention and mitigation of severe accidents, based on in-depth phenomenological analyses that identify potential design and operational vulnerabilities and address them appropriately in a manner that minimizes the consequential risk to the public and to the environment. The design and construction of the severe accident prevention and mitigation features are in compliance with USNRC regulations. These design features comply with USNRC SECY-93-087. In principle, a series of potential phenomena which can threaten the integrity of the containment needs to be screened, reviewed and assessed, since various individual phenomena can occur under severe accident conditions depending upon the design characteristics of the plant.

This report consists of the main body and supplemental appendices. The main body of this report has two parts. The first part describes the severe accident prevention and mitigation features. The second part covers the phenomenological analysis and assessment. The appendices contain the details for the following severe accident analysis.

- Hydrogen control
- Molten core-concrete interaction(MCCI) and Debris Coolability
- High pressure melt ejection(HPME) and direct containment heating(DCH)
- Fuel-coolant interaction(FCI)
- Containment performance capability
- Equipment survivability

The preventive and mitigative design features implemented in the design of ARP1400 include the HG, CFS, ECSBS, and structural designs of the containment and reactor cavity for severe accident loads. The structural design of the reactor cavity is intended to prevent failure from ex-Vessel severe accidents. In particular, the reactor cavity was designed to meet the requirements for prevention and mitigation of phenomena such as HPME/ DCH, EVSE and MCCI. The main design characteristics include a core debris chamber inside the reactor cavity, a convoluted gas vent path, large floor area, and the CFS.

The APR1400 are designed for safety functionality even during a very unlikely severe accident scenario. The design includes accident prevention and mitigation features that are based on the analyses of severe accidents. Sufficient robustness is provided in the design so that ample time exists for operator action to mitigate the consequences of a severe accident and minimize the radiological releases into the environment.

In the severe accident analysis for the APR1400, emphases have been laid on the following six topics: hydrogen control, MCCI and debris coolability, HPME and DCH, FCI, containment performance, and ES in order to ensure design adequacy and regulatory compliance. The regulatory compliance involves strict adherence to requirements and reasonable conformance with the guidelines set forth in USNRC, SECY-93-087 and other regulatory requirements such as 10 CFR 100, GDC of 10 CFR 50 Appendix A, and the TMI-related requirements of 10 CFR 50.34(f), 10 CFR 50.44, NRC RG 1.216, and SECY-90-016.

TABLE OF CONTENTS

1	INTRODUCTION	1
2	SEVERE ACCIDENT PREVENTION AND MITIGATION FEATURES	2
2.1	Severe Accident Prevention	2
2.1.1	Anticipated Transient without Scram	2
2.1.2	Mid-Loop Operation.....	2
2.1.2.1	Instrumentation for Shutdown Operations.....	3
2.1.2.2	SCS Design	3
2.1.2.3	Steam Generator Nozzle Dam Integrity	3
2.1.2.4	Alternate Inventory Additions and Decay Heat Removal Methods	3
2.1.3	Station Blackout.....	3
2.1.4	Fire Protection	4
2.1.5	Intersystem Loss of Coolant Accident	4
2.1.6	Other Severe Accident Preventative Features	5
2.2	Severe Accident Mitigation	6
2.2.1	Overview of the Containment Design.....	6
2.2.1.1	Description of the Containment.....	6
2.2.1.2	Containment Pressure Limits	7
2.2.1.3	Containment Penetrations	7
2.2.2	Cavity Flooding System.....	7
2.2.3	Hydrogen Mitigation System	8
2.2.4	Rapid Depressurization Function	9
2.2.5	Reactor Cavity Design.....	10
2.2.6	Emergency Containment Spray Backup System	10
3	SEVERE ACCIDENT PHENOMENOLOGICAL ANALYSIS AND ASSESSMENT	12
3.1	Hydrogen Control	12
3.1.1	Local Hydrogen Accumulation Evaluation and Summary	12
3.1.2	DDT	13
3.1.3	AICC Pressure Evaluation.....	13
3.2	MCCI and Debris Coolability	13
3.3	High Pressure Melt Ejection and Direct Containment Heating	14
3.3.1	Direct Containment Heating	14
3.3.2	Rapid Depressurization Analysis.....	15
3.4	Fuel-Coolant Interaction	15
3.5	Containment Performance	16

3.6 Equipment Survivability 17

4 CONCLUSIONS 33

5 REFERENCES 35

APPENDICES

- Appendix A** Severe Accident Analysis Report for Hydrogen Issue
- Appendix B** Severe Accident Analysis Report for MCCI
- Appendix C-1** Severe Accident Analysis Report for HPME/DCH
- Appendix C-2** Severe Accident Analysis Report for RD
- Appendix D** Severe Accident Analysis Report for FCI
- Appendix E** Severe Accident Analysis Report for Containment Performance
- Appendix F** Severe Accident Analysis Report for Equipment Survivability Evaluation

LIST OF TABLES

Table 3-1	Selected Severe Accident Scenarios for MCCI Analyses	18
Table 3-2	Summary of Cavity Structural Integrity Analysis Result.....	18

LIST OF FIGURES

Figure 3-1 Mole Fraction of Hydrogen in the Dome Region for LBLOCA 19

Figure 3-2 Mole Fraction of Hydrogen in the Dome Region for SBLOCA..... 22

Figure 3-3 Mole Fraction of Hydrogen in the Dome Region for SBO-Three-way valve 25

Figure 3-4 Mole Fraction of Hydrogen in the Dome Region for TLOFW-Three-way valve 28

Figure 3-5 Ablation Depths within 24 Hours for Several Severe Accident Scenarios 31

Figure 3-6 Containment Pressures within 24 Hours for Several Severe Accident Scenarios 31

Figure 3-7 Containment Pressure for Large Break LOCA with ECSBS Actuated 24 hours
after Onset of Core Damage..... 32

ACRONYMS AND ABBREVIATIONS

AC	alternative current
AFW	auxiliary feed water
AICC	adiabatic isochoric complete combustion
ALWR	advanced light water reactor
AOO	anticipated operational occurrence
ATWS	anticipated transient without scram
BDBA	beyond design basis accident
CCFP	conditional containment failure probability
CCW	component cooling water
CET	core exit temperature
CFS	cavity flooding system
CSS	containment spray system
DBA	design basis accident
DCH	direct containment heating
DDT	deflagration-to-detonation transition
DPS	diverse protection system
ECSBS	emergency containment spray backup system
EDG	emergency diesel generator
ES	equipment survivability
ESW	essential service water
EVSE	ex-vessel steam explosion
FA	flame acceleration
FCI	fuel coolant interaction
FLC	factored load category
HPME	high pressure melt ejection
HVT	holdup volume tank
ICI	in core instrumentation
IRWST	in-containment refueling water storage tank
ISLOCA	intersystem loss of coolant accident
IVSE	in-vessel steam explosion
LBLOCA	large break LOCA
LOCA	loss of coolant accident
LOOP	loss of offsite power

MAAP	modular accident analysis program
MBLOCA	medium break LOCA
MCCI	molten core concrete interaction
MWR	metal water reaction
PAR	passive autocatalytic recombiner
POSRV	pilot operated safety and relief valve
PRA	probabilistic risk assessment
RCGV	reactor coolant gas vent
RCP	reactor coolant pump
RCS	reactor coolant system
RD	rapid depressurization
RV	reactor vessel
RVLMS	reactor vessel level monitoring system
SBLOCA	small break LOCA
SBO	station black out
SCS	shutdown cooling system
SIS	safety injection system
TLOESW	total loss of essential service water
TLOFW	total loss of feed water
VB	vessel breach

1 INTRODUCTION

The likelihood of a severe accident, which postulates reactor core meltdown beyond the scope of design basis accidents and consequently can lead to releases of large amounts of radionuclides into the environment, is extremely low. However, in view of the postulated severe damage to the reactor core, the social and economical consequences of such an accident can be very significant.

The APR1400 is designed for the prevention and mitigation of severe accidents, based on in-depth phenomenological analyses that identify potential design and operational vulnerabilities and address them appropriately in a manner that minimizes the consequential risk to the public and to the environment. The design and construction of the severe accident prevention and mitigation features are in compliance with USNRC regulations. These design features comply with USNRC SECY-93-087, "Policy, Technical, and Licensing Issues Pertaining to Evolutionary and Advanced Light Water Reactor (ALWR) Designs."(Reference 1) In principle, a series of potential phenomena which can threaten the integrity of the containment needs to be screened, reviewed and assessed, since various individual phenomena can occur under severe accident conditions depending upon the design characteristics of the plant.

This report consists of the main body and supplemental appendices. The main body of this report has two parts. The first part describes the severe accident prevention and mitigation features. The second part covers the phenomenological analysis and assessment. The appendices contain the details for the following severe accident analysis.

- Hydrogen control
- Molten core-concrete interaction(MCCI) and Debris Coolability
- High pressure melt ejection(HPME) and direct containment heating(DCH)
- Fuel-coolant interaction(FCI)
- Containment performance capability
- Equipment survivability

2 SEVERE ACCIDENT PREVENTION AND MITIGATION FEATURES

This section describes the APR1400 features that are designed to prevent and mitigate severe accidents. The severe accident evaluation for the APR1400 design is consistent with the guidance in SECY-93-087 as well as the corresponding Staff Requirements Memorandum (SRM), dated July 21, 1993. The reactor and containment system designs are a vital portion of the defense-in-depth philosophy. Current reactors and containments are designed to withstand a loss-of-coolant accident (LOCA) and to comply with the siting criteria of 10 CFR 100 (Reference 2), General Design Criteria (GDC) of 10 CFR 50 Appendix A (Reference 3), and the Three Mile Island (TMI)-related requirements of 10 CFR 50.34(f) (Reference 4), 10 CFR 50.44 (Reference 5), NRC RG 1.216 (Reference 6), and SECY-90-016 (Reference 7).

2.1 Severe Accident Prevention

The APR1400 design includes features aimed at preventing the onset of a severe accident, including the severe accident precursors identified in SECY-90-016 and SECY-93-087. These precursors include anticipated transient without scram (ATWS), mid-loop operation, station blackout (SBO) event, fire, and intersystem loss-of-coolant accident (ISLOCA). Preventive features are described below for each of these events.

2.1.1 Anticipated Transient without Scram

An ATWS happens when an anticipated operational occurrence (AOO) occurs but is not followed by an automatic reactor trip. Reactor trip is necessary to terminate the transient and to shut down the plant. The APR1400 design includes a digital safety system and a diverse protection system (DPS) to minimize the possibility of an ATWS.

The plant protection system (PPS) is normally available to prevent and mitigate an ATWS. The PPS includes the electrical and mechanical devices and circuitry required to perform the functions of the reactor protection system (RPS) and the engineered safety features component control system (ESF-CCS). The RPS is the portion of the PPS that trips the reactor when required. A coincidence of two signals, due to the two-out-of-four trip logic, is required to generate a reactor trip signal. The ESF-CCS is the portion of the PPS that activates the engineered safety features (ESFs). Additionally, the reactor trip system includes the RPS portion of the PPS, reactor trip switchgear system (RTSS), and components that perform a reactor trip after receiving a signal from the RPS (either automatically or manually).

The DPS provides a diverse backup to the PPS when the PPS is not working. The DPS initiates a reactor trip signal on high pressurizer pressure to decrease the possibility of an ATWS and provides an auxiliary feedwater actuation signal (backup to the ESF-CCS of the PPS) to mitigate an ATWS.

2.1.2 Mid-Loop Operation

During plant shutdowns, certain maintenance and testing activities require the controlled drain-down of the reactor coolant system (RCS) to a partially filled condition. When the reduced RCS level is within the hot leg, the risk of losing shutdown cooling is increased due to the possibility of vortex formation at the shutdown cooling suction line interface with the hot leg. If a vortex is formed in the shutdown cooling suction line, a substantial amount of air could be entrained into the shutdown cooling suction piping and degrade or interrupt the SC pump performance. If sufficient shutdown cooling is not reestablished, coolant heatup and vaporization/boiling can lead to uncovering of the reactor core.

The APR1400 design features can accommodate loss of residual heat removal during the operation with reduced reactor water inventory. These design features include:

2.1.2.1 Instrumentation for Shutdown Operations

Diverse, accurate, and redundant instrumentation provides the operator with continuous system status and precise information to monitor the operation with reduced reactor water inventory and respond to the loss of shutdown cooling events.

2.1.2.2 SCS Design

System design features that improve shutdown cooling system (SCS) performance include:

1. The shutdown cooling suction lines do not contain loop seals, thereby minimizing the potential to trap gas. The suction piping layout allows self-venting of accumulated gas (or air).
2. The two redundant shutdown cooling suction lines are completely independent.
3. There are no auto-closure interlocks on the shutdown cooling suction piping valves, minimizing the potential for shutdown cooling isolation events.

2.1.2.3 Steam Generator Nozzle Dam Integrity

The APR1400 design addresses the regulatory concern of preventing significant pressurization in the upper plenum of the reactor vessel during core boiling scenarios. The APR1400 procedural guidance recommends a nozzle dam installation and removal sequence, which consists of the following:

1. Installation: The nozzle dams are installed in the cold legs first and in the hot legs second.
2. Removal: The nozzle dams in the hot legs are removed first and in the cold legs second.

The installation procedure requires that the pressurizer manway be opened so that a hot side vent pathway exists prior to blocking both RCS hot legs with nozzle dams.

In the APR1400 design, the ability of the RCS to withstand abnormal pressurization during reduced-inventory operations with the nozzle dams installed is limited by the design pressure of the nozzle dams. Based on overpressure tests performed on nozzle dams, the design pressure is estimated to be 3.52 kg/cm² (50 psia). The design pressure is sufficient to withstand an abnormal pressurization transient.

In order to provide reasonable assurance that the nozzle dam design pressure is not exceeded during reduced-inventory operations with boiling conditions in the reactor vessel, the APR1400 design requires that a mid-loop vent pathway is opened via the pressurizer manway prior to reduced-inventory operation. When the pressurizer manway is opened to the containment atmosphere, the surge line provides sufficient venting capacity to prevent RCS pressurization and preclude subsequent nozzle dam failure. The pressurizer surge line vent pathway has sufficient capacity to prevent core uncover due to pressurization of the hot side resulting from boiling coolant.

2.1.2.4 Alternate Inventory Additions and Decay Heat Removal Methods

If SCS is lost during Mode 5 reduced water inventory operations, containment spray (CS) pumps or the safety injection (SI) pumps are used to provide makeup. If all above methods of decay heat removal and inventory replenishment are unavailable, a charging pump or a boric acid makeup pump is used to provide makeup for Modes 5 and 6. If no method of pumped inventory addition is available, a source for gravity feed inventory addition can be used via the SI tanks.

2.1.3 Station Blackout

One alternate ac (AAC) source is provided to help mitigate the effects of an SBO. The AAC

automatically starts and is manually aligned to provide power to a Class 1E 4.16 kV bus in case Class 1E emergency diesel generators (EDGs) fail to start and load during loss of offsite power (LOOP) events. This standby unit is independent and diverse from the Class 1E EDGs. Successful startup of the AAC together with turbine-driven auxiliary feedwater pumps is sufficient to prevent core damage in SBOs.

2.1.4 Fire Protection

The systems and components required for safe shutdown are physically separated from functionally similar or redundant systems or components to maintain the ability to perform safe shutdown functions in the event of a fire. Fire protection features such as fire detection, automatic and manual fire suppression, and fixed fire barriers provide reasonable assurance that the plant does not enter an unrecoverable state as a result of a fire incident.

2.1.5 Intersystem Loss of Coolant Accident

An ISLOCA is defined as a class of events in which a break occurs outside the containment in a system connected to the RCS, leading to a loss of primary system water inventory. This is considered as a beyond-design-basis event for systems connected with the RCS. Pressurization of an interfacing system could result from the inadvertent opening of a valve or valves, failure of containment isolation, or valves that are otherwise fully open (e.g., check valves that are stuck open). The APR1400 design addresses ISLOCA challenges by including the following design features:

1. The design pressure of equipment or systems has been increased to 64.3 kg/cm² (900 psig) for the low-pressure systems that are connected with the RCS.
2. Equipment and instrumentation has been added to alert the operator to an ISLOCA challenge or terminate and limit the scope of an ISLOCA event.
3. Parts of systems considered unnecessary are deleted because their functions can be replaced by other existing systems.
4. The refueling water tank is located inside containment.
5. Capability is provided for leak testing pressure isolation valves.
6. Pressure isolation valve position indication and control is provided in the main control room (MCR).
7. High-pressure alarms are added to warn the operator when increasing pressure approaches the design pressure of low-pressure systems.

In the APR1400 design, the safety injection system (SIS), SCS, and chemical and volume control system (CVCS) are directly connected to the RCS and are potentially susceptible to one or more ISLOCA events (i.e., they have one or more ISLOCA pressurization pathways).

The safety injection lines are connected to the reactor vessel directly and are primary interfaces through which an ISLOCA can begin. Pressurization is postulated to move from the direct vessel injection (DVI) nozzles and out of containment through the containment isolation valves to the low-pressure sections of the system. The SIS design satisfies the ISLOCA acceptance criteria because all sections of the system and interfaces are designed to withstand full RCS operating pressure or have a leak-test capability. In addition, the valve position indications in the control room function even when the isolation valve operators are de-energized, and high-pressure alarms sound to warn operators when pressure is

approaching the design pressure. These design features protect the SIS lines and all interfacing systems from an ISLOCA challenge without adversely affecting performance or operations.

The shutdown cooling suction lines are connected to the RCS directly and are primary interfaces through which an ISLOCA event can begin. Pressurization is postulated from the hot leg and out of containment through the containment isolation valves to the low pressure sections of the system. The shutdown cooling return lines are connected to the RCS directly and are primary interfaces through which an ISLOCA event can begin. Pressurization is postulated from the DVI nozzles and out of containment through the containment isolation valves to the low-pressure sections of the SCS.

This SCS line design satisfies the ISLOCA acceptance criteria because all sections of the system and interfaces are designed to withstand full RCS operating pressure, or they have leak-test capabilities, valve position indications in the control room that function even when isolation valve operators are de-energized, and high-pressure alarms to warn operators when pressure is approaching the design pressure. Deletion of the interfaces from the SCS lines eliminates the potential for an ISLOCA without adversely affecting the performance or operations of the SCS. These design features satisfy the ISLOCA acceptance criteria for the SCS line.

The containment spray system (CSS) is not connected directly to the RCS during the modes of reactor operation for which an ISLOCA challenge can occur. However, there is an indirect interface through the SCS because the CS pumps, CS heat exchangers, SC pumps, and SC heat exchangers are interchangeable respectively. All connected CS sections are designed to 64.3 kg/cm² (900 psig). The only low-pressure system interface with the CSS is the spent fuel pool cooling and cleanup system (SFPCS) connection to the refueling pool. This connection provides the ability to fill the refueling pool directly rather than through the reactor vessel. A spool piece connection is available to provide a method of physical separation of the low-pressure SFPCS from any pressurization source in the CSS.

The CVCS letdown line is directly connected to the RCS and is a primary interface through which an ISLOCA event can begin. Pressurization is postulated from the letdown nozzle, through the regenerative and letdown heat exchangers, through the letdown orifices, and out of containment through the containment isolation and letdown control valves to the low-pressure sections of the system. The letdown line has a high-pressure alarm that is located downstream of the letdown control valves and warns the operator when the pressure is approaching the low-pressure system design pressure. When a warning is issued, the control room operator isolates the letdown line to terminate any further pressure communication downstream of the containment isolation valve.

The CVCS charging line is connected directly to the RCS and is a primary interface through which an ISLOCA event can begin. Pressurization is postulated from the charging nozzle, through the shell side of the regenerative heat exchanger, the charging control valve, and the charging pump to the low-pressure sections of the system. The charging pump suction line has a high-pressure alarm that warns the operator when the pressure is approaching the low-pressure system design pressure. When a warning is received, the control room operator isolates the charging line to terminate any further pressure communication downstream of the containment isolation valve. These design responses satisfy the ISLOCA acceptance criteria.

2.1.6 Other Severe Accident Preventative Features

The APR1400 design uses other features to prevent severe accidents including:

1. Feedwater can be supplied to a steam generator by a turbine-driven auxiliary feedwater pump when the motor-driven auxiliary feedwater pumps are not available. Two independent turbine-driven auxiliary feedwater pumps are available in the APR1400 design.

2. If the CS pumps are inoperable during a LOCA event, then the SC pumps can be used as a backup.
3. The CS pumps and CS heat exchangers can be used as backups for the SC pumps and SC heat exchangers to provide cooling of the in-containment refueling water storage tank (IRWST) during post-accident feed-and-bleed operations when the steam generators are not available to cool the RCS.
4. Cooling during a loss of all feedwater can be accomplished via feed-and-bleed operation using the SIS and the pilot-operated safety and relief valves (POSRVs).

The component cooling water system (CCWS) is composed of two separate but interconnected two-division systems. The systems are designed to automatically isolate the cross connection in an accident. One or both of these systems operate independently after isolation because their designs provide a high level of performance reliability. If the CCWS is inoperable at any time during reactor coolant pump (RCP) operation, the RCP seal injection function is performed by the supply of seal injection via the auxiliary charging pump.

2.2 Severe Accident Mitigation

If a severe accident cannot be prevented by the above design features, other APR1400 features mitigate the effects of a severe accident. Of particular importance are the containment design and the ability of mitigating equipment to survive severe accident conditions. This section describes the mitigation features in the context of various severe accident phenomena that could be encountered during severe accident progression.

2.2.1 Overview of the Containment Design

2.2.1.1 Description of the Containment

The APR1400 containment is a pre-stressed concrete structure composed of a right circular cylinder with a hemispherical dome and is founded on safety-related common basemat. The APR1400 containment encloses the reactor vessel, steam generators, reactor coolant loops, and portions of the auxiliary and engineered safety features systems. The containment provides reasonable assurance that leakage of radioactive material to the environment does not exceed the acceptable dose limit as defined in 10 CFR 50.34 even if a LOCA occurred.

The cylindrical containment shell has a constant thickness of ()^{TS} from the top of the foundation basemat to the spring line. The shell is thickened locally around the equipment hatch, two personnel airlocks, feedwater, and main steam line penetrations. The containment reinforcing consists primarily of hoop and meridional steel. Prestressing tendons are also arranged in hoop and meridional directions. The roof of the containment is a hemispherical dome. The buttresses are extended up to 48 degrees into the dome to provide anchorage for the dome hoop tendons. The 6.0 mm (0.25 in) steel liner plate is attached to inside of the dome and the cylindrical wall to provide leak-tightness.

The containment provides a large free volume with its internal structures arranged in a manner to (1) protect the inner containment from missile threats, (2) promote mixing throughout the containment atmosphere, and (3) accommodate condensable and noncondensable gas releases from design basis and severe accidents. The internal structures, which are made of reinforced concrete, enclose the reactor vessel and other primary system components. The internal structures provide radiation shielding for the containment interior and missile protection for the reactor vessel and containment shell.

2.2.1.2 Containment Pressure Limits

In severe accident scenarios, the containment vessel is the last fission product barrier protecting the public from radiation release. Therefore, it is of paramount importance to provide a strong containment design to meet severe accident internal pressurization challenges.

The containment is designed in accordance with ASME Section III, Division 2 (Reference 8), and for the design pressure of 4.218 kg/cm² (60 psig) and design basis temperature of 416.5 K (290 °F). The containment is analyzed to determine all membrane, bending, and shear stresses resulting from the specified static and dynamic design loads.

As stated in SECY 93-087, the conditional containment failure probability (CCFP) must be less than 0.1 or meet a deterministic containment performance goal that provides comparable protection so the following general criterion is met: The containment maintains its role as a reliable, leak-tight barrier by providing reasonable assurance that the containment factored load category (FLC) requirements are met for a period of approximately 24 hours following the onset of core damage, and following this 24-hour period, the containment continues to provide a barrier against the uncontrolled release of fission products. The APR1400 containment meets the FLC requirement of ASME Section III, Division 2, Subarticle CC-3720.

2.2.1.3 Containment Penetrations

The containment pressure boundary is made up of the containment shell and several mechanical and electrical containment penetrations. The penetrations include one equipment hatch; two personnel airlocks; containment piping penetration assemblies to provide for the passage of process, service, sampling, and instrumentation pipelines into the containment; electrical penetrations for power, control, and instrumentation; and a fuel transfer tube. All large penetrations are explicitly considered in the containment shell ultimate pressure capacity analyses. Smaller penetrations are sufficiently strong that they do not prematurely compromise the integrity of the containment shell.

2.2.2 Cavity Flooding System

The cavity flooding system (CFS) provides a means of flooding the reactor cavity during a severe accident to cool the core debris in the reactor cavity and to scrub fission product releases. The water delivery from the IRWST to the reactor cavity is accomplished by means of active components. The CFS is designed (in conjunction with the containment spray system) to provide an inexhaustible continuous supply of water to quench the core debris.

The components of the CFS include the IRWST, holdup volume tank (HVT), reactor cavity, connecting piping, valves, and associated power supplies. This system is used in conjunction with the containment spray system to form a closed recirculation water cooling system to provide a continuous cooling water supply to the core debris. The quenching of the corium produces steam, which is condensed by the containment spray flow. The CFS takes water from the IRWST and directs it to the reactor cavity. The water flows first into the HVT by way of the two HVT spillways and then into the reactor cavity by way of two reactor cavity spillways.

Once actuated, movement of the water from the IRWST source to the cavity occurs passively due to the natural hydraulic driving heads of the system. Actuation of the CFS results in the opening of the HVT spillway valves, allowing water from the IRWST to flood the HVT. This flow is driven by the differences in the static heads of water between the IRWST and the HVT. Flooding of the HVT progresses until the water level in the HVT reaches the reactor cavity spillway, at which time reactor cavity flooding commences. Flooding ceases when water levels in the IRWST, HVT, and reactor cavity equalize at 6.4 m (21 ft) from the reactor cavity floor (EL. 69 ft 0 in).

The HVT and cavity spillways are located as low as possible to provide the greatest head and maximize

usage of available water in the IRWST and HVT. Both spillways are equipped with remote manual motor-operated valves (MOVs). HVT flooding valves are normally closed and located in individual flow paths connecting the IRWST to the HVT. Reactor cavity flooding valves are normally closed and located in individual flow paths connecting the HVT to the reactor cavity. The valves are opened by the MCR operator to flood the reactor cavity in the event of a severe accident. Controls are provided to allow the valves to be opened either individually or simultaneously, to initiate reactor cavity flooding.

Flooding of the reactor cavity serves the following purposes in the strategy to mitigate the consequences of a severe accident:

1. Minimize or eliminate corium-concrete attack
2. Minimize the generation of combustible gases (hydrogen and carbon monoxide) and non-condensable gases
3. Scrub fission products released due to corium-concrete interaction
4. Remove heat from the core debris

The manual operation of the CFS provides a mechanism for the operator to most efficiently use plant resources and mitigate the consequences of a severe accident. It is envisioned that the CFS is actuated once a potential core melt condition is imminent or has been diagnosed as being in progress. Typical indications of core uncover include (1) core exit temperature (CET) in excess of 922.04 K (1,200 °F), (2) reactor vessel level monitoring system (RVLMS) readings indicative of no liquid above the fuel alignment plate, and (3) significant changes in readings of self-powered neutron detectors (SPND).

It is understood that steam explosions may pose a non-negligible threat to the cavity and containment integrity. Thus, there may be an incentive to delay actuation of the CFS until vessel breach (VB) is imminent or when the reactor vessel lower head has failed. While actuation of the CFS before VB is presently deemed desirable, the consequences of delayed CFS actuation (prior to extensive concrete erosion) may also achieve similar results. Flooding of the HVT progresses until the water levels in IRWST, HVT, and reactor cavity equalize at 6.4 m (21 ft) from the reactor cavity floor (EL. 69 ft 0 in).

Thus, it is currently believed that an acceptable stable state can be achieved ex-vessel as long as the CFS has been actuated prior to VB. Although providing water to the reactor cavity may not immediately terminate the concrete erosion, having a water-filled reactor cavity initially reduces and ultimately terminates the erosion, while simultaneously providing scrubbing of fission products released in the molten core-concrete interaction process.

2.2.3 Hydrogen Mitigation System

During a degraded core accident, hydrogen is generated at a greater rate than that of the design basis LOCA. The containment hydrogen control system is designed to accommodate the hydrogen generation from a metal-water reaction of 100 percent of the active fuel cladding and limit the average hydrogen concentration in containment to 10 percent consistent with 10 CFR 50.34(f) and 10 CFR 50.44 for a degraded core accident. These limits are imposed to preclude detonations in containment that might jeopardize containment integrity or damage essential equipment.

The containment hydrogen control system (HG) consists of a system of passive autocatalytic recombiners (PARs) complemented by glow plug igniters installed within the containment. The PARs are capable of controlling hydrogen in all accident sequences with moderate hydrogen release rates, and are located throughout the containment. The igniters supplement PARs for accidents in which rapid hydrogen release rates are expected, and are placed near anticipated source locations to promote the combustion

of hydrogen in a controlled manner. The HG design is composed of 30 PARs and 8 igniters. The HG PARs are strategically distributed so that the overall average concentration requirements are met. These locations are determined based on equipment and piping proximity as well as inspection and maintenance access. The PAR components and igniter assembly are designed to meet seismic Category I requirements.

The PARs are self-actuated and require no electric power. Therefore, no operator action is required. The igniters, which supplement PARs, are intended to control hydrogen concentration within containment once the operator confirms that an extended core uncover is in progress. The operators use specific accident management guidance that relies on RCS and containment instrumentation, such as in-vessel level monitoring instrumentation, core-exit thermocouples, containment and RCS pressure indications, and a direct measurement of containment hydrogen concentration.

Once activated, an igniter produces either periodic small local burns or a standing diffusion flame, either of which reduces the containment hydrogen concentration below the upward flammability limit. Thus, the HG system prevents hydrogen from accumulating to the point where a destructive hydrogen detonation might occur within the containment.

2.2.4 Rapid Depressurization Function

The rapid depressurization (RD) function is a multi-purpose dedicated system designed to serve important roles in severe accident prevention and mitigation.

In the APR1400 design, the POSRVs are designed to allow for depressurization of the RCS below the cutoff pressure for HPME to occur. For the APR1400 design, the rapid depressurization function is initiated by operator action as part of the severe accident management strategy. When CET exceeds 922.04K (1,200°F), the operator identifies entry into a severe accident condition and starts rapid depressurization by opening the required POSRVs.

The RD function design requirement related to severe accident mitigation is the capability to depressurize the RCS from approximately 175.8 kg/cm² (2,500 psia) to approximately 17.6 kg/cm² (250 psia) prior to reactor vessel breach. The target pressure of the RD function is determined on the basis of DOE/ID-10271 (Reference 9).

The power for each RD valve is supplied from a respective Class 1E direct current (dc) bus. The power is provided such that a bleed path can be established in case of a loss of offsite power, four EDGs, and the AAC source. Each train of dc loads is provided with a separate and independent battery charger and a standby charger. The battery chargers are powered from the 480 V ac Class 1E power distribution systems of the same trains. A load management strategy provides reasonable assurance of dc power availability for a minimum of 4 hours for Trains A and B and 16 hours for Trains C and D following an SBO.

The RD function provides a manual means of quickly depressurizing the RCS when normal and auxiliary feedwater are unavailable to remove core decay heat through the steam generators. This function is achieved via remote manual operator control. Whenever events, such as a total loss of feedwater (TLOFW), result in a high RCS pressure with a loss of RCS liquid inventory, the POSRVs may be opened by the operator, causing a controlled depressurization of the RCS. As the RCS pressure decreases, the SI pumps start, initiating feed flow to the RCS and restoring the RCS liquid inventory. The RD function allows for both short- and long-term decay heat removal.

The RD function also serves an important role in severe accident mitigation. In the event a high-pressure meltdown scenario develops and the feed portion of feed and bleed cannot be established due to unavailability of the SI pumps, the RD function can be used to depressurize the RCS and prevent HPME following a VB.

2.2.5 Reactor Cavity Design

The reactor cavity is configured to promote retention of, and heat removal from, the postulated core debris during a severe accident, thus serving several roles in accident mitigation. The large cavity floor area allows for spreading of the core debris, enhancing its coolability within the reactor cavity region.

The large free volume of the reactor cavity is a benefit when cavity pressurization issues are considered. Large, vented volumes are not prone to significant pressurization resulting from vessel breach or during corium quench processes. This design characteristic is illustrated in the cavity pressurization analysis results in that the possible peak pressure in the reactor cavity during severe accidents stays well below the allowable capacity.

The reactor cavity is designed to maximize the unobstructed floor area available for the spreading of core debris. The cavity floor is free from obstructions and comprises an area available for core debris spreading such that the floor area/reactor thermal power ratio is larger than $0.02 \text{ m}^2/\text{MWt}$. Uniform distribution of 100 percent of the corium debris within the reactor cavity results in a relatively shallow debris bed and consequently, effective debris cooling is expected in the reactor cavity. The containment liner plate in reactor cavity area is embedded 0.91 m (3 ft.) below from the cavity floor at the minimum.

Corium retention in the core debris chamber virtually eliminates the potential for significant DCH-induced containment loadings. When the vessel is breached under high pressure, the melt is ejected first followed by the high-speed steam and H_2 jet. The melt is entrained by the jet into small particles. The duration of the gas blowdown following melt ejection may be sufficiently long to cause complete sweep-out of the ejected melt. Therefore, it is reasonable, and conservative, to assume complete entrainment of ejected melt. Then, the mixture of steam, gas, and corium particles flow through available flow paths between the reactor cavity and the upper containment.

For flow entering the debris chamber, the lower-inertia steam/hydrogen/gas mixture negotiates right-angle turns and exit the reactor cavity while the corium particles carried by the flow impinge on walls and deposit in the subcompartment. For flow entering the in-core instrumentation (ICI) chase, the presence of the seal table prevents upward corium discharge through the instrument shaft. Even if the seal table fails due to overpressure in the reactor cavity, the flow first impinges on the wall at the end of the cavity and makes a 90-degree (upward) turn to the ICI chase where the seal table is located. It is shown that nearly all the entrained corium is captured by the impingement and only a small amount corium is released through the failed seal table. Therefore, the only flow path that leads directly to the upper containment without significant de-entrainment is the reactor pressure vessel (RPV) annulus. Because of the multiphase flow, the flow is choked in the reactor cavity, not in the reactor cavity access area. Thus, the fraction of the dispersed corium that enters the upper containment via the RPV annulus is given by the ratio of the area of RPV annulus, 1.96 m^2 , to the total flow area, which is the sum of the area of PRV and the area of reactor cavity, 23.76 m^2 , or 0.082.

2.2.6 Emergency Containment Spray Backup System

For a provision against a beyond-design-basis accident where either two SC pumps and two CS pumps or the IRWST is unavailable, the emergency containment spray backup system (ECSBS) is provided as an alternative to the CSS.

The ECSBS is designed to protect the containment integrity against overpressure and prevent the uncontrollable release of radioactive materials into the environment. The emergency containment spray flow path is from external water sources (the reactor makeup water tank, demineralized water storage tank, fresh water tank, or the raw water tank), through the fire protection system line via the diesel-driven fire pump, to the ECSBS line emergency connection located at ground level near the auxiliary building.

The ECSBS flow rate provides sufficient heat removal to prevent containment pressure from exceeding

()**TS**

3 SEVERE ACCIDENT PHENOMENOLOGICAL ANALYSIS AND ASSESSMENT

3.1 Hydrogen Control

3.1.1 Local Hydrogen Accumulation Evaluation and Summary

The evaluation of local hydrogen accumulation has been performed using MAAP 4.0.8 (Reference 10). This evaluation identifies local conditions within the containment with hydrogen exceeding 10%. The 10% hydrogen volume fraction is taken as a criterion for determining whether the accumulation should be further considered for deflagration-to-detonation transition (DDT) evaluation.

The analyzed accident sequences include five initiating events with a base case defined for each initiator type. For each initiator type, variations in the availability of accident mitigation systems are made such that their impact, if any, can be observed. The five initiating events are as follows:

- Large break LOCA (LBLOCA)
- Medium break LOCA (MBLOCA)
- Small break LOCA (SBLOCA)
- Station Blackout (SBO)
- Total loss of feedwater (TLOFW) that also represents total loss of essential service water (TLOESW) and loss of offsite power (LOOP)

These sequences represent the entire spectrum of severe accident conditions important to hydrogen accumulation and distribution in the containment. Other probabilistic risk assessment (PRA) accident sequences can be either represented or bounded by these analyzed sequences such that analysis of the specific sequence is not necessary.

All analyzed sequences have hydrogen generated in-vessel equivalent to 100% Metal Water Reaction (MWR) assuming minimum generation rate of 0.045 kg/s. The total amount of hydrogen generated during the analyzed sequences exceeded the equivalent of 100% MWR for sequences with MCCI.

The release of hydrogen was predicted at various containment compartments under severe accident scenarios. The possible hydrogen release points considered in the analysis include the hot-leg break (for LOCAs), IRWST spargers, failed reactor vessel lower head, and POSRV three-way valves. For LOCAs prior to vessel failure, hydrogen is released from the break in the hot leg into SG compartment. For non-LOCA sequences like SBO and TLOFW, hydrogen is first released to the IRWST through the pressure-lifted POSRVs. When three-way valve manual alignment is actuated, hydrogen is also released to SG compartment via the three-way valve. For high pressure sequences including SBO, TLOFW and SBLOCA, additional release point could come from the hot leg failure due to creep. After vessel failure, the failed lower head provides another hydrogen release point to the cavity area.

Figure 3-1 to Figure 3-4 show the hydrogen distribution in the dome region when applying all severe accident mitigation features. With all severe accident mitigation features available, the hydrogen concentration is less than 10 percent.

In the screening of 10% hydrogen limit exceedance for various accident scenarios, it was found that

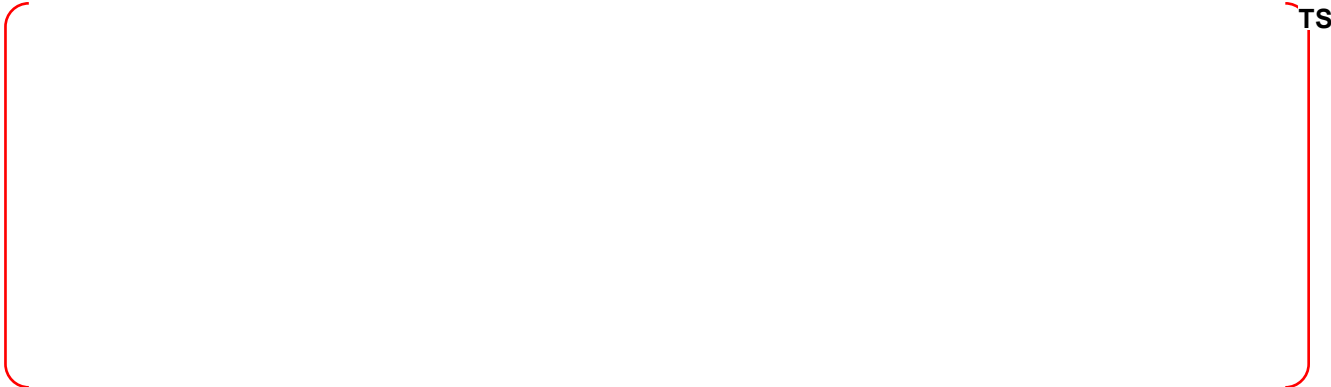
1. If the POSRV via the three-way valve is available, there is no limit exceedance anywhere in the containment except in the IRWST quarters and in the SG compartment for high pressure sequences (such as TLOFW, LOOP and TLOESW for delayed actuation timing of POSRV and three-way valve).
2. If the HG (i.e. igniters and PARs) is available and no containment sprays are actuated, there is no limit exceedance anywhere in the containment for all LOCA sequences.

3.1.2 DDT

The evaluation of the potential of DDT has been performed using MAAP 4.0.8. The DDT index condition refers to the gaseous mixture that has compositions that have the condition of flame acceleration (FA) and the detonation cell size that allow DDT to develop within the characteristic length of the compartment. When the DDT index condition is detected in the accident simulation, it means that all necessary conditions for DDT are present. Whether or not the condition is sufficient for DDT is beyond the capability of the criteria. However, as a conservative approach, one may assume that the presence of DDT index condition locally or globally in the containment means DDT will occur if ignited.

It was found that there is no DDT potential anywhere in the containment if the POSRV via the three-way valve is available.

3.1.3 AICC Pressure Evaluation



The details of hydrogen control analyses are provided in Appendix A.

3.2 MCCI and Debris Coolability

Potential threat to containment integrity due to MCCI was studied for the APR1400 plant. The postulated severe accident scenarios are the so-called “wet” cases, where the cavity flooding system (CFS) is assumed available to flood the reactor cavity following reactor core damage.

The computational tool used for this study is the severe accident code MAAP 4.0.8. Review of the modeling features of this code indicates that two modeling parameters, FCHF and ENT0C, must be calibrated against more sophisticated MCCI codes to achieve conservative predictions of key variables important to containment integrity, including concrete ablation depth and containment pressure. The MCCI code, CORQUENCH 3.03, was selected as the basis of the calibration process. This code has detailed modeling features for a corium-water interaction and a melt eruption. Based on the analysis results using this code, the ablation depth of a limestone common sand (LCS) concrete floor is within 0.3

m (1 ft) for the bounding large LOCA scenario. This result is considered conservative because it ignores initial molten corium jet breakup. If this effect was considered, the ablation depth would have been much smaller. The MAAP 4.0.8 input value of FCHF is calibrated to be 0.0235, which still leads to a conservative result for the ablation into the concrete floor, compared to the ablation depth predicted by CORQUENCH for the chosen bounding scenario. This ablation depth is much smaller than the depth of containment liner (about 0.9 m (3 ft)). Therefore, release of fission products from containment due to ablation damage is unlikely. The value of ENT0C, which is the entrainment coefficient in the initial jet breakup model, is set to a very small number, which is equivalent to ignoring the effect of jet breakup. It is conservative with respect to concrete ablation, because ignoring the jet breakup will generate a high temperature corium pool. The impact of this small value of ENT0C on containment pressurization has also been assessed and found consistent with modeling expectations.

The five severe accident scenarios were selected based on their core damage frequencies from Level I PRA analyses and potential bounding features, including such sequences as: loss of essential service water, loss of AC power with failure of auxiliary feedwater, medium break LOCA, and large break LOCA. Table 3-1 lists the identifiers of the scenarios along with brief scenario descriptions. For each scenario, up to 24 hours of the transient was simulated. The modeling parameter FCHF was set to 0.0235 and ENT0C was set to 1×10^{-5} .

TS

The details of MCCI and debris coolability analyses are provided in Appendix B.

3.3 High Pressure Melt Ejection and Direct Containment Heating

3.3.1 Direct Containment Heating

While DCH experiments have not been directed towards examining the consequences of DCH occurring in the APR1400 reactor, significant DCH pressurization of the APR1400 containment is judged to be most unlikely. It has been well established by the DCH laboratory research that containment structures and compartments have a first order mitigating influence on the pressurization potential of DCH. The number of compartments between the cavity and the containment dome of the APR1400 are not at all conducive to supporting a strong DCH event, as demonstrated in this report.

According to the NUREG/CR-6075 (Reference 12) methodology, the DCH issue is considered resolved if the containment failure probability due to DCH, obtained through a probabilistic evaluation of phenomenological analysis and its uncertainties, is found to be lower than a certain threshold value. The severe accident scenario that can lead to DCH in the APR1400 is identified as a small LOCA with RCS re-pressurization due to operator intervention and three representative scenarios were considered.

For each of the three scenarios, zero (0) containment failure case has resulted from 10,000 trials. Based on this outcome, the CCFP in the APR1400 due to DCH is estimated to be less than 0.01% (0.0001).

This indicates that the APR1400 meets the success criterion established in NUREG/CR-6338 (Reference 13) for PWR large dry containment, where DCH problem is considered resolved if CCFP is less than 1% (0.01).

3.3.2 Rapid Depressurization Analysis

The RD function is diverse roles during design basis accidents (DBAs), beyond design basis accidents (BDBAs), and even severe accidents. Depressurization for a severe accident using the POSRVs enables operation of the low pressure systems, such as the SCS, thus enabling additional means of core cooling. The RCS is maintained at a low pressure for cases involving a loss of core heat removal functions. This prevents the occurrence of HPME phenomenon, and prolongs the reactor vessel integrity.

In this report, the main focus is on the following three conditions that are required for a successful depressurization: (i) RD function is performed after the CET exceeds 922.04K (1,200°F); (ii) the POSRVs can only be guaranteed to open when the temperature is lower than 644K (700°F); and, (iii) the RCS should be depressurized below 1.72 MPa (250 psia) before the RV fails. The depressurization evaluation was considered successful if these three conditions were met.

HPME can be prevented for the 10 analyzed sequences. For certain sequences, vessel failure occurs at a sufficiently low pressure, while for other sequences, operator intervention is necessary. Operation of only two POSRVs within a half hour of the plant entering a severe accident is sufficient for all the sequences that are being considered. The results are in compliance with SECY-93-087.

The details of the analyses for DCH and rapid depressurization capability are provided in Appendix C-1 and Appendix C-2, respectively.

3.4 Fuel-Coolant Interaction

Steam explosion is a remaining risk-significant issue in nuclear power plant due to the threatening of integrity of the defense-in-depth barriers by explosive dynamic loadings that could lead to release radioactive fission product to public.

Therefore, it is needed to evaluate steam explosion risk when a new design reactor like the APR1400 is considered. The steam explosion risk can be categorized into two groups in terms of the locations of steam explosion initiation, that is, in-vessel and ex-vessel.

Comprehensive analyses on both in-vessel steam explosion (IVSE) and ex-vessel steam explosion (EVSE) are conducted using the TEXAS-V computer code and the most updated technical information on the phenomena, risk evaluation, and analysis methodology are collected and utilized for the assessment of steam explosion risk in the APR1400 design. The analysis results can be used for the evaluation of structure integrity relevant to the steam explosion issue in the APR1400 design, especially in the case of ex-vessel severe accident progression.

The IVSE loads are evaluated using the TEXAS-V computer code. Based on this analysis, the integrity of the reactor vessel is assessed using the ABAQUS computer code. This analysis concludes that IVSE provides no threat to fail RPV. For the EVSE analysis, the risk due to EVSE is analyzed using the TEXAS-V computer code and the reactor cavity structure with EVSE pressure loading is evaluated using LS-DYNA. The maximum displacements, concrete cracks, liner plate stresses, reinforcement re-bar stresses, RPV column support anchor bolt stresses and strains due to the EVSE loading on the reactor cavity are summarized in Table 3-2. EVSE also provides no threat to fail the reactor cavity.

Details of the FCI analysis are provided in Appendix D.

3.5 Containment Performance

As stated in SECY 93-087, the containment stress should not exceed Factored Load Category (FLC) presented in ASME Code, Section III, Division 2, Subarticle CC-3720, approximately 24 hours following the onset of core damage. In addition, USNRC RG 1.216 requires the containment integrity analysis to consider the FLC requirement presented in requirement position 5 of USNRC RG 1.7.

TS

The response of the APR1400 containment to gradual pressurization under severe accident conditions was investigated by using the MAAP 4.0.8 code for a range of possible sequences. The containment pressurization sequences considered in the analysis included the overpressurization by steam and non-condensable gases.

The sequences analyzed covered the most likely severe accident initiators for the APR1400. In accordance with the design of the APR1400, Cavity Flooding System (CFS) and ECSBS were included in the sequences.

Among the sequences, a large break LOCA resulted in the highest pressure in containment at 24 hours following the onset of core damage. Due to the break, primary system pressure rapidly drops and causes the reactor to scram. The break flow from the RCS rapidly pressurizes containment and the core is quickly uncovered. Due to the low primary system pressure, the coolant in SITs is injected temporarily recovering and cooling the core. Once the inventory in SITs has been depleted, the core uncovers again and begins to heat up. Core exit temperature soon reaches 922.04K (1,200°F), signaling the onset of core damage.

After 30 minutes following the onset of core damage, the actuation of the CFS, which allows the gravity-driven water flow from the IRWST into the reactor cavity, is assumed. The core begins to melt and relocate to the reactor vessel lower plenum. This produces a momentary pressure spike in the RCS due to the rapid steaming of the water pool that exists in the lower plenum.

The molten corium in the reactor vessel lower plenum eventually causes the vessel to fail at low pressure. The core debris slumps into the flooded reactor cavity. The corium causes the water pool in containment to heat up and boil. Due to the gradual steam generation in the cavity and non-condensable gas generation during MCCI, containment pressure steadily increases. Heat removal by the overlying water pool quenches the corium and eventually halts concrete ablation. At the time of complete quenching of the corium, the concrete ablation depth is much less than the depth of the steel containment liner in the reactor cavity.

TS

TS

The details of the analysis for containment performance are provided in Appendix E.

3.6 Equipment Survivability

The applicable regulations and criteria for equipment survivability assessment are reviewed. The required equipment and instrumentation for equipment survivability assessment are identified. Bounding radiation and thermal-hydraulic environmental conditions during a severe accident are determined. Each piece of essential equipment and instrumentation is assessed for equipment survivability.

Several potential design modifications may be considered if the equipment survivability of a given item cannot be demonstrated by analysis or use of existing test data. Typically localized high temperature conditions due to hydrogen burns within containment during postulated severe accident sequences constitute the greatest challenge to the component's survivability. Thus, detailed knowledge of the containment's response for a variety of bounding severe accident sequences can identify locations within the containment that have the least challenging thermal conditions. The relocation of some components to a position with less severe thermal conditions may better ensure their survivability.

Some devices, such as hydrogen igniters, must be appropriately located to ensure the successful operation of the system. Thus, relocating igniters may not be a useful approach given that they are intended to control the hydrogen in the regions of the containment where they are placed. These cases may require the use of redundancy or an understanding of the functional interval required for their operation.

Other design modifications include adding a thermal shield or wall to provide protection against the local severe accident environment, and modifying the component (replacing non-metallic material or changing its configuration).

The details of the methodologies for equipment survivability (ES) assessment are provided in Appendix F.

Table 3-1

Selected Severe Accident Scenarios for MCCI Analyses

TS



Table 3-2

Summary of Cavity Structural Integrity Analysis Result

TS



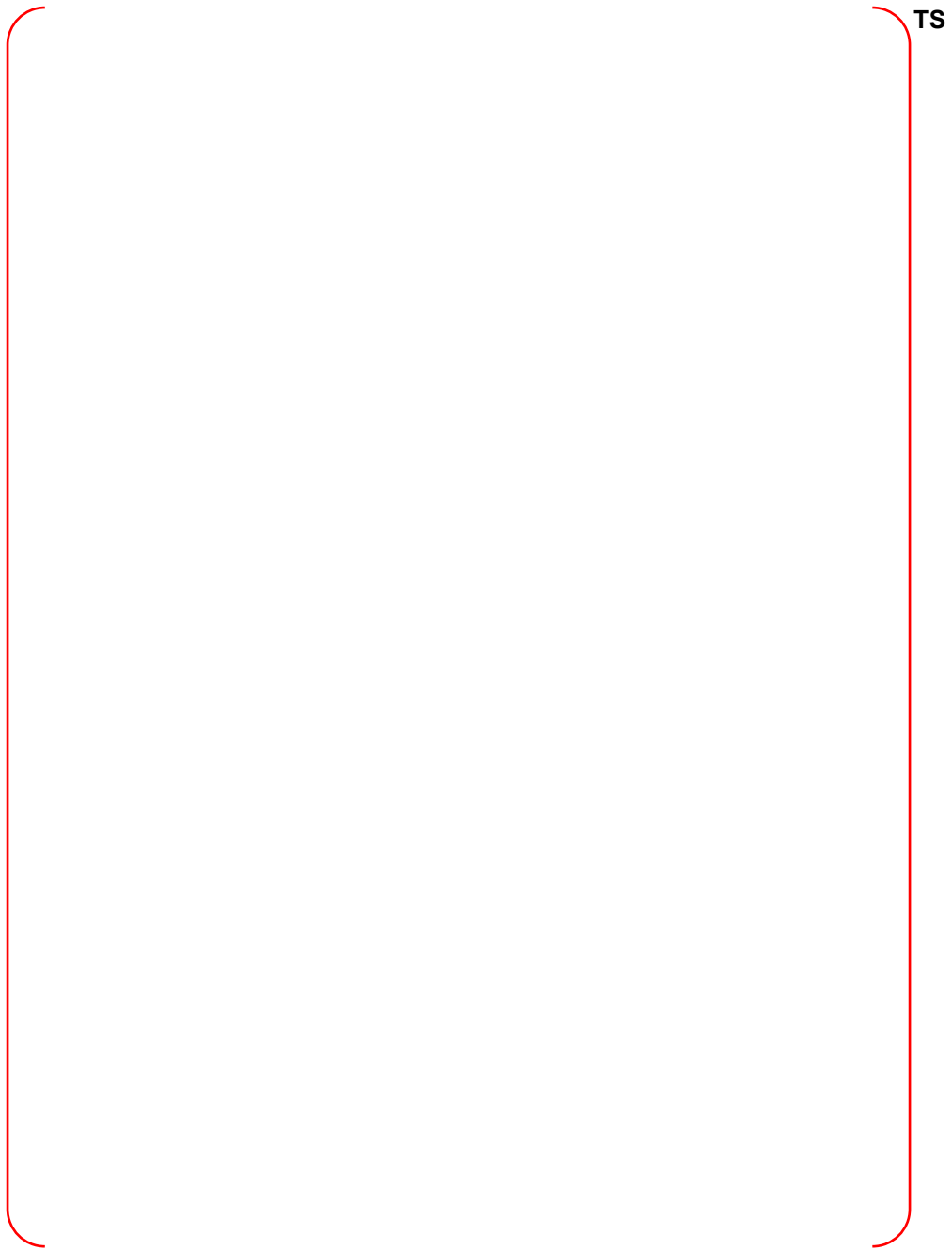


Figure 3-1 Mole Fraction of Hydrogen in the Dome Region for LBLOCA (1/3)

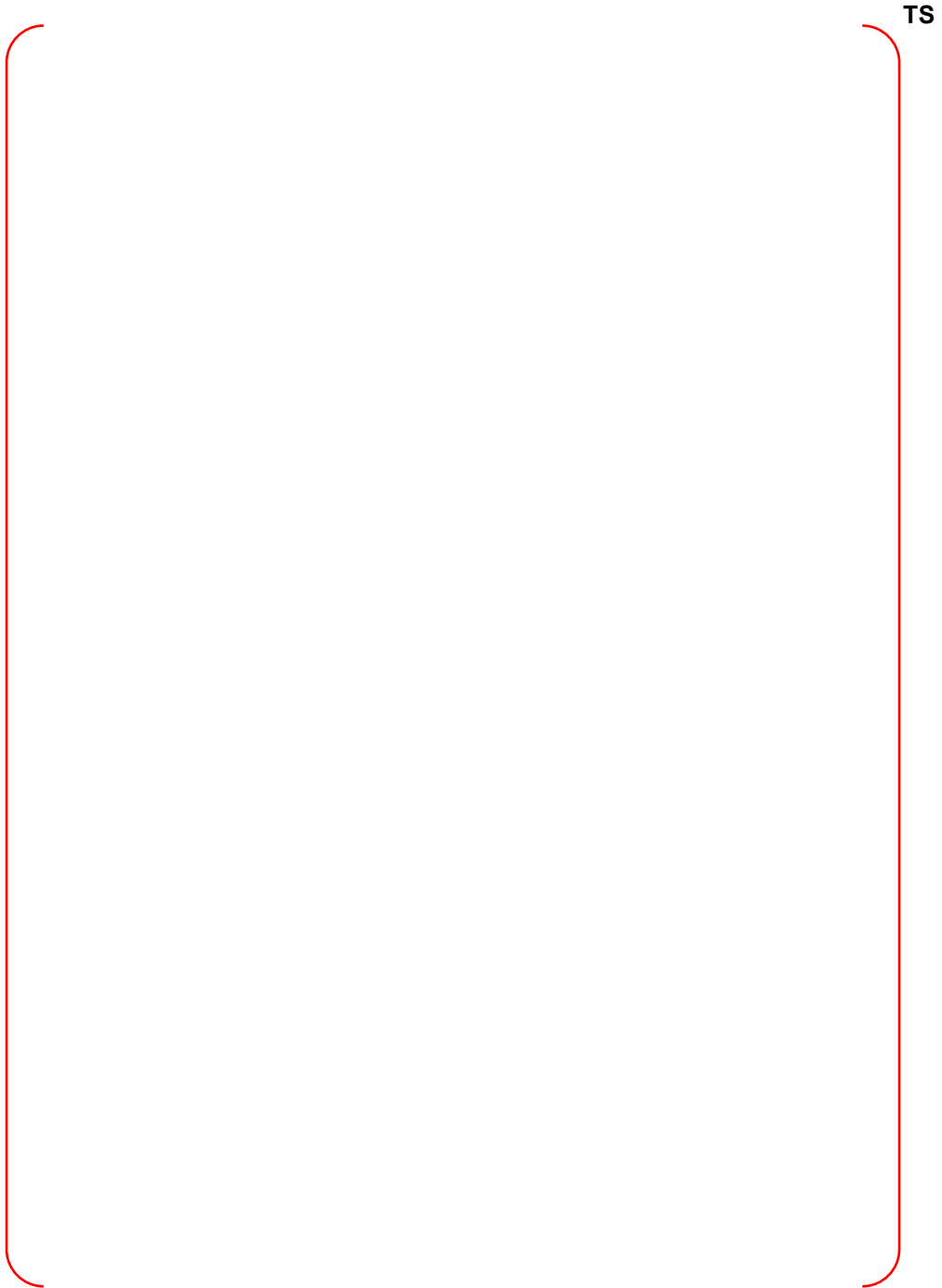


Figure 3-1 Mole Fraction of Hydrogen in the Dome Region for LBLOCA (2/3)

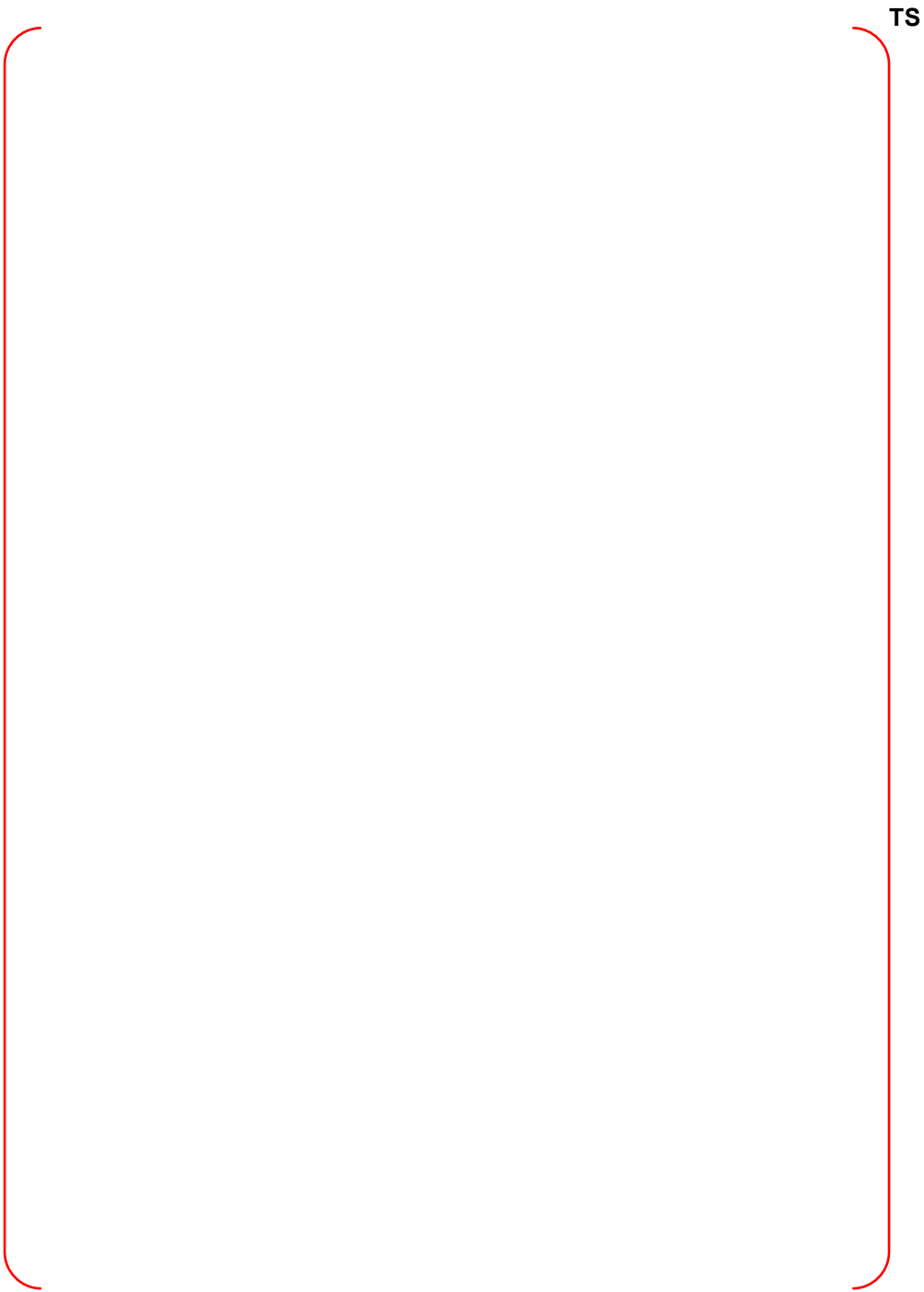


Figure 3-1 Mole Fraction of Hydrogen in the Dome Region for LBLOCA (3/3)

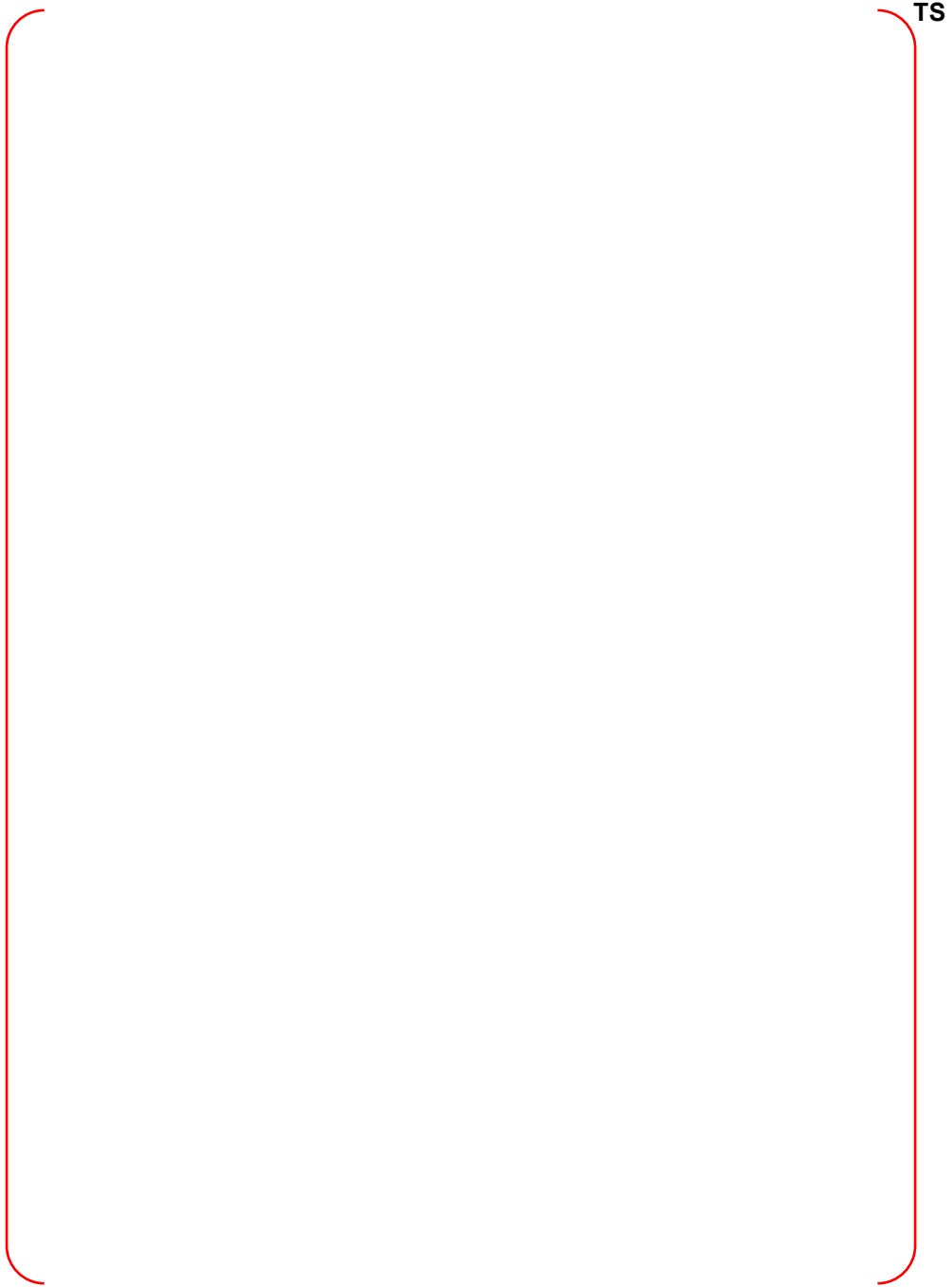
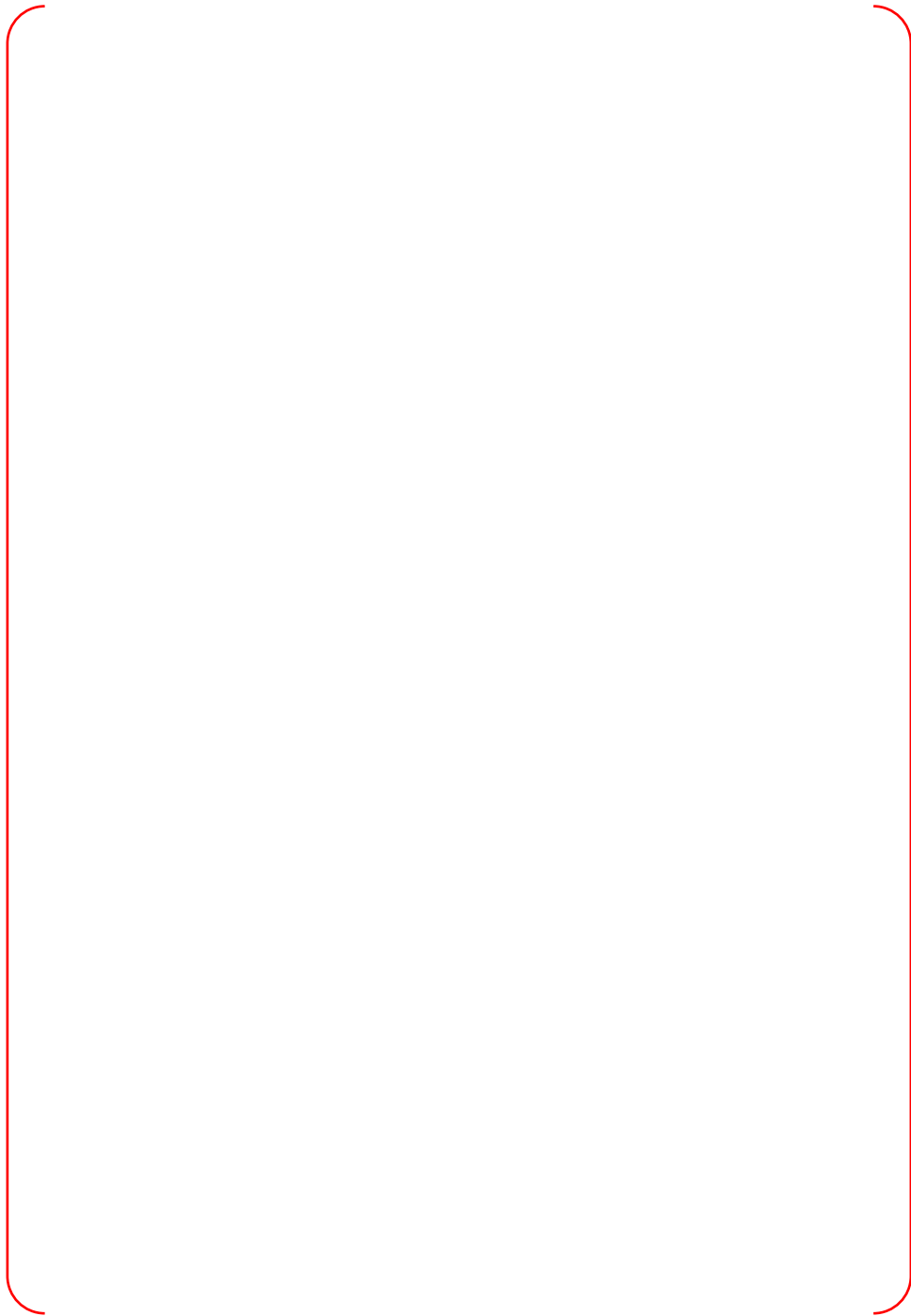


Figure 3-2 Mole Fraction of Hydrogen in the Dome Region for SBLOCA (1/3)



TS

Figure 3-2 Mole Fraction of Hydrogen in the Dome Region for SBLOCA (2/3)

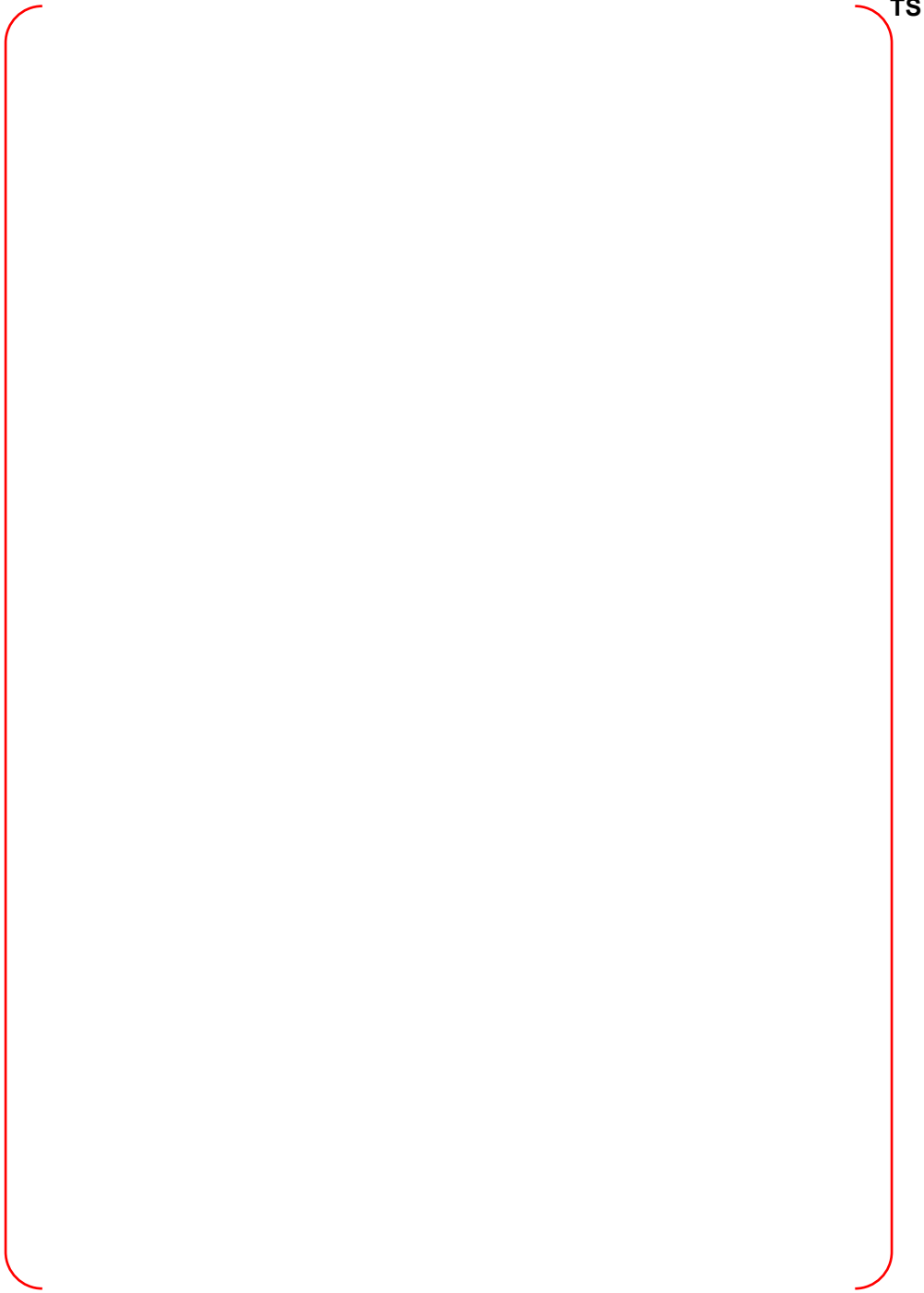


Figure 3-2 Mole Fraction of Hydrogen in the Dome Region for SBLOCA (3/3)

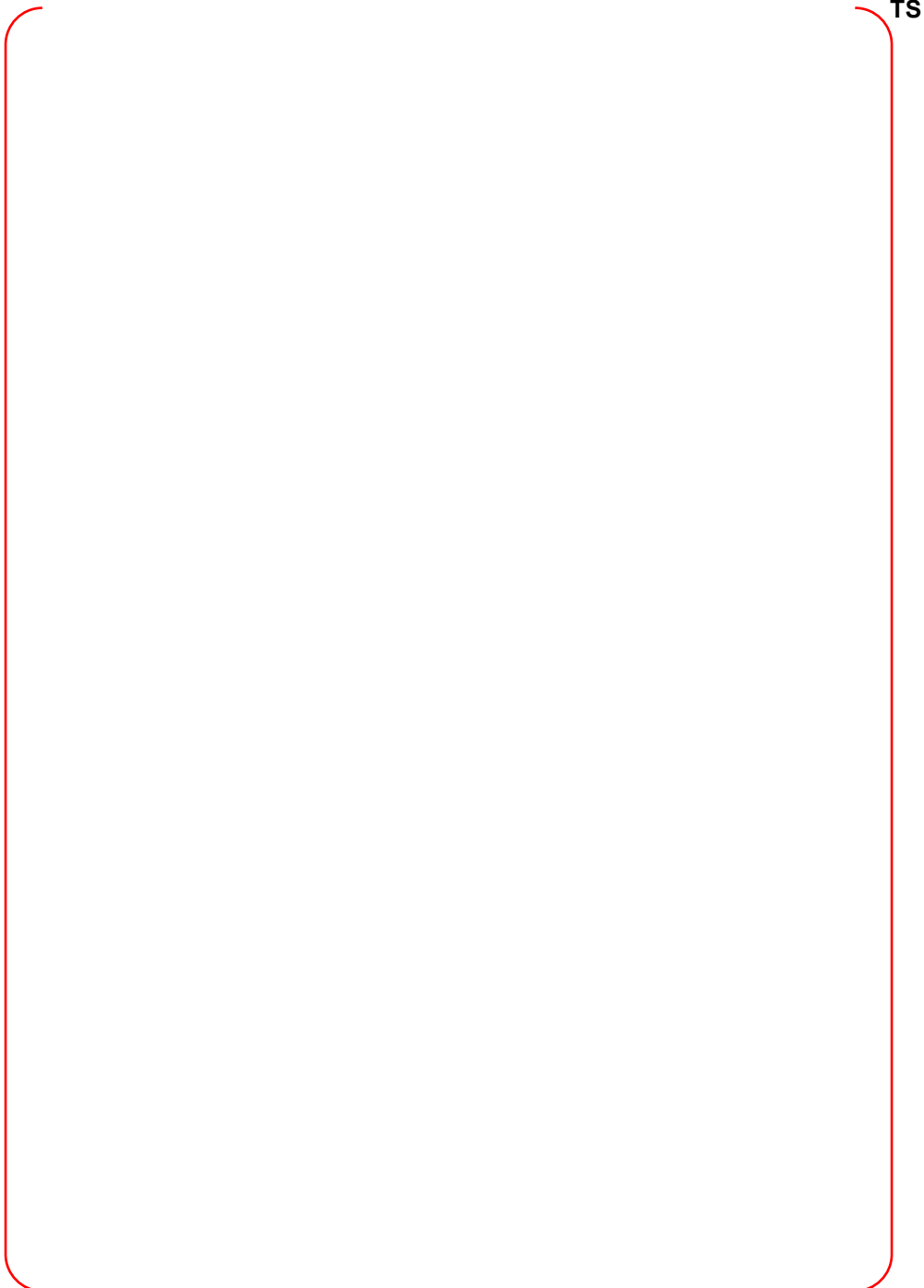


Figure 3-3 Mole Fraction of Hydrogen in the Dome Region for SBO-Three-way valve (1/3)

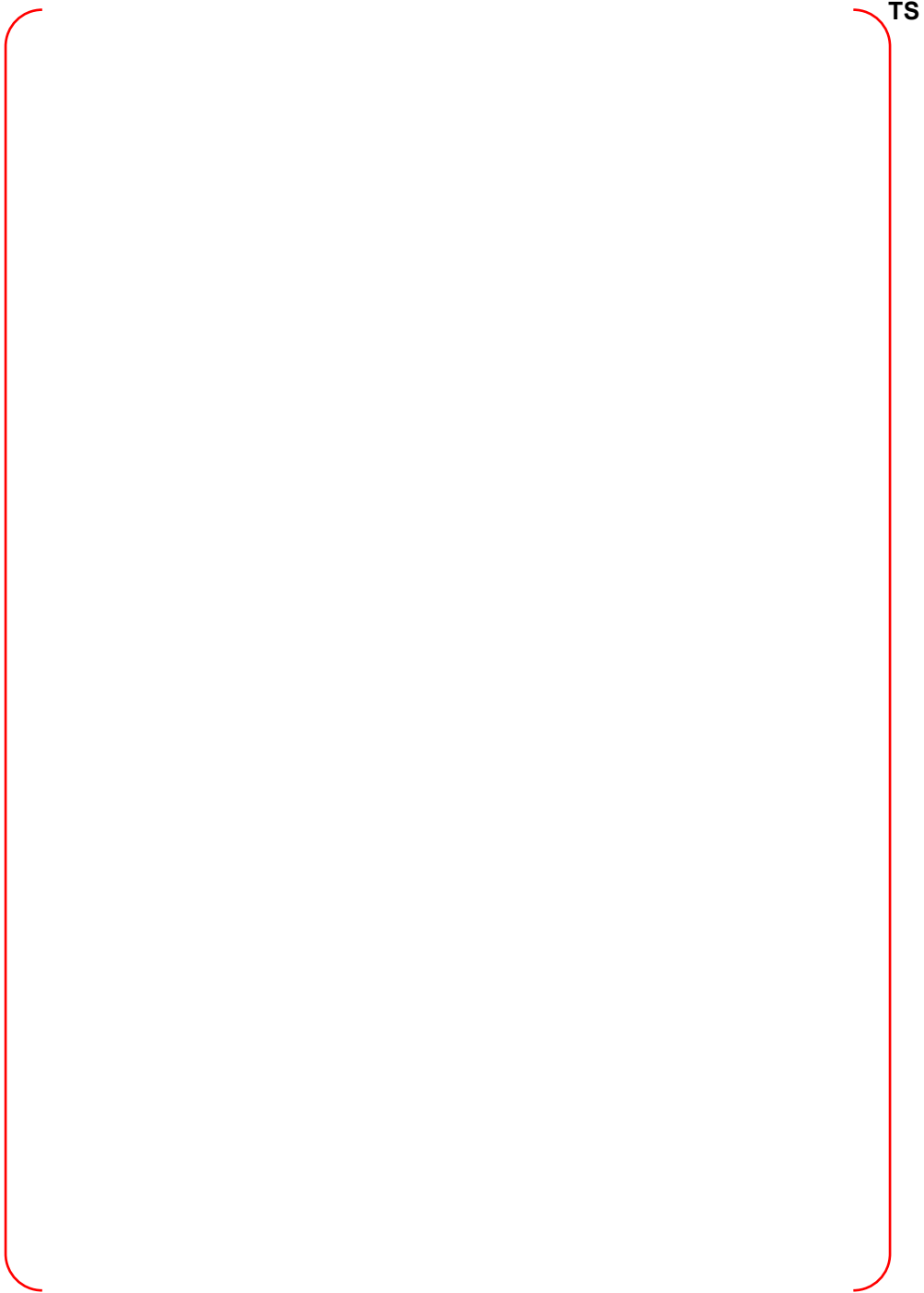


Figure 3-3 Mole Fraction of Hydrogen in the Dome Region for SBO-Three-way valve (2/3)

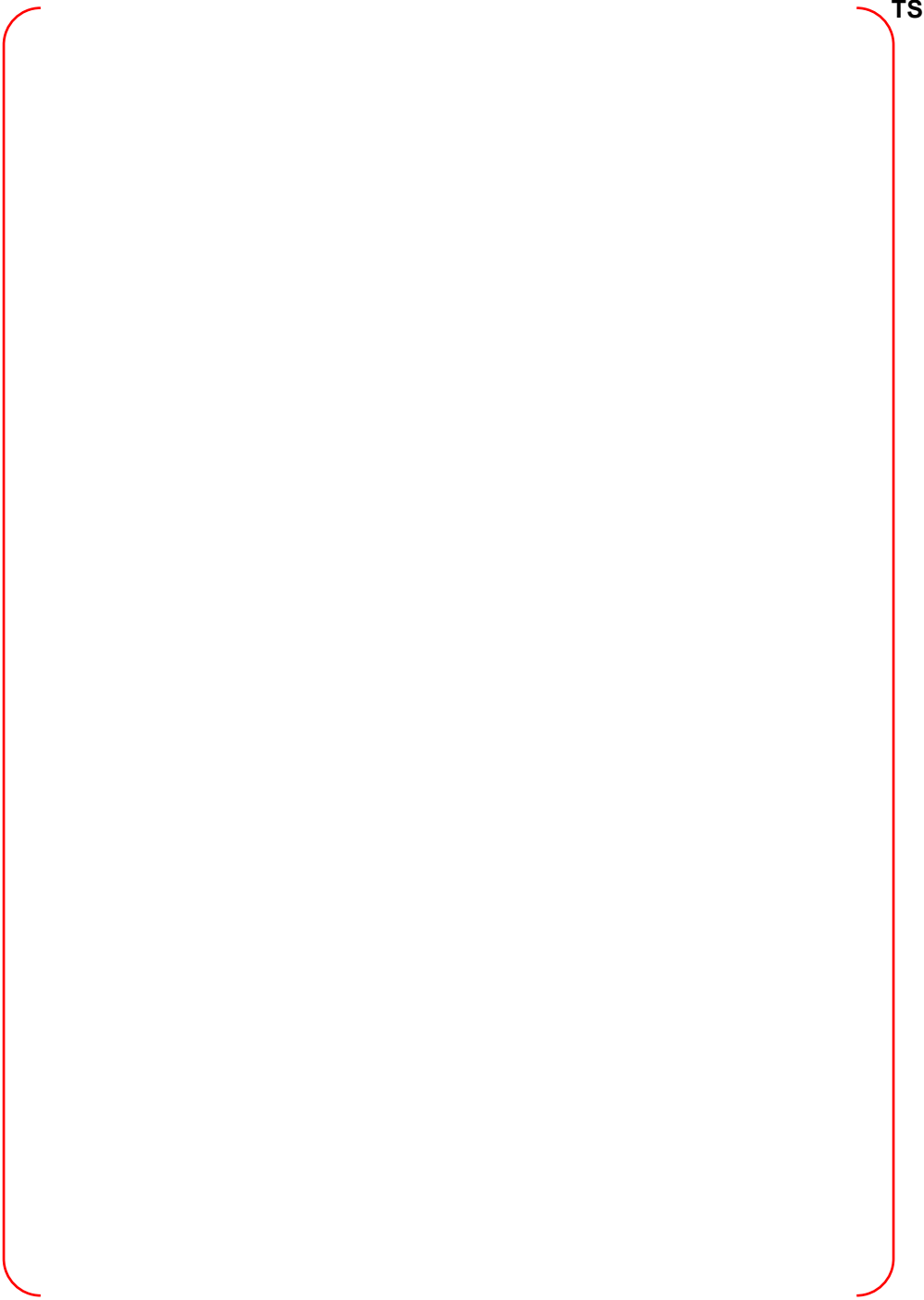


Figure 3-3 Mole Fraction of Hydrogen in the Dome Region for SBO-Three-way valve (3/3)

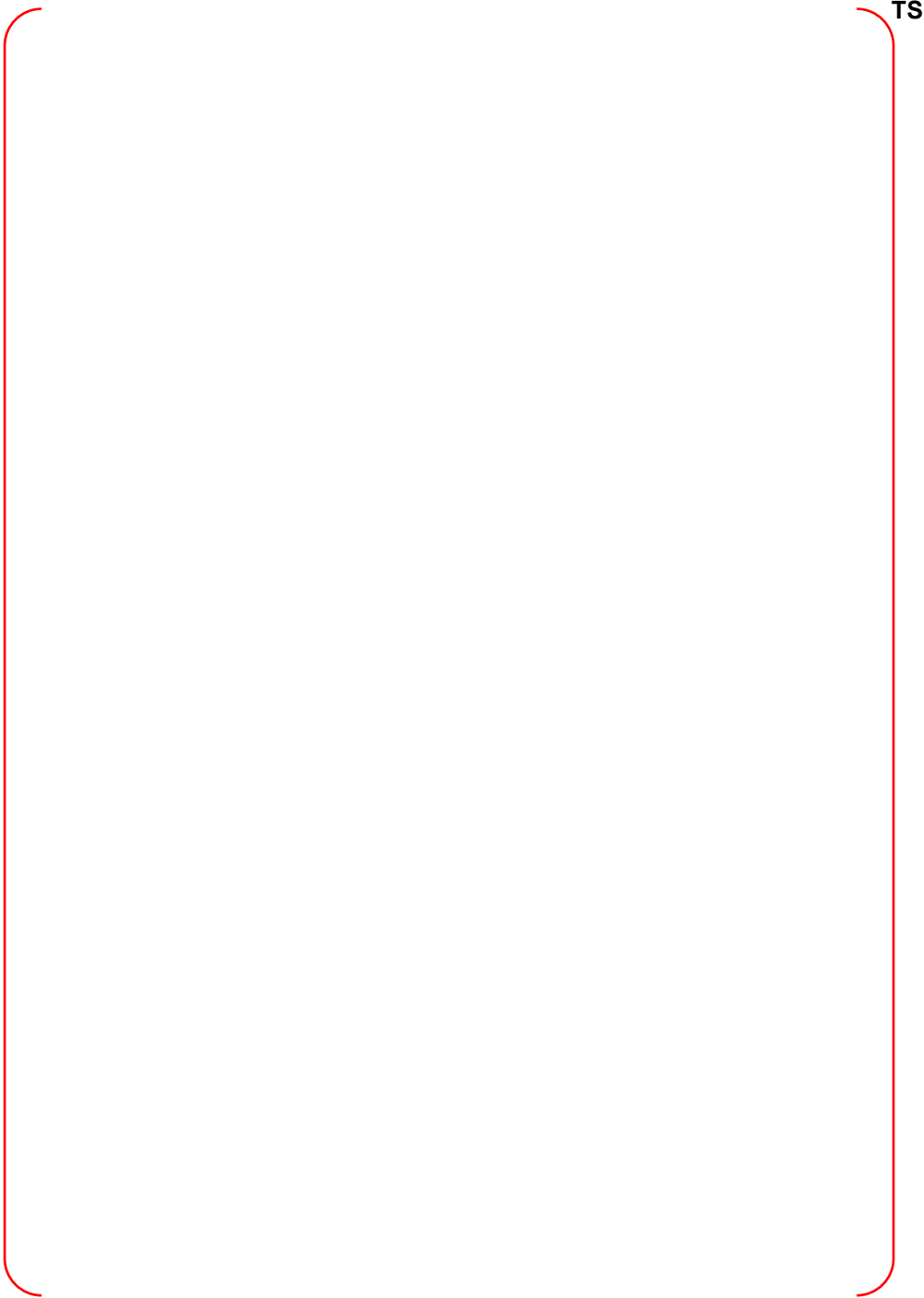


Figure 3-4 Mole Fraction of Hydrogen in the Dome Region for TLOFW-Three-way valve (1/3)

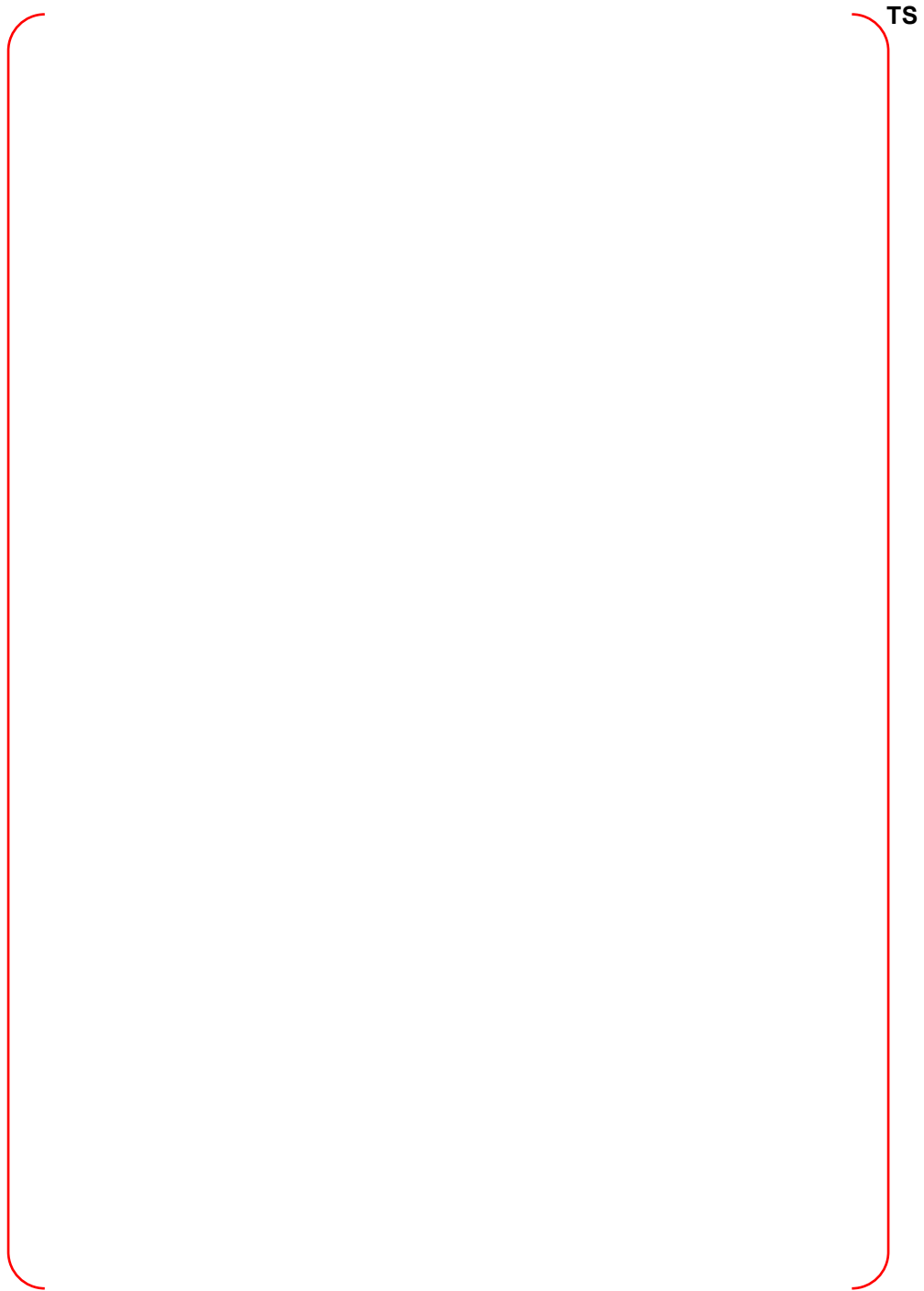


Figure 3-4 Mole Fraction of Hydrogen in the Dome Region for TLOFW-Three-way valve (2/3)

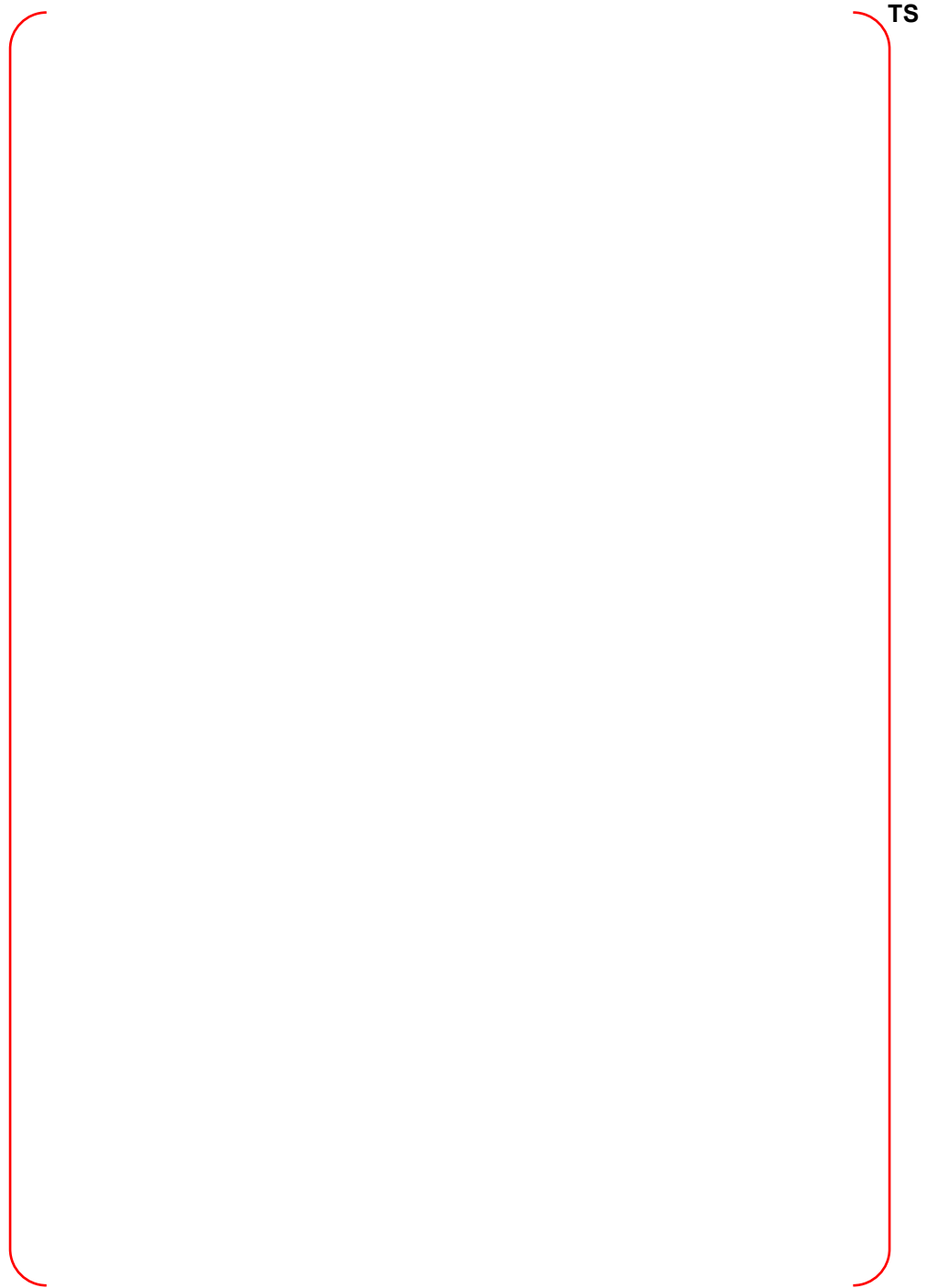


Figure 3-4 Mole Fraction of Hydrogen in the Dome Region for TLOFW-Three-way valve (3/3)



Figure 3-5 Ablation Depths within 24 Hours for Several Severe Accident Scenarios



Figure 3-6 Containment Pressures within 24 Hours for Several Severe Accident Scenarios



Figure 3-7 **Containment Pressure for Large Break LOCA with ECSBS Actuated 24 hours after Onset of Core Damage**

4 CONCLUSIONS

The preventive and mitigative design features implemented in the design of ARP1400 include the HG, CFS, ECSBS, and structural designs of the containment and reactor cavity for severe accident loads.

The structural design of the reactor cavity is intended to prevent failure from ex-Vessel severe accidents. In particular, the reactor cavity was designed to meet the requirements for prevention and mitigation of phenomena such as HPME/ DCH, EVSE and MCCI. The main design characteristics include a core debris chamber inside the reactor cavity, a convoluted gas vent path, large floor area, and the CFS.

The APR1400 are designed for safety functionality even during a very unlikely severe accident scenario. The design includes accident prevention and mitigation features that are based on the analyses of severe accidents. Sufficient robustness is provided in the design so that ample time exists for operator action to mitigate the consequences of a severe accident and minimize the radiological releases into the environment.

In the severe accident analysis for the APR1400, emphases have been laid on the following six topics: hydrogen control, MCCI and debris coolability, HPME and DCH, FCI, containment performance, and ES in order to ensure design adequacy and regulatory compliance. The regulatory compliance involves strict adherence to requirements and reasonable conformance with the guidelines set forth in USNRC, SECY-93-087 "Policy, Technical, and Licensing Issues Pertaining to Evolutionary and Advanced Light-Water Reactor (ALWR) Designs" and other regulatory requirements such as 10 CFR 100, GDC of 10 CFR 50 Appendix A, and the TMI-related requirements of 10 CFR 50.34(f), 10 CFR 50.44, NRC RG 1.216, and SECY-90-016 (Reference 7). The six phenomenological issues considered here are listed and summarized below.

1) Hydrogen control

In hydrogen control analysis, detailed containment hydrogen distribution were analyzed. The investigation of in-Vessel and ex-Vessel hydrogen release characteristics for different accident sequences considered the potential for DDT. It was concluded from the analysis that the APR1400 would have the capability to withstand the hydrogen generation and combustion risks following most severe core damage accident scenarios.

2) MCCI and debris coolability

As a result of the MCCI analyses using the MAAP 4.0.8 and CORQUENCH computer codes, it was determined that the integrity of the containment liner would not be challenged by core concrete attack and it would maintain its integrity under severe accident conditions with the CFS operation.

3) HPME and DCH

The assessment of containment integrity against the DCH risk evaluations concluded that the predicted CCFP values for scenarios V, Va and VI were smaller than the criterion of 0.01 presented in NUREG/CR-6338. Accordingly, it was concluded that the likelihood of containment failure due to DCH loads was negligibly small. Based on the results of the rapid depressurization analyses for preventing HPME under high RCS pressure conditions, it was confirmed that, if the operator could open two POSRVs at appropriate timings after core exit temperatures exceed 922.04K (1,200°F), the RCS pressure would decrease below the DCH cutoff pressure of 17.6 kg/cm² (250 psia).

4) FCI

The risk due to IVSE was analyzed by evaluating IVSE loads using the TEXAS-V computer code. Subsequently, the integrity of the reactor vessel was assessed using the ABAQUS computer code. It was confirmed that the integrity of the reactor vessel could be maintained even if an IVSE occurred. In the event there is a water pool in the reactor cavity due to the operation of the CFS, the resulting risk from EVSEs was analyzed using the TEXAS-V computer code. LS-DYNA computer code is employed in order to analyze the response of the cavity structures according to EVSE loads. All these evaluations confirmed that the integrity of the reactor cavity structure would be maintained even if ex-Vessel FCI occurred.

5) Containment performance capability

TS

6) ES

The ES performance and operability of vital equipment and instrumentation for severe accident prevention and mitigation were verified. This was accomplished by calculating the severe accident environmental conditions inside the containment for in-vessel and ex-vessel events, and then assessing equipment and instrumentation survivability during designated time intervals.

5 REFERENCES

1. SECY-93-087, "Policy, Technical, and Licensing issues Pertaining to Evolutionary and Advanced Light-Water Reactor (ALWR) designs," USNRC, April 1993.
2. 10CFR100, "Reactor Site Criteria," USNRC, July 2012.
3. 10CFR50 Appendix A, "General Design Criteria for Nuclear Power Plants," USNRC, November 2012.
4. 10CFR50.34, "Contents of Applications; Technical Information," USNRC, November 2012.
5. 10CFR50.44, "Combustible Gas Control for Nuclear Power Reactors," U.S. Nuclear Regulatory Commission, Washington, DC, November 2012.
6. Regulatory Guide 1.216, "Containment Structure Integrity Evaluation for International Pressure Loading above Design Basis Pressure" USNRC Aug. 2010
7. SECY-90-016, "Evolutionary Light-Water Reactor (LWR) Certification Issues and Their Relationship to Current Regulatory Requirements," USNRC, June 1990.
8. ASME Section III Division 2, "Rules of Construction of Nuclear Facility Components - Code for Concrete Containments," ASME, July 2006.
9. DOE/ID-10271, "Prevention of Early Containment Failure due to High Pressure Melt Ejection and Direct Containment Heating for Advanced Light Water Reactors," March 1, 1990.
10. Fauske & Associates, 2012(a), MAAP4 Modular Accident Analysis Program for LWR Power Plants, Transmittal Document for MAAP4 Code Revision MAAP 4.0.8, FAI/12-0005, February.
11. OECD Nuclear Energy Agency, Breitung, W., et al. (2000). Flame Acceleration and Deflagration to Detonation Transition (DDT) in Nuclear Safety. State-of-the-Art Report, Ref. NEA/CSNI/R/2000/7.
12. NUREG/CR-6075, Pilch, M. M., Yan, H. and Theofanous, T. G., 1994, "The Probability of Containment Failure by Direct Containment Heating in Zion," SAND93-1535, Sandia National Laboratory, Albuquerque, NM.
13. NUREG/CR-6338, Pilch, M. M., Allen M. D., and Klamerus E. W., "Resolution of the Direct Containment Heating Issue for All Westinghouse Plants With Large Dry Containments or Subatmospheric containments," SAND95-2381, Sandia National Laboratories, Feb. 1996.

Appendix-A

Severe Accident Analysis Report for

Hydrogen Issue

TABLE OF CONTENTS

1	BACKGROUND AND OBJECTIVES	A-7
1.1	Background	A-7
1.2	Objectives.....	A-8
2	HYDROGEN COMBUSTION PHENOMENA.....	A-9
2.1	Basics of Hydrogen Combustion.....	A-9
2.2	Ignition Source	A-10
2.3	Flammability Limits and Combustion Pressures	A-10
2.4	Incomplete Combustion.....	A-10
2.5	Flame Acceleration (FA) and Detonation.....	A-11
2.5.1	Deflagrations	A-11
2.5.2	Detonations	A-11
2.5.3	Deflagration to Detonation Transition (DDT).....	A-12
2.6	Detonation Cell Width.....	A-12
2.7	Correlations for Deflagration to Detonation Transition.....	A-13
2.8	Experimental Database for Flame Acceleration Criterion and Onset of Detonation Criterion ...	A-14
2.9	Effects of H ₂ Stratification on Deflagrations	A-16
2.10	Hydrogen Mixing and Distribution	A-16
2.10.1	Experiments	A-16
2.10.2	Code Prediction.....	A-17
2.10.3	Subnode Physics Model in MAAP4.....	A-17
2.11	Passive Auto-Catalytic Recombiners.....	A-18
2.12	Relationship to Containment Failure Mechanisms.....	A-18
3	METHODOLOGY.....	A-48
3.1	Methodology for Non-Detonative Slow Combustion Evaluation	A-48
3.2	Methodology for Local Hydrogen Accumulation Evaluation.....	A-48
3.3	Methodology for DDT Evaluation	A-49
3.3.1	Criterion for Flame Acceleration.....	A-49
3.3.1.1	MAAP4 Calculations of Expansion Ratios	A-50
3.3.2	Criterion for Deflagration-to-Detonation Transition Potential	A-50
3.3.2.1	Correlation for Detonation Cell Width.....	A-51
3.3.2.2	Other Correlation for Detonation Cell Width.....	A-52
3.3.2.3	Detonation Cell Width for CO.....	A-53
3.3.2.4	Characteristic Length of Compartments.....	A-53
4	EVALUATION AND RESULTS SUMMARY.....	A-61

4.1	AICC Pressure Evaluation and Summary	A-61
4.2	Local Hydrogen Accumulation Evaluation and Summary	A-61
4.3	DDT Evaluation and Summary.....	A-63
5	CONCLUSION	A-78
6	RERERENCE	A-79

LIST OF TABLES

Table 2-1	Experiments Used in Correlations for Flame Acceleration Criterion	A-37
Table 2-2	Experiments Used in the L/ λ Correlation for Onset of Detonations	A-39
Table 2-3	References Cited in Tables 2-1 and 2-2	A-40
Table 3-1	Critical Expansion Ratio as a Function of Initial Temperature	A-49
Table 3-2	Fitting Equation for Critical Expansion Ratio	A-49
Table 4-1	Summary of Locations with DDT Potential and Required Conditions	A-65

LIST OF FIGURES

Figure 2-1 Minimum Ignition Energy for Hydrogen Deflagrations..... A-20

Figure 2-2 Type of Ignition Source Energies with Sources Required for Detonation by Direct Energy Deposition..... A-21

Figure 2-3 Comparison of Ignition Source Energies with Sources Required for Detonation by Direct Energy Deposition..... A-22

Figure 2-4 Flammability Domain for upward Propagation for H₂-Air- H₂O vapor mixtures. A-23

Figure 2-5 Comparison of Lower Flammability Limits (LFL) and Upper Flammability Limits (UFL) of hydrogen-air-mixtures as a function of initial temperature..... A-24

Figure 2-6 Theoretical adiabatic, constant volume combustion pressure ratios of H₂-air mixtures A-25

Figure 2-7 Adiabatic, Isochoric, Complete Combustion (AICC) pressures for various containment initial conditions..... A-26

Figure 2-8 Degrees of Combustion in Hydrogen Air Steam Mixtures..... A-27

Figure 2-9 Hydrogen concentration during incomplete burning..... A-28

Figure 2-10 Combustion Completeness for Nevada Test Site Premixed Combustion Tests A-28

Figure 2-11 Comparative pressure profiles for three 8% (nominal) hydrogen combustion tests having different precombustion steam concentrations. A-29

Figure 2-12 Detonation pressure ratios and speed for hydrogen-air mixtures A-30

Figure 2-13 Measured values (McGrill, Sandia) of the detonation cell width (λ) as a function of hydrogen concentration..... A-31

Figure 2-14 Detonation Cell Width Data (Sandia HDT) and Predictions (Shepherd Model)..... A-32

Figure 2-15 Detonation cell width as a function of temperature A-33

Figure 2-16 Deflagration-to-detonation transition (DDT) results from the FLAME facility at Sandia A-34

Figure 2-17 Detonation Propagation and Transmission Correlations for Simple Geometries..... A-35

Figure 2-18 Illustration of Characteristic Size L for Channels with Obstacles and Varying Blockage Ratio A-36

Figure 2-19 Limits of Flame Acceleration for Hydrogen-Air-Steam Mixtures at 375 K and 1 atm..... A-41

Figure 2-20 Combustion regime as function of expansion ratio σ and Zeldovich number β for hydrogen-lean mixtures (i.e., $\beta(Le-1) < -2$)..... A-41

Figure 2-21 Combustion regime as function of expansion ratio σ and Zeldovich number β for hydrogen-rich (including stoichiometric) mixtures (i.e., $\beta(Le-1) > -2$)..... A-42

Figure 2-22 Expansion ratio and flame acceleration limits of hydrogen-air-steam mixtures at 373 K... A-42

Figure 2-23 L/ λ correlation for onset of detonations A-43

Figure 2-24 Hydrogen distribution and mixing tests	A-44
Figure 2-25 Gas temperatures at 0 m floor; comparison of MAAP4 results to HDR Test E11.2 data...	A-45
Figure 2-26 Hydrogen/helium concentration in the upper dome; comparison of MAAP4 results to HDR Test E11.2 data	A-46
Figure 2-27 Hydrogen/helium concentration at 10 m floor; comparison of MAAP4 results to HDR Test E11.2 data	A-47
Figure 3-1 Example of Expansion Ratio Calculated by STANJAN Code	A-50
Figure 3-2 Calculation Results of Detonation Cell Width from Eq. 3-15 vs. Experimental Data as a Function of Hydrogen Concentrations at Various Temperatures	A-57
Figure 3-3 Calculation Results of Detonation Cell Width from Eq. 3-15 vs. Experimental Data as a Function of Steam Concentrations at various hydrogen concentrations	A-57
Figure 3-4 Detonation Cell Width (cm) plotted in $[H_2]_{dry}$ - $[H_2O]$ Plane using Eq. 3-15	A-58
Figure 3-5 Comparison of Detonation Cell Width given by Eq. 3-15 and Gavrikov Method.....	A-59
Figure 3-6 Guidelines for Determination of Compartment Characteristic Length	A-60
Figure 4-1 Mole Fraction of Hydrogen in the Dome Region for LLOCA	A-60
Figure 4-2 Mole Fraction of Hydrogen in the Dome Region for SLOCA.....	A-63
Figure 4-3 Mole Fraction of Hydrogen in the Dome Region for SBO-3way valve	A-66
Figure 4-4 Mole Fraction of Hydrogen in the Dome Region for TLOFW-3way valve	A-75

1 BACKGROUND AND OBJECTIVES

1.1 Background

The potential failure of a nuclear power plant containment due to an energetic hydrogen burn has been a subject of concern for the nuclear regulatory agencies and the nuclear industry worldwide. The concern is that hydrogen, evolved during a core damage event, could accumulate in the containment building and subsequently ignite. If the combustion is energetic enough to fail the containment, the timing and uncertainties in location of the containment shell failure have two potentially important ramifications regarding the radiological source term. First, if the hydrogen burns early and causes containment failure before or shortly after vessel failure, natural fission product deposition mechanisms in the containment do not have sufficient time to significantly affect (reduce) the masses of fission products that could be released through the failure location. Second, fission products carried by gas flows from the failed containment would result in radiological releases to the environment.

The USNRC regulations clearly establish safety requirements related to the potential of hydrogen combustion or detonation as listed below:

10CFR50.34(f)(3)(v)(A)(1)

Containment integrity will be maintained during an accident that releases hydrogen generated from 100% fuel clad metal-water reaction accompanied by hydrogen burning. For concrete containments, containment integrity is maintained by meeting the requirements of the ASME Boiler Pressure Vessel Code, Section III, Division 2 Subsubarticle CC-3720, Factored Load Category, considering pressure and dead load alone.

10CFR50.34(f)(2)(ix)(A) and (B)

The hydrogen control system and associated systems shall provide, with reasonable assurance, that

(A) Uniformly distributed hydrogen concentrations in the containment do not exceed 10% during and following an accident that releases an equivalent amount of hydrogen as would be generated from a 100% fuel clad metal-water reaction, or that the post-accident atmosphere will not support hydrogen combustion.

(B) Combustible concentrations of hydrogen will not collect in areas where unintended combustion or detonation could cause loss of containment integrity or loss of appropriate mitigating features.

10CFR50.44(c)(1),(2) and (3)

(1) *Mixed atmosphere*. All containments must have a capability for ensuring a mixed atmosphere during design-basis and significant beyond design-basis accidents.

(2) *Combustible gas control*. All containments must limit hydrogen concentrations in containment during and following an accident that releases an equivalent amount of hydrogen as would be generated from a 100 percent fuel clad-coolant reaction, uniformly distributed, to less than 10 percent (by volume) and maintain containment structural integrity and appropriate accident mitigating features.

(3) *Equipment Survivability*. Containments that do not rely upon an inerted atmosphere to control combustible gases must be able to establish and maintain safe shutdown and containment structural integrity with systems and components capable of performing their functions during and after exposure to the environmental conditions created by the burning of hydrogen. Environmental conditions caused by local detonations of hydrogen must also be included, unless such detonations can be shown unlikely to occur. The amount of hydrogen to be considered must be equivalent to that generated from a fuel clad-coolant reaction involving 100 percent of the fuel cladding surrounding the active fuel region.

1.2 Objectives

There are three main objectives for this report:

1. To identify the different types of hydrogen combustion that can take place in the APR1400 containment and determine the limiting conditions for combustion.
2. To evaluate how the containment can be affected by the hydrogen combustion.
3. To provide a technical basis for determining whether the likelihood of containment rupture due to hydrogen combustion is big enough to consider it a credible cause of containment failure.

2 HYDROGEN COMBUSTION PHENOMENA

This section provides an up-to-date review of current knowledge on hydrogen combustion phenomena in relation to nuclear plant safety during severe accidents. The emphasis of this review is on establishing the technical basis for evaluation of the potential for detonations.

2.1 Basics of Hydrogen Combustion

Hydrogen combustion, or burning, is the result of a chemical reaction between gaseous hydrogen and gaseous oxygen. The products of this reaction are steam and energy; the energy is liberated as light and heat. Necessary conditions for hydrogen combustion are the presence of sufficient amounts of hydrogen and oxygen and the presence of an ignition source or trigger.

With a volume filled with only hydrogen and oxygen gases, minimum concentrations of hydrogen and oxygen are required for hydrogen combustion to occur. A mixture containing too little hydrogen to burn is called "lean", while a mixture containing too little oxygen to burn is called "rich" since there is an excess of fuel. The presence of another gas that does not participate in the combustion reaction (such as steam or nitrogen) acts to inhibit combustion. As the concentration of the inert gas increases, the threshold hydrogen concentration for lean hydrogen combustion increases, while the threshold concentration for rich hydrogen combustion decreases. Extensive research has been performed for numerous combinations of hydrogen, oxygen, and inert gases to map out the hydrogen and oxygen concentrations that are combustible. These maps display the flammability limits.

A trigger is generally necessary to initiate burning of a flammable hydrogen and oxygen mixture. Typically a spark is sufficient to ignite a flammable mixture. The required trigger energy decreases as the hydrogen gas temperature increases, until a threshold temperature is reached. Above this temperature the mixture itself is energetic enough to self-trigger (or auto-ignite). This threshold is therefore referred to as the minimum autoignition temperature.

With a volume containing a flammable mixture of hydrogen and oxygen and a trigger that initiates combustion, the energy release depends on the mass of hydrogen consumed by the chemical reaction. The combustion of one kmole of hydrogen releases 244 MJ of energy. Ignition of gas mixtures with compositions near the flammability limits have too little hydrogen or oxygen for the flame front to propagate throughout the entire volume and consume all of the available hydrogen; such burns are called "partial" burns. As the hydrogen concentration moves away from the flammability limits the associated burns become more complete. When a mixture of hydrogen and oxygen is well within the flammability limit an ignition will cause a complete combustion of the limiting reactant. This is called a "global burn." Global burns yield the maximum energy release that can be obtained by combustion of a given flammable mixture.

Hydrogen-air-steam mixtures can burn in several modes: diffusion flames, slow and accelerated deflagrations, and detonations. Combustion of hydrogen that has not been well mixed with oxygen results in a diffusion flame. Diffusion flames are stationary (standing flames) and the primary consequences are thermal loads on nearby structures and equipment. If hydrogen has mixed well with oxygen, the combustion involves flames moving or propagating through the combustible mixture. Two types of premixed flame propagation can occur. One is called deflagration, while the other is called detonation. Deflagration is a combustion process in which the flame front moves at subsonic (for slow deflagrations) or sonic (for accelerated deflagrations) velocity with respect to the unburned gas. Detonation is defined as supersonic propagation of the flame front.

It is important to understand how the velocity of the combustion front affects the system. The pressure in a subsonic deflagration cannot exceed the Adiabatic, Isochoric, Complete Combustion (AICC) pressure value, which can be readily calculated by equilibrium thermodynamics. Pressure is then assumed to be uniformly distributed since the flame is moving slowly with respect to the pressure waves. In a detonation,

transient overpressures can exceed this AICC value by a factor of three or more, and pressure can vary significantly across the detonation front. Calculating the maximum dynamic loads from accelerated flames and detonations requires a specialized shock wave physics model.

2.2 Ignition Source

For any type of combustion, an ignition source is required to provide a minimum amount of energy to a combustible mixture in order to ignite it. Relatively weak sources such as static discharge and sparks can cause ignition. Figure 2-1 presents the minimum ignition energy for hydrogen deflagrations. For the case of 13% by volume of hydrogen in air, approximately 0.07 mJ is sufficient to ignite a hydrogen burn. Figure 2-2 compares various potential ignition sources energies including a simple match. A match burning for one second can release one joule of energy which is over four orders of magnitude more energy than that required to initiate a hydrogen burn. The high energy sources shown in Figure 2-3 are not sufficient to directly initiate shock waves to further drive detonations, but are sufficient to cause a deflagration. As discussed in Section 2.5, a deflagration can develop into a detonation if certain conditions are met.

High temperatures lead to slow volumetric oxidation, and very high temperatures (~960 K) can cause immediate ignition, known as auto-ignition. Auto-ignition is most likely to occur for severe accident sequences that release very high temperature hydrogen-rich gases into non-inerted regions.

2.3 Flammability Limits and Combustion Pressures

Flammable conditions are determined by flammability limits. Flammability limits of a combustible gas mixture are defined as the limiting gas compositions, at a given temperature and pressure, in which a deflagration (once ignited) will propagate. There is relatively good information on flammability limits of hydrogen-air-steam mixtures at temperatures less than 149 °C [Reference 19, 32, 3]. At higher temperatures, such information is incomplete. For this reason, a systematic extrapolation of flammability limits to higher temperatures, as well as calculations of flammability limits of different gas compositions such as those used in the MAAP4 code [Reference 17], is a reasonable approach. Classical limits (i.e. derived from practical experience and experimentation) for flammability and AICC maximum equilibrium final pressure are presented in Figure 2-4 and Figure 2-5. In more recent flammability charts [Reference 6], the flammability limits for hydrogen/air/steam mixtures are drawn slightly wider into higher steam concentrations than that in Figure 2-4. The region of concern generally lies below the line of stoichiometric mixtures, where hydrogen is the limiting reactant. The minimum amount of hydrogen necessary for combustion is slightly over 4% in dry air. The minimum oxygen concentration necessary for combustion is about 5% in dry air, corresponding to about 75% hydrogen. Addition of steam to any mixture of hydrogen and air reduces the hydrogen volumetric concentration and increases the required threshold concentration for combustion.

Figure 2-6 presents the AICC overpressure ratio resulting from combustion of hydrogen in air and indicates classical deflagration and detonation limits [Reference 52]. However, the detonation limits shown in this figure are too simplistic for reactor applications because detonation limits depend on a number of parameters in complex and incompletely understood ways.

The effect of steam on post-combustion pressure is quantified for various initial saturation conditions as a function of hydrogen concentration in Figure 2-7. In this figure, the initial pressure is calculated by adding the partial pressure of hydrogen and steam to a humid air mixture originally at 1.0 atm total pressure and 300 K.

2.4 Incomplete Combustion

For hydrogen there are two lean propagation limits, upward and downward. At the lean upward propagation limit (~4.5%), flames will propagate upward. At lean downward propagation limits (~8%),

flames will propagate both upward and downward throughout the volume. Hence, the extent of flame propagation (or combustion completeness) for combustion at lean flammability limits is dependent on the hydrogen concentration. If the hydrogen concentration is above the upward propagation limits but below the downward propagation limits, combustion will be incomplete.

Incomplete burning occurs for hydrogen concentrations below ~8% which is the downward propagation limit (see Figure 2-8 and Figure 2-9). Concentrations that are above the downward propagation limit lead to fairly complete combustion. The effect of steam addition is also shown in these figures. There is close agreement between these sets of deflagration data despite a significant disparity in geometric scale of the vessel used in each experiment (i.e., 0.002 m³ and 2048 m³, respectively) [Reference 29, 44, 65]. In both cases, it is evident that the addition of steam has an effect on the completeness of combustion, shifting the required hydrogen concentration to a higher value as more steam is added.

Steam affects the combustion completeness, flame velocity, heat capacity, and emissivity of the combustible gas mixture which, in turn, affects the resultant system pressure rise. Figure 2-10 and Figure 2-11 illustrate this reduction in combustion pressure as a result of increasing the relative concentration of steam for two different size systems (6.3 m³ and 2048 m³ sphere) [Reference 24, 44]. Both sets of data were taken with initial hydrogen concentrations of 8%. This concentration was chosen to represent a condition that undergoes complete combustion in dry air. It was also selected to provide a common point of reference for comparing these two sets of tests. The pressure rise ratio is reduced by about 50% in the large apparatus and by even a greater factor in the smaller apparatus. In each case, combustion was only about 38% complete for the highest steam addition test.

2.5 Flame Acceleration (FA) and Detonation

2.5.1 Deflagrations

Slow deflagrations results in a flame that travels with a speed of approximately 100 m/s or less. This is much slower than the speed of sound. The pressure will be in equilibrium with the containment during the combustion. No dynamic loads are generated. Accelerated deflagrations or accelerated flames travel between ~100 and ~1000 m/s which can be fast enough to generate shock waves and significant dynamic loads [Reference 23]. Flame acceleration is likely to occur in a highly confined region rather than in a partially confined region, and is strongly influenced by the scale of the region and the size, shape, and spacing of obstacles within the region. The obstacles induce turbulence in the flow generated by the expansion of the burned gases. The turbulence widens the flame front area. This improves the transport properties. The result is an increased combustion rate. The positive feedback from the enhanced combustion rate makes the flame accelerate even more [Reference 25, 9].

For multi-compartments interconnected by junctions of relatively small flow area, an ignition in a single compartment could cause accelerated flames in the neighboring compartment due to hot gas expansion and turbulence at the junction [Reference 20]. The prediction of flame acceleration in simple geometries can be achieved by a combustion code that solves the Navier-Stokes equations and incorporates reasonable turbulence-combustion interaction models [Reference 20]. This method requires enormous computing resources even for a system of small scale and simple geometry. An application of a computational fluid dynamics (CFD) based combustion code to real plants with highly complex geometries is impractical at the present time. An attempt to address the issue of accelerated flames in multi-compartments with simple geometry within the framework of a lumped parameter code using MAAP4 was presented by Luangdilok et al. [Reference 30]. However, more development work is needed to extend this approach to a much more complicated geometry of a nuclear plant.

2.5.2 Detonations

Detonation of a hydrogen/oxygen mixture can occur if enough energy is introduced to the system to create initial shock waves. According to Figure 2-3 at least 100 GJ/s is required to detonate an ideal

mixture. No such source is present in the reactor containment so this form of detonation can be ruled out from this study report. The only type of detonation that can occur is therefore one that is generated from a deflagration-to-detonation transition.

The hydrogen/oxygen mixture condition can cause detonation. The flame can then accelerate above the speed of sound. The energy released from the combustion sustains a shock wave that further ignites and combusts the hydrogen/air mixture. This leads to a detonation. The phenomenon is usually called deflagration-to-detonation transition (DDT). The energy needed to ignite this form of detonation is equivalent to the energy needed to ignite a slow deflagration. Detonations travel between 1400 and 2200 m/s and may also generate significant dynamic loads [Reference 66]. Figure 2-12 shows the relation between detonation speeds and dynamic pressures for dry air as a function of hydrogen concentrations at 1 atm, 298 K. The degree of occurrence of DDT depends on a number of parameters. The detonation limits cannot currently be predicted by any principles theory.

Engineering correlations that are used to predict the limits have been developed based on a measurable quantity called the detonation cell width. The detonation cell width represents a characteristic length of a detonation wave that describes the sensitivity of the mixture to detonation. The smaller the detonation cell width is, the easier it is to get the mixture to detonate. The detonation cell width is a very important property for predicting the detonation behavior of the detonable mixture. It is further discussed in Section 2.6.

2.5.3 Deflagration to Detonation Transition (DDT)

Three methods for DDT evaluation have been proposed. The method of Sherman and Berman (1986) which gives the probability of DDT, requires too much qualitative engineering judgment that could be very subjective. The DDT criterion proposed by Peraldi et al. (1986) requires as a prerequisite that for a flame to accelerate to DDT the flame must reach the sonic speed. However, determining whether the flame is sonic or not is not an easy task. The latest method proposed by an expert group is commissioned by OECD/NEA. The group issued the so-called "State-of-the-Art Report on Flame Acceleration and Deflagration-to-Detonation Transition in Nuclear Safety" that set the standard for DDT evaluation at present time [Reference 6].

2.6 Detonation Cell Width

The detonation cell width (λ) is a very important property for predicting the detonation behavior of a mixture [Reference 65, 36, 2]. The smaller the detonation cell size is, the more sensitive a mixture is to detonation. Measured cell widths for mixtures of hydrogen in dry air at 25°C are shown in Figure 2-13. The curve always has a U-shape with a minimum value of λ near stoichiometry (29.7% hydrogen). The cell widths may vary from about 1 cm for 30% H₂ in air to several meters for very lean or rich mixtures. A general way of correlating the detonation cell widths to mixture composition is in terms of equivalence ratio, denoted by ϕ . The equivalence ratio is the ratio of the number of moles of hydrogen divided by the number of moles of air to that quotient at stoichiometry. The equivalence ratio ϕ , the hydrogen mole fraction X_{H_2} , and the steam mole fraction (or other diluent) X_s are related by

$$\phi = SX_{H_2} / (1 - X_{H_2} - X_s) \quad (2-1)$$

or

$$X_{H_2} = \phi(1 - X_s) / (\phi + S) \quad (2-2)$$

where $S = 2.387$. As an example, equivalence ratio for 13% hydrogen in dry air is 0.357. This value is unchanged by addition of steam to the dry mixture because the overall H₂ and O₂ mole fractions decrease in the same proportion.

The detonation cell width increases dramatically with the addition of steam as shown in Figure 2-14 for mixtures at 100°C. Figure 2-14 shows predictions given by a model developed by Shephard (1985). The addition of carbon dioxide to mixtures at 20°C and 1 atm and at 100°C and 1 atm increase the detonation cell width as much, or more than, the addition of steam [Reference 57]. Thus, steam or carbon dioxide as a diluent makes detonation more difficult to achieve. As temperature increases, detonation becomes easier as seen by the decrease in cell width in Figure 2-15. Comparing the two figures, one can clearly see that in this temperature range the steam inerting effect is far more pronounced than the heating effect on detonation cell size.

2.7 Correlations for Deflagration to Detonation Transition

Detonations are most likely to be initiated by a deflagration-to-detonation transition (DDT) in reactor accident scenarios. A mixture may be ignited by an ignition source, then accelerate to choked flow conditions where DDT is possible. The lowest hydrogen concentration for which DDT was observed was 15% (Sherman et al., 1989) at the FLAME facility at Sandia, which is a half-scale model of an ice condenser upper plenum, 2.44 m high, 1.83 m wide, and 30.5 m long. This long rectangular channel can be partially vented on top, and to promote turbulence, obstacles can be placed along the interior. The 15% low limit corresponds to a case with no venting and periodic obstacles every 1.83 m. In a case with no obstacles, 25% hydrogen was required, as shown by Figure 2-16, and for a case with obstacles and 50% venting, 20% hydrogen was required. However, according to the most recent state-of-the-art report, DDT is possible for mixtures at elevated temperatures even at hydrogen slightly higher than 10% [Reference 6].

The scale of the combustible mixtures and enclosure has been observed to be important for DDT. Larger scale appears to promote flame acceleration (a necessary condition for DDT) over a wider range of mixtures. Most experimental data were obtained in small scales which are not directly applicable to reactor scales. Since larger scales promote flame acceleration, most data can be regarded as non-conservative. Efforts to resolve this problem have been made to correlate the occurrence of DDT to the detonation cell width and the smallest dimension of the flow channel. This does not account for the presence of obstacles (such as blockage ratio and spacing) in the flow field. Hence, this type of correlation is not universal, but it is the only guideline available. Peraldi et al. (Reference. 42), based on experiments in circular tubes of up to 30 cm in diameter filled with orifice ring obstacles, proposed that a necessary condition for DDT is that the minimum transverse tube dimension (d) must be sufficiently large to accommodate at least one transverse detonation cell width (λ) characteristic of the mixture of the tube. Quantitatively this can be written as

$$d/\lambda \geq a \quad (2-3)$$

where $a=1$. Some other researchers suggested a more conservative value of $a = \pi$ (Lindstedt and Michels, 1989) for tubes. It is more conservative than that of $a=1$ because it says that DDT can occur at larger detonation cell width (i.e., less chemically sensitive mixture) for the same tube of diameter d . The important conclusion to draw from this is that a deflagration-to-detonation transition can take place in large scale containments even if the ideal chemical composition of the mixture for detonation does not exist.

Extensive research at Sandia leads to a summary of conditions for detonation propagation of various geometries as shown in Figure 2-17. It is noted that these geometries are still too simplistic for reactor applications.

More recent research as summarized (by Dorofeev) in Breitung et al [Reference 6], suggests a characteristic size L to represent a more complicated geometry such as tubes with obstacles and a system of connected rooms. The necessary condition for DDT is that $L > 7\lambda$. The characteristic size L for channels with obstacles and its changes with blockage ratio is illustrated in Figure 2-18. This is the most current criterion that is based on extensive experimental data and is acceptable for reactor applications. Further discussion on this is provided in section 2.8.

A review of more recent work in the methodology of DDT assessment compiled by an OCED-commissioned expert group [Reference 6] indicates that improvement in the characterizations of the nature of DDT has been achieved to the extent that quantitative prediction is possible, but still subject to large uncertainties. One of the combustion characterizations that was not mentioned in earlier work was the expansion ratio (unburned-to-burned mixture density ratio). It must be greater than the critical expansion ratio for flame acceleration (which is a prerequisite to DDT) to occur. This expansion ratio is a parameter representing the reactivity of the mixture, while the critical expansion ratio can be regarded as a boundary between slow flames and fast flames as shown in Figure 2-19 [Reference 6].

2.8 Experimental Database for Flame Acceleration Criterion and Onset of Detonation Criterion

As part of the OECD expert group, Dorofeev analyzed a large amount of experimental data on turbulent flame acceleration at conditions applicable to reactor accidents and came up with the idea of critical expansion ratio required for flame acceleration. The following list of experiments in Table 2-1 shows the most extensive database ever assembled together by the expert group [Reference 6]:

- (1) High-Temperature Combustion Facility (HTCF) at the Brookhaven National Laboratory (BNL) to study flame acceleration and DDT in hydrogen-air and hydrogen-air-steam mixtures with different hydrogen and steam concentrations. The experiments were performed without venting and with 5.1% venting at initial mixture temperatures up to 650K [Reference 11]. The HTCF is 21.3 m long and has an internal diameter of 27.3 cm. Periodic orifice plates were installed down the length of the entire detonation tube. The orifice plates have an outer diameter of 27.3 cm, an inner diameter of 20.6 cm, and a spacing of 1 tube diameter.
- (2) Heated Detonation Tube (HDT) Experiments conducted at the Sandia National Laboratories (SNL) with hydrogen-air-steam and hydrogen-air mixtures to determine the region of benign combustion (between the flammability limits and the DDT limits) [Reference 51]. The HDT is 12 m long and has internal diameter of 43 cm. Obstacles were used with 30% blockage ratio annular rings, and alternate rings and disks of 60% blockage ratio. The initial conditions were 383 K and 1 or 3 atm pressure.
- (3) RUT facility tests at Russian Research Centre "Kurchatov Institute" with hydrogen-air mixtures with and without steam dilution in a complex geometry [Reference 12, 13]. The first part of the facility was a channel of 2.5 x 2.3-m cross-section and 34.6 m long; the second part was a canyon of 6 x 2.5-m cross-section and 10.5 m long, and the third one was a channel of 2.5 x 2.3-m cross-section and 20 m long. Twelve concrete obstacles were placed along the first channel with a spacing of 2.5 m (blockage ratios were 0.3 and 0.6). Initial temperature in tests with steam was close to 375 K. Initial pressure in all the tests was 1 atm.
- (4) FLAME facility tests at the Sandia National Laboratories in a study of FA and DDT of hydrogen-air mixtures [Reference 53]. FLAME is a large (30.5 m long) rectangular channel that has an interior width of 1.83 m and a height of 2.44 m. The blockage ratio was 0.0 (no obstacles) or 0.33 in the tests. Initial conditions were normal in these tests.
- (5) FZK experiments [Reference 26] were performed in a 35-cm-diameter, 12-m-long length with equidistant rings as obstacles (blockage ratio was 0.6, spacing was 35cm). Flame acceleration was studied in hydrogen air mixtures and in hydrogen-oxygen (2:1) mixture, diluted with nitrogen, argon, helium and CO₂. Experiments were conducted under normal initial conditions.
- (6) CHANNEL, DRIVER, and TORPEDO experiments provided data on turbulent flame propagation regimes in obstructed areas at different scales [Reference 14, 15]. Blockage ratios ranged from 0.1 to 0.9. Distances between obstacles were equal to the transverse size of each tube for all these facilities. Mixture compositions were varied in the tests. Experiments were conducted under normal conditions.

- (7) The CHANNEL facility is a tube with a square cross-section of 80 mm x 80 mm and 5.28-m length. Rectangular obstacles were mounted along upper and bottom plates. Different hydrogen-air mixtures and stoichiometric hydrogen-oxygen, diluted by argon or helium were used in these tests.
- (8) The DRIVER facility is a detonation tube of 174 mm id and approximately 12-m length. Hydrogen-air mixtures and stoichiometric hydrogen-oxygen mixtures diluted with nitrogen, argon, or helium were used in this facility.
- (9) The TORPEDO facility is a 520 mm tube of 30.3 m length. Hydrogen-air mixtures and stoichiometric hydrogen-oxygen, diluted by helium were used in these tests.

This was an extensive undertaking that provided better insight into the combustion regime of slow and fast deflagrations. It also made possible a quantitative prediction of flame acceleration in code calculations. Figure 2-20 shows for hydrogen-lean mixtures the correlation between the expansion ratio, the Zeldovich number and the resulting combustion regime. Here, the Zeldovich number is defined as $\beta = Ea(T_b - T_u)/(RT_b^2)$ where Ea is the effective activation energy, T_u is the initial, and T_b is the maximum flame temperature. There is clearly a boundary between fast combustion and slow combustion. This boundary line defines the critical expansion ratios for a wide range of initial temperatures. Similarly, for hydrogen-rich (including stoichiometric) mixtures, the boundary line between fast and slow combustions shown in Figure 2-21 is a horizontal line with expansion ratio between 3.5 to 4.0. Based on these results, Dorofeev established the so-called " σ criterion" which states that for flame acceleration to occur, the expansion ratio of the mixture must be equal or greater than the critical expansion ratio. Figure 2-22 shows the relation between the acceleration limits and expansion ratios for hydrogen-air-steam mixtures at 373 K.

Dorofeev also correlated the onset conditions for DDT based on the above large amount of experimental data and some additional experiments that are listed below:

- (1) McGill University small-scale tests on DDT [Reference 63, 27],
- (2) Whiteshell Laboratories (AECL) data [Reference 8].
- (3) Large-scale DDT experiments with hydrogen-air, hydrogen-air-steam, and hydrogen-air-CO₂ mixtures at Russian Research Centre 'Kurchatov Institute' RUT facility [Reference 12, 13, 14, 33,54, 55, 56]
- (4) Small scale experiments in MINIRUT experimental apparatus at scale 1:50 of RUT facility [Reference 33, 14].
- (5) Data on DDT conditions obtained in obstructed channels with transverse sizes 80, 174, 350, 520 mm [Reference 33, 26] for a wide range of hydrogen mixtures

A summary of experiments is given in Table 2-2 and experimental results are presented in Figure 2-23. Data are marked with light and dark labels where "light" means no DDT and "dark" means DDT. Figure 2-23 shows combustion modes (DDT or no DDT) as a function of characteristic length L of the compartment or the mixture cloud, and detonation cell width λ . A good correlation is observed for $L/\lambda = 7$ within the accuracy of the cell size data over a wide range of scales. The minimum ratio of $L/\lambda = 5.6$ for few cases of DDT (i.e. dark data points above $L/\lambda = 7$ line) can be found among the general borderline of $L/\lambda = 7$ in the correlation presented in Figure 2-23. This is just a 20% deviation, which is much smaller than inaccuracy of the cell size data. Based on these results, the so-called " 7λ criterion" was recommended for reactor safety applications.

2.9 Effects of H₂ Stratification on Deflagrations

So far we have only considered combustion in a well-mixed mixture. However, in reality, stratified regions of hydrogen or steam concentrations may exist prior to complete mixing. Whitehouse et al. (1994) found, from a series of experiments in a 10.7 m³ cylinder, that combustion of a stratified mixture could be the same, less, or more severe than a well-mixed mixture for the same amount of hydrogen. For the case of stratified mixtures with average concentrations of hydrogen below the downward flammability limits, the combustion pressures were significantly greater than well-mixed mixtures when ignited at the top of the vessel and about the same when ignited at the bottom. A higher concentration at the top leads to a considerably higher burn completeness in the stratified mixture for top ignition.

For the case with average concentrations above the downward flammability limits, the combustion pressures were nearly the same for top ignition and lower for bottom ignition. The burn completeness was near 100% for top ignition. Much higher flame speeds for top ignition and slower flame speeds for bottom ignition were observed in the stratified mixtures. Since stratification could result in an incomplete burn, one can conservatively neglect the stratification effects on combustion by assuming a complete burn.

2.10 Hydrogen Mixing and Distribution

The ability to predict hydrogen concentrations in the containment is crucial to the prediction of the occurrence of combustion and its consequences. Distribution of hydrogen concentrations depend on gas mixing rates which depend on a number of mechanisms, (1) jet entrainment (entrainment of surrounding gases by high momentum jet from a pipe break), (2) inter-compartmental flow (driven by pressure differences among compartments), (3) forced flow (induced by containment fans or sprays), (4) natural convection (induced by density differences and steam condensation), and (5) diffusion (molecular process). The time scales for the above mixing mechanisms range, in increasing order, from less than seconds for jet entrainment to days for diffusion.

2.10.1 Experiments

Several experimental programs were aimed at understanding the behavior of hydrogen mixing in a containment during a LOCA. The major programs were, in order of increasing test facility volume, (1) the Containment Systems Test Facility (CSTF) experiments (876 m³) in the U.S. during the early 1980s (Bloom et al., 1983), (2) the NUPEC's hydrogen mixing and distribution tests (1300 m³) in Japan during the early 1990s [Reference 41], and the Heiss Dampf Reaktor (HDR) program (11,000 m³) in Germany during the late 1980s [Reference 68,69, 70, 72]. In all these experiments, helium was used as a simulant gas instead of hydrogen for safety reasons. As for the geometry of the test facility(Figure 2-24), the CSTF simulated the highly simplified PWR ice condenser containment. The NUPEC facility simulated the large dry PWR containment with delicate internal structures typical of the Japanese and U.S. design. The HDR facility simulated the highly compartmentalized containment with a large dome. Among these facilities, the size of the HDR containment in terms of free volume (10000 m³) is the largest.

Up-scaling the experimental results to the actual scale is another challenge faced by engineers in all fields [Reference 21, 43].

What we have learned so far from small and relatively large scale experiments is that homogeneous mixing within the source compartment can be expected if the jet entrainment dominates the mixing. This occurs when the injection rates are high such that the characteristic Froude number is high. When the injection rates are low the buoyant plumes form instead of jets. Vertical stratification develops such that the region above the injection point is relatively well mixed and the region below the injection point remains unmixed for a much longer (diffusion) time scale. Natural convection alone can provide good mixing after termination of the jet. Forced air recirculation can increase mixing significantly.

2.10.2 Code Prediction

Information obtained from the experimental programs are utilized for identifying various mixing processes as well as for guiding the construction and validation of mathematical models to be used in the computer codes. Only through the use of computational models, can experimental results be applied to the actual containment scale and realistic accident conditions.

Fast-running lumped-parameter codes have limits in their ability to predict hydrogen concentrations. The lumped-parameter approach, which has been the backbone of accident analysis codes (such as MAAP4, CONTAIN, MELCOR, RALOC, and HECTR) since their inception, is based on a small number (say, in the range of 4 to 10 for a containment) of nodes (or volumes) interconnected by flow junctions. The momentum equations for the flow network are solved. No momentum is treated within the nodes. Quantities (such as temperature, pressure, and gas compositions) within the nodes are assumed to be uniformly mixed. Hence, intrinsically, the lumped-parameter codes cannot predict stratification of gases within the nodes, and the rate of mixing among nodes depends on the flow rate through junctions.

A limited number of code validations against HDR (Reference 22, 37) and NUPEC tests [Reference 40, 58, 60, 61] were organized by OECD/NEA as international standard problems ISP-29 and ISP-35, respectively. We learned from these exercises that the lumped-parameter codes do a reasonable job of predicting mixing when the processes are dominated by either high momentum jet, inter-compartmental flow, or forced flow, but not so good with the stratified conditions controlled by natural convection. In analyzing NUPEC test M-7-1 which was well mixed throughout the facility due to water sprays, all participating codes had difficulty in matching, to a reasonable degree, the helium concentrations in the lowest compartment and in the dead-end compartments that were not greatly affected by global mixing due to sprays. This is also the major failure of the lumped-parameter codes in predicting the gas concentrations in the HDR test E11.2 where gases below the injection compartment remained relatively unmixed resulting in global stratification.

2.10.3 Subnode Physics Model in MAAP4

To overcome the deficiency in coping with stratified conditions in the lumped parameter code, the subnodal phenomena must be considered. In the MAAP4 code, the so called "subnode physics" model was developed to account for stratification. The subnode physics model determines the condition required for flow stagnation in the node in question (based on pressure equilibrium with its horizontally connected node). The required condition is that the penetration depth (within the node in question) of the lighter gas entering from the node above through a vertically oriented junction, or of the heavier gas entering from the node below exceeds the distance required to clear the nearest horizontally oriented junction, then the junction is shut off to any buoyancy-driven flow. The model, hence, does not always allow buoyancy-driven flow through the vertically-oriented junction. The rate of gas mixing among various nodes can be then properly predicted.

The results of MAAP4 calculations of the HDR Test E11.2 with and without the subnode physics model are compared in Figure 2-25, Figure 2-26 and Figure 2-27 (Reference 17). Figure 2-25 shows an excellent improvement in the calculated gas temperature at 0 m elevation from a maximum error of ~36 K to about 6 K. Figure 2-26 and Figure 2-27 also show a very good improvement in the calculated gas concentration in the upper dome and at the 10 m elevation. It can be noted that the trend of the test data, which is incorrectly predicted without the subnode physics model, is correctly predicted by the addition of the subnode model.

The subnode physics model offers no guarantee of success to applications involving more complex flow networks than considered for the HDR test. This is an area that has not been thoroughly investigated.

2.11 Passive Auto-Catalytic Recombiners

Passive autocatalytic recombiners (PARs) are a passive hydrogen removal device for used in post-accident conditions that chemically combines hydrogen and oxygen gas molecules on catalytic surfaces into water vapor. Each PAR consists of an open-ended stainless-steel box with catalyst-coated elements inside, and a cover to protect the elements from water sprays [Reference 34]. The catalytic reaction can take place at ambient temperature and significantly low hydrogen concentration (~1 vol.%). The resulting reaction heat induces a chimney flow which provides self-start and self-feeding of the device. These properties make PARs a passive safety device. Typical removal rates per PAR unit are in the order of 60 m³ hydrogen per hour, which correlates to a heat contribution of approx. 180 kW [Reference 45]. The basic technical ability of PARs to reduce the amount of hydrogen in the containment atmosphere has been proven in several studies over the last two decades Blanchat [Reference 4], and OECD/NEA [Reference 39]

According to Reineke [Reference 45], PARs have a quick start. However, water deposited on the catalyst as well as other air-borne substances—which are expected to be numerous during a severe accident—may slow down the initial startup process. The catalysts used are not strictly selective for hydrogen and oxygen, and consequently may influence or may be influenced by atmospheric components. Recent research by (OECD/NEA, 2010) also indicates that PAR operation can dissolve previously formed stratified layers prior to PAR operation. There is also a possibility of local combustion initiated by hot catalyst sheets at high hydrogen concentrations leading to a pressure rise inside the containment and significantly change the composition and thermal conditions of the containment atmosphere.

The potential poisoning effect of PAR was also investigated by the OECD research (OECD/NEA, 2010). As described by Reineke (2012), PAR was exposed to excessive aerosol concentrations of insoluble tin oxide (SnO₂) representing insoluble aerosols, highly hygroscopic and sticky lithium nitrate (LiNO₃) solution droplets, steam and iodine, a potential catalyst poison. The results showed that even under such challenging conditions, PAR recombination efficiency remained in the range of 50-70 %. This is comparable to the results of the THAI HR series with similar thermal-hydraulic conditions, but without aerosols and iodine. Also, the onset of recombination occurred at hydrogen concentrations comparable to corresponding tests from the HR series. No major negative effects of aerosols and/or iodine on PAR performance could be observed.

There was an attempt to define the failure probability of PARs among Probabilistic Risk Analysis (PRA) engineers working in new nuclear plant designs. But it has been difficult to find a failure mode for PARs. As a general rule supported by experiments, however, these PARs do not fail. There are no moving parts whatsoever. The natural convection of containment forces air through the slats and the rest is a chemical process.

2.12 Relationship to Containment Failure Mechanisms

Hydrogen combustion could be a potential threat to containment integrity because of the increase in pressure and temperature during the event. The pressure has two components; the dynamic load and the static load. For slow deflagrations, the dynamic load is zero. For accelerated deflagrations there is a continuous increase in dynamic pressure. Theoretical predictions of detonation pressures are shown in Figure 2-12. The static pressure load on the containment is bounded by the AICC pressure. The actual static pressure is generally lower due to heat transfer to structures during the event and in some cases due to incomplete combustion. The dynamic load during a detonation lasts only for a period of milliseconds and may be unable to cause containment failure, though equipment damage may still be possible. Because flames may accelerate during a deflagration, equipment damage may occur due to a local impulse loading. The deflagration temperature load is rather insignificant, in general, because it only lasts from tens of seconds to a few minutes, with a brief peak and sharp decay. An impulse (integral of pressure over time) analysis is required for dynamic pressures. The existence of a combustion event does not automatically imply containment failure. The combustion pressure must be compared against a

containment failure criteria. The containment failure criteria should include the pressure versus impulse curves for the containment failure modes and the maximum pressure and impulse available from combustion, if detonation impacts need to be evaluated.

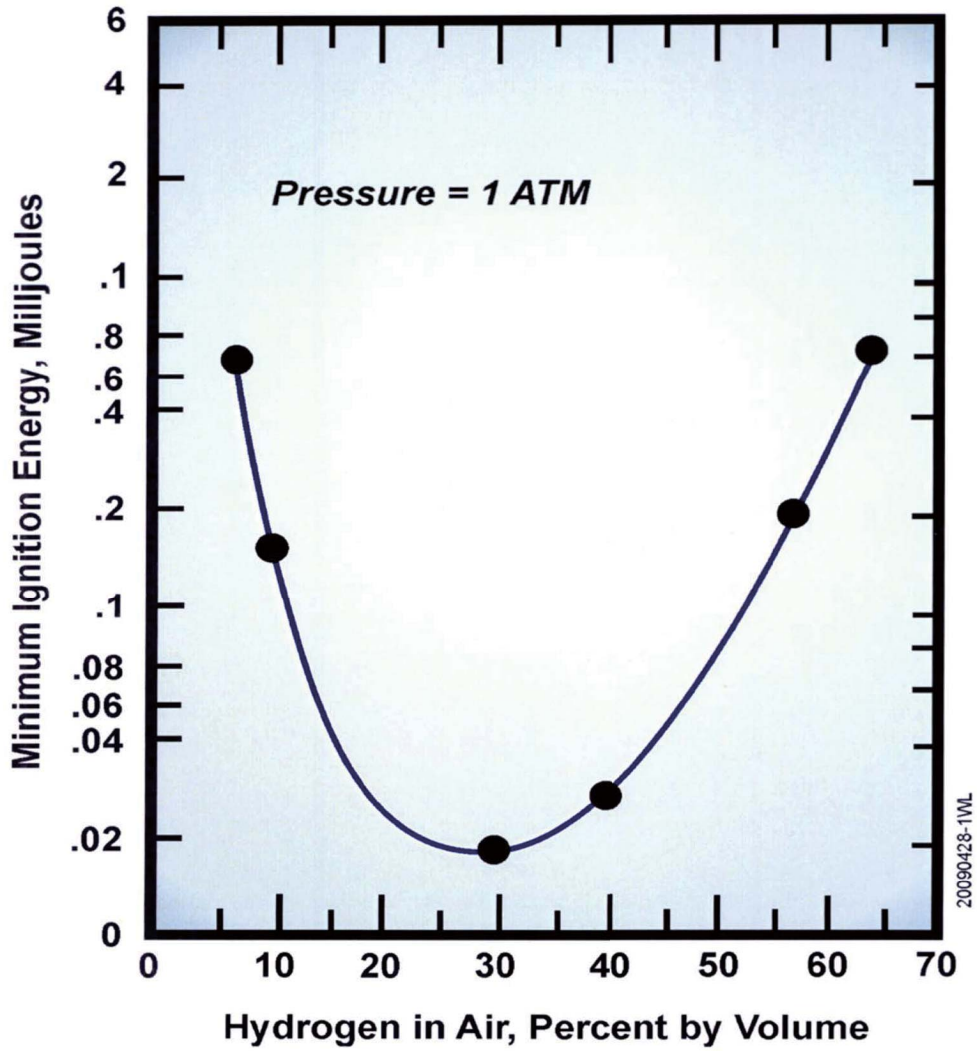


Figure 2-1 Minimum Ignition Energy for Hydrogen Deflagrations [Reference 7]

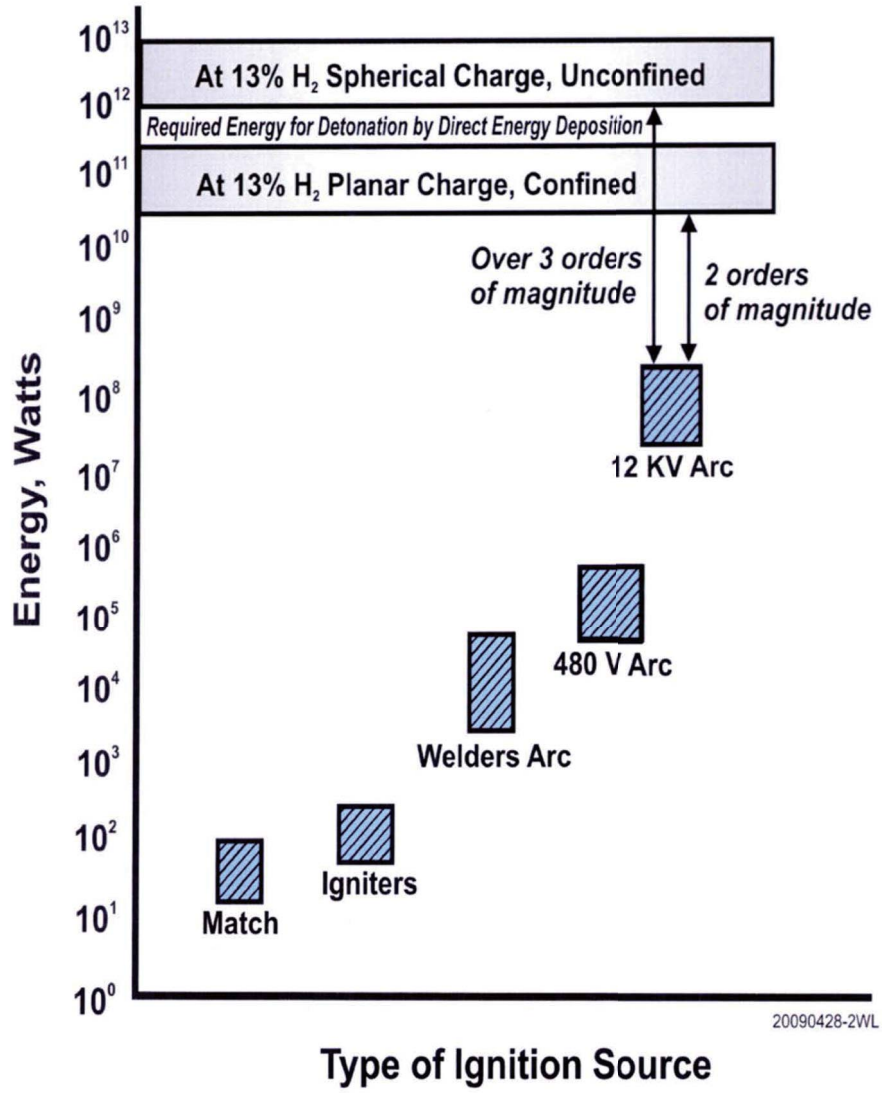


Figure 2-2 Type of Ignition Source Energies with Sources Required for Detonation by Direct Energy Deposition [Reference 16]

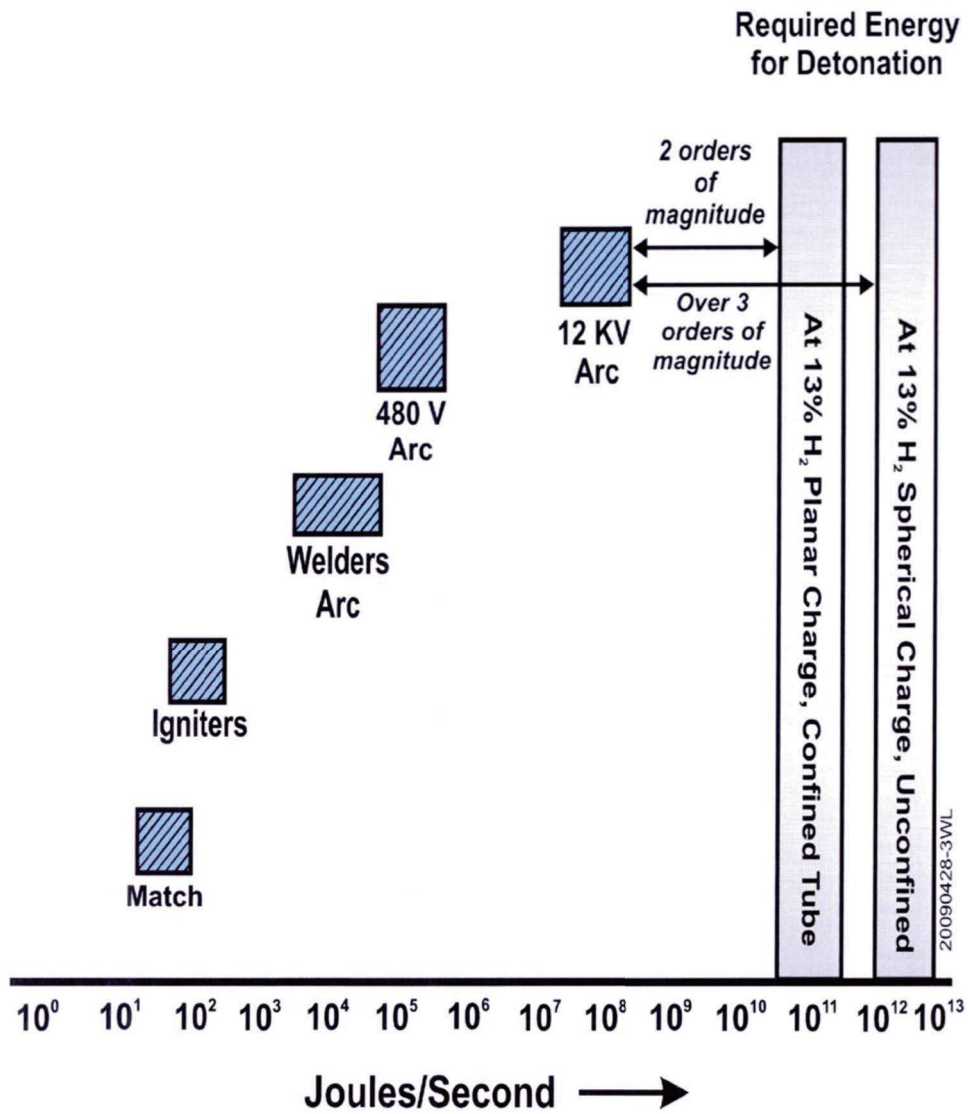


Figure 2-3 Comparison of Ignition Source Energies with Sources Required for Detonation by Direct Energy Deposition [Reference 16]

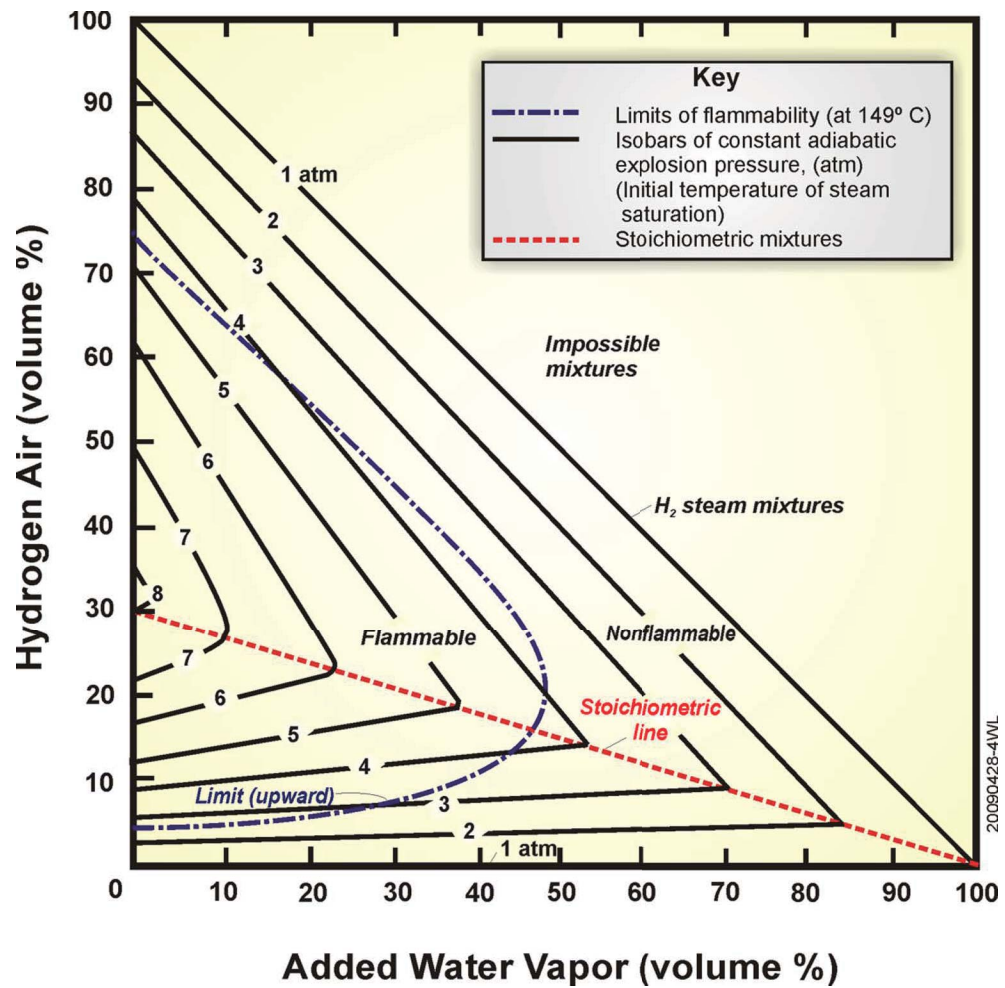


Figure 2-4 Flammability Domain for upward Propagation for H₂-Air- H₂O vapor mixtures.[Reference 19]

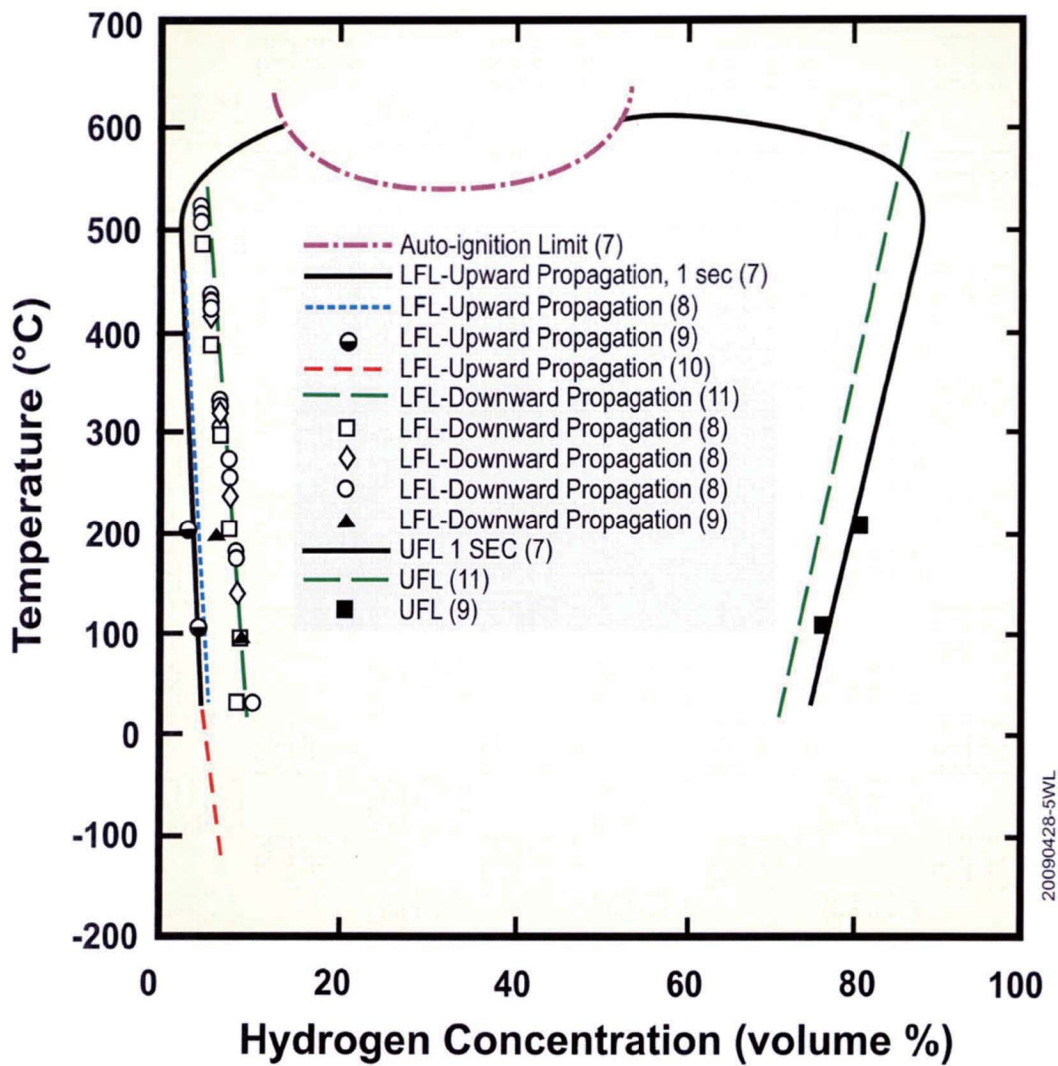


Figure 2-5 Comparison of Lower Flammability Limits (LFL) and Upper Flammability Limits (UFL) of hydrogen-air-mixtures as a function of initial temperature [Reference 53]

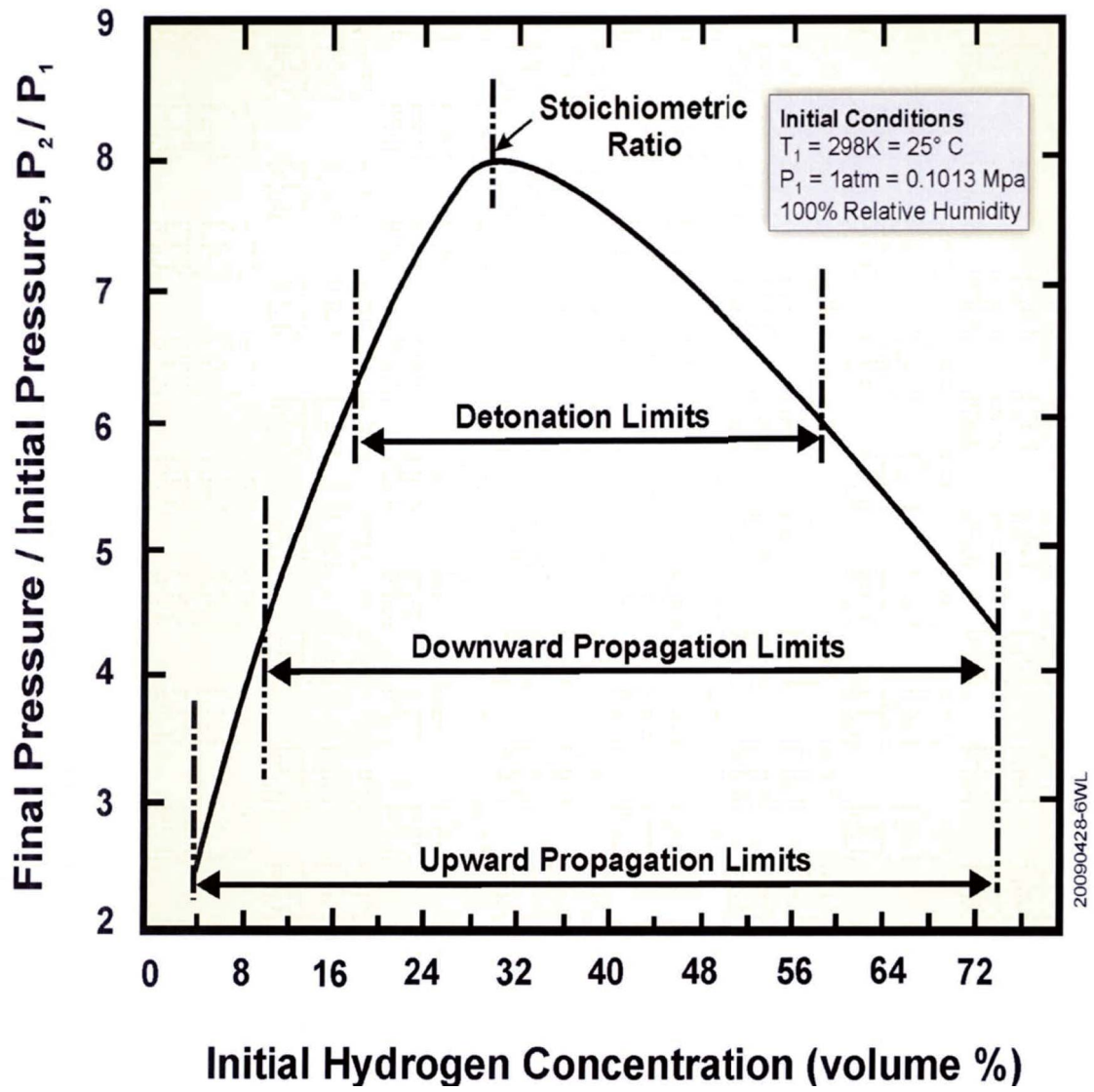


Figure 2-6 Theoretical adiabatic, constant volume combustion pressure ratios of hydrogen-air mixtures [Reference 52]

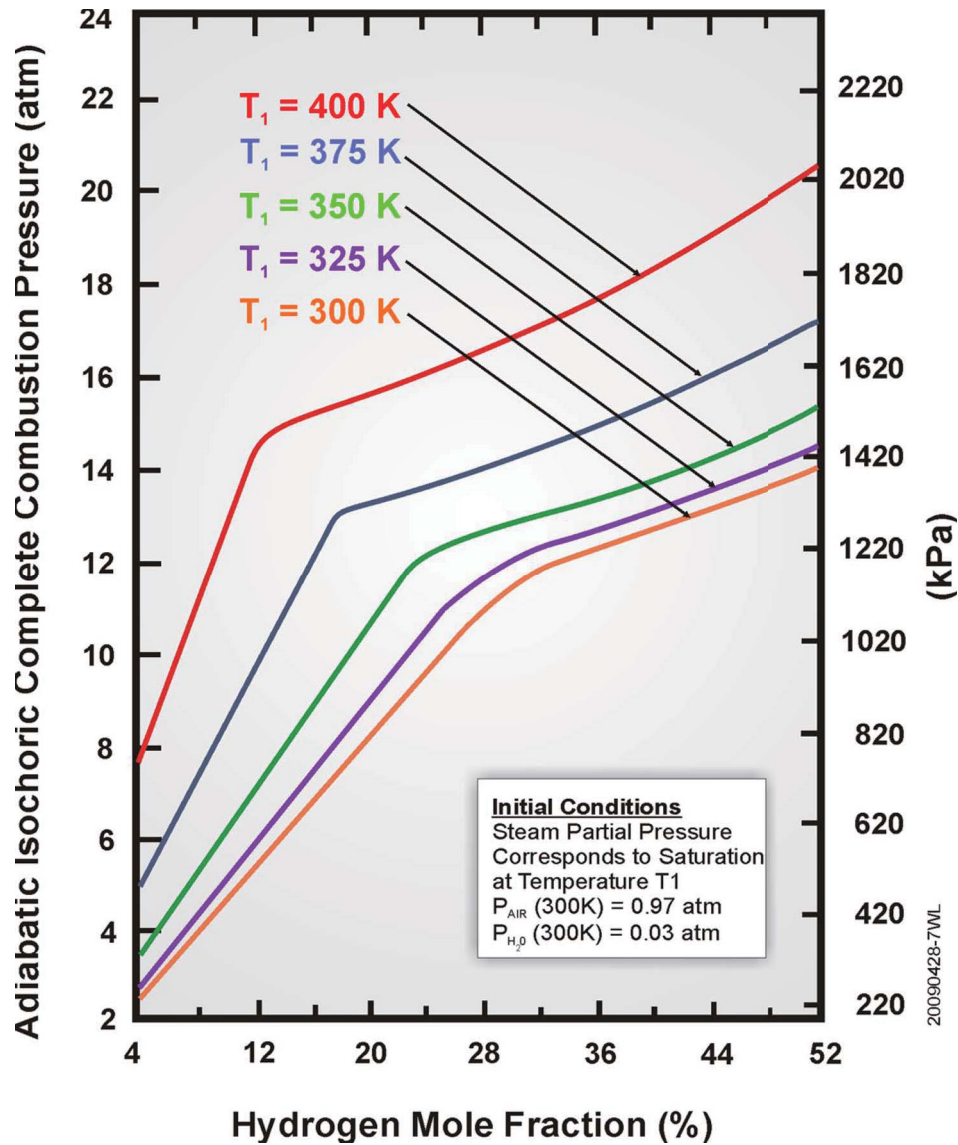


Figure 2-7 AICC pressures for various containment initial conditions [Reference 50]

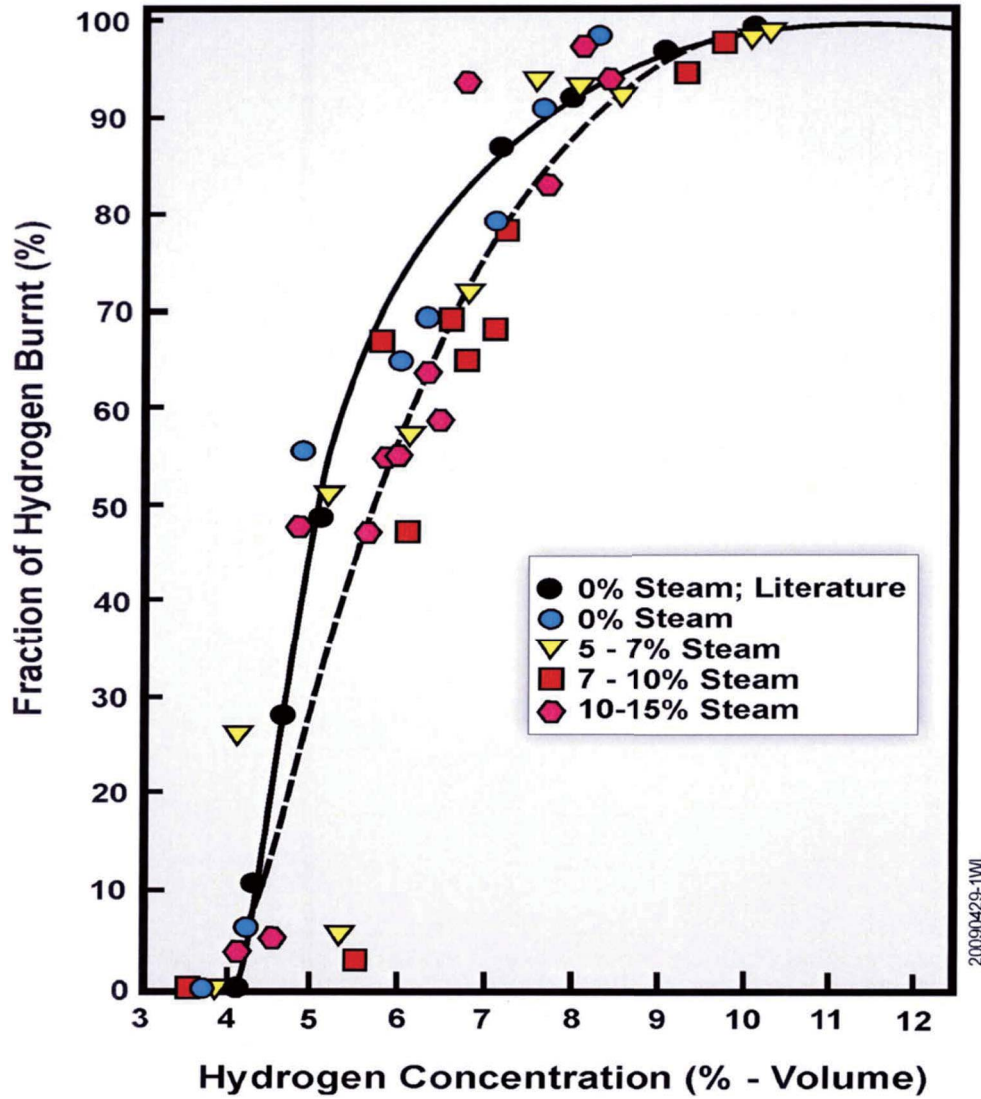


Figure 2-8 Degrees of Combustion in Hydrogen Air Steam Mixtures [Reference 29]

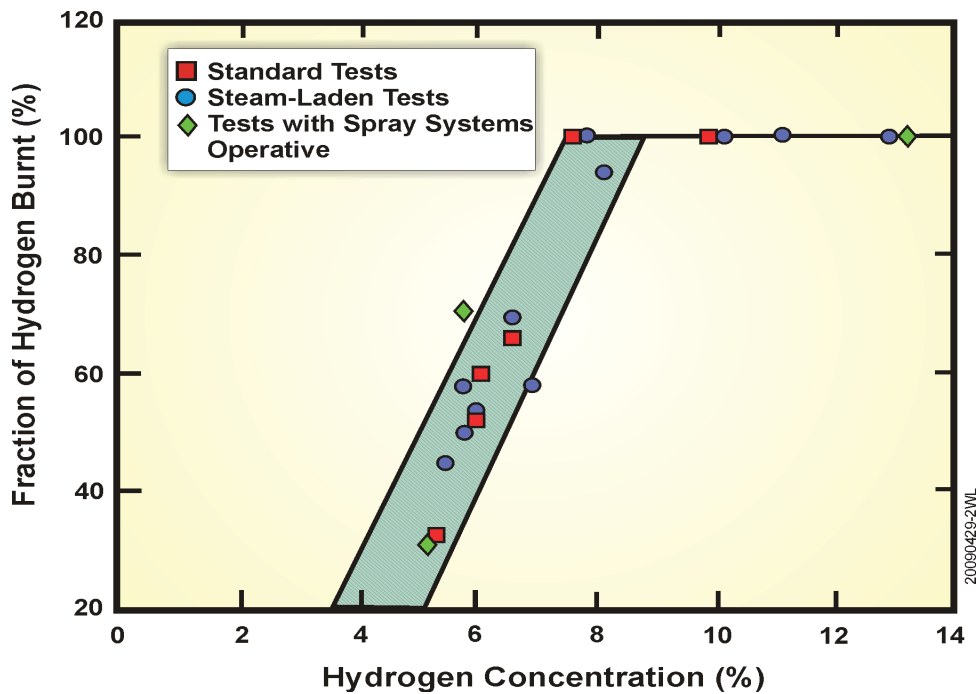


Figure 2-9 Hydrogen concentration during incomplete burning [Reference 44]

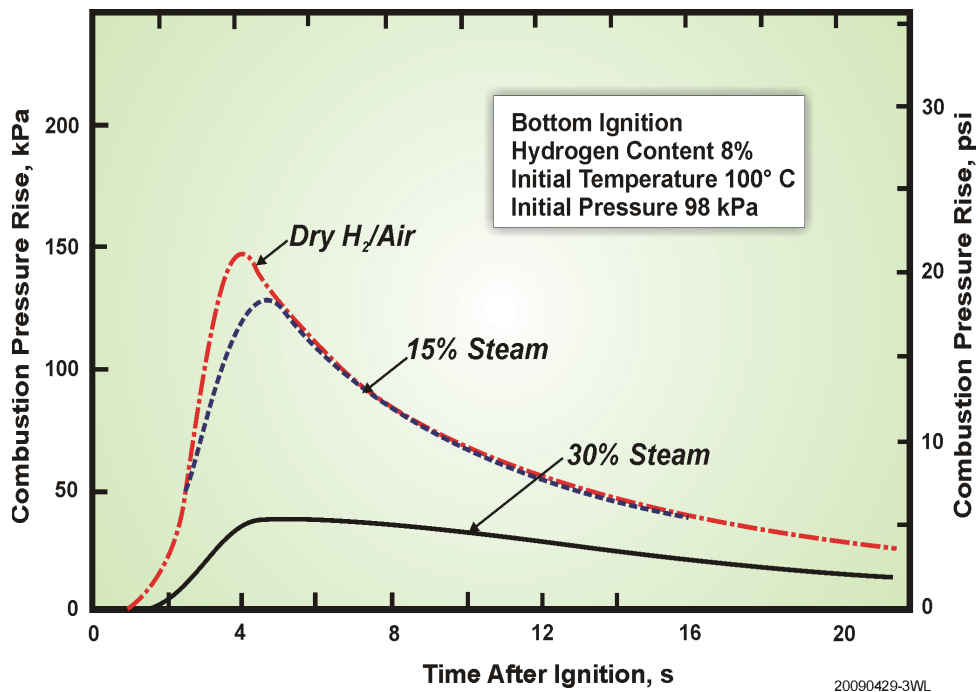
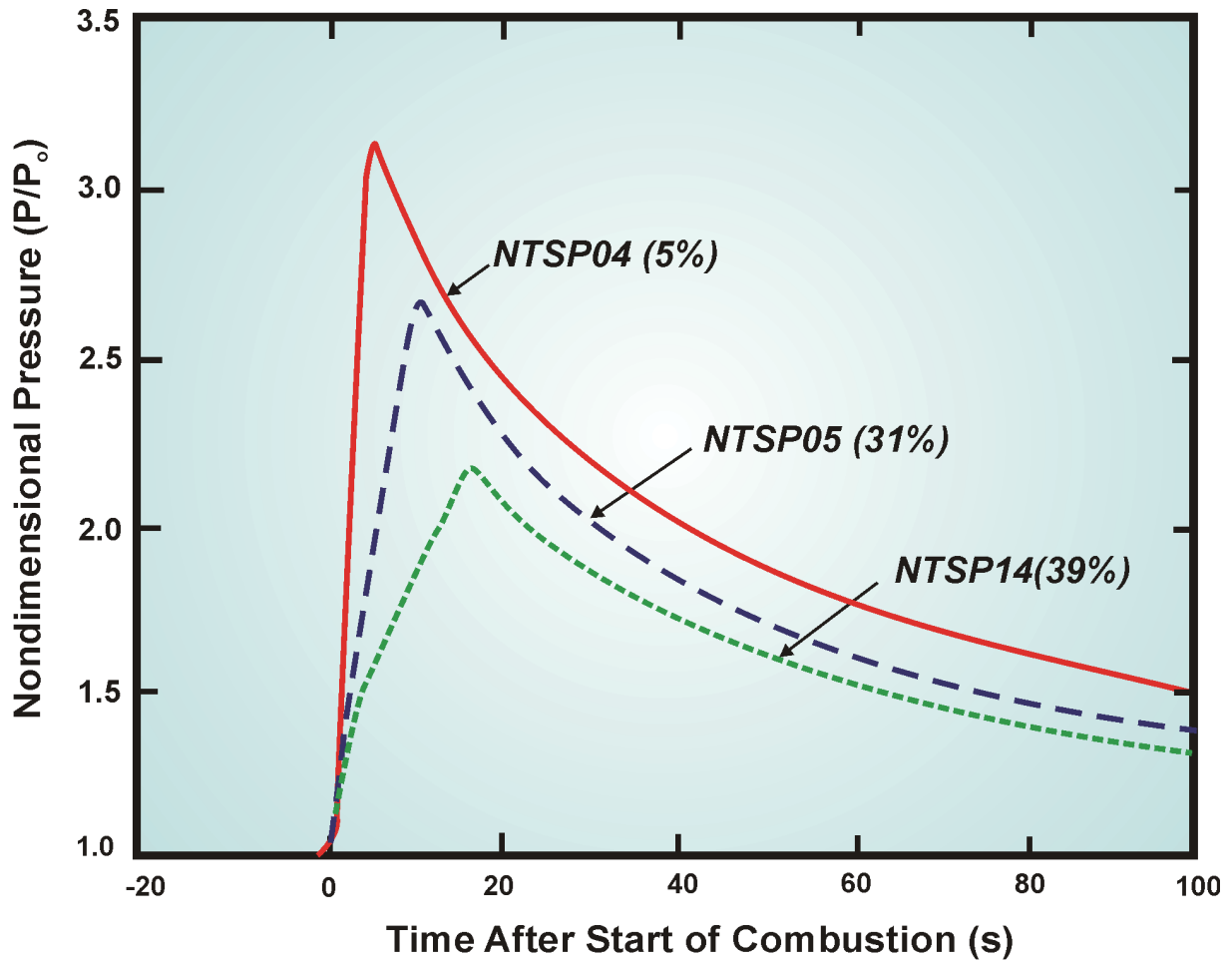


Figure 2-10 Combustion Completeness for Nevada Test Site Premixed Combustion Tests [Reference 44]



20090429-4WL

Figure 2-11 Comparative pressure profiles for three 8% (nominal) hydrogen combustion tests having different pre combustion steam concentrations. [Reference 44]

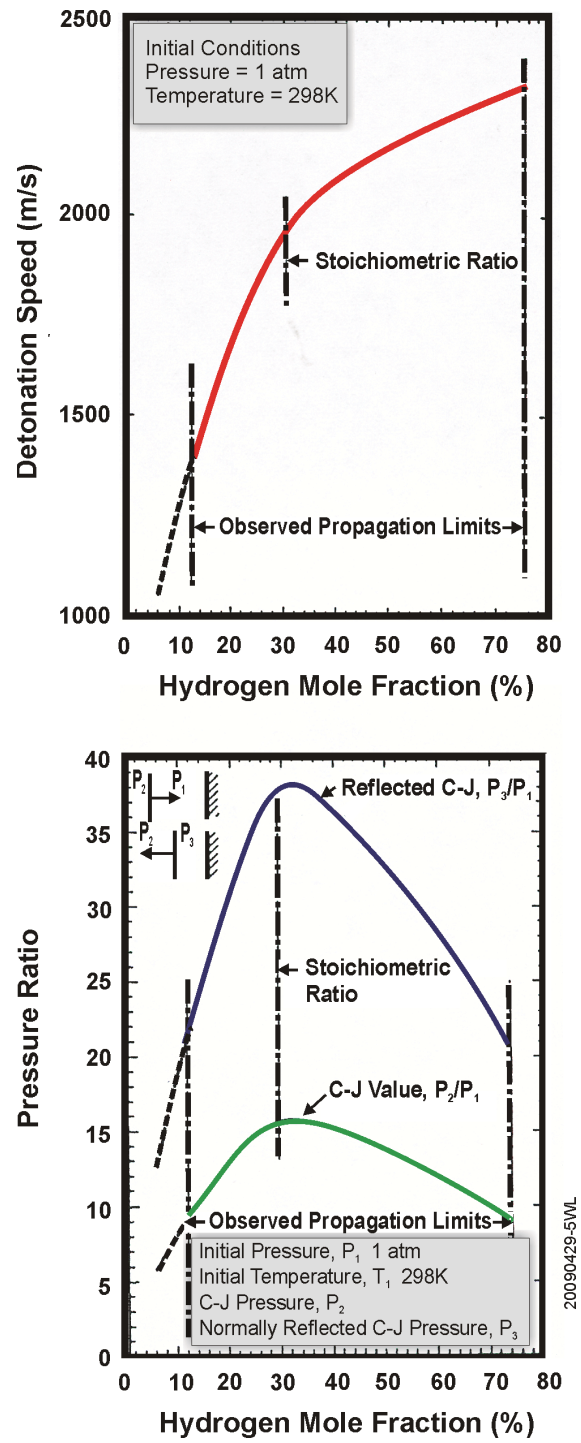


Figure 2-12 Detonation pressure ratios (below) and speed (above) for hydrogen-air mixtures [Reference 66]

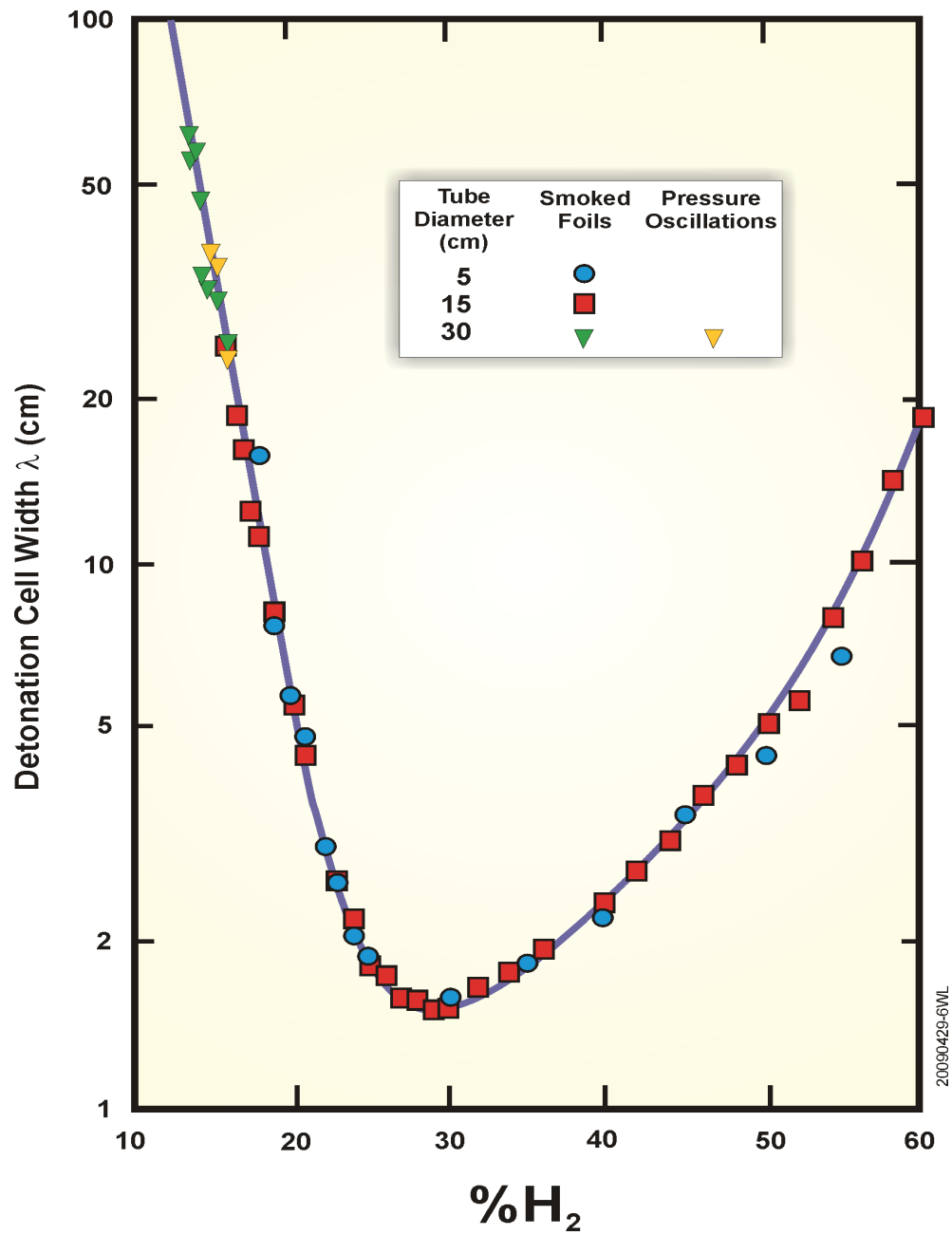


Figure 2-13 Measured values (McGrill, Sandia) of the detonation cell width (λ) as a function of hydrogen concentration [Reference 65]

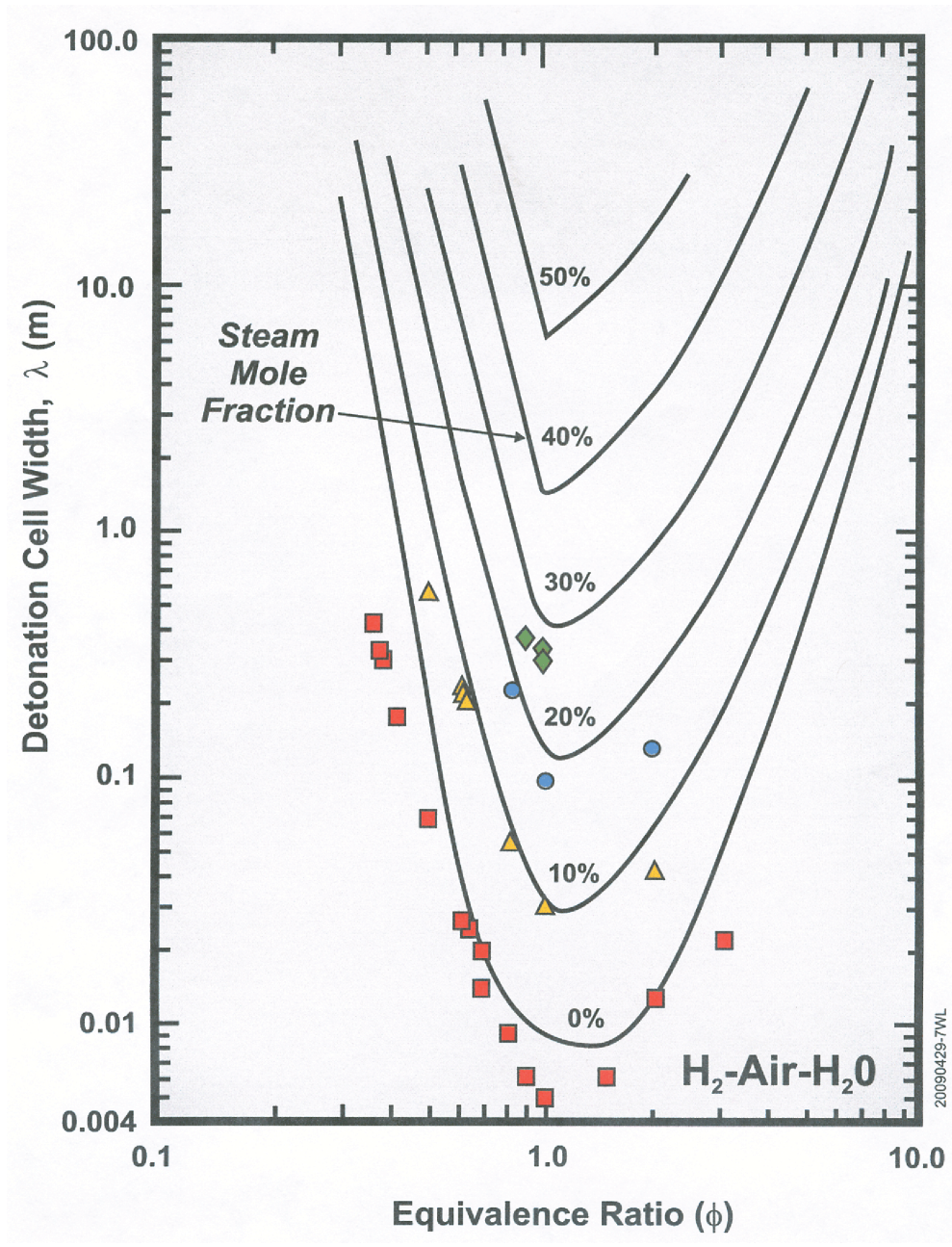


Figure 2-14 Detonation Cell Width Data (Sandia HDT) and Predictions (Shepherd Model) (H₂-air-steam, air density = 1.184 kg/m³, T = 100°C for data, T = saturation for prediction). [Reference 57]

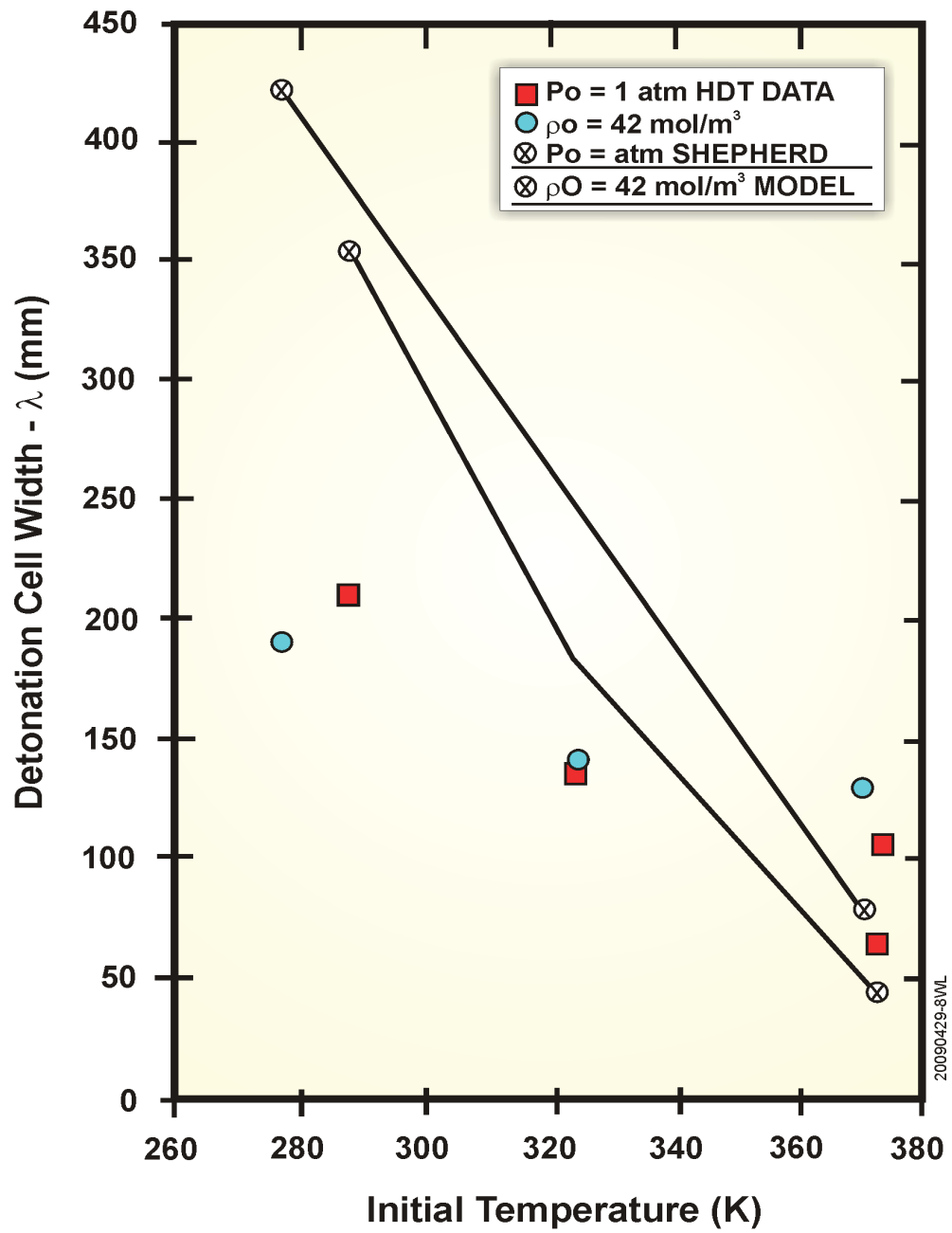
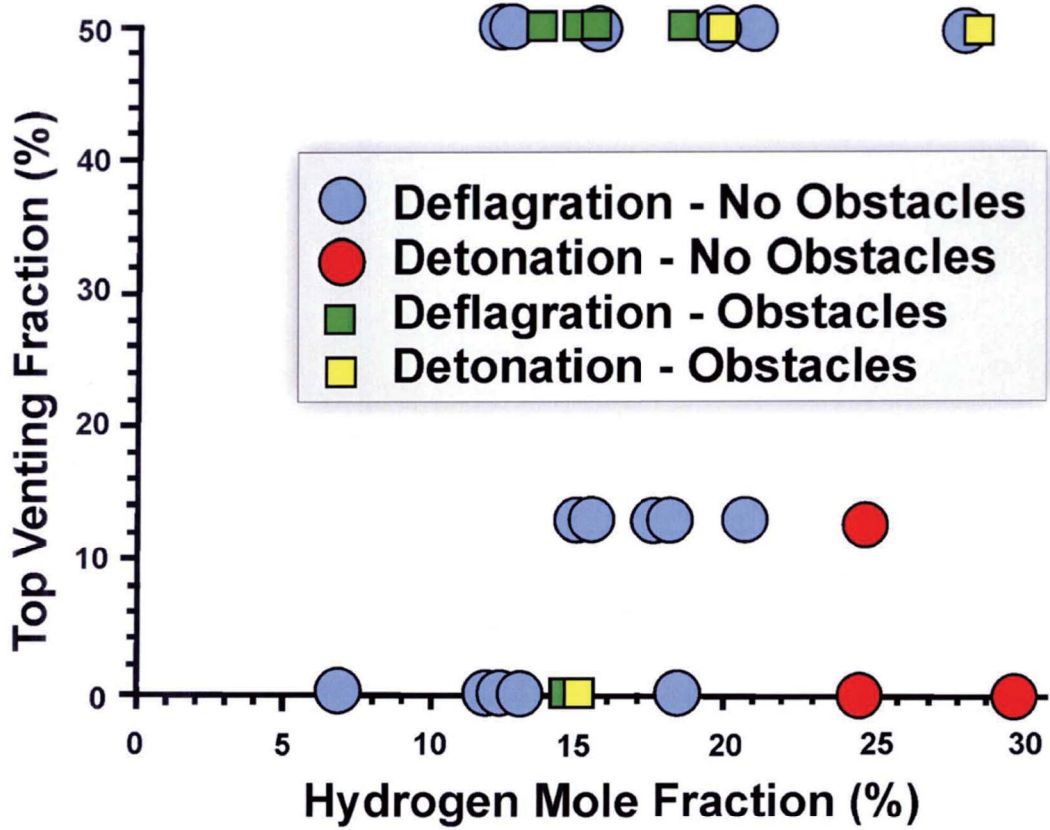
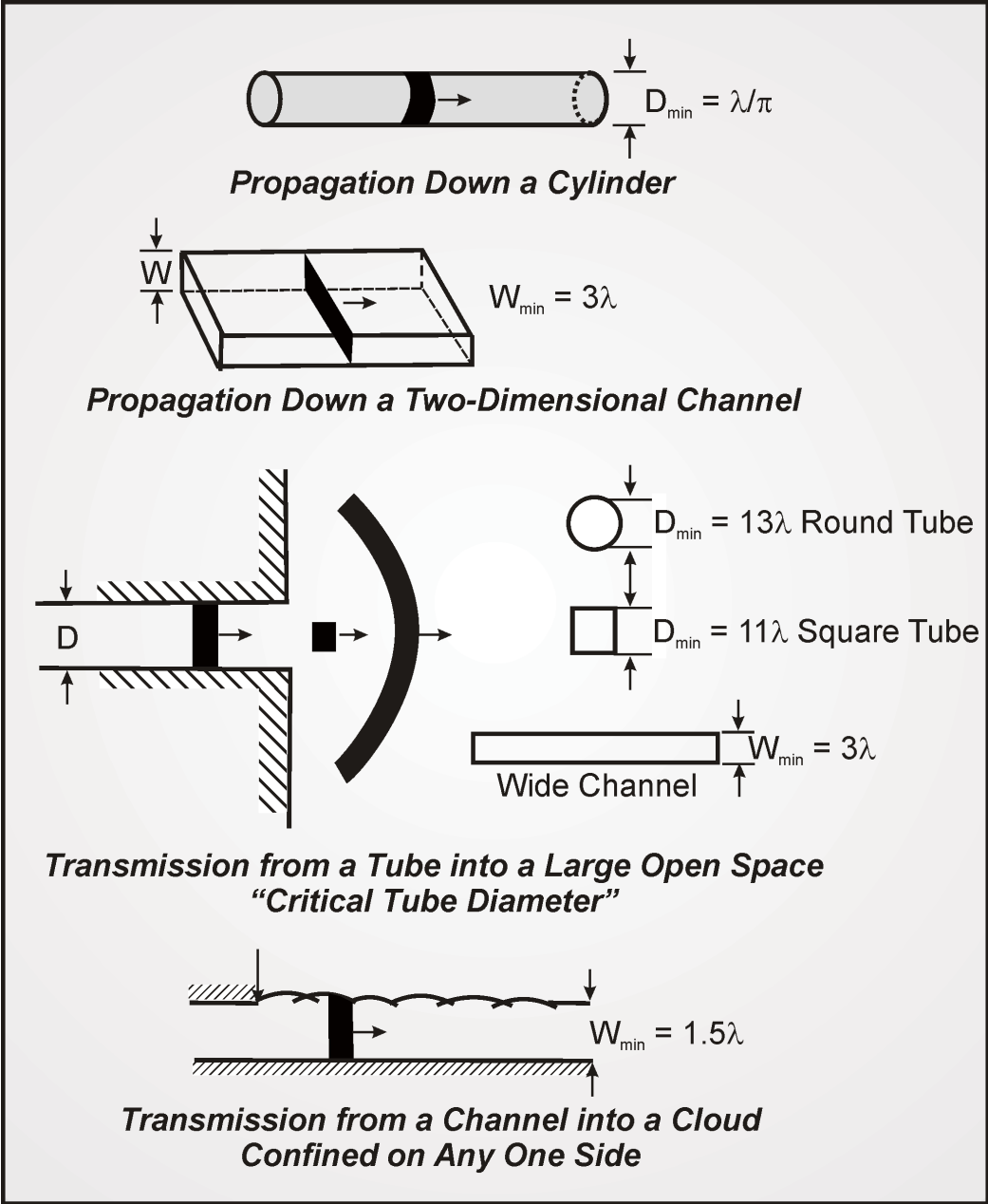


Figure 2-15 Detonation cell width as a function of temperature [Reference 65]



20090429-9WL

Figure 2-16 Deflagration-to-detonation transition (DDT) results from the FLAME facility at Sandia [Reference 53]



20090429-10WL

Figure 2-17 Detonation Propagation and Transmission Correlations for Simple Geometries [Reference 65]

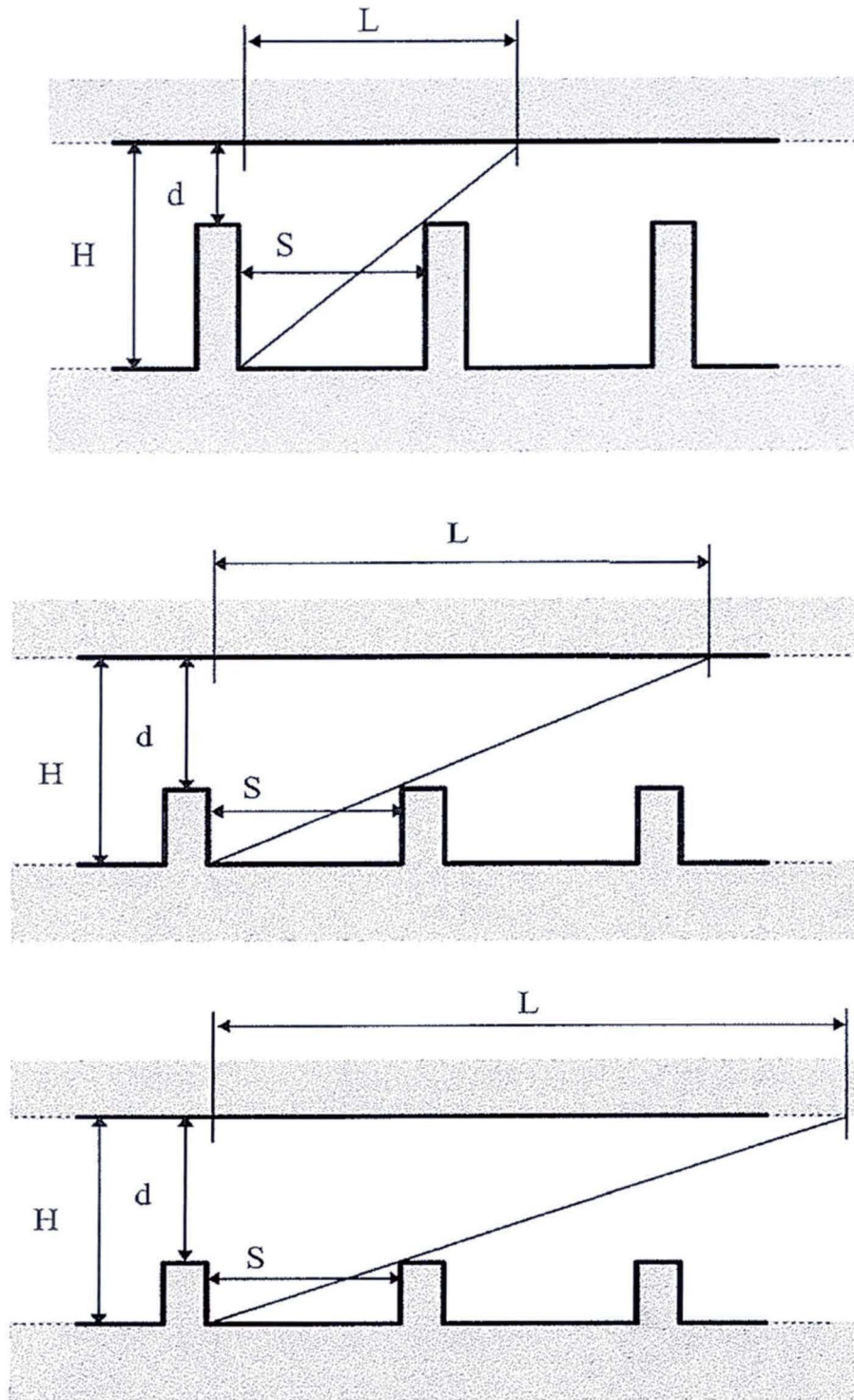


Figure 2-18 Illustration of Characteristic Size L for Channels with Obstacles and Varying Blockage Ratio [Reference 6]

Table 2-1 Experiments Used in Correlations for Flame Acceleration Criterion

Data source	Label	Blockage ratio BR	Tube or channel size L, mm	Initial temperature T, K	Mixture type	Equivalence ratio ϕ
HTCF-BNL [3.11]	b1	0.43	273	300	H ₂ /air	<1
HTCF-BNL [3.11]	b2	0.43	273	500	H ₂ /air	<1
HTCF-BNL [3.11]	b3	0.43	273	650	H ₂ /air	<1
HTCF-BNL [3.11]	b4	0.43	273	400	H ₂ /air/H ₂ O	<1
HTCF-BNL [3.11]	b5	0.43	273	500	H ₂ /air/H ₂ O	<1
HTCF-BNL [3.11]	b6	0.43	273	650	H ₂ /air/H ₂ O	<1
CHANNEL-RRCKI [3.9]	c1	0.1	80	293	H ₂ /air	<1; >1
CHANNEL-RRCKI [3.9]	c2	0.3	80	293	H ₂ /air	<1; >1
CHANNEL-RRCKI [3.9]	c3	0.6	80	293	H ₂ /air	<1; >1
CHANNEL-RRCKI [3.9]	c4	0.9	80	293	H ₂ /air	<1; >1
CHANNEL-RRCKI [3.9]	c5	0.6	80	293	H ₂ /O ₂ /He	1
CHANNEL-RRCKI [3.9]	c6	0.6	80	293	H ₂ /O ₂ /Ar	1
DRIVER-RRCKI [3.9]	d1	0.09	174	293	H ₂ /air	<1; >1
DRIVER-RRCKI [3.9]	d2	0.3	174	293	H ₂ /air	<1; >1
DRIVER-RRCKI [3.9]	d3	0.6	174	293	H ₂ /air	<1; >1
DRIVER-RRCKI [3.9]	d4	0.9	174	293	H ₂ /air	<1; >1
DRIVER-RRCKI [3.9]	d5	0.09	174	293	H ₂ /O ₂ /N ₂	1
DRIVER-RRCKI [3.9]	d6	0.3	174	293	H ₂ /O ₂ /N ₂	1
DRIVER-RRCKI [3.9]	d7	0.6	174	293	H ₂ /O ₂ /N ₂	1
DRIVER-RRCKI [3.9]	d8	0.9	174	293	H ₂ /O ₂ /N ₂	1
DRIVER-RRCKI [3.9]	e1	0.09	174	293	H ₂ /O ₂ /He	1
DRIVER-RRCKI [3.9]	e2	0.3	174	293	H ₂ /O ₂ /He	1
DRIVER-RRCKI [3.9]	e3	0.6	174	293	H ₂ /O ₂ /He	1
DRIVER-RRCKI [3.9]	e5	0.09	174	293	H ₂ /O ₂ /Ar	1
DRIVER-RRCKI [3.9]	e6	0.3	174	293	H ₂ /O ₂ /Ar	1
DRIVER-RRCKI [3.9]	e7	0.6	174	293	H ₂ /O ₂ /Ar	1
FLAME-SNL [3.15]	f1	0.33	1830	293	H ₂ /air	<1
FLAME-SNL [3.15]	f2	0	1830	293	H ₂ /air	<1
FZK [3.9]	g1	0.6	350	293	H ₂ /air	<1; >1
FZK [3.9]	g2	0.6	350	293	H ₂ /O ₂ /N ₂	1
FZK [3.9]	g3	0.6	350	293	H ₂ /O ₂ /He	1
FZK [3.9]	g4	0.6	350	293	H ₂ /O ₂ /Ar	1
FZK [3.9]	g5	0.6	350	293	H ₂ /O ₂ /CO ₂	1
FZK [3.9]	g6	0.6	350	293	H ₂ /air/CO ₂	.5
FZK [3.9]	g7	0.6	350	293	H ₂ /air/CO ₂	1
FZK [3.9]	g8	0.6	350	293	H ₂ /air/CO ₂	2
FZK [3.9]	g9	0.6	350	293	H ₂ /air/CO ₂	4

continued . . .

Table 2-1 Experiments Used in Correlations for Flame Acceleration Criterion
(Continued)

Data source	Label	Blockage ratio BR	Tube or channel size L, mm	Initial temperature T, K	Mixture type	Equivalence ratio ϕ
RUT-RRCKI [3.13]	r1	0.6	2250	293	H ₂ /air	<1
RUT-RRCKI [3.13]	r2	0.3	2250	293	H ₂ /air	<1
RUT-RRCKI [3.13]	r3	0	2250	293	H ₂ /air	<1
RUT-RRCKI [3.14]	r4	0.3	2250	375	H ₂ /air/H ₂ O	≤1
HDT-SNL [3.12]	s1	0.6	406	383	H ₂ /air	>1
HDT-SNL [3.12]	s2	0.3	406	383	H ₂ /air/H ₂ O	>1
TORPEDO-RRCKI [3.9]	t1	0.6	520	293	H ₂ /air	<1; >1
TORPEDO-RRCKI [3.9]	t2	0.6	520	293	H ₂ /O ₂ /He	1
TORPEDO-RRCKI [3.9]	t3	0.3	520	293	H ₂ /air	<1; >1
TORPEDO-RRCKI [3.9]	t4	0.1	520	293	H ₂ /air	<1; >1

Table 2-2 Experiments Used in the L/λ Correlation for Onset of Detonations

Data source	Label	Blockage ratio BR	Tube or channel size <i>D</i> (H), mm	Initial temperature <i>T</i> , K	Mixture type	Equivalence ratio ϕ
AECL [3.21]	a1	0.31	280	373	H ₂ /air/H ₂ O	
HTCF-BNL [3.11]	b1	0.43	273	300	H ₂ /air	<1
HTCF-BNL [3.11]	b2	0.43	273	500	H ₂ /air	<1
HTCF-BNL [3.11]	b3	0.43	273	650	H ₂ /air	<1
HTCF-BNL [3.11]	b4	0.43	273	400	H ₂ /air/H ₂ O	<1
HTCF-BNL [3.11]	b5	0.43	273	500	H ₂ /air/H ₂ O	<1
HTCF-BNL [3.11]	b6	0.43	273	650	H ₂ /air/H ₂ O	<1
CHANNEL-RRCKI [3.9]	c1	0.1	80	293	H ₂ /air	<1; >1
CHANNEL-RRCKI [3.9]	c2	0.3	80	293	H ₂ /air	<1; >1
CHANNEL-RRCKI [3.9]	c3	0.6	80	293	H ₂ /air	<1; >1
DRIVER-RRCKI [3.9]	d1	0.09	174	293	H ₂ /air	<1; >1
DRIVER-RRCKI [3.9]	d2	0.3	174	293	H ₂ /air	<1; >1
DRIVER-RRCKI [3.9]	d3	0.6	174	293	H ₂ /air	<1; >1
DRIVER-RRCKI [3.9]	d4	0.9	174	293	H ₂ /air	<1
FLAME-SNL [3.15]	f1	0.33	1830	293	H ₂ /air	<1
mini-FLAME-SNL [3.47]	f3	0.33	150	293	H ₂ /air	<1
FZK [3.9]	g1	0.6	350	293	H ₂ /air	<1; >1
FZK [3.9]	g2	0.6	350	293	H ₂ /O ₂ /N ₂	1
FZK [3.9]	g3	0.3	350	293	H ₂ /air	1
FZK [3.9]	g6	0.6	350	293	H ₂ /air/CO ₂	.5
FZK [3.9]	g7	0.6	350	293	H ₂ /air/CO ₂	1
FZK [3.9]	g8	0.6	350	293	H ₂ /air/CO ₂	2
FZK [3.9]	g9	0.6	350	293	H ₂ /air/CO ₂	4
McGill [3.25]	m1	0.44	16 x 57 x 50	293	H ₂ /air	<1
McGill [3.25]	m2	0.44	16 x 57 x 100	293	H ₂ /air	<1
McGill [3.26]	m3	0.43	50	293	H ₂ , CH-fuels/air	<1
McGill [3.26]	m4	0.43	150	293	H ₂ , CH-fuels/air	<1
McGill [3.26]	m5	0.43	300	293	H ₂ , CH-fuels/air	<1
McGill [3.27]	m6	0.44	65 x 52 x 32	293	H ₂ , CH-fuels/air	<1
McGill [3.27]	m7	0.44	65 x 52 x 64	293	H ₂ , CH-fuels/air	<1
McGill [3.27]	m8	0.44	65 x 52 x 128	293	H ₂ , CH-fuels/air	<1
RUT-RRCKI [3.13]	r1	0.6	2250	293	H ₂ /air	<1
RUT-RRCKI [3.13]	r2	0.3	2250	293	H ₂ /air	<1
RUT-RRCKI [3.13]	r3	room	10.5 x 6 x 2.3 m	293	H ₂ /air	<1
RUT-RRCKI [3.14]	r4	room	10.5 x 6 x 2.3 m	375	H ₂ /air/H ₂ O	≤1
RUT-RRCKI [3.14]	r5	0.3	2250	375	H ₂ /air/H ₂ O	≤1
RUT-RRCKI [3.40]	r6	0.3	2250	293	H ₂ /air/CO ₂	<1
RUT-RRCKI [3.40]	r7	room	10.5 x 6 x 2.3 m	293	H ₂ /air/CO ₂	<1
RUT-RRCKI [3.45]	ri	room	15 x 6 x 2.3 m	293	H ₂ -injection	≤1

continued . . .

Table 2-2 Experiments Used in the L/λ Correlation for Onset Detonations (Continued)

Data source	Label	Blockage ratio BR	Tube or channel size D (H), mm	Initial temperature T , K	Mixture type	Equivalence ratio ϕ
HDT-SNL [3.12]	s1	0.6	406	383	H ₂ /air	>1
HDT-SNL [3.12]	s2	0.3	406	383	H ₂ /air/H ₂ O	>1
TORPEDO-RRCKI [3.9]	t1	0.6	520	293	H ₂ /air	<1; >1
TORPEDO-RRCKI [3.9]	t3	0.3	520	293	H ₂ /air	<1; >1
TORPEDO-RRCKI [3.9]	t4	0.1	520	293	H ₂ /air	<1; >1
mini-RUT-RRCKI [3.44]	v1	0.3	46	293	H ₂ /air	<1
mini-RUT-RRCKI [3.44]	v2	room	210 x 120 x 50	293	H ₂ /air	<1

Table 2-3 References Cited in Tables 2-1 and 2-2

Number	References
3.9	[Kuznetsov et al. 1999]
3.11	[Cicarelli et al. 1998]
3.12	[Sherman et al. 1993]
3.13	[Dorofeev et al. 1996]
3.14	[Dorofeev et al. 1997]
3.15.	[Sherman et al. 1989]
3.21	[Chan et al. 1996]
3.25	[Teodorczyk et al. 1990]
3.26	[Lee et al. 1984]
3.27	[Teodorczyk et al 1988]
3.38	[Sidorov et al. 1998 (a)]
3.39	[Sidorov et al. 1998 (b)]
3.40	[Sidorov et al. 1999]
3.44	[Dorofeev et al. 1999]
3.45	[Matsukov et al. 1999]
3.47	[Sherman et al. 1989]

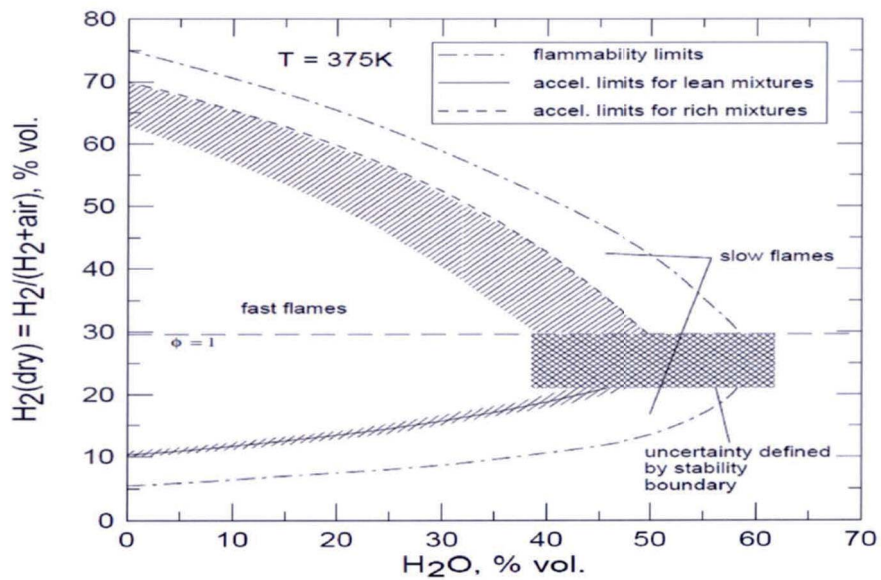


Figure 2-19 Limits of Flame Acceleration for Hydrogen-Air-Steam Mixtures at 375 K and 1 atm. [Reference 6]

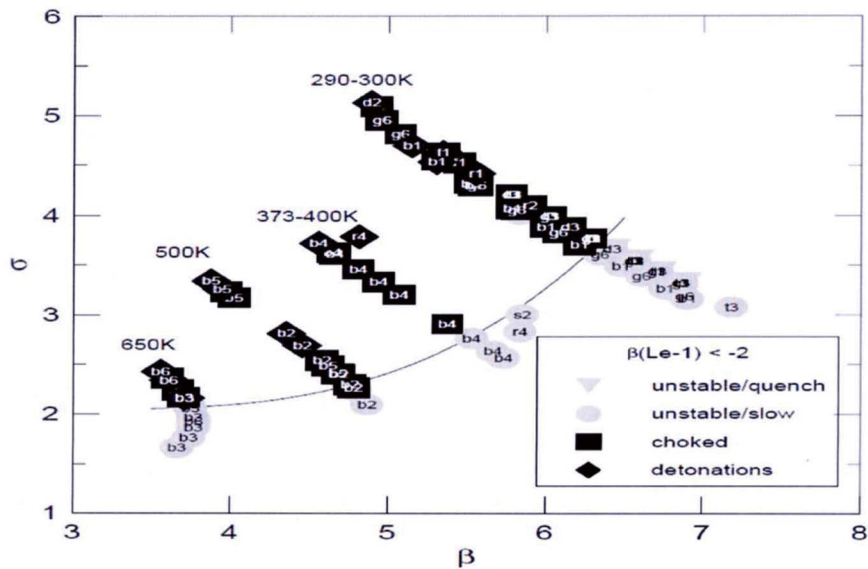


Figure 2-20 Combustion regime as function of expansion ratio σ and Zeldovich number β for hydrogen-lean mixtures (i.e., $\beta(Le-1) < -2$). [Reference 6]

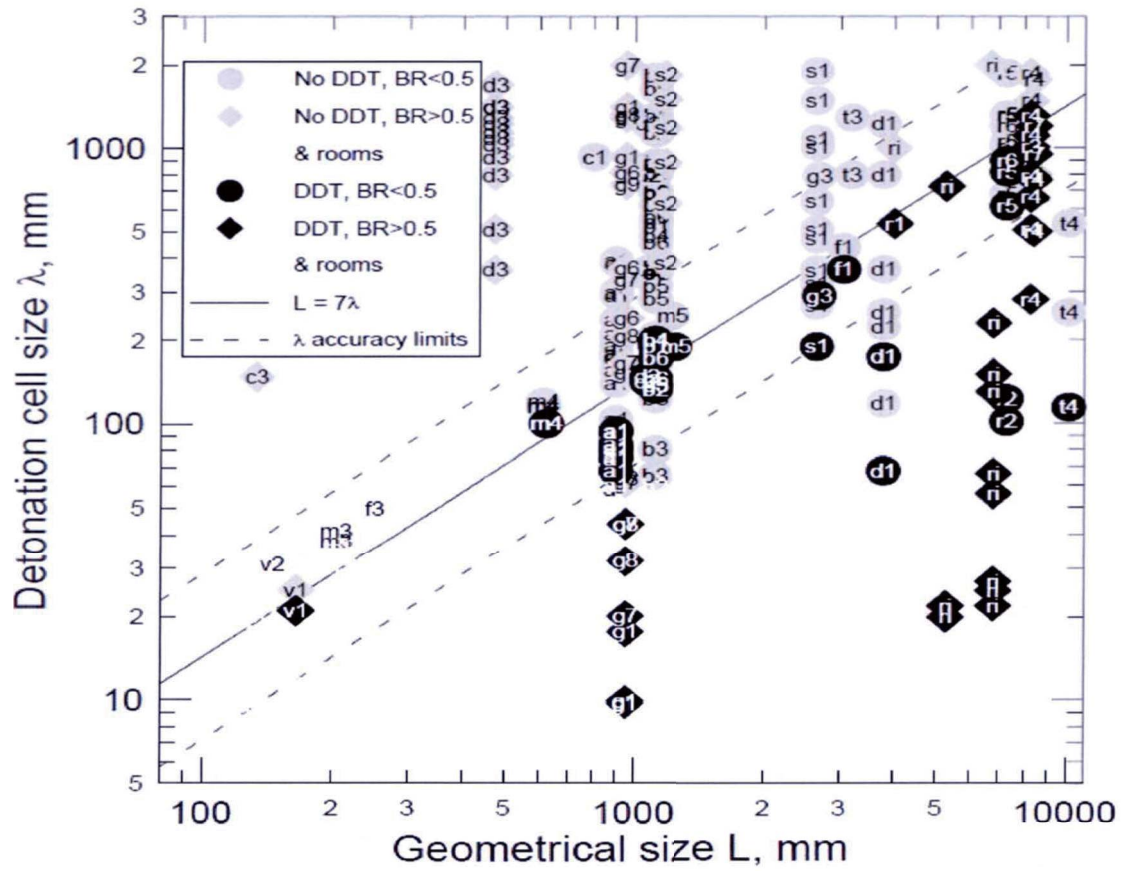
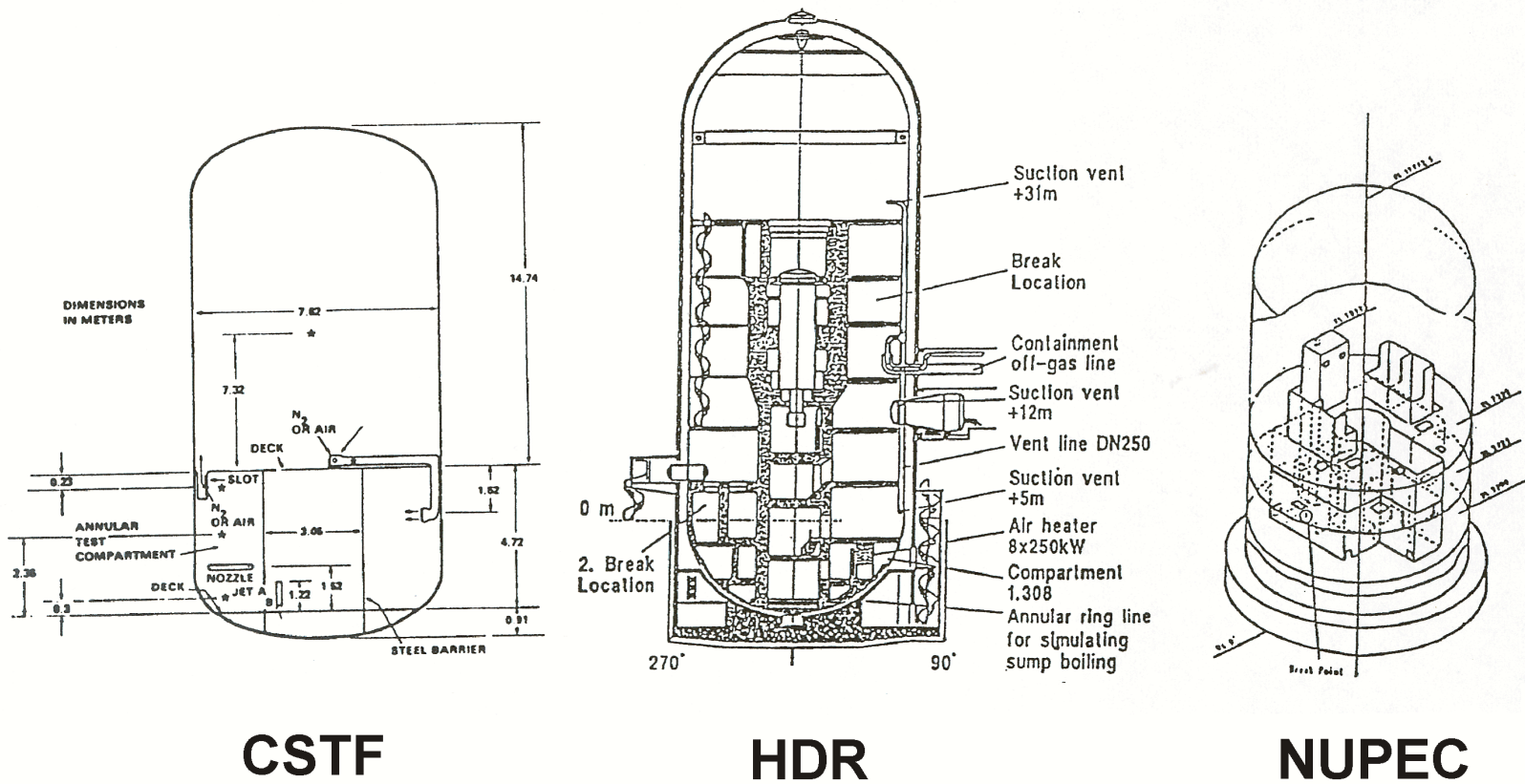


Figure 2-23 L/λ correlation for onset of detonations [Reference 6]



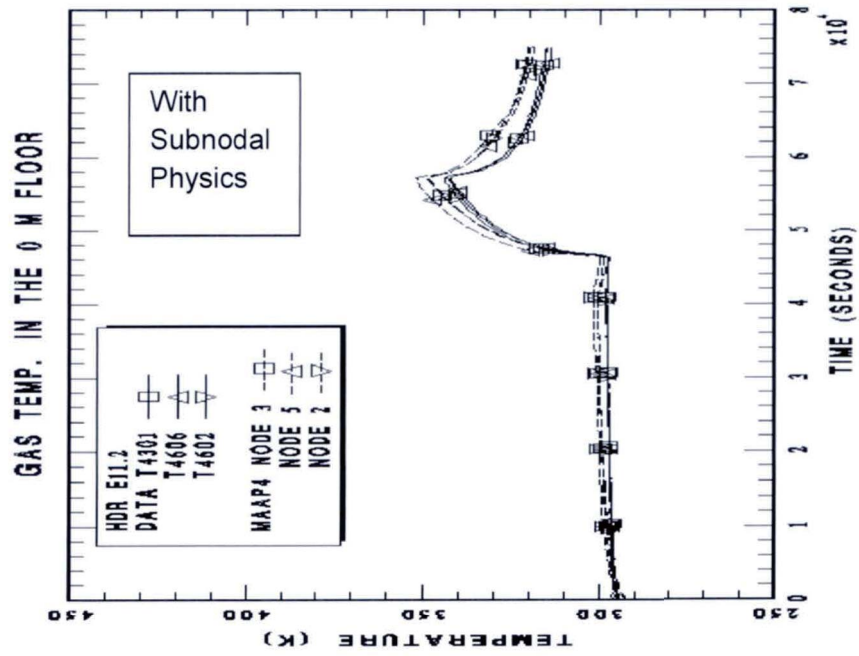
CSTF

HDR

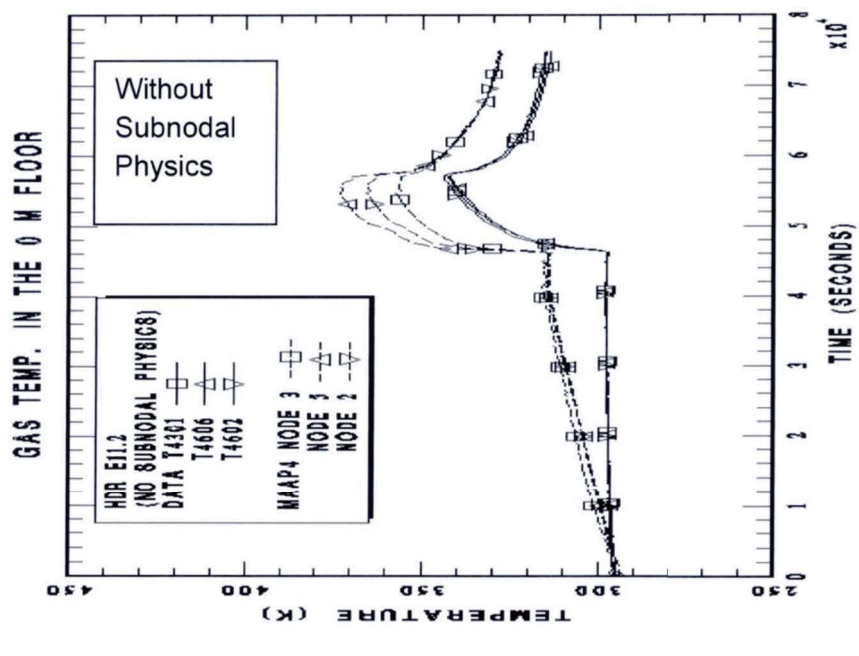
NUPEC

20090429-11CEH

Figure 2-24 Hydrogen distribution and mixing tests

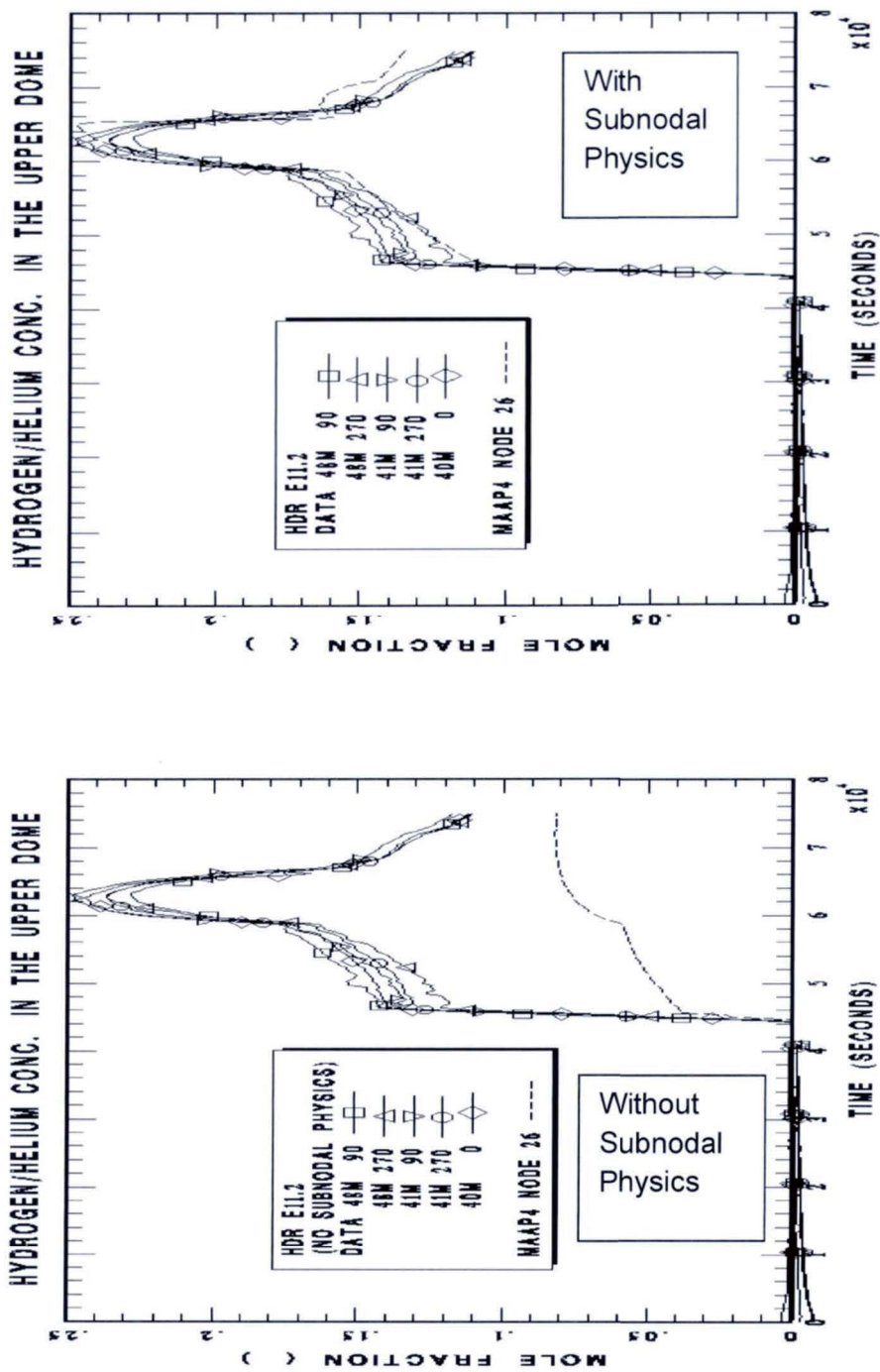


APR1400-E-P-NR-14003-NP-FIG-25-1



APR1400-E-P-NR-14003-NP-FIG-25-2

Figure 2-25 Gas temperatures at 0 m floor; comparison of MAAP4 results to HDR Test E11.2 data



HDR E11.2 (NO SUBNODAL PHYSICS) AND MAAP4 NODE 26

HDR E11.2 (WITH SUBNODAL PHYSICS) AND MAAP4 NODE 26

Figure 2-26 Hydrogen/helium concentration in the upper dome; comparison of MAAP4 results to HDR Test E11.2 data

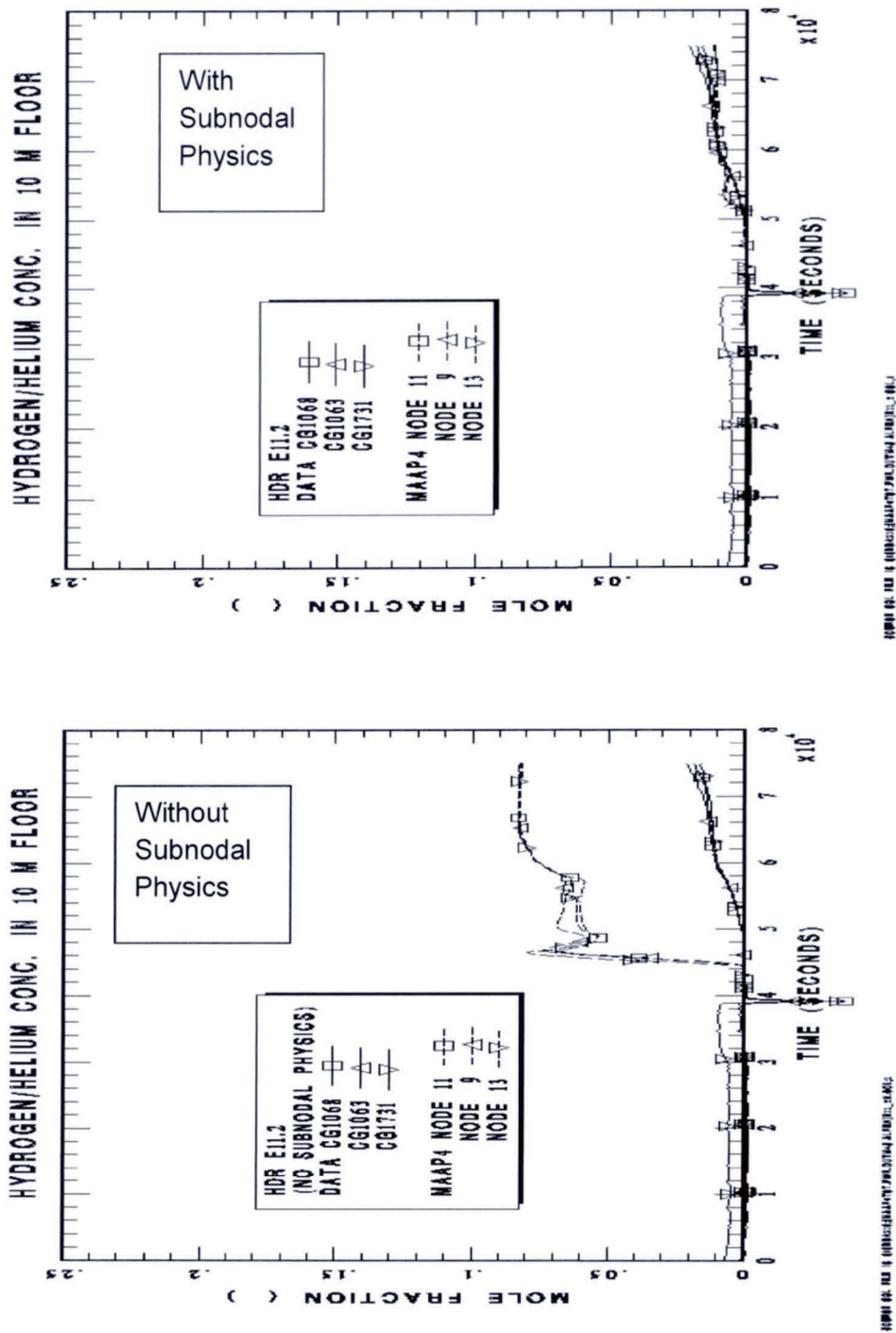


Figure 2-27 Hydrogen/helium concentration at 10 m floor; comparison of MAAP4 results to HDR Test E11.2 data

3 METHODOLOGY

The methodology for determining the potential and the effect of hydrogen combustion within the containment consists of:

1. Evaluation of the impact of non-detonative slow combustion on containment overpressure
2. Evaluation of local hydrogen accumulation beyond 10% in volume in the vicinity of hydrogen release sources
3. Evaluation of the potential for local and global occurrence of DDT.

3.1 Methodology for Non-Detonative Slow Combustion Evaluation

The methodology for the evaluation of the potential of containment failure due to non-detonative slow combustion of hydrogen is to compute the AICC pressure resulting from burning a containment-wide uniformly mixed hydrogen-air-steam mixture containing an equivalent amount of hydrogen as would be generated from 100% fuel clad metal-water reaction during an accident and compare its values to the ultimate pressure capacity of the containment. The AICC pressure is the bounding combustion pressure when hydrogen in the containment burns in a slow deflagration mode for any given initial conditions.

The computed AICC pressure is higher if the initial preborn pressure is higher. The highest AICC pressure is achieved when the pre-burn condition corresponds to the condition of a gaseous mixture with highest steam mole fraction that is barely, but still, flammable. On the flammability limit curves for hydrogen-air-steam mixtures, this point would correspond to the farthest tip of the curves along the steam axis. If the containment can survive the highest AICC pressure, the containment will survive any slow burns at all possible preburn conditions. Then, the containment would not be vulnerable to overpressure failure due to non-detonative slow deflagrations.

3.2 Methodology for Local Hydrogen Accumulation Evaluation

A containment-wide uniformly mixed hydrogen-air-steam mixture assumed in the calculation of AICC pressure would normally not be achieved during a progression of severe core melt accident in which a rapid hydrogen release is occurring from inside the RCS to the compartment where the release point is located. The rapid hydrogen release can lead to a significant local accumulation of hydrogen with concentrations much higher than other downstream compartments. Hence, the issue here is whether the local hydrogen accumulation is severe enough to lead to the conditions favorable to the occurrence of local DDT.

The methodology for the evaluation of local hydrogen accumulation beyond 10% in volume is to use the MAAP4 code with sufficient nodes representing compartments of the containment to analyze various "hydrogen" accident scenarios that represent the entire spectrum of hydrogen-significant accident sequences. Here, the 10% hydrogen volume fraction is taken as a criterion for determining whether the accumulation should be further considered for DDT evaluation. The 10% hydrogen volume fraction is the value identified in the USNRC regulation as the upper bound for a uniformly distributed hydrogen concentration during and following an accident that releases an equivalent amount of hydrogen as would be generated from a 100% fuel clad metal-water reaction. The result from this evaluation is not an end by itself, but rather is used as an input to the DDT evaluation.

3.3 Methodology for DDT Evaluation

The occurrence of DDT can potentially produce significant dynamic pressure loads at least 9 to several tens times initial pressure (Figure 2-12). Comparing the possible range of DDT dynamic pressure magnitude to the ultimate pressure capacity of the containment usually leads one to the conclusion of high probability of containment failure. Hence, for the DDT evaluation, it is considered reasonably sufficient (based on the current knowledge of DDT) to quantitatively evaluate whether the conditions that support the onset of DDT exist during the progression of all possible accident sequences without having to estimate the associated dynamic pressure.

The methodology for the evaluation of the potential of DDT is based on the method proposed by the expert group in the “OECD State of the Art Report (SOAR) on Flame Propagation and Deflagration-to-Detonation Transition in Nuclear Safety” issued in 2000 [Reference 6]. There are two main criteria established by the SOAR; the flame acceleration (FA) criterion also known as “the σ criterion,” and the detonation cell width criterion that is also known as “the 7λ criterion.” The two criteria are considered necessary conditions for DDT and are described in Sections 3.3.1 and 3.3.2 below.

3.3.1 Criterion for Flame Acceleration

The criterion for flame acceleration according to the SOAR [Reference 6] is based on the observation of a large amount of experimental data that correlates the expansion ratio of burned gas mixture to the occurrence of flame acceleration. It was found that there is a (minimum) critical value for the expansion ratios (later on to be referred to as $\sigma_{critical}$) required to support flame acceleration. The critical expansion ratio is a function of temperature. The critical expansion ratio decreases with increasing temperatures. This is one of the necessary conditions for DDT purely based on the thermodynamic properties of the mixture. There is no geometric factor in this criterion. The criterion can be stated as follows:

$$1) \quad \text{If } \sigma_{index} < 1, \text{ no FA is possible} \quad (3-1)$$

$$2) \quad \text{If } \sigma_{index} \geq 1, \text{ FA is possible} \quad (3-2)$$

Here, σ_{index} is defined as the ratio of the expansion ratio σ to the $\sigma_{critical}$

$$\sigma_{index} = \frac{\sigma(\bar{X}_{H_2}, \bar{X}_{H_2O}, \bar{X}_{O_2}, T)}{\sigma_{critical}(\bar{X}_{H_2}, \bar{X}_{O_2}, T)} \quad (3-3)$$

The expansion ratio σ is defined as the ratio of density of unburned gases to the density of burned gases. The expansion ratio is a function of averaged concentrations of hydrogen (\bar{X}_{H_2}), steam (\bar{X}_{H_2O}) and oxygen (\bar{X}_{O_2}), and temperature (T) of the compartment. On the other hand, the critical expansion ratio is a function of temperature for lean mixtures and is constant for rich mixtures as shown in Table 3-1. lists values of critical expansion ratios [Reference 6] that were used in the GASFLOW code [Reference 67] developed by FZK of Germany. These values can be fitted by a quadratic equation (in) that was developed by AECL and used in their DDTINDEX code [Reference 10].

As an example for a typical range of the values of the expansion ratios as a function of concentrations and temperatures for hydrogen-steam-air mixtures, shows expansion ratios calculated using STANJAN code, a well-known chemical equilibrium code developed at Stanford University [Reference 46]. Also shown is the critical expansion ratios above which flame acceleration is possible. It can be seen that at 300 K temperature, a gaseous mixture with steam not greater than 40% would meet the FA condition with hydrogen concentration in the range of 12-13%. At 400 K, the required hydrogen concentrations reduce to 10-11%.

3.3.1.1 MAAP4 Calculations of Expansion Ratios

An expansion ratio is not a variable in the MAAP4 code, but it can be calculated from other variables in the MAAP4 code. The expansion ratio is defined as the ratio of the density of unburned gas mixture (ρ_u) to the density of burned gas mixture (ρ_b);

$$\sigma = \frac{\rho_u}{\rho_b} \quad (3-4)$$

If one writes an ideal gas equation for an initial burned gas mixture, and then writes another ideal gas equation for the burned gas mixture at the same pressure as the unburned gas, i.e. undergoing an isobaric process, the density ratio derived from these two equations becomes:

$$\frac{\rho_u}{\rho_b} = \frac{T_b}{T_u} \frac{n_b}{n_u} \quad (3-5)$$

where T_b is flame temperature, T_u is unburned gas temperature, n_b is number of moles of gases after burn, and n_u is number of moles of gases before burn.

On the other hand, the AICC pressure P_{AICC} is a calculated quantity in MAAP4 and it is calculated from:

$$P_{AICC} = P_0 \frac{T_{AICC}}{T_u} \frac{n_b}{n_u} \quad (3-6)$$

Multiplying and dividing the right hand side of Eq. 3-6 with T_b , one obtains:

$$P_{AICC} = P_0 \frac{T_{AICC}}{T_b} \frac{T_b}{T_u} \frac{n_b}{n_u} \quad (3-7)$$

The right hand side of Eq. 3-5 can be seen as part of the right hand side of Eq. 3-7. Hence by substituting part of the right hand side of Eq. 3-7 with Eq. 3-5, the expansion ratio is then given by:

$$\sigma = \frac{\rho_u}{\rho_b} = \frac{P_{AICC}}{P_0} \frac{T_b}{T_{AICC}} \quad (3-8)$$

All four variables on the right hand side of Eq. 3-8 are MAAP4 variables. Hence, the expansion ratio can be calculated simultaneously in MAAP runs by defining the following term for a containment node in the input:

$$\sigma = \frac{\rho_u}{\rho_b} = \frac{PAICC(I)}{PRB(I)} \frac{TFLRB(I)}{TAICCB(I)} \quad (3-9)$$

3.3.2 Criterion for Deflagration-to-Detonation Transition Potential

For the potential of DDT, the “ 7λ criterion” proposed in the SOAR [Reference 6] is used for evaluation. This criterion represents another necessary but not sufficient condition in addition to the flame acceleration criterion discussed in Section 3.3.1. The criterion requires that the characteristic length of the compartment is greater than 7 times the detonation cell width. This criterion is generally in good agreement with experimental data over a wide range of scales and mixture compositions [Reference 6].

The 7λ criterion can be stated as follows:

$$1) \text{ If } 7\lambda_{\text{index}} < 1, \text{ DDT not possible} \quad (3-10)$$

$$2) \text{ If } 7\lambda_{\text{index}} \geq 1, \text{ there is possibility of DDT} \quad (3-11)$$

where the $7\lambda_{\text{index}}$ is a characteristic length index defined as the characteristic length divided by 7 times averaged detonation cell width λ as shown below:

$$7\lambda_{\text{index}} = \frac{\text{Characteristic Dimension}}{7 \times \text{Averaged Detonation Cell Width}} = \frac{L}{7\lambda} \quad (3-12)$$

Overall DDT Criteria

Since flame acceleration is a prerequisite to the onset of DDT, the flame acceleration criterion represented by σ_{index} in Eq. 3-2 must also be satisfied. This criterion implicitly implies that the mixture composition meets the downward flammability limits to support flame propagation in all directions.

Hence the overall DDT criteria to be used for this analysis require the following 2 criteria - 7λ criterion, and flame propagation criterion, to be satisfied simultaneously;

- 1) DDT condition - possible

$$\text{DDT index} = 7\lambda_{\text{index}} \times \sigma_{\text{index}} \geq 1 \quad \text{if } 7\lambda_{\text{index}} \geq 1 \text{ and } \sigma_{\text{index}} \geq 1 \quad (3-13)$$

- 2) DDT condition - not possible

$$\text{DDT index} = 0 \quad \text{if one of 2 conditions not satisfied} \quad (3-14)$$

The DDT index is used in the MAAP analysis to indicate whether DDT condition is possible or not possible by using a value of either 0 or ≥ 1 as an indicator.

3.3.2.1 Correlation for Detonation Cell Width

Detonation cell width is a length that characterizes the reactivity of the mixture. A smaller detonation cell width indicates that the mixture is more reactive. The detonation cell width can be calculated with an empirical correlation (function B67p) presented in Appendix D of the SOAR report [Reference 6] and is shown in Equation (3-15). According to this equation, the detonation cell width can be calculated with just four input parameters (i.e., hydrogen concentration, steam concentration and initial temperature and pressure). The calculation of this correlation is simple and can be conveniently applied in the MAAP include file for MAAP4 runs. The correlation (which is also used in the GASFLOW code) is adopted for this analysis and is expressed as follows:

$$\log_{10}(\lambda) = \left[a - m + \left[\frac{b}{(A - k/T)^f} + h \cdot (A - g \cdot T)^2 + i \cdot (A - g \cdot T) \right] \cdot \left[1 + d \cdot C + e \cdot T \cdot C^2 \right] \cdot \frac{j}{T} \right] \cdot [P - c] \cdot \left[\frac{1}{0.1 - c} + n \cdot (P - 0.1) \right] + m \quad (3-15)$$

where A is dry hydrogen volume fraction of hydrogen-steam-air mixture (vol%), i.e.,

$$[H_2]_{\text{dry}} = \frac{[H_2]}{[H_2] + [\text{air}]} \quad (3-16)$$

- T is initial temperature (K),
- C is steam volume fraction (vol%),

P is initial pressure (MPa),

λ is detonation cell size (cm),

and various constants in the correlation:

a	-1.13331E+00
b	4.59807E+01
c	-1.57650E-01
d	4.65429E-02
e	3.59620E-07
f	9.97468E-01
g	-2.66646E-02
h	8.74995E-04
i	-4.07641E-02
j	3.31162E+02
k	-4.18215E+02
m	2.38970E+00
n	-8.42378E+00

Examples of typical range for the values of detonation cell width are shown in Figure 3-2 and Figure 3-3 where both correlation results are compared with experiment data. Figure 3-2 shows detonation cell width as a function of hydrogen concentration for a mixture with no steam at various temperatures. The detonation cell width becomes smaller when the temperature is higher at the condition with same hydrogen and steam concentrations. Figure 3-3 shows that at any fixed hydrogen concentration, the detonation cell width increases with increasing steam concentrations. As shown in Figure 3-4, maps of the constant cell widths at 2 different pressures plotted in $[H_2]_{dry} - [H_2O]$ plane using Eq. 3-15 show that the detonation cell width is not sensitive to an increase in pressure.

3.3.2.2 Other Correlation for Detonation Cell Width

There is another method for calculating detonation cell width reported in the SOAR [Reference 6]. This method based on chemical kinetics was suggested by Gavrikov of Russian Research Center (RRC). It was developed from the Zeldovich-von Neumann-Döring (ZND) model for detonation. It is a semi-empirical approach to correlate the relation between a characteristic reaction zone width (δ) and the detonation cell width (λ). The Gavrikov correlation is as shown below:

$$\log_{10}(\lambda / \delta) = Y \cdot (a \cdot Y - b) + X \cdot [c \cdot X - d + (e - f \cdot Y) \cdot Y] \\ + g \cdot \ln(Y) + h \cdot \ln(X) + Y \cdot (i / X - k \cdot Y / X^m) - j \quad (3-17)$$

where, $X = E_a / RT_{ps}$, $Y = T_{vn} / T_0$, in the range of $3 < X < 16$ and $1.5 < Y < 8$, and other constants are

a	-0.007843787493
b	0.1777662961
c	0.02371845901
d	1.477047968
e	0.1545112857
f	0.01547021569
g	1.446582357
h	8.730494354
i	4.599907939
j	7.443410379
k	0.4058325462
m	1.453392165

It is not easy to apply the Gavrikov correlation. Some parameters are required to be pre-calculated with chemical kinetic theory. Gavrikov used the CHEMKIN-II code (the version of Prof. J. Shepherd of Caltech) for kinetic pre-calculations. This code, which can be executed in a command window, was developed with two types for hydrogen-steam-air mixture and C-H-O-N mixture respectively. The Gavrikov method is not used here because of its complexity. Its example calculation of detonation cell width are compared with results from Eq. 3-15 for standard air-hydrogen mixture ($T=375$ K, $p = 1$ bar) in Figure 3-5. The two correlations give slightly different results. For the same gas compositions, Eq. 3-15 give smaller detonation cell widths than the Gavrikov correlation. Hence the use of Eq. 3-15 to determine detonation widths in the 7λ criterion is a conservative approach.

3.3.2.3 Detonation Cell Width for CO

The correlation for detonation cell width using Eq. 3-15 is only valid for mixtures composed of air, hydrogen and steam. It is not applicable to gaseous mixtures in the containment during a severe accident involving generation of CO and CO₂ from Molten Core Concrete Interaction (MCCI). However, in order to estimate detonation cell widths for such mixtures, a conservative approach may be taken by assuming one mole of CO is as reactive as one mole (or a fraction of a mole) of hydrogen in the correlation of Eq. 3-15 while the presence of CO₂ would be treated as if it is nitrogen. A one-to-one mole assumption is believed to be a very conservative approach since CO is not as reactive as H₂. No detonation could be initiated in stoichiometric CO-O₂ mixture [Austin & Shepherd, 2000]. The lower flammability limit for CO in air is much higher than that of H₂, i.e. 12.5% for CO vs. 4% for H₂ [Reference 35].

3.3.2.4 Characteristic Length of Compartments

The characteristic length of a compartment is an important input parameter required in the 7λ criterion of Eq. 3-12. Characteristic length in the context of the 7λ criterion refers to the distance available while the 7λ length refers to the minimum distance required for DDT formation.

Determining characteristic length of the compartments or containment nodes of a nuclear plant can be very ambiguous because of the complex geometry of the plant.

In this analysis, the rules for determination of characteristic size in a lumped-parameter approach given in Appendix F of the SOAR [Reference 6] are utilized. In these rules, 4 simple shapes of rectangular boxes including long box, flat box, tall box and cubic box as shown in Figure 3-6 are used to characterize the

compartments found in the containment. The characteristic length is determined according to the formula shown next to individual compartment shapes shown in Figure 3-6.

For compartment nodes that can be flooded with water, actual compartment height is determined by taking into consideration the water height in the compartment. Due to the complexity of the containment geometry, rather than deciding the shape to individual compartment and calculating the characteristic length, a conservative approach can be taken such that the characteristic lengths of all 4 shapes are first calculated and the maximum is selected as the characteristic length. The calculated characteristic length cannot be longer than the longest dimension of the compartment.

Table 3-1 Critical Expansion Ratio as a Function of Initial Temperature

Temperature(K)	σ critical	
	$X_{H_2} < 2X_{O_2}$	$X_{H_2} > 2X_{O_2}$
300	3.75	3.75
400	2.80	3.75
500	2.25	3.75
600	2.10	3.75

Table 3-2 Fitting Equation for Critical Expansion Ratio [Reference 10]

Temperature(°C)	σ critical	
	$X_{H_2} < 2X_{O_2}$	$X_{H_2} > 2X_{O_2}$
T	$3.75 - 0.0115(T - 25) + 0.00002(T - 25)^2$	3.75

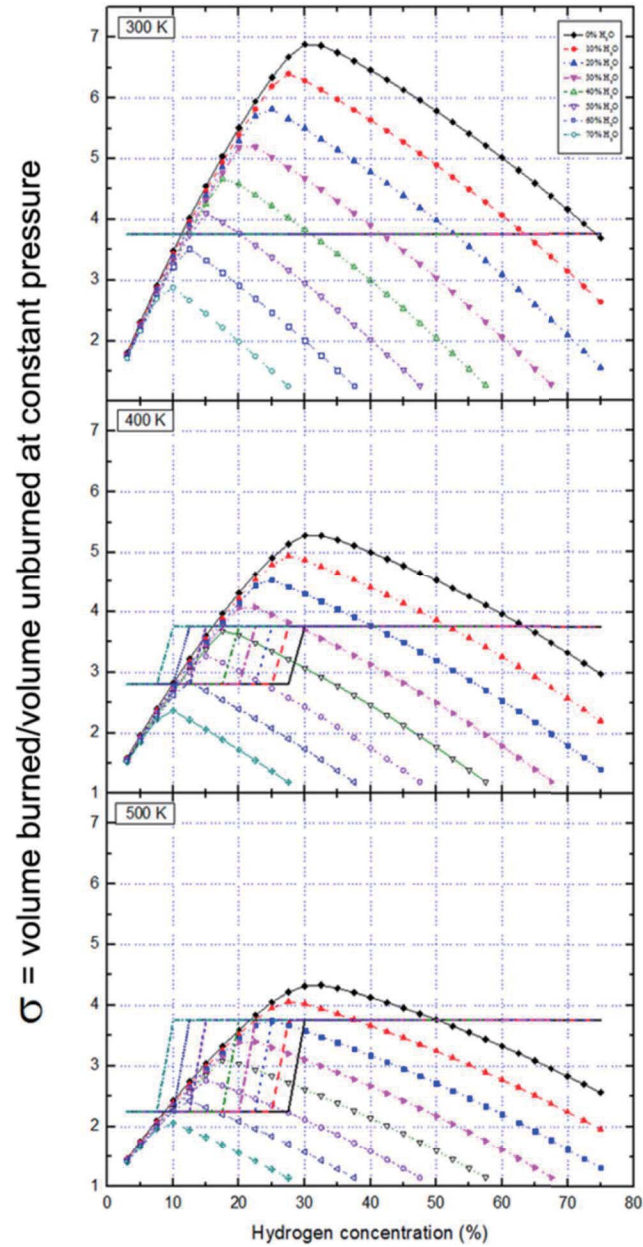


Figure 3-1 Example of Expansion Ratio Calculated by STANJAN Code

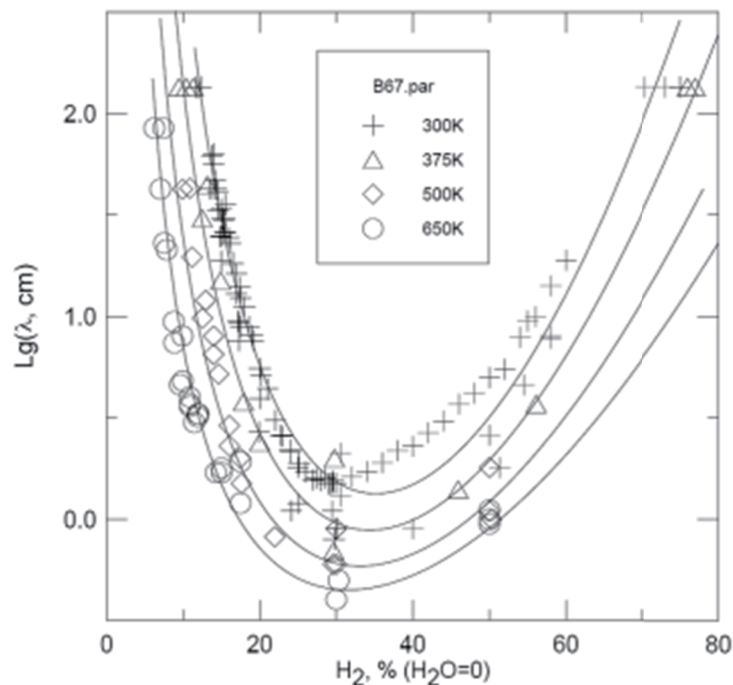


Figure 3-2 Calculation Results of Detonation Cell Width from Eq. 3-15 vs. Experimental Data as a Function of Hydrogen Concentrations at Various Temperatures [Reference 6]

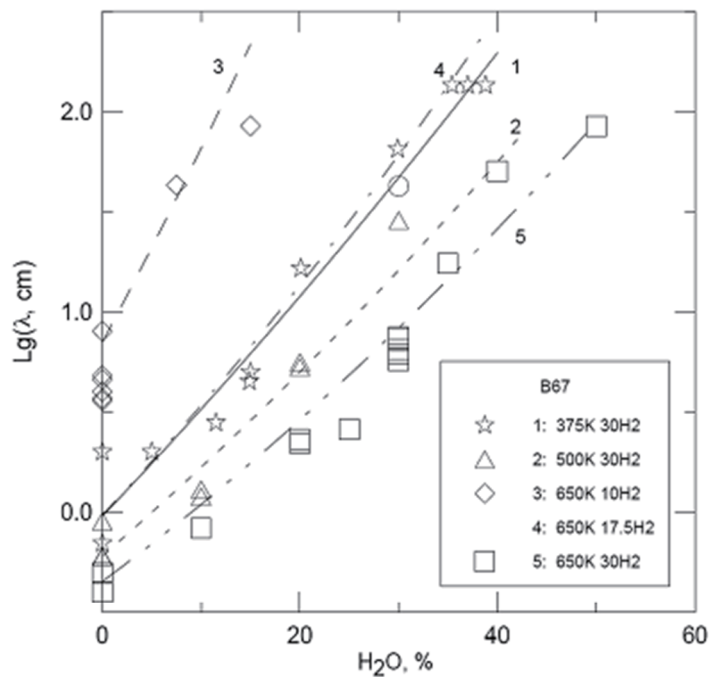


Figure 3-3 Calculation Results of Detonation Cell Width from Eq. 3-15 vs. Experimental Data as a Function of Steam Concentrations at various hydrogen concentrations [Reference 6]

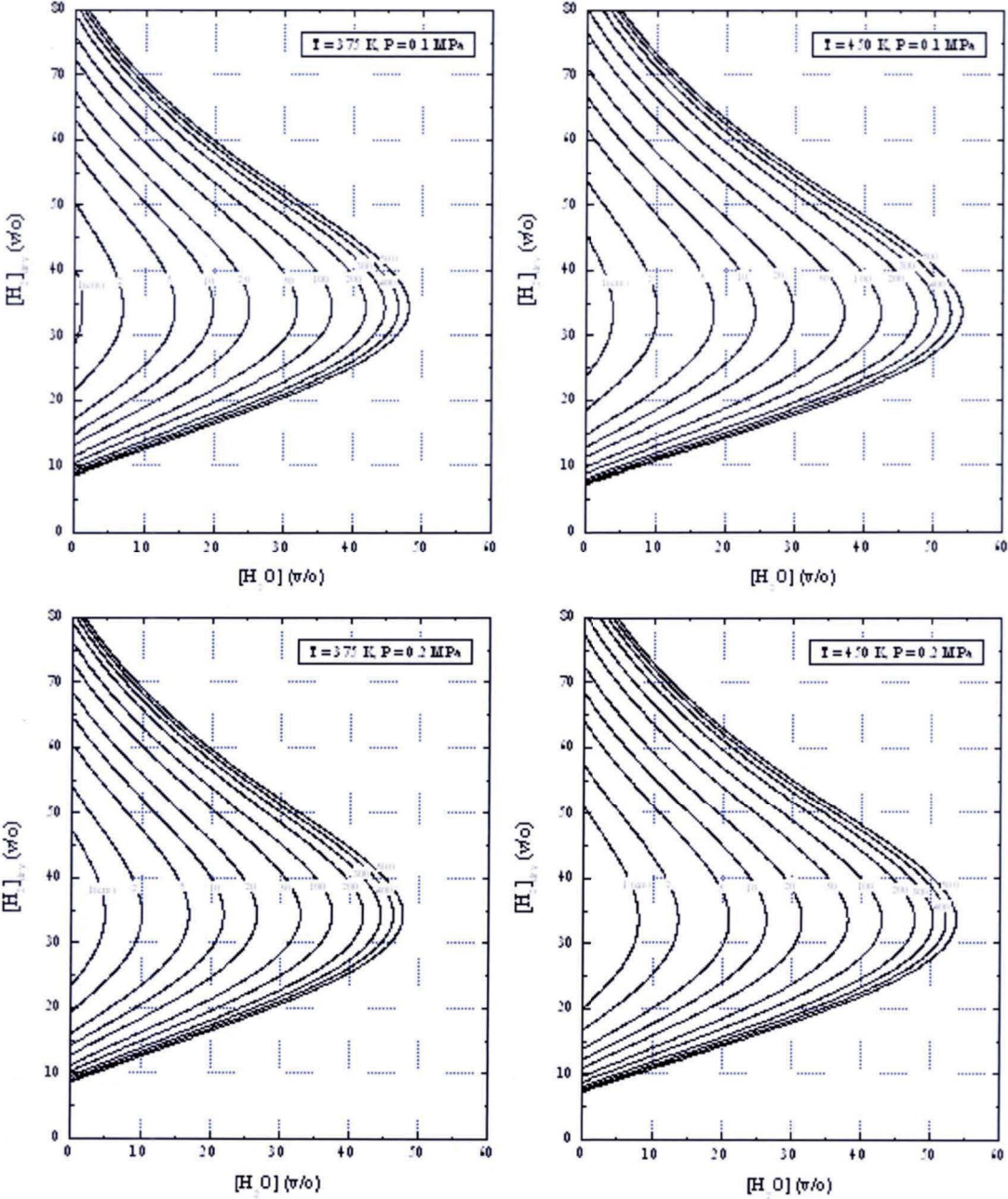
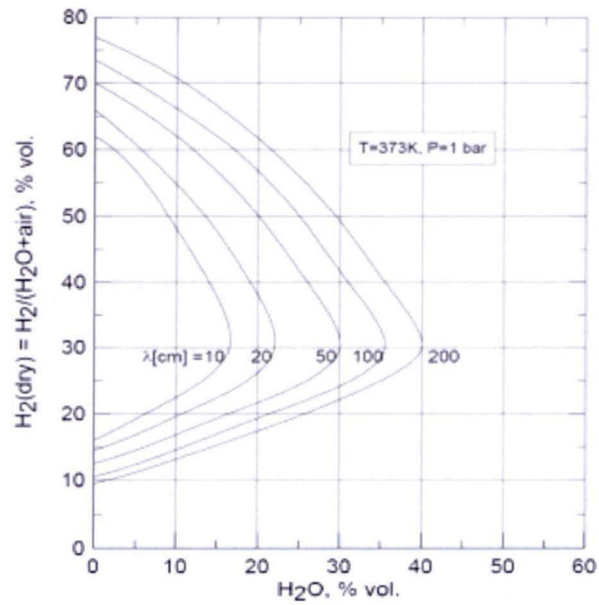
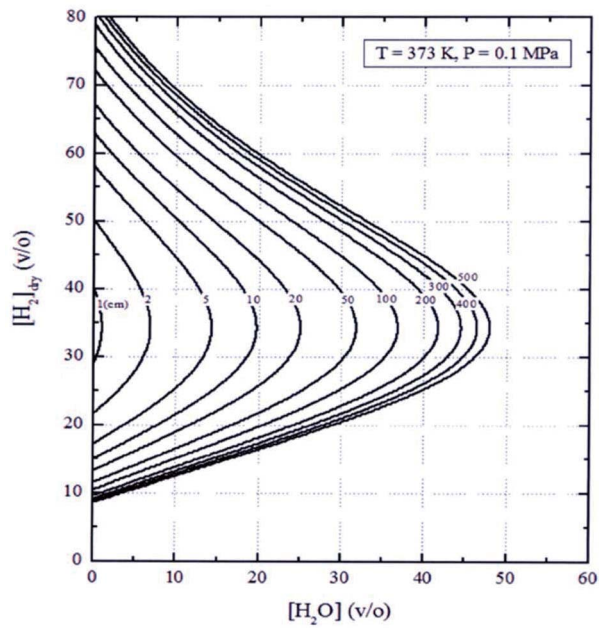


Figure 3-4 Detonation Cell Width (cm) plotted in $[H_2]_{dry}$ - $[H_2O]$ Plane using Eq. 3-15



(a) Cell Width Calculated with Gavrikov Correlation

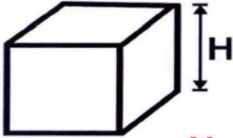
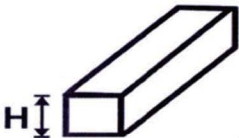
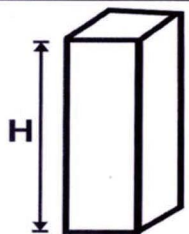
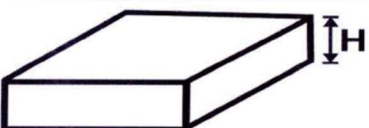


(b) Cell Width Calculated with Eq. 3-15

Figure 3-5 Comparison of Detonation Cell Width given by Eq. 3-15 and Gavrikov Method

Compartment Characteristic Length

V: compartment volume
H: compartment height

Shape	Characteristic Length L
 <p style="text-align: right; color: red;">$H \sim V^{1/3}$</p>	$L = \sqrt[3]{V}$
 <p style="text-align: right; color: red;">$H \ll V/H^2$</p>	$l = V/(H * H)$ $L = (l+H)/2$
 <p style="text-align: right; color: red;">$H \gg \sqrt{V/H}$</p>	$l = \sqrt{V/H}$ $L = (l+H)/2$
 <p style="text-align: right; color: red;">$H \ll \sqrt{V/H}$</p>	$L = \sqrt{V/H}$

20120621-2WL

Figure 3-6 Guidelines for Determination of Compartment Characteristic Length [Reference 6]

4 EVALUATION AND RESULTS SUMMARY

Evaluations of (1) AICC pressure, (2) hydrogen distribution and (3) potential of DDT for APR 1400 containment have been performed in three separate calculation notes, respectively. The results of each evaluation are summarized here.

4.1 AICC Pressure Evaluation and Summary

TS

4.2 Local Hydrogen Accumulation Evaluation and Summary

The evaluation of local hydrogen accumulation has been performed using MAAP4.0.8 [Reference 17]. This evaluation identifies local conditions within the containment with hydrogen exceeding 10%. The 10% hydrogen volume fraction is taken as a criterion for determining whether the accumulation should be further considered for DDT evaluation.

The analyzed accident sequences include 5 initiator types with a base case defined for each initiator type. For each initiator type, variations in the availability of accident mitigation systems are made such that their impact, if any, can be observed. Here, severe accident mitigation features refer to containment spray system, cavity flooding system, hydrogen mitigation system, and manual opening of Pilot Operated Safety Relief Valve (POSRV) for rapid RCS depressurization. The five initiator types are as follows:

- Large break LOCA (LLOCA)
- Medium break LOCA (MLOCA)
- Small break LOCA (SLOCA)
- Station Blackout (SBO)
- Total Loss Of Feed Water (TLOFW) that also represents Total Loss Of Essential Service Water (TLOESW) and Loss of Offsite Power (LOOP)

These sequences represent the entire spectrum of severe accident conditions important to hydrogen accumulation and distribution in the containment. Other PRA accident sequences can be either represented or bounded by these analyzed sequences such that analysis of that specific sequence is not necessary.

All analyzed sequences have hydrogen generated in-vessel equivalent to 100% Metal Water Reaction (MWR) assuming minimum generation rate of 0.045 kg/s. The total amount of hydrogen generated during the analyzed sequences exceeded the equivalent of 100% MWR for sequences with MCCI.

It was predicted the release of hydrogen at various containment compartments under severe accident scenarios. The possible hydrogen release points considered in the analysis include the hot-leg break (for LOCAs), IRWST spargers, failed reactor vessel lower head, and POSRV three way valves. For LOCAs prior to vessel failure, hydrogen is released from the break in the hot leg into SG compartment. For non-LOCA sequences like SBO and TLOFW, hydrogen is first released to the In-containment Refueling Water Storage Tank (IRWST) through the pressure-lifted POSRVs. When three way valve manual alignment is actuated, hydrogen is also released to SG compartment via the three way valve. For high pressure sequences including SBO, TLOFW and SLOCA, additional release point could come from the hot leg failure due to creep. After vessel failure, the failed lower head provides another hydrogen release point to the cavity area.

Figure 4-1 ~ Figure4-4 show the hydrogen distribution in the dome region when applying all severe accident mitigation features. With all severe accident mitigation features available, the hydrogen concentration is less than 10 percent.

In the screening of 10% hydrogen limit exceedance for various accident scenarios, it was found that

- (1) if the POSRV via the three way valve is available, there is no limit exceedance anywhere in the containment except in the IRWST quarters and in the SG compartment for high pressure sequences (such as TLOFW, LOOP, and TLOESW for delayed actuation timing of POSRV and three way valve).
- (2) If the Containment Hydrogen Control System (HG, i.e. igniters and PARs) is available and no containment sprays are actuated, there is no limit exceedance anywhere in the containment for all LOCA sequences.

Four locations during various accident scenarios were identified to exceed the 10% hydrogen limit. The 10% limit conditions for each of these locations are summarized as follows.

10% Limit Condition in the Reactor Annulus for LOCAs with Cavity Flooding System (CFS):

The 10% limit condition is exceeded in the reactor annulus when molten corium pours from the failed vessel to the flooded cavity for a very brief duration of about 20 to 40 seconds.

10% Limit Conditions in Lower Containment Regions: In-Core Instrument (ICI) chase, Corium Chamber room, and Reactor Cavity Access Area for LOCAs without CFS

The 10% hydrogen limit is exceeded in the cavity and its vicinity such as ICI chase, corium chamber room, and reactor cavity access area for cases where igniters are unavailable and the cavity is not flooded. Such conditions occur right after vessel failure when artificial hydrogen generation is still ongoing. At the time, the high hydrogen concentration is resulted from both the ex-vessel hydrogen generation from MCC1 in a dry cavity and the artificial in-vessel hydrogen generation intended to meet the 100% MWR requirement. The 10% limit condition in lower containment regions is not detected for cases with CFS actuated.

10% Limit Conditions in IRWST and Regions above IRWST:

The appearance of the 10% limit conditions in the IRWST is commonly found in non-LOCA accident sequences (such as SBO, TLOFW, and TLOESW) when POSRV fails to depressurize the RCS through realigned three way valve. This leads to accumulation of hydrogen in the pressurizer which is released into the IRWST through the intermittent POSRV opening.

In TLOFW sequence, the actuation of POSRV via three way valve reduces the number of locations with 10% limit exceedance significantly. With the POSRV via the three way valve, the 10% limit conditions are

eliminated in the IRWST quarters without spargers and in most areas above the entire IRWST quarters. However, the actuation of POSRV via three way valve does not entirely eliminate the 10% limit conditions in the IRWST quarters with spargers.

In contrast, for SBO sequences, the actuation of three way valve (without POSRV) entirely eliminates the 10% limit conditions in the IRWST.

The major difference in the 10% limit conditions between the analyzed SBO and TLOFW sequences is in the timing of POSRV actuation. In TLOFW sequences, POSRV is actuated 30 minutes after core damage. This actuation time is much later compared to the one used in the analyzed SBO sequences (which is 30 minutes after the first POSRV lifting). Variations in the availability of igniters, PARs, CFS, and containment spray make no differences.

10% Limit Condition in Steam Generator Compartment at Time of Hot Leg Creep Rupture

The 10% limit condition is detected in the steam generator compartment at the time of hot leg creep rupture for a high-pressure sequence. The 10% limit is also exceeded in the steam generator compartment when the three way valve is aligned to it. This 10% limit condition is caused by the assumption of the well-mixed condition (an intrinsic assumption of the MAAP code) in the steam generator compartment following the blowdown of the high-temperature, hydrogen-rich gases out of the hot leg break at the time of creep rupture failure. However, a well-mixed condition is unlikely achieved in the steam generator compartment. A more likely scenario is a hydrogen burn as a diffusion flame emanating from the pipe rupture location. A diffusion flame is considered a threat to nearby equipment rather than to the containment integrity.

4.3 DDT Evaluation and Summary

The evaluation of the potential of DDT has been performed using MAAP4.0.8. Based on the screening results of 10% hydrogen limit exceedance discussed in section 4.2, DDT index conditions as discussed in section 3.3.2 were further evaluated for the potential of DDT.

Here the DDT index condition refers to the gaseous mixture that has compositions that meet the criteria of flame acceleration (FA) and the detonation cell size that allow DDT to develop within the characteristic length of the compartment. When the DDT index condition is detected in the accident simulation, it means that all necessary conditions for DDT are present. Whether or not the condition is sufficient for DDT is beyond the capability of the criteria. However, as a conservative approach, one may assume that the presence of DDT index condition locally or globally in the containment means DDT will occur if ignited.

It was found that there is no DDT potential anywhere in the containment if the POSRV via the three way valve is available.

Four locations during various accident scenarios were identified to meet the DDT index conditions (criteria) when the POSRV via the three way valve is unavailable. The DDT potential for each of these locations and required conditions to meet the DDT index conditions are summarized in Table 4-1 and are discussed as follows.

DDT Index Conditions in the Reactor Annulus:

There is no potential of DDT in the reactor annulus.

DDT Index Conditions in Lower Containment Regions: ICI Chase, Corium Chamber room, and Reactor Cavity Access Area:

This DDT index condition is detected in the nodes around the cavity such as the ICI chase, corium chamber room, and reactor cavity access area. The conditions meet the 7λ criterion and the σ criterion (i.e., the DDT index ≥ 1) for extremely low probability cases in which igniters are unavailable and the cavity is not flooded. The timing of such conditions is after vessel failure with MCCI as a major source of ex-vessel hydrogen production and artificial hydrogen generation as a major source of in-vessel hydrogen production for cases in which the 100% MWR requirement has not been met at the time of vessel failure.

DDT Index Conditions in the IRWST and Areas above the IRWST:

The appearance of the DDT index condition in the IRWST is found commonly in non-LOCA accident sequences (such as SBO, TLOFW, LOOP, and TLOESW) when there is failure to depressurize the RCS through the POSRV via the three way valve early enough to avoid high accumulation of hydrogen in the pressurizer that can be released into the IRWST.

In TLOFW sequence, the actuation of the POSRV via the three way valve reduces the number of locations with DDT index conditions significantly. With the success of POSRV via the three way valve, the DDT index conditions are eliminated in the IRWST quarters without spargers and in all areas above the entire IRWST quarters. The actuation of POSRV via the three way valve does not entirely eliminate the DDT index conditions in the IRWST quarters with spargers. However, the cumulative duration for the DDT index conditions is substantially reduced. Furthermore, the detonation cell widths calculated at these conditions are larger than 4 m. No detonations have ever been observed in mixtures with detonation cell width greater than 2 m [Reference 6]. Therefore, the potential of DDT is very unlikely in this case.

For SBO sequences, the actuation of the three way valve entirely eliminates the DDT index conditions in the IRWST.

The major difference in the DDT index conditions between the analyzed SBO and TLOFW sequences is in the timing of POSRV actuation. In TLOFW sequences, POSRV is actuated 30 minutes after core damage. This actuation time is much later in time compared to the one used in the analyzed SBO sequences (which is 30 minutes after the first POSRV lifting). Variations in the availability of igniters, PARs, CFS, and containment spray make no differences.

DDT Index Conditions in the Steam Generator Compartment at the Time of Hot Leg Creep Rupture

The DDT index condition is also detected in the steam generator compartment at the time of hot leg creep rupture for a high-pressure sequence with a failure of POSRV and failure to align the three way valve. However, if the three way valve is aligned to the steam generator compartment the DDT index condition disappears. This DDT index condition is caused by the assumption of the well-mixed condition (an intrinsic assumption of the MAAP code) in the steam generator compartment following the blowdown of the high-temperature, hydrogen-rich gases out of the hot leg break at the time of creep rupture failure. Under this situation a well-mixed condition is unlikely achieved yet, and if the gas mixture is ignited a much more likely scenario would be the burning of hydrogen gas as a diffusion flame emanating from the pipe rupture location. The duration of the DDT index condition is also very short (less than 10 seconds). An ignition during Thus DDT in this mode is very unlikely.

Table 4-1 Summary of Locations with DDT Potential and Required Conditions

TS

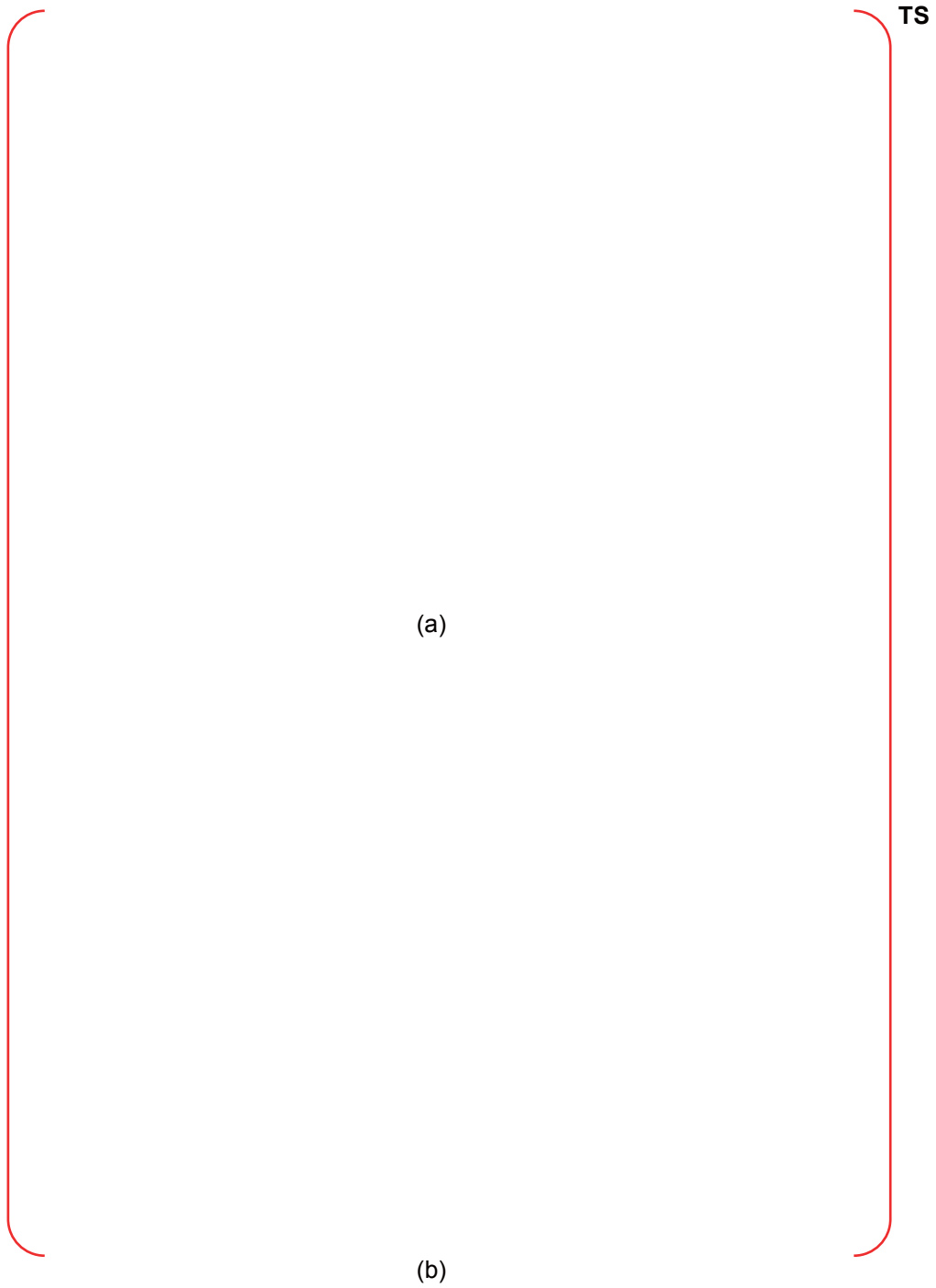


Figure 4-1 Mole Fraction of Hydrogen in the Dome Region for LLOCA (1/3)

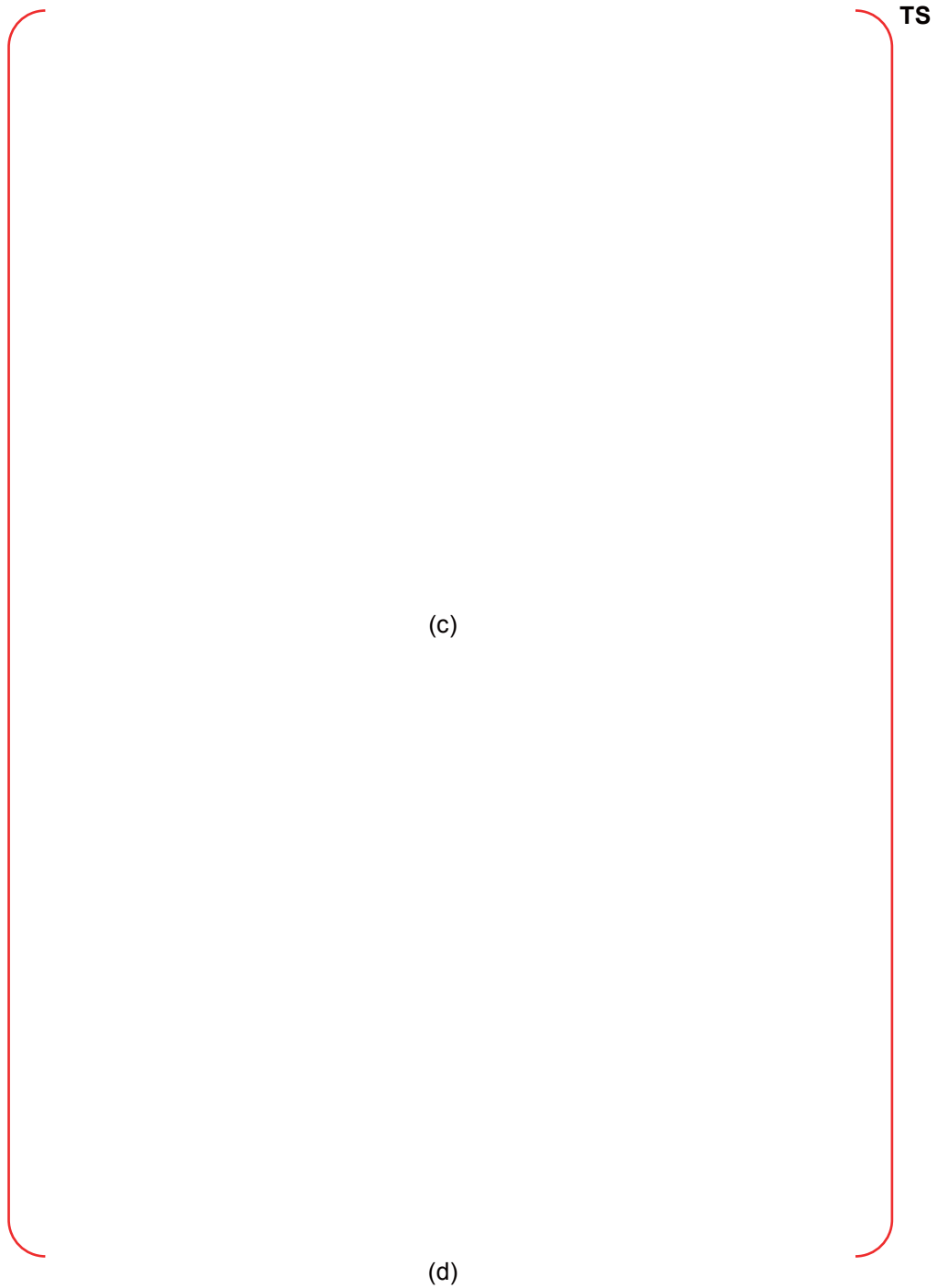


Figure 4-1 Mole Fraction of Hydrogen in the Dome Region for LLOCA (2/3)

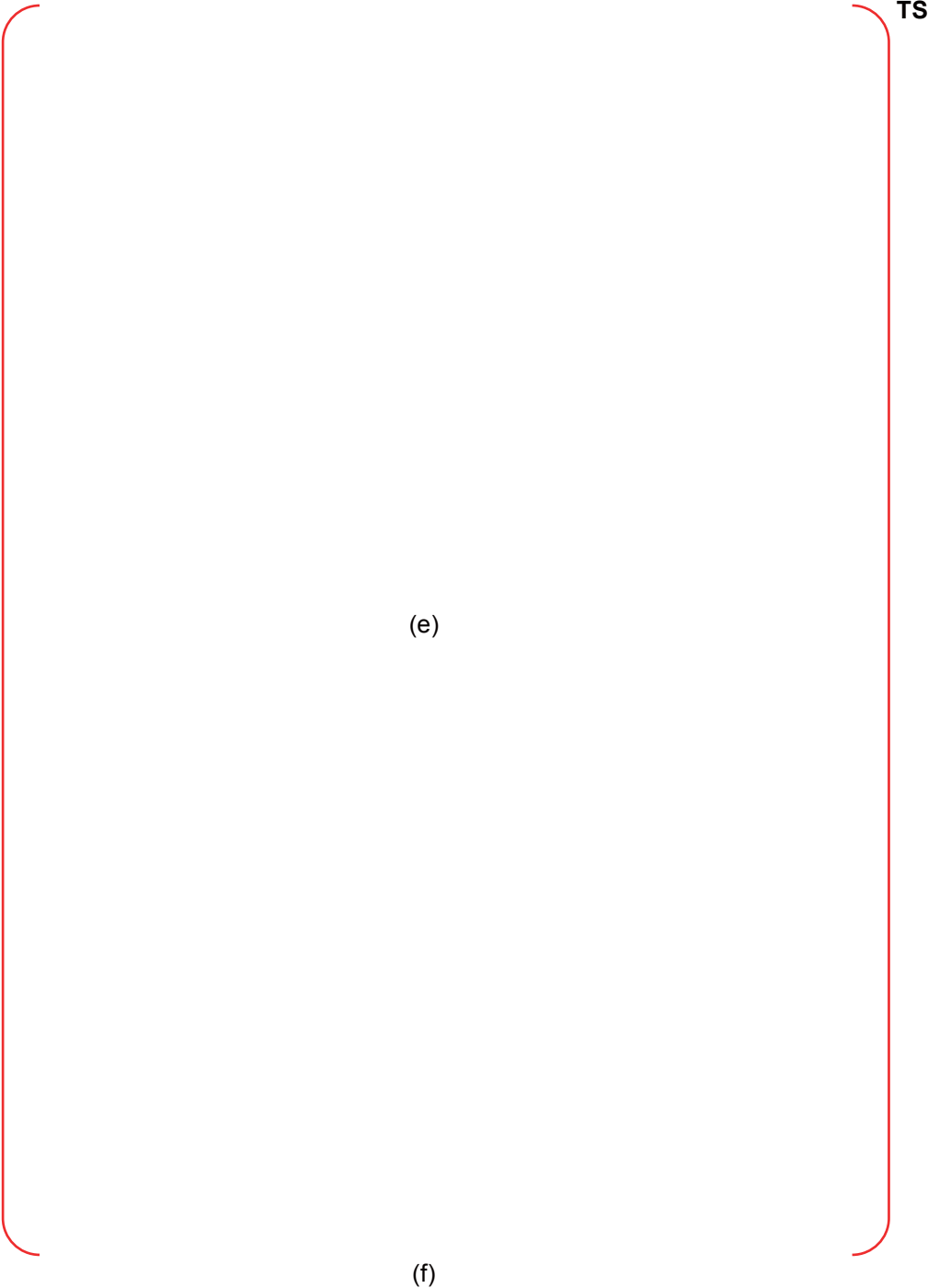


Figure 4-1 Mole Fraction of Hydrogen in the Dome Region for LLOCA (3/3)

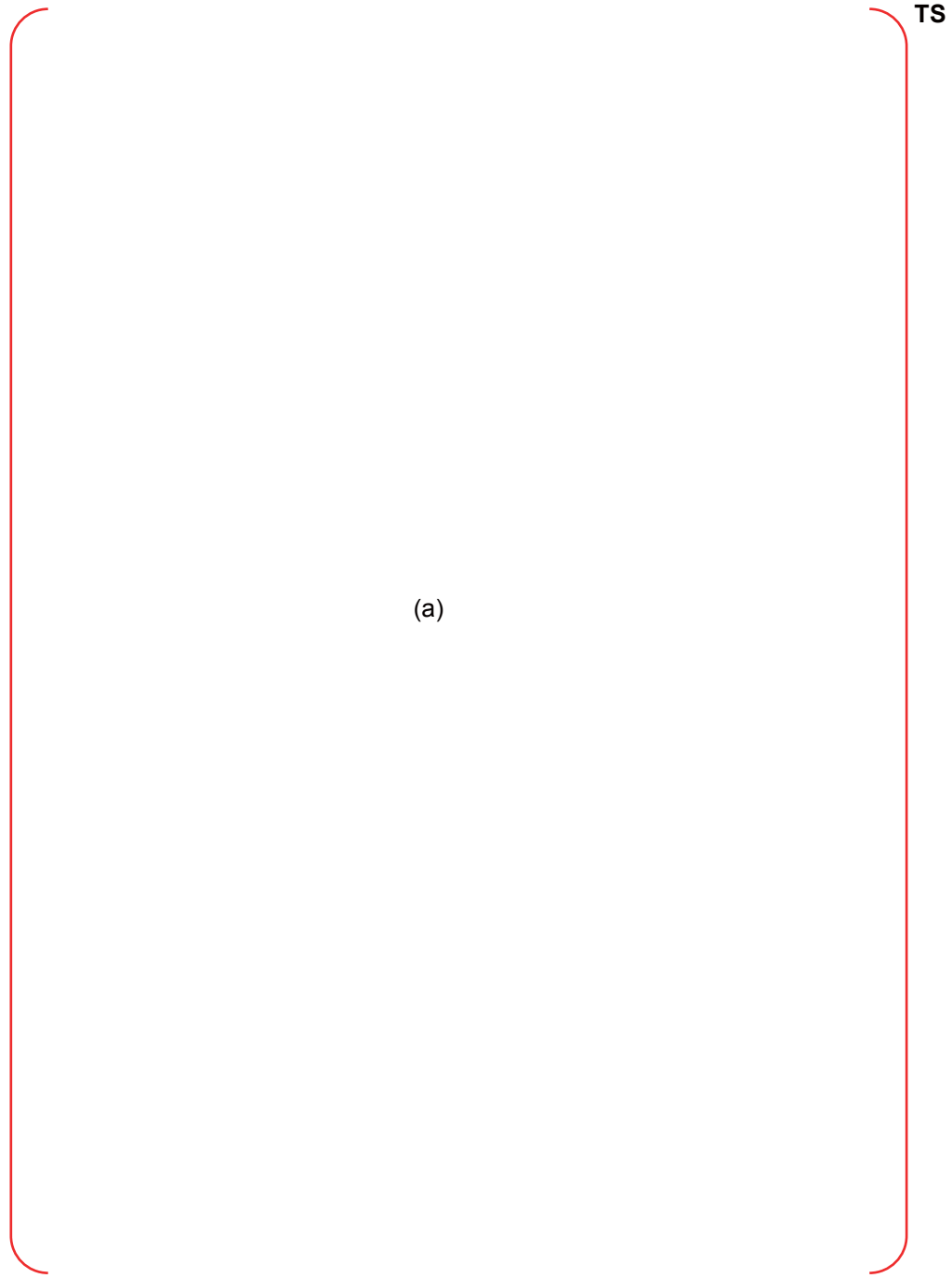


Figure 4-2 Mole Fraction of Hydrogen in the Dome Region for SLOCA (1/3)

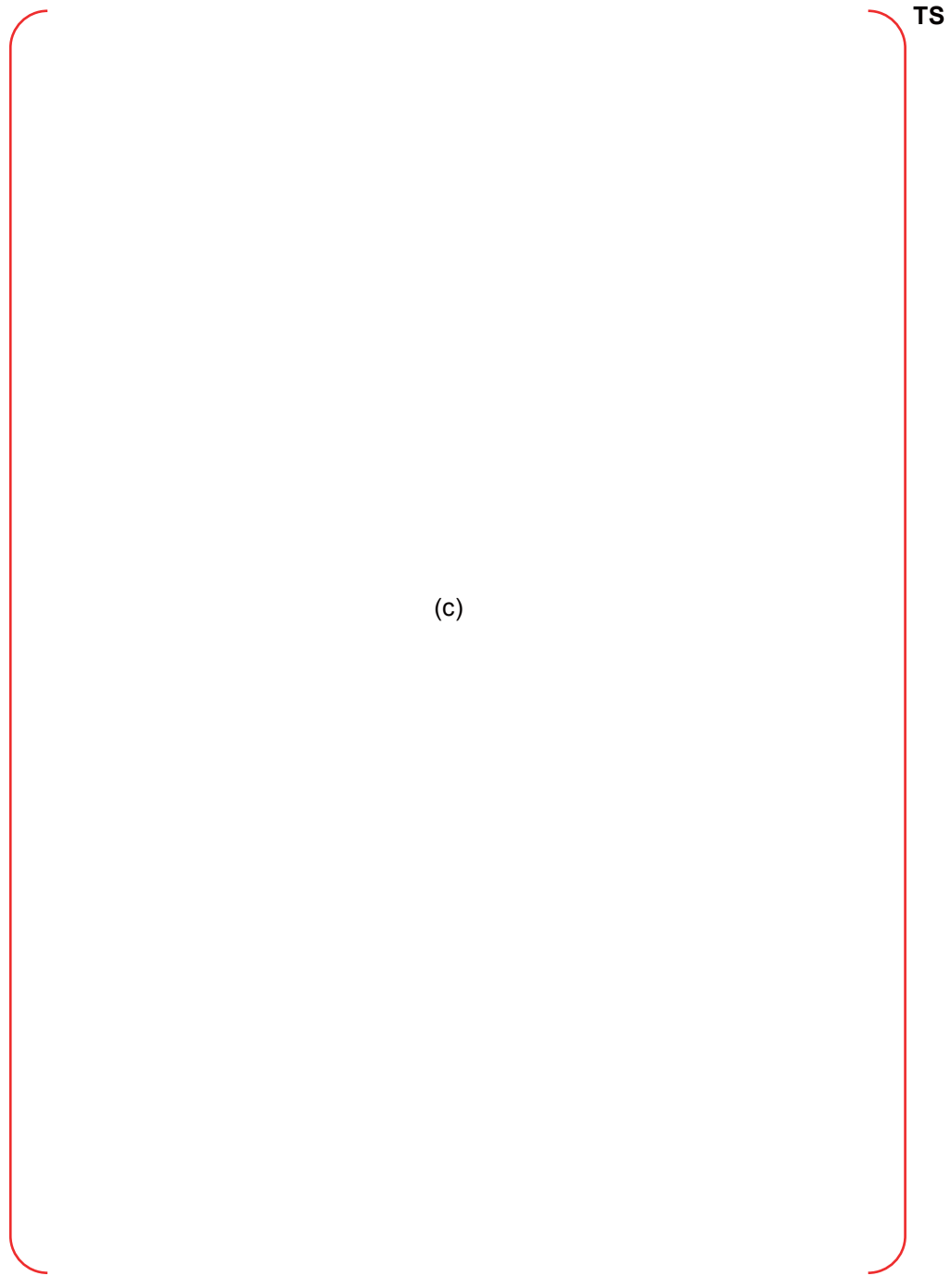


Figure 4-2 Mole Fraction of Hydrogen in the Dome Region for SLOCA (2/3)

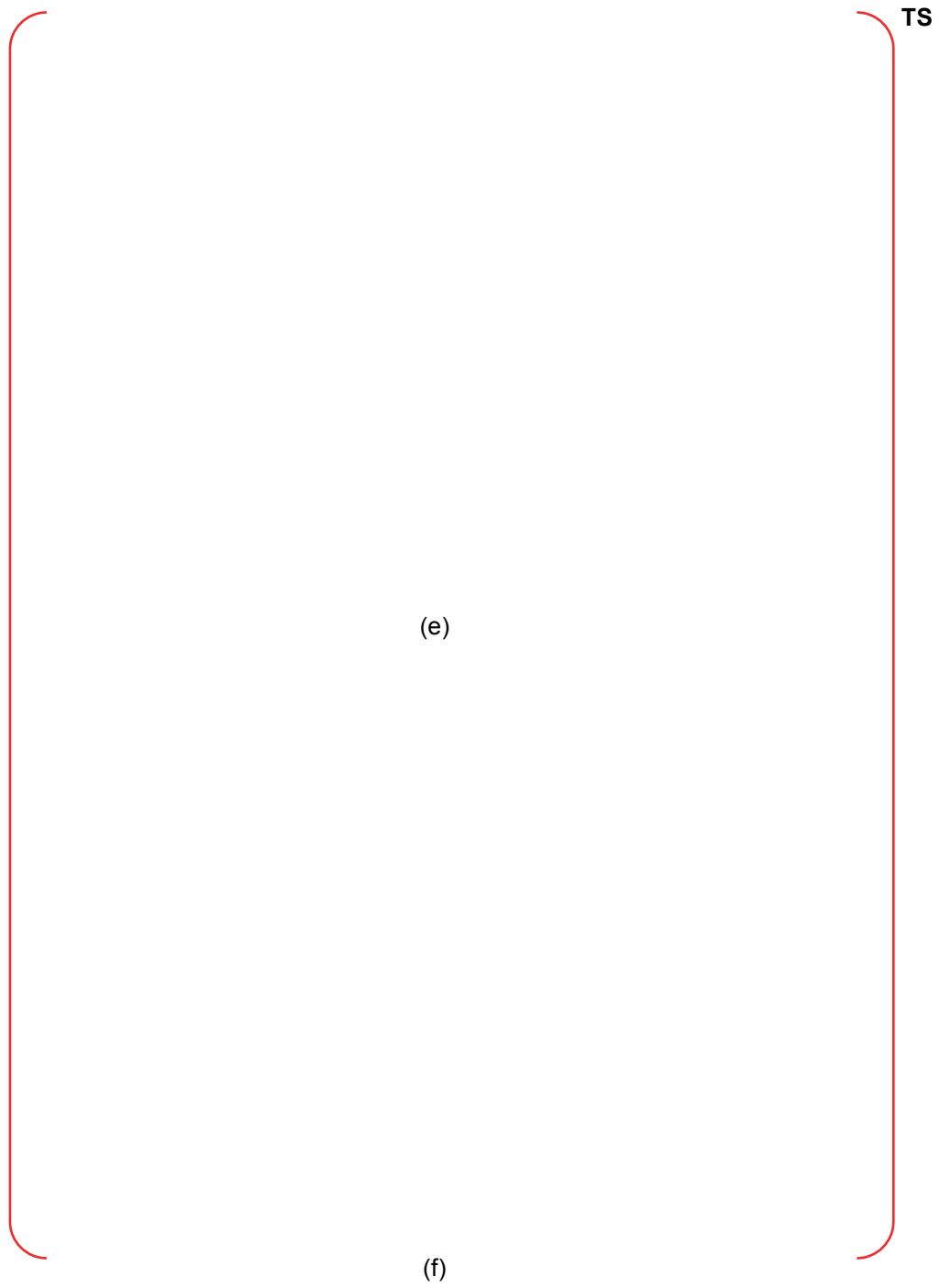


Figure 4-2 Mole Fraction of Hydrogen in the Dome Region for SLOCA (3/3)

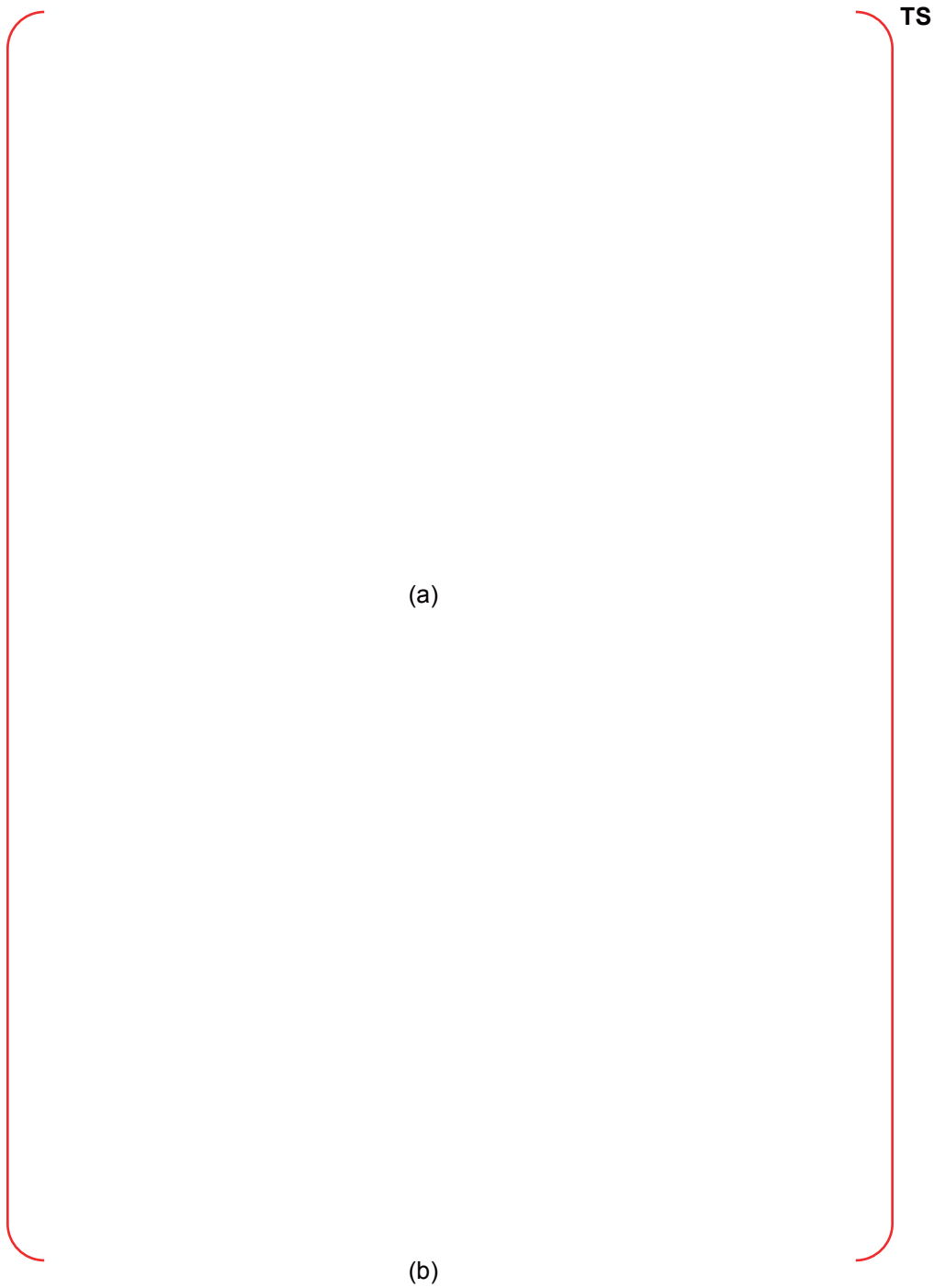


Figure 4-3 Mole Fraction of Hydrogen in the Dome Region for SBO-3way valve (1/3)

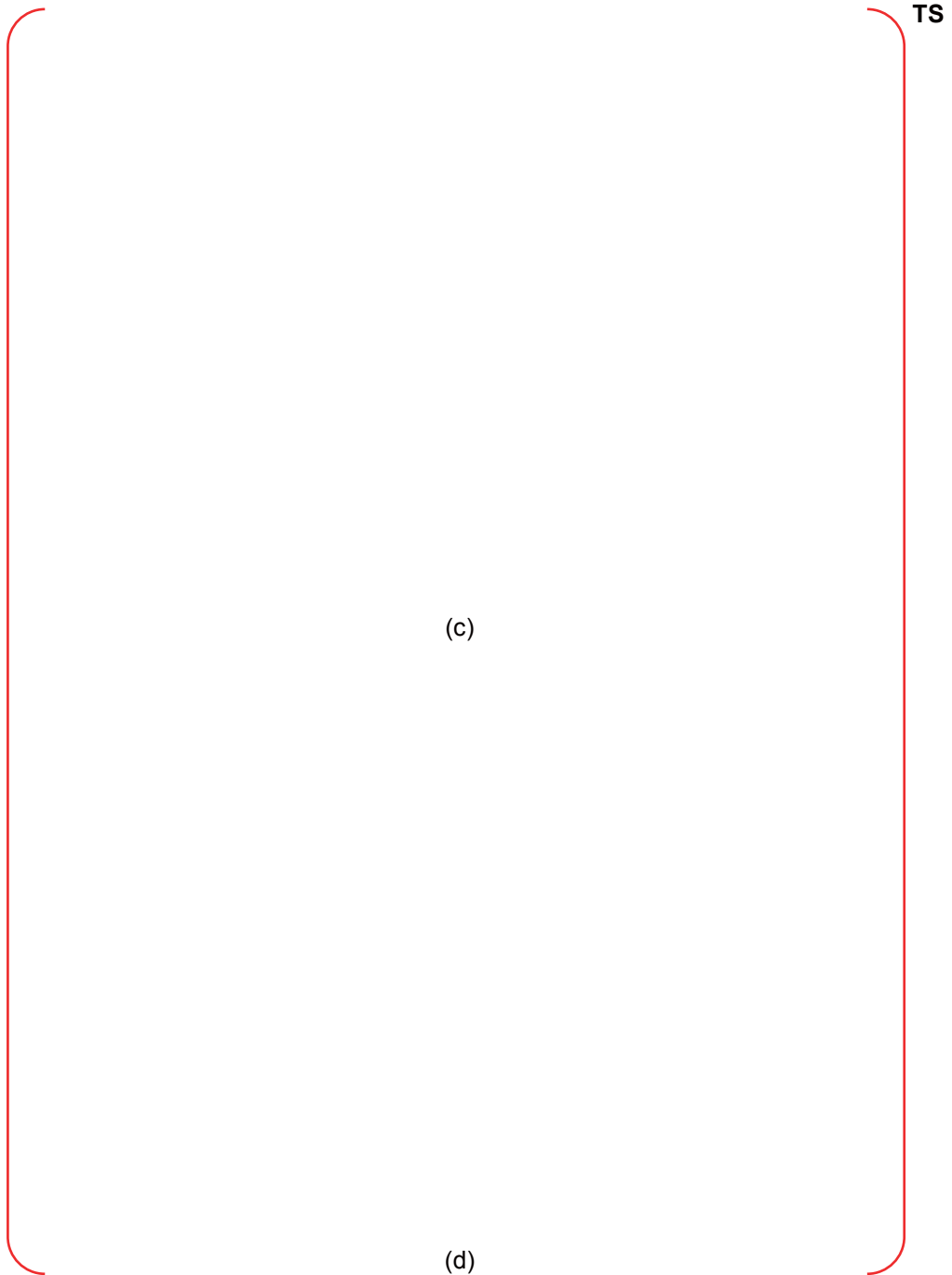


Figure 4-3 Mole Fraction of Hydrogen in the Dome Region for SBO-3way valve (2/3)

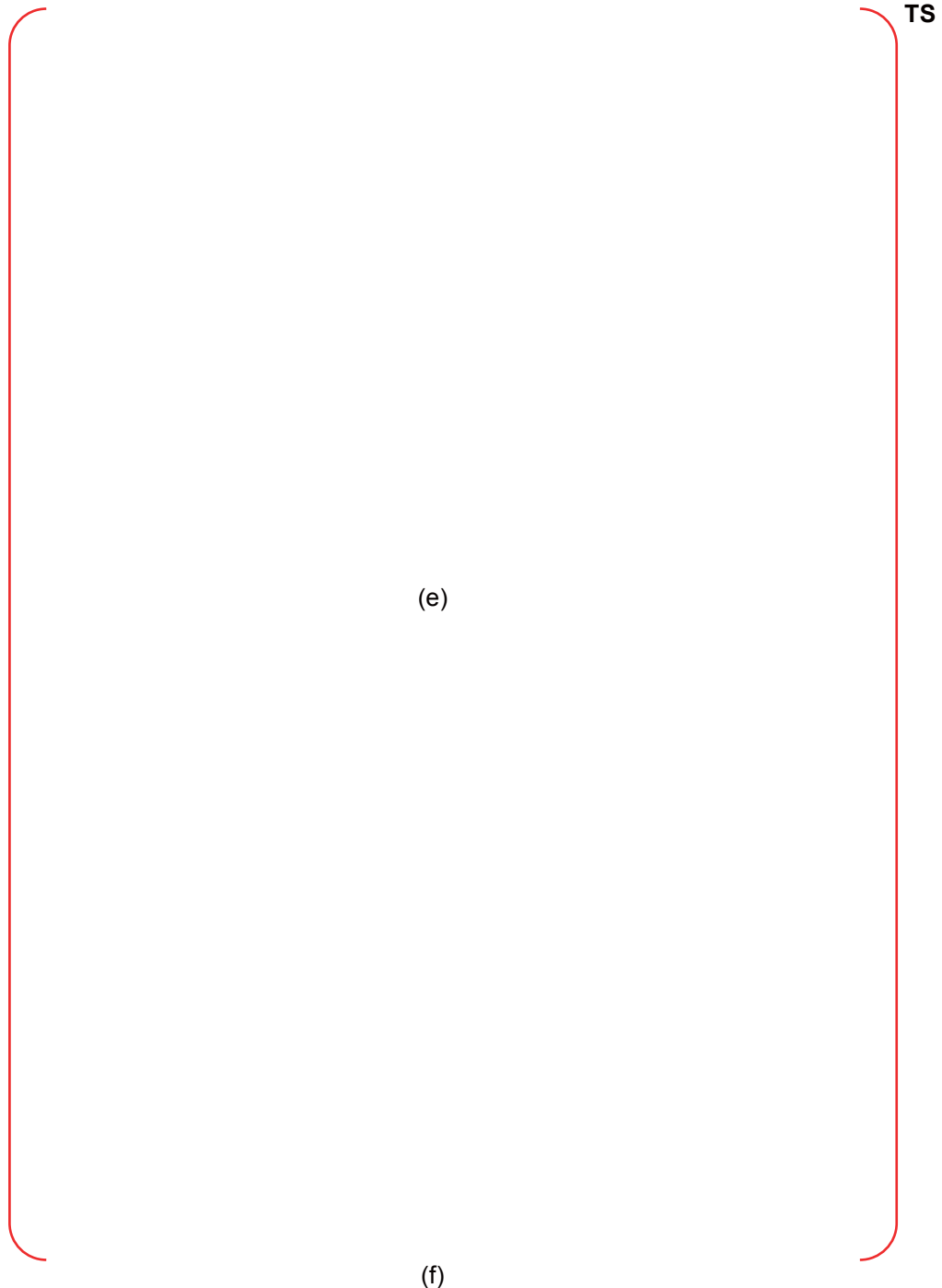


Figure 4-3 Mole Fraction of Hydrogen in the Dome Region for SBO-3way valve (3/3)

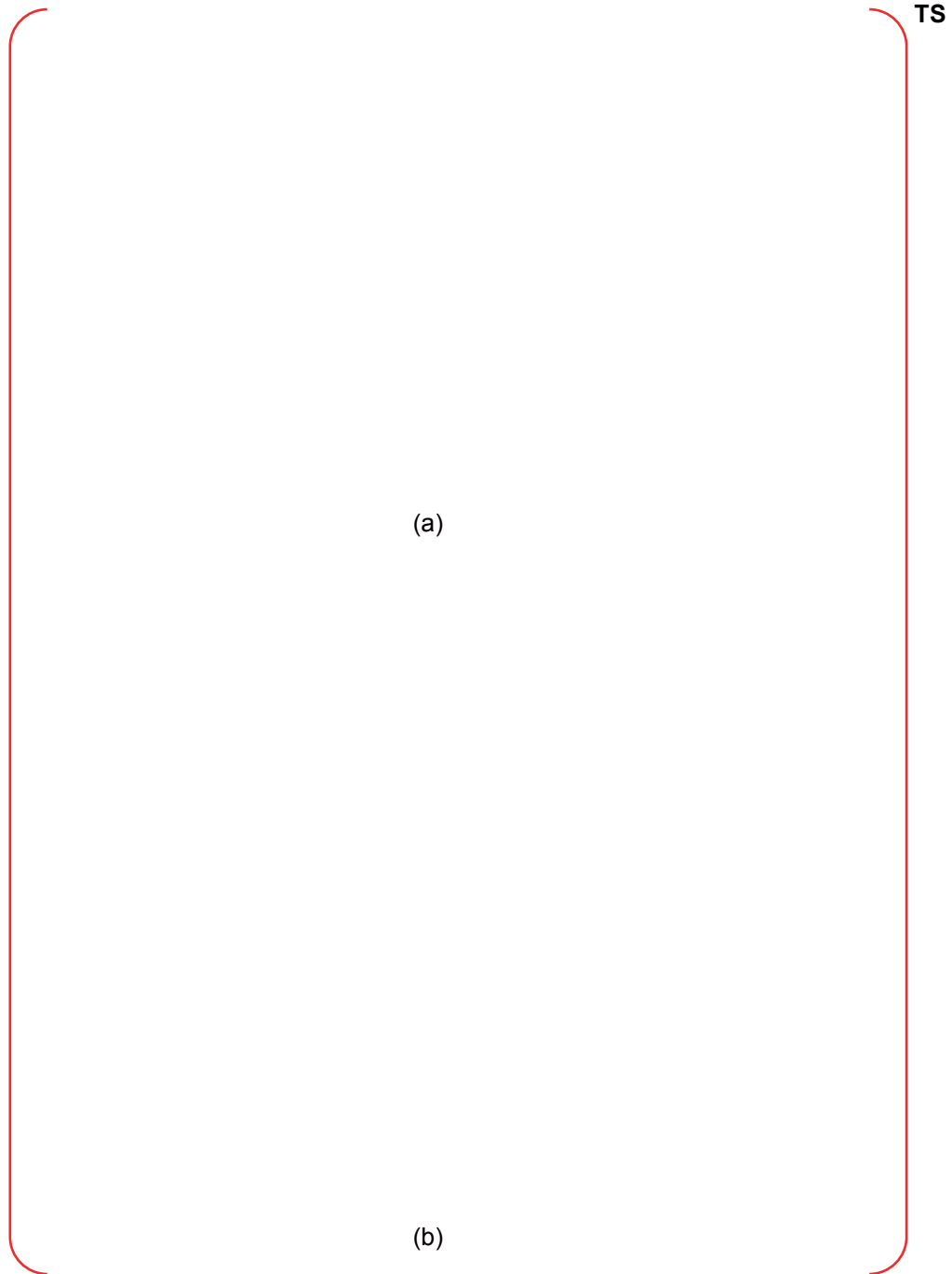


Figure 4-4 Mole Fraction of Hydrogen in the Dome Region for TLOFW-3way valve (1/3)

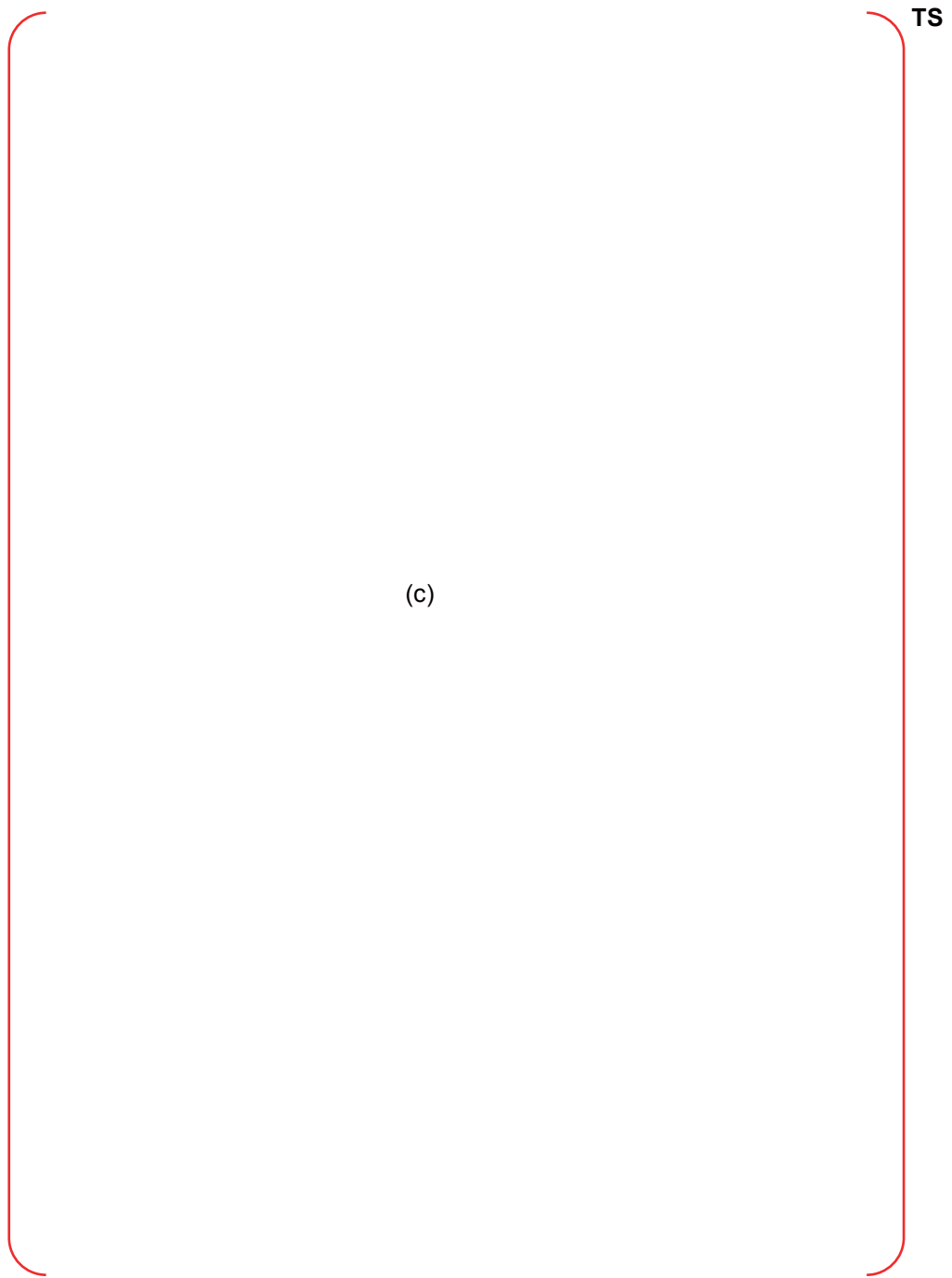
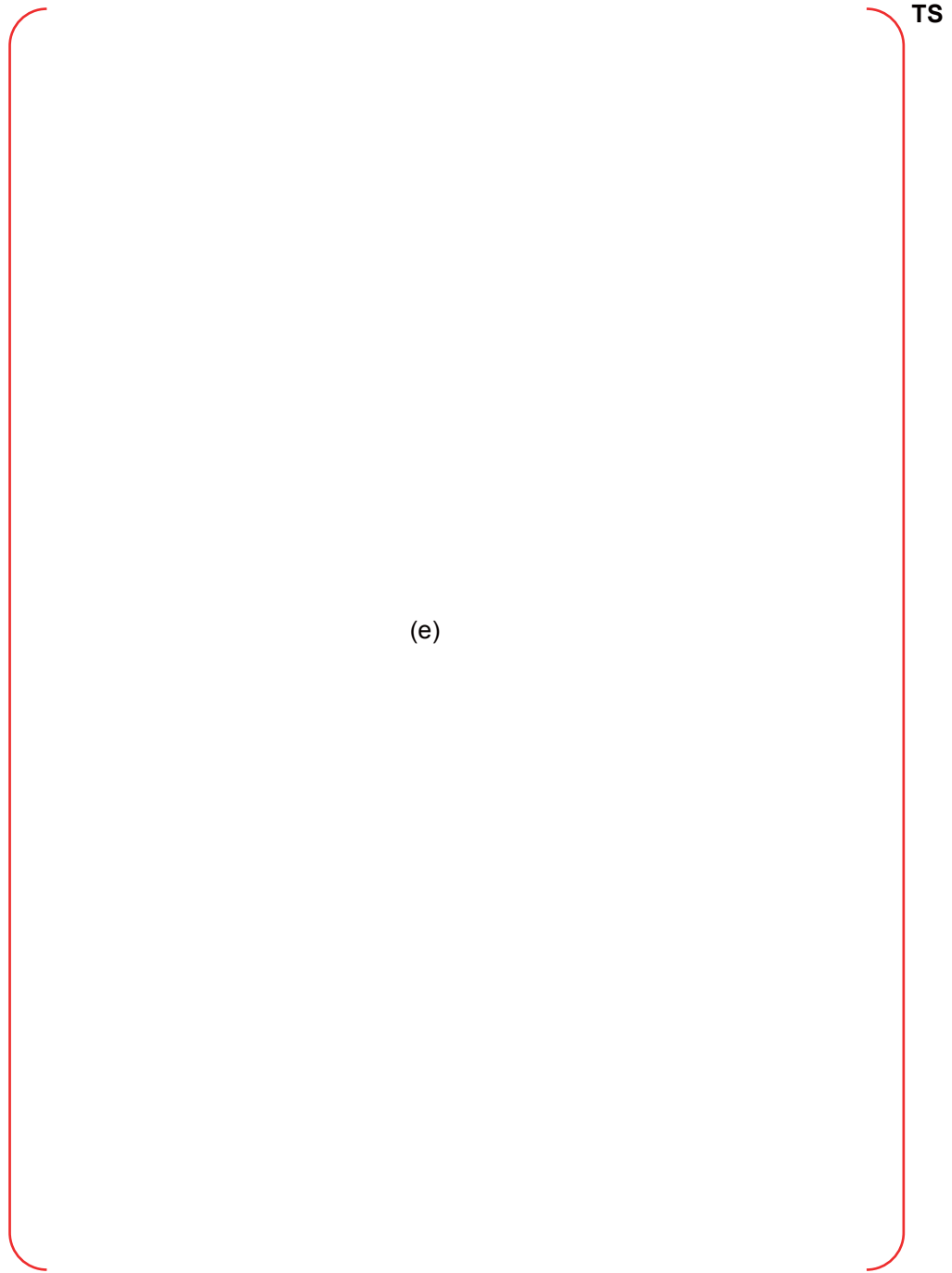


Figure 4-4 Mole Fraction of Hydrogen in the Dome Region for TLOFW-3way valve (2/3)



(f)
Figure 4-4 Mole Fraction of Hydrogen in the Dome Region for TLOFW-3way valve (3/3)

5 CONCLUSION

TS

Based on the evaluation of local hydrogen accumulation of a wide spectrum of accident sequences, it was found that:

- (1) If the POSRV via a three way valve is available, there is no 10% hydrogen limit exceedance anywhere in the containment except in the IRWST quarters and in the SG compartment for high pressure sequences (such as TLOFW, LOOP, and TLOESW for delayed actuation timing of POSRV and three way valve).
- (2) If the HG (Igniters and PARs) is available and no containment sprays are actuated, there is no 10% hydrogen limit exceedance anywhere in the containment for all LOCA sequences.

Based on the evaluation of DDT potential due to local hydrogen accumulation, it was found that:

- (1) There is no DDT potential anywhere in the containment if the POSRV via a three way valve is available.
- (2) If the POSRV via a three way valve is not available in high pressure sequences, the IRWST and areas above it have the potential of DDT.
- (3) DDT potential exists in the lower containment areas for any sequences with igniter failure and dry cavity (due to CFS failure).

With severe accident mitigation features available, there is no potential for DDT anywhere in the containment. The mitigation features include HG, CFS, and manual opening of POSRVs with alignment of the three way valve.

6 RERERENCE

- 1 Austin, J.M., and Shepherd, J.E., 2000, Detonations in Hydrocarbon Fuel Blends, Explosive Dynamics Laboratory Report FM99-6, California Institute of Technology, July.
- 2 Berman, M., 1986, "A Critical Review of Recent Large-Scale Experiments on Hydrogen-Air Detonation," Nuclear Science and Engineering, 93, pp. 321-347.
- 3 NUREG/CR-6530, Blanchat, T.K., & Stamps, D.W. (1997). Deliberate Ignition of Hydrogen-Air-Steam Mixtures in Condensing Steam Environments. Sandia National Laboratories. SAND94-1676.
- 4 NUREG/CR-6580, Blanchat, T. (1998), Performance Testing of Passive Autocatalytic Recombiners, June.
- 5 NP-2669, Bloom, G. R., et al., 1983, "Hydrogen Mixing and Distribution in Containment Atmospheres," Electric Power Research Institute.
- 6 Breitung, W., et al. (2000). Flame Acceleration and Deflagration to Detonation Transition (DDT) in Nuclear Safety. State-of-the-Art Report, OECD Nuclear Energy Agency, Ref. NEA/CSNI/R/2000/7
- 7 NUREG/CR-2726, Camp, A., et al., 1983, "Light Water Reactor Hydrogen Manual," SAND82-1137, Sandia National Laboratories, Albuquerque, NM.
- 8 Chan, C. K. and Dewit, W. A., 1996, Deflagration to Detonation Transition in End Gases, 26th International Symposium on Combustion, The Combustion Institute, Pittsburgh, PA, 2679-2684.
- 9 Chan, C. K., et al., 1994, "Modeling Maximum Flames Speeds," 3rd Int. Conf. on Containment Design and Operation, Toronto, October.
- 10 Chan, C.K. and Wojciechowski, L., "Code Package for Assessing the Potential for DDT in a Post-Accident Nuclear Containment," AECL Whiteshell Laboratories, IAEA-IHMTFCV Cologne, June 2001.
- 11 NUREG/CR-6509, Ciccarelly G., Boccio, J., Ginsberg, T., Finfrock, C., Gerlach, L., Tagava, H. and Malliakos, A., 1998, The Effect of Initial Temperature on Flame Acceleration and Deflagration-to-Detonation Transition Phenomenon, BNL-NUREG-52515.
- 12 Dorofeev, S. B., Sidorov, V. P., Dvoinishnikov, A. E. and Breitung, W., 1996, Deflagration to Detonation transition in Large Confined Volume of Lean Hydrogen-Air Mixtures, Combustion and Flame Vol. 104, 95-110.
- 13 Dorofeev S. B., Sidorov, V. P., Dvoinishnikov, A. E., Denkevits, A., Efimenko, A. and Lelyakin, A., 1997, Large Scale Hydrogen-Air-Steam DDT Experiments in the RUT Facility. Test Series 1996. Report RRC KI 80-05/16, RRC "Kurchatov Institute".
- 14 Dorofeev, S. B., Kuznetsov, M.S., Alekseev, A. A., Efimenko, A. A., Bezmelnitsyn, A. V., Yankin, Yu. G. and Breitung, W., 1999, Effect of Scale and Mixture Properties on Behaviour of Turbulent Flames Preprint IAE-6127/3, RRC "Kurchatov Institute", Report FZKA-6268, Forschungszentrum Karlsruhe.

- 15 Dorofeev, S. B., Sidorov, V. P., Kuznetsov, M. S., Matsukov, I. D. and Alekseev, V. I., 1999, Effect of Scale on the Onset of Detonations, In: CDROM Proceedings of 17th International Colloquium on Dynamics of Explosions and Reactive Systems, Heidelberg, Germany, ISBN 3-932217-01-2.
- 16 DOE/ID-10290, Fauske & Associates, 1990, "Technical Support for the Hydrogen Control Requirements for the EPRI Advanced Light Water Reactor Requirements Document," U.S. Department of Energy.
- 17 Fauske & Associates, 2012(a), MAAP4 Modular Accident Analysis Program for LWR Power Plants, Transmittal Document for MAAP4 Code Revision MAAP 4.0.8, FAI/12-0005, February.
- 18 Gavrikov, A. I., Efimenko, A. A. and Dorofeev, S. B., 2000, "A Model for Detonation Cell Size Predictions from Chemical Kinetics," Combustion and Flame, Vol. 120, 19-33.
- 19 NUREG/CR-2017, Hertzberg, Martin, 1981, "Flammability Limits and Pressure Development in Hydrogen-Air Mixtures," Proc. Workshop on the Impact of Hydrogen on Water Reactor Safety, Volume III, SAND81-0661, Sandia National Laboratories, September 1981.
- 20 Kanzleiter, T. F., and Fisher, K. O., 1994, "Multi-Compartment Hydrogen Deflagration Experiments and Model Development," Nuclear Engineering and Design, 146, pp. 417-426.
- 21 Karwat, H., 1987, "Scaling and Extrapolation of Hydrogen Distribution Experiment," Nuclear Engineering and Design, Vol. 104, pp. 285-294.
- 22 Karwat, H., 1992, "OECD Standard Problem OECD-CSNI-ISP 29, Distribution of Hydrogen within the HDR-Containment Under Severe Accident Conditions," Final Comparison Report (Draft), August 1992
- 23 Kevin, W. B., et al., 1992, "Loads from the Detonation of Hydrogen-Air-Steam Mixtures," SAND92-0544, Sandia National Laboratories.
- 24 NP-2955, Kumar, R. K., et al., 1984, "Intermediate Combustion Studies of Hydrogen-Air-Steam Mixtures," Electric Power Research Institute, Palo Alto, California, June 1984.
- 25 Kumar, R. K., et al., 1994, "Combustion of Hydrogen/Air/Steam Mixtures in a Repeated Obstacle Field," 3rd Int. Conf. on Containment Design and Operation, Toronto, October.
- 26 Kuznetsov, M.S., Alekseev, V. I., Bezmelnitsyn, A. V., Breitung, W., Dorofeev, S. B., Matsukov, I. D., Veser, A. and Yankin, Yu. G., 1999, Effect of Obstacle Geometry on Behavior of Turbulent Flames. Preprint IAE-6137/3, RRC "Kurchatov Institute", Report FZKA-6328, Forschungszentrum Karlsruhe.
- 27 Lee, J. H., Knystautas, R. and Chan, C. K., 1984, Turbulent Flame Propagation in Obstacle-filled Tubes, 20th Symposium International on Combustion. The Combustion Institute, Pittsburgh, PA, 1663-1672.
- 28 Lindstedt, R. P., and Michels, H. J., 1989, "Deflagration of Detonation Transitions and Strong Deflagrations in Alkane and Alkene Air Mixtures," Combustion and Flame, Vol. 76, pp. 169-181.
- 29 NUREG/CR-2017, Liu, D. D., et al., 1981, "Some Results of WRNE Experiments on Hydrogen Combustion," Proc. Workshop on the Impact of Hydrogen on Water Reactor Safety, Volume

- III, SAND81-0661, Sandia National Laboratories, September.
- 30 Luangdilok, W., et al. (2002). Modeling of Hydrogen Flame Propagation in Multicompartiment Buildings. Nuclear Technology, 138, 44-57.
 - 31 Manninen, M., Silde, A., Lindholm, I., Huhtanen, R., and Sjövall, (2002), "Simulation of Hydrogen Deflagration and Detonation in a BWR Reactor Building", Nuclear Engineering and Design, 211, 27-50.
 - 32 Marshall, B. W., 1986, "Hydrogen:Air:Steam Flammability Limits Combustion Characteristics in the FITS Vessel,": NUREG/CR-3468, SAND84-0383, Sandia National Laboratories.
 - 33 Matsukov, I. D., Kuznetsov, M. S., Alekseev, V. I. and Dorofeev, S. B., 1999, Photographic Study of Transition from Fast Deflagrations to Detonations, 22nd International Symposium on Shock Waves, London, UK, 370-375.
 - 34 Moffett, R., 2012, A Canadian Perspective on Passive Autocatalytic Recombiner, Nuclear Engineering International, September 3 (Online Article).
 - 35 N. Cohen, 1992, Flammability and Explosion Limits of H₂ and H₂/CO: A literature Review, Aerospace Report No. TR-92(2534)-1, Aerospace Corporation, September 10.
 - 36 National Research Council, 1987, "Technical Aspects of Hydrogen Control and Combustion in Severe Light-Water Reactor Accidents," National Research Council Report, National Academy Press, Washington, D.C.
 - 37 Narula, J. S., and Woodcock, J., 1994, "Westinghouse-Gothic Distributed Parameter Modeling of HDR Test," 3rd Int. Conf. on Containment Design and Operation, Toronto, October.
 - 38 NUREG-1417, 1990, "Safety Evaluation Report," related to Hydrogen Control Owners Group Assessment of Mark III Containment, October.
 - 39 OECD/NEA, 2010, THAI Project: Hydrogen and Fission Product Issues Relevant for Containment Safety Assessment under Severe Accident Conditions, Final Report, NEA/CSNI/R(2010) .
 - 40 Ofstun, R. P., et al., 1994, "Westinghouse-Gothic Modeling of NUPEC's Hydrogen Mixing and Distribution Test M-4-3," 3rd Int. Conf. on Containment Design and Operation, Toronto, October.
 - 41 Ogata, J., et al., 1995, "NUPEC's Large Scale Hydrogen Mixing Test in a Reactor Containment Vessel (1) Hydrogen Mixing and Distribution Test," 3rd JSME/ASME Joint Int. Conf. on Nuclear Engineering, Kyoto, Japan, April 23-27, Vol. 2, pp. 1149-1154.
 - 42 Peraldi, O., et al., 1986, "Criteria for Transition to Detonation in Tubes," 21st Symp. on Combustion, the Combustion Institute, Pittsburgh, pp. 1629-1638
 - 43 Peterson, P. F., 1994, "Scaling and Analysis of Mixing in Large Stratified Volumes," Int. J. Heat Mass Transfer, Vol. 37, Suppl. 1, pp. 97-106.
 - 44 NUREG/CR-4238, Ratzel, A. C., 1985, "Data Analysis for Nevada Test Site (NTS) Premixed Combustion Tests," SAND85-0135, Sandia National Laboratories, May.

- 45 Reinecke, E., 2012, Operational Behavior of Passive Auto-Catalytic Hydrogen Recombiners, Nuclear Engineering International, September 3 (Online Article).
- 46 Reynolds, W.C., 1995, "The Element-Potential Method for Chemical Equilibrium Analysis: Implementation in the Interactive Program STANJAN," Dep't of Mechanical Engineering, Stanford University, 1981 and STANJAN chemical equilibrium solver, v 3.96, IBM-PC, (c).
- 47 Rodgers, M., et al., 1995, "NUPEC's Large Scale Hydrogen Mixing Test in a Reactor Containment Vessel (3) Visualization of the Mixing Test and the Test Analyses," 3rd JSME/ASME Joint Int. Conf. on Nuclear Engineering, Kyoto, Japan, April 23-27, Vol. 3, pp. 1161-1165.
- 48 Shephard, J. E., 1985, "Chemical Kinetics and Hydrogen-Air-Diluent Detonations," Tenth international Colloquium on Dynamics of Explosions and Reactive Systems, Berkeley, CA, August 4-9.
- 49 NUREG/CR-4803, Sherman, M. P. and Berman, M., 1987, "The Possibility of Local Detonation During Degraded Core Accidents in the Bellefonte Nuclear Plant," SAND86-1180, Sandia National Laboratories, January.
- 50 Sherman, M. P., 1984, "Hydrogen Combustion in Nuclear Plant Accidents and Associated Containment Loads," Nuclear Engineering and Design, 83, p. 13-24.
- 51 Sherman, M. P., Berman, M. and Beyer, R. F., 1993, Experimental Investigation of Pressure and Blockage Effects on Combustion Limits in H₂-air-steam Mixtures, Sandia National Laboratories Report No. SAND91-0252.
- 52 NUREG/CR-2017, Sherman, M. P., et al, 1981, "Deliberate Ignition and Water Fogs as H₂ Control Measures for Sequoyah, Proc. Workshop on the Impact of Hydrogen on Water Reactor Safety, Volume IV, SAND81-0661, Sandia National Laboratories, September.
- 53 NUREG/CR-5275, Sherman, M. S., Tieszen, S., and Benedick, W., 1989 The Effect of Obstacles and Transverse Venting on Flame Acceleration and Transition to Detonation for Hydrogen-Air Mixtures at Large Scale, SAND 85-1264.
- 54 Sidorov, V. P. and Dorofeev, S. B., 1998 (a), Influence of Initial Temperature, Dilution and Scale on DDT Conditions in Hydrogen-air mixtures, Arhivum Combustionis, Vol. 18, No 1-4, 87-103.
- 55 Sidorov, V. P. and Dorofeev, S. B., 1998 (b), Large-Scale Experiments and Scaling of DDT Conditions in Hydrogen-Air-Steam Mixtures - an Overview, Proceedings of the Workshop on Severe Accident Research in Japan (SARJ-97) JAERI-Conf 98-009, 162-182.
- 56 Sidorov, V. P., Kuznetsov, M. S., Matsukov, I. D., Alekseev, V. I., Denkevits, A. V. and Dorofeev, S. B., 1998, Large Scale DDT and Detonation Transmission Experiments with Hydrogen Containing Mixtures in the RUT Facility. Test Series 1998. Report RRC "Kurchatov Institute" RRC KI 80-05/17, April.
- 57 NUREG/CR-5525, Stamps, D., Benedick, W. B., Tieszen, S. R., 1991, "Hydrogen-Air-Diluent Detonation Study for Nuclear Reactor Safety Analyses," SAND89-2398, Sandia National Laboratories.
- 58 Stamps, D. W., 1995, "CONTAIN Assessment of the NUPEC Mixing Experiments," SAND94-

- 2880, Sandia National Laboratories.
- 59 NUREG/CR-5525, Stamps, D., Benedick, W. B., Tieszen, S. R., 1991, "Hydrogen-Air-Diluent Detonation Study for Nuclear Reactor Safety Analyses," SAND89-2398, Sandia National Laboratories.
 - 60 Tezuka, H., and Hirose, T., 1994, "Final Comparison Report on ISP-35 NUPEC's Hydrogen Mixing and Distribution Test - Test M-7-1, ISP35-092 Rev. 5, Nuclear Power Engineering Corporation, Japan, September 10.
 - 61 Tezuka, H., et al., 1995, "NUPEC's Large Scale Hydrogen Mixing Test in a Reactor Containment Vessel (2) MELCOR Analysis of the Mixing Tests," The 3rd JSME/ASME Joint Int. Conf. on Nuclear Engineering, Kyoto, Japan, April 23-27, Vol. 3, pp. 1155-1159.
 - 62 Teodorczyk, A., Lee, J. H. S. and Knystautas R., 1988, Propagation Mechanisms of Quasi-detonations, 22nd Symposium International on Combustion. The Combustion Institute, Pittsburgh, PA, 1723-1731.
 - 63 Teodorczyk, A., Lee, J. H. S., and Knystautas, R., 1990, Photographic Studies of the Structure and Propagation Mechanisms of Quasi-Detonations in a Rough Tube, In: AIAA Progress in Astroautics and Aeronautics, Vol. 133, 233-240.
 - 64 NP-3878, Thomson, R. T., et al., 1988, "Large-Scale Hydrogen Combustion Experiments, Vol. 1: Methodology and Results," Electric Power Research Institute.
 - 65 NUREG/CR-4905, Tieszen, S. R., et al., 1987, "Detonability of H₂-Air-Diluent Mixtures," SAND85-1263, Sandia National Laboratories, Albuquerque, New Mexico, July.
 - 66 Tieszen, S. R., et al., 1993, "Hydrogen Distribution and Combustion," in Ex-Vessel Accident Review for the Heavy Water New Production Reactor (e.d. by K. D. Bergeron), SAND 90-0234, NPRW-SA90-3, Sandia National Laboratories.
 - 67 Travis, J.R., 2001, "Compilation of Work Reports on GASFLOW Extensions between March 1995 and February 2001," FZK, March 14.
 - 68 Valencia, L., and Wolf, L., 1990a, "Overview of First Results on H₂-Distribution Tests at the Large Scale HDR-Facility," 2nd Int. Conf. on Containment Design and Operation, Toronto, October.
 - 69 NUREG/CP-0114, Valencia, L., and Wolf, L., 1990b, "Large-Scale HDR Hydrogen Mixing Experiments Test Group #11," Proceeding of the U.S. Nuclear Regulatory Commission, 18th Water Reactor Safety Information Meeting, Vol. 2.
 - 70 Wenzel, H. H., et al., 1989, "Wasserstoffverteilungsversuche HDR-Versuchsgruppe CON Versuch E11.2," Kernforschungszentrum Karlsruhe, PHDR-Arbeitsbericht Nr. 10.010/89.
 - 71 Whitehouse, D. R., et al., 1994, "Combustion of Stratified Hydrogen-Air Mixtures in the 10.7 m³ CTF Cylinder," 3rd Int. Conf. on Containment Design and Operation, Toronto, October.
 - 72 NUREG/CP-0105, Wolf, L., and Valencia, L., 1989, "Hydrogen Mixing Experiments in the HDR-Facility," Proceeding of the U.S. Nuclear Regulatory Commission, 17th Water Reactor Safety Information Meeting, Vol. 2.

- 73 M. P. Sherman, S. R. Tieszen and W. B. Benedick, Sandia National Laboratories Report No. SAND89-0859, 1989.

Appendix-B

Severe Accident Analysis Report for MCC

TABLE OF CONTENTS

1	INTRODUCTION	B-7
2	ANALYSIS METHODOLOGY	B-9
2.1	Major Assumptions.....	B-9
2.1.1	MAAP 4.0.8 MCCI Model.....	B-9
2.1.2	Other.....	B-9
2.2	Main Features of MCCI Model.....	B-10
2.2.1	Corium Thermal Property Evaluation.....	B-10
2.2.1.1	Element Partition.....	B-10
2.2.1.2	Phase Diagrams.....	B-11
2.2.1.3	Temperature Calculating Procedure.....	B-12
2.2.2	Corium- Concrete Chemical Reactions.....	B-12
2.2.3	Concrete Ablation.....	B-12
2.2.4	Effects of Water.....	B-14
2.3	MAAP 4.0.8 Model Limitations.....	B-15
2.4	Quantifications of Key Inputs.....	B-16
2.4.1	CORQUENCH 3.03 Results.....	B-16
2.4.2	Selection of the FCHF Value.....	B-17
2.4.3	Selection of the ENT0C Value.....	B-17
2.4.4	Summary of MCCI Parameters Used in MAAP 4.0.8 Analyses for APR1400.....	B-17
3	DETAILED ANALYSIS	B-30
3.1	Scenario Selection.....	B-30
3.1.1	Sequence Identifier: R1-TLOES-003-MCCI.....	B-30
3.1.2	Sequence Identifier: R2_MLOCA003-MCCI.....	B-31
3.1.3	Sequence Identifier: R3_LOOP-004-MCCI.....	B-31
3.1.4	Sequence Identifier: R9_SBO-006-MCCI.....	B-32
3.1.5	Sequence Identifier: LLOCA-C04-NoECSBS-MCCI.....	B-32
3.2	Results of analysis.....	B-33
3.2.1	Sequence Identifier: R1-TLOES-003-MCCI.....	B-33
3.2.2	Sequence Identifier: R2-MLOCA003-MCCI.....	B-34
3.2.3	Sequence Identifier: R3_LOOP-004-MCCI.....	B-35
3.2.4	Sequence Identifier: R9_SBO-006-MCCI.....	B-35
3.2.5	Sequence Identifier: LLOCA-C04-NoECSBS-MCCI.....	B-36
4	CONCLUSIONS	B-56
5	REFERENCES	B-59

LIST OF TABLES

Table 2-1	Basis Equations and Species.....	B-19
Table 2-2	METOXO Compound List.....	B-20
Table 2-3	MCCI Parameters Used in MAAP4.0.8 Analyses for APR1400.....	B-21
Table 2-4	Additional Set of MCCI Parameters Used in Hydrogen Distribution and DDT Analyses for APR1400	B-21
Table 3-1	Ten PRA Sequences with High Core Damage Frequencies	B-30
Table 3-2	Run Equipment Availability for R1_TLOES-003-MCCI	B-31
Table 3-3	Run Equipment Availability for R2_MLOCA003-MCCI	B-31
Table 3-4	Run Equipment Availability for R3_LOOP-004-MCCI.....	B-32
Table 3-5	Run Equipment Availability for R9_SBO-006-MCCI	B-32
Table 3-6	Run Equipment Availability for LLOCA-C04-NoECSBS-MCCI	B-33
Table 4-1	Selected Severe Accident Scenarios for MCCI Analyses for the APR1400 Plant.....	B-57

LIST OF FIGURES

Figure 2-1	MAAP 4.0.8 Model of Corium Pool, Crusts, and Concrete Slab	B-22
Figure 2-2	Organization of Materials for Energy-Temperature Relations.....	B-23
Figure 2-3	Pseudo-Binary Phase Diagram with Dashed Lines Indicating Constant Liquid Fraction.....	B-24
Figure 2-4	Energy-Temperature Relationship for a Pseudo-Binary System	B-25
Figure 2-5	Major Metallic Phase Diagram	B-26
Figure 2-6	Ablation Depth in Cavity Floor for Different FCHF	B-27
Figure 2-7	Heat Flux from Corium to Water for Different FCHF	B-27
Figure 2-8	Heat Transfer Rate from Corium to Water for Different FCHF.....	B-28
Figure 2-9	Containment Pressure for Different FCHF	B-28
Figure 2-10	Comparison of Pressure in the Containment for the Cases with ENT0C=10-5, and ENT0C=0.045.....	B-29
Figure 3-1	Pressure in RCS for the PRA sequence of loss of essential service water (R1_TLOES-003-MCCI).....	B-38
Figure 3-2	Core exit temperature for the PRA sequence of loss of essential service water (R1_TLOES-003-MCCI).....	B-38
Figure 3-3	Pressures in steam generators for the PRA sequence of loss of essential service water (R1_TLOES-003-MCCI)	B-39
Figure 3-4	Water levels in steam generators for the PRA sequence of loss of essential service water (R1_TLOES-003-MCCI)	B-39
Figure 3-5	Masses in the core, lower plenum and reactor cavity for the PRA sequence of loss of essential service water (R1_TLOES-003-MCCI)	B-40
Figure 3-6	Ablation depth in floor and sidewall for the PRA sequence of loss of essential service water (R1_TLOES-003-MCCI).....	B-40
Figure 3-7	Pressure in containment dome for the PRA sequence of loss of essential service water (R1_TLOES-003-MCCI)	B-41
Figure 3-8	Pressure in RCS for the PRA sequence of medium break LOCA (R2_MLOCA003-MCCI)	B-41
Figure 3-9	Core exit temperature for the PRA sequence of medium break LOCA (R2_MLOCA003-MCCI)	B-42
Figure 3-10	Pressures in steam generators for the PRA sequence of medium break LOCA (R2_MLOCA003-MCCI)	B-42
Figure 3-11	Water levels in steam generators for the PRA sequence of medium break LOCA (R2_MLOCA003-MCCI)	B-43
Figure 3-12	Masses in the core, lower plenum and reactor cavity for the PRA sequence of medium break LOCA (R2_MLOCA003-MCCI)	B-43
Figure 3-13	Ablation depth in floor and sidewall for the PRA sequence of medium break LOCA (R2_MLOCA003-MCCI)	B-44
Figure 3-14	Pressure in containment dome for the PRA sequence of medium break LOCA (R2_MLOCA003-MCCI)	B-44

Figure 3-15	Pressure in RCS for the PRA sequence of loss of offsite power (R3_LOOP-004-MCCI)	B-45
Figure 3-16	Core exit temperature for the PRA sequence of loss of offsite power (R3_LOOP-004-MCCI)	B-45
Figure 3-17	Pressures in steam generators for the PRA sequence of loss of offsite power (R3_LOOP-004-MCCI)	B-46
Figure 3-18	Water levels in steam generators for the PRA sequence of loss of offsite power (R3_LOOP-004-MCCI)	B-46
Figure 3-19	Masses in the core, lower plenum and reactor cavity for the PRA sequence of loss of offsite power (R3_LOOP-004-MCCI)	B-47
Figure 3-20	Ablation depth in floor and sidewall for the PRA sequence of loss of offsite power (R3_LOOP-004-MCCI)	B-47
Figure 3-21	Pressure in containment dome for the PRA sequence of loss of offsite power (R3_LOOP-004-MCCI)	B-48
Figure 3-22	Pressure in RCS for the PRA sequence of loss of AC power with short battery life (R9_SBO-006-MCCI)	B-48
Figure 3-23	Core exit temperature for the PRA sequence of loss of AC power with short battery life (R9_SBO-006-MCCI)	B-49
Figure 3-24	Pressures in steam generators for the PRA sequence of loss of AC power with short battery life (R9_SBO-006-MCCI)	B-49
Figure 3-25	Water levels in steam generators for the PRA sequence of loss of AC power with short battery life (R9_SBO-006-MCCI)	B-50
Figure 3-26	Masses in the core, lower plenum and reactor cavity for the PRA sequence of loss of AC power with short battery life (R9_SBO-006-MCCI)	B-50
Figure 3-27	Ablation depth in floor and sidewall for the PRA sequence of loss of AC power with short battery life (R9_SBO-006-MCCI)	B-51
Figure 3-28	Pressure in containment dome for the PRA sequence of loss of AC power with short battery life (R9_SBO-006-MCCI)	B-51
Figure 3-29	Pressure in RCS for the PRA sequence of large break LOCA (LLOCA-C04-NOECSBS-MCCI)	B-52
Figure 3-30	Core exit temperature for the PRA sequence of large break LOCA (LLOCA-C04-NOECSBS-MCCI)	B-52
Figure 3-31	Pressures in steam generators for the PRA sequence of large break LOCA (LLOCA-C04-NOECSBS-MCCI)	B-53
Figure 3-32	Water levels in steam generators for the PRA sequence of large break LOCA (LLOCA-C04-NOECSBS-MCCI)	B-53
Figure 3-33	Masses in the core, lower plenum and reactor cavity for the PRA sequence of large break LOCA (LLOCA-C04-NOECSBS-MCCI)	B-54
Figure 3-34	Ablation depth in floor and sidewall for the PRA sequence of large break LOCA (LLOCA-C04-NOECSBS-MCCI)	B-54
Figure 3-35	Pressure in containment dome for the PRA sequence of large break LOCA (LLOCA-C04-NOECSBS-MCCI)	B-55

Figure 4-1 Ablation Depths within 24 Hours for Different Severe Accident Scenarios for the APR1400 Plant..... B-58

Figure 4-2 Containment Pressures within 24 Hours for Different Severe Accident Scenarios for the APR1400 Plant..... B-58

1 INTRODUCTION

Molten corium-concrete interaction (MCCI) is a severe accident phenomenon occurring when corium is relocated from the vessel into the reactor cavity. The interaction involves melting and decomposition of concrete, chemical reactions between the concrete and corium materials, and heat transfer from the corium to its surroundings. It can potentially cause: a) a large amount of non-condensable and flammable gases being released from concrete decomposition; b) a large amount of heat due to the chemical reactions between the corium and the concrete; c) fission product release from the corium to the containment atmosphere; and d) significant amount of concrete erosion. Uranium dioxide, zirconium dioxide, zirconium and stainless steel comprise the core melt. The major constituents of concrete are SiO_2 , CaO , Al_2O_3 , MgO , Fe_2O_3 , K_2O , Na_2O , free water, chemically bound water and CO_2 . When the molten core material contacts the concrete and the temperature of the concrete reaches the ablation temperature the concrete begins to ablate and a layer of molten concrete or slag forms that separates the solid concrete below from the overlying core melt. The formation of the concrete melt may be accompanied by the appearance of a crust of core material that grows on the slag layer. Beneath the ablating surface of the concrete the solid concrete decomposes and releases water and CO_2 gas stored in the concrete. Thus gas bubbles evolve from the concrete ablation front and rise through the core melt pool. Portions of the concrete slag layer may be removed by the evolving gas bubbles and thereby enter and mix with the core melt. Since concrete is less dense than the overlying core melt material, buoyancy will also cause the concrete slag to rise and mix with the core melt. Thus the core melt pool is stirred by both gases and rising concrete slag. An intervening crust of frozen core material may temporarily impede or cut off the mixing of the concrete slag below the crust with the core melt pool above the crust.

As concrete slag continues to mix with the core melt pool additional complications arise. Core melt/concrete mixtures possess a wide temperature range between the liquidus and solidus temperatures where liquid and solid coexist. High viscosity conditions are likely to exist in the relatively cool boundary layers just above the concrete slag layer and beneath the surface of the pool. In these regions the core melt/concrete mixture temperature may be below the mixture liquidus temperature and at a point where the mixture carries a considerable quantity of precipitate solids. In fact, the whole MCCI pool may be at a temperature below the liquidus. Thus MCCI ablation heat transfer involves three phases: gas, liquid and solid. The viscosity of the mixture is known to increase sharply with increasing solids concentration (or, equivalently, decreasing temperature), making it difficult to assign an effective Newtonian viscosity to the mixture. The presence of a significant concentration of solids in core melt/concrete mixtures may cause foaming.

Most of the energy emitted by the pool's surface is transported to the containment walls or an overlying water pool via thermal radiation. However the surface temperature of the pool, which dictates the magnitude of the emitted radiation will be influenced by the presence of a crust cover, below-surface turbulent natural convection, and/or the passing of gas bubbles through the surface of the pool. Also, thermal radiation from the melt could be strongly attenuated by the particle cloud that obviously exists in the atmosphere above the pool. The MCCI process is sustained for a relatively long period of time by the radioactive decay of fission products and by a number of in-pool chemical reactions involving, say, the reduction of steam, CO_2 and SiO_2 by zirconium.

If there is any water in the reactor cavity, the underlying corium can be cooled by this water, and the released fission products can be scrubbed by the water pool. Therefore, MCCI in a flooded reactor cavity is generally less severe than MCCI in a dry cavity. However, heat transfer from corium to water can potentially generate a large amount of steam, in addition to the non-condensable gases generated during concrete decomposition, becoming another source of containment pressurization.

It is crucial to assess the consequences of MCCI and its threat to containment integrity to ensure that proper regulatory criteria are being satisfied. Specifically, for APR1400, there are two concerns with regard to MCCI: a) whether the containment pressure will exceed the containment failure pressure in the first 24 hours after core damage; and b) whether the concrete erosion will cause breach of the leak-tight boundary (liner) of the containment.

TS

Clearly, the MCCI is a particularly difficult problem to deal with by mathematical modeling alone, and it was recognized early on that little progress would be made on this problem in the absence of experiments with prototypic reactor materials. Real material testing of the MCCI phenomenon began in 1975 and MCCI issue has continued unabated to this day. The early experiments as well as some recent ones involved metallic and oxidic melts poured onto concrete in the absence of an applied heat source. Later on emphasis was placed on the conduct of tests with sustained heating in the melt to simulate radioactive decay heating, but concrete ablation was limited to the downward direction only. Because sideward heat losses (ablation) from an MCCI pool is important in terms of the overall pool energy balance and because of the threat to containment structures in some plants, so called two-dimensional (2D) experiments were ultimately performed, which included both downward and sideward concrete ablation. Finally, the real material MCCI testing included flooding the interacting materials from above with water to see if the MCCI could be terminated by quenching.

2 ANALYSIS METHODOLOGY

Integral severe accident analysis code MAAP 4.0.8 was used to calculate the containment pressure and concrete floor and side ablation depths through MCCI phenomena for APR1400 plant under severe accident scenarios. This section discusses the assumptions and main features of the MAAP 4.0.8 model, followed by quantifications of key modeling parameters FCHF and ENT0C.

2.1 Major Assumptions

2.1.1 MAAP 4.0.8 MCCI Model

The following assumptions were used in the MCCI model in MAAP 4.0.8 (Reference 1) to simplify the complexity of the physical and chemical processes:

- 1) The corium is homogeneously mixed due to the agitation by the off-gases from concrete ablation, i.e., no stratification is considered in the corium.
- 2) The corium pool is represented by a single average internal energy.
- 3) The oxide corium is treated as a pseudo-binary system of core oxides (UO_2 , ZrO_2) and concrete oxides (SiO_2 , CaO , MgO , Al_2O_3 , etc.).
- 4) Chemical reactions can be treated by an equilibrium model.
- 5) Corium crust has the same composition as molten debris.
- 6) Temperature distribution in the crust is close to steady-state profile.
- 7) All energy involved in the concrete phase change and endothermic chemical reactions can be lumped together as a single effective latent heat.
- 8) The temperature profile in the concrete slab is essentially one-dimensional in the direction of erosion. Fine nodes are used near the erosion interface to track the melting front.
- 9) Gases released from the concrete floor ablation will enter the corium mixture at 100%. Gases released from the (vertical) concrete sidewall ablation will also enter the corium mixture at a user specified fraction.
- 10) The heat transfer rate from the corium to water above it is given by a formulation for CHF rate, which can be adjusted by a user specified parameter FCHF.
- 11) The reactor cavity floor is a flat one-piece concrete slab, i.e., it has no deep concaving part such as sump.

2.1.2 Other

TS



The assumed pressure limit will be referred to as the "FLC" throughout this report.

2.2 Main Features of MCCI Model

Figure 2-1 illustrates how MAAP 4.0.8 models the interaction between corium and its surrounding in the reactor cavity. Specifically, it models corium contacting a concrete floor and sidewall, while losing heat by boiling heat transfer to water if the cavity is flooded or by thermal radiation to upper walls and by convection to the atmosphere if the cavity is dry. The floor and sidewall are modeled as one horizontal and one vertical heat sink that can be ablated by, and react with the corium pool. As the concrete heat sink ablates, it releases decomposed non-gaseous constituents, namely "slag", and gaseous constituents, namely "off-gases", which enter the corium pool and react with corium materials to generate heat and gases such as CO and H₂.

2.2.1 Corium Thermal Property Evaluation

One of the evaluations in MCCI model is to determine thermal properties in the corium mixture based on bulk constituents and total internal energy, including temperature, solid fraction, viscosity, and other properties. MAAP 4.0.8 follows a simplified approach, including partitioning the elements into oxidic and metallic phases, constructing pseudo-binary phase diagram, and finding the temperature and other properties.

2.2.1.1 Element Partition

Corium in the reactor cavity typically consists of UO₂, Zr, ZrO₂, Fe, Cr, Ni, either B₄C or Ag-In-Cd plus fission product compounds (such as SrO, BaO, La₂O₃, etc.) and trace materials contained in alloys (such as Sn, Mn, etc.). It also includes the compounds from concrete slag (such as SiO₂, CaO, MgO, etc.) as the molten core-concrete interaction progresses. The compounds in the corium can form solutions in which the oxygen initially associated with oxides is partly dissolved in a metallic phase and partly remains in an oxidic phase. Other elements, such as U would be preferentially present in the oxide phase, while Fe, Cr and Ni, would be preferentially present in the metallic phase. In general, every element will partition in some proportion between these two phases.

If material data was available for an applicable range, an equilibrium calculation could be used to evaluate the composition of the metal and oxide phases by minimizing the Gibbs free energy of both phases at constant temperature. Unfortunately, functional forms for chemical potentials (Gibbs free energies) have only been created for a small subset of the compounds of interest, namely UO₂, ZrO₂, SiO₂, CaO, and MgO. Thus, a rigorous model cannot be applied to the entire corium system. However, it can be applied to some subsystems to yield pseudo-binary data.

A simplification was made to replace the free energy minimization calculations with two types of data: equilibrium compositions within each phase as a function of temperature and bulk composition (a phase diagram for each phase), and internal energy functions for each compound in each phase (enthalpies of mixing). The means of combining these data constitute the solution technique for temperature, either for each phase separately or for both phases isothermally. Figure 2-2 illustrates how various elements are expected to be partitioned between metal and oxide phases of core debris. MAAP 4.0.8 assumes that U and Zr will essentially oxidize to completion before B₄C, Fe, Cr, and Ni begin to oxidize. It also assumes that reduction of slag oxides such as SiO₂ and CaO may be neglected for the temperature calculation. PWR control rod material constituents Ag-In-Cd (minor metals) are excluded from the metal phase diagram because they are assumed to have a negligible influence compared to other materials; however, their internal energy is considered. Trace materials such as Sn and Mn are assumed to have both negligible energy and influence on the phase equilibria, and are excluded from the phase diagrams and the temperature calculation.

Materials defined for the energy calculation are therefore:

- 1) U-Zr-O + (SO + CN): Oxides, a combination of U-Zr-O, steel oxides and concrete slag oxides;
- 2) BCS: Major metals, a combination of B-C-Fe-Cr-Ni-Zr;
- 3) Ag-In-Cd: Minor metals for PWR control materials.

2.2.1.2 Phase Diagrams

For oxidic phase, core-concrete oxides are characterized by a large difference in the melting range between core debris (typically between 2900 K to 3100 K) and concrete slag (typically 1300 K to 1700 K). The pseudo-binary phase diagram approach has therefore been applied to this system using core oxide and concrete slag as two pseudo-compounds.

Based on the best-estimate calculations for a core-oxide – concrete-oxide pseudo-binary system (Reference 3) a generic core-concrete pseudo-binary phase diagram, as shown in Figure 2-3 is developed. The solidus and liquidus of each pseudo-compound and the solidus, liquidus, and liquid fraction for the mixture of the two pseudo-compounds are shown as a function of composition and temperature. Key parameters of the phase diagram of core-oxide – concrete are user inputs in the concrete property section of MAAP 4.0.8 parameter file.

The energy-temperature constitutive relationship for a pseudo-binary oxide mixture is plotted in Figure 2-4. Given the composition and selecting a temperature, one can obtain the liquid fraction, and solidus and liquidus temperature by interpolation. The oxide mixture energy is then given by:

$$U = (1 - f_L) \sum_i X_{iS} U_{iS} + f_L \sum_i X_{iL} U_{iL} \quad (2-1)$$

where U is the energy, X_{iS} and X_{iL} are the solid and liquid composition of component i respectively, and f_L is the liquid mass fraction.

For metallic phase, it is assumed that the metal phase can be represented as a pseudo-binary mixture of Fe plus other metals, for three reasons. First, unless large quantities of un-oxidized Zr are present, Fe will be by far the most abundant metal. Second, even when there is more Zr than Fe, the amount of other metals (except U) relative to Fe would be small and hence a binary Fe-Zr (or pseudo-binary Fe-(U,Zr)) diagram may be a good first approximation to the real system. Last, binary Fe - other metal phase diagrams are commonly available.

The pseudo-binary phase diagram can be generated from binary metal phase diagram data. It is assumed that dissolved oxygen has a negligible impact on the metal phase diagram. This is a good approximation when Fe dominates the metals, though it is not as clearly valid for Zr. Therefore, dissolved oxygen will only be considered to influence the melting point of otherwise pure Zr. The calculated phase diagram for the metal phase is shown in Figure 2-5.

The temperature-energy relationship for the metallic phase is assumed to be the same as for the oxides, except that there is no congruent melting at the liquidus, or the solidus.

2.2.1.3 Temperature Calculating Procedure

Given the energy and composition of the corium mixture, MAAP 4.0.8 determines its temperature with the phase diagram. The first step is to find the phase change temperatures, i.e., the solidus and the liquidus, for each of the three pseudo-compounds: the oxide, the major metal, and the minor metal. The energy of each material at phase change is obtained from the “pure” substance material properties. Total energy of the mixture at each phase change temperature is then calculated as the sum of energies of all materials.

To find the upper and lower bounds of temperature for the iteration, input energy is compared with the mixture total energy at every phase change temperature. When input energy is between the upper and lower bounds of a phase change, the temperature is known and the solid fraction can be directly solved. When the mixture input energy is between the phase change energies at two temperatures, Newton's method is applied to find the temperature iteratively. A linear programming method is used to find the temperature if Newton's method does not converge within the expected number of iterations.

Once the temperature is determined, properties of the corium such as density, volume, and viscosity are determined from averaging those of individual constituents.

2.2.2 Corium - Concrete Chemical Reactions

Chemical reactions between the concrete and corium materials are the major cause generating large amount of heat and non-condensable gases, including the combustible gases of H₂ and CO. The chemical reactions are calculated by a module in the MAAP 4.0.8 model that assumes chemical equilibrium reached at each time step.

Table 2-1 lists the reactions and the basic chemical species considered in the model. In addition to the basic species listed in Table 2-1, a number of intermediate (auxiliary) species shown in Table 2-2 are also considered. At the equilibrium, the partial pressures of the reactants and products follow a temperature dependent ratio. An example is given here for the reaction of H₂ plus CO₂ to generate H₂O and CO (equation 1 in Table 2-1):

$$k_1 = \frac{p(\text{H}_2) p(\text{CO}_2)}{p(\text{H}_2\text{O}) p(\text{CO})} \quad (2-2)$$

where k_1 is a temperature-dependent chemical reaction ratio evaluated at each time step, and $p(\)$ designates the partial pressure of a particular species in the mixture. Taking the natural logarithm of each side and noticing that the total pressure and total number of gas moles cancels out, p can be replaced by n , or the number of moles, yielding:

$$r_1 = 0 = -\ln(k_1) + \ln[n(\text{H}_2)] + \ln[n(\text{CO}_2)] - \ln[n(\text{H}_2\text{O})] - \ln[n(\text{CO})] \quad (2-3)$$

where r_1 is the residual function for the first basic species. Similar equations can be written for all the basic species and auxiliary species. Ultimately, Newton-Raphson technique can be used to find the number of mole for each species that reduces the residual function r to zero.

Through this technique, the compositions at the equilibrium are solved at each time step based on the instantaneous temperature, and the heat and gases generations are determined by comparing the current time step equilibrium compositions and the previous time step compositions. The non-condensable gases released from the chemical reactions are added to containment gas space to assess pressurization rate in the containment.

2.2.3 Concrete Ablation

Ultimately, the objective of MCC1 studies is to evaluate the potential failing the containment integrity, either through too much concrete ablation, or too much pressurization. The evaluation must be performed by calculating the heat transfer from the corium into the concrete and concrete ablation rate.

If the corium-concrete mixture pool is substantially deep to prevent removal of the heat generated by fission product through conduction, the central region of the pool remains molten. Three pieces of solid crusts are tracked, including: the lower crust interacting with the concrete floor, the side crust interacting with the concrete sidewall, and the upper crust at the top transferring heat to water, gas or reactor cavity upper wall heat sink. Each crust may have different thickness depending on the convective heat transfer from the molten pool to the crust, and from the crust to its interfaced heat sink. The heat flux from the molten pool to the crust can be represented by the convective term given in the following equation

$$q'' = \begin{cases} h_d (T_F - T_{F,m}) & , \text{ for bottom crust} \\ h_s (T_F - T_{F,m}) & , \text{ for side crust} \\ h_u (T_F - T_{F,m}) & , \text{ for upper crust} \end{cases} \quad (2-4)$$

where q'' is the heat flux from the molten pool to the crust, h_d , h_s and h_u are the downward, sideward and upward heat transfer coefficients, T_F is the bulk temperature of the molten debris, and $T_{F,m}$ is the melting temperature of the debris. The convective heat transfer coefficient is affected by viscosity, and the viscosity increases rapidly with increasing debris solid fraction. The solid fraction of the oxide debris can be treated as a pseudo-binary system of core oxide (UO_2 , ZrO_2) and concrete oxide (SiO_2 , CaO , MgO , Al_2O_3 , etc.). As discussed in the previous section, the solid fraction is governed by the system temperature, which, in turn, is controlled by the heat transfer from the pool. When the pool is 100% liquid, the maximum convective heat transfer is achieved, and when the debris is completely solidified, the convective term disappears. Downward, sideward, and upward heat transfer coefficients are modeled as functions of the corium solid fraction, expressed by the following mathematical formulation:

$$h_i = h_{i,0} (1 - f_s)^n \quad (2-5)$$

where subscript i represents downward ($i=d$), sideward ($i=s$) or upward ($i=u$) heat transfer coefficient, $h_{x,0}$ is the nominal maximum value of the coefficient, f_s is the solid fraction in the molten pool, and n is an exponent. Experimental data were used to determine the nominal heat transfer coefficient and the exponent.

Heat transfer from the crust to its interfaced heat sink is calculated with the assumption that the temperature distribution in the crust is close to the steady-state profile. Due to internal heat generation, the steady-state profile in the crust is a parabolic function. The exact temperature distribution is determined with the boundary conditions at the interfaces between the molten pool and the crust, and between the crust and heat sink. In most cases, the temperature between the interface of the molten pool and the crust stays at the corium melting (solidus) temperature; the temperature between the interface of the crust and concrete is at the concrete melting temperature. Once the temperature profiles are evaluated with the given boundary conditions of the temperatures at the interfaces, the crust growing or shrinking rate is evaluated through energy balance, given as

$$\frac{dX_{cr,i}}{dt} = \frac{q_i'' + q_v'' X_{cr,i} - k_{cr} \left. \frac{dT_{cr,i}}{dx} \right|_{x=X_{cr,i}}}{r_{cr} LH_{cr}} \quad (2-6)$$

where $X_{cr,i}$ is the thickness of crust, q_i'' is the convective heat transfer rate from the molten corium pool to the crust, q_v''' is the volumetric decay power generation rate in the crust, $k_{cr} \left. \frac{dT_{cr}}{dx} \right|_{x=X_i}$ term represents the heat conduction rate from the crust to the concrete, ρ_{cr} is the density of the crust, LH_{cr} is the latent heat from the crust to form or melt. Based on the temperature profile, the heat flux from the crusts to the heat sinks q_{cn}'' is easily evaluated through conduction heat transfer equations.

Once the energy loss to the concrete q_{cn}'' is determined, response of the concrete material to the imposed heat flux is solved by considering energy balance at the ablation front. The concrete heat sink is modeled as one-dimensional slab, and the temperature distribution in the slab is simulated with a fully implicit solution of the one-dimensional heat conduction equation. For a given the heat flux from the core debris into the concrete, its ablation rate is calculated through the energy balance as:

$$\frac{dX_{cn,i}}{dt} = \frac{q_{cn,i}'' - k_{cn} \left. \frac{dT_{cn,i}}{dx} \right|_{x=0}}{\rho_{cn} LH_{cn}} \quad (2-7)$$

where $\frac{dX_{cn,i}}{dt}$ is the ablation rate, $T_{cn,i}$ is the temperature in the concrete slab, $k_{cn} \left. \frac{dT_{cn,i}}{dx} \right|_{x=0}$ is the heat flux conducted away from the interface, ρ_{cn} is the concrete density. The latent heat term LH_{cn} is a bulk latent heat of concrete including the latent heat for both melting and decomposition processes.

2.2.4 Effects of Water

Corium-water interaction is a model separate from MCCI in MAAP 4.0.8. However, MCCI severity can be substantially reduced by a large amount of water in the cavity, and the heat transfer rate evaluation between corium and water has a significant impact on MCCI progression.

Two phenomena can be identified for corium-water interaction from an MCCI perspective: initial jet breakup, and water ingress. First, initial jet breakup is the phenomenon occurring when a corium jet forms between the vessel and the bottom of a deep water pool. Corium particles can be stripped off from the corium jet due to intensity of the corium-water interaction. These particles can eventually settle on top of the upper crust of corium pool, forming a layer known as the particle bed. As a result of this process, the mass of the molten corium pool can be significantly reduced, making the MCCI less severe. Second, water ingress is the phenomenon occurring once corium is fully settled on top of the cavity floor. As the corium is covered by water, the large heat removal from the top surface can produce a thick upper crust. According to experimental data, heat removal rate by water in this configuration would by far exceed the maximum heat transfer rate through the upper crust layer, if the layer were continuous and impermeable. The upper crust is not a continuous, impermeable layer; instead, numerous deep cracks can develop, as the solidified corium in the upper crust is subjected to a large temperature gradient. Water and steam can ingress (infiltrate) into the corium through these cracks, contacting the hotter region of the corium. As the solidification progresses, both the temperature gradient and the cracks extend deeper into the corium pool.

The model in MAAP 4.0.8 evaluates the heat transfer and oxidation of metal during the process of the initial jet breakup. However, it does not simulate the formation of the particle bed on top of the upper crust. MAAP 4.0.8 assumes that the particles formed during the initial jet breakup are promptly merged into the corium pool. The mass stripping rate off of a jet is calculated using a formulation similar to the Ricou-Spalding model (Reference 4):

$$\frac{dr_{dj}}{dt} = ENT0C \cdot \left(\frac{\rho_w}{\rho_{dj}} \right)^{1/2} u_{dj} \quad (2-8)$$

where r_{dj} is the radius of the corium jet, ρ_w is the density of water, ρ_{dj} is the density of corium jet, and u_{dj} is the velocity of the corium jet. Model parameter ENT0C is a coefficient multiplier to the total mass of stripped particles (the higher the coefficient, the larger the fraction is). The recommended range for the parameter ENT0C in the MAAP 4.0.8 code is from 0.025 to 0.06 (Reference 1).

MAAP 4.0.8 models water ingress by assuming the heat flux from a corium pool to its overlying water is prescribed by CHF heat flux, or higher, because water always ingresses into the hot region in the corium. The heat flux formulation is given by:

$$q''_{cr-wt} = FCHF \cdot \left[\frac{g\sigma(\rho_l - \rho_g)}{\rho_g^2} \right]^{1/4} \rho_g (h_g - h_l) \quad (2-9)$$

where g is the gravity constant, ρ_l and ρ_g are densities of saturated water and steam, and h_l and h_g are enthalpies of saturated water and steam. Modeling parameter FCHF is the Kutateladze number (Reference 5) for corium to water heat transfer, which controls the magnitude of the heat flux. The recommended of values for FCHF is from 0.0036 to 0.3.

2.3 MAAP 4.0.8 Model Limitations

The MCCI model in MAAP 4.0.8 was created and benchmarked against experiments designed for a dry cavity case (Reference 1), where the corium is mostly homogeneous in terms of temperature, geometry, and composition. For this case, assumptions and methodology of the MCCI model in MAAP 4.0.8 work reasonably well compared with the experiments. However, for a wet cavity case, the model has several limitations: one is that the MAAP 4.0.8 model does not consider the effects of melt eruption, which occurs when corium is ablating a type of concrete with rich gaseous constituents, such as Limestone or Limestone Common-Sand concrete. In this case, the released off-gases from concrete can entrain the molten corium into particles, and carry those particles through many ventilation channels (eruption sites) to the top of the upper crust. A number of experiments have confirmed the phenomenon of melt eruption (Reference 6, Reference 7, and Reference 8). The significance of this phenomenon is that it transforms portions of the continuous corium pool into a particle bed, which is much more easily cooled by the overlying water. The second limitation is that the MAAP 4.0.8 model does not address the particle bed formed by melt eruption and/or initial jet breakup. As discussed in the section 2.2.4, MAAP 4.0.8 considers heat transfer and metal oxidation during the jet breakup, but it does not consider the particle bed formed by the particles stripped off from the corium jet or entrained by off-gases during melt eruption. The heat transfer from the particle bed to water is thus not a part of the corium and water interaction model. The third limitation of MAAP 4.0.8 is that it assumes a homogeneous corium pool (assumption 1 and 2 in the section 2.1). The homogeneous assumption in the MAAP 4.0.8 code causes all the layers (molten pool and crusts at the top, bottom, and sides) to be lumped into one pool, having a single average temperature, which may lead to an optimistic prediction of the time to completely quench (solidify) the corium. However, a corium pool can develop a thick, quenched upper crust, with a much lower temperature than the molten pool, when a large amount of water is in the cavity. On top of this crust, a particle bed can form. Essentially, experimental data (Reference 9) support a stratified geometry of the corium, with a particle bed at the top, a thick upper crust in the middle, and a molten pool at the bottom.

In addition to the limitations in wet cavity scenarios, the MAAP 4.0.8 model has limited capabilities of modeling a reactor cavity with a sump in its floor. In this case, the corium pool in the sump has a different cross-section area from the pool in the remaining cavity, and the walls and the floor in the sump may be subject to deeper ablation than the remaining cavity walls and floor. The way for MAAP 4.0.8 to handle

such geometry is to split the corium pool in the cavity into two: one in the sump, and the other in the remaining part of the cavity.

For calculations presented herein, the MAAP 4.0.8 model limitations for the wet cavity scenario are accommodated by calibrating the two model parameters FCHF and ENT0C discussed in section 2.2.4. The objective is to have MAAP4.0.8 generating conservative results in terms of key variables. Model parameter FCHF is adjusted based on the results calculated by more sophisticated MCCI codes. This will allow for conservative predictions of ablation depth and long term containment pressurization. However, time required to completely quench the corium pool may not be correctly predicted, and it must be obtained through experiments or other more sophisticated codes. Details of calibrating FCHF and ENT0C are given in the next section.

The model limitation of the cavity floor geometry with a sump is not handled in this analysis report. Detailed CORQUENCH calculations show that the corium in the sump is quenched before the ablation depth reaches the liner plate. (Reference 10)

2.4 Quantifications of Key Inputs

For the MCCI cases considered in this analysis report, default and case specific inputs for running the MAAP 4.0.8 code have been documented in the parameter file and input decks for APR1400. Besides these default inputs, two key modeling parameters, FCHF and ENT0C, must to be calibrated to accommodate the modeling deficiency discussed in the previous section. The objective in selecting the parameter values is to conservatively predict the key variables important to containment performance of APR1400. These include the ablation depth in the cavity floor and the containment pressure 24 hours after core damage. The code chosen as the basis for calibration of MAAP 4.0.8 model parameters is CORQUENCH 3.03 (Reference 10), which is a MCCI code developed by Argonne National Laboratory. This code models a stratified corium pool structure consisting of an upper crust, a bottom crust, and a molten pool; it also models the effects of melt eruption.

2.4.1 CORQUENCH 3.03 Results

CORQUENCH 3.03 analysis was performed by Argonne National Laboratory, for Siliceous, and LCS (Limestone and common sand) concrete types. The initial conditions used in these calculations are summarized as the following:

- 1) Sequence initiator is a Large LOCA. To add more conservatism, core support plate is assumed to fail at about 6000 seconds, dumping the entire core into the RPV lower plenum. Reactor vessel fails at about 7,100 seconds.
- 2) About 118 tons of UO_2 and 29.6 tons of Zr are relocated from the vessel into the cavity, which correspond to 100% of inventory in the core.
- 3) Oxidation fraction of Zr is about 52%
- 4) Initial temperature of the melt is about 2500 K

The CORQUENCH 3.03 calculation is based on a very conservative assumption, which ignores the particle bed created during the initial jet breakup phase. This means that the particle bed can only be created through melt eruption when MCCI occurs. CORQUENCH 3.03 calculation also assumes that the containment pressure stays at a constant pressure of 1 bar during the entire MCCI process due to activation of containment sprays. The results indicate that the corium is quenched in about 8 hours and the ablation depth of the concrete floor is about 27 cm. The average heat flux from the corium pool to water is about 415 kW/m^2 during MCCI.

2.4.2 Selection of the FCHF Value

TS

2.4.3 Selection of the ENT0C Value

TS

2.4.4 Summary of MCCI Parameters Used in MAAP 4.0.8 Analyses for APR1400

Table 2-3 and Table 2-4 show two sets of values for MCCI parameters FCHF and ENT0C. The set of parameters in Table 2-3 leads to conservative results for ablation depth and containment pressure within 24 hours of core damage, as discussed in the previous two sections. Therefore, for all the APR1400 MAAP4.0.8 analyses, both in this and other analysis, this set of MCCI parameters is used.

The second set of MCCI parameters (listed in Table 2-4) has the merit to capture the rapid steam and hydrogen generation occurring right after vessel failure. This set of parameters impacts the potential of local high hydrogen concentration and DDT. Therefore, all the severe accident sequences are additionally analyzed with this set of parameters, for the hydrogen analysis.

Table 2-1 Basis Equations and Species

1.	H ₂	$H_2 + CO_2 \rightleftharpoons H_2O + CO$
2.	C	$C + H_2O \rightleftharpoons CO + H_2$
3.	Zr	$Zr(1) + 2H_2O \rightleftharpoons ZrO_2(1) + 2H_2$
4.	Cr	$2Cr(1) + 3H_2O \rightleftharpoons Cr_2O_3(1) + 3H_2$
5.	Fe	$Fe(1) + H_2O \rightleftharpoons FeO(1) + H_2$
6.	SiO ₂	$SiO_2(1) + H_2 \rightleftharpoons SiO + H_2O$
7.	CaO	$CaO(1) + H_2 \rightleftharpoons Ca + H_2O$
8.	Al ₂ O ₃	$Al_2O_3(1) + 3H_2 \rightleftharpoons 2Al + 3H_2O$
9.	K ₂ O	$K_2O(1) + H_2 \rightleftharpoons 2K + H_2O$
10.	H ₂ O	Hydrogen element balance
11.	CO	Oxygen element balance
12.	CO ₂	Carbon element balance
13.	Cr ₂ O ₃	Chromium element balance
14.	FeO	Iron element balance
15.	B ₄ C	$B_4C(1) + 7H_2O \rightleftharpoons 2B_2O_3(1) + CO + 7H_2$
16.	UO ₂	$UO_2(1) + 2H_2 \rightleftharpoons U(1) + 2H_2O$
17.	O ₂	$H_2O \rightleftharpoons H_2 + 1/2 O_2$
18.	KOH	Potassium element balance
19.	B ₂ O ₃	Boron element balance
20.	Ni	$Ni(1) + H_2O \rightleftharpoons NiO(1) + H_2$
21.	NiO	Nickel element balance
22.	H	$H_2 \rightleftharpoons 2H$
23.	Silicon element balance	

Table 2-2 METOXA Compound List

1.	Liquid Metals	Liquid Oxides	Gases			
			O ₂	OH	H	O
1.	H ₂	H ₂ O	O ₂	OH	H	O
2.	C		CO	CO ₂		
3.	Zr	ZrO ₂	ZrO	ZrO ₂		
4.	Cr	Cr ₂ O ₃	Cr	CrO	CrO ₂	CrO ₃
5.	Fe	FeO	Fe	Fe(OH) ₂		
6.		SiO ₂	SeO	Si ₃		
7.		CaO	Ca	CaOH	Ca(OH) ₂	
8.		Al ₂ O ₃	Al	Al ₂ O	AlOH	Al(OH) ₂
9.		K ₂ O	K	KOH		
10.		Na ₂ O	Na	NaOH		
11.	Ni	NiO	Ni	NiH	Ni(OH) ₂	
12.	B ₄ C	B ₂ O ₃	BO	B ₂ O ₃	BO ₂	
13.	Ag		Ag	AgH		
14.	In		In			
15.	Cd		Cd			
16.	Sr	SrO	Sr	SrOH	Sr(OH) ₂	
17.	Ba	BaO	Ba	BaO	BaOH	Ba(OH) ₂
18.	La	La ₂ O ₃	LaO	La(OH) ₂		
19.	Ce	CeO ₂	CeO	CeO ₂		
20.	U	UO ₂	UO	UO ₂	UO ₃	UO ₂ (OH) ₂
21.		MgO	Mg	MgOH	Mg(OH) ₂	
22.	Sn	SnO ₂	Sn	SnH	SnO	
23.	Mn	MnO	Mn	MnH	Mn(OH) ₂	H ₂ MoO ₄ *
24.	Mo	MoO ₂ , MoO ₃		Mo	MoO ₂	MoO ₃
25.	Ru		Ru	RuO	RuO ₃	
26.	Te		Te	SnTe	AgTe	SbTe
27.	Nb	NbO, NbO ₂		NbO	NbO ₂	
28.	Sb		Sb	SbO		

* There are 7 total Mo compounds.

Table 2-3 MCCI Parameters Used in MAAP4.0.8 Analyses for APR1400



TS

Table 2-4 Additional Set of MCCI Parameters Used in Hydrogen Distribution and DDT Analyses for APR1400



TS

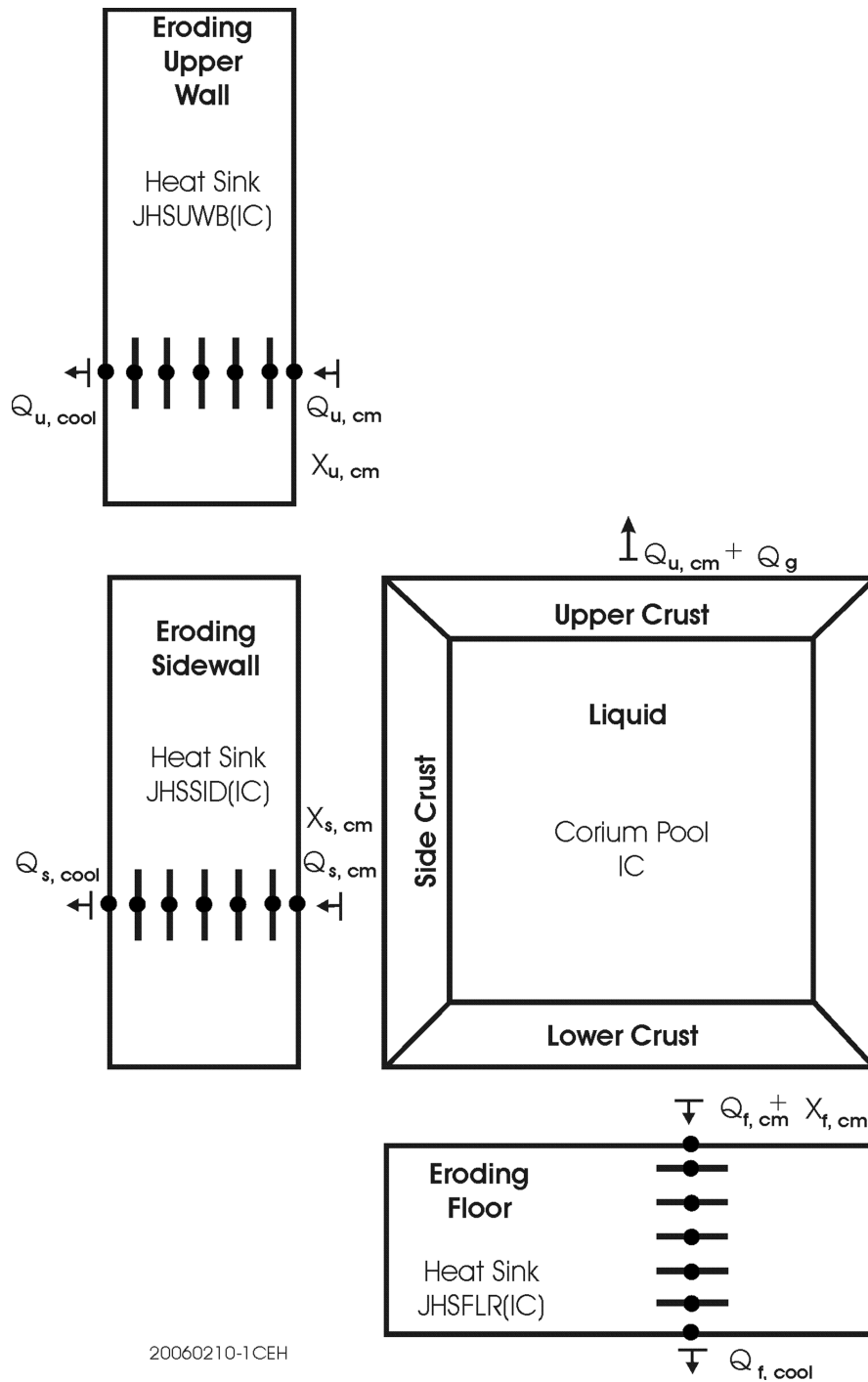
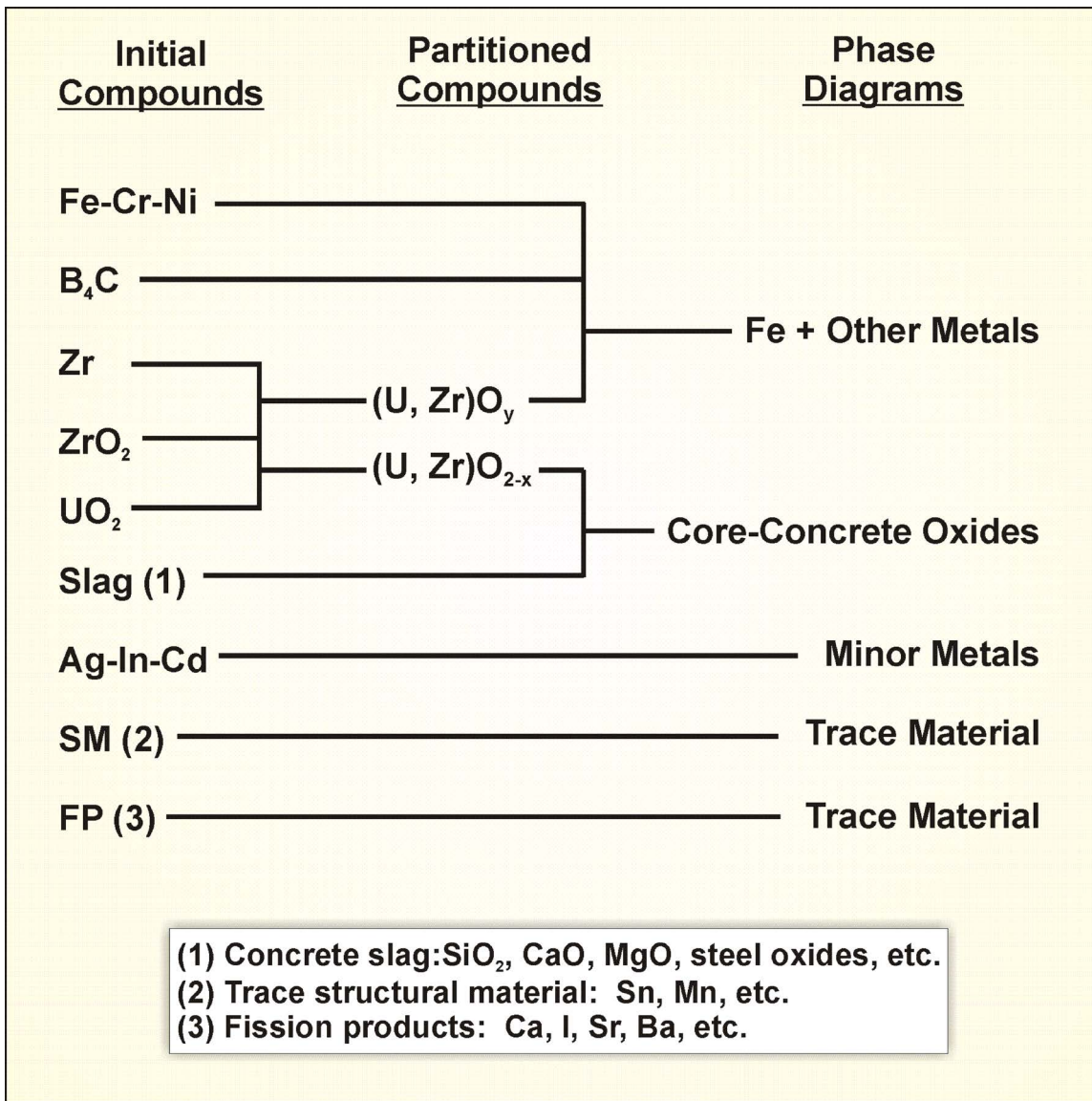
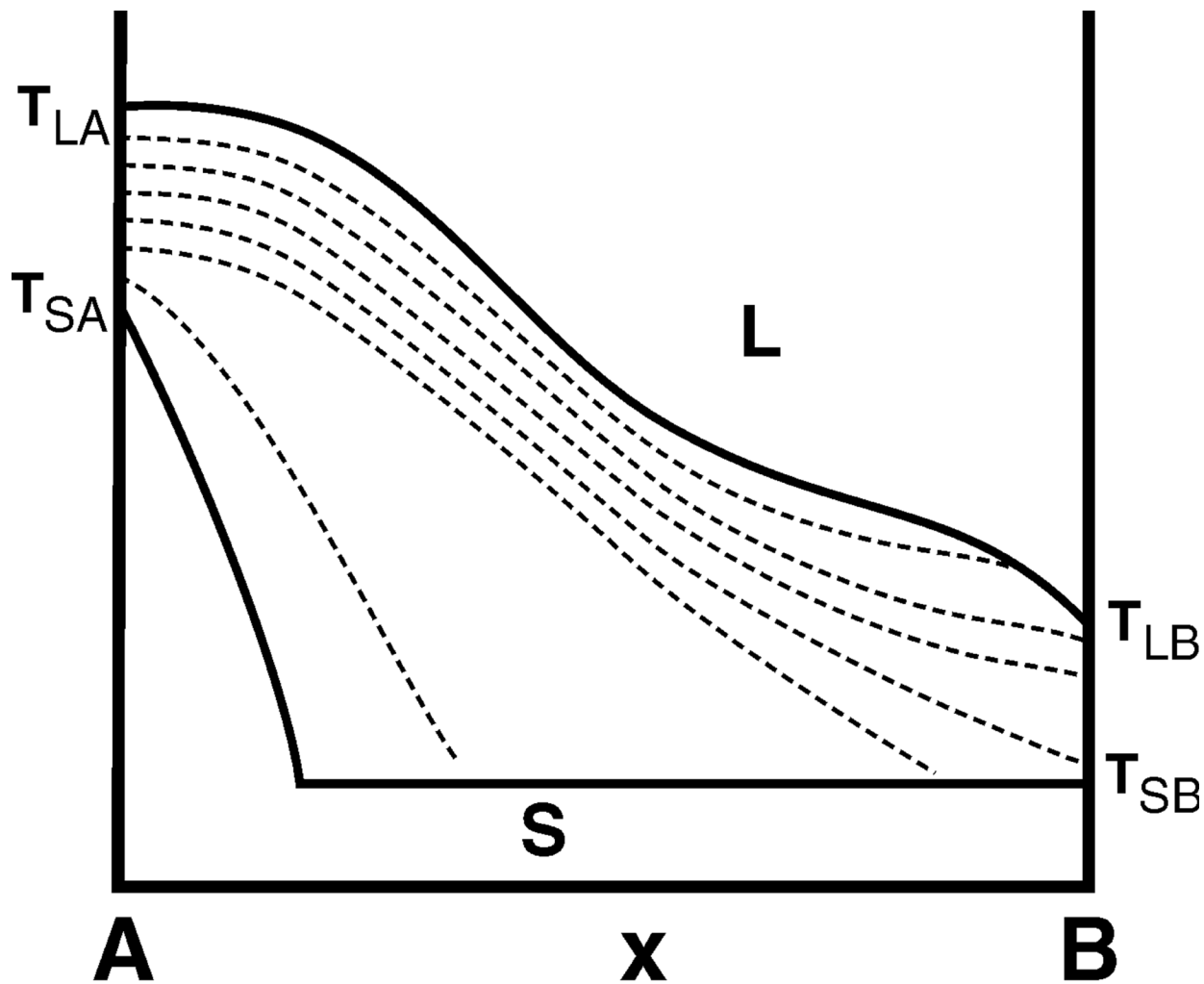


Figure 2-1 MAAP 4.0.8 Model of Corium Pool, Crusts, and Concrete Slab
 Q= Power and X= Eroded Distance



20110421-4QZ

Figure 2-2 Organization of Materials for Energy-Temperature Relations



MP925065.CDR

Figure 2-3 Pseudo-Binary Phase Diagram with Dashed Lines Indicating Constant Liquid Fraction.

Equilibrium composition pairs are not shown. For a selected bulk composition and temperature, the liquid fraction is found. This liquid fraction may be used together with an assumed solid (or liquid) composition to yield the liquid (or solid) composition.

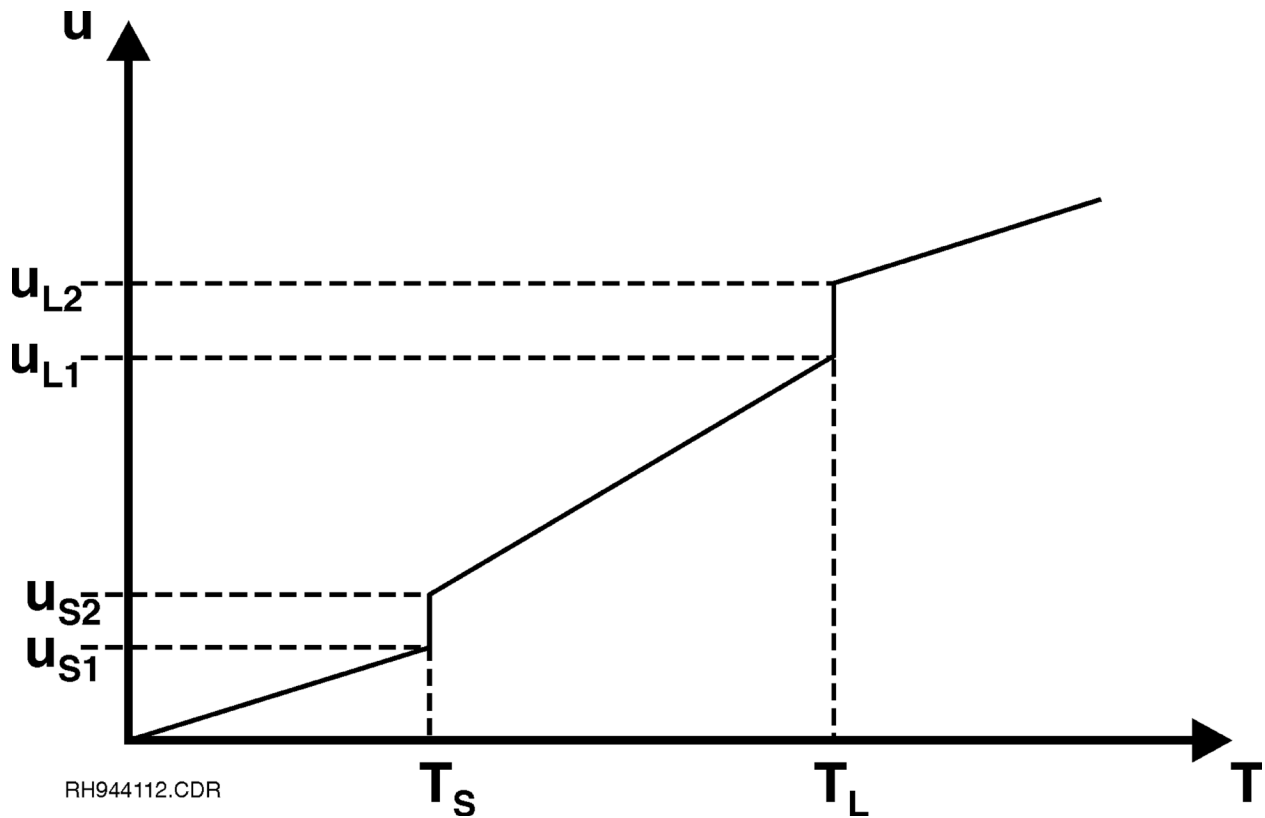


Figure 2-4 Energy-Temperature Relationship for a Pseudo-Binary System

The slope in the two-phase range is, in general, not constant because the liquid fraction may vary non-linearly and because the latent heat depends upon the liquid composition. Note that partially congruent melting may occur at both the solidus and liquidus where the slope is vertical.

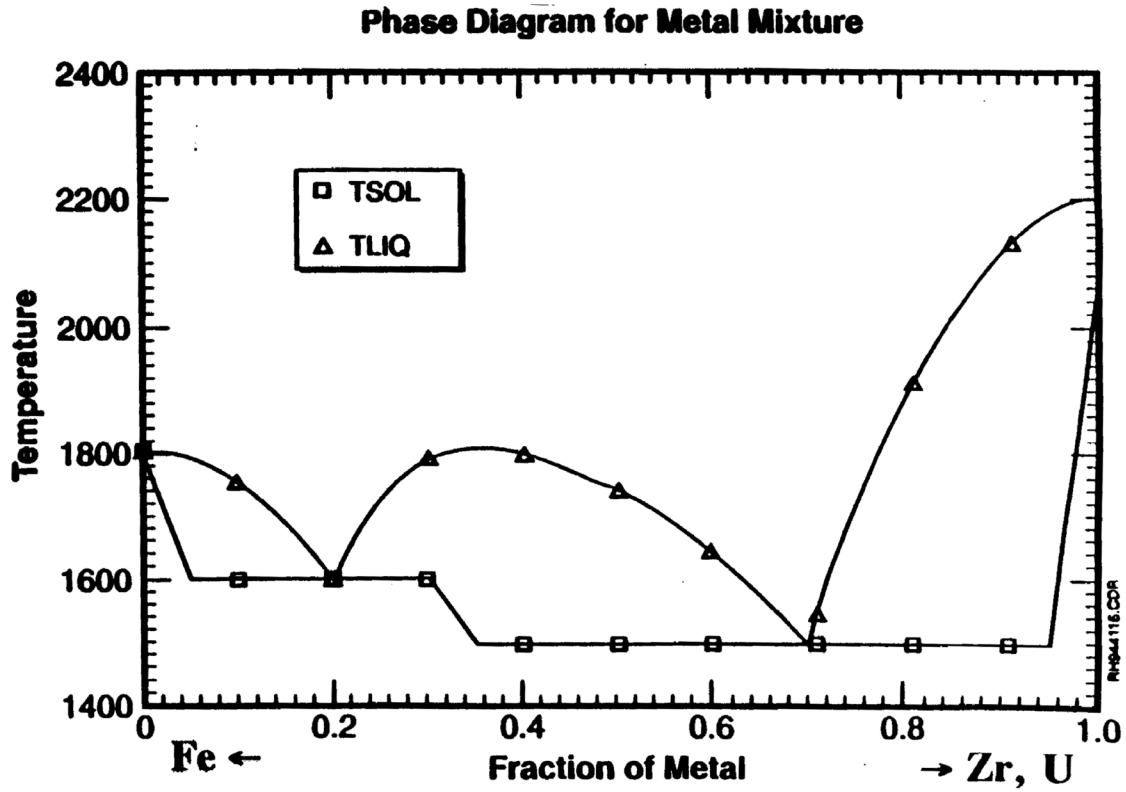


Figure 2-5 Major Metallic Phase Diagram



Figure 2-6 Ablation Depth in Cavity Floor for Different FCHF



Figure 2-7 Heat Flux from Corium to Water for Different FCHF



Figure 2-8 Heat Transfer Rate from Corium to Water for Different FCHF



Figure 2-9 Containment Pressure for Different FCHF



Figure 2-10 Comparison of Pressure in the Containment for the Cases with $ENT0C=10^{-5}$, and $ENT0C=0.045$

3 DETAILED ANALYSIS

3.1 Scenario Selection

Sequences were selected for MCCI analysis based on their core damage frequencies and bounding features. The following ten sequences are identified having high core damage frequencies:

Table 3-1 Ten PRA Sequences with High Core Damage Frequencies

TS

Out of the ten sequences, four were selected for MCCI analysis. These include: total loss of essential service water (R1_TLOES-003-MCCI), Medium LOCA (R2_MLOCA003-MCCI), Temporary Loss of AC power (R3_LOOP-004-MCCI), and Loss of AC power with turbine-driven AFW off after 2 hours (R9_SBO-006-MCCI). The other six sequences were ignored because they will lead to significantly delayed core damage, therefore, not being the limiting sequences for MCCI analysis. In addition to the four PRA sequences, a Large LOCA sequence from containment performance analysis (LLOCA-C04-NoECSBS-MCCI) was also selected, because it leads to very quick core damage and vessel breach. Equipment availability and sequence progression for each of those sequences is discussed next.

3.1.1 Sequence Identifier: R1-TLOES-003-MCCI

TS

The following table summarizes availabilities of key systems in this sequence.

TS

3.1.2 Sequence Identifier: R2_MLOCA003-MCCI

The initiating event of this sequence is a medium break LOCA occurring at full power. The break is equivalent to a 6 inch diameter hole in loop 1 hot leg. Four Safety Injection Tanks and Motor-Driven AFW are available. Charging Pumps are assumed to be unavailable. Safety Injection pumps are available initially but are assumed to fail 2 hours into the sequence at the time of switchover to hot leg injection. RCS depressurization using the SDVS, CFS actuation, and alignment of the Three-Way Valves to the steam generator compartment, are assumed to occur 30 minutes after the onset of core damage. ECSBS (Emergency Containment Spray Backup System) is assumed not to be available for this sequence.

The following table summarizes availabilities of key systems in this sequence:

TS

3.1.3 Sequence Identifier: R3_LOOP-004-MCCI

The initiating event for this sequence is a loss of AC power causing reactor scram almost immediately. Following the initiating event, charging pumps, safety injection pumps, and AFW pumps are lost. Although the diesel generator starts in 10 minutes, charging pump, safety injection pumps and AFW do not recover. One hour into the sequence, two POSRVs are manually opened by operator to relieve RCS pressure.

The following table summarizes availabilities of key systems in this sequence.

TS

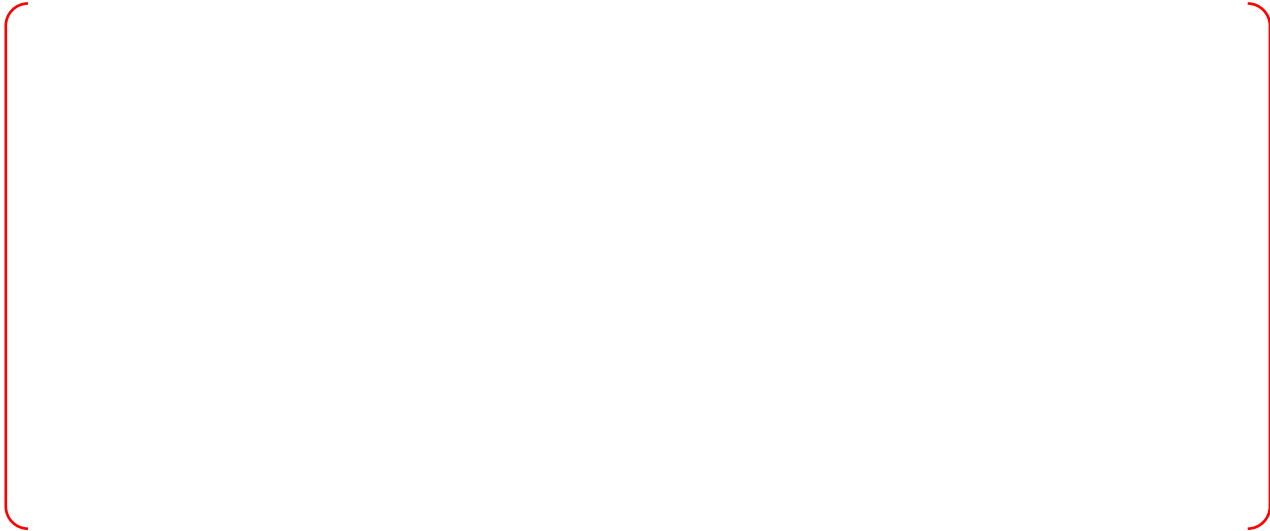


3.1.4 Sequence Identifier: R9_SBO-006-MCCI

The initiating event for this sequence is a sudden loss of AC power at full reactor power. Following the loss of AC power, safety injection pumps, charging pump, and motor-driven AFW are unavailable. Turbine-driven AFW is assumed available, until 2 hours into the sequence, once the when battery runs out.

The following table summarizes availabilities of key systems in this sequence.

TS



3.1.5 Sequence Identifier: LLOCA-C04-NoECSBS-MCCI

The initiating event for this sequence is a large break occurring at full power. The break is equivalent to a 9.5 inch diameter hole in the loop 1 hot leg. Four safety injection tanks (SITs) are available, but safety injection pumps and charging pumps are unavailable.

The following table summarizes availabilities of key systems in this sequence.

3.2 Results of analysis

3.2.1 Sequence Identifier: R1-TLOES-003-MCCI

This sequence is defined as a loss of Essential Service Water (ESW) at full power resulting in reactor scram at sequence initiation. Four Safety Injection Tanks are available. Auxiliary Feedwater, Safety Injection Pumps, Containment Spray Pumps, and Charging Pumps are assumed to be unavailable. RCS depressurization using the SDVS, CFS actuation, and alignment of the Three-Way Valves to the steam generator compartment, are assumed to occur 30 minutes after the onset of core damage. ECSBS is assumed not to be available for this sequence. Due to the loss of ESW, a 21 gpm per pump seal LOCA is assumed to occur half an hour into the sequence.

Figure 3-1 to Figure 3-4 show RCS pressure, core exit temperature, SG pressures and SG levels. Once reactor scram occurs and main feedwater is isolated, the steam generators begin to boil off their inventories. Because AFW is assumed unavailable, SG 1 and 2 quickly boil dry at 2546 seconds, and stop removing decay heat. Half an hour into the sequence, a 21 gpm per pump seal LOCA occurs, but the flow rate is not sufficient to depressurize the RCS. The primary system heats up and pressurizes, reaching the POSRV relief set points at about 2900 seconds, and causing the valves to open. Primary system inventory is steadily lost through the POSRVs and RCP seals, causing the core water level to decrease. The discharge from the POSRVs is sparged into the IRWST, condensing the steam and preventing additional containment pressurization. The core is soon uncovered, causing the core exit temperature to reach 1,200° F, signaling the onset of core damage.

Thirty minutes after the onset of core damage (30 minutes after 5168 seconds), operators are assumed to align the Three-Way Valves to the steam generator compartment and open all four POSRVs to depressurize the primary system into the containment atmosphere. At the same time, operators are assumed to actuate the CFS, allowing for gravity-driven water flow from the IRWST into the reactor cavity. Depressurization of the primary system allows the available Safety Injection Tanks to inject. However, injection of the SITs is not sufficient to quench the core. The core begins to melt and relocate to the RPV lower plenum.

Figure 3-5 shows the remaining mass in the core, corium mass in the lower plenum, and corium mass in the reactor cavity. The molten corium in the reactor vessel lower plenum eventually causes the vessel to fail at low pressure. About 124 metric tons of corium, which is 62% of the molten material that has accumulated in the lower plenum, is relocated into the flooded reactor cavity at 24,257 seconds. As previously stated, the effects of initial jet breakup were ignored. This results in a molten corium pool that is capable of ablating the concrete at the bottom of the flooded reactor cavity. Figure 3-6 shows the

ablation depths in the concrete floor and sidewall. The corium causes the water pool in containment to heat up and boil. Due to boiling in the cavity, and non-condensable gas generation during decomposition of concrete, containment steadily pressurizes. Figure 3-7 shows pressure in the containment dome. Heat removal by the overlying water pool eventually halts concrete ablation and quenches the corium. At the time when the corium is quenched, the concrete ablation depth of about 7.1 cm is well short of the depth of the steel containment liner (about 90 cm into the floor) in the reactor cavity.

The quenched core debris at the bottom of the reactor cavity continues to steam away the cavity water pool for the duration of this sequence. The containment pressure does not reach the FLC of 8.5 bar within 24 hours of the onset of core damage. However, due to a lack of ECSBS availability for this sequence, containment pressurization continues unabated. Containment failure eventually occurs due to overpressure.

3.2.2 Sequence Identifier: R2-MLOCA003-MCCI

This sequence is defined as a medium break LOCA occurring at full power. The break is equivalent to a 6 inch diameter hole in one of the hot legs. Four Safety Injection Tanks, and Motor-Driven AFW, are available. Charging Pumps and Containment Spray Pumps are assumed to be unavailable. Safety Injection pumps are available initially, but are assumed to fail 2 hours into the sequence, at the time of switchover to hot leg injection. RCS depressurization using the SDVS, CFS actuation, and alignment of the Three-Way Valves to the steam generator compartment, are assumed to occur 30 minutes after the onset of core damage. ECSBS is assumed not to be available for this sequence.

Figure 3-8 to Figure 3-11 shows RCS pressure, core exit temperature, SG pressures and levels. Due to the 6 inch break, primary system pressure rapidly drops and generates an SI signal. The SI signal causes the reactor to scram and actuates the available Safety Injection Pumps. The RCS break effluent rapidly pressurizes the containment. Injection from the Safety Injection Pumps and the Safety Injection Tanks keep the core covered and cooled.

Two hours into the sequence, Safety Injection Pumps are assumed to become unavailable. RCS injection stops and primary system inventory is quickly lost out the hot leg break. Core uncovers and begins to heat up at 7,954 seconds. Core exit temperature reaches 1,200° F at 8,861 seconds, signaling the onset of core damage.

Thirty minutes after the onset of core damage, operators are assumed to align the Three-Way Valves to the steam generator compartment and open all four POSRVs. At the same time, operators are assumed to actuate the CFS, allowing for gravity-driven water flow from the IRWST into the reactor cavity. Since the break size is large, actuation of the SDVS has no impact on primary system pressure. The core begins to melt and relocate to the RPV lower plenum (Figure 3-12) at 13,302 seconds. This produces a brief pressure spike in the RCS due to the rapid steaming of the water pool that exists in the lower plenum.

The molten corium in the reactor vessel lower plenum eventually causes the vessel to fail, as shown in Figure 3-12. About 128 tons, or 82% of this molten material, is relocated to the reactor cavity at the time of this low-pressure vessel failure. As previously stated, the effects of initial jet breakup were ignored. This results in a molten corium pool that is capable of ablating the concrete at the bottom of the flooded reactor cavity. Figure 3-13 shows the ablation depths of the concrete floor and sidewall. The corium causes the water pool in containment to heat up and boil. Due to boiling in the cavity and non-condensable gas generation during the decomposition of concrete, containment steadily pressurizes. Figure 3-14 shows the pressure in the containment dome. Heat removal by the overlying water pool eventually halts concrete ablation and quenches the corium. At the time that the corium is quenched, the concrete ablation depth of 13.1 cm is well short of the depth of the steel containment liner in the reactor cavity.

The quenched core debris at the bottom of the reactor cavity continues to steam away the cavity water pool for the duration of the sequence. The containment pressure does not reach the FLC within 24 hours after the onset of core damage. However, due to a lack of ECSBS availability for this sequence, containment pressurization continues unabated. Containment failure eventually occurs due to overpressure.

3.2.3 Sequence Identifier: R3_LOOP-004-MCCI

This sequence is defined as a Loss of Offsite Power (LOOP) at full power resulting in reactor scram at sequence initiation. Diesel Generators are assumed to be started to provide backup power. Four Safety Injection Tanks are available. Auxiliary Feedwater, Safety Injection Pumps, Containment Spray Pumps, and Charging Pumps are assumed to be unavailable. RCS depressurization using the SDVS, CFS actuation, and alignment of the Three-Way Valves to the steam generator compartment, are assumed to occur 30 minutes after the onset of core damage. ECSBS is assumed not to be available for this sequence.

Figure 3-15 to Figure 3-18 shows RCS pressure, core exit temperature, SG pressures and levels. Once the LOOP occurs, steam generators begin to boil off their inventories. Diesel Generators are assumed to start successfully, but no ESF systems are recovered. Because AFW is unavailable, both steam generators quickly boil dry at 2,698 seconds and stop removing decay heat. Primary system heats up and pressurizes, soon reaching the POSRV relief setpoints at 2,984 seconds, and causing the valves to open. Primary system inventory is steadily lost through the POSRVs, causing the core water level to decrease. The discharge from the POSRVs is sparged into the IRWST, condensing the steam and preventing containment pressurization. The core is soon uncovered, causing the core exit temperature to reach 1,200° F, signaling the onset of core damage.

Thirty minutes after the onset of core damage (thirty minutes after 4,896 seconds), operators are assumed to align the Three-Way Valves to the steam generator compartment and open all four POSRVs to depressurize the primary system into the containment atmosphere. At the same time, operators are assumed to actuate the CFS, allowing for gravity-driven water flow from the IRWST into the reactor cavity. Depressurization of the primary system allows the available Safety Injection Tanks to inject. However, injection of the SITs is not sufficient to quench the core. The core begins to melt and relocate to the RPV lower plenum.

The molten corium in the reactor vessel lower plenum eventually causes the vessel to fail at 20,039 seconds, as shown in the Figure 3-19. About 107 tons, or 80% of this molten material, is relocated to the flooded reactor cavity at the time of this low-pressure vessel failure. As previously stated, the effects of initial jet breakup were ignored. This results in a molten corium pool that is capable of ablating the concrete at the bottom of the flooded reactor cavity. Figure 3-20 shows the ablation depths in the concrete floor and sidewall. The corium causes the water pool in containment to heat up and boil. Due to this boiling in the cavity and non-condensable gas generation during concrete decomposition, containment steadily pressurizes. Figure 3-21 shows the containment pressure. Heat removal by the overlying water pool eventually halts concrete ablation and quenches the corium. At the time that the corium is quenched, the concrete ablation depth of 16.8 cm is well short of the depth of the steel containment liner in the reactor cavity.

The quenched core debris at the bottom of the reactor cavity continues to steam away the cavity water pool for the duration of the sequence. The containment pressure does not reach the FLC within 24 hours after the onset of core damage. However, due to a lack of ECSBS availability for this sequence, containment pressurization continues unabated. Containment failure eventually occurs due to overpressure.

3.2.4 Sequence Identifier: R9_SBO-006-MCCI

This sequence is defined as a loss of AC power at full power resulting in reactor scram at sequence initiation. Turbine-driven AFW is available initially, but assumed to fail 2 hours into the sequence, when batteries run out. Four Safety Injection Tanks are available. Motor-driven Auxiliary Feedwater, Safety Injection Pumps, Containment Spray Pumps, and Charging Pumps are all assumed to be unavailable. ECSBS is assumed not to be available for this sequence.

Figure 3-22 to Figure 3-25 shows RCS pressure, core exit temperature, and SG pressures, and levels. Once the loss of AC power occurs, reactor scrams, and the steam generators begin to boil off their inventories. Turbine-driven AFW (TDAFW) starts to inject water into the secondary side of the SGs at 2,293 seconds, when SG levels drop below the TDAFW setpoint. This increases SG water level and keeps the RCS pressure lower than the POSRV setpoint. One hour into the sequence, operators are assumed to: align the Three-Way Valves to the steam generator compartment (to prevent hydrogen accumulation in the IRWST), actuate the CFS (to allow for gravity-driven water flow from the IRWST into the reactor cavity), and open the POSRVs (to depressurize the primary system). The discharge from the POSRVs is sparged into the IRWST, condensing the steam, and preventing containment pressurization. Primary system inventory is quickly lost through the POSRVs, causing the core water level to decrease. Core is uncovered at 6822 seconds, causing the core exit temperature to reach 1,200° F at 10,061 seconds, which in turn signals the onset of core damage. Core begins to melt and relocate to the RPV lower plenum at 19,198 seconds.

Figure 3-26 shows the masses of the remaining core, corium in the lower plenum, and corium in the reactor cavity. Molten corium in the reactor vessel lower plenum eventually causes the vessel to fail at a low pressure, at 24,878 seconds. About 93 tons of corium is relocated from the lower plenum to the completely flooded cavity at the time of vessel failure, which is about 68% of the molten material accumulated in the lower plenum. Shortly after, as the remaining 54 tons of core material collapses, additional molten material drops into the cavity. As previously stated, the effects of initial jet breakup were ignored. This results in a molten corium pool that is capable of ablating the concrete at the bottom of the flooded reactor cavity. Figure 3-27 shows the ablation depths in the concrete floor and sidewall. The corium causes the water pool in containment to heat up and boil. Due to boiling in the cavity and non-condensable gas generation during the decomposition of concrete, containment steadily pressurizes. Figure 3-28 shows the containment pressure. Heat removal by the overlying water pool eventually halts concrete ablation and quenches the corium. At the time when the corium is quenched, the concrete ablation depth of 13 cm is well short of the depth of the steel containment liner in the reactor cavity.

The quenched core debris at the bottom of the reactor cavity continues to steam away the cavity water pool for the duration of the sequence. The containment pressure does not reach the FLC within 24 hours after the onset of core damage. However, due to a lack of ECSBS availability for this sequence, containment pressurization continues unabated. Containment failure eventually occurs due to overpressure.

3.2.5 Sequence Identifier: LLOCA-C04-NoECSBS-MCCI

This sequence is defined as a large break LOCA at full power resulting in reactor scram at sequence initiation. The break area is equivalent to a 9.5 inch diameter hole in loop 1 hot leg. Motor-driven AFW and four Safety Injection Tanks are available. Safety Injection Pumps, Containment Spray Pumps, and Charging Pumps are all assumed to be unavailable. RCS depressurization using the SDVS is assumed unnecessary. CFS actuation and alignment of the Three-Way Valves to the steam generator compartment are assumed to occur 30 minutes after the onset of core damage. ECSBS is assumed not to be available for this sequence.

Figure 3-29 to Figure 3-32 shows RCS pressure, core exit temperature, SG pressures, and levels. As the large break occurs, RCS inventory is quickly lost. Four Safety Injection Tanks start to inject water almost immediately, but the injection flow rate is much smaller than the break discharge flow rate. Core is

quickly uncovered at 152 seconds, causing the core exit temperature to reach 1,200° F at 1,360 seconds, signaling the onset of core damage. By 4,044 seconds, the core is severely damaged, and a fraction of molten mass is relocated into the lower plenum, causing a brief RCS pressure spike.

Thirty minutes after the onset of core damage, operators are assumed to align the Three-Way Valves to the steam generator compartment. At the same time, operators are assumed to actuate the CFS, allowing for gravity-driven water flow from the IRWST into the reactor cavity.

Figure 3-33 shows the remaining mass in the core, corium mass in the lower plenum, and corium mass in the reactor cavity. The molten corium in the reactor vessel lower plenum eventually causes the vessel to fail at low pressure at 7,258 seconds. The reactor vessel fails because penetration tube weld in the second (axial) row of the lower plenum wall melts. About 107 tons of molten corium is relocated from the vessel into the completely flooded reactor cavity at the time of vessel failure, which is about 80% of the molten material accumulated in the lower plenum. About 5,900 seconds later, another major relocation occurs, as the remaining 24 tons of core material collapses into the lower plenum, dumping additional molten material into the reactor cavity. As previously stated, the effects of initial jet breakup were ignored. This results in a molten corium pool that is capable of ablating the concrete at the bottom of the flooded reactor cavity. Figure 3-34 shows the ablation depths in the concrete floor and sidewall. The corium causes the water pool in containment to heat up and boil. Due to boiling in the cavity and non-condensable gas generation during decomposition of concrete, containment steadily pressurizes. Figure 3-35 shows the containment pressure. Heat removal by the overlying water pool eventually halts concrete ablation and quenches the corium. At the time when the corium is quenched, the concrete ablation depth of 24 cm is well short of the depth of the steel containment liner in the reactor cavity.

The quenched core debris at the bottom of the reactor cavity continues to steam away the cavity water pool for the duration of the sequence. The containment pressure does not reach the FLC within 24 hours after the onset of core damage. However, due to a lack of ECSBS availability for this sequence, containment pressurization continues unabated. Containment failure eventually occurs due to overpressure.



Figure 3-1 Pressure in RCS for the PRA sequence of loss of essential service water (R1_TLOES-003-MCCI)



Figure 3-2 Core exit temperature for the PRA sequence of loss of essential service water (R1_TLOES-003-MCCI)



Figure 3-3 Pressures in steam generators for the PRA sequence of loss of essential service water (R1_TLOES-003-MCCI)



Figure 3-4 Water levels in steam generators for the PRA sequence of loss of essential service water (R1_TLOES-003-MCCI)



TS

Figure 3-5 Masses in the core, lower plenum and reactor cavity for the PRA sequence of loss of essential service water (R1_TLOES-003-MCCI)



TS

Figure 3-6 Ablation depth in floor and sidewall for the PRA sequence of loss of essential service water (R1_TLOES-003-MCCI)



Figure 3-7 Pressure in containment dome for the PRA sequence of loss of essential service water (R1_TLOES-003-MCCI)



Figure 3-8 Pressure in RCS for the PRA sequence of medium break LOCA (R2_MLOCA003-MCCI)

TS

Figure 3-9 Core exit temperature for the PRA sequence of medium break LOCA (R2_MLOCA003-MCCI)

TS

Figure 3-10 Pressures in steam generators for the PRA sequence of medium break LOCA (R2_MLOCA003-MCCI)



Figure 3-11 Water levels in steam generators for the PRA sequence of medium break LOCA (R2_MLOCA003-MCCI)



Figure 3-12 Masses in the core, lower plenum and reactor cavity for the PRA sequence of medium break LOCA (R2_MLOCA003-MCCI)



Figure 3-13 Ablation depth in floor and sidewall for the PRA sequence of medium break LOCA (R2_MLOCA003-MCCI)



Figure 3-14 Pressure in containment dome for the PRA sequence of medium break LOCA (R2_MLOCA003-MCCI)



Figure 3-15 Pressure in RCS for the PRA sequence of loss of offsite power (R3_LOOP-004-MCCI)



Figure 3-16 Core exit temperature for the PRA sequence of loss of offsite power (R3_LOOP-004-MCCI)



Figure 3-17 Pressures in steam generators for the PRA sequence of loss of offsite power (R3_LOOP-004-MCCI)

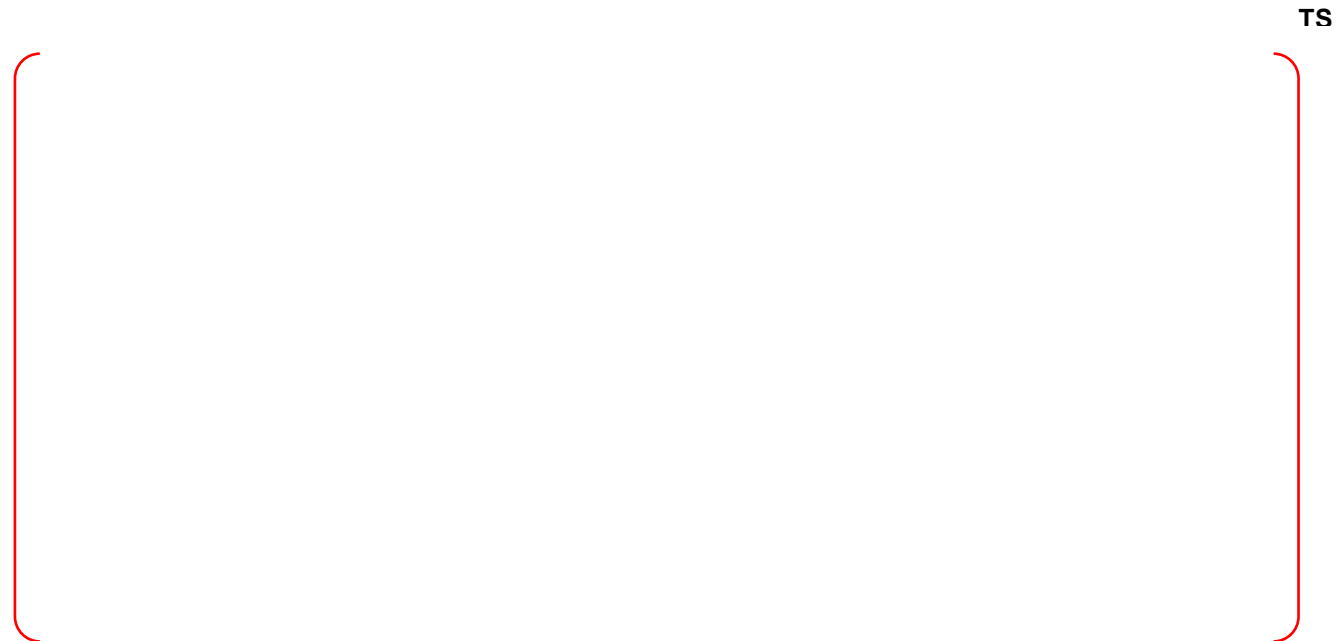


Figure 3-18 Water levels in steam generators for the PRA sequence of loss of offsite power (R3_LOOP-004-MCCI)



Figure 3-19 Masses in the core, lower plenum and reactor cavity for the PRA sequence of loss of offsite power (R3_LOOP-004-MCCI)



Figure 3-20 Ablation depth in floor and sidewall for the PRA sequence of loss of offsite power (R3_LOOP-004-MCCI)



Figure 3-21 Pressure in containment dome for the PRA sequence of loss of offsite power (R3_LOOP-004-MCCI)



Figure 3-22 Pressure in RCS for the PRA sequence of loss of AC power with short battery life (R9_SBO-006-MCCI)



Figure 3-23 Core exit temperature for the PRA sequence of loss of AC power with short battery life (R9_SBO-006-MCCI)



Figure 3-24 Pressures in steam generators for the PRA sequence of loss of AC power with short battery life (R9_SBO-006-MCCI)



Figure 3-25 Water levels in steam generators for the PRA sequence of loss of AC power with short battery life (R9_SBO-006-MCCI)



Figure 3-26 Masses in the core, lower plenum and reactor cavity for the PRA sequence of loss of AC power with short battery life (R9_SBO-006-MCCI)

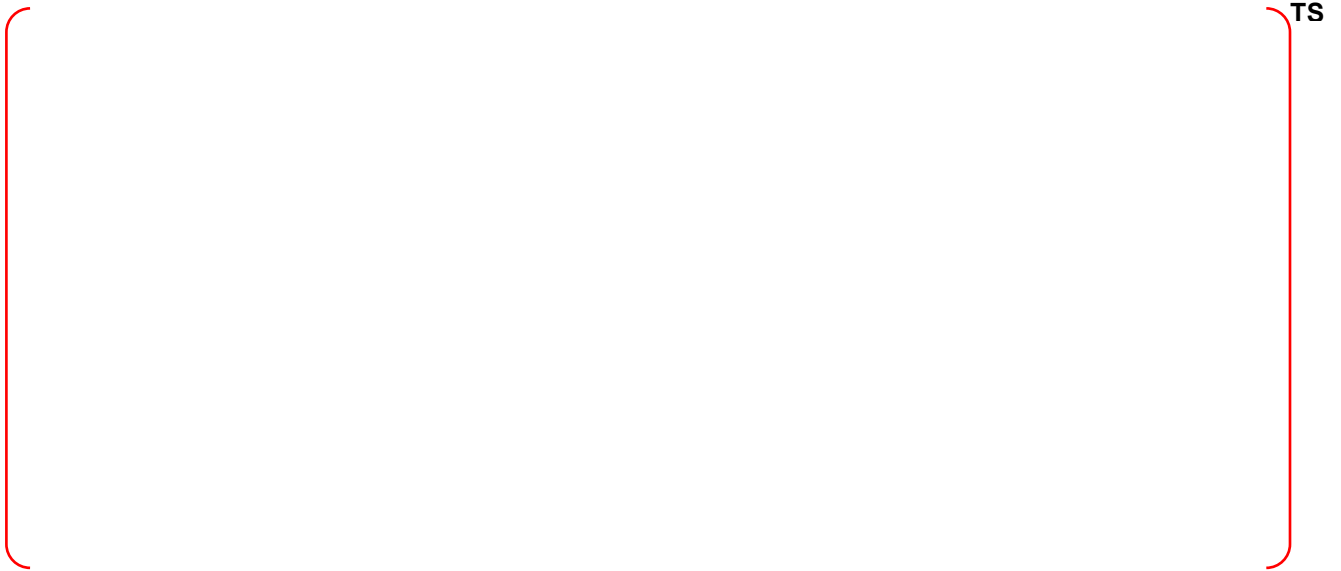


Figure 3-27 Ablation depth in floor and sidewall for the PRA sequence of loss of AC power with short battery life (R9_SBO-006-MCCI)



Figure 3-28 Pressure in containment dome for the PRA sequence of loss of AC power with short battery life (R9_SBO-006-MCCI)



Figure 3-29 Pressure in RCS for the PRA sequence of large break LOCA (LLOCA-C04-NOECSBS-MCCI)



Figure 3-30 Core exit temperature for the PRA sequence of large break LOCA (LLOCA-C04-NOECSBS-MCCI)



Figure 3-31 Pressures in steam generators for the PRA sequence of large break LOCA (LLOCA-C04-NOECSBS-MCCI)



Figure 3-32 Water levels in steam generators for the PRA sequence of large break LOCA (LLOCA-C04-NOECSBS-MCCI)



Figure 3-33 Masses in the core, lower plenum and reactor cavity for the PRA sequence of large break LOCA (LLOCA-C04-NOECSBS-MCCI)



Figure 3-34 Ablation depth in floor and sidewall for the PRA sequence of large break LOCA (LLOCA-C04-NOECSBS-MCCI)



Figure 3-35 Pressure in containment dome for the PRA sequence of large break LOCA (LLOCA-C04-NOECSBS-MCCI)

4 CONCLUSIONS

Potential threat to containment integrity due to MCCI was studied for the APR1400 plant. The postulated severe accident scenarios are the so-called “wet” cases, where the containment flooding system (CFS) is assumed available to flood the reactor cavity following reactor core damage.

The computational tool used for this study is the severe accident code MAAP 4.0.8. Review of the modeling features of this code indicates that two modeling parameters, FCHF and ENT0C, must be calibrated against more sophisticated MCCI codes to achieve conservative predictions of key variables important to containment integrity, including concrete ablation depth and containment pressure. The MCCI code CORQUENCH 3.03 was selected as the basis of the calibration process, given its detailed modeling features of corium-water interaction and melt eruption.

TS

The five severe accident scenarios were selected based on their core damage frequencies from Level I PRA analyses and potential bounding features, including such sequences as: loss of essential service water, loss of AC power with failure of auxiliary feedwater, medium break LOCA, and large break LOCA.

TS

Figure 4-1 and Figure 4-2 show the ablation depths and containment pressures of the scenarios for the first 24 hours.

TS

According to SECY 93-087 (Reference 12), the containment liner must be protected during MCCI, and the pressure resulting from MCCI should not exceed the FLC (Factored Load Category) pressure within 24 hours.

TS

It can be seen that the ablation depth and containment pressure resulting from MCCI do not exceed the limits even for the most bounding scenario. MAAP4.0.8 results are based on the assumption that the cavity floor is a flat surface without a sump. When a cavity sump is considered, CORQUENCH shows that the corium in the sump is quenched before the ablation depth reaches the containment liner, given a cavity floor made of LCS concrete.

Table 4-1 Selected Severe Accident Scenarios for MCCI Analyses for the APR1400 Plant



TS

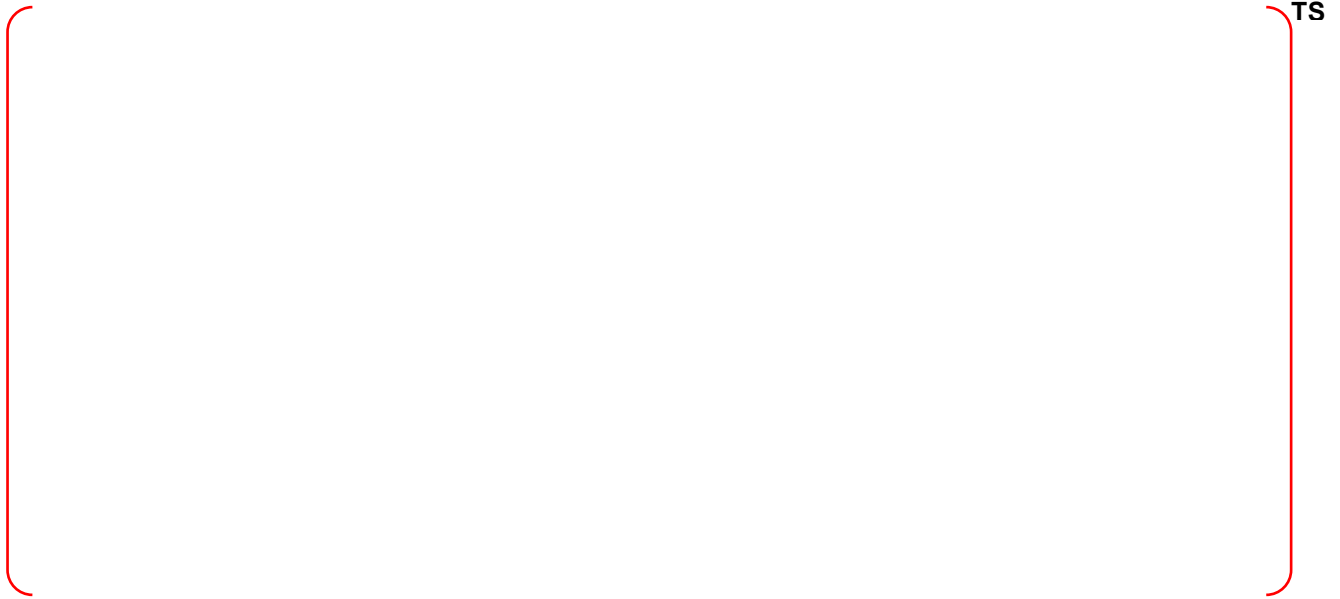


Figure 4-1 Ablation Depths within 24 Hours for Different Severe Accident Scenarios for the APR1400 Plant



Figure 4-2 Containment Pressures within 24 Hours for Different Severe Accident Scenarios for the APR1400 Plant

5 REFERENCES

1. EPRI, 2012, "Modular Accident Analysis Programs for LWR Power Plants, Transmittal Document for MAAP4 Code Revision MAAP 4.0.8" FAI/12-0005.
2. P. Y. Chevalier, 1991, "Presentation of OXY5-GEMINI Code to the ACE-TAC Meeting at Palo Alto," November 4-8, ACE-TAC Meeting, Palo Alto, California, USA.
3. P.Y. Chevalier, G. Cenerino, 1992, "Thermodynamic Data Bases and Calculation Code Adapted to the Modeling of Molten Core Concrete Interaction (MCCI) Phenomena, Developed Jointly by THERMDATA and Institut de Protection et de Surete Nucleaire (France)," Proceedings of second OECD (NEA) CSNI Specialist Meeting on Molten Core Debris-Concrete Interaction, Karlsruhe, Germany, April 1-3.
4. F. B. Ricou, D. B. Spalding, 1961, "Measurements of Entrainment by Axisymmetrical Turbulent Jets," Journal of Fluid Mechanics, Volume 11, pp. 21-32.
5. S. S. Kutateladze, 1951, "A Hydrodynamic Theory of Changes in the Boiling Process under Free Convection," Izv. Akad. Nauk. SSSR Otd, Thekh. Nauk., 4, 529.
6. K. R. Robb, M. L. Corradini, 2010, "Towards Understanding Melt Eruption Phenomena During Molten Corium Concrete Interactions," Proceedings of: ICONE 18, Paper 30116, Xi'an China (May 17-21).
7. M. T. Farmer, R. Aeschlimann, D. J. Kilsdonk, S. Lomperski, 2010a, "Category 4: The CCI-6 Large Scale Core-Concrete Interaction Experiment Examining Debris Coolability Under Early Cavity Flooding Conditions," Viewgraph Presentation at MCCI Seminar, Cadarache France (November 15-17).
8. OECD/MCCI-2010-TR04, M. T. Farmer, D. J. Kilsdonk, R. W. Aeschlimann, S. Lomperski, 2010b, "OECD MCCI Project Category 4 Integral Test to Validate Severe Accident Codes: Core-Concrete Interaction Test Six (CCI-6) Final Report," Rev. 2 (November).
9. M. T. Farmer, Kilsdonk D. J., Aeschlimann R. W., 2009 "Corium Coolability under Ex-Vessel Accident Conditions for LWRs," Nuclear Engineering Technology, Volume 41, 575.
10. OECD/MCCI-2010-TR03, M. T. Farmer, 2011 "the CORQUENCH Code for Modeling of Ex-Vessel Corium Coolability under Top Flooding Conditions, Code Manual-Version 3.03, Rev. 2,".
11. Farmer M. T., 2012, "CORQUENCH Analysis for Siliceous and Limestone Common Sand Concretes for APR1400 Cavity," Transmittal Documents and Data from Argonne National Laboratory to Fauske & Associates, LLC on March 3.
12. United States Nuclear Regulatory Commission, Policy Issue SECY-93-087, 1993, "Policy, Technical, and Licensing Issues Pertaining to Evolutionary and Advanced Light-Water Reactor (ALWR) Designs", April 2

Appendix-C1

Severe Accident Analysis Report for DCH

TABLE OF CONTENTS

1	INTRODUCTION	C1-7
2	REVIEW ON THE EXISTING EXPERIMENTS	C1-8
2.1	Sandia High Pressure Melt Streaming (HIPS) Experiments.....	C1-8
2.2	Argonne Wood's Metal Tests.....	C1-9
2.3	Argonne Corium/Water Thermal Interaction (CWTI) Tests.....	C1-12
2.4	Sandia Surtsey Experiments (Initial).....	C1-15
2.5	Fauske & Associates, Inc. DCH Experiments.....	C1-18
2.6	Argonne 1/40 Liner Scale DCH Experiments for a Zion-Like Containment.....	C1-23
2.7	Sandia 1/10 Scale DCH Experiments for a Zion-Like Containment.....	C1-30
2.8	Purdue Air-Water DCH Simulation Experiments.....	C1-39
2.9	FAUSKE & ASSOCIATES 1/25TH SCALED DCH EXPERIMENTS FOR VANDELLOS AND ASCO CONTAINMENTS	C1-39
2.10	Sandia Scaled DCH Experiments for a Surry-Like Containment.....	C1-47
2.11	Sandia Scaled DCH Experiments for a Calvert Cliffs-Like Containment.....	C1-53
2.12	Karlsruhe Scaled DCH Experiments for European Reactor-Like Containments.....	C1-53
3	REVIEW ON METHODOLOGY OF DCH ANALYSIS	C1-58
3.1	CLCH Model.....	C1-58
3.1.1	Assumptions.....	C1-58
3.1.2	Equations of Pressure and Temperature Increases.....	C1-58
3.1.3	Considerations of Iron Chemical Reaction and Pre-existing H2 Combustion.....	C1-60
3.1.4	Comparison with Experiments.....	C1-60
3.2	TCE Model.....	C1-64
3.2.1	Assumptions.....	C1-64
3.2.2	Prototype SCE Model.....	C1-64
3.2.3	Extension from SCE Model with Consideration of Trapping Corium in the SubCompartment.....	C1-65
3.2.4	Probabilistic Framework.....	C1-67
3.3	Modeling of Accident Scenarios.....	C1-72
3.3.1	Scenario V (Va) - SBLOCA with Repressurization of RCS by Operator Intervention.....	C1-72
3.3.2	Scenario VI - SBLOCA Under Wet Core Conditions.....	C1-73
4	DCH ANALYSIS IN APR1400	C1-74
4.1	Melt Transport in Compartmentalized Containments.....	C1-74
4.1.1	Cut-Off Droplet Size for Corium Deposition.....	C1-74
4.1.2	Cavity Pressure and Two-Phase Flow Velocity.....	C1-75
4.1.3	Fraction of Drops that Impinge on the Wall.....	C1-77
4.1.4	Fraction of Entrained Melt Transported Through Reactor Vessel Annulus.....	C1-77

4.2	DCH model for APR1400	C1-79
4.2.1	Generation of probabilistic distribution and sampling for uncertain input parameters	C1-79
4.2.2	Quantification of point input parameters	C1-79
4.2.3	TCE calculation	C1-80
5	SUMMARY OF RESULTS FOR APR1400 DCH ANALYSIS	C1-81
6	CONCLUSIONS	C1-83
7	REFERENCES	C1-84

LIST OF TABLES

Table 2-1	Selected HIPS Experiments.....	C1-8
Table 2-2	Summary of Wood's Metal Injection/Dispersion Tests	C1-11
Table 2-3	ANL CWTI DCH-Related Experiments	C1-15
Table 2-4	SNL-DCH Experiments	C1-18
Table 2-5	CECo/FAI-DCH Experiments	C1-19
Table 2-6	Experimental Initial Conditions.....	C1-24
Table 2-7	Summary of Test Results.....	C1-27
Table 2-8	Initial Conditions for the IET Experiments.....	C1-31
Table 2-9	Initial Conditions	C1-42
Table 2-10	Comparison of Maximum Pressure Increase (psig).....	C1-46
Table 2-11	Post-Test Debris Distribution	C1-46
Table 2-12	Initial Conditions for the IET Experiments.....	C1-49

LIST OF FIGURES

Figure 2-1	Sectional view of the experimental apparatus for the ANL Wood's metal tests	C110
Figure 2-2	ANL thermite apparatus for the CWTI tests.....	C1-14
Figure 2-3	Schematic of the Surtsey Direct Heating Test Facility.....	C1-17
Figure 2-4	Elevation view of the vessel interconnection to simulate the containment configuration.....	C120
Figure 2-5	Cross-section of the melt generator, reactor cavity, instrument tunnel and the simulated lower compartment with structures	C1-21
Figure 2-6	Relationship of the test configuration to the Zion containment buildings.....	C1-22
Figure 2-7	Cross-sectional view of Zion subcompartment and cavity model.....	C1-25
Figure 2-8	Three-dimensional view of the Zion subcompartment model.....	C1-26
Figure 2-9	Containment loads obtained in the IET tests	C1-28
Figure 2-10	Containment loads obtained in the corium experiments.....	C1-29
Figure 2-11	Surtsey vessel, high-pressure melt ejection system, and subcompartment structures used in the 1/10 scale IET experiments.....	C1-33
Figure 2-12	Schematic of the 1:10 linear scale model of the Zion reactor Cavity.....	C1-34
Figure 2-13	Isometric view of the subcompartment structures inside the Surtsey 1/10 scale vessel	C1-35
Figure 2-14	Surtsey vessel pressure versus time for Test IET-5.....	C1-36
Figure 2-15	Surtsey vessel pressure versus time in the IET-6 experiment	C1-37
Figure 2-16	Validation of the TCE model against all experiments with compartmentalized geometry.	C1-38
Figure 2-17	DCH test facility configuration.....	C1-41
Figure 2-18	Scaled reactor cavity and instrument tunnel configuration used for the Vandellos test.....	C1-44
Figure 2-19	Scaled reactor cavity and instrument tunnel configuration used for the Asco test.....	C1-45
Figure 2-20	Isometric view of the subcompartment structures and RPV model inside the CTTF vessel	C1-48
Figure 2-21	CTTF vessel pressure versus time in the IET-9 experiment.....	C1-50
Figure 2-22	CTTF vessel pressure versus time in the IET-11 experiment.....	C1-51
Figure 2-23	Surtsey vessel pressure versus time in the IET-12 experiment	C1-52
Figure 2-24	Scheme of the DISCO-H facility with the model of the EPR cavity	C1-55

Figure 2-25	Model of the Konvoi cavity and compartments	C1-56
Figure 2-26	Measured containment peak pressure rise over amount of burnt hydrogen per containment volume; the line represents the theoretical pressure increase by thermal energy of hydrogen combustion without heat loss to structure	C1-57
Figure 3-1	Comparisons of pressure increase predicted by CLCH model and the experiment data measured by SNL IET series of experiments. Lower limit of hydrogen generation is assumed for steel oxidation.	C1-61
Figure 3-2	Comparisons of pressure increase predicted by CLCH model and the experiment data measured by SNL IET series of experiments. Upper limit of hydrogen generation is assumed for steel oxidation.	C1-62
Figure 3-3	Comparisons of pressure increase predicted by CLCH model and the experiment data measured by ANL IET series of experiments. Upper limit of hydrogen generation is assumed for steel oxidation.	C1-63
Figure 3-4	Comparisons of pressure increase between SCE model and experiments.	C1-69
Figure 3-5	Comparison of coherence ratio and hydrogen generation between the model prediction and the experiment data.	C1-70
Figure 3-6	Comparison of pressure increase between the model prediction and the experiment data.	C1-71
Figure 5-1	Comparison of pressure due to DCH and the containment failure for APR1400	C1-76

1 INTRODUCTION

The phenomena of HPME and DCH were first considered in the Zion Probabilistic Safety Study (ZPSS) (Reference 1). Until this time, analyses, such as those in the Reactor Safety Study (Reference 2), considered that if the reactor vessel should fail as a result of a severe core damage event, the molten core debris would reside in the reactor cavity. In the ZPSS, it was considered that the spectrum of accident sequences could potentially result in a situation wherein the RPV would fail due to high temperature core debris in the lower plenum and with the RCS at a significant pressure. As a result, the core debris would be initially released to the reactor cavity, but the subsequent blowdown of saturated water, steam and hydrogen from the RCS could displace, push, and entrain the core debris out of the reactor cavity to other regions of the containment. In the ZPSS it was also considered that this high temperature core debris could potentially heat the containment atmosphere.

Subsequent to this study, numerous experiments were performed to determine if dynamic removal of core debris from the reactor cavity would occur should the RPV fail under significant pressure. These experiments, summarized in this report, demonstrate that high density, high temperature melt could indeed be dynamically removed from various types of reactor cavities for situations in which the RCS pressure was greater than approximately 2 MPa at the time of RPV failure. Since this covers a spectrum of accident conditions, dynamic removal was considered in more depth with respect to its potential for directly heating the atmosphere. Hence, the issue of DCH was identified and was the central focus of numerous studies, both analytical and experimental. In the next section, the key experiments that have added to the knowledge base and led towards resolution of this issue for USA cavity designs with large instrument tunnels are described. The section ends with a review of the DCH experiments directed at providing data for European-type reactor designs. Most of these experiments relate to dispersal of molten debris from the reactor cavity and the potential for heating of the containment atmosphere.

The successful DCH modeling tools are reviewed in section 3. The first successful modeling tool for DCH model is CLCH (Convection Limited Containment Heating) model (Reference 35) which is described in section 3.1. The key argument of CLCH model is that the heat transfer between the melt and the gas is limited by the amount of blow-down gases that have intimate (coherent) contact with the melt. Once the melt particles are trapped and deposited in the subcompartment, the heat transfer between the melt and the containment atmosphere becomes negligible, and the major energy addition into the atmosphere is through the combustion of the so-called pre-existing hydrogen. The other modeling tool for DCH is TCE (Two-Cell Equilibrium) model (Reference 36) which is described in section 3.2. The TCE model is another model used to assess the DCH risk, which is an extension of the SCE (Single-Cell Equilibrium) model to account for the effect of containment compartmentalization. The detailed information for TCE model is provided in section 3.2. Section 3.3 is described the accident scenarios used for DCH analysis. These scenarios are selected based on the NUREG/CR-6075, Supplement 1 (Reference 35).

The application of DCH analysis to APR1400 is described in section 4. Section 4.1 is described the assessment of melt transport toward upper compartment. This section is included the interpretation on the behavior of the corium in the reactor cavity applying APR1400 design. Section 4.2 is described the actual methodology used in DCH analysis for APR1400.

An assessment result on the APR1400 containment to DCH effects is described in section 5. The assessment was performed using TCE model with selected accident scenarios in section 3.3. According to the assessment result, APR1400 meets the success criterion established in NUREG/CR-6338 (Reference 46), where DCH problem is considered resolved if Conditional Containment Failure Probability (CCFP) is less than 1% (0.01).

2 REVIEW ON THE EXISTING EXPERIMENTS

2.1 Sandia High Pressure Melt Streaming (HIPS) Experiments

The Sandia HIPS experiments (Reference 3) were conducted to confirm the dispersal of debris from a simulated cavity geometry and to assess the phenomena of jet geometry, gas solubility, and aerosol generation (Reference 4). In the tests reported (Reference 5 and 6), a 1:10 linearly scaled model of the Zion cavity was used. This cavity was either open to the atmosphere or placed within an expansion chamber with one end open to the atmosphere. No attempts were made to maintain the geometric similarity of containment internal structures of Zion for these experiments. Iron-alumina thermite charges with masses of about 80 kg were used. A table of reported tests presented in Pilch and Tarbell is reproduced here in Table 2-1.

Table 2-1 Selected HIPS Experiments

Test Name	Scale	Thermite Mass		Initial Vessel Pressure		Extent Dispersal (%)	Water In Cavity
		(kg)	(lbm)	(MPa)	(psia)		
SPIT-19	1:20	10.3	22.7	12.6	1827	95	No
HIPS-2C	1:20	80.0	176	11.7	1697	99	No
HIPS-4W	1:10	80.0	176	11.7	1697	~95*	Yes
HIPS-5C	1:10	80.0	176	6.7	972	99	No
HIPS-6W	1:10	80.0	176	3.8	551	~95*	Yes
HIPS-7C	1:10	81.5	179	5.5	798	98	No
HIPS-8C	1:10	80.0	176	3.7	537	98	No

* Cavity destroyed during test.

In experiments HIPS-7C and -8C carbon dioxide was used as a cover gas, at pressures between about 3 MPa and 5.6 MPa. Pressures as high as 11.7 MPa were used in two other tests (HIPS-2C and -4W). In two reported experiments (HIPS-4W and -6W), a water-filled cavity was used and destroyed by overpressure during the blowdown due to the small amount of space available for gas expansion. One experiment (HIPS-8C) featured an annular gap around the thermite generator, simulating the gap around the RPV if the insulation were assumed to be removed. During all the HIPS tests, dense aerosol clouds surrounded the debris jet, and sweepout from the cavities was nearly complete in all cases, above 95%. After tests in which the cavity was placed inside the confinement room, this debris was found either within the room or on the concrete pad just outside its open end. This test series demonstrated the substantial influence of structures to capture the debris outside of the reactor cavity/instrument tunnel.

In the HIPS-7C tests, over 30% of the debris was found in the rear of the confinement chamber, much of it against the rear wall. Observations with high speed films show debris exiting the cavity splashing off the ceiling and raining down in that location. Over 97% of the original melt mass was recovered from the chamber and concrete pad, and the rest either landed on the ground beyond the pad or was in the aerosol cloud which billowed out. Thus, the confinement chamber does not model the containment lower compartment structures. On the other hand, it does illustrate that a minimal representation of the structure results in substantial removal of the debris from the gas stream.

In the HIPS-8C tests, aluminum collection pans were placed on the chamber floor to determine the spatial distribution of debris exiting the cavity, and deduce which fraction exited through the keyway outlet, and which fraction exited through the angular gap around the melt generator. About 25% of the debris was concluded to have been released through this gap, deflected off the ceiling, and fallen into pans around the melt generator. This corresponds to the area fraction taken up by the annular opening.

2.2 Argonne Wood's Metal Tests

The influence of the containment configuration outside the reactor cavity and instrument tunnel was demonstrated by the isothermal Wood's metal experiments (Reference 7). In these tests, the Zion reactor cavity-instrument tunnel configuration was mocked-up along with the seal table and biological shield inside the crane wall (missile barrier). Wood's metal, which has a melting temperature of 73°C and a density of about 9500 kg/m³, was used to simulate the debris. The experimental configuration is illustrated in Figure 2-1, and the experimental conditions are summarized in Table 2-2. As shown in the table the parameters investigated included various masses of water initially accumulated within the reactor cavity as well as different gas velocities through the cavity following molten metal discharge from the simulated reactor vessel.

The final debris configuration was reported in terms of (1) the material left within the reactor cavity, (2) that which was dispersed within one equivalent diameter of the instrument tunnel exit, and (3) that fraction of debris dispersed beyond one equivalent diameter of the instrument tunnel. High speed movies showed a large fraction of the debris is initially transported as a large wave moving along the outer sloping surface of the instrument tunnel, impacting upon the bottom surface of the seal table. The results demonstrate the structure in the lower compartment is very effective in separating the debris from the high velocity gas stream and depositing the debris on the containment floor in close proximity to the instrument tunnel. More specifically, the structure has a first order effect on the debris distribution in the simulated containment.

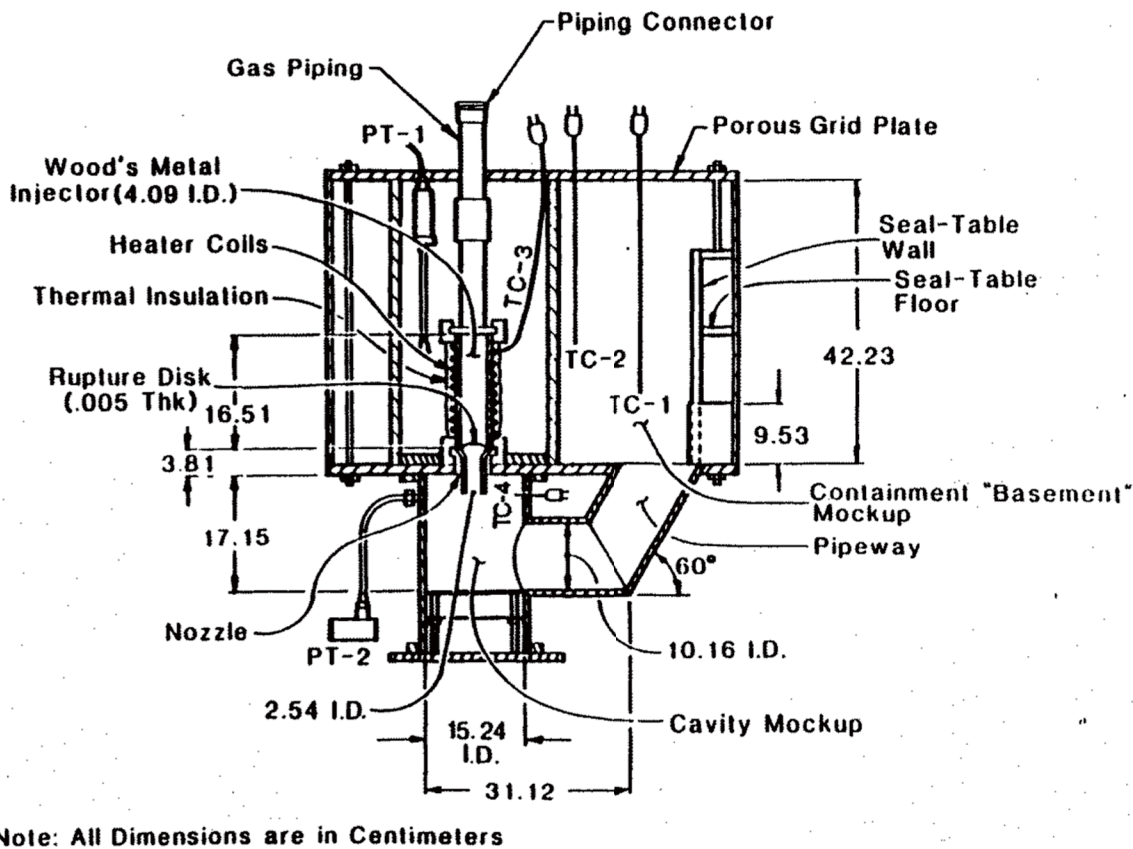


Figure 2-1 Sectional view of the experimental apparatus for the ANL Wood's metal tests

Table 2-2 Summary of Wood's Metal Injection/Dispersal Tests

Test Number (Old Ref.)	1 (17)	2 (18)	3 (19)	4 (20)	5 (21)	6 (22)	7 (24)	8 (25)	9 (26)	10 (27)	11 (28)
Injected Material ¹⁾	Gas Only	WM	WM	WM	WM	WM	WM	WM	WM	WM	WM
Cavity Water Level, h/D _t ²⁾	0.5	Dry	0.1	0.1	0.5	1.0	0.1	0.1	0.5	1.0	Dry
Injector Temperaure, °C/°F	--	89/ 192.2	91/ 195.8	75/ 192.2	89/ 192.2	90/ 194	89/ 192.2	88/ 190.4	87/ 188.6	88/ 190.4	89/ 192.2
Injection Pressure, MPa/psia	0.65/ 94.25	0.70/ 101.5	0.68/ 98.6	(3)	0.55/ 79.75	0.68/ 98.6	0.68/ 98.6	0.30/ 43.5	0.25/ 36.25	0.25/ 36.25	1.40/ 203
WM Injection Velocity, m/s/ft/s	7.8/ 25.57	7.8/ 25.57	7.8/ 25.57	7.8/ 25.57	7.8/ 25.57	7.8/ 25.57	7.8/ 25.57	5.4/ 17.70	5.4/ 17.70	5.4/ 17.70	11.7/ 37.0
Gas Velocity (4" pipe), m/s/ft/s	28/ 91.80	29/ 95.08	27/ 88.52	28/ 91.80	27/ 88.52	29/ 95.08	9.7/ 31.80	9.3/ 30.49	9.3/ 30.49	9.4/ 30.82	35/ 114.75
Maximum Cavity Pressuriza-tion, kPa	--	10	35	20	80	190	33 (4)	10	60	120	50
NOTES: (1) WM = Woods Metal (T _{mp} = 73°C). (2) D _t = pipeway diameter, 10.2 cm. (3) WM frozen in PT standoff line. (4) High pressure caused cavity apparatus to rupture at 60° pipe elbow.											

2.3 Argonne Corium/Water Thermal Interaction (CWTI) Tests

The CWTI series of reactor material DCH experiments were performed by Spencer et al., Spencer et al. and Spencer, et al. (Reference 8, 9, and 10). The experimental configuration represented some major features of the Zion reactor lower containment compartment cavity, and the upper compartment at a 1:30 linear scale. Reactor materials (principally UO_2 and stainless steel) were used and created by an exothermic thermite reaction. Molten debris was injected downward into a simulated cavity and keyway (see Figure 2-2), connected to an expansion volume partitioned like the lower and upper compartments of a containment. In some tests, water was present either in the cavity or the expansion volume or both. The objectives of these tests were to examine heat transfer between core debris and water, sweepout of water and core debris from the cavity, steam generation, hydrogen generation, and to characterize the spatial distribution of dispersed debris.

The test apparatus included the thermite reaction vessel (the source of the molten core debris), an interaction vessel (representing the reactor cavity), a pipe simulating the instrument tunnel, an expansion vessel representing the containment, a "trap" above the pipe discharge to simulate a seal table and a baffle plate to separate the expansion vessel into upper and lower compartments. It is noted that the geometric similarity of the simulated cavity was somewhat distorted (from the Zion cavity design) because of the use of a 90°-bend circular pipe as a keyway instead of a 64°-bend rectangular duct. The simulated core debris produced by the thermite reaction was composed of 60% UO_2 , 16% ZrO_2 , 24% stainless steel (67% Fe, 21% Cr, 12% Ni) and had a temperature of about 3100 K.

Tests were performed with low (less than 0.5 MPa) and high (~ 5 MPa) pressure blowdowns as well as with inert and oxidizing atmospheres. Several different initial water level conditions were tested in the interaction vessel ranging from completely empty to essentially full of water before the melt was released from the thermite furnace. Initial conditions and results for DCH-related CWTI tests are listed in Table 2-3.

The DCH-related tests were conducted by starting the thermite reaction at nominally atmospheric pressure. The melt was subsequently pressurized (by gas from external high pressure gas cylinders) to burst a bottom diaphragm and initiate melt ejection. The duration of the gas blowdown was sufficiently long to assure sweepout of all available melt. Debris not swept out remained as a 1 ~ 3 mm thick crust uniformly deposited on the wall of the interaction vessel and the entire pipe surface (for CWTI-5 and -6).

Various mass fractions of debris were observed to be dispersed from the reactor cavity into the simulated containment volume. Debris was collected at various locations in the apparatus including (1) the interaction vessel and pipe, (2) the "particle trap reflector" at the top of the pipeway as it exited into the bottom of the expansion vessel, (3) on the floor of the simulated containment, and (4) on the top of the simulated lower compartment representing the operating deck. Characteristic particle sizes for the particles swept out into the air atmosphere ranged from 64 to 700 microns for tests CWTI-11 and -13, which had no water in the cavity. Most particles were in the range 100 ~ 300 microns. The experiments with water in the interaction vessel or expansion volume prior to melt ejection demonstrated the effectiveness of water for removing heat from dispersed debris, including the energy released due to oxidation. These tests exhibited little or no direct containment heating. Results for test CWTI-12 show no significant contribution to DCH with the co-dispersal of debris and water into the containment atmosphere. Test CWTI-12 was performed without the presence of the impeding structure and clearly demonstrates the influence of co-dispersed water. Modest direct containment heating was observed in tests CWTI-6 and -11 which had water only in the pan of the expansion vessel (containment floor). The largest atmospheric heating occurred in test CWTI-13 where no structures and no water were present in either the interaction vessel (cavity) or expansion vessel (containment). This heatup was caused by a sweepout mass of only 0.2 kg. Hydrogen generation and/or oxygen depletion occurring during these tests were also measured to determine the extent of oxidation and its contribution to the overall energy input to the system.

The most important observation from the ANL experiments concerns the influence of structure on debris dispersal. The "particle reflector" in this experiment was a simulation of the in-core instrument tube seal table configuration in a Zion-like containment. The horizontal baffle plate above the "particle reflector" represented the floor separating the Zion containment into upper and lower compartments. Comparison of results from CWTI Tests 6, 11, and 13 reveals the effect of structure on direct containment heating. All three were performed with a dry interaction vessel (reactor cavity), but Tests 6 and 11 included structure in the expansion vessel (containment) while Test 13 had no structure. The DCH efficiencies whose definition is given in Table 2-3 and calculated in reference 10 for Tests 6 and 11 were 5% and 1%, respectively, while the DCH efficiency for Test 13 was reported at 62%. Thus, the substantial effect of the seal table structure was to prevent a significant fraction of the debris from entering the containment atmosphere directly. Because of the structure, a major fraction of the entrained debris was deposited on the lower containment floor.

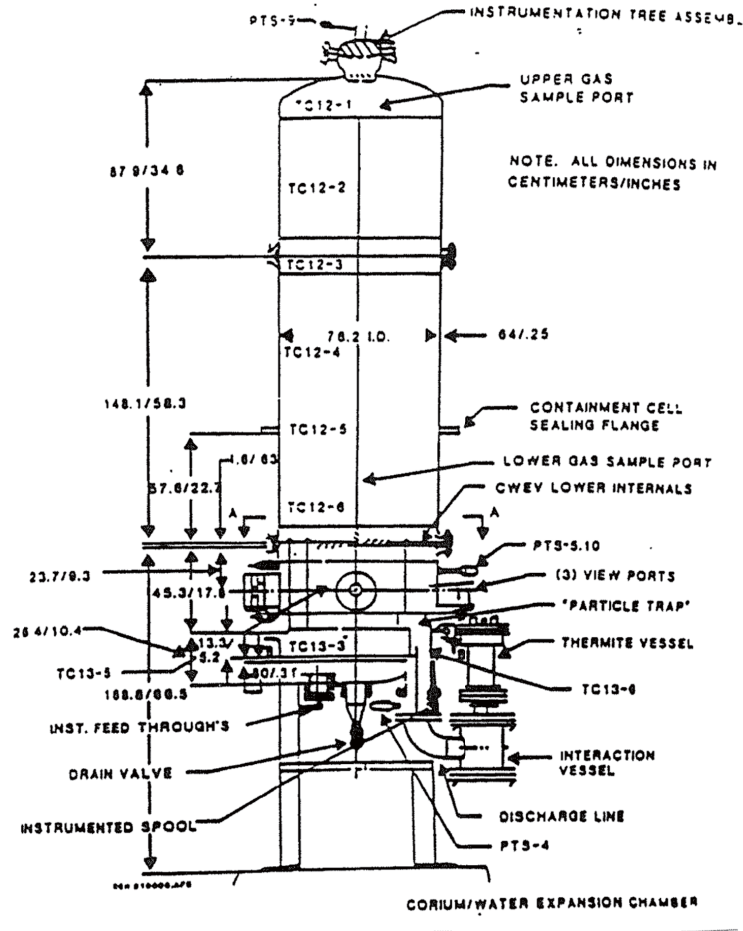


Figure 2-2 ANL thermite apparatus for the CWTI tests

Table 2-3 ANL CWTI DCH-Related Experiments¹

Test No.	5	6	11	12	13
Driving Pressure, MPa/psia	5.0/725	4.7/681.5	5.1/739.5	2.8/406	4.0/580
Atmosphere	AR	AR	air	air	air
Corium Mass Injected, kg/lbm	3.94/8.67	3.75/8.25	2.93/6.45	2.69/5.92	2.27/4.99
Corium Mass Swept Out, kg/lbm	2.44/5.37	1.21/2.66	0.88/1.94	1.31/2.77	0.20/.44
Corium Mass Remained, kg/lbm	1.5/3.3	2.54/5.59	2.05/4.51	2.38/3.04	2.07/4.55
Water in Cavity, kg/lbm	5.6/12.32	dry	dry	4.6/10.12	dry
Dispersal Impediments	s/b ²	s/b	s/b	none	none
Atmosphere Initial Temp, K/°F	419/294.2	408/274.4	411/279.8	422/299.6	298/76.4
Atmosphere Peak Temp, K/°F	417/290.6	461/369.8	435/523	407/272.6	621/657.8
Atmosphere Initial Pressure, MPa/psia	0.52/75.4	0.22/31.9	0.22/31.9	0.37/53.65	0.32/46.4
DCH Efficiency, %	0	5	1	0	62
¹ 3.33 % linear scale model of Zion. ² s/b - shroud/baffle. ³ DCH efficiency = $\frac{\text{Measured Atm. Heatup}}{\text{Max. Equilibrium Atm. Heatup}} \times 100.$					

2.4 Sandia Surtsey Experiments (Initial)

A series of experiments designated as Surtsey was conducted at Sandia (Reference 11, 12, 13, 14, and 15). Experiments DCH-1, 2, 3 and 4 used cavity configurations similar to those of the HIPS 1:10 linear-scale Zion mockups. These cavities were completely enclosed in a large expansion vessel (called SURTSEY) of 103 m³ capacity and a 1.0 MPa design pressure. No attempts were made to represent the geometry of the Zion containment internal structures such as the seal table, the lower compartment, the operating deck, etc. Four tests were performed, and results were presented in the detailed reports referenced above.

DCH-1 involved 20 kg of molten iron-alumina thermite injected into a 1:10 linear scale model of the Zion cavity only, with a nonprototypic exit guide box added to the instrument tunnel exit to direct debris upward along the centerline of the vessel. Figure 2-3 illustrates the Surtsey facility (Reference 16). The thermite was propelled with nitrogen gas initially at 2.55 MPa. Peak pressures ranged from 0.09 MPa to 0.13 MPa and were achieved less than one second after debris dispersal. High speed film shows debris shooting upward at 40 m/s, expanding laterally and filling the entire chamber cross-section within a few meters of the cavity exit. About 11.6 kg were dispersed from the cavity, including the correction for estimated oxidation. Melt retained within the cavity and chute was in the form of a thin crust, and a 1.2 kg mass was found at the base of the keyway inclination. Aerosol measurements indicated that much material was fragmented to a size under 10 microns, but the measurements may be inaccurate and a large uncertainty is present in the actual amount of such material. The calculated range of aerosolized debris was 5 to 25% of the dispersed mass. Mechanical sieving of debris collected in the chamber showed a log-normal size distribution with a mass mean size of 0.55 mm. Thus the bulk of the debris ejected from the cavity was of millimeter size. This test was analyzed using the methodology described in Henry (Reference 17) and good agreement was obtained when the specific configuration without structure was considered.

DCH-2 involved 80 kg of molten iron-alumina thermite injected into a 1:10 linear scale model of the Zion cavity and instrument tunnel only, with a nonprototypic exit guide box added to the exit to direct debris

upward along the centerline of the vessel. The thermite was propelled with nitrogen gas initially at 6.77 MPa and peak pressures ranged from 0.22 MPa to 0.31 MPa and were achieved less than one second after debris dispersal. High speed film showed that debris leaving the guide box expanded laterally and filled the entire chamber cross-section within a fraction of a second, likely indicating the debris-gas two-phase mixture was "choked" at the exit of the guide box. The total mass recovered from the test chamber, cavity, and melt generator was about 99.5 kg, representing an increase in mass above that injected of 24%. This was attributed to several potential sources related to the construction of the apparatus and test conduit as well as oxygen uptake by oxidation of the iron in the thermite. The latter source was considered to be the most dominant mechanism. About 91.3 kg were dispersed from the cavity. Five types of debris were identified, with each type being generally associated with a particular area of the apparatus. On the upper third of the vessel in line with the cavity exit, 1-2 mm thick sheets of brittle debris were tightly bonded to the wall. Debris stuck to lower portions of the vessel wall was loosely bonded and formed sheets of 2-4 mm thickness. On horizontal surfaces, debris was found to be approximately 1-mm diameter spheres, and agglomerations of such spheres with irregularly-shaped masses of previously molten debris. Melt retained within the cavity and chute was in the form of a thin crust, and a 2 kg mass was found directly underneath the melt generator. This test was also analyzed using the methodology proposed by Henry and found to be consistent with the methodology considering the simplified geometry used in the experiment.

DCH-3 and DCH-4 have been fully reported. The overall results of Tests DCH-1 to DCH-4 are summarized in Table 2-4. Test DCH-1 had the largest efficiency of energy transfer from the debris to the atmosphere (> 90%), while the DCH-4 test was lowest with nominally 35%. The latter was affected strongly by the absence of chemical energy release because of the lack of oxygen in the chamber atmosphere. For consumption of oxygen in the chamber, the degree of oxidation in the DCH-1 test was the greatest, while the DCH-3 debris was the least oxidized.

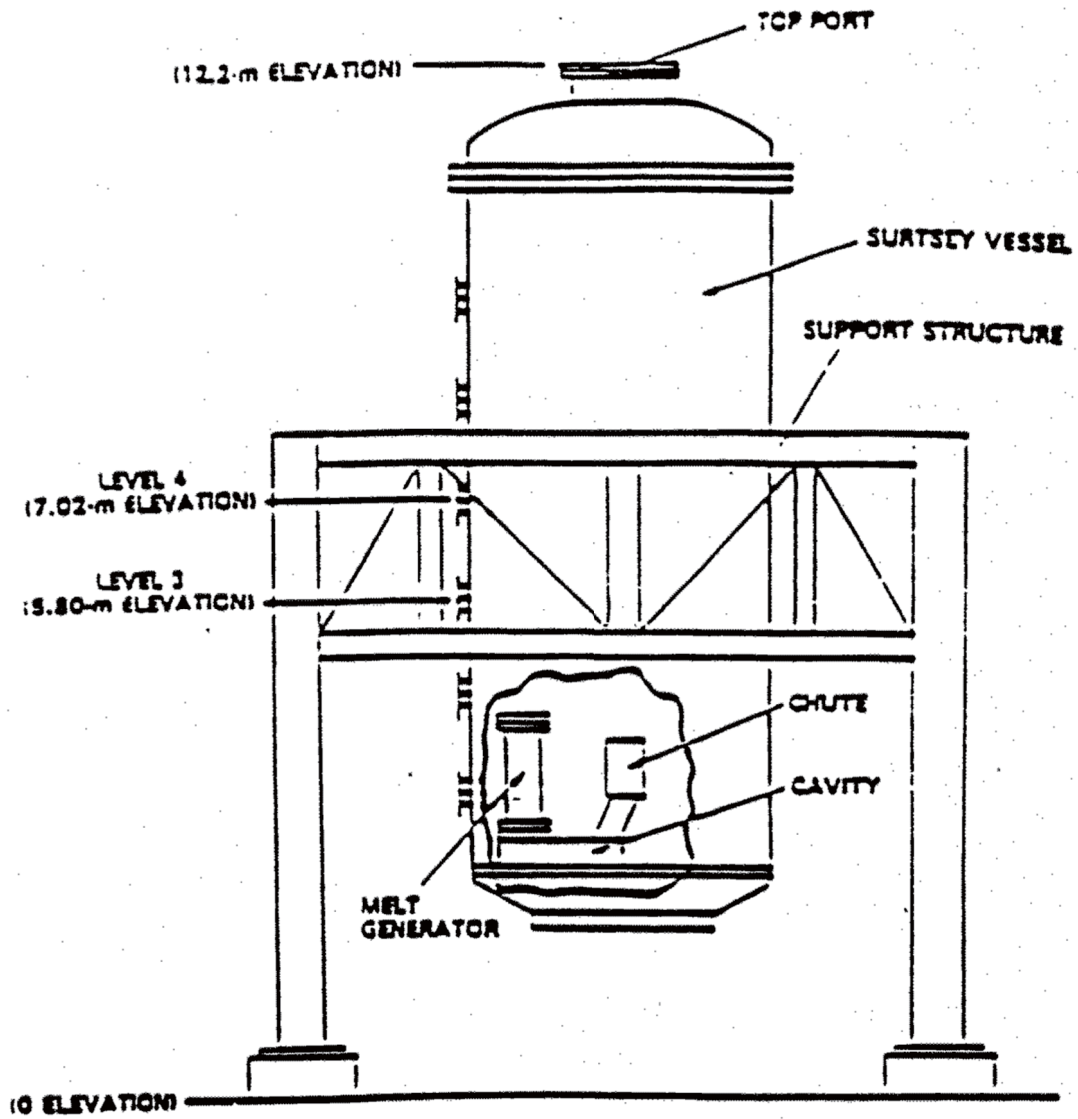


Figure 2-3 Schematic of the Surtsey Direct Heating Test Facility

Table 2-4 SNL-DCH Experiments^{1,2}

Test	Driving Pressure MPa/psia	Driving Gas	Thermite Mass (kg/lbm)			Peak Temp °C/°F	Peak Press MPa/psia
			Initial	Swept-Out	Remained		
DCH-1	2.4/348	N ₂	20/44	~10/22	~10/22	260/500	0.18/26.1
DCH-2	6.8/986	N ₂	80/176	~76/167.2	~4/8.8	880/1616	0.33/47.9
DCH-3	6.0/870	N ₂	80/176	~75/165	~5/11.0	860/1580	0.28/40.6
DCH-4 ³	6.9/1000.5	N ₂	80/176	~74/162.8	~6/13.2	860/1580	0.27/39.2

¹ 10% linear scale model of Zion cavity only, no representation of the containment structures outside of the reactor cavity/instrument tunnel.

² Dry cavity and containment.

³ Inert atmosphere.

2.5 Fauske & Associates, Inc. DCH Experiments

The Fauske & Associates, Inc. program addressed the issue of direct containment heating in support of the Zion IPE (Reference 18). In keeping with lessons learned from smaller scaled tests, these experiments were conceived and designed to have a 5% linear scale simulation of the reactor cavity, instrument tunnel, lower compartment (including two steam generators, two reactor coolant pumps and the refueling canal wall) and upper compartment of the Zion containment building. Figure 2-4 and Figure 2-5 show the experimental apparatus and Figure 2-6 describes how the experiment represents the reactor containment. Iron-aluminum thermite was used to simulate the molten core material, with the 20 kg thermite mass representing about twice the scaled debris mass and energy content of the Zion reactor. This was done to compensate for the greater propensity of freezing on the reactor cavity walls in small scale experiments. The experiments can also be viewed as a study of the effect of lower containment structures on the dispersal of iron-aluminum debris when compared with the Sandia DCH tests, which also used iron-aluminum as a core material simulant, but had no containment internal structures. This work represents the most complete geometric similarity of the Zion cavity and containment internal structures for the scaled DCH experiments performed to date.

The experimental matrix included four tests, all with 20 kg of thermite, three driven by nitrogen and one by steam. Water was available on the containment floor in all tests and was also available, to different extents, in the various tests; two having about 1 cm of water on the cavity floor, one having 8 cm and the other was performed with a dry reactor cavity. Table 2-5 presents the test conditions for the experimental matrix. Table 2-5 also summarizes the test results and clearly demonstrates that (1) the tests were very similar in their response and (2) very little pressurization occurred in the upper containment compartment. Measurements of the containment pressurization showed very little, if any, contribution to direct heating even though 90% of the material was dispersed. Pressurization in the reactor cavity and instrument tunnel, as well as the lower compartment, was essentially due to debris-water thermal interactions in the reactor cavity, the blowdown of the melt generator, and steam generated in the debris quenching process on the lower compartment floor. The measured peak temperatures of the lower compartment atmosphere were mostly the results of rapid steam generation due to quenching, followed by slow heating of the gas due to debris frozen on structures. This latter energy transfer did not contribute to the pressurization because of the cooling provided by other heat sinks.

Maximum local DCH efficiency of about 2%, based on the peak pressure, was measured in FAI-DCH-1 where only a limited water mass was present in the reactor cavity before the blowdown. This is an upper-bound estimate of DCH efficiency because the steam partial pressure was conservatively estimated (underestimated). The temperature increase in the lower compartment was about five to six times as high as in the upper compartment but was dominated by the rapid steam generation since the

measured peak temperature was only slightly superheated. The results for all four tests were very consistent with respect to the extent of debris dispersed, the peak temperature in the lower compartment and the pressurization transient in the containment. The only differences are the response caused by dynamic interactions in the reactor cavity (determined by the water mass in the cavity) and the hydrogen generated which is a function of the water in the cavity and the driving medium. Given the similarity of the global response for all four tests, these differences have a second order influence on the containment response.

The results were consistent with the Argonne CWTI-DCH tests in that significant heatup of the containment atmosphere was not observed in any runs including the important structural barriers of a seal table and the lower containment compartment. In fact, the capacity of structures to mitigate DCH can be seen by comparing these results to the Sandia DCH results which did not represent these structures. It is to be noted that the use of steam to eject the debris simulant yielded a containment temperature and pressure response virtually identical to the nitrogen blowdown tests, even though more hydrogen was generated, i.e., from 7% to 15% of the metal

Table 2-5 CECO/FAI-DCH Experiments

Test	Driving Pressure (MPa/psia)	Driving Gas	Thermite Mass (Kg/lbm)		Measure Peak Containment Pressure		Water (kg/lbm)	
			Initial	Swept-Out	kPa	Psia	Cavity	Compartment Floor
DCH-1	3.3/478	N ₂	20/44	~18/~39.6	165	23.9	1.1/2.4	90/198
DCH-2	2.9/420	N ₂	20/44	~18/~39.6	170	24.7	5.3/11.7	47/103
DCH-3	3.2/464	N ₂	20/44	~18/~39.6	155	22.5	Dry	47/103
DCH-4	2.3/333	Steam	20/44	~18/~39.6	172	25.0	1.1/2.4	47/103

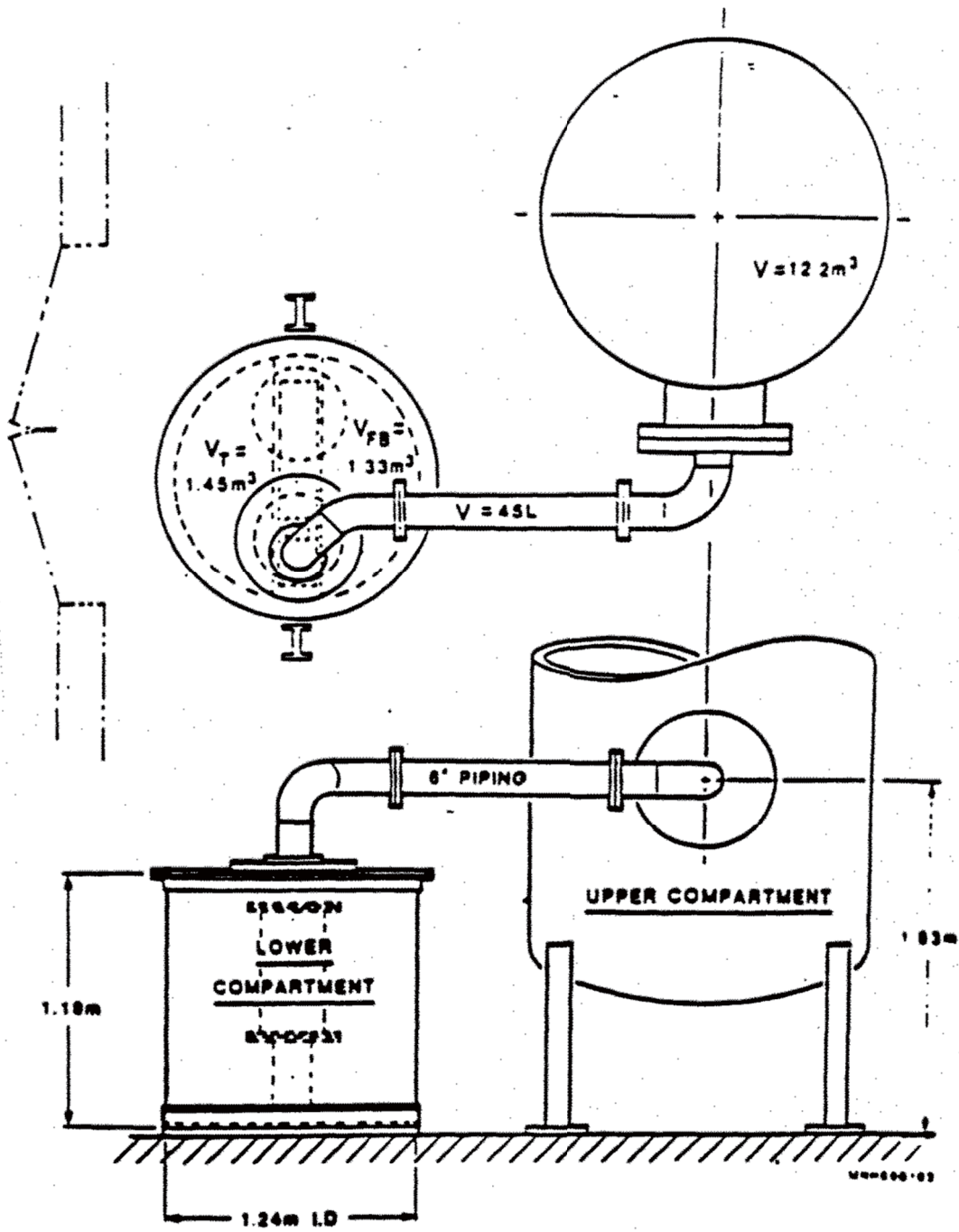


Figure 2-4 Elevation view of the vessel interconnection to simulate the containment configuration

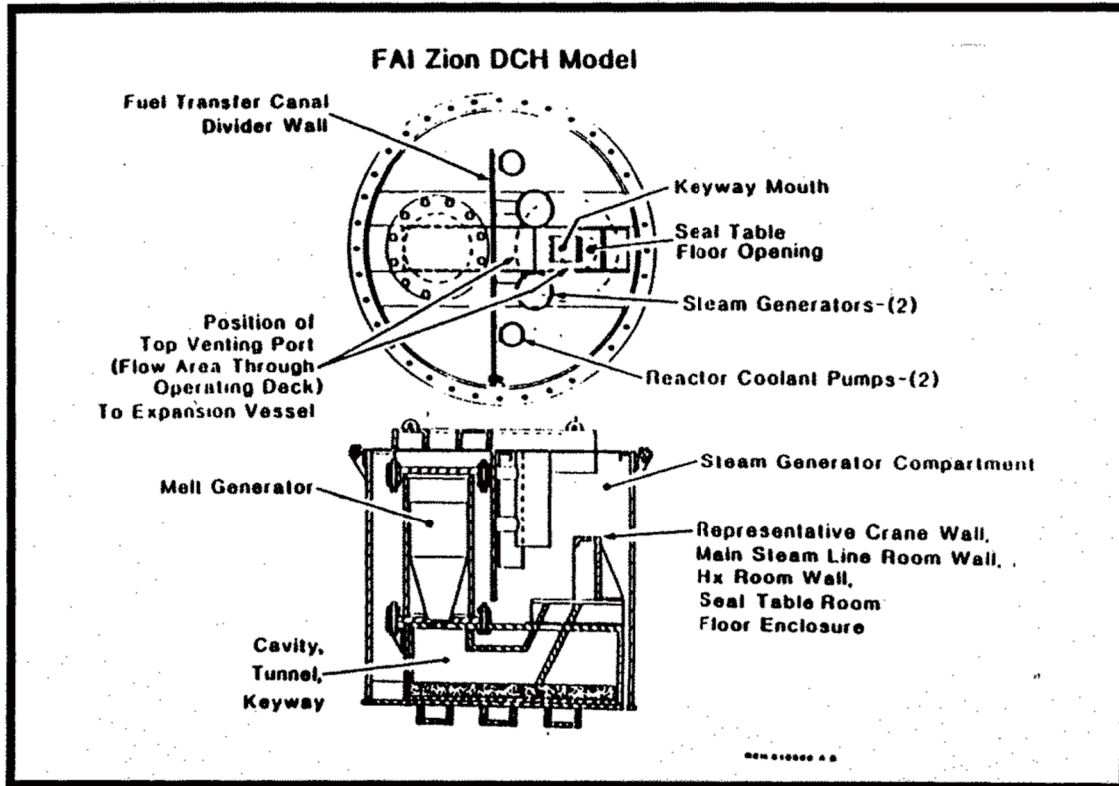


Figure 2-5 Cross-section of the melt generator, reactor cavity, instrument tunnel and the simulated lower compartment with structures

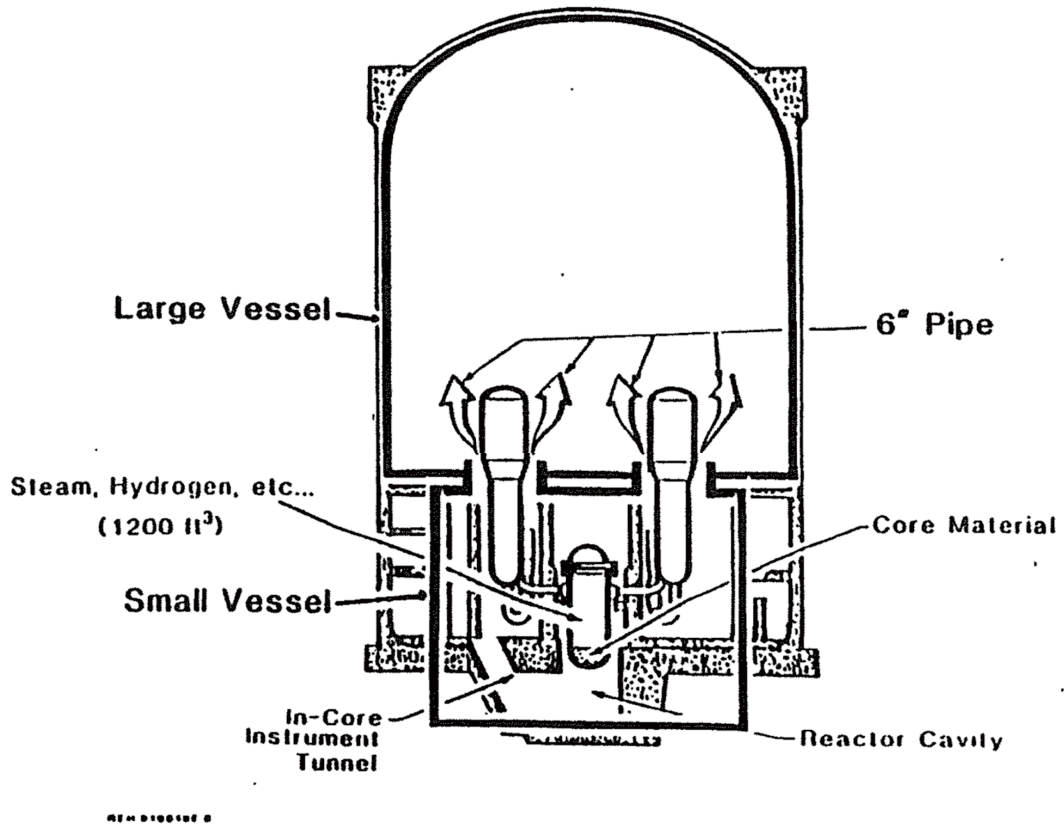


Figure 2-6 Relationship of the test configuration to the Zion containment buildings.

2.6 Argonne 1/40 Liner Scale DCH Experiments for a Zion-Like Containment

Table 2-6 (Reference 19) lists the initial conditions for the various experiments performed as part of the Argonne test program. As indicated by this table, the tests varied the materials used to represent the molten core debris, the reactor coolant system pressure at the time of vessel failure, the initial containment pressure, the initial containment temperature, and most importantly the conditions within the containment atmosphere. Specifically, tests were performed where the atmosphere was inerted with nitrogen, inerted with steam, and experiments were also run with an atmosphere supporting combustion.

Figure 2-7 illustrates the technique used to represent the Zion reactor vessel lower head, reactor cavity, the instrument tunnel and the exit into the steam generator compartment. As illustrated by this figure, also taken from reference 19, the length of the instrument tunnel is somewhat distorted as a result of this experimental configuration. This is not viewed as a substantial shortcoming of the experiment, and if anything, enables more entrainment to take place in the instrument tunnel; therefore it is a potential conservatism in the experimental configuration. It is to be noted that this particular aspect was also part of the Sandia 1/10 linear scale test as will be discussed later. Figure 2-8 illustrates the compartmentalization used for the Zion subcompartment model. Particularly, note the location of the "cavity exit", which is the exit of the instrument tunnel into steam generator compartment. With the substantial compartmentalization provided by the seal table room and the concrete walls defining the steam generator compartment, including the cylindrical wall supporting the crane, there is large amount of structure obstructing the flow path of core debris as it would exit the instrument tunnel and flow towards the major open volumes of the containment. Consequently, this structure, as noted by the numerous experiments discussed above, could separate the core debris from the flowing gaseous medium, deposit this material to a large extent within the steam generator compartment and result in localized high temperatures within the containment (in the steam generator compartment), but with minimal pressurization of the containment atmosphere. As will be discussed, this is the focus of the MAAP model and the Sandia two cell equilibrium model (TCE), which has been used to correlate the numerous experiments as well as to extrapolate to nuclear power plant conditions.

Figure 2-9 and Figure 2-10 illustrate the major result of these experiments, i.e. the containment pressure increase resulting from the HPME is typically between 1.5 to 2.5 bars depending upon the specific conditions. Also, as illustrated in Figure 2-10, the pressure increases resulting from using uranium thermite (Tests U1A, U1B and U2) are less than or equal to those resulting from iron thermite. Table 2-7 summarizes the test results from the ANL experiments and clearly illustrates that while substantial fractions of the molten material were swept out of the cavity (sweepout fraction), the maximum pressure increases in the containment for all the experiments lie well within the capabilities of a large dry containment such as Zion.

The 1/40 scale experimental program paid substantial attention to the details of linearly scaling the containment geometry for a Zion-like system. They showed that the subcompartment structures effectively trapped the molten debris and that there was only limited energy transfer with the containment atmosphere. Furthermore, experiments with uranium dioxide thermite showed that there was very little influence of real materials on the results.

Table 2-6 Experimental Initial Conditions

	IET-1RR	IET-3	IET-6	IET-7	IET-8	U1A	U1B	U2
Melt	Fe/Al ₂ O ₃	Corium	Corium	Corium				
Mass, kg	0.82	0.82	0.71	0.71	0.71	1.13	1.13	1.13
D _H	1.3	1.1	1.1	1.1	1.1	1.1	1.1	1.1
P _{RCS,0} , MPa	6.7	5.7	6.6	6.1	6.5	3.0	6.0	4.3
N _B , g-moles	9.84	8.43	9.65	8.88	9.36	4.18	8.87	5.89
P _{c,0} , MPa	0.1	0.2	0.2	0.1	0.2	0.2	0.2	0.2
T _{c,0} , K	318	315	310	310	473	300	300	301
Atm., mol%								
H ₂	0.0	0.0	2.0	0.0	3.9	0.0	0.0	2.6
O ₂	0.1	10.8	9.9	10.1	7.7	0.6	0.5	11.6
Steam	0.0	0.0	0.0	0.0	49.0	0.0	0.0	0.0
N ₂	99.9	88.8	87.5	89.4	37.4	99.0	99.0	84.6

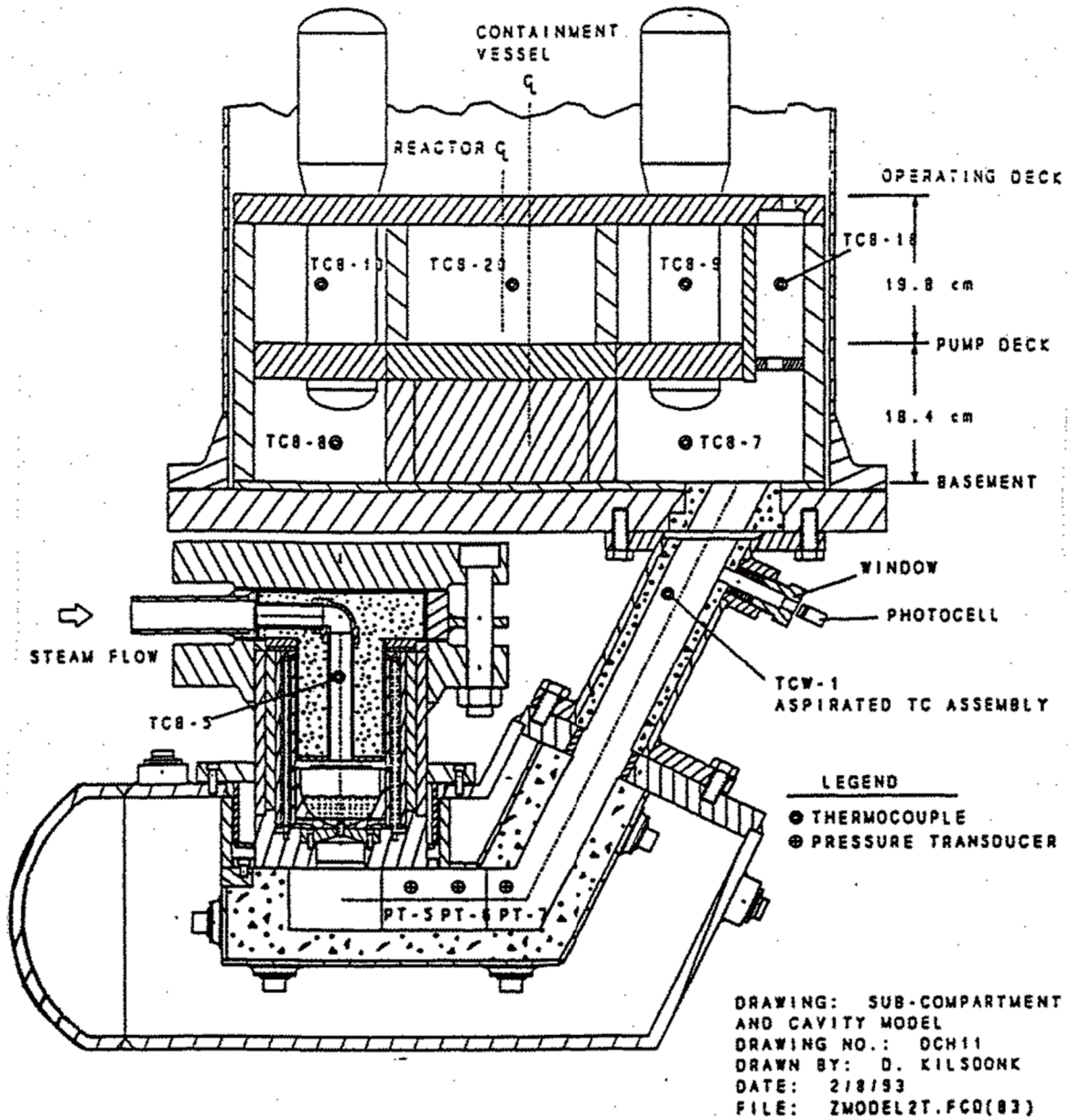


Figure 2-7 Cross-sectional view of Zion subcompartment and cavity model

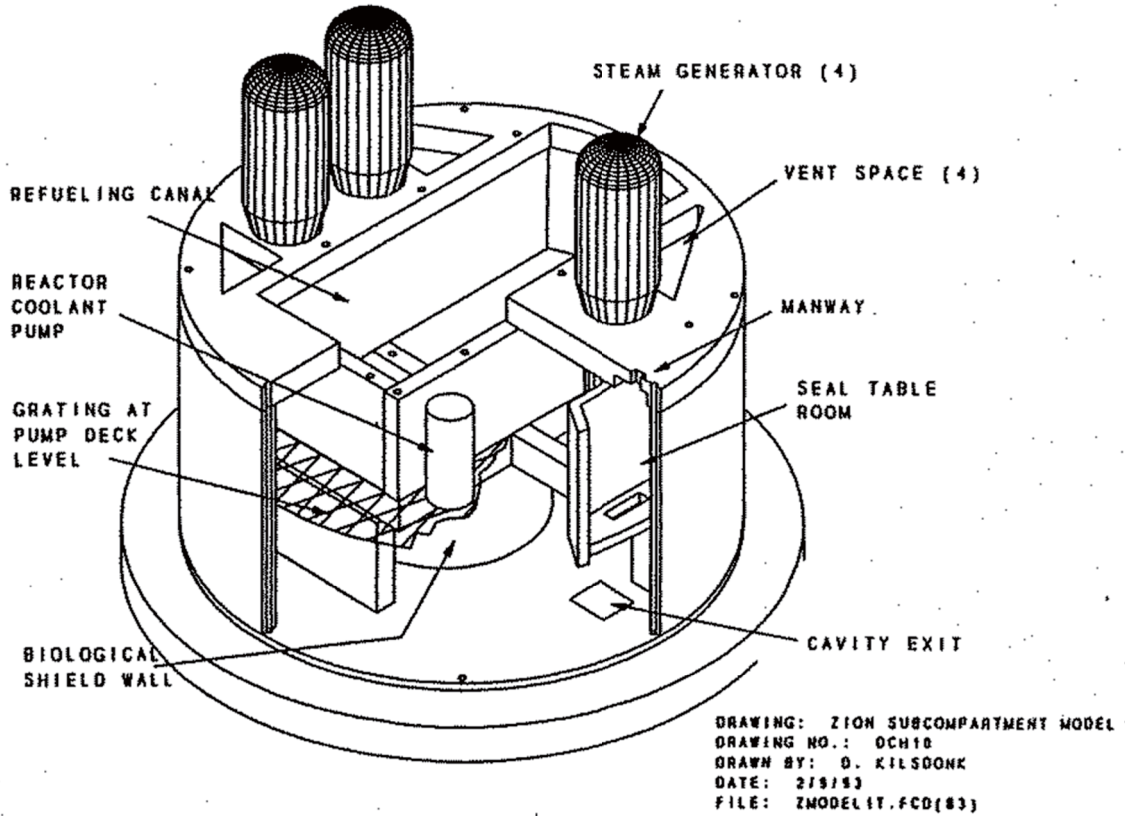


Figure 2-8 Three-dimensional view of the Zion subcompartment model

Table 2-7 Summary of Test Results

	IET-1RR	IET-3	IET-6	IET-7	IET-8	U1A	U1B	U2
Driving Pressure, $P_{RCS,0}$, MPa	6.7	5.7	6.6	6.1	6.5	3.0	6.0	4.3
Blowdown Steam, g-moles	9.84	8.43	9.65	8.88	9.36	4.18	8.87	5.89
Melt Mass, kg	0.79	0.75	0.71	0.69	0.70	1.130	1.130	1.130
Initial Cont. Pressure, $P_{CONT,0}$, MPa	0.2	0.2	0.2	0.1	0.2	0.2	0.2	0.2
Blowdown Time Constant, τ_s , secs	0.23	0.41	0.28	0.32	0.33	0.38	0.54	0.49
Initial Containment Atmosphere Composition, mole%								
H ₂	0.0	0.0	2.0	0.0	3.9	0.0	0.0	2.6
O ₂	0.1	10.8	9.9	10.1	7.7	0.6	0.5	11.6
Steam	0.0	0.0	0.0	0.0	49.0	0.0	0.0	0.0
N ₂	99.9	88.8	87.5	89.4	37.4	99.0	99.0	84.6
$\Delta P_{MAX,CAVITY}$, kPa	550	200	480	430	290	90	400	185
$\Delta P_{MAX,Cont}$, kPa	150	190	250	166	133	45	111	185
Sweepout Fraction	0.705	0.735	0.691	0.793	0.766	0.190	0.795	0.295
H ₂ Pre-existing, g-moles	0	0	2.3	0	3.0	0	0	3.1
H ₂ Produced, g-moles	4.1	4.7	4.9	5.2	5.2	5.0	6.0	6.0
O ₂ Depleted, g-moles	~0	1.8	2.1	1.8	0.4	~0	~0	3.0

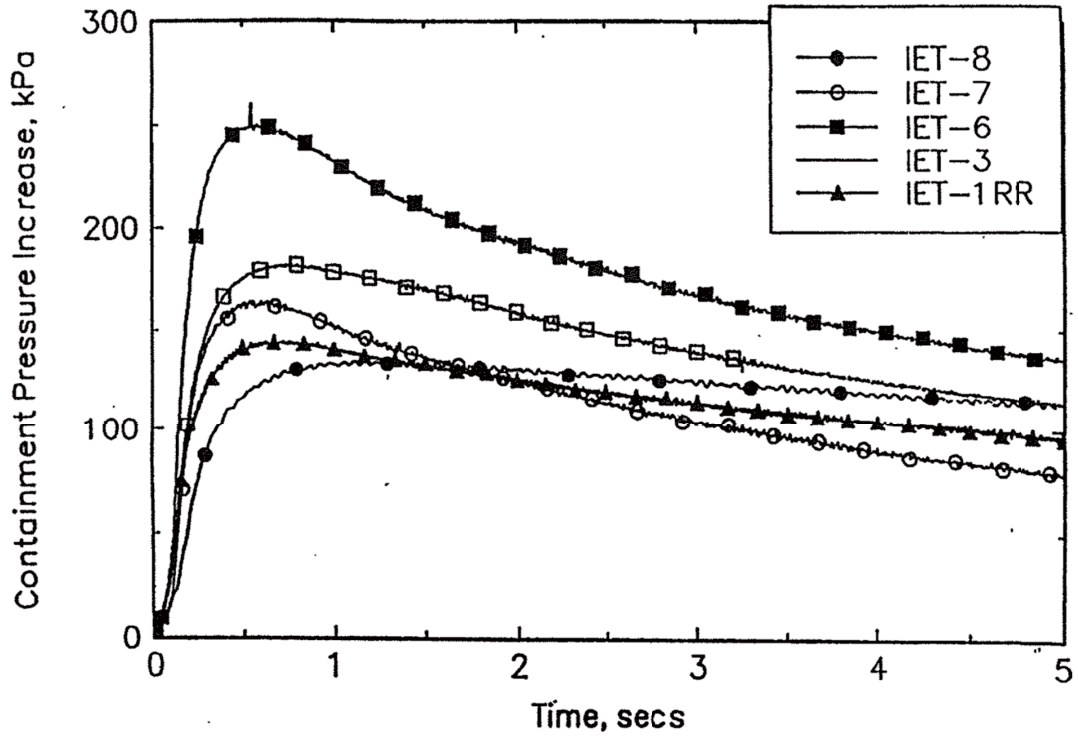


Figure 2-9 Containment loads obtained in the IET tests

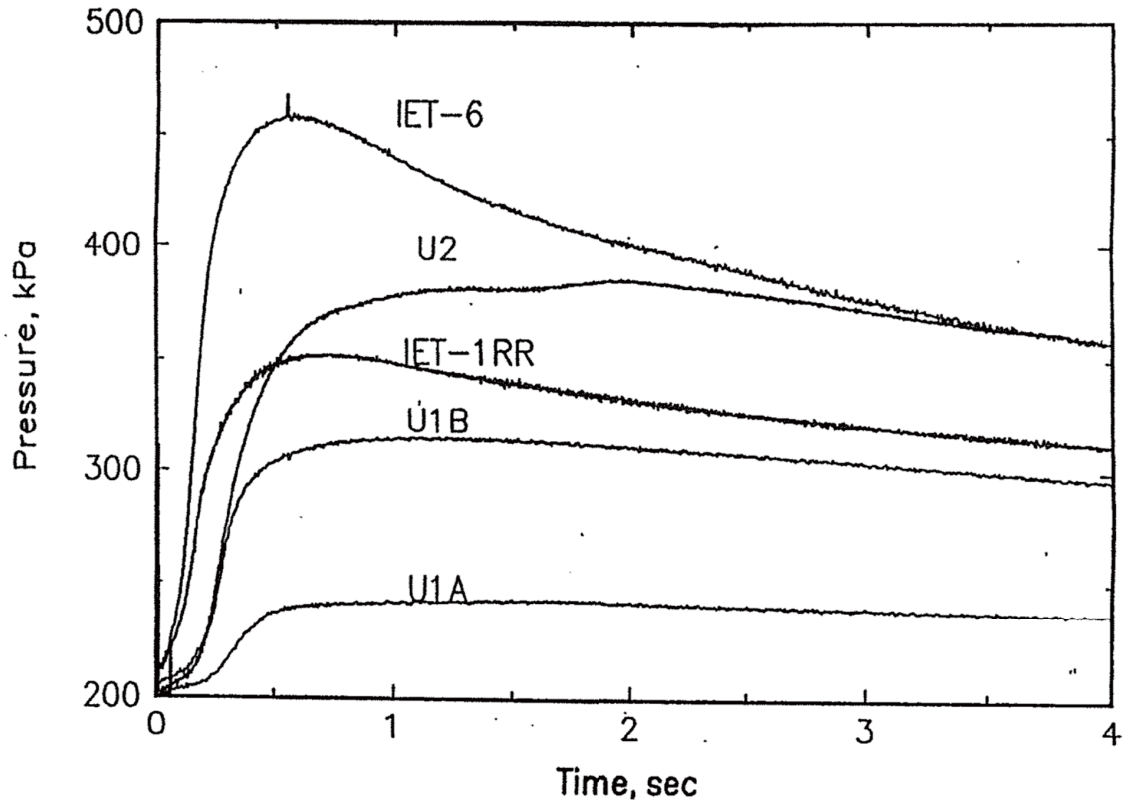


Figure 2-10 Containment loads obtained in the corium experiments

2.7 Sandia 1/10 Scale DCH Experiments for a Zion-Like Containment

To experimentally address the scaling issues, the 1/40 scale Argonne test had counterpart tests performed at 1/10 scale in the Sandia Surtsey facility. These experiments are documented in reference 15, 20, 21, 22, 23, 24, 25, 26 and summarized in reference 27. The Surtsey facility is a large vessel that can simulate a large dry containment at a 1/10 linear scale.

Figure 2-11 shows the Surtsey facility configuration with a Zion-like reactor cavity configuration added outside of the Surtsey vessel. Also, this figure shows the steam driven accumulator used to pressurize the simulated RPV lower head to cause the melt dispersion. This figure was taken from reference 27 and presents a general characterization of the significant scale used in this counterpart test series. Figure 2-12 and Figure 2-13 are taken from the same reference and show the details of the simulation for the Zion-like reactor cavity and instrument tunnel, as well as the containment structures in the steam generator compartment room illustrated in Figure 2-13. As was noted for the 1/40 scale ANL test, the reader should take note of the exit of the instrument tunnel noted by No.7 in Figure 2-13, and the large amount of structure that could separate melt from the blowdown gases, thereby limiting the melt dispersion to this compartment. If this is the case, only the gases within this compartment are substantially heated to temperatures approaching the melt temperature, meaning only a limited extent of pressurization as a result of HPME. Furthermore, note in Figure 2-12 that the ex-Surtsey location of the reactor cavity results in a somewhat longer instrument tunnel than is typical of the reactor system. This does not provide any substantial shortcoming of the experiment, and if anything represents a conservatism in the experimental configuration since more entrainment would likely occur as the melt moves upward through this tunnel in the presence of high velocity gases.

The initial conditions for the SNL counterpart tests at 1/10 scale are given in Table 2-8, also taken from reference 27. As is illustrated by this table, the conditions of RCS pressure, containment temperature and containment gas compositions follow similar variations to those for the Argonne tests. In particular, the containment conditions included atmospheres inerted by nitrogen (IET-1), steam, carbon dioxide as a simulant for steam (IET-5) and atmospheres where combustion of hydrogen generated during the blowdown, as well as pre-existing hydrogen, could occur. With these various atmospheric conditions, the experiments investigated a broad range of accident conditions, including a range of clad oxidation fractions with subsequent release to the containment atmosphere. It should also be noted, in this regard, that the thermite used in these experiments had a significant amount of chromium added to represent molten zirconium that could be ejected with the melt and which had not been oxidized as part of the core degradation. This very active metal (chromium) tended to be oxidized by the steam blowdown and provide hydrogen at very high temperatures that could burn (recombine) as it enters the atmosphere where oxygen was present. It is to be noted that later experiments deleted this chromium component since integral code calculations for the core melt progression and slumping to the RPV lower head have shown little, if any, unreacted metals in the molten core debris if the reactor vessel were to fail under pressure. Therefore, the inclusion of chromium in these experiments was an additional conservatism (tending to provide higher pressures in Surtsey than would be the case in the actual containment) along with the minor conservatism represented by the longer instrument tunnel.

Table 2-8 Initial Conditions for the IET Experiments

	IET-1	IET-1R	IET-3	IET-4	IET-5	IET-6	IET-7	IET-8A	IET-8B	
Date performed	9/13/91	2/7/92	12/13/91	3/20/92	5/13/92	6/18/92	7/9/92	7/30/92	8/26/92	
Steam pressure (MPa)	7.1	6.3	6.1	6.7	6.0	6.3	5.9	1.06	6.2	
Steam temperature (K)	600	585	585	555	586	571	599	421	554	
Steam driving gas (g•moles)	468	507	485	582	453	505	416	4.1 (N ₂)	545	
Cavity water (kg)	3.48	3.48	3.48	3.48	3.48	3.48	3.48	62.0	62.0	
Basement water (kg)	0	0	0	71.1	71.1	0	71.1	71.1	71.1	
Surtsey pressure (MPa)	0.200	0.197	0.189	0.200	0.205	0.199	0.200	0.200	0.203	
Surtsey temperature (K)	295	275	280	295.0	302	308	303	304	298	
Surtsey gas moles (g•moles)	7323	7737	7291	7323	7318	6961	7129	7105	7360	
Initial gas composition in Surtsey (mol.%)	N ₂	99.90	99.78	90.60	90.00	16.90	87.10	85.95	85.32	85.80
	O ₂	0.03	0.19	9.00	9.59	4.35	9.79	9.57	9.85	9.79
	H ₂	0.00	0.02	0.00	0.00	2.76	2.59	3.97	4.33	3.91
	CO ₂	0.01	0.00	0.02	0.02	75.80	0.00	0.03	0.03	0.03
	Other	0.06	0.01	0.38	0.39	0.19	0.52	0.48	0.47	0.47
Initial hole diameter (cm)	3.5	3.5	3.5	3.5	3.5	3.5	3.5	3.5	3.5	
Final hole diameter (cm)	4.04	4.02	4.53	4.22	4.31	3.91	4.08	3.50	4.10	
Plug in STR ceiling	Yes*	No	Yes	No	No	No	No	No	No	
Thermite composition	29.26 4.65 <u>9.09</u> 43.00 4.65 m ³ 85.25 m ³ 89.8 m ³									
iron oxide (kg)										
chromium (kg)										
aluminum (kg)										
Thermite charge (kg)										
Freeboard volume inside subcompartment structures										
Freeboard volume in Surtsey dome										
Total freeboard volume										
* The concrete plug in the ceiling of the seal table room was forcibly ejected by the thermite/water interaction in the cavity.										

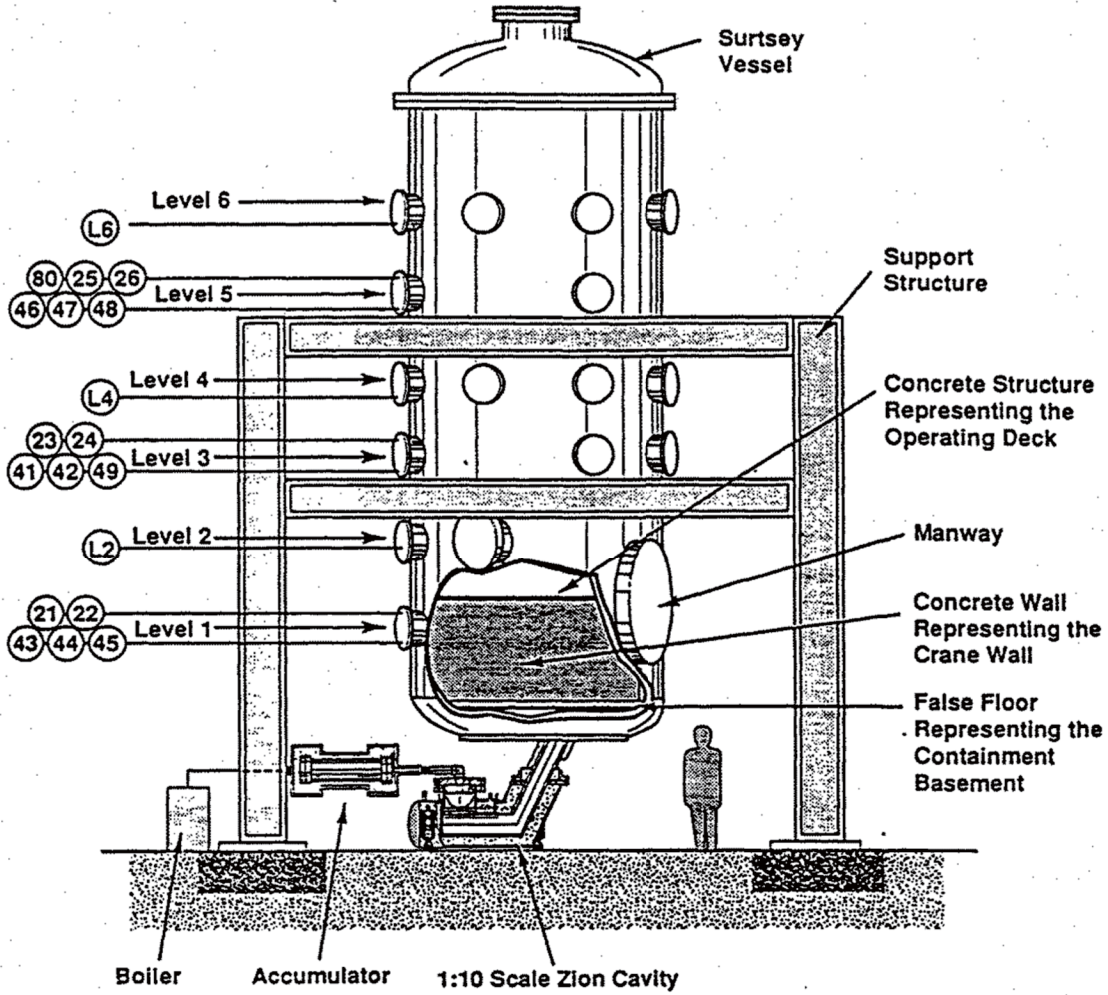
The results for the Zion-like experiments are plotted in Figure 2-14 and Figure 2-15, illustrating the containment pressurization in inerted and non-inerted atmospheres, respectively. In an inerted atmosphere, the pressure increase is approximately 1 bar, and in a non-inerted atmosphere, including the potential for burning of combustible gases as they are produced, as well as pre-existing hydrogen, the pressure increase is 2.8 bars. Both of these illustrate that the pressure increase resulting from a high pressure melt ejection in a geometry representing the internal structure of a containment is limited to values far below those which would challenge the containment integrity. Furthermore, these results are quite close to the pressure increase observed in the Argonne 1/40 scale experiments, hence, the

counterpart experiments performed at Argonne and Sandia at two different scales have illustrated that linear scaling is the appropriate approach for performing these experiments. Furthermore, this is also the appropriate approach for extrapolating to the reactor system. Specifically, the pressure increases observed in the Argonne and Sandia experiments would be expected to be the same in the reactor case given this type of accident sequence. As indicated above, the accident sequences envisioned and the experimental configurations, if anything, provide a worst case scenario for reactor systems.

Figure 2-16 shows a comparison of the predicted pressurization efficiencies versus the predicted pressurization efficiencies for a wide range of experiments and many different scales using the two cell equilibrium model (TCE). This approach is summarized later on, but is used here to illustrate the fact that these results, at many different scales, show quite good agreement in terms of the potential containment pressurization. Also, when a linear scale is used, the predicted pressure increases are, for all practical purposes, identical. This provided a substantial point for resolving this issue with respect to nuclear power plants, both experimentally and analytically.

The major conclusions for this counterpart set of experiments were that:

1. Approximately 77% of the melt released from the RPV was dispersed into the Surtsey vessel.
2. Of the material dispersed into the Surtsey vessel, typically 10% was found outside of the steam generator compartment. The remainder of the material was separated from the gas flow stream and deposited within the steam generator compartment.
3. The hydrogen produced by oxidation of the chromium during the blowdown process was burned during the HPME and contributes significantly to the measured pressurization. In particular, this caused an additional 1.5 bar increase over the inerted experiments. However, pre-existing hydrogen did not appear to burn on a timescale that had a significant influence on the peak vessel pressure.
4. All of the counterpart tests resulted in containment pressure increases far below those providing a challenge to containment integrity.



Note: All pressure transducers have individual penetrations.

Figure 2-11 Surtsey vessel, high-pressure melt ejection system, and subcompartment structures used in the 1/10 scale IET experiments

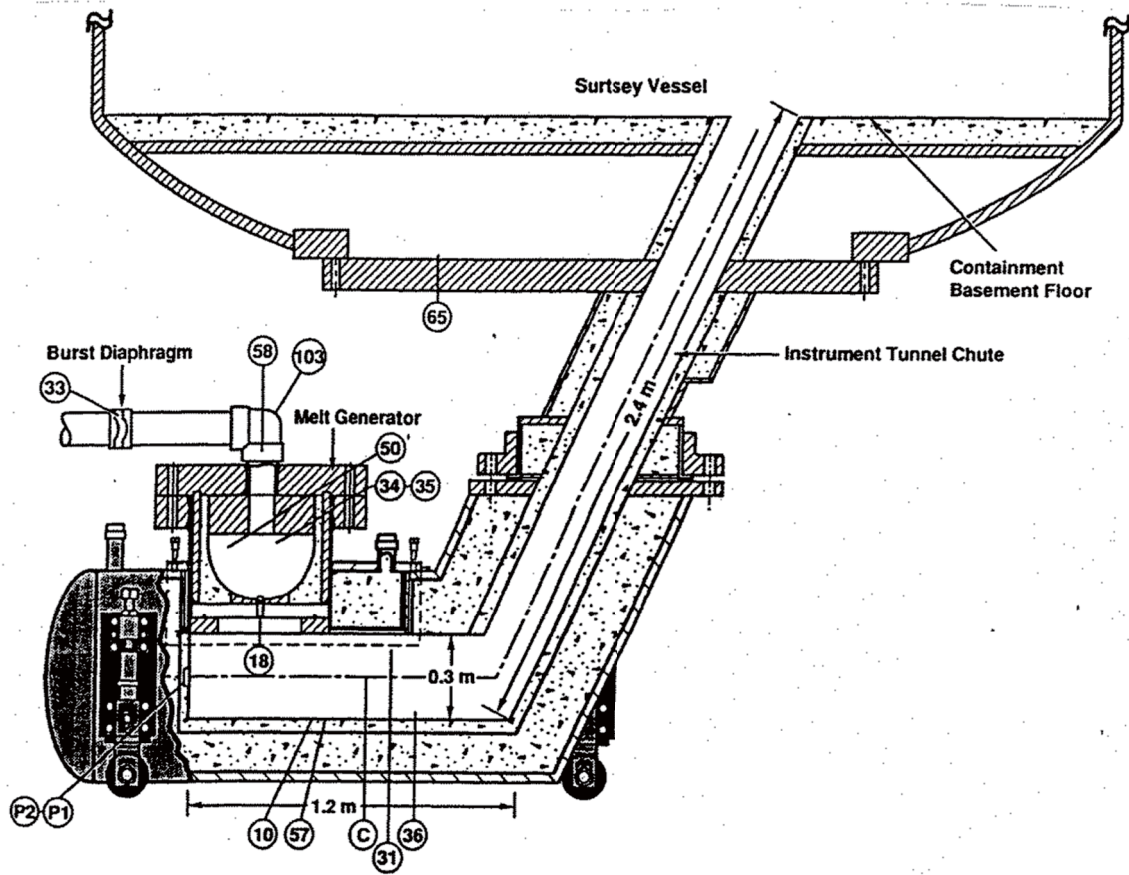


Figure 2-12 Schematic of the 1:10 linear scale model of the Zion reactor Cavity

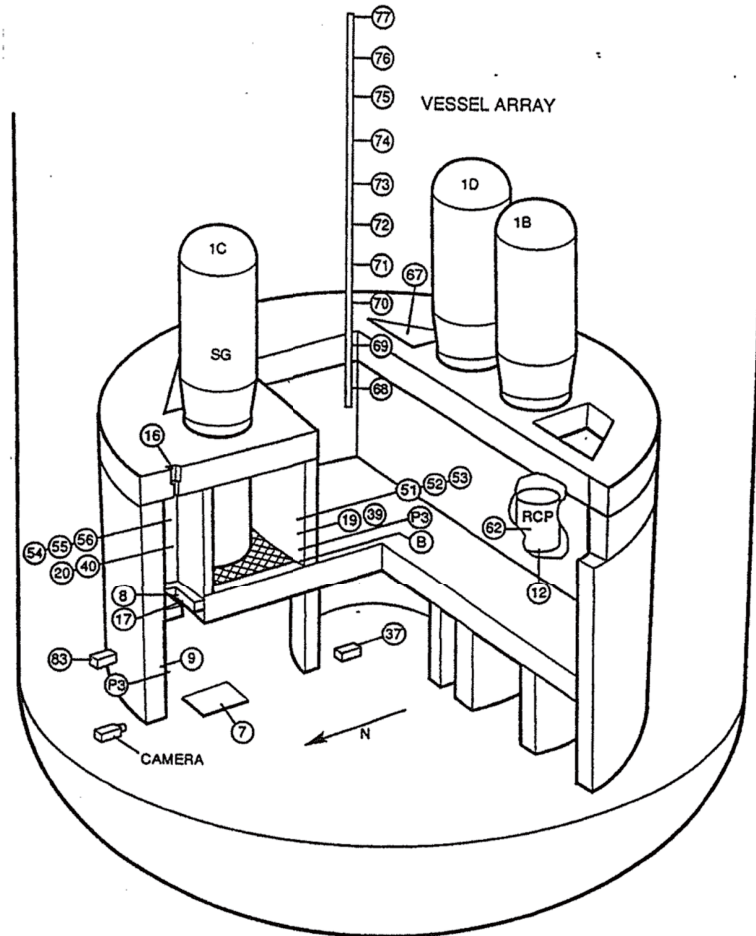


Figure 2-13 Isometric view of the subcompartment structures inside the Surtsey 1/10 scale vessel

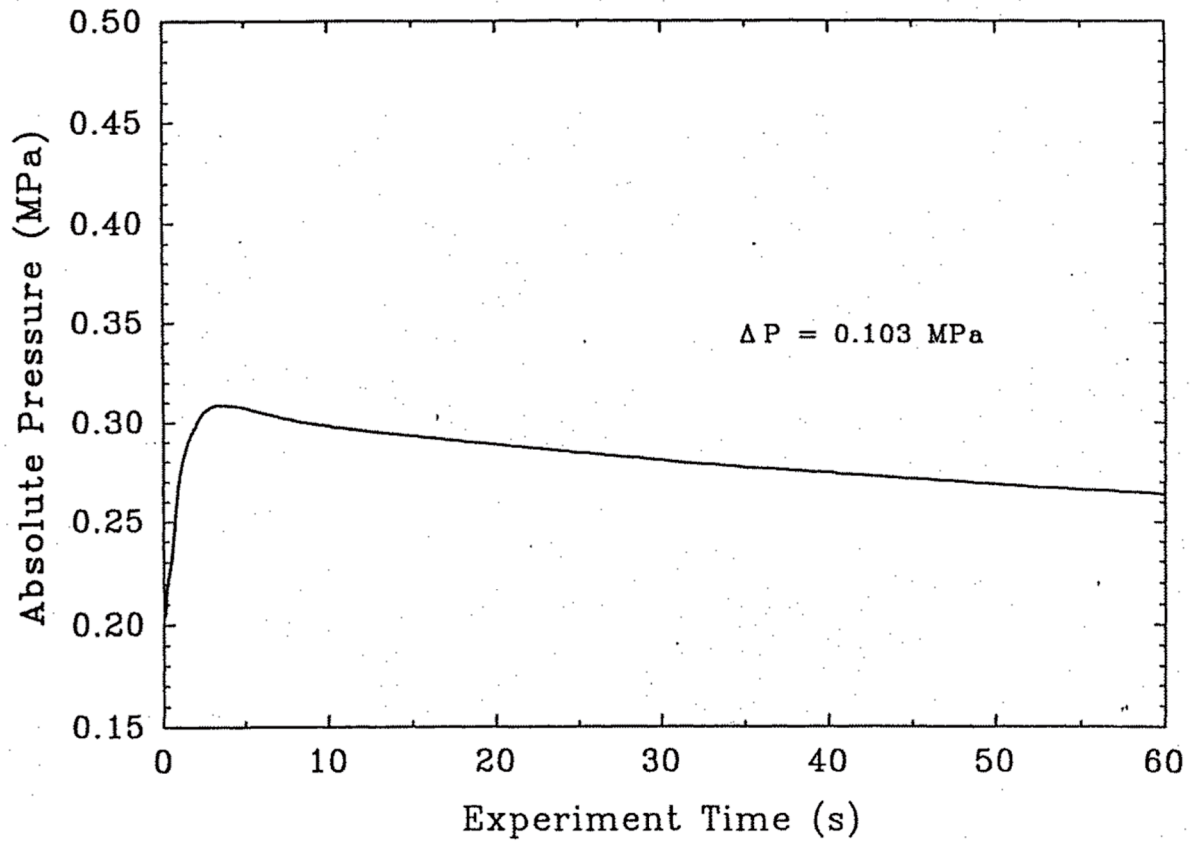


Figure 2-14 Surtsey vessel pressure versus time for Test IET-5

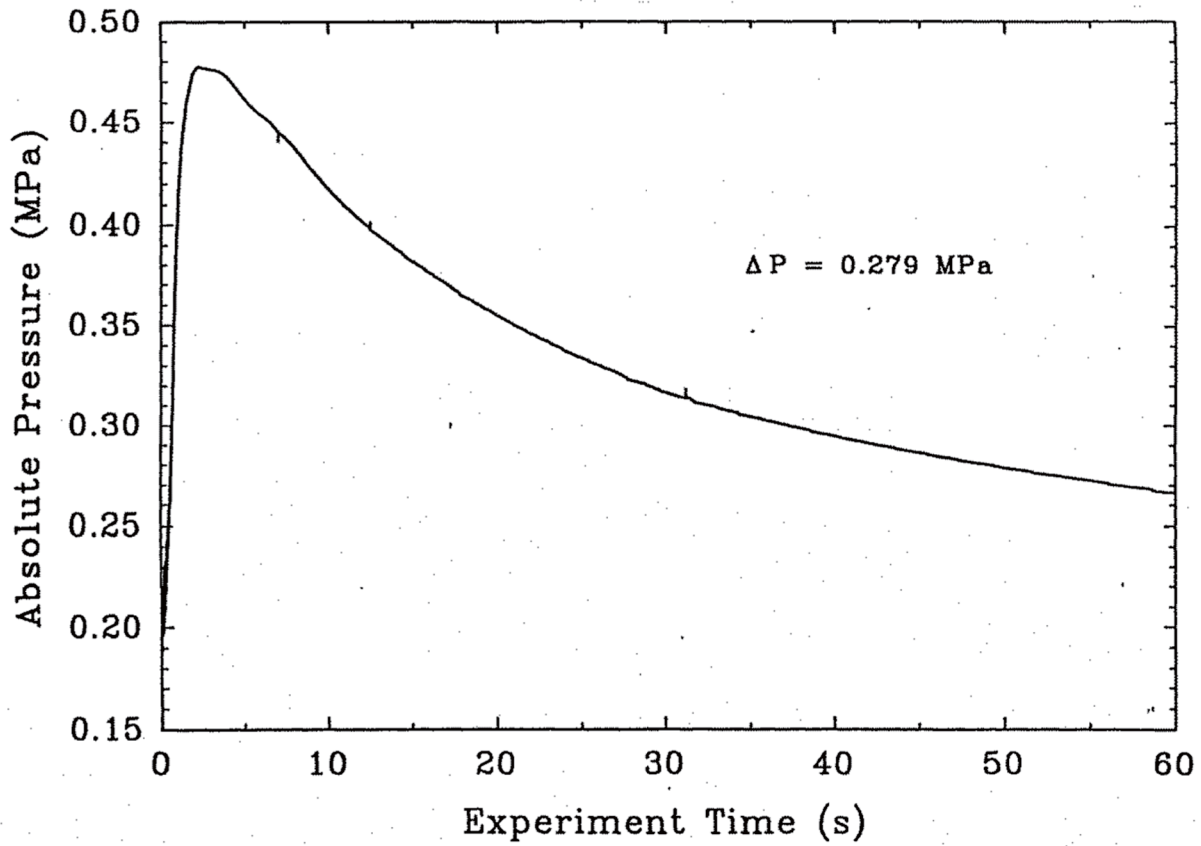


Figure 2-15 Surtsey vessel pressure versus time in the IET-6 experiment

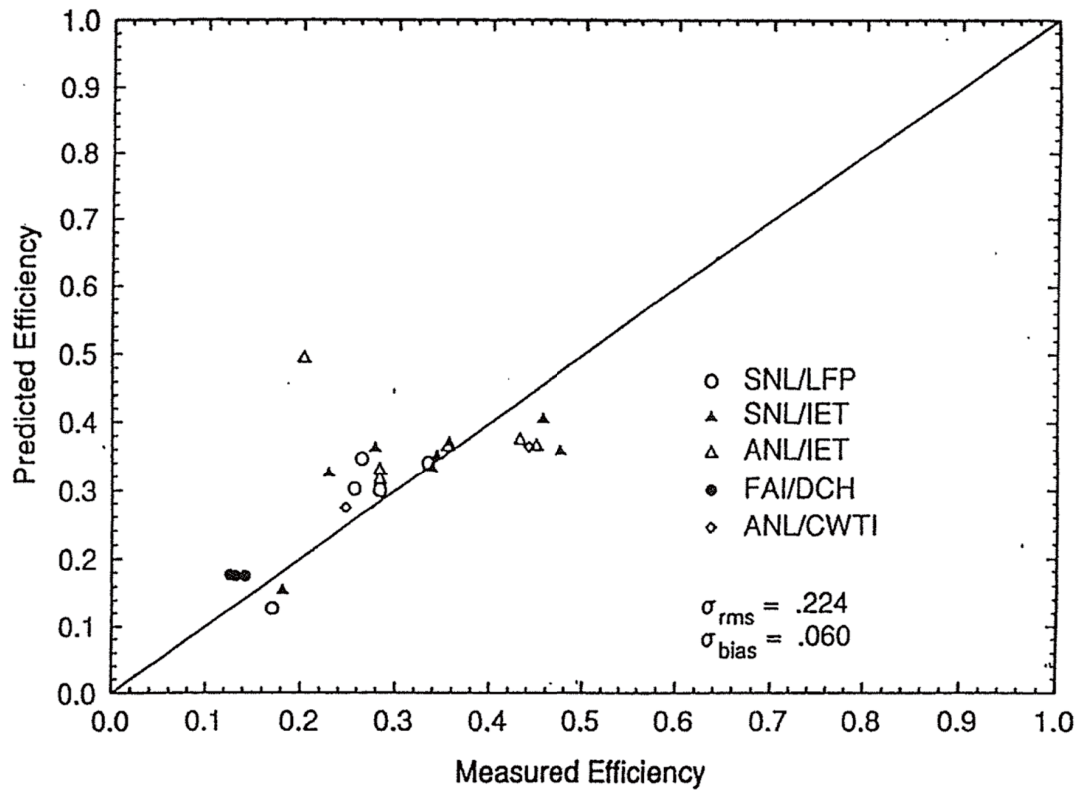


Figure 2-16 Validation of the TCE model against all experiments with compartmentalized geometry.

2.8 Purdue Air-Water DCH Simulation Experiments

Debris entrainment in the reactor cavity, movement of the debris out of the reactor cavity, impingement of the debris on containment structures immediately downstream of the reactor cavity, re-entrainment of the debris and dispersal of the debris to other containment compartments are the most important individual physical processes affecting direct containment heating. To address these processes, simulant fluid experiments were performed at Purdue University using water-air and Wood's metal-air systems to investigate these separate effects behaviors (Reference 28 and 29). These tests were specifically directed at understanding the dispersion mechanisms and the trapping behavior that would occur in subcompartments immediately downstream from the reactor cavity/instrument tunnel.

The experiments were performed for a Zion-like configuration. The reactor cavity and instrument tunnel were represented in the scaled configuration with the liquid being discharged from a separate vessel, followed by the gas blowdown from gas tanks through a separate discharge nozzle into the reactor cavity. The substantial containment structures that could intercept entrained and non-entrained debris as it exits the instrument tunnel were included in the simulant tests, as they were also included in the integral effects experiments performed with the thermite melts.

Numerous parametric studies were performed with this scaled separate effects facility. These tests indicated very interesting results with respect to the liquid film behavior in the reactor cavity, the extent of entrainment and the extent of carryover out of the lower compartment structures. As a result of the incoming momentum from the discharging liquid (water in this case) it was found that a liquid film spreads along the reactor cavity floor and up the walls of the reactor cavity and eventually the instrument tunnel. It was found that approximately one liter of water could flow out of the reactor cavity without entrainment. This corresponds to about 15% of the liquid mass inventory and this is removed from the reactor cavity before the entrainment process begins. For higher liquid inventories, approximately 30% of the liquid inventory was carried out of the cavity before the gas blowdown was initiated. Furthermore, it was found that during the entrainment process a significant fraction of the remaining mass (about 42%) was entrained droplets with the rest being transported out of the reactor cavity as a liquid film; however, the entrained droplet size is relatively large. This is important since this has a significant influence on the rate at which droplets can be deposited when flow direction changes are encountered as the two-phase mixture exits the instrument tunnel.

The entrainment of the two-phase mixture is clearly observed in this transparent apparatus. The first major entrainment occurs at the seal table and this is principally due to the droplet momentum and trajectory. The observation is this entrainment is mainly through the view factor and the ratio of the area opening in the cavity cross-sectional area. It is also observed that the larger droplets impact on structural surfaces and de-entrain to form liquid films. Only the very small droplets continue to remain entrained in the gas stream and they have a significant potential for being carried out of the subcompartment configuration and into the upper regions of the containment. However, the magnitude of the liquid mass observed to be transported out of the subcompartment region was quite small. Typically, only a few percent of the total liquid mass was carried to the upper compartment.

The observed substantial removal of debris from the airborne fluid stream as a result of interactions with structure in the containment subcompartments and the small fraction of liquid mass entrained into the upper compartment region are clearly in agreement with the integral effects test reported elsewhere in this document.

2.9 Fauske & Associates 1/25th Scaled DCH Experiments for Vandellos and Asco Containments

As part of the plant specific IPE studies for Vandellos and Asco, the utilities operating these plants elected to perform scaled tests for HPME conditions to address the issue directly through experiments. Because of the specific reactor cavity and instrument tunnel designs for these two plants, and because of the

proximity of the containment liner to the exit from the instrument tunnel in Vandellos, it was judged that plant specific scaled experiments were a more direct means of addressing the IPE questions than attempting to use experiments directed at other plant configurations. These experiments were performed in the Fauske & Associates, Inc. experimental facility using a 4% linear scale model of the reactor cavity, instrument tunnel, steam generator compartment and upper containment compartment (Reference 30).

Figure 2-17 shows the test facility configuration used for the two tests representing the different plant geometries. Plant drawings were used to determine the dimensions for the 1/25th scale representation of the reactor cavity, instrument tunnel, seal table room, adjacent containment liner, lower compartment/annular compartment and upper containment regions. The test facility consisted of (1) a melt delivery assembly, (2) the test assembly, (3) the lower containment volume, (4) the upper containment volume, and (5) the steam generator. Iron thermite was used to represent the high temperature melt with the specific initial conditions used for the two different experiments listed in Table 2-9. Based on the linear scaling, an iron thermite mass of 4.3 kilograms would be required to simulate the core inventory of uranium dioxide and zircaloy. However, with the greater propensity of freezing on cold walls in small scaled experiments, the scaled mass was increased to 10 kg. With this larger mass, that which could be released to the lower compartment was equal to or greater than that required to satisfy the volumetrically scaled behavior. With the higher energy content of the aluminum oxide in the thermite mass compared to the uranium dioxide in the reactor system, this results in a substantial conservatism in the scaled experiments.

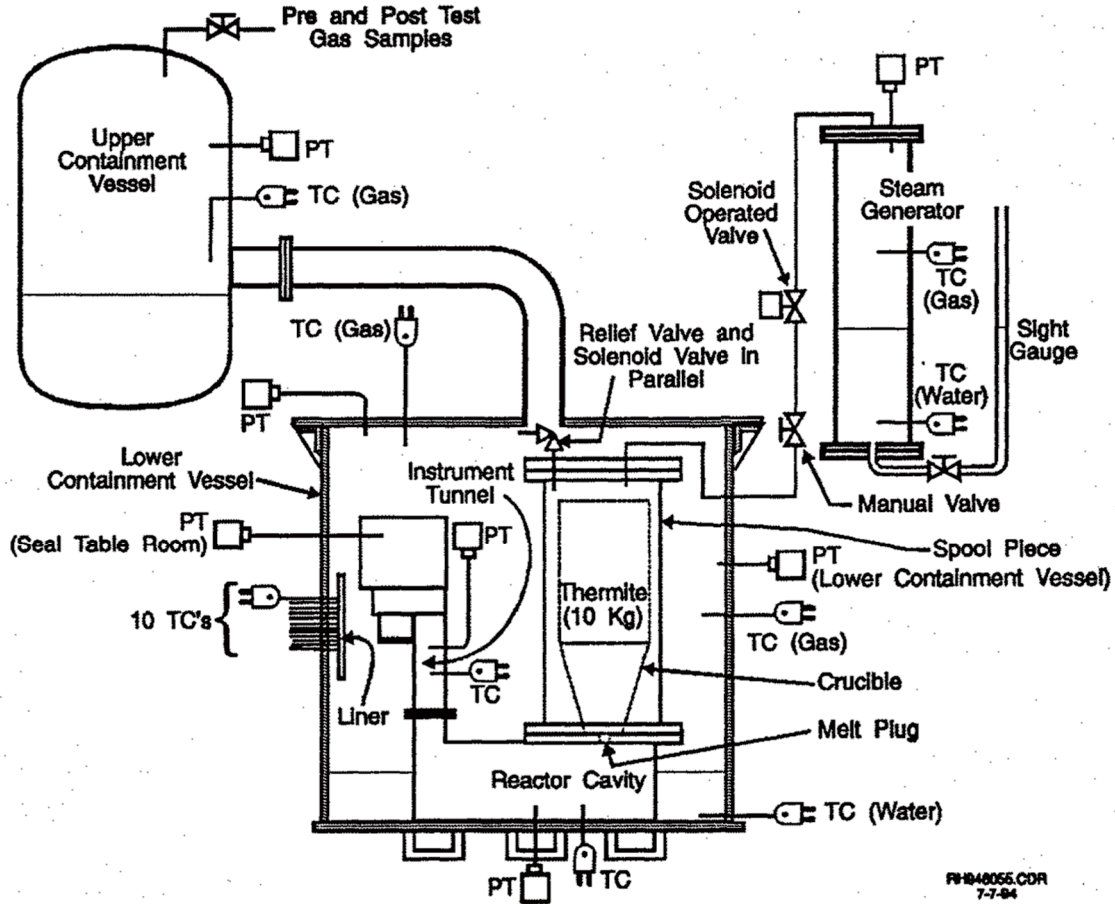


Figure 2-17 DCH test facility configuration

Table 2-9 Initial Conditions

Test	Mass of Thermite (kg)	Cont. Gauge Pressure (MPa)	Crucible Gauge* Pressure (MPa)	Containment Temperatures	
				Gas Space (°K)	Water (°K)
Vandellos	10	-0.025	1.90	296	296
Asco	10	0.018	2.94	298	298
* Steam pressure in crucible at time of vessel (melt plug) failure.					

The pressure and temperature information used in these experiments is summarized in Figure 2-17. The carbon steel containment liner was represented in each test with the carbon steel plate located opposite the ventilation openings in the vertical instrument tunnel for the Vandellos test and opposite the seal table room for the Asco experiment. Figure 2-18 shows the scaled reactor cavity and instrument tunnel configuration for the Vandellos experiment and Figure 2-19 shows the configuration for the Asco test. In the experiments, water was added to the floor of the annular compartment (approximately 54 kg) as indicated in Figure 2-17. For the Asco experiment 4.7 kg of water were added to the reactor cavity, corresponding to a water depth of approximately one half the height of the horizontal portion of the instrument tunnel. There was no water in the reactor cavity for the Vandellos test.

Table 2-10 shows the peak pressures measured in the various containment compartments for the two different experiments. Of particular note for both experiments is that the net containment pressurization was limited being 5 psig in the upper compartment for the Vandellos test and 5.4 psig for the Asco experiment.

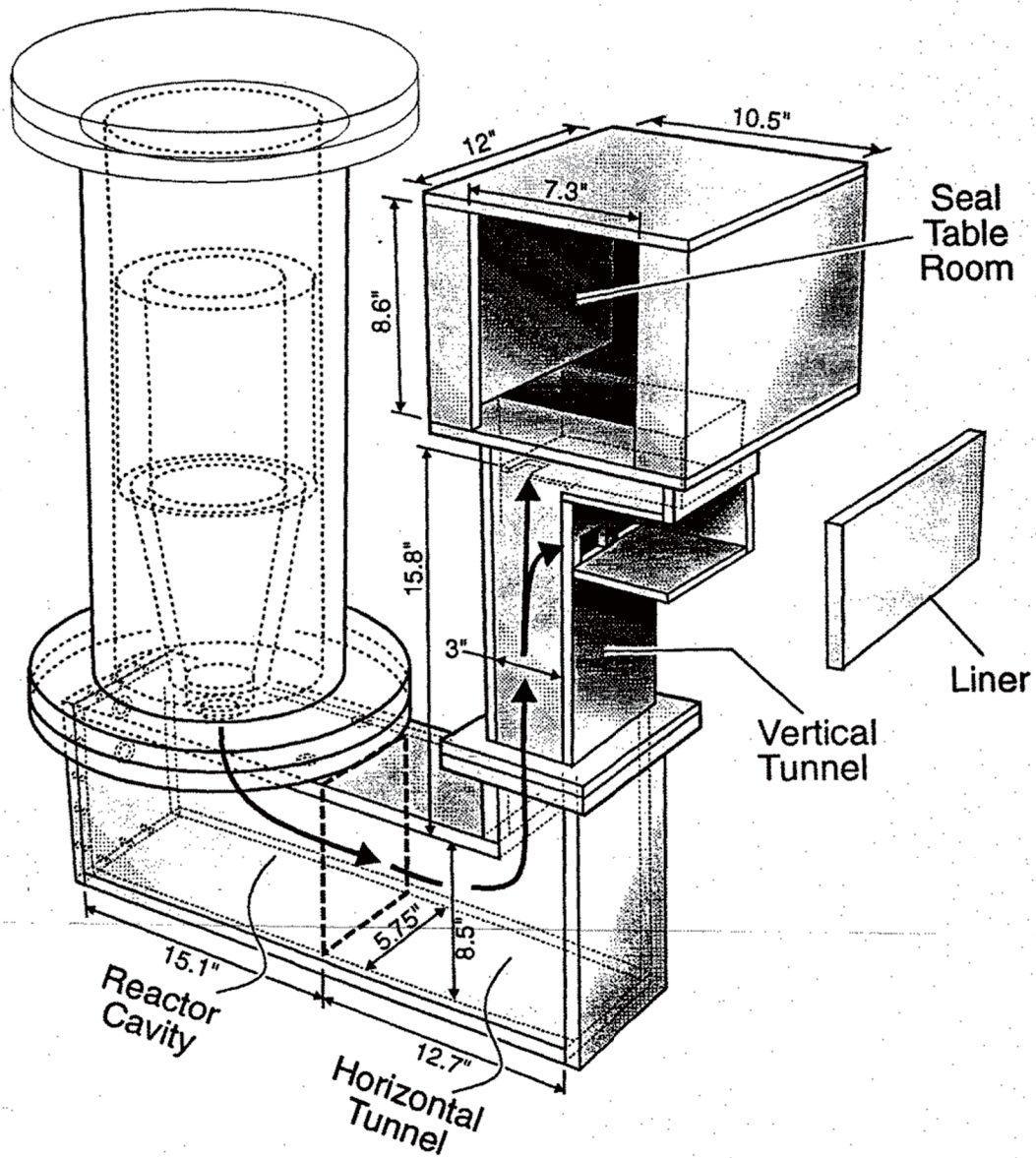
For both experiments, the debris was collected and weighed. Table 2-11 summarizes the debris masses found in the several regions. As is noted a significant fraction (50-60%) of the debris was discharged from the instrument tunnel and seal table for the Vandellos experiment. About one third of this mass was found to be a frozen film on the vessel wall during the post-test examination, with the balance collected on the floor of the lower compartment and therefore submerged in water. A very small amount of debris particulation was found and no debris was detected in the upper containment compartment or the pipe connecting the upper and lower compartments. Pre-test and post-test gas samples taken from the upper containment compartment were examined for hydrogen. There was no detected amount of hydrogen observed for the dry reactor cavity test used for the Vandellos configuration.

As mentioned previously, the Asco experiment used a configuration in which the reactor cavity was half full of water. A dynamic debris-water interaction was observed in the reactor cavity, causing substantial pressurization of this region as indicated in Table 2-10. For this configuration, a single vent path connected the instrument tunnel to the seal table room, with the area of this vent being only about 1.5 times the failure area in the bottom of the melt crucible. The temperature within the reactor cavity and horizontal segment of the instrument tunnel reached a maximum value near 240°C, corresponding to the saturation temperature of the measured peak pressure.

As illustrated in Table 2-11, virtually all of the debris remained within the reactor cavity for the Asco configuration. No debris was observed in the upper compartment or the pipe connecting the upper and lower compartment. Also, the liner plate was found to have a layer of frozen debris covering the impingement surface. Pre-test and post-test gas samples were taken from the upper containment volume to examine the potential for hydrogen generation. A limited amount was detected (0.1 to 0.4

volume percent) which was the result of oxidation of the high temperature molten iron by the steam and water in the wet reactor cavity.

The observed pressure responses in both experiments for the upper and lower containment regions for both experiments were far less than the design basis pressure for these containments. Hence, these linear scaled experiments demonstrated no significant challenge to containment integrity as the result of a high pressure melt ejection.



RH94095.CDR 4-18-94

Figure 2-18 Scaled reactor cavity and instrument tunnel configuration used for the Vandellos test

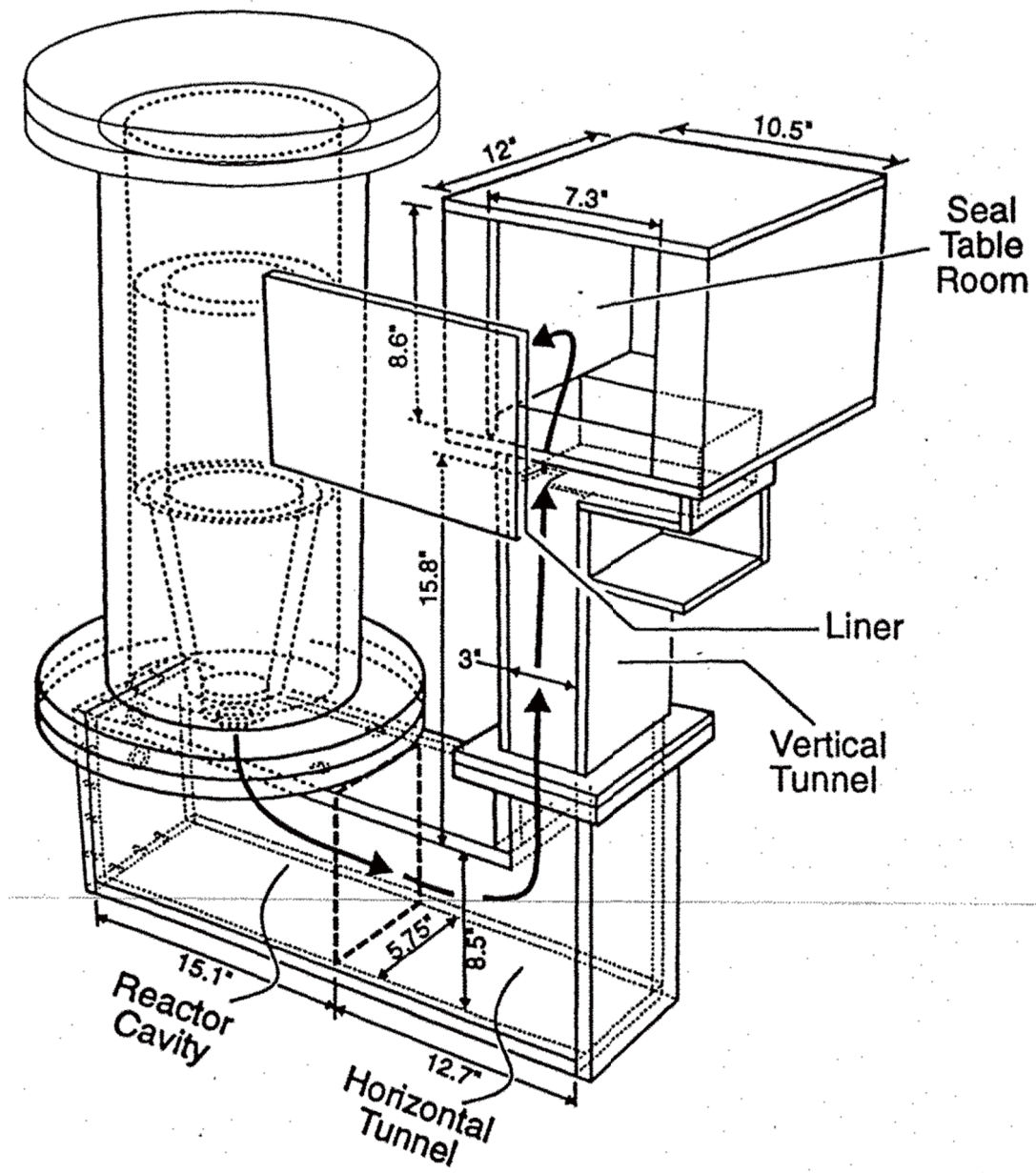


Figure 2-19 Scaled reactor cavity and instrument tunnel configuration used for the Asco test

Table 2-10 Comparison of Maximum Pressure Increase (psig)

Location	Maximum Measured Pressure Increase (psig)	
	Vandellos	Asco
Reactor Cavity	45.5	450
Instrument Tunnel	43.4	440
Seal Table Room	9.2	11.4
Lower Containment	7.3/7.3	7.2/7.0
Upper Containment	5.0	5.4

Table 2-11 Post-Test Debris Distribution

Debris Location	Vandellos		Asco	
	Debris Mass (kg)	% of Recov. Mass	Debris Mass (kg)	% of Recov. Mass
1. Cavity/instrument tunnel.	2.9	32	5.4	70
2. Seal table room.	0.6	7	1.1	14
3. Lower containment vessel.	4.7	52	0.3	4
4. Upper containment vessel.	0	0	0	0
5. Residual in crucible.	0.9	9	0.9	12
Recovered Mass	9.1		7.7	
Unrecovered Mass	0.9		2.3	

2.10 Sandia Scaled DCH Experiments for a Surry-Like Containment

Large scale experiments at Sandia to investigate the response of the Surry-like containment to a HPME were run in both the 1/40 scale Surtsey facility as well as the 1/6 scale Containment Technology Test Facility (CTTF). Since the Surtsey facility has already been discussed, we will focus on the CTTF configuration.

Figure 2-20 (Reference 31) shows the containment simulation, including the various internal structures for the containment, the simulated RPV lower head, the different reactor cavity and instrument tunnel configuration (as compared to the Zion-like studies), and the instrumentation in the upper regions of the containment. As indicated by this figure, the simulation of the containment subcompartments was extensive. Table 2-12 lists the initial conditions for the Surry-like experiments, and as indicated for those experiments in the CTTF facility, the initial thermite charge was 158 kg and the charge also included chromium to represent unreacted zircaloy metal that could be dispersed with the melt. Subsequent analyses to these experiments indicated there would be little, if any, zirconium present in a melt that would undergo HPME. Hence, this 17 kg of chromium represents a conservatism in the experimental system. It should also be noted that some of these experiments were performed with substantial steam in the containment environment (IET-9).

Figure 2-21 represents the experimental result from test IET-9 and shows that the containment pressurization was approximately 2.8 bars. Figure 2-22 illustrates the result from IET-11, which had a combustible atmosphere in containment, and shows an observed pressure increase of 4.3 bars. Test IET-12 is represented in Figure 2-23, which was a steam inerted atmosphere in the Surtsey facility and illustrates a pressure increase of approximately 2 bars, close to that observed for the steam inerted test IET-9. As is illustrated by the summary of all these experiments, the pressure increase is much less than that which would threaten a Surry-like containment. In particular, the extensive structures of the containment provided for substantial limitations on the melt dispersion throughout the containment atmosphere. As a result, the regions of very high temperature were limited to those subcompartments immediately downstream from the exit of the instrument tunnel. Hence, the pressure increase was limited even with a reactive atmosphere and much less than those which would challenge the containment integrity.

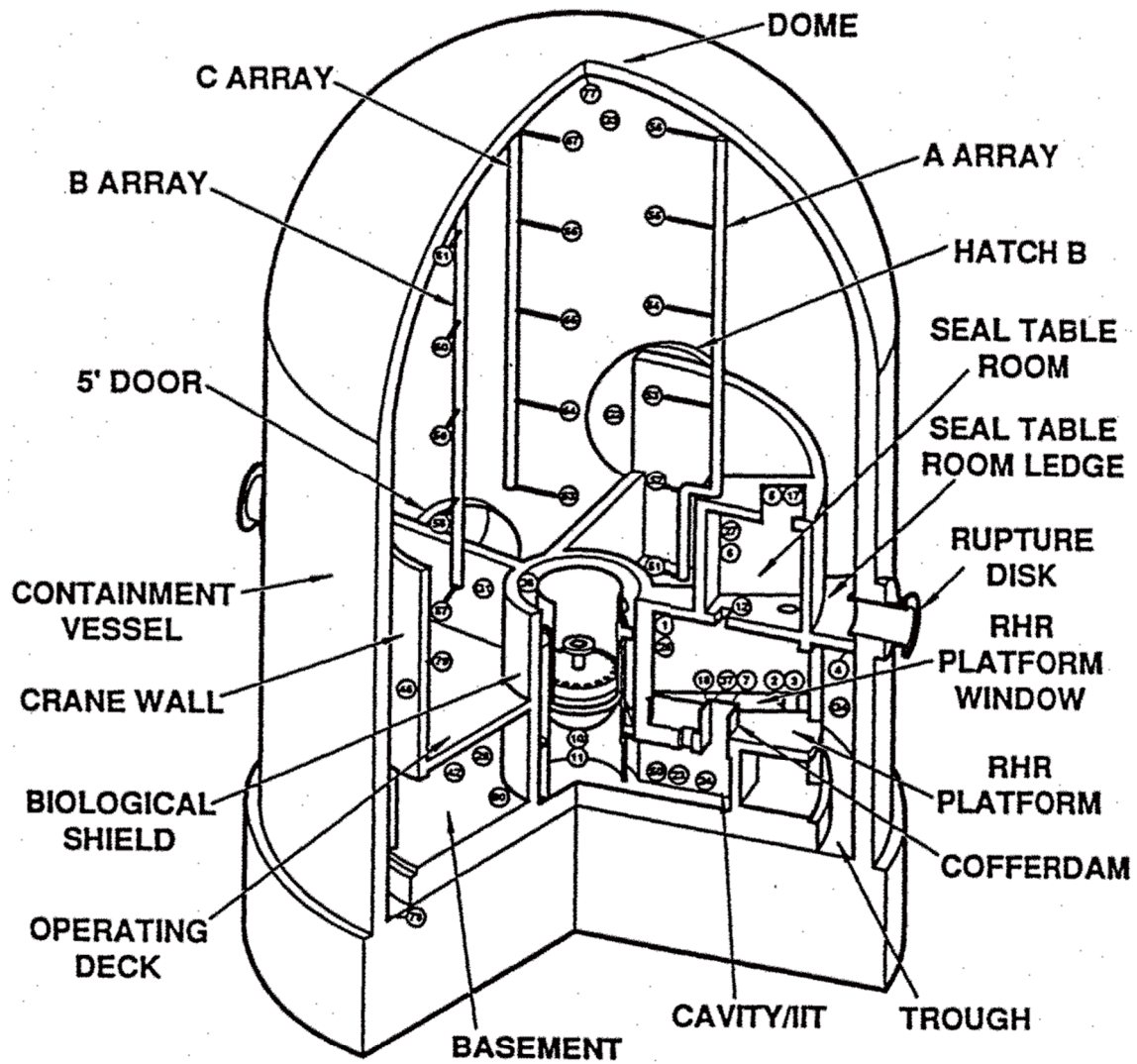


Figure 2-20 Isometric view of the subcompartment structures and RPV model inside the CTTF vessel

Table 2-12 Initial Conditions for the IET Experiments

	IET-9	IET-10	IET-11	IET-12	
Test date	01/29/93	03/19/93	05/02/93	08/12/93	
Thermite composition (kg)					
iron oxide	107.52			22.89	
chromium	17.08			0.00	
aluminum	<u>33.40</u>			<u>7.11</u>	
Mass of the initial thermite charge (kg)	158.00			30.00	
Mass of the RPV SS insulation (kg)	0	0	29	0	
Gas pressure at plug failure (MPa)	12.9	12.1	13.2	11.2	
Gas temperature at plug failure (K)	787	713	693	696	
Moles of driving gas (g•moles)	3005	3275	4705	604	
Initial hole diameter (cm)	7.0	7.0	7.0	5.6	
Final hole diameter (cm)	7.4	9.8	7.6	5.6	
Initial annular gap area (m ²)	0	0	0.0174	0	
Final annular gap area (m ²)	0.012	0	0.0360	0	
Seal table model	No	Yes	Yes	Yes	
Water on basement floor (kg)	372	0	703	0	
Initial vessel absolute pressure (MPa)	0.1351	0.1791	0.2209	0.1635	
Initial vessel gas temperature (K)	392	410	399	408	
Initial vessel gas moles (g•moles)	11870	15027	18802	2461	
Initial gas composition in the containment vessel (mol.%)	Steam	67.24	48.20	32.25	57.98
	N ₂	24.01	38.47	50.98	28.45
	O ₂	6.14	10.17	13.66	7.28
	H ₂	2.20	1.98	2.39	5.66
	CO	0.00	0.51	0.00	0.03
	CO ₂	0.13	0.21	0.02	0.26
	Other	0.28	0.46	0.70	0.34
Freeboard volume inside subcompartment structures (m ³)	83.1		79.1	12.8	
Freeboard volume in upper dome (m ³)	<u>202.9</u>		<u>202.9</u>	<u>38.2</u>	
Total freeboard volume (m ³)	286.0		282.0	51.0	

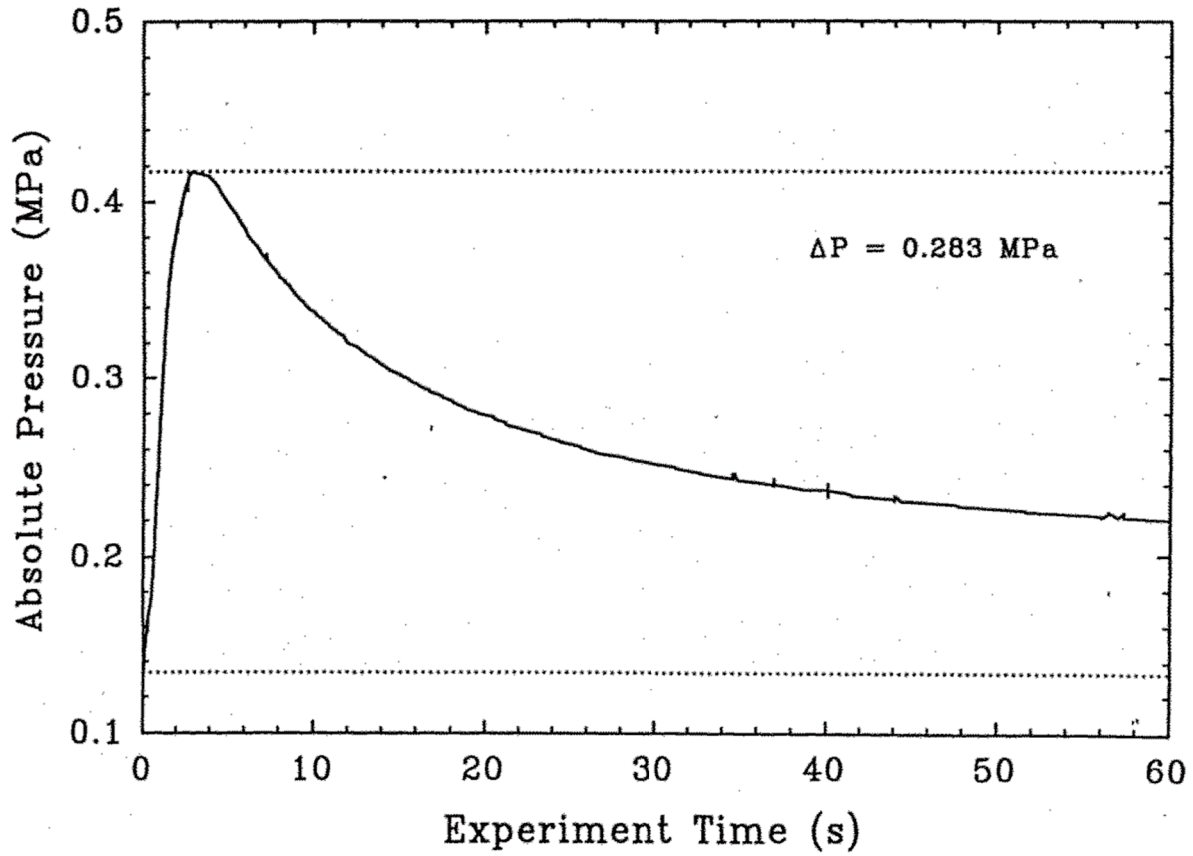


Figure 2-21 CTF vessel pressure versus time in the IET-9 experiment

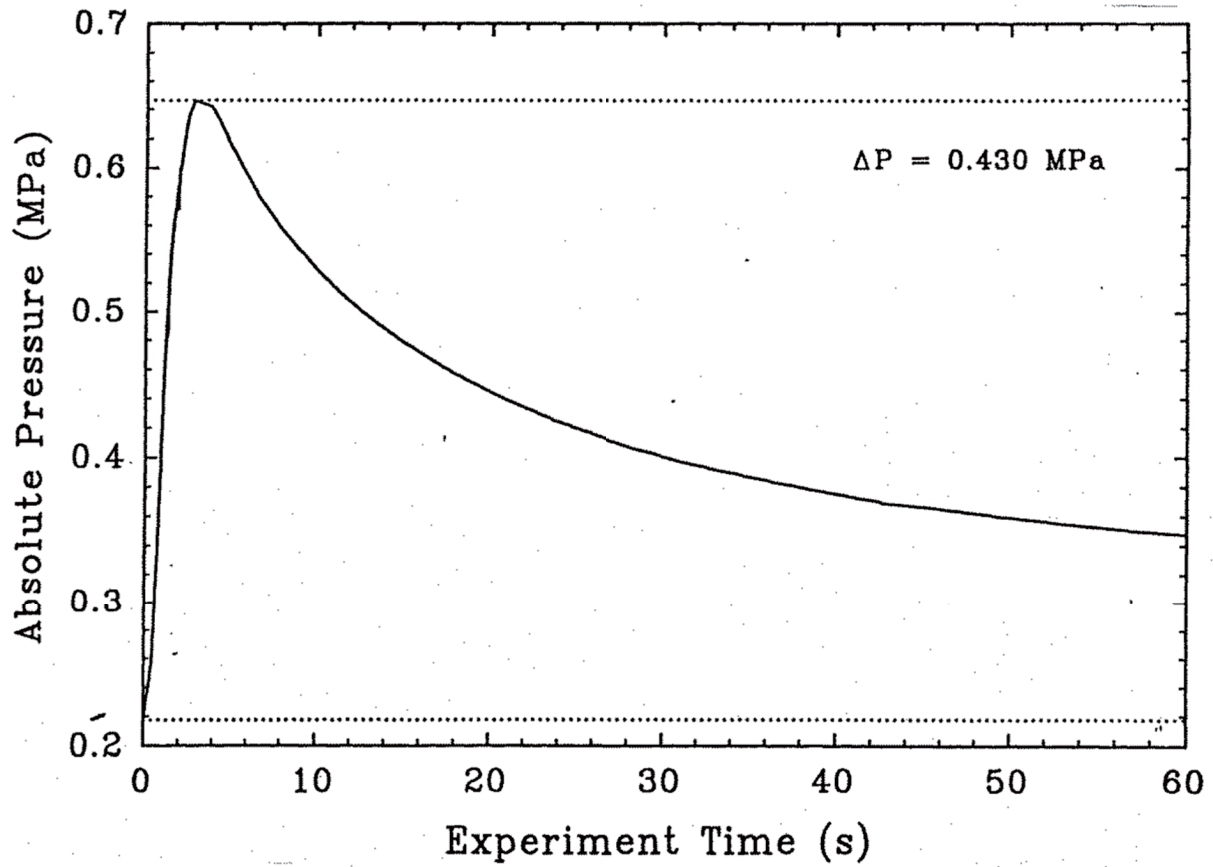


Figure 2-22 CTF vessel pressure versus time in the IET-11 experiment

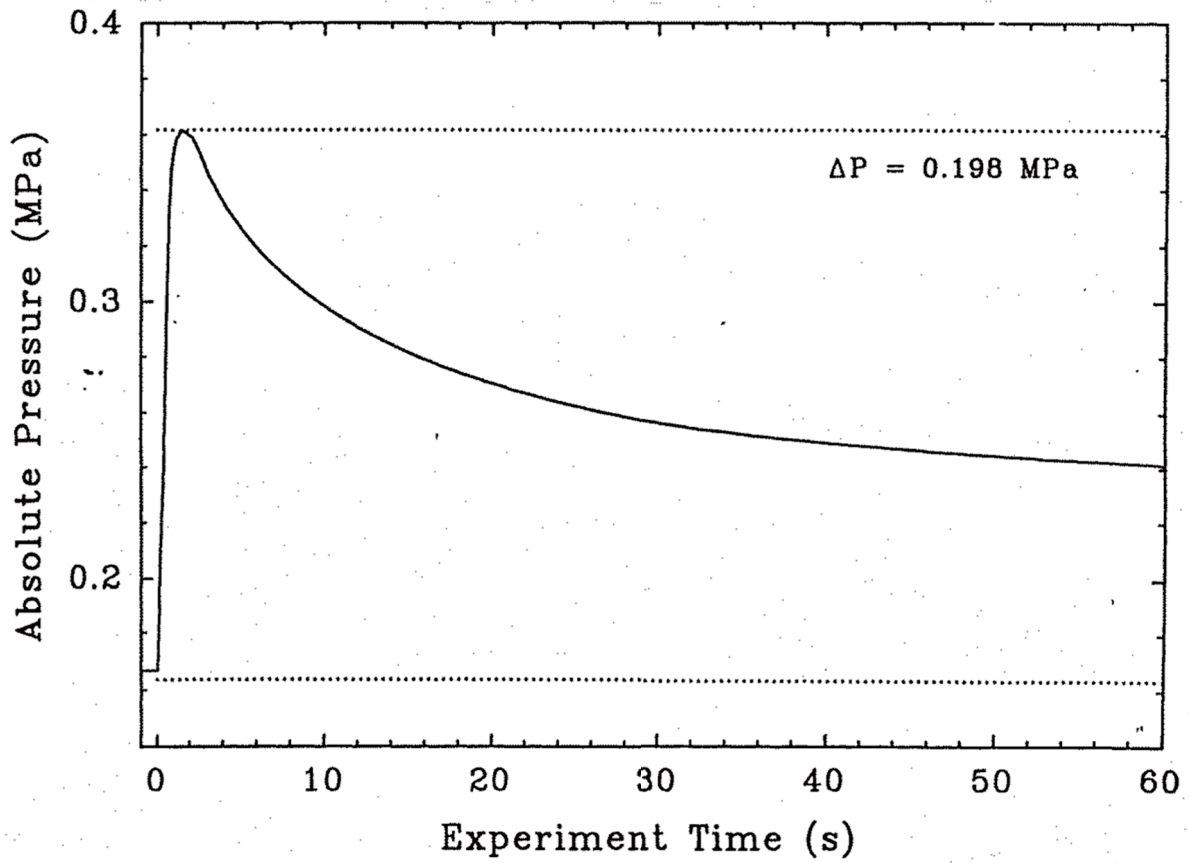


Figure 2-23 Surtsey vessel pressure versus time in the IET-12 experiment

2.11 Sandia Scaled DCH Experiments for a Calvert Cliffs-Like Containment

All the experiments discussed so far were focused on cavity designs with large instrument tunnels leading into subcompartments. Blanchat performed experiments on a Calvert Cliffs-like cavity where the main pathway from the cavity to the containment is the annular gap that separates the reactor pressure vessel (RPV) from the cavity wall (Reference 32 and 33). In the initial test series an iron-alumina melt was generated by a thermite reaction in the cavity and steam was released from the RPV onto the melt. In Test CE-3 the RPV steam pressure was 8.0 MPa and about 48% of the melt was transported to the cavity. Nevertheless, the measure pressure increase of 0.25 MPa was similar to that observed in scaled containments with instrument tunnels, perhaps because most of the hydrogen in the containment reacted before the thermite melt was ejected from the cavity. In two supplementary tests (Sup 1 and Sup 2) the thermite melt was generated in the RPV and ejected by steam at pressures in the range 1.0-1.5 MPa. The diameter of the RPV breach opening in Sup 1.0 was 2.5 times the diameter of the breach in Sup 2.0. As might be expected in Sup 1.0 70% of the melt was dispersed into the containment and the containment pressure increase was 0.38 MPa, compared with the corresponding values of 22% and 0.2 MPa in Sup 2.0. Again, the containment pressure in the Sup 1 test, while high compared to Sup 2.0, was no different than that observed during the Sandia 1/10 scale Zion-containment tests (see Figure 2-15).

2.12 Karlsruhe Scaled DCH Experiments for European Reactor-Like Containments

By the year 2000, experimental research on the DCH problem in the USA came to an end. Work on this subject, however, began in Europe (at Karlsruhe) around 2003 and an important paper that summarizes this work appeared in the literature in 2009. DCH experiments were performed by Meyer (Reference 34) using test models that were scaled-down versions of European nuclear power plants. The reactor cavity models investigated in the tests were: EPR (1/18 scale), French 1300 MWe P'4 (1/16 scale), Russian VVER (1/15 scale) and the German Konvoi (1/19 scale). In addition to the different cavity geometries and pathways to the containment used, the RPV breach sizes, RPV initial pressures and containment hydrogen concentrations were varied from test to test.

The simulant corium was generated by a thermite reaction resulting in an iron/aluminum oxide melt mixture. The facility used in the experiments is shown in Figure 2-24. The facility is known as the DISCO facility. The primary system was represented by a vertical pipe. The melt was generated at the lower end of the pipe which served as the RPV. The reactor cavity was constructed of concrete which was placed inside a steel vessel. Eight horizontal steel cylinders served as the hot and cold legs and each cylinder was surrounded by an annular space which served as flow paths to a model size equipment room. The reactor cavity was covered, but four or eight openings (depending on reactor design) penetrated the cover to represent flow paths from the cavity to the containment or refueling room above. The containment room was a 5.8-m high pressure vessel of 14 m³ volume.

The actual arrangement of the compartments depended on the type of reactor plant geometry that was tested. As an example, the model of the Konvoi cavity and adjacent compartments is shown in Figure 2-25 where an additional compartment can be seen on top of the cavity which represented the refueling room. The side of this compartment had two small openings that connected to the equipment room compartment. Eight openings in the cavity cover connected the cavity with the refueling room. In this 1/18th linear scaled model experiment the flow areas were: 315 cm² around the RPV, 80 cm² through the annular paths around the hot legs and 73 cm² to the refueling room. Presumably there was a wide open area between the refueling room and the containment above, since this area was not given in reference 34.

Qualitatively speaking, the experimental findings at the DISCO facility were no different than those reported during the previous DCH experiment in the USA; namely, the final distribution of the corium debris is mainly a function of the pathways between the cavity and the containment dome and that this distribution determines the pressure rise in containment. In all the DISCO tests the measured pressure

rise was in the range observed in the tests for the Zion, Surry and Calvert Cliffs plants, namely between 0.09 and 0.35 MPa. The low end of this pressure range was measured in scaled reactor models with no direct pathway from the cavity to the containment dome. In those reactor models where significant fractions of corium reached the containment dome and hydrogen was present in flammable concentrations, the pressure rise was about 0.3 MPa with most of this rise due to hydrogen combustion.

From the initial inventory of gases and melt (containing Fe and Al) and the data from periodically sampling of the upper containment atmosphere, Meyer estimated the amount of hydrogen burned in their DISCO facility tests and in some of the Sandia tests. The measured containment pressure increase versus the estimated amount of hydrogen burned is shown in Figure 2-26. The experimental peak pressure correlates well with the amount of hydrogen burned, indicating the important contribution of hydrogen combustion to the containment pressure rise. Note that the data from the Sandia IET tests, which used cavities having large instrument tunnel pathways, lie along a line that is above the line of data produced using annular cavity designs (Karlsruhe DISCO tests and Sandia Test CE-sup). Indeed, hydrogen does burn in amounts at least partly dictated by containment design. The solid line in Figure 2-26 is the theoretical maximum pressure rise due to hydrogen burning. This solid line does not include heat transfer (conduction) from the debris to the containment gas so that some of the measured values are close to or exceed the theoretical pressure increase.

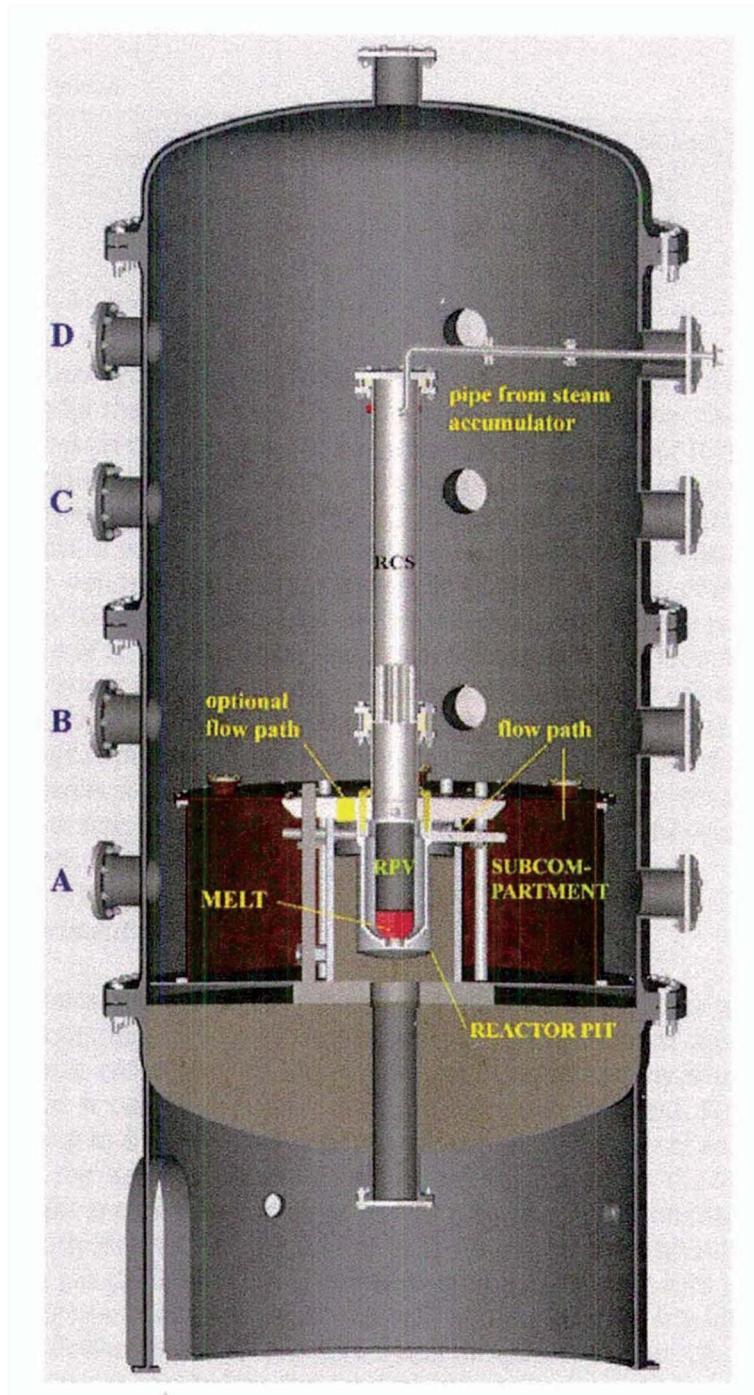


Figure 2-24 Scheme of the DISCO-H facility with the model of the EPR cavity

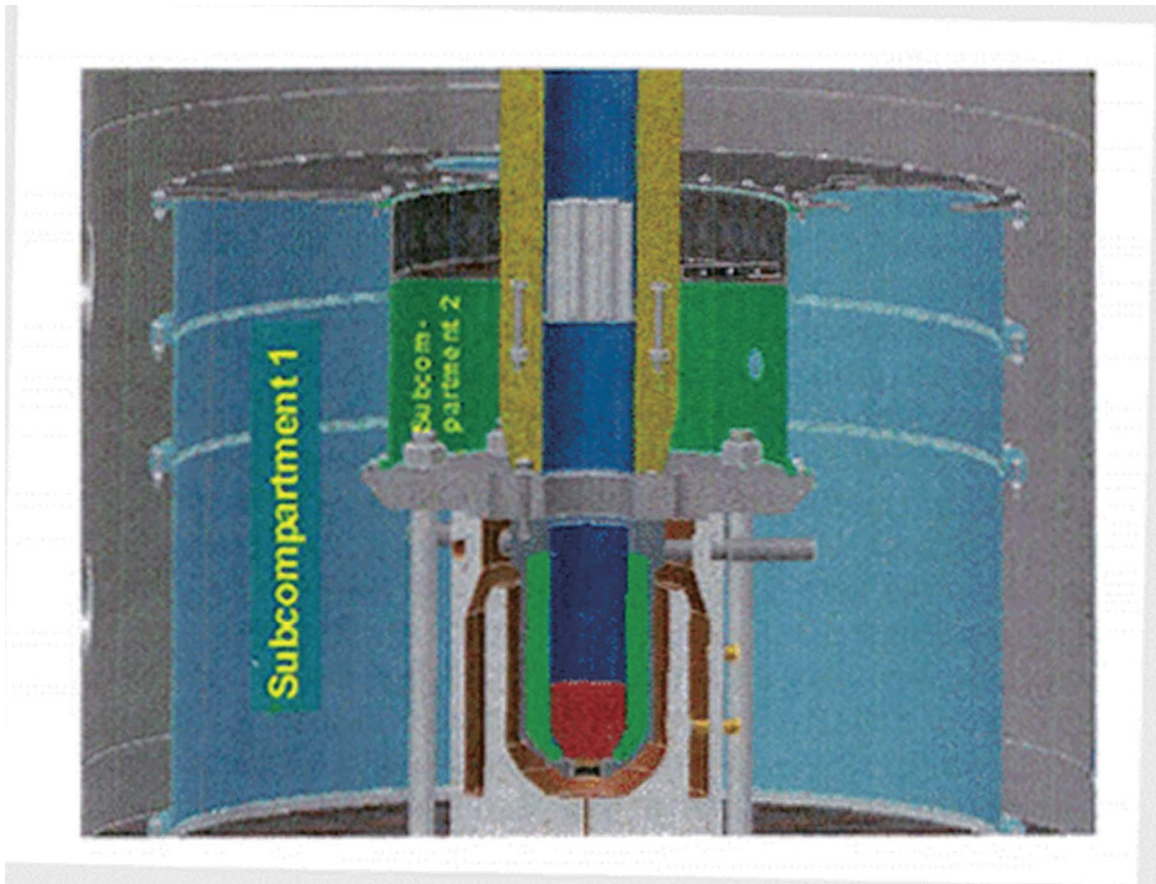


Figure 2-25 Model of the Konvoi cavity and compartments

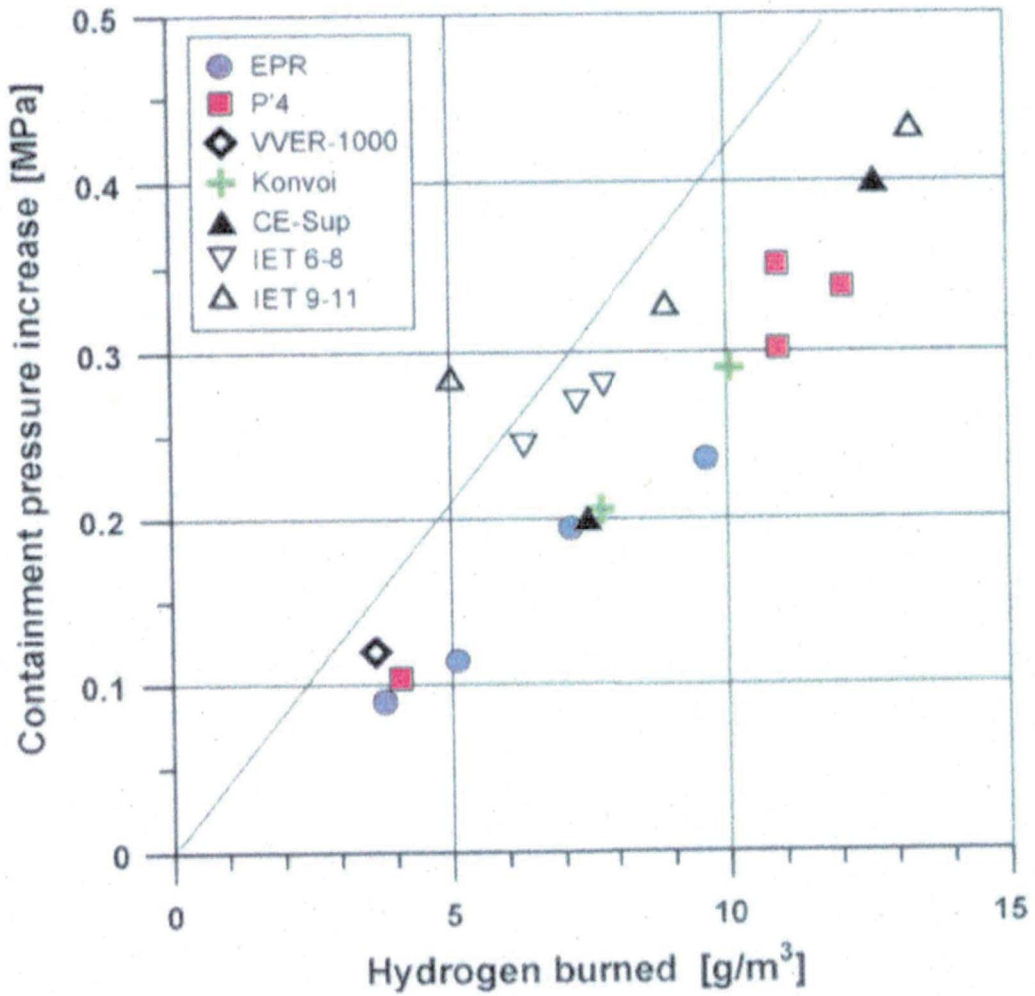


Figure 2-26 Measured containment peak pressure rise over amount of burnt hydrogen per containment volume; the line represents the theoretical pressure increase by thermal energy of hydrogen combustion without heat loss to structure

3 REVIEW ON METHODOLOGY OF DCH ANALYSIS

DCH has been extensively studied in the past 2 decades and a number of modeling approaches were proposed and tested. These include the CLCH model (Reference 35) and the TCE model (Reference 36), which were used for assessments of DCH risks for all nuclear plants in the US. Features of these models are described as follows.

3.1 CLCH Model

The key argument of this model is that the heat transfer between the melt and the gas is limited by the amount of blow-down gases that have intimate (coherent) contact with the melt. Once the melt particles are trapped and deposited in the subcompartment, the heat transfer between the melt and the containment atmosphere becomes negligible, and the major energy addition into the atmosphere is through the combustion of the so-called pre-existing hydrogen.

3.1.1 Assumptions

A number of assumptions were made in this model, which are summarized below:

- a) When the vessel is breached under high pressure, the melt is ejected first followed by the high speed steam and H₂ jet. The flow pattern within the reactor cavity (PWR) or pedestal (BWR) is a recirculation flow, which induces a strong interaction between the gas the melt. The melt is entrained by the jet into small particles. Heat transfer between the gas and melt allow them to reach thermal equilibrium quickly. In the meantime, chemical reactions between the two cause depletion of the steam constituent and increase of the hydrogen constituent.
- b) Once the multiple phases of steam, gas and corium particles flow through the inclined junction, or so-called chute, between the cavity and subcompartment, the gas flow is significantly slowed down because the volume of the subcompartment is much larger than the cavity. The flow speed is expected to be less than the threshold speed to levitate the particles, and most of the corium particles carried by the flow, except those with very small diameters, are deposited in the subcompartment. Once they are deposited, their ability to transfer significant amount of heat and be oxidized is assumed minimal compared to the finely particulate state.
- c) Hydrogen generated during DCH is assumed from Zr, Cr, and Steel oxidation, where Zr and Cr are considered as highly reactive metals, while steel is the less reactive metal. The rates of Zr and Cr oxidation are only limited by the amount of reactant steam. Chemical equilibrium is assumed between the steel, steam, and hydrogen reactants. Pre-existing hydrogen in the containment is assumed to combust when the temperature in the containment reaches the auto-ignition temperature.

3.1.2 Equations of Pressure and Temperature Increases

An implication in the assumptions is that significant heat transfer occurs only in the time frame when the blow-down gas speed is large enough to disperse and levitate the particles. The time is denoted as the coherent time τ_m . For the blow-down gas, adiabatic expansion is assumed, and the blow-down gas pressure, mass flow rate, and temperature are given by assuming an ideal gas, so that

$$\frac{P_{s,v}}{P_{sO,v}} = \left[1 + \frac{\gamma-1}{2} \Gamma \frac{t}{\tau_s} \right]^{2\gamma/(1-\gamma)} \quad (3-1)$$

$$\dot{m}_{s,b} = \eta A_b \rho_{sO,v} a_{sO} \Gamma \left(1 + \frac{\gamma - 1}{2} \Gamma \frac{t}{\tau_s} \right)^{(\gamma+1)/(1-\gamma)} \quad (3-2)$$

$$T_{s,v} = T_{sO,v} \left(\frac{P_{s,v}}{P_{sO,v}} \right)^{(\gamma-1)/\gamma} \quad (3-3)$$

where γ is the ratio of specific heat of C_p/C_v of the gases, A_b is the break area, η is the discharge coefficient, $P_{sO,v}$, $T_{sO,v}$ and $\rho_{sO,v}$ are the pressure, temperature and gas density in the RCS before the blow-down, a_{sO} and Γ are related to the ratio γ and the temperature $T_{sO,v}$. The characteristic depressurization time τ_s is given by

$$\tau_s = \frac{V_v}{\eta A_b a_{sO}} \quad (3-4)$$

where V_v is the volume of the RCS. As stated before, thermal and chemical equilibriums are assumed between the blow-down gases and the corium particles during the coherent time of τ_m . A simple energy balance between the blow-down gases and the corium particles lead to an equation for the temperature of the hot gas and corium mixture:

$$T_{s,c} = \frac{\dot{m}_m C_{p,m} T_m + \dot{m}_{s,b} C_{p,s} T_{s,v} + \Delta H_{r,Zr} \dot{m}_m (\omega_{Zr}) + \Delta H_{r,Fe} \dot{m}_m (\omega_{Fe}) r_{Fe}}{\dot{m}_m C_{p,m} + \dot{m}_{s,b} C_{p,s}} \quad (3-5)$$

where $\dot{m}_m = m_{mO} / \tau_m$ is the entrainment rate in the cavity, m_{mO} is the total mass of corium ejected from the vessel, $C_{p,m}$ and $C_{p,s}$ are the specific heat of the melt and the gas, ω_{Zr} and ω_{Fe} are the mass fractions of Zr+Cr and steel in the melt, $\Delta H_{r,Zr}$ and $\Delta H_{r,Fe}$ are the reaction heat per mass when Zr+Cr and steel are oxidized. As assumed, Zr and Cr are assumed highly reactive and a complete oxidation of these metals is expected, while iron is less reactive, and partial oxidation is considered when chemical equilibrium is reached between the reactants of steel, steam, and hydrogen. The factor r_{Fe} is the constant which account for partial oxidation, which is evaluated based on the chemical equilibrium constant of the iron oxidation equation.

When the hot gas enters the open space in the containment, it mixes with the bulk atmosphere in the containment and elevates the temperature and pressure in the containment. The gas temperature in the containment is thus given in the following formulation by considering an energy balance in the entire containment:

$$\left(m_s C_{v,s} + m_a C_{v,a} \right) \frac{dT_a}{dt} = \dot{m}_s C_{p,s} T_{s,c} - \dot{m}_s C_{v,s} T_a, \text{ for } t \leq \tau_m, \quad (3-6)$$

$$T_{a,f} = \frac{m_{s,v}(\tau_m) C_{v,s} T_{s,v}(\tau_m) + m_{s,a}(\tau_m) C_{v,s} T_a(\tau_m) + m_a C_{v,a} T_a(\tau_m) + \Delta H_{H_2} m_{H_2}}{m_{sO} C_{v,s} + m_a C_{v,a}}, \text{ for } t > \tau_m \quad (3-7)$$

where T_a is the containment bulk temperature, m_s is the mass of blow-down gases, and $\Delta H_{H_2} m_{H_2}$

represents the energy addition due to H₂ combustion. Finally, the pressure in the containment is given by the ideal gas law as

$$P_{a,f} = \left(\frac{m_{sO,v}}{V_v + V_a} R_s + \frac{m_a}{V_v + V_a} R_a \right) T_{a,f} \quad (3-8)$$

3.1.3 Considerations of Iron Chemical Reaction and Pre-existing H₂ Combustion

Steel in the melt ejected from the reactor vessel can be oxidized by the blow-down steam to generate hydrogen. The oxidation is limited by the chemical equilibrium among the reactants of iron, FeO, hydrogen, and steam. If the rate of iron consumption is denoted by \dot{r} , the chemical equilibrium is expressed by a temperature-dependent equilibrium coefficient of K, as

$$K = \frac{\dot{r}(\dot{M}_{H_2} + \dot{r})}{(\dot{M}_m \chi_{Fe} - \dot{r})(\dot{M}_s - \dot{r})} \quad (3-9)$$

where \dot{M}_{H_2} includes the blow-down rate of hydrogen which is originally in the RCS and the rate generated by oxidation of Zr and Cr. The rate of iron consumption can be easily solved from the above equation, and applied to Eq. (3-5).

Besides the oxidation during the blow-down phase, more hydrogen can be generated through oxidation of steel, when 1) certain amount of steel can be trapped in the cavity, therefore subject to oxidation following the dispersion of the main body of the melt; 2) certain amount of steel can be expelled to the open space of the containment, subject to the oxidation in the space. The additional hydrogen generated by these two mechanisms are referred to as the hydrogen sources of “captured” and “dispersed”. A lower limit of total hydrogen in the containment can be made if the additional hydrogen generation is considered for only the “captured” iron oxidation; while an upper limit can be made if both the “captured” and “dispersed” iron oxidations are considered.

Combustion of the hydrogen in the containment is assumed only when the containment atmosphere temperature is above the auto-ignition temperature, which is estimated around 850 K to 1070 K, and the hydrogen concentration is above the lean flammability limit of about 5%. Once the hydrogen is considered flammable, its reaction heat is added into the term in Eq. (3-7).

3.1.4 Comparison with Experiments

The CLCH model was compared with the IET series of experiments done in SNL (Sandia National Laboratory) and ANL (Argonne National Laboratory). Figure 3-1 and Figure 3-2 show the comparisons between the model and SNL IET series of experiments, where the curved lines are predictions of the model and the flat lines are experiment data. Figure 3-1 is based on the lower limit of hydrogen generation due to steel oxidation, while Figure 3-2 is based on the upper limit. The data, as shown, is between the lower and upper limit predictions of steel oxidation. Figure 3-3 shows the comparison between the model and ANL IET series of experiments, which is based on the upper limit of hydrogen generation. The model slightly over-predicts the pressure increase compared to the experiments. This is probably because the ANL IET experiments were using a much smaller scale facility, and heat loss to the wall has a larger impact on the measured pressure rise. In general, the CLCH results are reasonable compared to the experiments in the range of the characteristic time ratio of τ_m/τ_s .

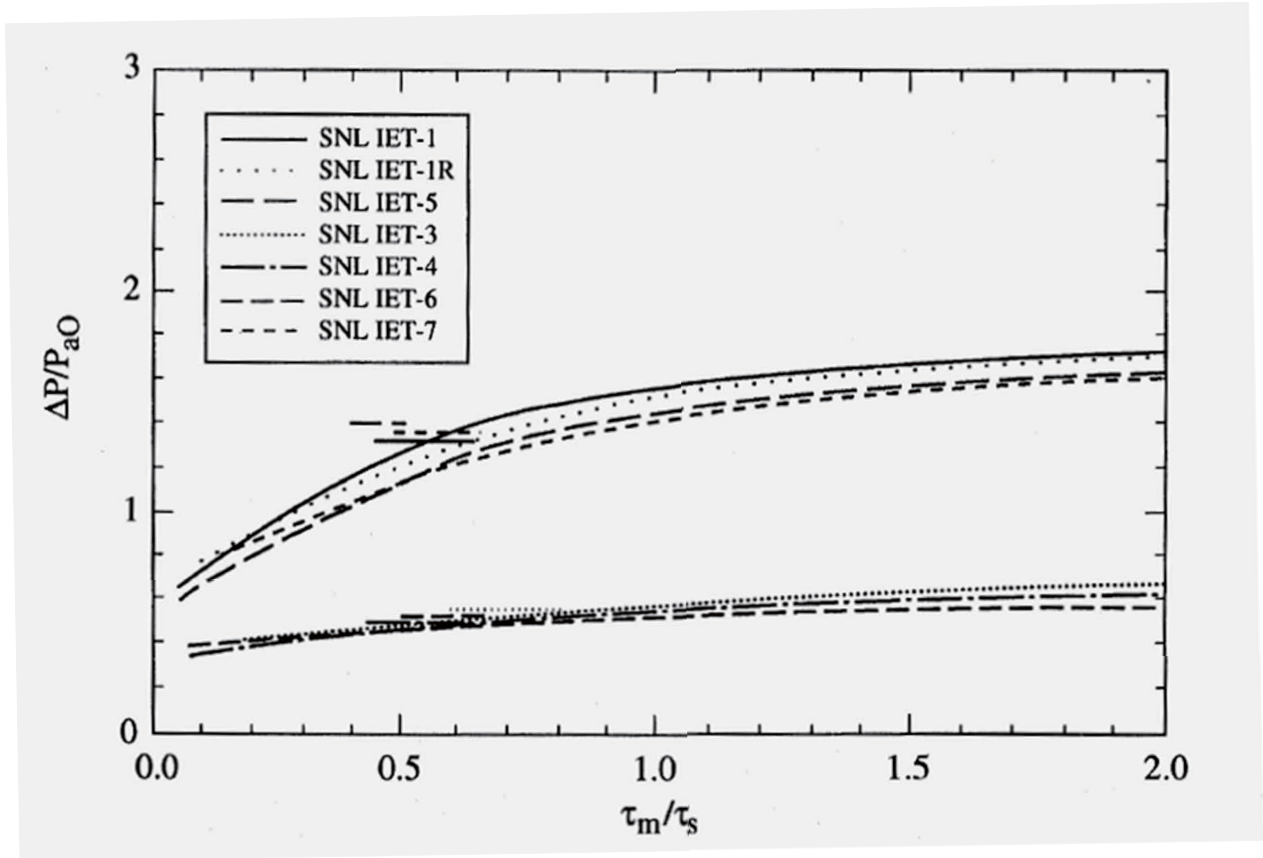


Figure 3-1 Comparisons of pressure increase predicted by CLCH model and the experiment data measured by SNL IET series of experiments. Lower limit of hydrogen generation is assumed for steel oxidation.

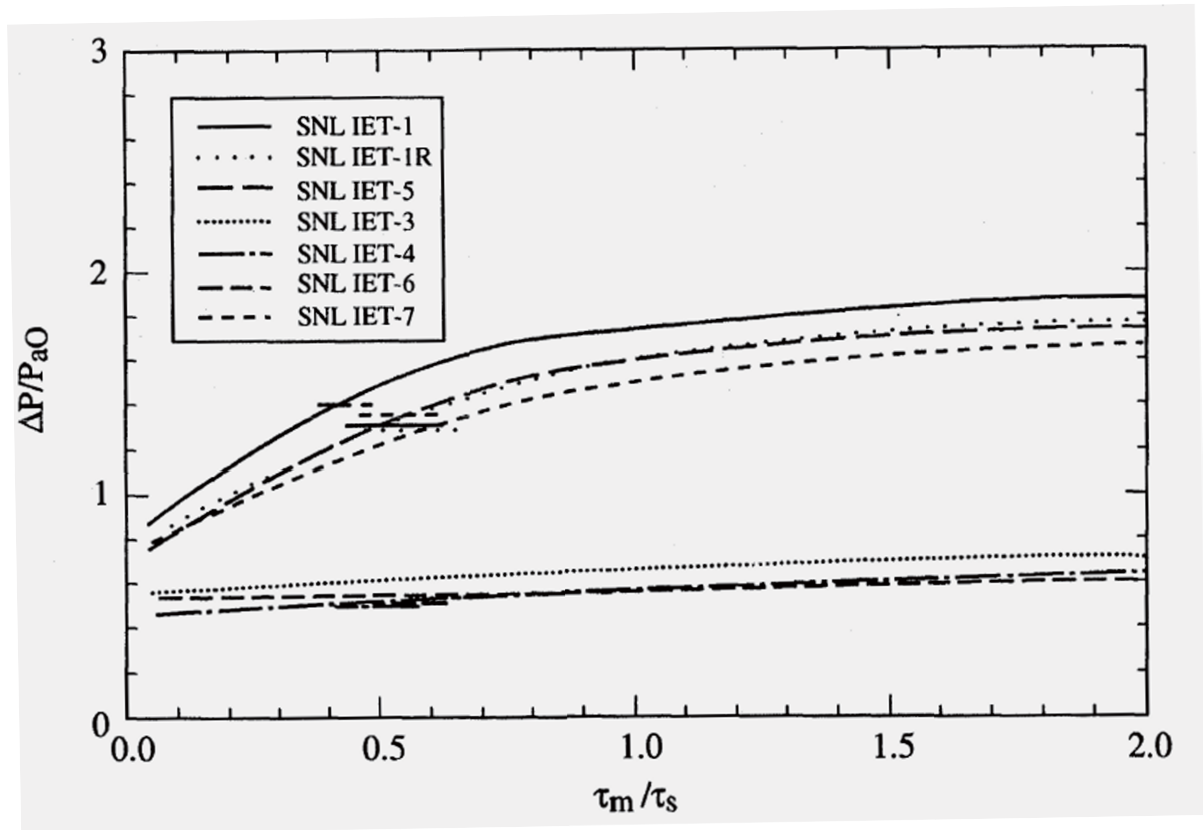


Figure 3-2 Comparisons of pressure increase predicted by CLCH model and the experiment data measured by SNL IET series of experiments. Upper limit of hydrogen generation is assumed for steel oxidation.

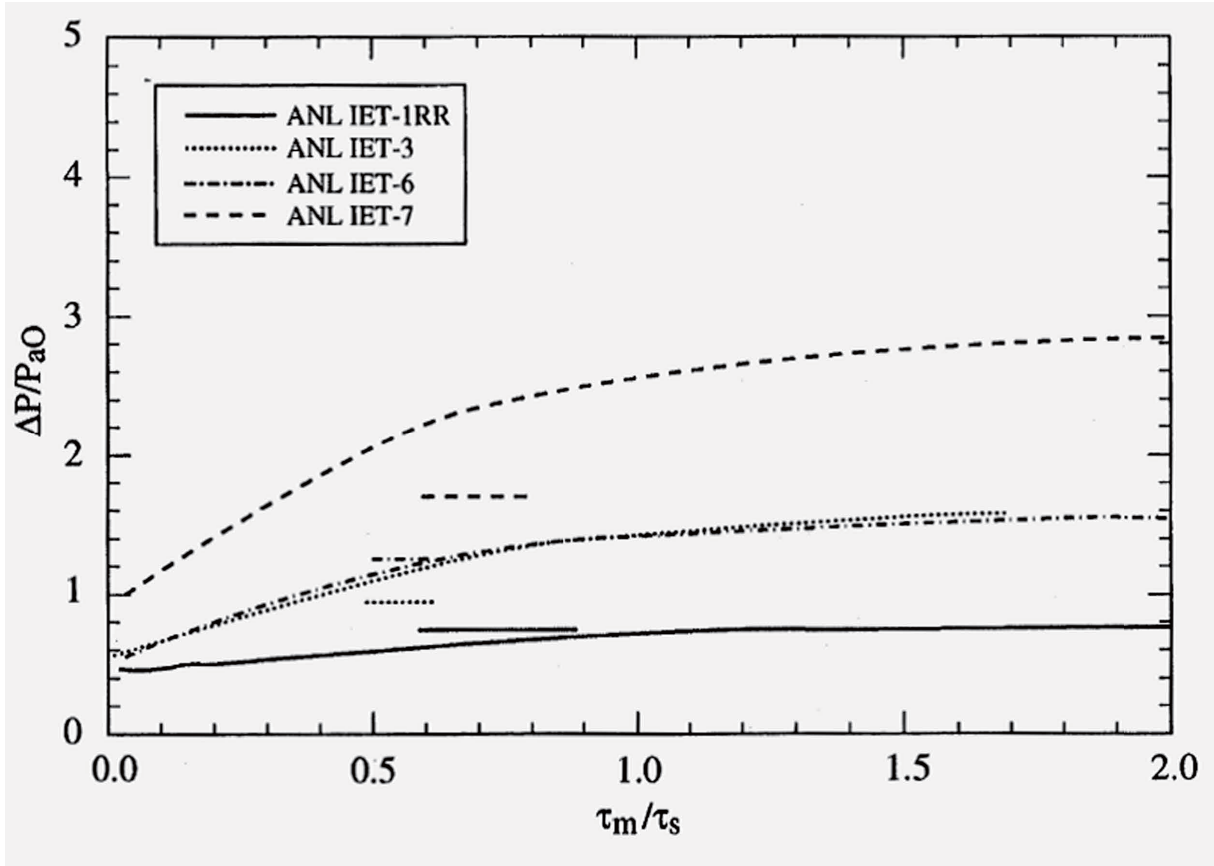


Figure 3-3 Comparisons of pressure increase predicted by CLCH model and the experiment data measured by ANL IET series of experiments. Upper limit of hydrogen generation is assumed for steel oxidation.

3.2 TCE Model

The TCE model is another model used to assess the DCH risk, which is an extension of the SCE model to account for the effect of containment compartmentalization. The major difference between the TCE and CLCH model is that: a) In the TCE model, both the gases in the containment and the gases blowing-down to the RCS exchange energy with the melt particles, while the CLCH model only considers the blow-down gases; b) the TCE model considers the limit to the heat transfer due to trapping of the melt particles in the subcompartment by using two nodes in the containment; c) two modes of combustion of hydrogen are considered in the TCE model: diffusion flame and bulk deflagration, while the CLCH only considers the deflagration when the bulk temperature is above the auto-ignition temperature.

3.2.1 Assumptions

A number of conservative modeling assumptions are made in the SCE and TCE models, and these are listed in the following:

- a) The entire containment space can be modeled with two compartments, and each of them receives a fraction of the dispersed corium particles. The subcompartment includes the reactor cavity and surrounding areas such as the corium chamber, ICI chase, and access area; the upper dome includes the remaining open space in the containment. Thermal and chemical equilibrium is reached between the gas space and the dispersed particles in each compartment.
- b) The containment atmosphere is adiabatic during the DCH process. The maximum pressure and temperature in the containment are determined by the thermal and chemical reaction heat transfer between the dispersed corium particles and containment gas.
- c) The mass of gases in the subcompartment that can reach thermal equilibrium with the corium particles is the maximum between the mass of gases in the sub-compartment prior to the vessel failure and the mass of the gases and steam which is coherent with the dispersal process during the blow-down. The blow-down is assumed to be an isentropic (adiabatic) process. A coherence ratio is defined as the time required for dispersing all the corium in the cavity to the blowdown time. The fraction of the mass of gases and steam coherent with the corium is calculated as a function of the coherence ratio.
- d) Hydrogen combustion occurs only in the upper dome compartment. Three sources of the hydrogen are considered: pre-existing hydrogen that is released from the RCS to the containment before vessel failure, the hydrogen released from the RCS as part of the blowdown gases, and the hydrogen generated from metal oxidation during the DCH process.
- e) The hydrogen generated from oxidation of Zr, Cr and Al is limited only by the amount of steam coherent with the dispersal process. The hydrogen generated from oxidation of steel is limited not only by the amount of steam available, but also by the chemical equilibrium between the steel and steam.
- f) A diffusion flame is the expected mode of hydrogen combustion in the upper dome compartment. The lowest oxygen mole fraction that can sustain the diffusion flame is determined through the balance of chemical reaction heat and the heat required raising the temperature of entrained air.

3.2.2 Prototype SCE Model

The SCE model assumes that the entire containment volume can be treated as a single control volume. The dispersed debris is assumed to mix completely with the entire containment atmosphere and to

remain airborne long enough to enable all thermal and chemical interactions to come to equilibrium.

Based on these assumptions, the maximum pressure rise in the containment resulting from DCH is obtained by combining the energy balance equation and the ideal gas law. That is,

$$\frac{\Delta P}{P^0} = \frac{\Delta U}{U^0} = \frac{\sum \Delta E_i}{U^0 (1 + \psi)} \quad (3-10)$$

where ΔP and ΔU are the pressure increase and internal energy increase in the containment gas space, P^0 and U^0 are the initial pressure and energy. ΔE_i represents the energy input into the containment, and ψ is the ratio of the total heat capacitances in the RCS and in the containment.

The energy input is the sum of the energies due to blow-down gases ΔE_b , melt ΔE_t , metal oxidation ΔE_r , and hydrogen combustion ΔE_{H_2} , i.e.,

$$\sum \Delta E_i = \Delta E_b + \Delta E_t + \Delta E_r + \Delta E_{H_2} \quad (3-11)$$

In the above equation ΔE_b and ΔE_t are evaluated by assuming that the blow-down gas pressure is reduced to the initial containment pressure and that the melt is cooled to the initial containment temperature. The chemical reaction term ΔE_r is evaluated for the metals in the melt in the order of Zr, Cr, and steel. The blow-down steam is considered as the source of oxidant of the reaction, and it reacts with the most reactive metal, then the less reactive ones, until all the steam is exhausted. The combustion term ΔE_{H_2} is evaluated for the hydrogen coming from three sources: pre-existing hydrogen in the containment, hydrogen in the RCS, and hydrogen generated during metal oxidation. The combustion is assumed to be complete when all the oxygen within the containment is exhausted.

Figure 3-4 shows a comparison of the pressure increase predicted by the SCE model with those measured in the experiments. As shown, the SCE model tends to over-predict the pressure increase, mainly because it fails to consider the limitation to the energy exchange when melt particles are trapped in the subcompartment.

3.2.3 Extension from SCE Model with Consideration of Trapping Corium in the SubCompartment

In light of the insufficiency of the SCE model, a more sophisticated TCE model was developed to account for the trapping of the melt. As stated in the assumption section, the entire containment was split into a subcompartment and the upper dome.

When the vessel fails, the melt particles can be carried into the two compartments at the same time. The premise of the TCE model is that DCH occurs independently in the subcompartment and in the upper dome. The energy balance in each compartment shows that the individual contributions to the containment energy can be written as the product of the efficiency and the maximum internal energy change based on the SCE model, so the containment pressurization can be written as

$$\frac{\Delta P}{P^0} = (\eta_1 + \eta_2) \left(\frac{\Delta P}{P^0} \right)_{1C} \quad (3-12)$$

In the above equation, η represents the efficiency, the subscripts 1, 2, and 1C mean the subcompartment, upper dome, and SCE model respectively.

The efficiency of the DCH process in the subcompartment can be derived through an energy balance equation for the subcompartment. Since the hydrogen combustion is assumed to occur in the upper dome, the energy exchange in the subcompartment includes only the terms due to blowing down gas and melt, and metal oxidation. If the fraction of blow-down gases and melt entering the subcompartment is denoted as f_{a1} , the energy addition into the subcompartment is given by

$$\Delta U_1 = \frac{f_{a1}(\Delta E_b + \Delta E_t + \Delta E_r) - f_{a1}N_d C_d(T_1 - T_r)}{1 + \psi_1} \quad (3-13)$$

where $f_{a1}N_d C_d$ is the heat capacitance of the melt entering the subcompartment, and T_r is the reference temperature, typically the initial temperature in the containment. The term T_1 is an average temperature of the blowing-down gases coherent with the melt, and the gases pre-existing in the subcompartment. ψ_1 is the ratio of heat capacitance between the melt and the amount of gases available for heat transfer in the subcompartment. Note: the amount of the gases for heat transfer in the TCE model is assumed the maximum between the blowing-down gases coherent with the melt and the pre-existing gas mass in the subcompartment. Therefore, the term ψ_1 can be written as

$$\psi_1 = \frac{f_{a1}N_d C_d}{\max[f_{a1}f_{coh}N_{RCS}^0, f_{v1}N^0]C_v} \quad (3-14)$$

where f_{coh} is the so-called coherence ratio, f_{v1} is the volumetric fraction of the subcompartment (to the entire volume of the containment), N_{RCS}^0 and N^0 are the total moles of gases originally in the RCS and containment, and C_v is the specific heat (per mole) at the constant volume. If the subcompartment volume is large, the mass of gas pre-existing in the subcompartment will dominate the heat transfer. This is one of the major differences between the TCE model and the CLCH model. With these definitions, the efficiency in the subcompartment is thus formulated by dividing the ΔU_1 by the ΔU in the SCE model, that is

$$\eta_1 = f_{a1} \frac{1 + \psi}{1 + \psi_1} \left[1 - \left(\frac{\Delta E_{H2}}{\sum \Delta E_i} \right)_{IC} \frac{T_1 - T_r}{T_d^0 - T_r} \right] \quad (3-15)$$

Similar derivation can be made for the efficiency in the upper dome, which is given by the following formulation

$$\eta_2 = \frac{1 + \psi}{1 + \psi_2} \left[f_{a2} - (f_{a2} - f_{burn}) \left(\frac{\Delta E_{H2}}{\sum \Delta E_i} \right)_{IC} - f_{a2} \left(\frac{\Delta E_{H2}}{\sum \Delta E_i} \right)_{IC} \frac{T_2 - T_r}{T_d^0 - T_r} \right] \quad (3-16)$$

One of the key variables in the efficiency formulations is the coherence ratio f_{coh} , which is defined as the fraction of the blow-down gases participating intense heat transfer and oxidation with the melt particles. The coherence ratio is a function of the time ratio R_t of the entrainment time and the blowing down time. If the blow-down is assumed an adiabatic expansion process, the coherence ratio is given by

$$f_{\text{coh}} = 1 - \left(1 + \frac{\gamma - 1}{2} R_{\tau} \right)^{-2/(\gamma - 1)} \quad (3-17)$$

where γ is the ratio of c_p/c_v of the blowing down gases. The time ratio must be determined through the momentum equation for the corium particles in the cavity. Here the flow regime in the cavity is assumed to be finely dispersed corium particles carried by the high speed gases. If the particle sizes are assumed to be independent with the gas flow speed, and drag on the particles by the gas flow is considered, the time ratio can be written as a function of the geometric and physical parameters of the RCS and the cavity:

$$R_{\tau} = \frac{\tau_e}{\tau_b} = C_{R_{\tau}} f_d \left(\frac{T_{\text{RCS}}^0}{T_d^0} \right)^{1/4} \left(C_{d,h} \frac{M_d^0}{M_g^0} \frac{A_h V_c^{1/3}}{V_{\text{RCS}}} \right)^{1/2} \quad (3-18)$$

where $C_{R_{\tau}}$ is a modeling parameter matching the experimental data, and $C_{d,h}$ is the dragging coefficients of the gas flow, f_d is the dispersal fraction, which is normally very close to 1, T_{RCS}^0 and T_d^0 are the initial temperatures of the RCS and the particles, M_d^0 and M_g^0 are the initial masses of the melt and the gases in the RCS, A_h is the break area of the vessel, V_c and V_{RCS} are the total volumes of the cavity and the RCS.

The second key variable in the TCE model is the term of hydrogen combustion in the equation of the efficiency η_2 . Several hydrogen sources are considered: (1) hydrogen injected into the atmosphere at the time of vessel breach as part of the blow-down gases, (2) hydrogen produced from reactive metals (Zr, Ni, and Cr)-steam reactions with the coherent part of the blowdown gases, (3) hydrogen produced from iron-steam reaction, and (4) pre-existing hydrogen in containment. Similar to the CLCH model, hydrogen from the iron-steam reaction is subject to chemical equilibrium limitation. As the hot jet of steam and hydrogen mixture enters the upper dome, the combustion of the jet flame is considered, which is capable of burning as long as the jet temperature is above the auto-ignition temperature of the jet flame. The jet flame can entrain the pre-existing hydrogen into the burning zone of the flame, so that it contributes to the total hydrogen combustion heat. If the upper dome temperature is higher than the auto-ignition temperature for deflagration, a global combustion is also considered for the energy release.

The TCE model has been compared with experiments extensively. Figure 3-5 shows comparisons of the coherence ratio and hydrogen generation in Zion-like containments between the model prediction and the measured data. Figure 3-6 shows the comparison of the measured and predicted containment pressure increase. TCE model predictions are reasonable compared with the experiments in general.

3.2.4 Probabilistic Framework

Besides phenomenological modeling factors in TCE model, the DCH loads depend on parameters that characterize the system initial conditions; that is, primary system pressure, temperature and composition (i.e., hydrogen mole fraction), melt quantity and composition (zirconium and stainless steel mass fraction), initial containment pressure and composition (hydrogen mole fraction), and geometry (containment volume and the size of the breach). The key component of the framework, therefore, is the casual relation between these parameters and the resulting containment pressure (and temperature) under the influence of the uncertainty in the coherence ratio. Of these parameters, some are fixed, some vary only over a narrow range, and some are so uncertain that they can be approached only in a bounding sense. The following features were considered in coming up with the final choice of a framework in:

(a) Geometry: The specific geometry is fixed for a given plant; however, the basic features are that that is an intermediate compartment between the cavity and the main containment volume and that the lower head fails in a local (rather than global) manner. In addition, the geometry is characterized by the free volume of the containment and the primary system volume.

(b) Containment Conditions: Typically, high-pressure scenarios evolve with significant primary system venting prior to vessel breach; this venting increases the containment pressure to ~ 0.25 MPa with temperatures near saturation. This pressure will be lower if any of the active containment heat removal systems are operational. The containment atmosphere will also contain hydrogen at a concentration of a few mole percent. Pre-existing hydrogen is limited by the quantity of zirconium available to react in the core, and thus there is a constrained relationship between pre-existing hydrogen in the containment and the hydrogen produced by steam/zirconium reactions in the DCH event.

(c) Primary System Conditions: Reasonable consistency between reactor coolant system (RCS) pressure (and temperature) and melt mass and composition is emphasized here.

TCE model predictions indicate that DCH loadings are insensitive to the temperature of the primary system. Pressure can be enveloped rather than predicted. This leaves only the expelled melt parameters in need of quantifications: melt quantity, composition and temperature. These are the variables that drive the DCH process; however, they are highly uncertain. They depend on the complex interactions and the many scenario bifurcations in the core meltdown, relocation, and lower head failure processes, and are hence in need of very careful quantification.

The probabilistic framework can be structured in the manner. The initial melt parameters are to be quantified as independent probability density functions, representing modeling uncertainty in the parameters (variations from stochastic processes are assessed as insignificant relative to modeling uncertainty). These functions are formed into a joint probability density/function for the peak containment pressure. This distribution function is combined with the set of containment fragility curves (probabilistically distributed themselves) to obtain a probability distribution of the containment failure frequency.

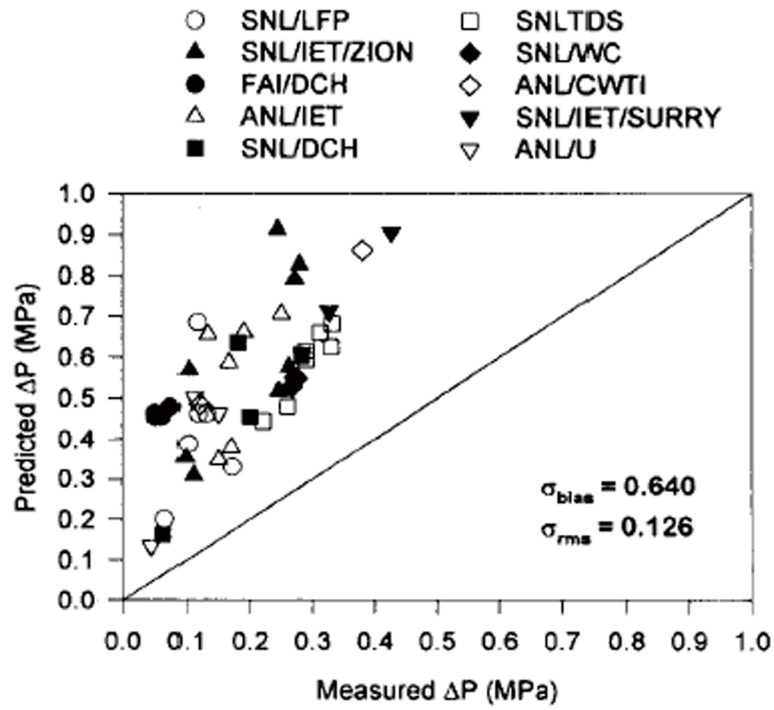


Figure 3-4 Comparisons of pressure increase between SCE model and experiments.

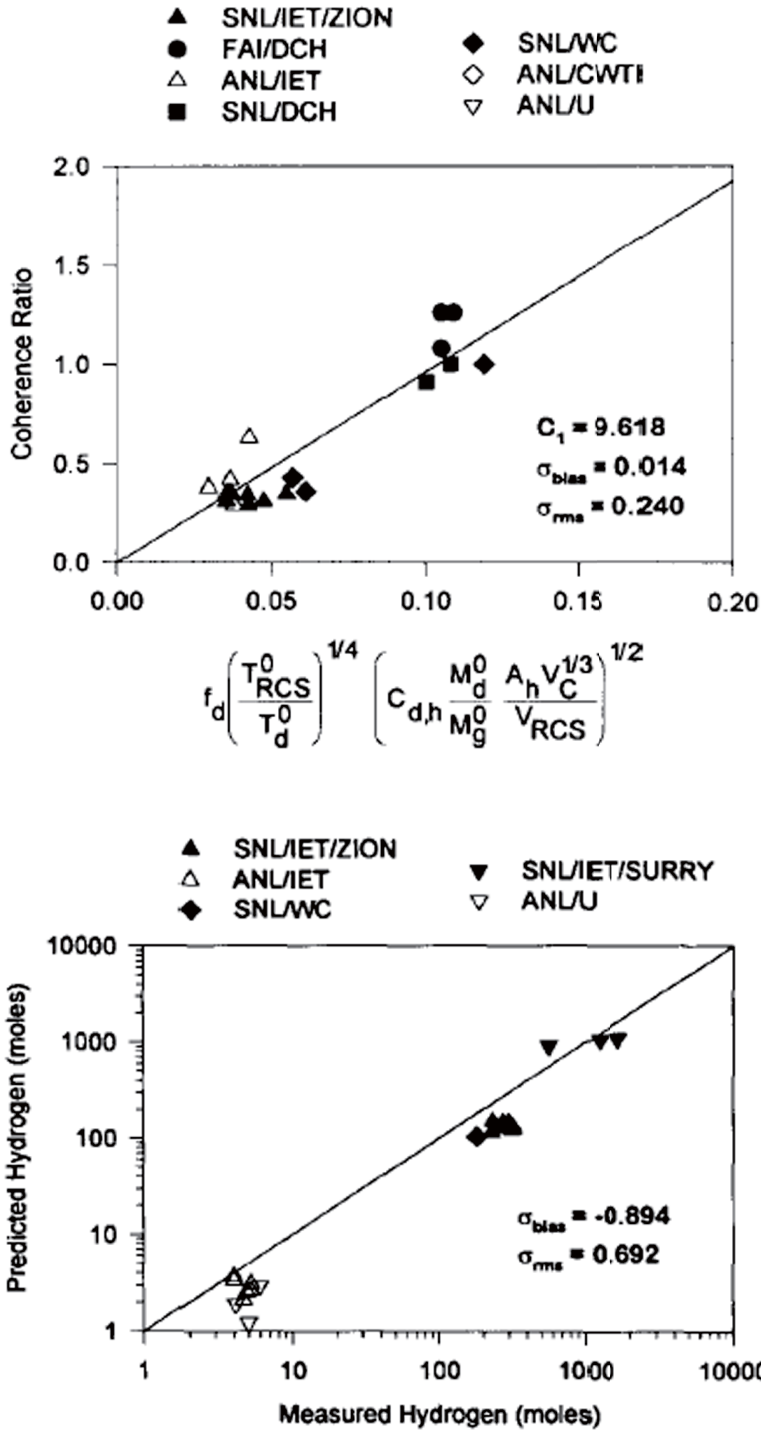


Figure 3-5 Comparison of coherence ratio and hydrogen generation between the model prediction and the experiment data.

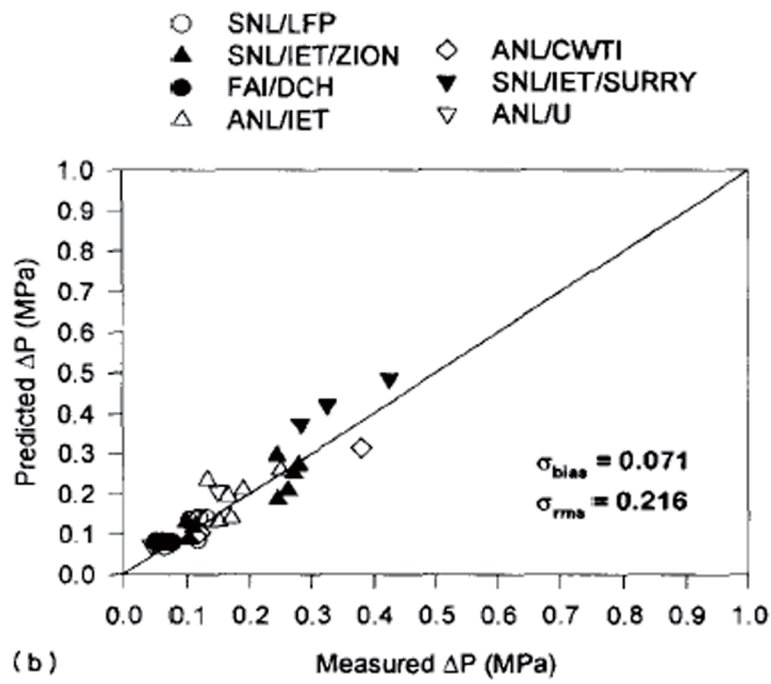


Figure 3-6 Comparison of pressure increase between the model prediction and the experiment data.

3.3 Modeling of Accident Scenarios

For the evaluation of DCH loads on the APR1400 containment, initial and boundary conditions were determined in advance, which include the APR1400 specific geometries of RCS and containment, the initial inventories of core materials, T/H condition of RCS and containment at the time of vessel breach (VB), the inventories of molten debris at VB and the characteristics of debris dispersal. Since DCH is possible only for high pressure sequences, appropriate scenarios had to be selected first.

Three scenarios were selected from the DCH studies of Zion (Reference 3) and Surry (Reference 5) where the efforts were consolidated into DCH issue resolution for Westinghouse and CE nuclear power plants. (Reference 4 and 6) These, designated as Scenario V, Va and VI in conformity with the references, simulated small break LOCAs with repressurization by operator intervention and were considered as conservative initiators in terms of DCH loads on the containment integrity. These scenarios will be described below in details.

Given an accident scenario, the initial and boundary conditions need to be prepared depend upon the DCH assessment methodology. For APR1400, two methodologies were used: the NUREG method and the mechanistic CONTAIN analysis. Whereas the NUREG method usually requires probabilistic distribution for major physical quantities, the CONTAIN analysis requires point-values for the same quantities. Moreover, the NUREG method requires plant-specific data from which it calculates related quantities internally. Thus, except for modeling-specific conditions required by each method, only general conditions are produced herein which can be classified in three subgroups: plant-specific information, quantification of initial conditions of molten corium in the lower plenum and thermo-hydraulic conditions, and quantification of the DCH phenomena. The bounding scenarios for DCH assessments are described as follows:

3.3.1 Scenario V (Va) - SBLOCA with Repressurization of RCS by Operator Intervention

Scenario V simulates a small break LOCA with repressurization of the RCS by operator intervention. It represents a core melt accident that progresses with water still present in the lower portions of the core. Such conditions lead to formation of a crust within the core followed by a massive release of melt when the crust fails. Accumulation of core material on the lower head of the RPV causes the lower head to heat up, eventually to the point where its structural strength is so degraded that it can no longer withstand the stresses induced in the lower head by elevated RCS pressures. Thus, creep rupture of the lower head is the expected failure mechanism.

Operator actions are assumed to repressurize the RCS to pressurizer safety valve opening setpoint. Operator intervention refills the RPV with water to the hot leg nozzles and quenches any steam remaining in the RCS to near saturation condition (~ 700 K). A non-condensable gas bubble prevents operators from refilling the entire RCS.

Consistent with TMI-II, the potential release of molten material to the lower head is controlled by the formation of a hemispherical crucible that excludes only the outer assemblies of the core. The outer assemblies are generally not in a severely degraded state because the RPV is flooded. Asymmetries in crucible growth ensure that localized penetration of the outer assembly and the core barrel would most likely occur when the crucible has grown (on average) to the outer assembly.

The containment conditions assume that active containment cooling systems (i.e., fan coolers or sprays) are not operational. However, the branch Scenario Va simulates the containment sprays in operation. It represents an accident in which the containment air temperature is very high and the steam mole fraction is very low to better envelop the range of containment conditions, so that the burning of hydrogen is highly likely. Even though these conditions are in the flammable regime, we do not guarantee that a random ignition source (unless intentional) will burn off the hydrogen prior to vessel failure even if the flammability limits are exceeded.

3.3.2 Scenario VI - SBLOCA Under Wet Core Conditions

Scenario VI simulates a small break LOCA with partial repressurization of the RCS by operator intervention. In the absence of any RCS leaks, hot leg failure would occur long before RV bottom head failure. These fully depressurize the RCS and are of no interest for DCH. Scenario VI can exist as the consequence of partial operator intervention that partially refills the RPV with water. Owing to the similarity in Scenarios V and VI, we emphasize only the differences in RCS pressure, RCS temperature and melt mass, with all other parameters developed in a manner similar to that for Scenario V.

The RCS gas at the time of vessel breach clearly must be superheated. In conjunction with the pressure and volume, the moles of gas in the RCS can be computed with the RCS temperature. The gas temperatures in each region of the RCS are estimated to be between 650K and 2800K. For this analysis, an average of 1,000K is assigned to this scenario. (Reference 3)

The potential release of molten material to the lower head is again controlled by the formation and failure of a crucible in the core region. Water occupies only the lowest regions of the core, so radial cooling of a growing crucible is reduced in this situation, and the crucible cold take on the bounding shape of an upright cylinder. We note that the molten pool must grow to the core boundary as a condition for core relocation, thus it shows some localized involvement of the outer assemblies. We expect, however, that asymmetries in crucible growth ensure that localized penetration of the outer assembly and core barrel would likely occur when the crucible has grown (on average) to the outer assembly. Consequently, the outer assemblies are excluded from our assessments.

4 DCH ANALYSIS IN APR1400

4.1 Melt Transport in Compartmentalized Containments

4.1.1 Cut-Off Droplet Size for Corium Deposition

Most reactor containments have many compartments so that the entrained melt drops will impinge and deposit on structures and walls which prevents efficient energy transport (thermal and chemical) from the cavity to the containment atmosphere. Assuming that all of the melt in the cavity is entrained by the vessel blowdown gas, the problem reduces to determining where the molten debris ultimately comes to rest, and how much of it was dispersed into the containment dome. The evaluation of debris transport can only be done on a plant by plant basis and here we focus our attention on the APR1400 containment geometry.

There are two main entrained corium transport paths from the cavity to the reactor dome: (i) through the annular gap between the reactor vessel and the cavity wall and (ii) through the cavity access area (i.e. staircase). While the flow up through the annular gap is redirected somewhat by neutron shield plugs and hot and cold legs, it will be conservatively assumed that all of the corium that enters the annular gap reaches the containment dome.

In order for the entrained corium to reach the cavity access staircase it must take a 90 degree turn in the cavity toward the sump. From the sump region it must turn upwards by 90 degrees to the corium chamber room. Then the entrained corium has to take another 90 degree turn toward the staircase. Finally the entrained corium has to take another 90 degree turn to flow up the staircase. Each 90 degree turn involves corium impingement on the wall that deflects the flow in the next lateral direction. Consider the first wall that deflects the flow, which is in the cavity itself.

As the flow approaches the wall it feels the presence of the solid surface and becomes deflected. Obviously, the gas component of the flow does not enter the wall but, instead, is completely deflected by the surface. As the droplets move with the gas, their paths will deviate from the gas streamlines because of droplet inertia and drag force and possibly because of gravity and Brownian motion if the droplets are small ($< 1.0 \mu\text{m}$). Here we assume that the droplets are large enough so that only droplet inertia and drag determine the droplet trajectories in the vicinity of the wall. The trajectories of the droplets in the flow deflection region are similar to the trajectories of the droplets in an inertial impactor, which consists of a particle/gas flow through a nozzle aimed at an impactor plate. Thus if the outer streamline of the flow (the effective width W of the wall) is replaced by an imaginary nozzle of inside radius W , calculated or experimental results for the droplet removal efficiencies of inertial impactors can be applied to estimate the droplet capture efficiency of the cavity wall during the HPME.

The most comprehensive numerical study of particle motion in an inertial impactor was performed by Marple (Reference 37, 38, and 39). Their numerical results for a circular impactor are well represented by the following correlations for the cut-off Stokes number St_{cut} or cut-off particle (or droplet) diameter D_{cut} :

$$St_{\text{cut}} = \frac{\rho_c D_{\text{cut}}^2 u_n}{9 \mu_g d_n} = 0.24 \quad (4-1)$$

where μ_g is the gas viscosity, ρ_c is the density of the liquid drop material (corium), d_n is the nozzle diameter, u_n is the nozzle gas velocity, and D_{cut} is the droplet diameter below which the droplets do not deposit on the impactor plate (or cavity wall in the present application). Equation (4-1) is in good quantitative agreement with the experimental data of Mercer and Stafford (Reference 40).

To use Eq. (4-1) we choose an imaginary nozzle in the flow deflection (or stagnation) region and we identify u_n and d_n with the oncoming two-phase corium/gas flow velocity $u_{2\phi}$ through the cavity toward the wall and with the effective width of the wall W . Therefore, Eq. (4-1) for the cut-off droplet diameter becomes

$$D_{\text{cut}} = 1.47 \left(\frac{\mu_g W}{\rho_c u_{2\phi}} \right)^{1/2} \quad (4-2)$$

Yuu and Jotaki (Reference 41) apparently were the first to suggest that the central part of an actual impactor nozzle can be regarded as a stagnation flow. Chiang (Reference 42) used this idea (Eq. 4-2) to predict water droplet deposition from a flashing jet impinging onto a plate. The next step in the analysis is the calculation of the two-phase flow velocity in the cavity.

4.1.2 Cavity Pressure and Two-Phase Flow Velocity

We consider the period in the direct containment heating transient in which all of the molten corium in the lower head has been displaced to the cavity by the in-vessel high pressure steam. While the pressure in the cavity P_{cav} is high it is assumed to be sufficiently below the vessel pressure P_0 so that the steam flow \dot{m}_g (in kg s^{-1}) from the vessel to the cavity is given by the critical flow equation:

$$\dot{m}_g = 0.61 A_0 \sqrt{P_0 \rho_{g,0}} \quad (4-3)$$

where A_0 is the area of the vessel failure opening and $\rho_{g,0}$ is the in-vessel steam density. The numerical coefficient 0.61 corresponds to isothermal critical flow. The choked two-phase corium/steam flow $\dot{m}_{2\phi}$ through the cavity cross-section toward the sump is

$$\dot{m}_{2\phi} = C_0 A_{\text{cav}} \sqrt{P_{\text{cav}} \rho_{2\phi}} \quad (4-4)$$

where A_{cav} is the cross-sectional flow area in the cavity, $\rho_{2\phi}$ is the two-phase density of the corium/steam mixture that occupies the cavity and the annular region and C_0 is a numerical constant whose value depends on the steam volume (void) fraction α in the two phase mixture and whether the flow is frozen (steam is thermally insulated from the corium) or the steam and corium are in thermal equilibrium (Reference 43).

The density of the two-phase mixture in the cavity region is

$$\rho_{2\phi} = \alpha \rho_g + (1 - \alpha) \rho_c \quad (4-5)$$

where ρ_g is the steam density in the cavity region and ρ_c is the density of the molten corium. Since $\alpha \rho_g \ll (1 - \alpha) \rho_c$, Eq. (4-5) may be simplified to

$$\rho_{2\phi} \cong (1 - \alpha) \rho_c \quad (4-6)$$

Turning our attention to the value of α , the volume of the cavity is denoted by the symbol V_{cav} . The portion of this volume occupied by the corium is

$$V_c = \frac{m_c}{\rho_c} \quad (4-7)$$

where m_c is the total mass of corium ejected from the vessel. The fraction of the total volume (V_{cav}) occupied by steam is then

$$\alpha = 1 - \frac{V_c}{V_{cav}} = 1 - \frac{m_c}{\rho_c V_{cav}} \quad (4-8)$$

We will also need to know the steam quality (mass fraction Y) in the cavity and annular regions. The quality is related to α by the formula

$$Y = \frac{\rho_g \alpha}{\rho_g \alpha + (1 - \alpha)\rho_c} \cong \frac{\rho_g}{\rho_c} \left(\frac{\alpha}{1 - \alpha} \right) \quad (4-9)$$

From the ideal gas law the density of the steam in the cavity is

$$\rho_g = \frac{P_{cav} M_g}{R_{id} T_0} \quad (4-10)$$

where M_g is the molecular weight of the steam, R_{id} is the ideal gas constant and T_0 is the temperature of the steam in the cavity. The subscript "0" signifies that T_0 is also identified with the steam temperature in the vessel since frozen two-phase flow is assumed.

The steam mass flow through the annular gap is assumed to be small compared with that through the cavity. This assumption will be justified by the result of the analysis. It follows that the steam mass flow rate through the cavity must match the steam mass flow rate from the vessel; therefore

$$Y \dot{m}_{2\phi} = \dot{m}_g \quad (4-11)$$

Combining Eqs. (4-3), (4-4), (4-6), (4-9), (4-10) and (4-11) and solving the result for P_{cav} gives

$$P_{cav} = \left(\frac{0.61 A_0 R_{id} T_0}{M_g C_0 A_{cav}} \right)^{2/3} \left[\frac{P_0 \rho_{g,0} \rho_c (1 - \alpha)}{\alpha^2} \right]^{1/3} \quad (4-12)$$

The reactor operating pressure is about $P_0 = 1.7 \times 10^7$ Pa. The steam in the vessel is assumed to be superheated to $T_0 = 1000$ K. From the ideal gas law $\rho_{g,0} = 36.8$ kg m⁻³. We assume that $m_c = 97.5 \times 10^3$ kg of corium is ejected from the reactor vessel and that the density of corium $\rho_c \cong 9250$ kg m⁻³. The volume of the APR1400 cavity is $V_{cav} = 368$ m³. Therefore, from Eq. (4-8) $\alpha = 0.971$. From the choked flow charts in reference 43, for $\alpha = 0.971$ and the assumption of frozen flow, $C_0 \cong 0.6$. The flow area in the cavity is $A_{cav} = 21.8$ m². The failure area can be calculated through modeling the ablation of reactor vessel wall when the corium is ejected by the high pressure. TCE model calculations were performed to

show that the diameter of the failure in the vessel wall can be as large as 0.5 m, corresponding to a failure area of 0.2 m². The cavity pressure is, from Eq. (4-12),

$$P_{cav} = 1.48 \times 10^6 \text{ Pa} \quad (4-13)$$

The two-phase flow velocity toward the cavity wall that deflects the flow is, from Eqs. (4-4) and (4-6)

$$u_{2\phi} = \frac{\dot{m}_{2\phi}}{\rho_{2\phi} A_{cav}} = C_0 \sqrt{\frac{P_{cav}}{\rho_c (1-\alpha)}} = 44.9 \text{ m s}^{-1} \quad (4-14)$$

4.1.3 Fraction of Drops that Impinge on the Wall

Post-DCH-test measurements of particle sizes with sieves have shown that particles are distributed lognormally with a mass median diameter \bar{D} of approximately 0.5 mm and a geometric standard deviation $\sigma_g \cong 4.0$ (Reference 5, 20 and 44). For a log-normal distribution the fraction F of the total mass of particles with diameters less than D_{cut} are

$$F = \frac{1}{2} - \frac{1}{2} \operatorname{erf} \left[-\frac{1}{\sqrt{2} \ln \sigma_g} \ln \left(\frac{D_{cut}}{\bar{D}} \right) + \frac{3}{2\sqrt{2}} \ln \sigma_g \right] \quad (4-15)$$

Inserting $u_{2\phi} = 44.9 \text{ m s}^{-1}$ (Eq. 4-14), $\mu_g = 3.55 \times 10^{-5} \text{ kg m}^{-1} \text{ s}^{-1}$ (for H₂O at 1000 K), $\rho_c = 9250 \text{ kg m}^{-3}$ and $W \cong 5.0 \text{ m}$ for the effective width of the cavity wall into Eq. (4-2) gives

$$D_{cut} = 3.04 \times 10^{-5} \text{ m} \quad (4-16)$$

From Eq. (4-15) we get

$$F = \frac{1}{2} - \frac{1}{2} \operatorname{erf}(2.9) = 2.05 \times 10^{-5} \quad (4-17)$$

for the fraction of corium drops that are not captured by the wall. While it is likely that a higher mass fraction of droplets than this escapes the cavity the calculation does show that most of the melt that flows toward the entrance to the corium chamber room deposits on the cavity wall. The corium melt film on the wall drains to the cavity floor only to be re-entrained again and cycled back to the wall. Note that re-entrainment of melt from the surface of the liquid film on the wall is unlikely since the instability of the Kelvin-Helmholtz type is bounded in stagnation counter flow fields (Reference 45).

4.1.4 Fraction of Entrained Melt Transported Through Reactor Vessel Annulus

The two-phase corium/steam flow through the reactor vessel annulus obeys the same equation as that for flow through the cavity, namely Eq. (4-4) with A_{cav} replaced by the cross-sectional flow area A_{an} in the annulus:

$$\dot{m}_{2\phi} = C_0 A_{an} \sqrt{P_{cav} \rho_{2\phi}} \quad (4-18)$$

Thus the fraction of the dispersed corium that enters the containment dome via the reactor annulus is

$$f_{\text{dom}} = \frac{A_{\text{an}}}{A_{\text{cav}} + A_{\text{an}}} \quad (4-19)$$

This fraction represents all of the corium that enters the containment dome since we just demonstrated that practically all of the corium that travels towards the compartments will be trapped. For the ARP1400 containment $A_{\text{an}} = 1.96 \text{ m}^2$ and $A_{\text{cav}} = 21.8 \text{ m}^2$ and

$$f_{\text{dom}} = 0.082 \quad (4-20)$$

It should be mentioned that the NUREG/CR-6075 (Reference 35) analyzed a number of DCH experiments and concluded that Eq. (4-19) represents the debris flow through the annular gap.

A word of caution must be inserted here in that the predicted cavity pressure $P_{\text{cav}} = 1.48 \times 10^6 \text{ Pa}$ (Eq. 4-13) exceeds the differential pressure of $7.5 \times 10^5 \text{ Pa}$ to fail the seal table. Whether or not the seal table fails depends on the instantaneous pressure in the containment dome and the pressure drop through the ICI chase from the reactor cavity to the seal table. However, even if the seal table is indeed failed, it is expected the opening is a gap-type of opening, instead of the line-of-sight pathway allowing the direct transport of corium to the open space of the containment. Also, for the flow to go through the path of the failed seal table, it must first impinge the wall at the end of the cavity and make a 90 degree (upward) turn to ICI chase chamber, where the seal table is located. The previous discussion has shown that nearly all the entrained corium will be captured by the impingement and very little corium will be released through the failed seal table.

4.2 DCH model for APR1400

DCH induced loads in APR1400 were calculated using the TCE model. In the calculations, three scenarios were considered which are described in NUREG/CR-6338 (Reference 46).

4.2.1 Generation of probabilistic distribution and sampling for uncertain input parameters

The high uncertain parameters considered in the TCE model are to be quantified as probability density functions. In this calculation, initial mass of UO_2 in melt at vessel breach, fraction of Zr oxidized, coherence ratio, containment fragility curve are selected as probabilistic input parameters. The initial mass of UO_2 in melt at vessel breach, the fraction of Zr oxidized and variations in the coherence ratio were quantified as probability density curves. For the TCE model analysis, each probabilistic input parameter is sampled using the LHS (Latin Hypercube Sampling) method. In this calculation, the 10,000 samples per each probabilistic input parameter are used.

4.2.2 Quantification of point input parameters

Referring to the specific design information of APR1400 and the initial and boundary conditions for selected scenarios, the point input parameters are quantified. In this calculation, the point input parameters are as follows:

- Lower head wall thickness (m)
- Lower plenum volume (m^3)
- Initial lower head hole diameter (m)
- Lower head wall temperature at VB (K)
- Mass of Control Rod Material in melt (metric ton)
- Mass of UO_2 in core (metric ton)
- Mass of Zr in core (metric ton)
- Mass of steel in lower plenum (metric ton)
- Reactor cavity specific multiplier in coherence ratio
- RCS pressure at VB (MPa)
- RCS volume (m^3)
- RCS temperature at VB (K)
- Containment pressure at normal operation (MPa)
- Containment temperature at normal operation (K)
- Containment pressure at VB (MPa)
- Containment temperature at VB (K)
- Containment free volume (m^3)

- Reactor cavity free volume (m³)
- Fraction of debris remaining in subcompartment
- Volume fraction of subcompartment
- Auto-ignition temperature (K)
- Temperature of debris melt (K)
- Fraction of Zr block relocated
- Fraction of H₂ generated in RCS that stays in RCS
- Melt fraction ejected into the reactor cavity
- Fraction of ejected melt dispersed from reactor cavity

4.2.3 TCE calculation

The TCE calculation is performed to evaluate the DCH loads. The probabilistic and point input parameters are used to evaluate the equations. In each trial the calculated DCH pressure is compared against the failure pressure sampled from the containment fragility curve. The process is repeated 10,000 times and the number of cases where the DCH pressure exceeds the containment failure pressure is recorded. The number of "failed" cases divided by 10,000 gives the containment failure probability.

5 SUMMARY OF RESULTS FOR APR1400 DCH ANALYSIS

DCH induced loads in APR1400 were calculated using the TCE model. In the calculations, three scenarios were considered which are similar to those considered in NUREG/CR-6338 (Reference 46). The initiation event of these scenarios is considered to be a small LOCA and re-pressurization of RCS due to operator's intervention. Scenario V and Va assume the RCS pressure before the vessel failure is at the pressurizer PORV set point of 17 MPa, and the water level in the RCS is high enough to cover the core region. The containment pressure for the scenario V is about 2.5 bar while the pressure for the scenario Va is about 1.25 bar. A corium pool in the shape of a hemisphere forms in the core region. Eventually the crust surrounding the pool fails and the corium is relocated into the lower plenum, where it causes the vessel failure. The amount of corium relocated into the lower plenum is assumed to follow a distribution with the maximum and best estimate about 81 tons and 40 tons respectively. Scenario VI assumes the RCS pressure before the vessel failure is at one half of the pressurizer set point, about 9 bars. The water level in the vessel covers only the lower portion of the core, and an upright cone shape of corium pool forms in the core region. The crust fails and the corium relocates into the lower plenum. The distribution of the mass of corium in the lower plenum has the maximum and best estimate values of about 98 tons and 49 tons respectively. Besides the mass of corium, several other parameters are assumed for each scenario to follow probabilistic distributions, including the containment failure pressure, fraction of Zr oxidation, and coherence time ratio in the TCE model.

Although most of the corium is expected to be captured by the wall at the end of the cavity, the calculations assume adjacent compartments around the cavity are capable of exchanging energy with the corium particle. The subcompartment in the TCE model is comprised of the cavity, corium chamber, ICI chase compartment, reactor cavity access area, and regenerative heat exchanger room. The total volume of these spaces is about 2% of the entire volume of the containment. The fraction of corium going directly into the containment upper dome is about 0.28, which is estimated based on the projected area of the reactor vessel, divided by the floor area of the cavity. The fraction is much more conservative than that estimated in the previous section based on the area fraction.

Based on the conservative assumptions described above, the loads (pressures) caused by DCH were compared with the containment failure pressure. Figure 5-1 shows the maximum pressure distributions for all three scenarios compared with the distributions of the containment failure pressure. As shown, there is only small pressure interval of intersection between the DCH pressures and the failure pressure (for the very high DCH pressure and very low containment failure pressure). The conditional probability of containment failure in DCH is estimated less than 0.1%, which, according to reference 46, can be considered as an acceptable risk.



Figure 5-1 Comparison of pressures due to DCH and the containment failure pressure for APR1400.

6 CONCLUSIONS

An extensive database from integral tests on DCH has been developed over the last three decades. The database covers cavity designs with large instrument tunnels connected to subcompartments and cavity designs of the annular type where one of the paths to the containment is the annular space between the reactor and the vessel. The most important conclusions derived from these experiments are:

1. The containment pressure is limited significantly by the presence of compartments between the reactor cavity and the containment dome which prevent the transport of large quantities of fine, hot debris to the containment dome.
2. As a result of the compartmentalization mentioned above, the DCH containment pressures are not sufficient to challenge containment integrity for the plant types investigated.
3. A linear scaling approach to experiments at substantially different scales has been demonstrated to be valid for plants with compartmentalized geometry.
4. The hydrogen produced and burned during the DCH event contributes significantly to the containment pressure rise.
5. The experimental containment pressure rise results can be adequately correlated by considering the regions in the containment (e.g., the TCE model).
6. The experiments performed with water in the cavity and/or on the basement floor have not revealed a large effect of water on containment pressurization. However, significant cavity pressurization has been observed in some tests with water in the cavity.

While DCH experiments have not been directed towards examining the consequences of DCH occurring in the APR1400 reactor, significant DCH pressurization of the APR1400 containment is judged to be most unlikely. It has been well established by the DCH laboratory research that containment structures and compartments have a first order mitigating influence on the pressurization potential of DCH. The number of compartments between the cavity and the containment dome of the APR1400 reactor are not at all conducive to supporting a strong DCH event, as demonstrated in this report.

According to the NUREG/CR-6075 (Reference 35) methodology, the DCH issue is considered resolved if the containment failure probability due to DCH, obtained through a probabilistic evaluation of phenomenological analysis and its uncertainties, is found to be lower than a certain threshold value. The severe accident scenario that can lead to DCH in APR1400 is identified as a small LOCA with RCS re-pressurization due to operator intervention and three representative scenarios were considered.

For each of the three scenarios, zero (0) containment failure case has resulted from 10,000 trials. Based on this outcome, the CCFP in APR1400 due to DCH is estimated to be less than 0.01% (0.0001). This indicates that APR1400 meets the success criterion established in reference 46 for PWR large dry containment, where DCH problem is considered resolved if CCFP is less than 1% (0.01).

7 REFERENCES

1. Commonwealth Edison Company (CECo), 1981, Zion Probabilistic Safety Study, Chicago, Illinois.
2. WASH-1400, Nuclear Regulatory Commission (NRC), 1975, "Reactor Safety Study,".
3. NUREG/CR-3025, Tarbell, W. W., et al., 1984, "High-Pressure Melt Streaming (HIPS) Program Plan," SAND82-2477, Sandia National Laboratories.
4. Tarbell, W. W., et al., 1986, "Melt Expulsion and Direct Containment Heating in Realistic Plant Geometries," Proc. of the International ANS/ENS Topical Meeting on Thermal Reactor Safety, San Diego, California.
5. NUREG/CR-4512, Tarbell, W. W., et al., 1986, "Pressurized Melt Ejection into Scaled Reactor Cavities," SAND86-0153, Sandia National Laboratories.
6. NUREG/CR-4455, Pilch, M. and Tarbell, W. W., 1986, "Preliminary Calculations on Direct Heating of a Containment Atmosphere by Airborne Core Debris," SAND85-2439, Sandia National Laboratories.
7. Spencer, B. W., et al, 1983, "Corium/Water Dispersal Phenomena in Ex-Vessel Cavity Interactions," Paper TS-15.5, proc. Int'l. Mtg. on LWR Severe Accident Evaluation, Vol. 2, Cambridge, MA.
8. Spencer, B. W., et al., 1983b, "Overview and Recent Results of ANL/EPRI Corium/Water Thermal Interaction Investigations," Paper TS-15.2, Proc. Int'l. Mtg. on LWR Severe Accident Evaluation, Vol. 2, Cambridge, MA.
9. NP-5127, Spencer, B. W., et al., 1987, "Hydrodynamics and Heat Transfer Aspects of Corium-water Interactions," Argonne National Laboratory.
10. Spencer, B. W., et al., 1988, "Results of EPRI/ANL DCH Investigations and Model Development," ANS/ENS Conference on Thermal Reactor Safety, Avignon, France.
11. Tarbell, W. W., et al., 1987, "DCH Experiments and Analyses at Sandia National Laboratories," Containment Loads and Molten Core Containment Expert Opinion Meeting, Albuquerque, New Mexico.
12. NUREG/CR-4817, Tarbell, W. W., et al., 1987, "Results from the DCH-I Experiment," SAND86-2483, Sandia National Laboratory.
13. NUREG/CR-4917, Tarbell, W. W., et al., 1988, "DCH-2: Results from the Second Experiment Performed in the Surtsey Direct Heating Test Facility," SAND87-0976, Sandia National Laboratory.
14. Tarbell, W. W., et al., 1988, "Direct Containment Heating and Aerosol Generation During High-Pressure-Melt Expulsion Experiments," Trans. Am. Nucl. Soc., 57, 361.
15. Allen, M. D., et al, 1991, "Experimental Results of Direct Containment Heating by High-Pressure Melt Ejection Into the Surtsey Vessel: The DCH-3 and DCH-4 Tests," SAND90-2138, Sandia National Laboratory.
16. Marx, K. D., 1989, "A Computer Model for the Transport and Chemical Reaction of Debris in Direct Containment Heating Experiments," Nuclear Sci. & Eng., 102, 391-407.

17. Henry, R. E. , 1989, "An Evaluation of Fission Product Release Rates During Debris Dispersal," Proc. of the ANS/ENS Intl. Topical Mtg. on Probability, Reliability and Safety Assessment, Vol. 1, pp. 375-383.
18. Henry, R. E., et al., 1991, "Direct Containment Heating Experiments in a Zion-Like Geometry," AIChE Sym., Series, Vol. 87, No. 293, Heat Transfer - Minneapolis 1991, pp. 86-98.
19. NUREG/CR-6168, Binder, J. L., et al., 1994, "Direct Containment Heating Integral Effects Tests at 1/40 Scale in Zion Nuclear Power Plant Geometry," Argonne National Laboratory, ANL-94/18.
20. Allen, M. D., Pilch, M., Griffith, R. O. and Nichols, R. T., 1992, "Experimental to Investigate the Effect of Water in the Cavity on Direct Containment Heating (DCH) in the Surtsey Test Facility - The WC-1 and WC-2 Tests," SAND91-1173, Sandia National Laboratories, Albuquerque, NM, March.
21. Allen, M. D., et al., 1992, "Quick-Look Report on the Second Integral Effects Tests (IET-2): Thermite Temperature Measurements," Sandia National Laboratories.
22. Allen, M. D., Blanchat, T. K., Pilch, M. and Nichols, R. T., 1992, "The Effects of Condensate Levels of Water on Direct Containment Heating (DCH) in Zion-like Geometry: The Fourth Integral Effects Test (IET-4) Conducted in the Surtsey Test Facility," SAND92-1241, Sandia National Laboratories, Albuquerque, NM, September.
23. Allen, M. D., Blanchat, T. K., Pilch, M. and Nichols, R. T., 1992, "Experimental Results of an Integral Effects Test in a Zion-like Geometry to Investigate the Effects of a Classically Inert Atmosphere on Direct Containment Heating: The IET-5 Experiment," SAND92-1623, Sandia National Laboratories, Albuquerque, NM, November.
24. Allen, M. D., et al., 1992, "Quick-Look Report on the Sixth Integral Effects Test (IET-6) in the Surtsey Test Facility," Sandia National Laboratory.
25. Allen, M. D., Blanchat, T. K., Pilch, M. and Nichols, R. T., 1992, "An Integral Effects Test to Investigate the Effects of Condensate Levels of Water and Preexisting Hydrogen on Direct Containment Heating in the Surtsey Test Facility: The IET-7 Experiment," SAND92-2021, Sandia National Laboratories, Albuquerque, NM, December.
26. Allen, M. D., Blanchat, T. K., Pilch, M. and Nichols, R. T., 1993, "Experiments to Investigate the Effects of Fuel/Coolant Interactions on Direct Containment Heating - The IET-8A and IET-8B Experiments," SAND92-2849, Sandia National Laboratories, Albuquerque, NM, February.
27. NUREG/CR-6044, Allen, M. D., et al., 1994, "Experiments to Investigate Direct Containment Heating Phenomena with Scaled Models of the Zion Nuclear Power Plant in the SURTSEY Test Facility," Sandia National Laboratory, SAND93-1049.
28. NUREG/CR-6267, Ishii, M., Revankar, S. T., Zhang, G., Wu, Q. and O'Brien, P., 1994, "Air-Water Simulation of Phenomena of Corium Dispersion and Direct Containment Heating," PU NE-93-1.
29. Zhang, G. J. and Ishii, M., 1995, "Entrance Effect on Droplet Entrainment in DCH," ANS Proceedings, HTC-Volume 8, 1995 National Heat Transfer Conference, Portland, Oregon, pp. 375-383.
30. Hammersley, R. J. et al., 1995, "Direct Containment Heating Experiments for Vandelllos and Asco Nuclear Power Plants," ANS Proceedings, Vol. 8, pp. 384-392, 1995 National Heat Transfer Conference, Portland, OR.

31. NUREG/CR-6152, Blanchat, T. K., et al., 1994, "Experiments to Investigate Direct Containment Heating Phenomena with Scaled Models of the Surry Nuclear Power Plant," Sandia National Laboratories, SAND93-2519.
32. NUREG/CR-6469, Blanchat, T. K., Pilch, M. M. and Allen, M. D., 1997, "Experiments to Investigate Direct Containment Heating Phenomena with Scaled Models of the Calvert Cliffs Nuclear Power Plant," SAND96-2289, Sandia National Laboratories, Albuquerque, NM.
33. NUREG/CR-5746, Blanchat, T. K., et al., 1999, "Direct Containment Heating Experiments at Low Reactor Coolant System Pressure in the Surtsey Test Facility," SAND99-1634, Sandia National Laboratories, Albuquerque, NM. Meyer, L., Albrecht, G., Caroli, C. and Ivanov, I., 2009, "Direct Containment Heating Integral Effects Tests in Geometries of European Reactors," Nucl. Engng. & Design 239, pp. 2070-2084.
34. Pilch, M. M., Yan, H. and Theofanous, T. G., 1994, "The Probability of Containment Failure by Direct Containment Heating in Zion," SAND93-1535, Sandia National Laboratory, Albuquerque, NM.
35. Pilch, M. M., 1996, "A Two-Cell Equilibrium Model for Predicting Direct Containment Heating," Nuclear Engineering and Design, Vol. 164, p.61~94.
36. Marple, V. A., 1970, "A Fundamental Study of Inertial Impactors," PhD. Thesis, University of Minnesota, Minneapolis, MN.
37. Marple, V. A. and Liu, B. Y. H., 1974, "Characteristics of Laminar Jet Impactors," Environmental Sci. and Tech. 8, pp. 648-654.
38. Marple, V. A. and Rubow, K. L., 1986, "Theory and Design Guidelines," In Cascade Impactor Sampling and Data Analysis, American Industrial Hygiene Association Monograph, J. P. Lodge and T. L. Chan (editors), pp. 79-101.
39. Mercer, T. T. and Stafford, R. G., 1969, "Impaction from Round Jets," Annals Occupation Hygiene 12, pp. 41-48.
40. Yuu, S. and Jotaki, T., 1978, "The Calculation of Particle Deposition Efficiency Due to Inertia, Diffusion and Interception in the Plane Stagnation Flow," Chem. Engng, Sci. 33, pp. 971-978.
41. Chiang, H. W., 1983, "A Model for the Removal of Water Droplet Aerosols from a Flashing Jet Impinging Onto a Plate," Presented at OECD/CSNI Specialist Meeting Nuclear Aerosols in Reactor Safety, Cologne, Germany (June 15-18).
42. Leung, J. C. and Epstein, M., 1990, "A Generalized Correlation for Two-Phase Nonflashing Homogeneous Choked Flow," J. Heat Transfer 112, pp. 528-530.
43. Allen M. D., et al., 1994, "Test Results on Direct Containment Heating by High-Pressure Melt Ejection into the Surtsey Vessel: the TDS Test Series," Sandia National Laboratories Report, SAND91-1208.
44. Erickson, G. G. and Olfe, D. B., 1978, "Growth and Decay of Perturbations at an Interface in a Stagnation Counterflow," J. Fluid Mech. 84, pp. 401-409.
45. Pilch, M. M., Allen M. D., and Klamerus E. W., "Resolution of the Direct Containment Heating Issue for All Westinghouse Plants With Large Dry Containments or Subatmospheric containments," NUREG/CR-6338, SAND95-2381, Sandia National Laboratories, Feb. 1996.

Appendix-C2

**Severe Accident Analysis Report
for Rapid Depressurization**

TABLE OF CONTENTS

1	INTRODUCTION	C2-5
2	REQUIREMENTS AND CRITERIA	C2-5
3	ANALYSIS METHODOLOGY	C2-7
3.1	Selection of Accident Scenarios	C2-7
3.2	MAAP Model of APR1400	C2-9
4	ANALYSIS RESULTS	C2-19
4.1	R1_TLOESW003	C2-19
4.2	R3 LOOP004	C2-23
4.3	R4 SBO002	C2-27
4.4	R5 SBO005	C2-31
4.5	R9 SBO006	C2-35
4.6	R10 SGTR10	C2-39
5	CONCLUSION	C2-43
6	REFERENCES	C2-44

LIST OF TABLES

Table 3-1	Dominant PRA Sequences	C2-8
Table 3-2	APR1400 Containment Node Description	C2-10
Table 4-1	R1_TLOESW003 Success Criteria Based on Operator Interventions.....	C2-22
Table 4-2	R3_LOOP004 Success Criteria Based on Operator Interventions	C2-26
Table 4-3	R4_SBO002 Success Criteria Based on Operator Interventions	C2-30
Table 4-4	R5_SBO005 Success Criteria Based on Operator Interventions	C2-34
Table 4-5	R9_SBO006 Success Criteria Based on Operator Interventions	C2-38
Table 4-6	R10_SGTR10 Success Criteria Based on Operator Interventions	C2-42

LIST OF FIGURES

Figure 3-1	Containment Nodalization Diagram for APR1400	C2-11
Figure 3-2	Containment Nodes in Section A-A	C2-12
Figure 3-3	Containment Nodes in Section B-B.....	C2-13
Figure 3-4	Containment Nodes at EL. 78' – 0".....	C2-14
Figure 3-5	Containment Nodes at EL. 100' 0".....	C2-15
Figure 3-6	Containment Nodes at EL. 114' – 0".....	C2-16
Figure 3-7	Containment Nodes at EL. 136' – 0".....	C2-17
Figure 3-8	Containment Nodes at EL. 156' – 0".....	C2-18
Figure 4-1	R1_TLOESW003 Primary Pressures.....	C2-20
Figure 4-2	R1_TLOESW003 Pressurizer Gas Temperatures.....	C2-21
Figure 4-3	R3_LOOP004 Primary Pressures.....	C2-24
Figure 4-4	R3_LOOP004 Pressurizer Gas Temperatures	C2-25
Figure 4-5	R4_SBO002 Primary Pressures	C2-28
Figure 4-6	R4_SBO002 Pressurizer Gas Temperatures	C2-29
Figure 4-7	R5_SBO005 Primary Pressures	C2-32
Figure 4-8	R5_SBO005 Pressurizer Gas Temperatures	C2-33
Figure 4-9	R9_SBO006 Primary Pressures	C2-36
Figure 4-10	R9_SBO006 Pressurizer Gas Temperatures	C2-37
Figure 4-11	R10_SGTR10 Primary Pressures.....	C2-40
Figure 4-12	R10_SGTR10 Pressurizer Gas Temperatures	C2-41

1 INTRODUCTION

The Rapid Depressurization (RD) function plays diverse roles during Design Basis Accidents (DBA), Beyond DBAs (BDBA), and severe accidents. The depressurization for a severe accident using RD function enables operation of the low pressure systems, such as Shutdown Cooling (SC) system. Additional contingencies for core cooling are made available by maintaining a low Reactor Coolant System (RCS) pressure when primary core heat removal functions are lost. Finally, maintaining a low RCS pressure prevents the High Pressure Melt Ejection (HPME), and prolongs the reactor vessel integrity.

In this report, the RD analysis was performed for APR1400. The RD function is performed for prevention of HPME, which would result in corium entrainment and direct containment heating. The depressurization capability was evaluated using MAAP (Modular Accident Analysis Program) 4.0.8 (Reference 1).

2 REQUIREMENTS AND CRITERIA

The RD function is implemented in compliance with SECY-93-087 (Reference 2), which prescribes the necessity of mitigation of the potential containment risks due to Direct Containment Heating (DCH) resulting from HPME via depressurization of the RCS before the reactor vessel fails.

To mitigate the DCH phenomena resulting from HPME, the RCS pressure should be kept below a certain level before vessel failure, and the reactor cavity should be able to reduce the entrained transport of the core melt to the containment dome region. The criterion of RCS pressure for the RD is prescribed as below 1.72 MPa (250 psia). This criterion of 1.72 MPa (250 psia) was obtained from a number of relevant experiments and has been considered as a cutoff pressure below which the entrainment of the melt can be prevented. Additional information can be found in the Reference 3 and Reference 4.

It is assumed that the operator begins RD after recognizing that the plant enters the severe accident stage. For this report, three conditions are defined as severe accident entry conditions. The first condition is the generally recognized, Core Exit Temperature (CET) exceeding 922K (1,200°F). The second condition is once a Pilot Operated Safety and Relief Valve (POSRV) has been first automatically opened, provided that there is also a loss of ac power, after the steam generator is empty. This condition is imposed since the POSRV must be opened before loss of dc power. Similarly, the last condition to begin RD is one hour before battery depletion.

In addition to the criterion of RCS pressure at the time of vessel failure, there is another criterion that the POSRV temperature should not exceed 644K (700°F), or the design temperature of POSRVs when opened manually. The operability of the POSRV can be assured only when the temperature is lower than the design temperature.

Thus, the following three conditions are the basis of this report:

- The RD function operation is performed at the onset of severe accident, which for the purpose of this report is defined as either:
 - After CET exceeds 922 K (1,200 °F), or,
 - Once a POSRV has been first automatically opened, provided that there is also a loss of ac power, after the steam generator is empty, or,
 - One hour before battery depletion for a station blackout.
- POSRVs can be opened only when the pressurizer gas temperature is lower than 644 K (700 °F)

- RCS should be depressurized below 1.72 MPa (250 psia) before the vessel fails.

The depressurization evaluation is considered successful if the last condition is met for each of the sequences considered.

3 ANALYSIS METHODOLOGY

In order to determine the containment performance of the APR1400 design under severe accident conditions, the MAAP 4.0.8 code is used to analyze a range of possible sequences. The method of selecting the sequences to be analyzed is discussed in Section 3.1. And the MAAP model of APR1400 is discussed in Section 3.2.

3.1 Selection of Accident Scenarios

Accident scenarios were selected by probabilistic means. The ten most likely core damage scenarios were selected based on the PRA results as shown in Table 3-1.

The following sequences will result in a low-pressure vessel failure, based on the sequence definition alone. Therefore, no further analysis will be performed for the following sequences:

- R2_MLOCA003
- R6_SLOCA008
- R7_PR-A-SL007
- R8_MLOCA002

•

Table 3-1 Dominant PRA Sequences

TS



3.2 MAAP Model of APR1400



Table 3-2 APR1400 Containment Node Description

TS



¹ All elevations in the table are the values that have been used in the MAAP containment modeling. Thus, the elevations in the table may have difference with actual elevations.

TS



Figure 3-1 Containment Nodalization Diagram for APR1400

TS

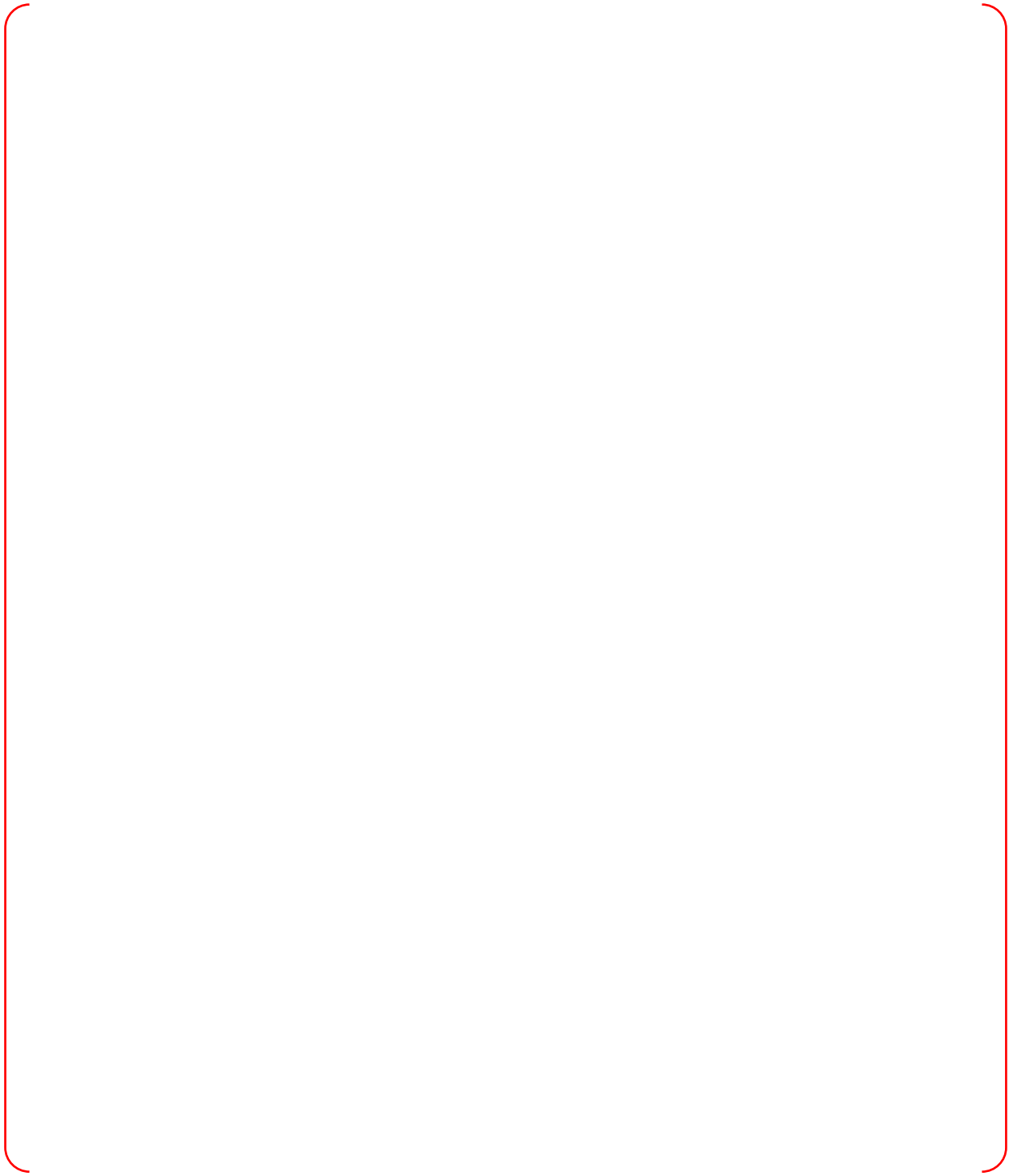


Figure 3-2 Containment Nodes in Section A-A

TS

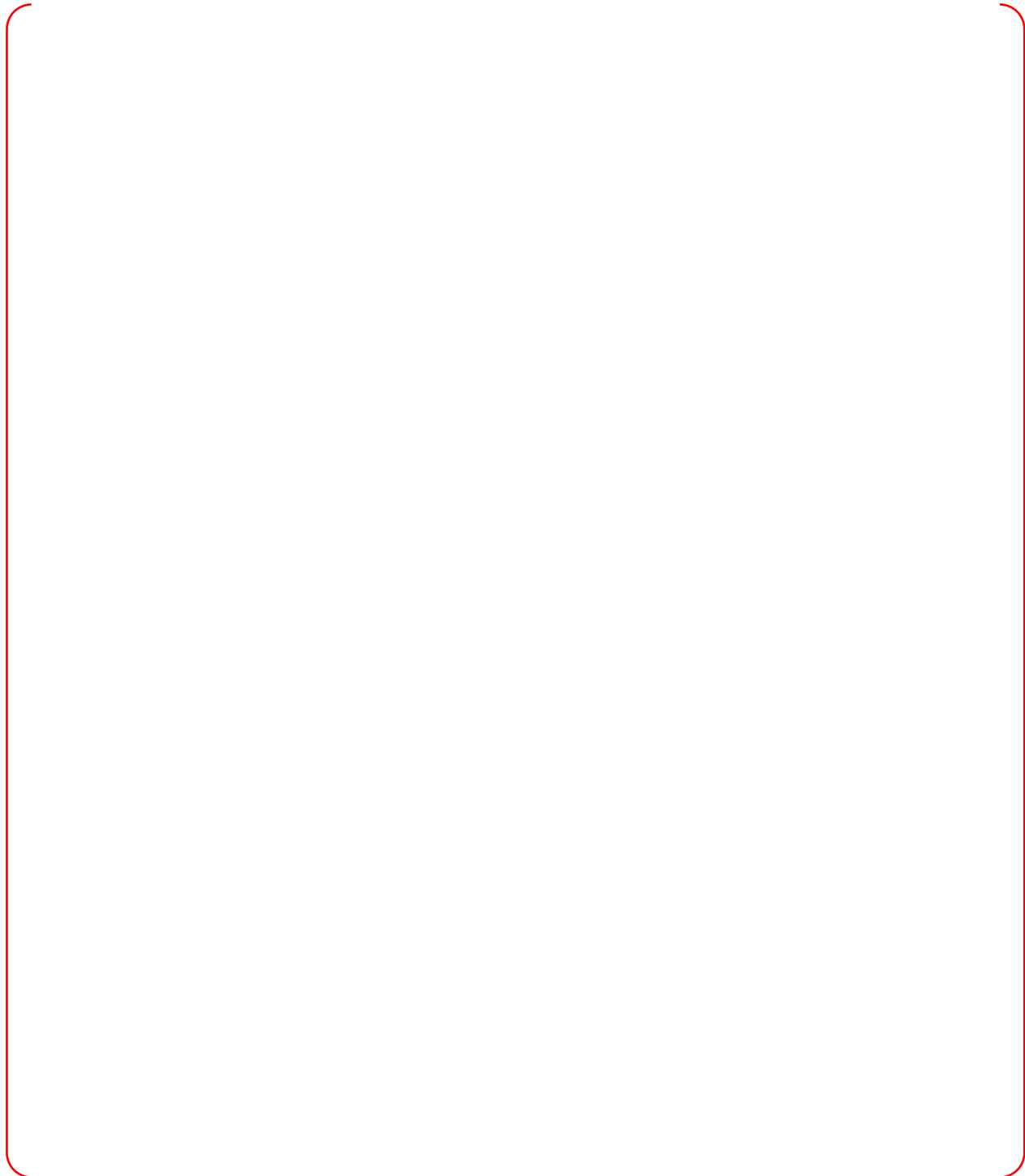


Figure 3-3 Containment Nodes in Section B–B



TS

Figure 3-4 **Containment Nodes at EL. 78' – 0"**



Figure 3-5 Containment Nodes at EL. 100' 0"



Figure 3-6 Containment Nodes at EL. 114' – 0"

TS



Figure 3-7 Containment Nodes at EL. 136' – 0"

TS

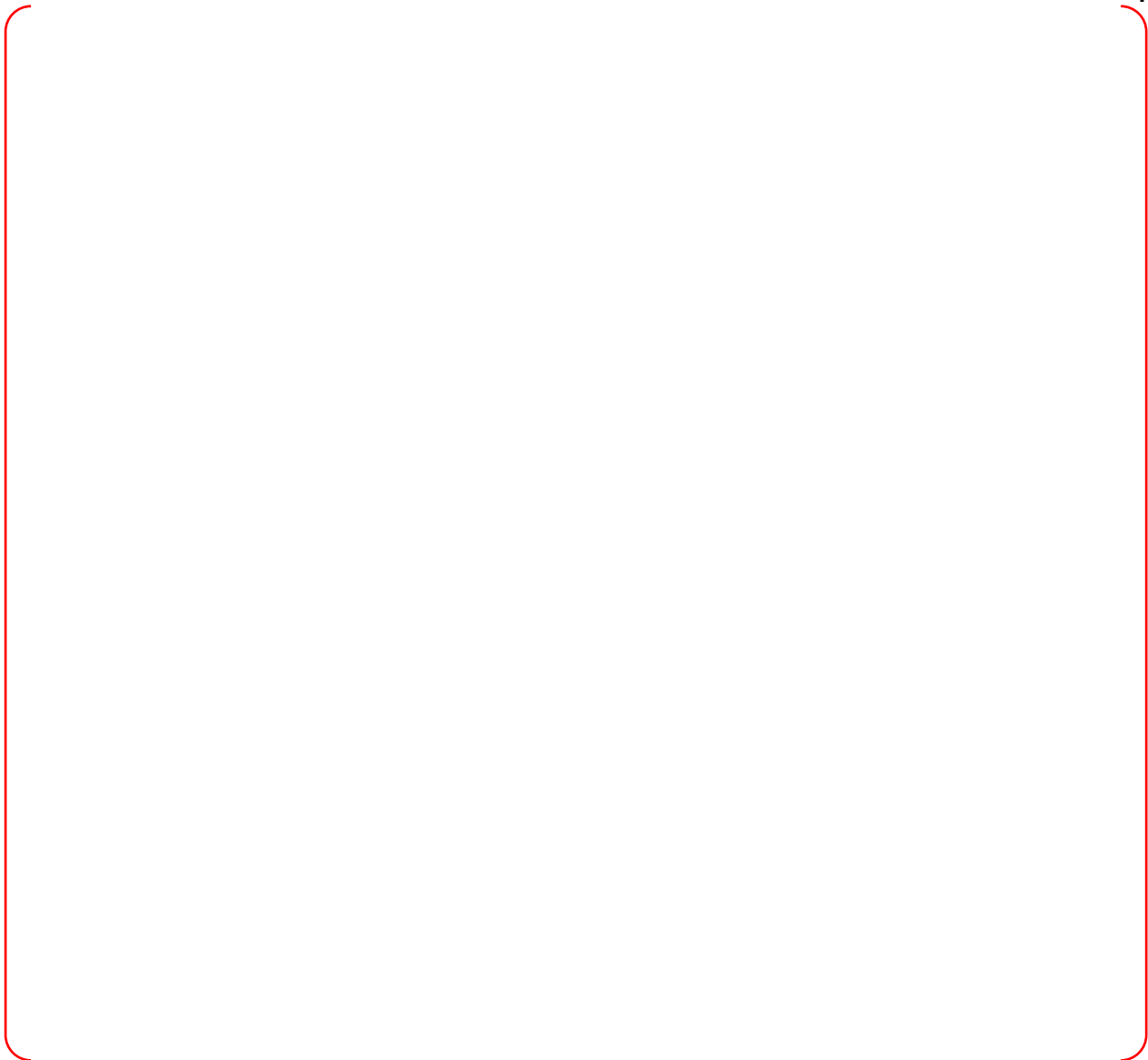


Figure 3-8 Containment Nodes at EL. 156' – 0"

4 ANALYSIS RESULTS

The sequences analyzed in this section were selected to be a representative sample of Level I PRA sequences, disabling the hot leg creep rupture model as necessary to predict a higher-pressure vessel failure. All sequences in this section are run with the Cavity Flooding System (CFS) and the Emergency Containment Spray Backup System (ECSBS) available. The CFS is actuated after the onset of core damage to ensure that a significant pool of water exists in the reactor cavity at the time of vessel failure. This mitigates concrete ablation but provides a challenge in terms of containment pressurization. Actuation of the CFS during a severe accident is the expected behavior of the plant. The intent of this section is to demonstrate that for all of the sequences not predicting vessel failure below 1.72 MPa (250 psia), operator intervention of manually opening the POSRVs can indeed depressurize the primary system below 1.72 MPa (250 psia) prior to vessel failure.

4.1 R1_TLOESW003

This sequence is defined as a loss of Essential Service Water (ESW) at full power resulting in reactor scram at sequence initiation. Four Safety Injection (SI) tanks are available. AF pumps, SI pumps, Containment Spray (CS) pumps, and charging pumps are assumed to be unavailable. Due to the loss of ESW, a 21 gpm per pump seal LOCA is assumed to occur half an hour into the sequence.

Once reactor scram occurs and main feedwater is isolated, the steam generators begin to boil off their inventories. Because AF is assumed unavailable, both steam generators quickly boil dry and stop removing decay heat. Half an hour into the sequence, a 21 gpm per pump seal LOCA occurs, but the flow rate is not sufficient to depressurize the RCS. The primary system heats up and pressurizes, soon reaching the POSRV relief setpoints and causing the valves to open. Primary system inventory is steadily lost through the POSRVs and RCP seals, causing the core water level to decrease. The discharge from the POSRVs is sparged into the In-containment Refueling Water Storage Tank (IRWST), condensing the steam and preventing additional containment pressurization. The core is soon uncovered, causing the CET to reach 1,200°F, signaling the onset of core damage.

Several sensitivities are executed, varying the number of POSRVs manually opened (0, 2, or 4), and time of operating the POSRV after entering severe accident conditions (0.00 hr, 0.50 hr, and 1.00 hr). Plots of primary pressure and pressurizer gas temperature are shown in Figure 4-1 and Figure 4-2 while detailed sensitivity analysis is presented in Table 4-1. Depressurization is successful for this sequence if two POSRVs are opened within 0.50 hours after entering severe accident conditions, or if four POSRVs are opened within 1.00 hours after entering severe accident conditions.



Figure 4-1 R1_TLOESW003 Primary Pressures



Figure 4-2 R1_TLOESW003 Pressurizer Gas Temperatures

Table 4-1 R1_TLOESW003 Success Criteria Based on Operator Interventions

TS



4.2 R3 LOOP004

This sequence is defined as a Loss of Offsite Power (LOOP) at full power resulting in reactor scram at sequence initiation. Diesel Generators (DG) are assumed to be started to provide backup power. Four SI tanks are available. AF pumps, SI pumps, SC pumps, and charging pumps are assumed to be unavailable.

Once the LOOP occurs, the steam generators begin to boil off their inventories. DGs are assumed to start successfully, but no Engineering Safety Feature (ESF) systems are recovered. Because AF system is unavailable, both steam generators quickly boil dry and stop removing decay heat. The primary system heats up and pressurizes, soon reaching the POSRV relief setpoints and causing the valves to open. Primary system inventory is steadily lost through the POSRVs, causing the core water level to decrease. The discharge from the POSRVs is sparged into the IRWST, condensing the steam and preventing containment pressurization. The core is soon uncovered, causing the CET to reach 1,200°F, signaling the onset of core damage.

Hot leg creep rupture is disabled for this sequence. Several sensitivities are executed, varying the number of POSRVs manually opened (0, 2, or 4), and time of operating the POSRV after entering severe accident conditions (0.00 hr, 0.50 hr, and 1.00 hr). Plots of primary pressure and pressurizer gas temperature are shown in Figure 4-3 and Figure 4-4, while detailed sensitivity analysis is presented in Table 4-2. Depressurization is successful for this sequence if at least two POSRVs are opened within 1.00 hours after entering severe accident conditions.



Figure 4-3 R3_LOOP004 Primary Pressures



Figure 4-4 R3_LOOP004 Pressurizer Gas Temperatures

Table 4-2 R3_LOOP004 Success Criteria Based on Operator Interventions

TS

4.3 R4 SBO002

This sequence is defined as a station blackout occurring at full power. Four SI tanks are available. Alternate AC (AAC) power is assumed to become available 30 minutes into the sequence. When AAC becomes available, only motor-driven AF system is recovered. SI pumps, CS pumps, and charging pumps are unavailable for the entirety of the sequence. It is assumed that no RCP seal LOCA occurs for this sequence.

At sequence initiation, all ac and dc power is lost, leading to a loss of all ESF systems. 30 minutes into the sequence, AAC power is recovered, allowing for the operation of motor-driven AF system. Motor-driven AF system is capable of removing decay heat from the primary system until Condensate Storage Tank (CST) inventory is eventually depleted. Once CST inventory is depleted, the steam generators begin to boil off their inventories. Both steam generators eventually boil dry and stop removing decay heat. The primary system heats up and pressurizes, soon reaching the POSRV relief setpoints and causing the valves to open. Primary system inventory is steadily lost through the POSRVs, causing the core water level to decrease. The discharge from the POSRVs is sparged into the IRWST, condensing the steam and preventing containment pressurization. The core is soon uncovered, causing the CET to reach 1,200°F, signaling the onset of core damage.

Hot leg creep rupture is disabled for this sequence. Several sensitivities are executed, varying the number of POSRVs manually opened (0, 2, or 4), and time of operating the POSRV after entering severe accident conditions (0.00 hr, 0.50 hr, 1.00 hr, 1.50 hr, and 2.00 hr). Plots of primary pressure and pressurizer gas temperature are shown in Figure 4-5 and Figure 4-6, while detailed sensitivity analysis is presented in Table 4-3. Depressurization is successful for this sequence if at least two POSRVs are opened within 2.00 hours after entering severe accident conditions.



TS

Figure 4-5 R4_SBO002 Primary Pressures

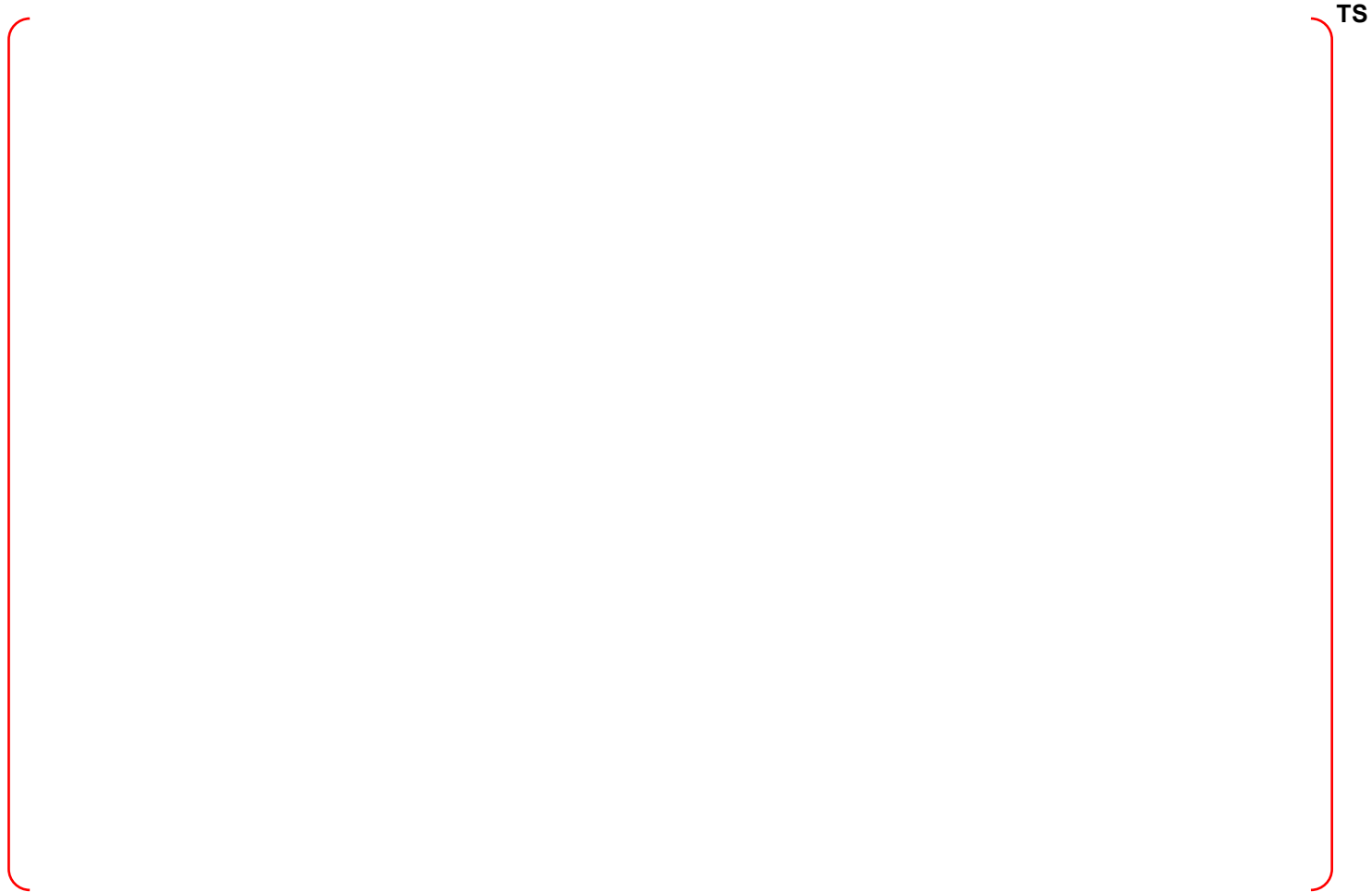


Figure 4-6 R4_SBO002 Pressurizer Gas Temperatures

Table 4-3 R4 SBO002 Success Criteria Based on Operator Interventions

TS

4.4 R5 SBO005

This sequence is defined as a station blackout occurring at full power. AAC power is assumed to be unavailable. Four SI tanks are available. Backup batteries are available, allowing the operation of turbine-driven AF system for 16 hours. SI pumps, CS pumps, and charging pumps are unavailable for the entirety of the sequence. RCS depressurization using the RD function, alignment of the three-way valves to the steam generator compartment, and CFS actuation are assumed to occur one hour prior to battery depletion. It is assumed that no RCP seal LOCA occurs for this sequence.

At sequence initiation, ac power is lost, leading to a loss of all ESF systems. Due to the availability of the backup batteries, turbine-driven AF system is able to operate for the first 16 hours, supplying feedwater to both steam generators and cooling the RCS. 15 hours into the sequence, operators are assumed to align the three-way valves to the steam generator compartment in order to prevent hydrogen accumulation in the IRWST, actuate the CFS to allow for gravity-driven water flow from the IRWST into the reactor cavity, and open the POSRVs to depressurize the primary system. Depressurization of the primary system allows the available SI tanks to inject. The core initially remains covered; however, the steam generators are unable to remove decay heat from the RCS due to the low primary system pressure. The inventory in the primary system is steadily boiled off and the core is eventually uncovered, causing the CET to reach 1,200°F and signaling the onset of core damage. The core begins to melt and relocate to the Reactor Pressure Vessel (RPV) lower plenum. This produces a brief pressure spike in the RCS due to the rapid steaming of the water pool that exists in the lower plenum.

Hot leg creep rupture is disabled for this sequence. Several sensitivities are executed, varying the number of POSRVs manually opened (0, 2, or 4). Sequence time of 15 hours, or one hour before battery is depleted, is reached before severe accident criteria are met; therefore, only the number of POSRVs to be manually opened is varied for this sequence. Plots of primary pressure and pressurizer gas temperature are shown in Figure 4-7 and Figure 4-8, while detailed sensitivity analysis is presented in Table 4-4. Depressurization is successful for this sequence if at least two POSRVs are opened.



TS

Figure 4-7 R5_SBO005 Primary Pressures

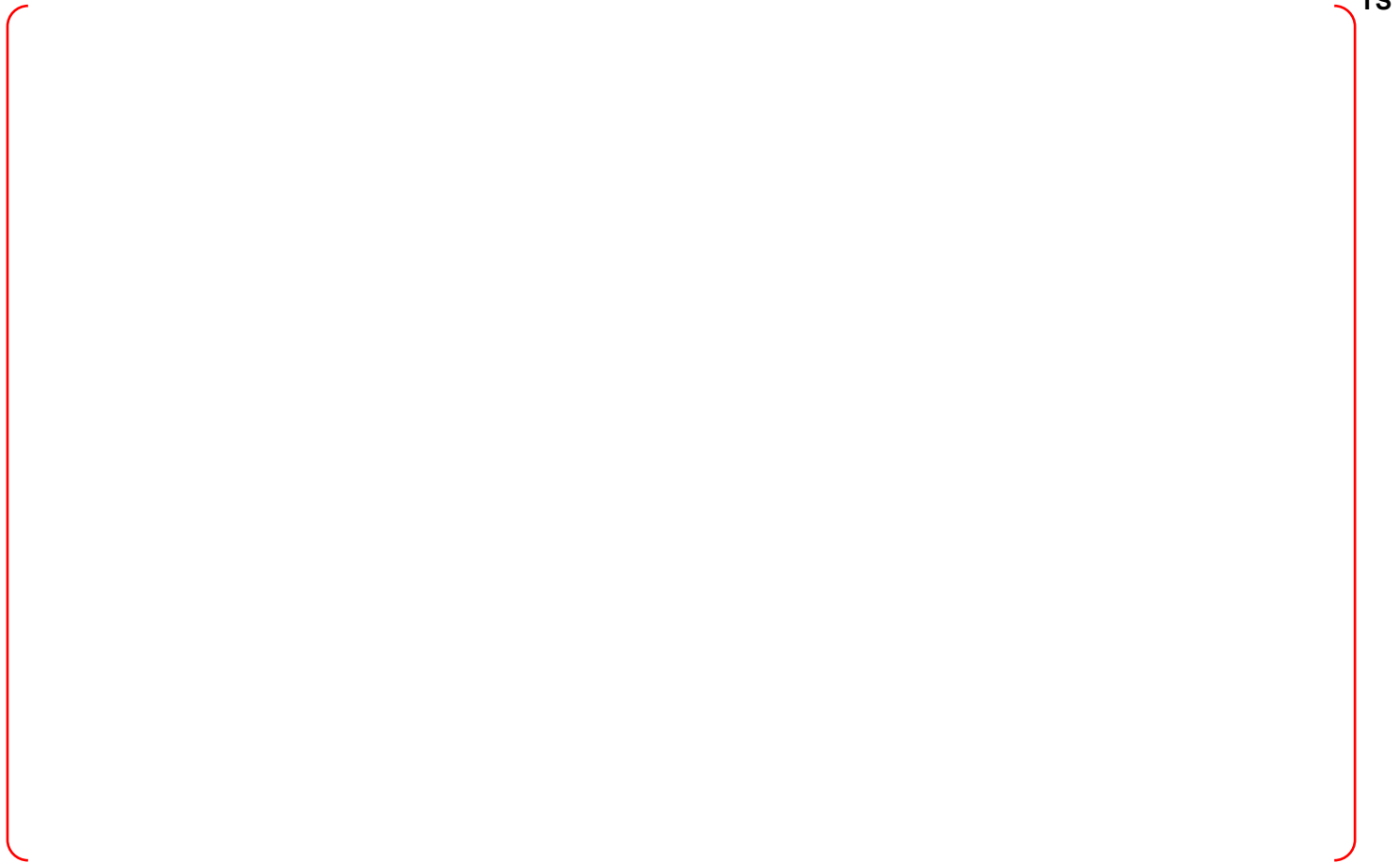


Figure 4-8 R5_SBO005 Pressurizer Gas Temperatures

Table 4-4 R5_SBO005 Success Criteria Based on Operator Interventions

TS

A large, empty red bracketed area that spans most of the width of the page, positioned below the caption. It appears to be a placeholder for a table that is not present in this version of the document.

4.5 R9 SBO006

This sequence is defined as a station blackout occurring at full power. AAC power is assumed to be unavailable. Four SI tanks are available. Backup batteries are available, allowing the operation of turbine-driven AF system for 2 hours. SI pumps, CS pumps, and charging pumps are unavailable for the entirety of the sequence. RCS depressurization using the RD function, alignment of the three-way valves to the steam generator compartment, and CFS actuation are assumed to occur one hour prior to battery depletion. It is assumed that no RCP seal LOCA occurs for this sequence.

At sequence initiation, ac power is lost, leading to a loss of all ESF systems. Turbine-driven AF system is initiated and operates until battery depletion occurs at 2 hours, supplying feedwater to both steam generators and cooling the RCS. One hour into the sequence, operators are assumed to align the three-way valves to the steam generator compartment in order to prevent hydrogen accumulation in the IRWST, actuate the CFS to allow for gravity-driven water flow from the IRWST into the reactor cavity, and open the POSRVs to depressurize the primary system. Depressurization of the primary system allows the available SI tanks to inject. The core initially remains covered; however, the steam generators are unable to remove decay heat from the RCS due to the low primary system pressure. The inventory in the primary system is steadily boiled off and the core is eventually uncovered, causing the CET to reach 1,200°F and signaling the onset of core damage. The core begins to melt and relocate to the RPV lower plenum. This produces a brief pressure spike in the RCS due to the rapid steaming of the water pool that exists in the lower plenum.

Hot leg creep rupture is disabled for this sequence. Several sensitivities are executed, varying the number of POSRVs manually opened (0, 2, or 4). Sequence time of one hour, or one hour before battery is depleted, is reached before severe accident criteria are met; therefore, only the number of POSRVs to be manually opened is varied for this sequence. Plots of primary pressure and pressurizer gas temperature are shown in Figure 4-9 and Figure 4-10, while detailed sensitivity analysis is presented in Table 4-5. Depressurization is successful for this sequence if at least two POSRVs are opened.



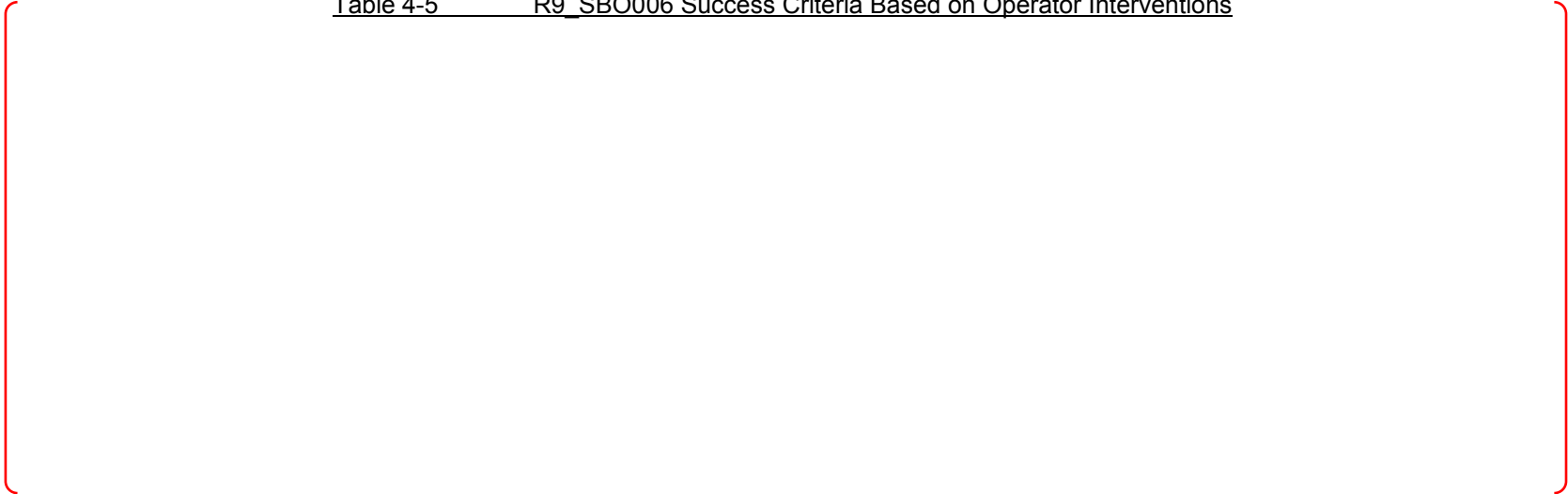
Figure 4-9 R9_SBO006 Primary Pressures



Figure 4-10 R9_SBO006 Pressurizer Gas Temperatures

Table 4-5 R9_SBO006 Success Criteria Based on Operator Interventions

TS

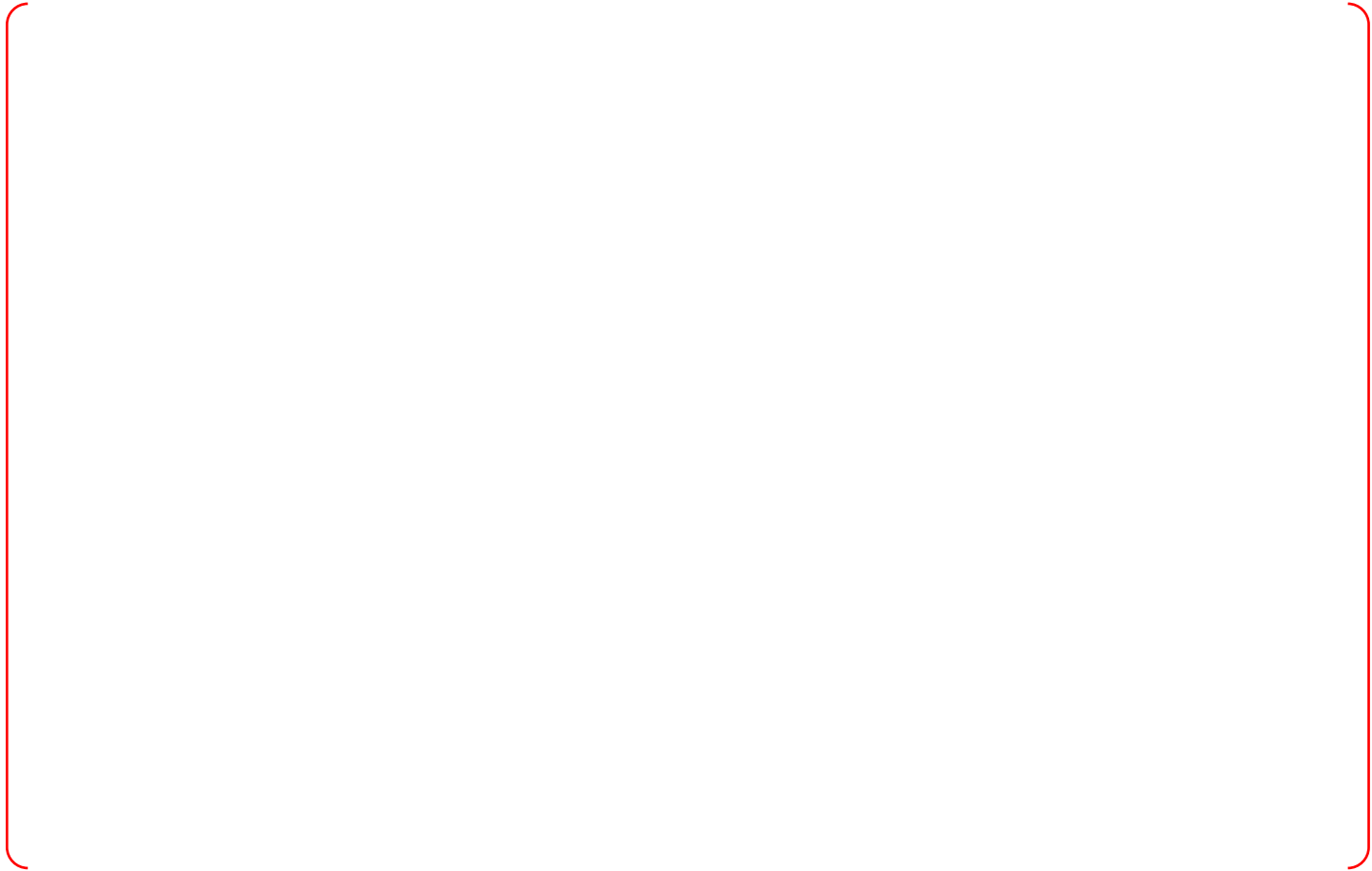


4.6 R10 SGTR10

This sequence is defined as a steam generator tube rupture occurring at full power. The break is a double ended rupture of one generator tube nine meters above the tube sheet of a single steam generator. Four SI tanks and motor-driven AF system are available. SI pumps, CS pumps, and charging pumps are assumed to be unavailable. Three hours into the sequence, operators are assumed to initiate cooldown and depressurization of the RCS at a rate of 100°F per hour by the manual actuation of two steam generator Pilot Operated Relief Valves (PORV) in the intact steam generator.

Due to the tube rupture, primary system pressure drops as RCS water flows into the ruptured steam generator. Reactor scram occurs and motor-driven AF system is initiated, pumping to both steam generators. Motor-driven AF system is capable of maintaining level in the steam generators and keeping the core cooled. Three hours into the sequence, operators initiate cooldown and depressurization of the RCS using two steam generator PORVs in the intact steam generator. Due to the cooldown, the primary system depressurizes, allowing SI tanks to begin injecting. Injection of the SI tanks maintains primary system pressure. This configuration is capable of cooling the core until CST inventory eventually runs out. Once CST inventory is depleted, the core begins to boil. Steam generator and core levels are boiled down, leading to core uncover. Once the core is uncovered, it begins to heat up. CET soon reaches 1,200°F, signaling the onset of core damage.

Several sensitivities are executed, varying the number of POSRVs manually opened (0, 2, or 4), and time of operating the POSRV after entering severe accident conditions (0.00 hr, 0.50 hr, 1.00 hr, 1.50 hr, and 2.00 hr). Plots of primary pressure and pressurizer gas temperature are shown in Figure 4-11 and Figure 4-12, while detailed sensitivity analysis is presented in Table 4-6. Depressurization is successful for this sequence if at least two POSRVs are opened within 2.00 hours after entering severe accident conditions.



TS

Figure 4-11 R10_SGTR10 Primary Pressures



Figure 4-12 R10_SGTR10 Pressurizer Gas Temperatures

Table 4-6 R10_SGTR10 Success Criteria Based on Operator Interventions

TS

5 CONCLUSION

The goal for resolving the HPME/DCH issue is to demonstrate that HPME/DCH carries insignificant risk of uncontrolled fission product release during postulated severe accident scenarios. This is accomplished by evaluating the likelihood of containment failure as a consequence of DCH. It includes investigation of the possibility of RCS depressurization for prevention of HPME/DCH. Using the guidance contained in the SECY 93-087, APR1400 can be depressurized by opening the POSRVs, thus minimizing the potential for HPME/DCH. In this report, the RD analysis was performed for APR1400.

The RD function is diverse roles during DBAs, BDBAs, and even severe accidents. Depressurization for a severe accident using the POSRVs enables operation of the low pressure systems, such as the SC System, thus enabling additional means of core cooling. The RCS is maintained at a low pressure for cases involving a loss of core heat removal functions. This prevents the occurrence of HPME phenomenon, and prolongs the reactor vessel integrity.

In this report, the main focus is on the following three conditions that are required for a successful depressurization: (i) RD function is performed after the CET exceeds 922K (1,200°F); (ii) the POSRVs can only be guaranteed to open when the temperature is lower than 644K (700°F); and, (iii) the RCS should be depressurized below 1.72 MPa (250 psia) before the RV fails. The depressurization evaluation was considered successful if these three conditions were met.

As shown in Section 4 of this report, HPME can be prevented for the 10 analyzed sequences. For certain sequences (R2_MLOCA003, R6_SLOCA008, R7_PR-A-SL007, R8_MLOCA002), vessel failure occurs at a sufficiently low pressure, while for other sequences, operator intervention is necessary. Operation of only two POSRVs within a half hour of the plant entering a severe accident is sufficient for all the sequences that are being considered. The results are in compliance with SECY-93-087.

6 REFERENCES

1. FAI/12-0005, "MAAP 4.0.8 Transmittal document," EPRI, Palo Alto, CA, Feb 15, 2012.
2. SECY-93-087, "Policy, Technical, and Licensing issues Pertaining to Evolutionary and Advanced Light-Water Reactor (ALWR) designs", USNRC, April 2, 1993.
3. DOE/ID-10271, "Prevention of Early Containment Failure due to High Pressure Melt Ejection and Direct Containment Heating for Advanced Light Water Reactors", March 1, 1990
4. BNL-NUREG-41753, N. K. Tutu, et. Al., "Low-Pressure Cutoff for Melt Dispersal from Reactor Cavities", Brookhaven National Laboratory. Jan, 1988

Appendix-D

Severe Accident Analysis Report for FCI

TABLE OF CONTENTS

1 INTRODUCTION D-8

1.1 BACKGROUND AND OBJECTIVES D-8

1.2 REACTOR CASE ANALYSIS OF STEAM EXPLOSION PHENOMENA..... D-10

1.2.1 ASSESSMENT OF IVSE FOR EXISTING NUCLEAR POWER PLANTS D-10

1.2.2 ASSESSMENT OF EVSE FOR EXISTING NUCLEAR POWER PLANTS D-10

1.2.3 ASSESSMENT OF EVSE FOR NEW NUCLEAR REACTOR DESIGNS D-12

2 METHODOLOGY OF STEAM EXPLOSION ANALYSIS FOR APR1400 D-19

2.1 INTRODUCTIONS D-19

2.2 STEAM EXPLOSION ANALYSIS METHODOLOGY FOR APR1400 D-19

2.2.1 IN-VESSEL STEAM EXPLOSIONS (IVSE)..... D-19

2.2.2 EX-VESSEL STEAM EXPLOSION (EVSE)..... D-20

2.3 DESCRIPTION OF THE TEXAS-V CODE D-21

2.3.1 STEAM EXPLOSION MODELS: FRAGMENTATION MODELS D-21

2.3.2 NEW TEXAS CODE: TEXAS-VI D-23

3 IN-VESSEL STEAM EXPLOSION ANALYSIS RESULTS FOR APR1400 D-25

3.1 INTRODUCTION D-25

3.2 INITIAL AND BOUNDARY CONDITIONS D-25

3.2.1 CORIUM CHARACTERISTICS D-25

3.2.2 COOLANT CHARACTERISTICS D-26

3.3 TEXAS-V MODELING D-26

3.3.1 MODEL NODALIZATION D-26

3.3.2 MODEL PARAMETERS..... D-26

3.4 EVALUATION OF DYNAMIC LOADS OF IVSE D-28

3.4.1 MIXING PHASE OF IVSE..... D-28

3.4.2 EXPLOSION PHASE OF IVSE..... D-28

3.4.3 SENSITIVITY STUDY: MULTI-JET EFFECT..... D-29

3.5	INTRODUCTION OF RPV STRUCTURE ANALYSIS	D-29
3.5.1	DESIGN CRITERIA	D-29
3.5.2	DYNAMIC LOADS TO RPV DUE TO STEAM EXPLOSION.....	D-29
3.6	EVALUATION OF RPV STRUCTURE ANALYSIS.....	D-29
3.6.1	STRESS ANALYSIS RESULT FOR DESIGN CONDITIONS	D-30
3.6.2	STRESS ANALYSIS RESULT FOR IVSE CONDITIONS.....	D-30
3.7	SUMMARY AND CONCLUSIONS.....	D-31
4	EX-VESSEL STEAM EXPLOSION ANALYSIS RESULTS FOR APR1400	D-54
4.1	INTRODUCTIONS.....	D-54
4.2	INITIAL AND BOUNDARY CONDITIONS OF EVSE ANALYSIS	D-54
4.2.1	CORIUM CHARACTERISTICS	D-55
4.2.2	CORIUM DISCHARGE CHARACTERISTICS.....	D-55
4.2.3	SUMMARY.....	D-57
4.3	TEXAS-V MODELING	D-58
4.4	EVALUATION OF DYNAMIC LOADS OF EVSE – BASE CASE	D-58
4.4.1	MIXING PHASE OF EVSE	D-58
4.4.2	EXPLOSION PHASE OF EVSE	D-58
4.5	SENSITIVITY STUDY.....	D-59
4.5.1	REACTOR VESSEL FAILURE MODE ISSUES	D-59
4.5.2	SAMG RELATED ISSUES: IN-VESSEL CORIUM MELT RETENTION (IVR)	D-60
4.5.3	EFFECTS OF KEY PHYSICAL PARAMETERS ON EVSE ENERGETICS	D-60
4.6	CORIUM MATERIAL EFFECTS ON EVSE ENERGETICS	D-61
4.7	REACTOR CAVITY STRUCTURAL INTEGRITY ASSESSMENT.....	D-61
4.7.1	INTRODUCTION	D-61
4.7.2	SKN 3&4 REACTOR CAVITY STRUCTURAL ASSESSMENT ON EVSE LOADING.....	D-62
5	CONCLUSIONS	D-105
6	REFERENCES	D-107

LIST OF TABLES

Table 1- 1	Summary of Relevant Studies on In-Vessel Steam Explosion	D-14
Table 1- 2	Summary of Relevant Studies on Ex-Vessel Steam Explosion	D-15
Table 1- 3	Alpha-Mode Failure Probability Estimates given Core Melt Accident (Cited from Table E.1 in Reference 3).....	D-16
Table 3- 1	Corium Properties	D-32
Table 3- 2	Initial and Boundary Conditions for the IVSE analysis with TEXAS-V.....	D-33
Table 3- 3	The TEXAS-V Model Parameters Selected for the Analysis	D-34
Table 3- 4	Sensitivity Studies for Multi-jets	D-35
Table 3- 5	Summary of the results of the simplified steam explosion cases (50, 100 and 150	D-35
Table 4- 1	Corium Pool Configuration and Thermal Loads with respect to Accident Scenarios (Reference 31, Table 3.1.6 and 3.1.7).....	D-64
Table 4- 2	Accident Scenarios Considered in the MAAP Analysis [Reference 32]	D-66
Table 4- 3	Melt Conditions at Vessel Failure with Penetrations (IOXIDHT=0) [Reference 32].....	D-67
Table 4- 4	Melt Conditions at Vessel Failure without Penetration (IOXIDHT=0) [Reference 32] ..	D-69
Table 4- 5	Melt Conditions at Vessel Failure with Penetrations (IOXIDHT=1) [Reference 32].....	D-71
Table 4- 6	Mean and Standard Deviation of Corium Flow Results at Vessel Failure [Reference 32]....	D-73
Table 4- 7	Corium Material Properties	D-74
Table 4- 8	Initial and Boundary Conditions for EVSE Analysis.....	D-75
Table 4- 9	The TEXAS-V Model Parameters Selected for the Analysis	D-76
Table 4- 10	Results of the TEXAS-V Analyses for the Base Cases	D-77
Table 4- 11	Predicted Pressure at the Cavity Wall based on the TEXAS-V Analyses	D-77
Table 4- 12	Effect of Accident Progression Scenarios.....	D-78
Table 4- 13	Effect of Corium Temperature.....	D-78
Table 4- 14	Effect of Corium Ejection Velocity.....	D-79
Table 4- 15	Effect of Corium Jet Diameter.....	D-79
Table 4- 16	Effect of Cavity Water Temperature.....	D-79

Table 4- 17 Summary of Cavity Structural Integrity Analysis Result..... D-80

Table 5- 1 Summary of the IVSE and EVSE Analysis for the APR1400 D-106

LIST OF FIGURES

Figure 1-1	CFD Simulation of Steam Explosion Shock Propagation in a Typical PWR Cavity Geometry done by Cizelj et al. [Reference 16].....	D-17
Figure 1-2	ABAQUS/Explicit Simulation of the Dynamic Response of the Cavity Wall due to Steam Explosion Loadings done by Cizelj et al. [Reference 16].....	D-18
Figure 2-1	Conceptual Diagram of Fine Fragmentation Model in the TEXAS-V Code [Reference 38]	D-24
Figure 3-1	TEXAS-V Nodalization for the In-Vessel Steam Explosion in the APR1400 RPV	D-36
Figure 3-2	Corium Jet Penetration (a) and Axial Distribution of Void and Fragmented Melt Fraction at the time of Triggering (b).....	D-37
Figure 3-3	Void Fractions along the Axial Direction during Mixing Phase	D-38
Figure 3-4	Fragmented Melt Fractions along the Axial Direction during Mixing Phase	D-39
Figure 3-5	Void Fractions and Fragmented Melt Fraction History during Mixing Phase.....	D-40
Figure 3-6	Pressures Calculated for the Base Case in terms of Variation of the User-Specific Mixing Diameter with respect to the Corium Jet Diameter	D-41
Figure 3-7	Void Fractions along the Axial Direction during Explosion Phase	D-42
Figure 3-8	Impulses, Energy Transfer to Coolant, maximum Kinetic Energies of Coolant and the Conversion Ratio calculated for the Base Case	D-43
Figure 3-9	Pressure and Void Fractions History during Mixing Phase.....	D-44
Figure 3-10	Models for the Reactor Case Analysis in the SERENA-I Project	D-45
Figure 3-11	Simplified Steam Explosion Pressure Profile for the Structure Analysis	D-46
Figure 3-12	Axisymmetric Sketch of Reactor Vessel: (a) Geometry, (b) Grid and (c) Boundary Conditions	D-47
Figure 3-13	Results for the Maximum Pressure of 50 MPa: (a) Maximum Equivalent Plastic Strain, (b) Equivalent Plastic Strain at the Maximum Strain Node, and (c) Von Mises Stress at the Maximum Strain Node.....	D-48
Figure 3-14	Results of Stress Analysis: (a) Von Mises Stress and (2) Equivalent Plastic Strain	D-49
Figure 3-15	Results for the Maximum Pressure of 100 MPa: (a) Maximum Equivalent Plastic Strain, (b) Equivalent Plastic Strain at the Maximum Strain Node, and (c) Von Mises Stress at the Maximum Strain Node.	D-50
Figure 3-16	Results for the Maximum Pressure of 150 MPa: (a) Maximum Equivalent Plastic Strain, (b) Equivalent Plastic Strain at the Maximum Strain Node, and (c) Von Mises Stress at the Maximum Strain Node.	D-51

Figure 3-17	Maximum Hoop Strain in terms of Explosion Impulse	D-52
Figure 3-18	Maximum Plastic Equivalent Strains in terms of Explosion Impulse for the comparison with the Failure Criteria.	D-53
Figure 4-1	Schematic Diagram of the Cavity Flooding System of APR1400	D-81
Figure 4-2	Nodalization for the Ex-Vessel Steam Explosion in the APR1400 Cavity	D-82
Figure 4-3	Void Fractions Calculated for the Base Case during Mixing Phase	D-83
Figure 4-4	Melt Fractions Calculated for the Base Case during Mixing Phase.....	D-84
Figure 4-5	Pressures Calculated for the Base Case	D-85
Figure 4-6	Void Fractions Calculated for the Base Case during Explosion Phase	D-86
Figure 4-7	Impulses, Conversion Ratio, Energy Transfer to Coolant, Kinetic Energies of Coolant calculated for the Base Case	D-87
Figure 4-8	Pressures and Impulses Calculated for the Base Case	D-88
Figure 4-9	Schematic Drawing of APR1400 Reactor Cavity	D-89
Figure 4-10	Comparison of TEXAS-V Calculation for TROI TS-4 Experimental Pressure Data	D-90
Figure 4-11	Comparison of Ex-Vessel Steam Explosion Pressure	D-91
Figure 4-12	Side View of the General Arrangement of the Reactor Cavity	D-92
Figure 4-13	Top View of the General Arrangement of the Reactor Cavity	D-93
Figure 4-14	Isometric View of all Reinforcement Bars in the Reactor Cavity	D-94
Figure 4-15	Isometric View of the RPV Model	D-95
Figure 4-16	Isometric View of the Global Model	D-96
Figure 4-17	Pressure Time Histories for the Zones	D-97
Figure 4-18	Applied Pressure Loads to the Reactor Cavity Walls	D-98
Figure 4-19	Maximum Resultant Displacement Contours for the Concrete Cavity.....	D-99
Figure 4-20	Crack Pattern of the Reactor Cavity	D-100
Figure 4-21	Plastic Strain Contours for Liner Plates	D-101
Figure 4-22	Plastic Strain Contours in Vertical Rebars	D-102
Figure 4-23	Vertical Displacement and Anchor Bolt Reaction of RPV	D-103
Figure 4-24	Vertical Displacements of Cold Leg and Hot Leg Pipes	D-104

1 INTRODUCTION

1.1 Background and Objectives

Steam explosion is a phenomenon that rapid heat transfer between a hot and volatile cold liquid occurs and results in explosive dynamic pressure that may threaten the integrity of surrounding structures. This phenomenon has been a special interest as risk-significant events in nuclear power plants during severe accidents. In the accidents, reactor fuel and materials melt due to the lack of adequate cooling capability as observed in Fukushima accident and form a molten material, called corium. To mitigate and eventually terminate the severe accident progression, the cold water should be provided to cool the corium. In this process, molten corium contacts water, resulting in steam explosions that may provide mechanical and functional damages to the surrounding structures and safety systems. Therefore, it is important to evaluate the energetics of steam explosions in the process of the safety assessment of nuclear power plants. In nuclear power plants, steam explosions can be classified into two categories in accident progression; in-vessel and ex-vessel. In-Vessel Steam Explosions (IVSE) occurs in the Reactor Pressurized Vessel (RPV) and Ex-Vessel Steam Explosions (EVSE) in the outside of RPV.

In the 1970s, the steam explosion process was intensively studied for the fast breeder reactor, in which uranium oxide and sodium were used as fuel and coolant, respectively. While search was continued on steam explosions for the safety of the fast breeder reactor, a comprehensive risk assessment to estimate the likelihood of containment failure in Light Water Reactors (LWR) due to a steam explosion was conducted in 1975 and reported in WASH-1400 [Reference 1]. This study focused on two specific reactor designs; the Surry PWR and the Peach Bottom BWR-Mark I. For the steam explosion process, it was determined that the containment could be threatened by three possible damage mechanisms; (a) dynamic liquid phase pressures on structures, (b) static over-pressurization of the containment by steam production, and (c) solid missile generation from the impact of a liquid slug accelerated by the steam explosion.

In this analysis, the primary concern was a direct failure of containment caused by an energetic Fuel Coolant Interaction (FCI) causing missile generation (designated " α -mode" failure). The probability of this phenomenon was estimated to be about 10^{-2} per reactor year with the likelihood of water availability and triggering of the explosion as the major uncertainties. A group of steam explosion experts performed a series of periodic review on the potential risk of steam explosion by the α -mode failure in every 5, 10 years; SERG-I [Reference 2], SERG-II [Reference 3], and the OECD/NEA FCI Specialist Meeting [Reference 4]. The outcomes of the review were mainly focused on the risk of the α -mode failure. The expert group recognized that α -mode failure required (1) large amount of corium relocation to the lower plenum, (2) large amount of corium-water mixing and (3) large energy conversions during steam explosions. However, those requirements are very difficult to be satisfied in the in-vessel scenarios because of (1) large vapor generation during the corium-water mixing due to the near saturation of water temperature and (2) less corium relocation due to internal structures and complex passages. Therefore, the estimated conditional probability of the α -mode failure had reached a consensus of resolution in a risk perspective, in the series of expert reviews as following (See Table 1-3);

SERG-I: $< 10^{-4} \sim 10^{-2}$, vanishingly small

SERG-II: $< 10^{-5} \sim 10^{-3}$, physically unreasonable

Until that time, the experiments showed a distinctive result that prototypic corium melts were difficult to be triggered to initiate an energetic explosion and generated low energy conversion while single oxidic melt like alumina provided a very energetic explosion. These observations triggered a debate of "melt material effects" on steam explosion energetics. The scaling of material characteristics had been an issue; sharp increase of viscosity during freezing, non-uniform freezing (surface freezing), non-condensable gas generation like hydrogen etc. However, limited theoretical understanding hinders to figure out the scaling involved. For the corium tests, limited numbers of experimental databases are available and most of date

there are large uncertainties in corium temperature (superheat), composition and properties. Although the difficulties in performing experiments, uncertainties in results and different definitions of explosion efficiency evaluations exist, there is a tendency that corium tests consistently provide lower energetics (conversion efficiency) compared with single oxide and metal tests such as Alumina tests in the KROTOS facility. Corium tests provide their low explosion efficiencies in many cases, meaning no steam explosion. However, most of simulant tests show high explosion efficiencies. In particular, the alumina tests performed in KROTOS facility provided very strong energetics and have been considered the upper bounds of the experimental results. For the reason, many computational modeling for steam explosion have been validated with the alumina tests and consequently most of codes tend to estimate their explosion energetics more conservatively.

The SERENA-I project [2002-2005] [Reference 5] aimed to make a status of the steam explosion codes capabilities to calculate steam explosion in reactor situations and to find out what would be strictly necessary to understand the phenomena and predictability of steam explosion energetics to desirable levels for risk management. The conclusions drawn from the projects despite the differences in modeling and approaches and the large scattering of hypothesis and results for explosion processes that the reactor calculations indicated clear tendencies; for the in-vessel case the calculated loads were far below the capacity of the defined model intact vessel and for the ex-vessel case, the calculated loads, even low, are above the capacity of the defined model cavity walls. The scattering of the results raises the question of quantifying the containment safety margin for ex-vessel steam explosions. Two main uncertainties were accentuated; uncertainties in the pre-mixing flow patterns and geometry due to the lack of detailed experimental data and uncertainties on material influence on the energetics.

The SERENA-II project [2007-present] [Reference 6] has two objectives to reduce the uncertainties identified in the SERENA-I project for computer code validation; (1) to obtain more detailed data on pre-mixing flow patterns in particular distribution and geometry and (2) to determine explosion behavior of a spectrum of corium melt compositions reflecting accident scenarios by performing two experiments, TROI (KAERI, Korea) and KROTOS (CEA, France). For that purpose, the KROTOS facility is equipped with a level meter to measure averaged void fraction and a high-energy X-ray radiography to visualize the pre-mixing of steam explosions. The TROI facility is equipped with a differential pressure meter for an average void fraction and an electro-capacitance tomography. At present, reliable experimental data for the quantification of void fraction in the pre-mixing phase of steam explosion were not obtained yet. For the analytical activities, the similar activities still continues but tries to model the material effects, such as solidification modeling. For instance, one of mechanistic codes developed in the framework of the SERENA-II, TEXAS-V implements the solidification model to update their capability of simulating the corium tests performed in the project [Reference 7]. In summary, the development of adequate models to describe the steam explosion is challenging but made much progress in understanding of the steam explosion in reactor application to make a conclusion.

In summary, based on experiments and related analyses, the α -mode failure due to an in-vessel steam explosion is not considered as a credible threat to containment integrity. However, in-vessel steam explosion is still a potential risk of reactor vessel failure, affecting to the accident management including in-vessel melt-retention strategy. In general, the vessel failure criteria are about a few hundreds kPa-s of impulse and depend on the specific reactors. Therefore, most of the in-vessel steam explosion analyses are conformed with the RPV structure analysis for their risk of vessel failure. Since the most of RPVs fulfill the criteria, the risk of in-vessel steam explosions was not the issue of resolution but the confirmation for old and new power plants. EVSE, on the other hand, has been one of the long pending unresolved issues in LWRs since in some existing LWRs water discharged from the reactor primary system accumulates in the reactor cavity under the vessel.

Therefore, this report describes a comprehensive analysis of the hazard potentials involved in in-vessel and ex-vessel steam explosions in the APR1400 design. For steam explosion, the energetics and resulting loadings to RPV in the case of IVSE and to the cavity structure in the case of EVSE are evaluated. The analysis methodology employs the base case analysis with a mechanistic code for steam

explosion, TEXAS-V.

1.2 Reactor Case Analysis of Steam Explosion Phenomena

1.2.1 Assessment of IVSE for Existing Nuclear Power Plants

Corradini et al. [Reference 49] extended the analysis of WASH-1400 with models for fuel-coolant mixing and explosion, i.e., expansion work into a Monte Carlo analysis to estimate the α -mode failure probability; namely given a core melt, the probability of α -mode failure was estimated less than 10^{-4} per reactor year. In 1985, in NUREG-1116 [Reference 2], the Steam Explosion Review Group (SERG) estimated the probability of the α -mode failure. This group of experts performed independent analyses and estimated that the conditional probability of the α -mode failure was much less likely than in WASH-1400 (10^{-2} ~ 10^{-4} /yr as upper bound given a core melt). This group also recognized that these estimates were founded on the judgment that the amount of fuel-coolant was limited and/or the explosion yield was less than the maximum thermodynamic values. Included in their findings was the consensus recommendation that fundamental experiments needed to be performed at large scales to characterize fuel-coolant mixing and measure explosion yield as well as the effect of mixing on yield.

Theofanous et al. [Reference 8] performed a comprehensive analysis of α -mode failure and found the upper bound value to be quite low ($<10^{-4}$ per reactor year). Recently, Turland et al. [Reference 9] investigated a methodology for quantifying the conditional probability of the α -mode failure in the Sizewell B PWR. They estimated that the probability was approximately 10^{-4} and the effect of the system pressure elevation on the probability of this mode of failure was modest. Theofanous et al. [Reference 10] updated their original risk assessment [Reference 11] and concluded that vessel failure by steam explosions might be regarded as physically unreasonable. Table 1-1 summarizes the relevant studies on the effort of the IVSE issue resolution.

1.2.2 Assessment of EVSE for Existing Nuclear Power Plants

Theofanous et al., [Reference 12] performed a comprehensive approach to examine the steam explosion energetics in detail for the requirement of the design of nuclear systems by providing the dynamic aspects of explosions and the resulting dynamic loads on adjacent structures. The results were provided on two-dimensional explosions from their micro-interaction model in the ESPROSE.m code.

Chu et al. [Reference 13] performed the analysis for the Swedish BWRs to examine their SAM strategy of the lower drywell flooding to mitigate against the effects of melt release into the drywell during severe accident. With the use of the THERMAL-1 code, they investigated the effectiveness of the water pool to protect lower drywell penetrations by fragmenting and quenching the melt as it relocated downward through the water.

The SERENA Phase I (SERENA-I) project [Reference 5] was the most comprehensive international collaboration exercise on steam explosion, aiming to verify the prediction capability of the FCI codes and to identify the major uncertainties which limit the confidences in those predictions. The major uncertainties related to the explosion processes were identified in the projects. For the uncertainties in the pre-mixing phases, it was noted that the codes tends to overestimate void generation with respect to the integral experimental data (not local but overall average such as level swell data), resulting underestimation of heat transfer and difficulties to reproduce the pressure data. The void distribution is a key parameter of steam explosion processes and resulting energetics, considering as a key limiting factor on steam explosion strength. In general, void fraction of over 50%, i.e., high water depletion in the FCI mixture, drastically reduces the steam explosion energetics. For the uncertainties in the explosion phases, the material effect that associates with melt fine fragmentation is one of significant factors. There is no model to describe this effect. Also, the composition of corium melt is specifically scenario-dependent as well as design-dependent.

Based upon the model verification exercise of the codes, the SERENA-I conducted the code applicability and identification of uncertainties on estimation of steam explosion loads in reactor cases, Figure 2.3 illustrates the initial and boundary conditions for the reactor case analyses (in-vessel and ex-vessel) in the SERENA-I project. The analysis aimed to verify the codes participated at the project with plausible generic reactor situations; i.e., for in-vessel, the multi-jet configuration and for ex-vessel, a large single jet ejecting from the bottom of the reactor vessel.

Magallon et al., [Reference 5] summarized the main conclusions of the SERENA Phase-I projects after the exercise of the FCI codes to reactor situations: (1) in the absence of pre-existing loads, IVSE would not challenge the integrity of the vessel, (2) damage to the cavity which may challenge the integrity of the containment is to be expected for ex-vessel explosion, and (3) the level of the loads cannot be reliably predicted due to the large scatter of results. Those conclusions suggested the need of further efforts on EVSE to decrease the scatter of the predictions to acceptable levels for reactor situations and led to the Phase-II of the SERENA project initiated 2007 to the present (2011). The project focuses on the increase of confidence level in the calculated containment safety margins for ex-vessel reactor case conditions by performing well-controlled and well-defined prototypic corium experiments, TROI (KAERI) and KROTOS (CEA) as well as increasing the capabilities of FCI models/codes. At present, four FCI codes, JASMINE by JNES, JEMI (IKEMIX/IKEJET) with IDEMO by IKE, MC3D with a group of participants and TEXAS-V by UWM and VTT are used [Reference 6].

Zuchuat et al. [Reference 14] performed the assessment of the in-vessel and ex-vessel steam explosion risk for three Swiss Beznau (Westinghous PWR) nuclear power plants, Gösgen (Siemens/KWU PWR) and Leibstadt (GE BWR-6) nuclear power plants. For the ex-vessel analysis, their analysis methodology for the assessment of uncertainties in the potential ex-vessel FCI impulse loads was based on the work of Khatib-Rahbar et al. [Reference 47] which considered the uncertainties in the accident progression variables and the model parameters in probabilistic manner. Khatib-Rahbar et al. [Reference 47] constructed probability density functions for key parameters in SA scenarios and code models and prepared about 1000 to 4000 samples using the stratified Mote-Carlo method (LHS: Latin Hypercube Sampling) code [Reference 48]. Their analysis used the TEXAS code for the deterministic analysis and formulated the probabilistic analysis to treat the EVSE uncertainties. Their results showed that the conditional failure probabilities of the pedestals at the Beznau plant and at Leibstadt were varied between 0.26 and 0.73 and 0.1 and 0.5, respectively. However, since the conditional probability of containment failure given an EVSE energetics is not only the EVSE but also other conditional failure probabilities such as steam generator support failure by the pedestal failure and containment penetration tear failure due to steam generator support failure, the mean conditional containment failure probabilities for Beznau and Leibstadt plants due to EVSE were determined to be 8×10^{-4} and 1×10^{-2} .

Moriyama et al. [Reference 15] evaluated the containment failure probability due to ex-vessel steam explosions using the similar methodology performed by Zuchuat et al. [Reference 14] for typical Japanese LWR plants. The analysis was performed with the 200 sampled stratified Monte Carlo method (LHS) and the 2-D JASMINE code for steam explosion calculation. The analysis estimated the mean conditional containment failure probabilities of 6.4×10^{-2} , 2.2×10^{-3} and 6.8×10^{-2} , for the BWR suppression pool case, the BWR pedestal case and the PWR cavity case, respectively. For the PWR cavity case, the mean conditional failure probabilities were much higher than those for Zuchuat's Beznau plant [Reference 14] since their analysis did not considered other possible conditional failure probabilities due to limited information about the plant structure.

Cizelj et al, [Reference 16] perform an analysis to provide an estimation of the pressure loads on the typical PWR power plant cavity structures due to the steam explosion and to assess the cavity integrity. They used a simplified conceptual steam explosion model for the steam explosion load analysis and a structure analysis model in CFX-5.7.1. They analysis results show that their proposed steam explosion model estimated the conversion ratio of 1% that corresponds to the steam explosion pressure of 40 MPa. The structure analysis simulated by the ABAQUS code for this case showed no damage to the cavity walls. For taking account of the large uncertainties involved in steam explosion model and phenomena, they performed another calculation considered to be more conservative case; the steam explosion energy

conversion ratio is 10%. The analysis suggested the maximum steam explosion pressure of 250 MPa (see, Figure 1-1). Figure 1-2(a) indicates that the maximum pressure of approximately 115 MPa is estimated at the cavity wall. The corresponding impulse of 345 kPa-s is deducted from the plot by assuming a triangular pressure profile at the cavity wall with the maximum number of 115 MPa and the pulse width of about 3 ms. Structure analysis results as shown in Figure 1-2(b) shows some minor to medium localized damage in the cavity wall, suggesting that the cavity wall maintains its structural integrity.

Table 1-2 summarizes the relevant studies to evaluate the risk of EVSE in nuclear power plants. The information suggested that the evaluation of EVSE risk requires the accurate structural response analyses against the steam explosion loads in parallel to perform uncertainty analyses against the key parameters influenced by accident scenarios.

1.2.3 Assessment of EVSE for New Nuclear Reactor Designs

Murphy et al. [Reference 17] evaluated the ex-vessel steam explosion loads against the cavity structure of advanced light water reactors. They proposed and demonstrated a three-step analysis methodology to overcome a drawback of applicability of 1-D TEXAS code to reactor cases. It consisted of (1) analysis for mixing of molten fuel in a large coolant pool with IFCI for obtaining 2-D mixing characteristics and with TEXAS for calculating detailed mixing parameters and subsequent explosion calculation, (2) simulation of explosion with TEXAS, IFCI for explosion propagation, and (3) evaluation of dynamic pressure loading with a hydrodynamic code like CTH for far-field propagation. For the SBWR specific conditions, explosion pressure at the center of the explosion at the axial depth of 3.5 m up from bottom reached about 60 MPa at maximum and decreased down to 20 MPa at 0.75 m apart from the center. It was cautiously concluded that the usefulness of the proposed methodology was identified and needed to be verified with direct comparison with FCI energetic data as it comes available.

The assessment of the ex-vessel steam explosion for the plant design and operation certificate for the AP600 nuclear power plant [Reference 18] was performed. The analysis assumed the global hinged mode of vessel failure and performed with the PM-ALPHA/ESPROSE.m code and the TEXAS-V codes. The estimated maximum impulse at the bottom of cavity was ranged about 150 and 650 kPa-s. Although the typical impulse of 25 kPa-s may cause damage to the cavity wall, only about 5% elongation of the containment liner due to the maximum impulse of 650 kPa-s was estimated. This result confirmed that the likelihood of the containment failure was remote and thus USNRC granted its design certificate and construction license for AP600.

For the licensing for the AP1000 power plant, the similar analysis [Reference 19] to the AP600 plant was performed by the consideration of the bottom and the side vessel failures. The estimated impulse at the bottom of the cavity was ranged between 9 and 300 kPa-s. Since the maximum impulse of ex-vessel steam explosion for AP1000, 300 kPa-s, was well below that for AP600, the likelihood of the containment failure was bounded to the AP600 plant.

A number of new nuclear reactor designs are under the review process which includes APWR (Mitsubishi Heavy Industry), ESBWR (GE-Hitachi), etc. The APWR design employs the SAM strategy of cavity flooding as a severe accident mitigation and prevention measures. Therefore, the risk of the EVSE is needed to be evaluated. Although the detailed analysis is not readily available, the limited information showed that the analysis has been performed with the TEXAS-V code and the JASMINE code. The EVSE loads to cavity wall were evaluated with the LS-DYNA code. From the analysis, it suggests that the risk of EVSE is remote because of the maximum pressure less than 84 MPa, remaining the cavity wall below the elastic strain and also the displacement of the reactor vessel less than 0.1 m (4 inches).

Aya and Corradini [Reference 20] performed the ex-vessel steam explosion analysis using the TEXAS-V code to model FCI phenomena to obtain the maximized energetics and the CFD package (ANSYS V11.0) to model the impact of the explosion dynamic loading in the cavity wall.

Moriyama et al. [Reference 15, 21] performed analysis at JAEA for the typical Japanese BWRs and PWRs. In this analysis, the failure criteria for the wall failure in the BWR Mark-II suppression pool, RPV support failures at the pedestal area in the BWR Mark-II reactors and in typical PWR cavity were used.

- Suppression pool wall failure fragility was defined as a failure at the lateral displacement of 20% of the structure thickness by the fluid-structure analysis with AUTODYN-2D code, i.e., impulse of 46.5 MN-s at 50% of log-normal probability distribution with error factor of 2.
- Fragility for the RPV support failure at the pedestal area in Japanese BWR Mark-II Reactors was defined as a failure of the anchor bolts that support RPV, i.e., kinetic energy of 39 MJ at 50% of log-normal probability distribution with error factor of 3.5.
- Fragility for the RPV support wall failure in typical Japanese PWR cavity was defined as a failure in terms of the vessel up-thrust by considering the failure energy of the wall structure that gives a constraint on the hot/cold legs against upward movement of the RPV, i.e., assuming 0.5~2% steel ratio (fraction of rebar cross section in the wall), the energy absorption of 14~94 MJ is obtained and thus kinetic energy of 30 MJ at 50% log-normal probability distribution with error factor of 2.5.

Esmaili et al., [Reference 19] estimated impulses of steam explosion for AP1000 at the bottom of the cavity ranged between 9 and 300 kPa-s. Since the maximum impulses of ex-vessel steam explosion of AP1000, 300 kPa-s, was well below that of AP600, the likelihood of the containment failure was not expected.

The ESBWR design also adopts the cavity flooding strategy as a severe accident measure with the core-catcher, called BiMAC. The risk of the EVSE was analyzed by the PM-ALPHA/ESPROSE.m code with the DYNA3D structure analysis code. The analysis shows that the maximum pressure and the impulse at the bottom of the cavity reach up to 500 MPa and 150 kPa-s, respectively. However, the DYNA3D analysis on the cavity wall and the BiMAC core catcher structures shows that the violation of the containment leak-tightness and of the BiMAC function was unreasonable. In general, the PWR cavity walls can hold higher dynamic loadings comparing to those of BWR and the core catcher is not designed for withstanding high dynamic pressure or impulses.

MHI [Reference 23] performed the structure analysis using the LS-DYNA code to evaluate the explosion loads to the APWR cavity wall. The maximum dynamic pressure of less than 84 MPa remains the cavity wall below the elastic strain and also the displacement of the reactor vessel less than 0.1 m (4 inches). It is also reasonable to postulate that the structural strength of the APWR cavity can be similar to that of the APR1400 cavity.

Hwang, et al., [Reference 24] performed analysis to assess the integrity of cavity walls in the KNGR empirically examined by evaluating the maximum loading on the cavity wall from the experimental evidence that the maximum conversion ratio of steam explosion observed was approximately 3%. The resulted maximum loading on the wall was less than 2.5 psi-s that is safely lower than the criteria of the containment failure.

Table 1-1 Summary of Relevant Studies on In-Vessel Steam Explosion

	Sources	Results
Expert Review	WASH-1400 (1975)	α -mode failure probability of $10^{-2}/\text{yr}$
	NUREG-1116 (1985)	α -mode failure probability of $10^{-2}\sim 10^{-4}/\text{yr}$
	NUREG-1524 (1995)	α -mode failure probability of $< 10^{-3}/\text{yr}$ Vanishingly small Physically unreasonable
Experiment	OECD/NEA-SRMFCI (1997)	No new evidence that would change or violate the conclusion of NUREG-1525 that ALPHA-mode failure is not risk significant
	ALPHA Tests (1995)	No steam explosion at pressure > 1.0 MPa and at saturated water Negligible α -mode failure probability for medium and high pressure accident scenarios
	FARO Tests (1997)	No or weak steam explosion for $\text{UO}_2\text{-ZrO}_2$ mixture
	KROTOS Tests (1997)	
Plant Analysis	Corradini & Swanson (1981)	α -mode failure probability of $< 10^{-4}/\text{yr}$
	AP600 (1999)	α -mode failure is physically unreasonable (ROAAM)
	SERENA-I (2005)	Steam explosion would not challenge the integrity of the vessel in the absence of pre-existing loads.

Table 1- 2 Summary of Relevant Studies on Ex-Vessel Steam Explosion

Sources		Results
Expert Review	NEA/CSNI/R(99)24 (1999)	Insufficient experimental database Real material tests are needed
Experiment	FARO Tests (1997) <hr/> KROTOS Tests (1997) <hr/> SERENA-I (2005)	No or weak steam explosion for UO ₂ -ZrO ₂ mixture Damage to the cavity which may challenge the integrity of the containment is to be expected
Plant Analysis	Zuchuat et al. (1997) <hr/> AP600 (1998) <hr/> AP1000 (2004) <hr/> Moriyama (2006) <hr/> Cizelj (2006)	Conditional containment failure probability of < 1.0x10 ⁻² Likelihood of the containment failure is remote Likelihood of the containment failure is bounded to the AP600 plant Conditional containment failure probability of < 6.8x10 ⁻² Some minor to medium localized damage in the cavity wall, suggesting that the cavity wall maintains its structural integrity

Table 1-3 Alpha-Mode Failure Probability Estimates given Core Melt Accident (Cited from Table E.1 in Reference 3)

Participant	NUREG-1116 (SERG-1, 1985)	NUREG-1524 (SERG-2, 1995)	View on Status of Alpha-Mode Failure Issue
Bankoff (USA)	$< 10^{-4}$	$< 10^{-5}$	Resolved from risk perspective
Berthoud (France)	-	Very unlikely	No statement on resolution
Cho (USA)	$< \text{WASH-1400}^*$	$< 10^{-3}$	Resolved from risk perspective
Corradini (USA)	$10^{-4} - 10^{-2}$	$< 10^{-4}$	Resolved from risk perspective
Fauske (USA)	Vanishingly small	Vanishingly small	Resolved from risk perspective
Fletcher (Australia)	-	$< 10^{-4}$	Resolved from risk perspective
Henry (USA)	-	Vanishingly Small	Resolved from risk perspective
Jacob (Germany)	-	Probably Low	Not resolved from risk perspective, needs more quantitative evaluation
Sehgal (Sweden)	-	Physically Unreasonable	Resolved from risk perspective
Theofanous (USA)	$< 10^{-4}$	Physically Unreasonable	Resolved from risk perspective
Turland (UK)	-	$< 10^{-3}$	Resolved from risk perspective

*WASH-1400 best estimate $< 10^{-2}$, SERG-1 consensus estimate $< 10^{-3}$

The SERG-1 column in this table shows the range of estimates to be 10^{-2} to 10^{-4} . The NUREG-1116 shows the range to be 10^{-2} to 10^{-5} . The latter document contains estimates from additional SERG-1 experts are not listed here

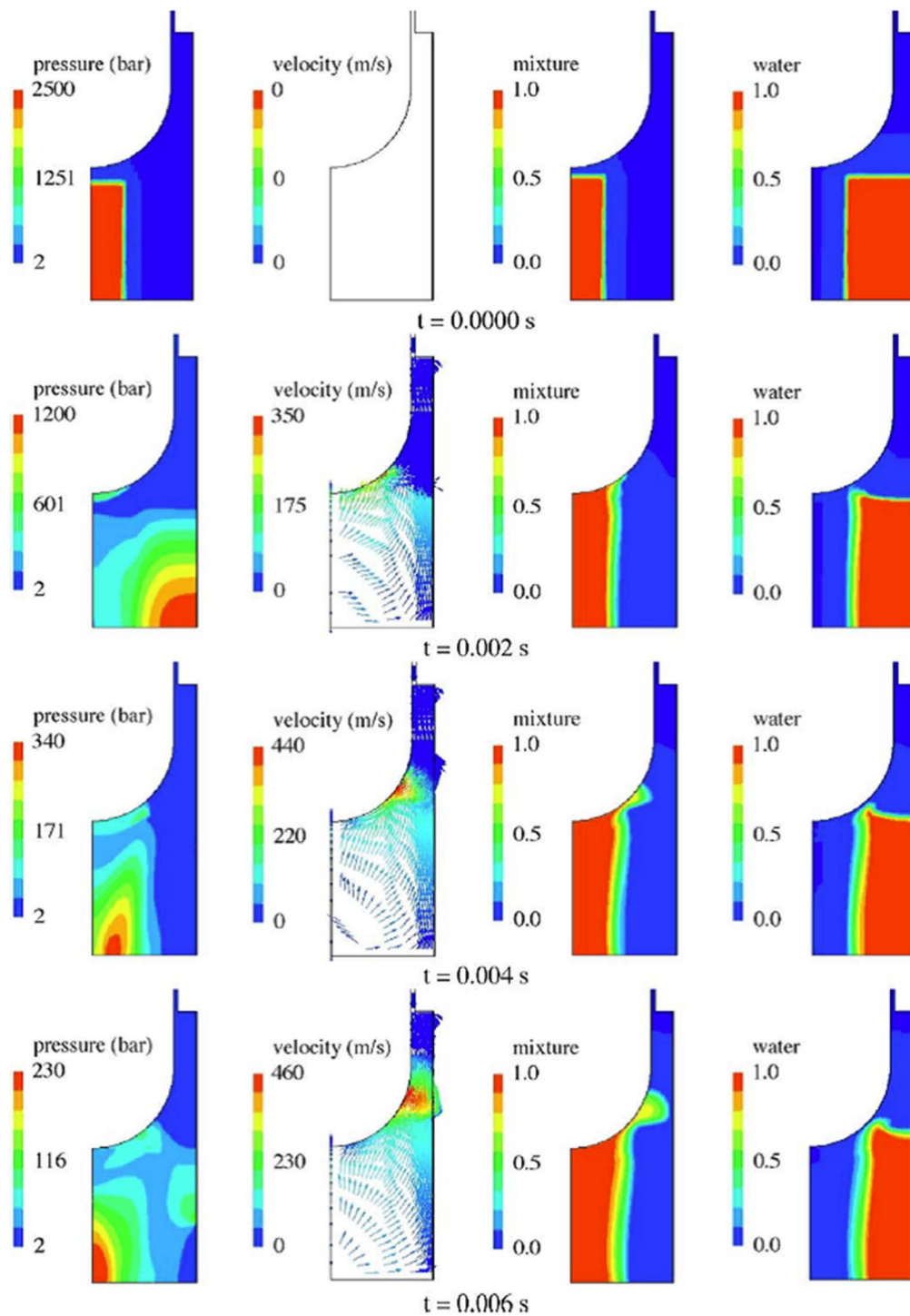
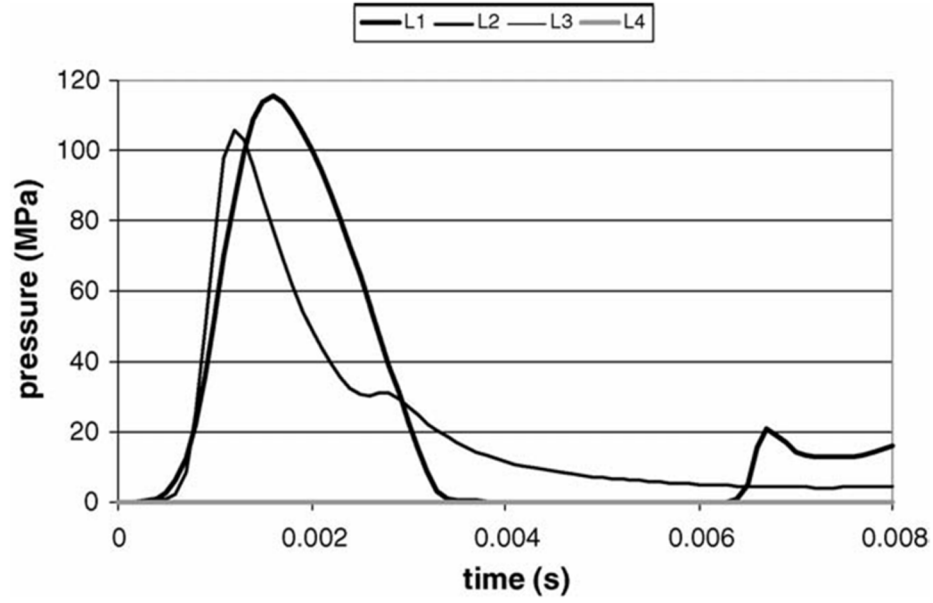
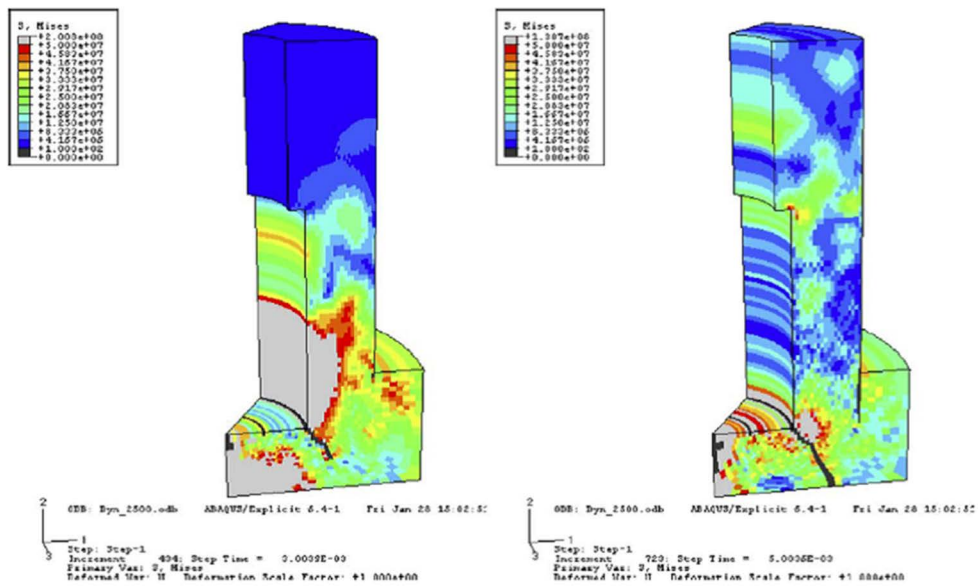


Figure 1-1 CFD Simulation of Steam Explosion Shock Propagation in a Typical PWR Cavity Geometry done by Cizelj et al. [Reference 16]



(a)



(b)

Figure 1-2 ABAQUS/Explicit Simulation of the Dynamic Response of the Cavity Wall due to Steam Explosion Loadings done by Cizelj et al. [Reference 16]

2 METHODOLOGY OF STEAM EXPLOSION ANALYSIS FOR APR1400

2.1 Introductions

In this chapter, the methodologies of steam explosion analysis for APR1400 are described. General methods of the analysis include several steps; determination of initial and boundary conditions, evaluation of steam explosion loads, assessment of structure integrity and sensitivity analysis. First, the initial and boundary conditions with the parameter ranges for the sensitivity analyses for both IVSE and EVSE are determined by the severe accident analysis codes, such as MAAP4.0.8. Second, the steam explosion energetics and corresponding loads to the structures in questions such as RPV for IVSE and cavity wall for EVSE are evaluated by the FCI mechanistic code such as TEXAS-V. Third, ABAQUS calculations are carried out to evaluate the RPV structure integrity against the estimated IVSE loads for the IVSE case and to evaluate the cavity structure integrity against the estimated EVSE loads for the EVSE case. Finally, sensitivity analyses of the initial and boundary conditions of key parameters affecting to the steam explosion loads against the surrounding structures are performed. In the case where the safety margin of the structure against the steam explosion loads, uncertainty analysis for the ranges of key parameters against the structure fragility curves is performed to evaluate the conditional failure probability.

2.2 Steam Explosion Analysis Methodology for APR1400

2.2.1 In-Vessel Steam Explosions (IVSE)

The analysis of steam explosion in the real reactor vessel depends on the mass of corium available, the location of the corium contact with water, the corium jet characteristics such as diameter, velocity as well as number of corium jets, etc. Those parameters is not easily estimated in accuracy since they are significantly depends on the accident progression and interaction among available materials and structures. Therefore, for the conservative point of view in the analysis, it is assumed that the RPV internal structures that may influence to the consequence of IVSE are not considered. This simplified configuration allows maximizing the interaction between the corium and water, resulting more bounding estimation compared to the geometry-constraint IVSE. In addition, the TEXAS-V code provided more conservative estimation of IVSE loading since the code is one-dimensional in nature providing the maximum energetics at the given FCI conditions by adjusting the radial mixing zone.

The steam explosion energetics depends largely upon the corium mass participated in the interaction. Therefore, it is assumed that the artificial trigger is provided by the corium jet contact at the bottom of RPV. The less conservative results will be obtained if the corium jet is triggered before or after the bottom contact of corium leading edge to the RPV wall.

2.2.1.1 Failure Criteria of RPV for IVSE

For the RPV failure criteria, there are number of approaches in literature. In this section, those criteria are reviewed to be used in the present analysis to evaluate the integrity of RPV in the APR1400 power plants.

Bang et al, [Reference 25] had reviewed several failure criteria as described below. They recognized that Berman [Reference 26] as well as Bohl and Butler [Reference 27] used failure criteria based on phenomenological continuum dynamics. In failure criteria based on equivalent plastic strain, $\bar{\varepsilon}_p$, formulation of equivalent plastic strain is given as

$$\bar{\varepsilon}_p = \frac{\sqrt{2}}{3} [(\varepsilon_1 - \varepsilon_2)^2 + (\varepsilon_2 - \varepsilon_3)^2 + (\varepsilon_3 - \varepsilon_1)^2] \quad (\text{Eq. 2.1})$$

Bohl and Butler used that failure occurred within 12% of equivalent plastic strain while Berman placed the criterion of 18%. For metallographic rupture, failure occurs for following case,

$$\varepsilon_{pg} \leq \varepsilon_{pmax} \quad (\text{Eq. 2.2})$$

ε_{pmax} is maximum principal plastic strain, ε_{pg} is failure plastic strain and failure plastic strain is obtained from following formulation.

$$\varepsilon_{pg} = 126.1 \left[\frac{1 + \beta^2 - 1.2\beta}{1 + \beta} \right] (1 + \delta^2 + 1.2\delta)^{-0.5} \quad (\text{Eq. 2.3})$$

β and α are defined as

$$\beta = \frac{1.5+2.5\delta}{2.5+2.5\delta}, \quad \delta = \frac{\varepsilon_1}{\varepsilon_2} \quad (\text{Eq. 2.4})$$

If this criterion is applied, failure occurs at same location but failure reaction is slightly delayed compared to 12% or 18% criteria mentioned above. Failure criteria for ductile material are generally based on plastic equivalent strains and ranges from 13% to 18% are conservative [Reference 11].

Shockey [Reference 28] adopted concept of ductile fracture apparatus based on void generation and growth. He found that void was generated from precipitation particle and critical strain required for void nucleus generation is 11%. This is also modification of maximum tensile strength that corresponds to beginning of necking. Bang [Reference 25] used this design criterion for the evaluation of the KNGR reactor vessel integrity against IVSE loads estimated by the TRACER code [Reference 29].

Recently, Corradini et al., [Reference 30] evaluated the vessel integrity of a new design reactor, NuScale PWR. They modeled the RPV wall by an elastic-plastic deformation model to determine the failure threshold for the dynamic pressure loads with a given peak-pressure and pulse width. By assuming the stress is constant (and equal to the yield stress), they modeled the shell by the following second order differential equation:

$$\frac{d^2y}{dt^2} = \frac{(rP - 2t\sigma)}{rt\rho} \quad (\text{Eq. 2.5})$$

where y is the radial displacement, P is the internal pressure, r is the mean radius of the shell, t is the shell wall thickness, σ is the yield stress of the shell material, and ρ is the density of the shell material. In this model, they assumed that significant yielding occurred in the solid and the material was perfectly plastic. They assumed that the failure occurred a hoop strain limit of 50%, reduced by a factor of 2.25 to account for biaxiality effects. In summary, for the failure criterion of the APR1400 RPV against IVSE loads, the Shockey criterion is selected for the conservatism.

It is assumed that the boundary pressure loading on the RPV inner wall be the maximum pressure pulse calculated by the TEXAS-V code over the entire inner wall boundary without the consideration of the pressure attenuation while travelling from the location of the explosion to the wall for the conservatism standpoint. ABAQUS 6.10 is used for stress analysis FEM tool. To apply real time to stress analysis, explicit mode of ABAQUS is used.

2.2.2 Ex-Vessel Steam Explosion (EVSE)

EVSE occurs when RPV failed due to the lack of adequate cooling of the corium relocated to the lower plenum in the vessel while water is available outside the reactor vessel. For the EVSE analysis, it is necessary to know the thermal conditions of corium at the time of vessel failure such as corium composition for the thermo-physical properties, corium temperature etc., the modes of vessel failure that

include the vessel failure location, size and corium ejection velocity and the conditions of cavity environment that includes the thermal conditions of water, ambient pressure and flooded water heights. Those parameters are considered as initial and boundary conditions that strongly depend on the accident sequences and scenarios. Therefore for the adequate definition of the conditions, it is required that rigorous accident analyses should be performed. For the reason, information to characterize the corium flow in EVSE are obtained from accident system code analysis for the corium formation in RPV such as the SCDAP/RELAP5, and MAAP analysis results [Reference 31, 32] as well as experimental evidences available in literatures and separate studies will be used as the initial and boundary conditions for EVSE.

TEXAS-V is also employed as an analysis tool to evaluate the EVSE energetics. As described in the previous section, the one-dimensional code will provide a conservative estimation for the given EVSE specific conditions. In particular for the estimation of explosion pressure on the cavity wall that is located at a distance away from the potential steam explosion interaction zone, underwater pressure attenuation should be considered.

2.3 Description of the TEXAS-V Code

TEXAS is a mechanistic model used for FCI analysis. The following is a brief description of the TEXAS models relevant to quenching calculations. It is essentially a condensed version of the description of the TEXAS model from Chu's and Tang's PhD thesis [Reference 33, 34].

The original TEXAS code was a parametric model developed by Young [Reference 35] for the design and analysis of fuel-coolant interaction experiments for LMFBR safety related issues. In an attempt to extend the capabilities of TEXAS, Chu and Corradini [Reference 36] incorporated a dynamic fragmentation model and a complete set of constitutive correlation's for interfacial mass, momentum, and energy transport terms; i.e., TEXAS-II. Since then, several improvements to the explosion propagation modeling, in particular, have been introduced by Tang [Reference 34]. A chemical reaction model to account the heat generation by oxidation of metallic melt was added by Murphy [Reference 17]. These updates warranted a new release of the model, TEXAS.

The TEXAS code is a transient, three fluid, one-dimensional model capable of simulating fuel-coolant mixing interactions. The three fields include two Eulerian fields for coolant liquid and vapor, and one Lagrangian field for fuel particles. The multifield feature of the code allows it to model thermal and mechanical nonequilibrium between coolant liquid and vapor which is very likely the case for fuel-coolant interactions. The code has the ability to handle flow regime transitions, which is also important to realistically model the heat transfer process. The "Lagrangian" treatment for the fuel field makes it easier to track the fuel particle movement, and eliminates some numerical difficulties encountered in pure Eulerian codes. The fragmentation model used in the code is based on hydrodynamic instabilities (i.e., Rayleigh-Taylor). The code also provides choices of velocity, pressure, and reflective (or closed) boundary conditions, giving more flexibility to users in different applications. A semi-implicit numerical technique is used in TEXAS which is a modified version of the SIMMER-II method, the actual forerunner of the TEXAS hydrodynamic formulation. With this method, the pressure iteration is done in a loop in which the energy and momentum equations are solved semi-implicitly, whereas the continuity equations are solved implicitly by adjusting the pressure distribution such that the errors of the continuity equations for all cells are reduced to a given tolerance. The Newton-Raphson method is employed in this pressure iteration.

2.3.1 Steam Explosion Models: Fragmentation Models

The key constitutive relation in TEXAS-V is the hydrodynamic fuel fragmentation model. This model was developed by Chu and Corradini [Reference 36] based on Pilch's original concept [Reference 37] of a multi-step fragmentation theory for liquid particles. The model considers the fuel particles to be deformed and dynamically fragmented into a discrete number of particles from its initial diameter to smaller sizes. The fragmentation mechanism assumed in the model is Rayleigh-Taylor instabilities. The shear forces

caused by the parallel velocity (e.g., Kelvin-Helmholtz instabilities and boundary layer stripping) are neglected because of their limited effects with a vapor film present. The correlation of this theoretical model reads as:

$$D(T^+) = D(0)\exp[-C_1(T^+)^{C_2}We^{C_3}] \quad (\text{Eq. 2.6})$$

By averaging the fragmentation rate, the above equation can be simplified to a linear time-independent form, which is used in TEXAS-V:

$$D_f^{n+1} = D_f^n(1 - C_0\Delta T^+We_e^{1/4}) \quad (\text{Eq. 2.7})$$

where the superscripts $n, n+1$ designate old and new time step values; We is the Weber number for the fuel particles; T^+ is a dimensionless time step; and C_0 is the constant:

$$We = \frac{\rho_c U_r^2 D_f^n}{\sigma_f} \quad (\text{Eq. 2.8})$$

$$\Delta T^+ = \frac{U_r(t^{n+1} - t^n)}{D_f^n} \left(\frac{\rho_c}{\rho_f}\right)^{1/2} \quad (\text{Eq. 2.9})$$

$$C_0 = 0.1093 - 0.0785 \left(\frac{\rho_c}{\rho_f}\right)^{1/2} \quad (\text{Eq. 2.10})$$

where U_r is the relative velocity; D is the fuel diameter; and ρ_f and ρ_c is the densities of fuel and coolant.

The conceptual model based on Corradini and Kim's model [Reference38] as shown in Figure 2-1 was employed in the TEXAS code in a semi-empirical relationship as shown in Eq. (2.12) depicting the fine fragmentation rate is proportional to the micro liquid jet velocity generated by the Rayleigh-Taylor instabilities and a function of fine fragmentation rate.

$$\begin{aligned} \dot{m}_{fr} &\sim u_j F(t_f) \\ u_j &= \left(\frac{\Delta P}{\rho_c}\right)^{0.5} \end{aligned} \quad (\text{Eq. 2.11})$$

The final expression for the fine fragmentation becomes

$$\dot{m}_{fr} = 6C_{fr}m_p \left(\frac{P - P_{th}}{\rho_f D_p^2}\right)^{0.5} F(\alpha)g(\tau) \quad (\text{Eq. 2.12})$$

Here, the fine fragmentation rates depend strongly on local pressure, mixing particle diameter and model parameters such as the fragmentation coefficient, C_{fr} and the local phase factor, F . In this analysis, C_{fr} of 0.002 was used, since the value was well evaluated with experimental data [Reference 39]. Local void fraction of 0.3 is used for the threshold value for the F factor, meaning the fine fragmentation process terminated at the local void fraction of 0.3. The threshold pressure of vapor film collapse surrounding melt particles, P_{tr} , is set to 0.2 MPa. The function, $g(\tau)$ is a characteristic time function which is defined by

$$g(\tau) = \begin{cases} 1 & \text{for } \tau < \tau_c \\ 0 & \text{for } \tau > \tau_c \end{cases}, \quad (\text{Eq. 2.8})$$

where τ_c is the characteristic time for fine fragmentation and is given to 2~4 ms as observed in single drop experiments [Reference 40].

The TEXAS-V model does not consider all the processes that may occur during melt jet mixing or the explosion phase. A key empirical observation from the KROTOS and FARO tests is that energetics with molten corium is substantially reduced from what had been observed with simulants (e.g., aluminum oxide).

Although this has been empirically seen in a number of experiments, there is still no clear reason for this observation. One possible explanation is that the corium partially solidifies and develops a solid 'skin' resisting rapid fuel fragmentation. No FCI model has the ability to locally model the effects of fuel partial solidification within a large collection of fuel drops in the coolant. This large reduction in energetics is not considered in these analyses, to be conservative, but is the focus of current modeling that briefly discussed in the next section.

2.3.2 New TEXAS Code: TEXAS-VI

Chen and Corradini [Reference 7] recently upgrade the TEXAS code, denoting the new TEXAS model as TEXAS-VI, by employing the fuel particle solidification model and solidifying fuel particle fragmentation criteria based on thermal stress and the modified Aeroelastic number. The new model has been verified with the FARO test, L14, and OECD standard problem [Reference 5] for FCI analysis.

This implementation is able to take account of the material solidification issues to examine the lower steam explosion energetics associated with the low superheat corium. In this model, the corium is considered as totally opaque for thermal radiation and the energy balance for fuel particle is formatted by heat conduction. The criterion of fragmentation for solidifying particle was set in terms of the modified Aeroelastic number and thermal stress.

The validation results with the FARO-L14 test demonstrated the effect of solidification on the mixing phase of steam explosion, especially for jet breakup, showing the good agreement of the L14 experiment data and also the slower increase of the fuel surface area prediction than one by TEXAS-V due to the limited rapid fragmentation. No validation efforts of the TEXAS-VI code for the explosion phase of steam explosion have been reported.

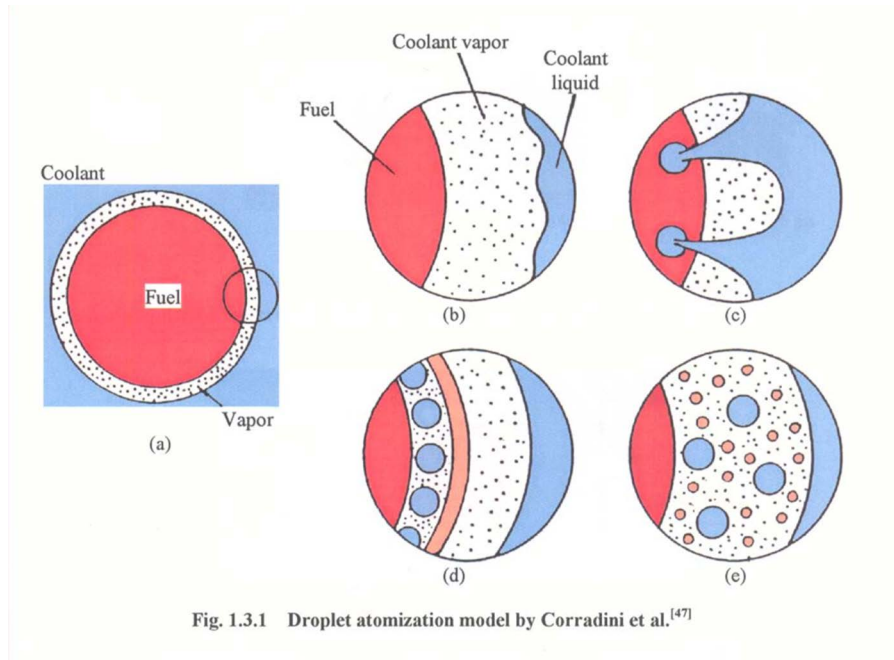


Figure 2-1 Conceptual Diagram of Fine Fragmentation Model in the TEXAS-V Code [Reference 38]

3 IN-VESSEL STEAM EXPLOSION ANALYSIS RESULTS FOR APR1400

3.1 Introduction

In this chapter, the APR1400 design specific analysis for the evaluation of in-vessel steam explosion risk will be discussed. The analysis consists of determination of initial and boundary conditions for the in-vessel steam explosions, the structure analysis for the APR1400 RPV against the explosion loading, sensitivity analysis for key parameters that vary with the consideration of severe accident scenarios, measures and progression. Finally, the analysis results will be discussed to evaluate the IVSE risk in the APR1400 design.

3.2 Initial and Boundary Conditions

In the IVSE analysis, the complex internal structure of RPV is not considered and assumed to be divided by two regions; the molten corium region in the core region and the residual water filled in the lower plenum. This assumption is considered conservative since the complex internal structure disrupts a corium flow path and provides steam explosion triggering source, causing pre-mature steam explosion. In addition, it is assumed that corium jet is introduced at the center of the RPV and steam explosion is triggered by the bottom contact of the corium jet. This assumption also provides additional conservatism on the analysis of IVSE. The summary of the initial and boundary conditions for the TEXAS-V analysis is shown in Table 3-2. The following sub-sections describe the rationales for the selection of the quantities of the key parameters.

3.2.1 Corium Characteristics

Corium composition and thermal properties: The reference corium composition 90%UO₂-10%ZrO₂ with its thermal and transport properties as shown in Table 3-1 is chosen. Table 3-1 indicates also the properties of corium composition of 80%UO₂-20%ZrO₂ that often used in experiments that most of thermo-physical properties are similar and no significant effects of those difference on the steam explosion energetics.

Corium temperature: The base case corium temperature of 3000 K is selected. This corium temperature corresponds to the superheat of 150 K. The corium temperatures at the vessel failure are estimated by considering the results of the MAAP analysis [Reference 32], the SCDAP/RELAP 5 analysis [Reference 31] and compared with other reactor case analyses such as SERENA-I reactor application [Reference 5], AP1000 analysis [Reference 19], Japanese LWR application [Reference 15, 21].

For the oxidic layer of the corium, most of reactor case analyses used the corium temperature considering the melt superheat of 150 K. Since the oxidic layer corium temperature of 3150 K was used in AP1000 as a conservatively bounding case, sensitivity analyses for the corium temperature up to 3150 K is performed.

Corium jet diameter: The base case corium jet diameter of 0.3 m was chosen. In the in-vessel conditions, it is not feasible to consider the large diameter expected in the ex-vessel case where the RPV failure may create a major release of melt that accounts a large corium jet diameter such as 0.5m or more. In addition, it has a possibility to have multiple jets relocated from the core locations to the lower plenum. In this situation, each jet could be much thinner than one for the single jet case. For the multi-jet case, a total of 24 jets with a diameter of 0.05 m was considered for testing the effect of multi-jet on the IVSE energetics.

Corium jet velocity: The corium jet velocity of 3 m/s is selected for the base case analysis. For the in-vessel scenario, it is not expected that corium jet is accelerated by any additional forces but by gravity.

3.2.2 Coolant Characteristics

RPV ambient pressure: The RPV pressure of 0.5 MPa is considered for the base case analysis. In general, since the effect of the ambient pressure has little effect on the steam explosion energetics, the sensitivity ranges of this parameter is not considered.

Water level and free-fall height: The depth of water level of 2.4 m is determined by the consideration that water is completely filled in the lower plenum of RPV. The free-fall height of 0.1 m is also selected by considering the distance between the core supporting plate and the water surface level.

Water temperature: Water temperature in RPV is assumed to be near saturation with the subcooling of 5 K.

3.3 TEXAS-V Modeling

3.3.1 Model Nodalization

The plant geometry of APR1400 for the TEXAS-V analysis is shown in Figure 3-1(a). The computational nodalization of the TEXAS code for the RPV is built as shown in Figure 3-1(b). The first nodalization group that represents the coolant RPV has 24 nodes that have the thickness of 0.1 m and the location of corium introduction is at 2.5m. At the bottom of the nodes, trigger cell is located to provide the trigger pressure to initiate the explosion process.

3.3.2 Model Parameters

In the TEXAS-V code, number of steam explosion model parameters, which influence the code performance and the calculation result are needed to be determined. The parameters include the jet breakup model, fine fragmentation model etc. Table 3-3 summarizes the selected parameters for the analysis. The present selections of the model parameters were intensively tested and validated during the reactor case exercise performed in the OECD/NEA SERENA-I project [Reference 5].

3.3.2.1. Melt Jet and Droplet Breakup Models for Mixing

TEXAS-V models the melt jet breakup by calculating the “blob” local relative velocity and then applying mechanistic models governed by fluid instabilities. Theoretically such a jet breakup modeling is quite complex and not well understood. Corradini and co-workers [Reference 33] have reviewed the various models for jet breakup and associated nozzle flow and categorized four mechanisms that are operative during jet breakup:

- Long-wavelength breakup of the jet as it leaves the nozzles producing discrete masses (blobs);
- Breakup of the jet along the jet column length due to Kelvin-Helmholtz (KH) instabilities;
- Breakup at the leading edge due to Boundary Layer Stripping (BLS); and
- Breakup of discrete liquid masses and the jet leading-edge by Rayleigh-Taylor instabilities.

The first form of breakup is difficult to mechanistically model, but it assists in determining the discretization of the jet as it issues forth from the nozzle. This is an active area of research, and currently TEXAS-V allows the user to fix the initial number of discrete masses at the leading edge of the jet pour (parameter NBREAK [Reference 41]). For the analysis of the OECD-CSNI standard problem (ISP-39), which is patterned after FARO L-14, the TEXAS-V analysis used NBREAK = 2 to match test results. The FARO tests were scaled to examine large jet pours of 100-500 kg/s and thus be prototypical of what may

occur in a severe accident for similar size gravity jet pouring events. Similarly, for these steam explosion analyses, we have used the same logic and have assumed NBREAK = 2.

The next two forms of breakup have been modeled by TEXAS-V [Reference 41]. However, the researchers have consistently urged caution in the use of these models, since the KH and BLS mechanisms fundamentally produce very small melt particles (micron-size length scale). Such debris sizes have not been observed in actual test data. In addition, it has been found that the KH and the BLS mechanisms would be minimized by the presence of film boiling particularly when the pool is subcooled. Thus, although modeled, these breakup mechanisms have a negligible effect on jet breakup.

The final form of breakup, via Rayleigh-Taylor instabilities (RTI), is operative throughout the jet pouring process; i.e., at the jet leading-edge for discrete masses formed from the jet and for subsequent melt particles that are produced by any breakup mechanism. The work by Chu [Reference 33] developed the model that is used in TEXAS-V.

The key constitutive relation in TEXAS is this hydrodynamic fragmentation model, designated as the RTI jet breakup mechanism. This model was developed by Chu based on Pilch's original concept of a multi-step fragmentation theory for liquid particles. The model considers the fuel particles to be deformed and dynamically fragmented into a discrete number of particles from their initial diameter to smaller diameters. The fragmentation mechanism assumed in the model is Rayleigh-Taylor instabilities. The shear forces caused by the parallel velocity (e.g., Kelvin-Helmholtz instabilities and boundary layer stripping) are neglected because of their limited effects with a vapor film present and with subcooling.

The final part of the jet breakup model that needs to be explained is that the whole jet is not available for breakup by this RTI mechanism, since it is coherent and is not made up of discrete masses. Thus, after the leading edge begins to breakup with its discrete masses (blobs), any subsequent melt jet breakup can only occur when the jet overtakes and passes these discrete masses. Lagrangian modelling continually takes account of the relative position of each discrete blob and will only allow further RTI breakup after the jet leading edge "blob" passes the other particles.

For the jet breakup model, two parameters, IENTRY and IENTRY2 with the values of 1 and 0 for both parameters, respectively, represent the jet breakup phenomena in which the stream of particles is treated as a coherent jet and the trailing edge model is the main particle break-up mechanism. In the trailing edge model, a number of independent leading particles are broken up first and the subsequent breakup occurs when the upstream particles become free and leading edge particles.

3.3.2.2. Melt Jet and Droplet Breakup Models for the Explosion

Given the triggering of an energetic FCI (or vapor explosion) by an external pressure pulse or film boiling collapse, the fuel is rapidly fragmented into fine particles (100 microns or less) due to local hydrodynamic and thermally driven instabilities. Tang and co-workers modified the original TEXAS model for fuel-coolant mixing and developed a rapid fuel fragmentation model for the explosive propagation phase of the FCI. This thermal fragmentation rate model for the fuel during this explosive propagation phase is a semi-empirical formulation based on the concept of vapor film boiling collapse and coolant jet impingement on the fuel surface to model single droplet FCI experiments. The fuel mass fragmentation rate, \dot{m}_{fr} , for a specific Lagrangian 'master particle' is given by the expression:

$$\dot{m}_{fr} = 6C_{fr}m_p \left(\frac{P - P_{th}}{\rho_f D_p^2} \right)^{0.5} F(\alpha)g(\tau) \quad (\text{Eq. 3.1})$$

The constant, C_{fr} , is estimated by past theoretical work and was empirically determined by analysis of the KROTOS tests to be between 0.001 - 0.002. We use 0.002 for this constant in this analysis.

The factor, F , is a binary variable (1 or 0) that goes from 1 to 0 when the fuel fragmentation ceases (as

the void fraction becomes large enough to become the continuous phase, fragmentation stops). This is considered a conservative value since fuel solidification effects are not considered. This fragmentation time was empirically found to vary from 0.5 to 2.0 milliseconds for good agreement with all of the KROTOS initial tests. KROTOS tests indicated that 2.0 ms was a bounding value for its one-dimensional geometry. The physical significance of this fragmentation time originates from the time it takes the explosion shock wave to propagate to the nearest free-surface, thus beginning to relieve the explosion pressure to the surroundings; i.e., the acoustic relief time. This is also correlated with the increase of the void fraction in the fuel-coolant mixture following the rapid fragmentation and the subsequent coolant vaporization. This corresponds to a void fraction of about 30 – 40 % based on analyses.

3.4 Evaluation of Dynamic Loads of IVSE

3.4.1 Mixing Phase of IVSE

Figure 3-2 (a) illustrate the corium jet penetration during the mixing phase of the base case. The corium reached to the bottom of the RPV about 0.7 s. The penetration velocity profile shows the typical corium penetration behavior in TEXAS where the corium jet is injected with the initial velocity and rapidly decelerated where the initial jet break-up occurs and start accelerating again. The jet break-up phenomena in the analysis can also be observed in Figure 3-2 (b) that shows the axial distribution of void and fragmented melt fractions.

Figures 3.3 and 3.4 show the void and fragmented melt fraction estimated all the axial nodes, respectively. The stacked plots for the void and fragmented melt fractions can also be found in Figure 3-5. The void fractions at all nodes in a single plot format that helps comparing the magnitudes of data while the stacked format plot in Figure 3-5 provides the progression of void fractions along with the corium penetration. The maximum void fraction reached up to 80% at the upper location where the jet velocity was rapidly decelerated. However, the void fractions in the lower region were very low although the corium jet fragmented as shown in Figure 3-5. Therefore, it is expected that steam explosion occurs due to the bottom triggering and propagates upward, triggering subsequent explosions. However, due to the large volume of void at the upper location, shock pressure will be diminished. It is also noted that the near saturation water temperature is responsible for this large volume of steam generation.

3.4.2 Explosion Phase of IVSE

Figures 3.6 and 3.9(a) show the steam explosion pressure profiles in terms of the explosion time. The maximum pressure and impulse of 37.5 MPa and 62.3 kPa-s, respectively. the steam explosion pressures along the axial direction in terms of the explosion time. Figures suggest that the explosion pressure reached its maximum of 37.5 MPa. The pressure profiles show the typical shock characteristics as the rapid build-up of pressure front and a long tail with respect to time. The explosion pressure front traveled with velocity of 1400~1500 m/s up to the location of L7 and dissipated in the upper axial location due to the presence of a volume of steam as shown in the mixing phase.

Figures 3.7 and 3.9 (b) shows the void fraction profiles during the explosion phase. The lower part of the lower head where steam explosion was triggered builds up their steam due to the explosion near 100% during the period the explosion phase. The upper region where the steam generated in the mixing phase shows the rapid condensation during the explosion phase period, 20 ms.

The impulse asserted to the surrounding structure was estimated by the integration of the explosion shock pressure during the explosion period. The evaluated impulses at each node are shown in Figure 3-8(a). The impulse at the node of cavity floor reached 62.3 kPa-s. The maximum possible energetics of steam explosion in this case estimated by the 1-D TEXAS-V analysis will travel (and be attenuated) to the surrounding internal structure in RPV. However, in this analysis to evaluate the RPV structure response against the explosion loading, the maximum pressure and impulse are assumed to be applied on the inner RPV wall. Therefore, no shock attenuation is considered.

Figures 3.8(b), (c) and (d) show more insights of the explosion phase of the steam explosions in RPV that include the energy partitioning, the coolant kinetic energy and the conversion ratio history during the explosion phase. In particular, the conversion ratio of the steam explosion reaches its maximum of near 1.0% after the triggering of explosion.

3.4.3 Sensitivity Study: Multi-Jet Effect

For the sensitivity study, three additional cases for investigating the effect of multi-jet configuration are studied. The cases includes (a) multi-jet case with the single jet diameter of 0.05m and 36 jets, (b) multi-jet case with the single jet diameter of 0.1 m and 9 jets and (c) the SERENA-I configuration with the single jet diameter of 0.08m and 24 jets as shown in Figure 3-10.

Table 3-4 summarized the results of the analyses and compared with the base case. The cases (a) and (b) were design to keep the equivalent diameters for both cases equal to one in the base-case single jet analysis, 0.3m. However, the equivalent diameter of the case (c) was larger.

The peak pressures estimated ranges from 50 to 87 MPa. The SERENA case shows the maximum peak among the cases. However, the maximum impulse was observed in the case (a), estimated near 100 kPa-s. For the multi-jet cases, the total mixing times are longer than one for the base case due to the steam generation induced drag forces. It is also observed that the mixing time increases when the number of jet increases. The maximum impulses are also increases with the number of jets. It can be explain that in the case of multi-jet the longer mixing time allows more melt jets to be fragmented. It is possible in TEXAS-V analysis because TEXAS was set to provide an optimal mixing conditions for the given jet-water configuration to maximize the energetics. However, in the real situation, the multi-jet configuration may produce more a steam rich mixing zone caused by (a) more fragmentation of jets and (b) limited radial dispersion of fragmented melts and thus result lower energetics. In this sensitivity analysis, it is now expected that the ranges of the maximum impulses that impose on the RPV inner wall will be approximately 60-100 kPa-s.

3.5 Introduction of RPV Structure Analysis

3.5.1 Design Criteria

The design criteria used in the APR1400 reactor vessel [Reference 25] are based on the ASME Boiler & Pressure Vessel Design Code Section III NR-3200 [Reference 42]. Detailed stress analysis for all of major components would be prepared to satisfy stress limit of NB-3220 and NB-3230 when load of NB-3110 is the main component. In this report, reactor vessel designs and stress limit are same with the design use in APR1400 reactor vessel report but stress analysis method is different.

In this study, the most conservative failure criteria suggested by Shockey who adopted the concept of ductile fracture apparatus based on void generation and growth is used. He suggested that void was generated from precipitation particle and critical strain required for void nucleus generation at 11%.

3.5.2 Dynamic Loads to RPV due to Steam Explosion

The RPV structure analysis is required to evaluate the dynamic response of RPV against the impeding IVSE pressure loadings. First, using the simplified pressure profile, the pressure and impulse criteria that cause the RPV failure will be examined. In so doing, a simplified explosion pressure profile that has a triangular pressure pulse with a given P_{max} at the center and pulse with Δt as shown in Figure 3-11 is used. In this study, the pulse with of 5ms was used.

3.6 Evaluation of RPV Structure Analysis

This part calculates the effect of dynamic pressures from a steam explosion on APR1400 reactor vessel

and evaluates integrity of structure. It is hard to know where the start point of explosion and it can cause much different result in stress analysis because it is related to applying time of dynamic pressure to wall in reactor vessel. We assume explosion happen at center of bottom head. It makes dynamic pressure apply to whole wall of the bottom head at same time. In real condition, liquid is pressure carrier and pressure damper when steam explosion happens. However, it is assumed that liquid is a pressure carrier without any attenuation. Therefore, the steam explosion pressure is applied directly to the inner wall of RPV.

For the analysis, ABAQUS 6.10 is used for the stress analysis FEM tool. To apply real time to stress analysis, the explicit mode of ABAQUS is used. Figure 3-12 shows the axisymmetric model of the RPV that the lower head is hemisphere.

ABAQUS has a large finite element library for 2-D and 3-D, cell, and solid. Figure 3-12 shows the basic dimension of geometric configuration of lower head. The lower head material is the SA508 class3 with characteristic of elastic-linear plastic including strain hardening effect. The material characteristics at 500°F are as follows.

$$\text{Young's modulus } E = 0.27 \times 10^8 \text{ psi}$$

$$\text{Poisson's ratio } \nu = 0.3$$

$$\text{Yield stress } \sigma_y = 50,000 \text{ psi}$$

$$\text{Allowable stress intensity } S_m = 30,000 \text{ psi}$$

$$\text{Tangent modulus } E_T = 0.235 \times 10^6 \text{ psi}$$

$$\text{Density } \rho = 0.283 \frac{\text{lb}}{\text{in}^3}$$

Figure 3-12 shows finite element model for the numerical grid that consists of four nodes elements, CAX4R, with the axi-symmetry boundary conditions. The total number of nodes is 440 and the total number of elements is 348.

Two boundary conditions should be specified in this model. Y-direction symmetry is applied at top side. X-direction symmetry is applied at left side. Y axi-symmetry is applied at model. Pressure is applied at inside and tabular data is used.

3.6.1 Stress Analysis Result for Design Conditions

The design pressure of 17.2 MPa (2,500 psi) acts on the inner lower head of the APR1400 design. In the analysis the maximum stress of 165.4 MPa and allowable value of 344 MPa (50,000 psi) have been obtained. In the case, the maximum equivalent strain is 0 % that is much less value than 11 % of allowable.

3.6.2 Stress Analysis Result for IVSE Conditions

For the analysis, the initial pressure of 0.5 MPa that was assumed in the in-vessel pressure is applied on the inner lower head. Pressure increases to its maximum pressure linearly during 2.5ms and decreases to the initial pressure during additional 2.5ms. The initial vessel pressure of 0.5MPa is maintained. In this analysis, the peak explosion pressures of 25, 50, 75, 100, 125, 150 and 175 MPa have been applied to the reactor vessel to map the allowable criteria of the maximum plastic equivalent strain of the reactor

vessel. The peak pressures correspond to the impulses of 62.5, 125, 187.5, 250, 312.5, 375 and 437.5 kPa-s.

Three different cases with the peak pressure of 50, 100, 150 MPa are discussed to illustrate the responds on RPV structure against explosion loadings and shown in Table 3-5. In case of the maximum pressure of 50MPa, the maximum plastic equivalent strain is 0.618% at 3.5ms, as shown in Figure 3-13. Time histories for plastic equivalent strain and von Mises stress of node that show maximum plastic equivalent strain are shown in Figure 3-14. These stress and strain are increased with time and vibrate under specific maximum plastic equivalent strain.

In case of maximum pressure 100 MPa, maximum plastic equivalent strain is 17.29% at 9.5ms. Time histories for plastic equivalent strain and von Mises stress of node that show maximum plastic equivalent strain are shown in Figure 3-15. These stress and strain are increased with time and vibrate under specific maximum plastic equivalent strain.

In case of the maximum pressure of 150MPa, the maximum plastic equivalent strain is 61.36% at 10ms. Time histories for plastic equivalent strain and von mises stress of node that show maximum plastic equivalent strain are shown in Figure 3-16. These stress and strain are increased with time and vibrate under specific maximum plastic equivalent strain. In this study, the stress limit on the node that plastic deformation occurred was observed at about 350MPa.

Figure 3-17 show the maximum hoop strain in terms of explosion impulse. The failure criteria limit of 50% maximum hoop strain corresponds to the explosion impulse of about 400 kPa-s. For the strain based failure criteria, Figure 3.18 summarized the structure responses on the explosion impulse. It shows the the Shockey criteria of 11% is the most conservative among others. For the criteria, the APR1400 RPV design can be safely maintain its integrity up to 215 kPa-s. The analysis evaluates the effect of dynamic pressures from a steam explosion on the integrity of the APR1400 reactor vessel. The present IVSE energetics of 62.3 kPa-s shows near zero strain in the RPV, well below the failure criteria. It is concluded that no threat of the APR1400 lower head due to the in-vessel steam explosion is expected.

3.7 Summary and Conclusions

For the IVSE analysis, there are number of assumptions that contribute to the analysis conservative. Those assumptions include;

- (a) Simplified internal geometry in RPV provides conservative assumptions on the corium configuration and early triggering
- (b) Bottom trigger of corium jet provides the maximized corium mixing and melt participation for explosion without additional build-up for the steam before the triggering of steam explosion
- (c) No explosion pressure shock attenuation from the location of IVSE to the RPV inner wall
- (d) One-dimensional analysis using TEXAS-V provides the maximum explosion energetics for the given mixing condition
- (e) No shock pressure attenuation from the location of explosion to the inner wall of RPV for the RPV structure analysis
- (f) Shiocky's criteria is conservative among other failure criteria evaluated in this study.

Under the consideration of the conservative assumptions, the structure analysis shows that no threat of the APR1400 lower head due to the in-vessel steam explosion is expected.

Table 3-1 Corium Properties

TS

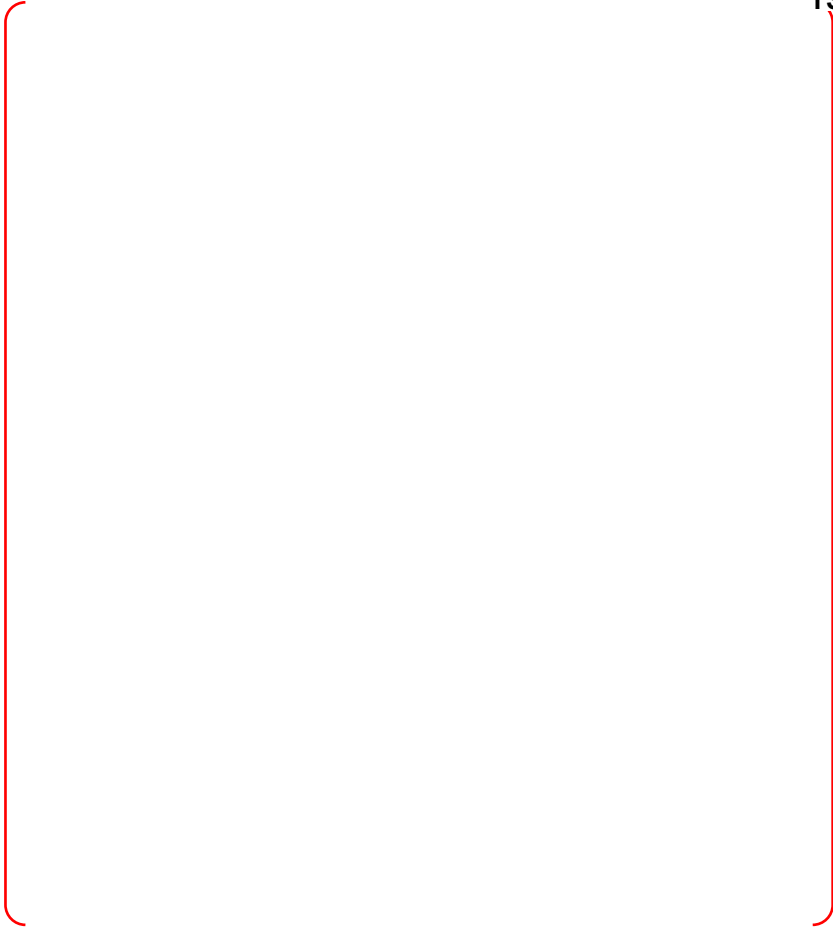


Table 3-3 The TEXAS-V Model Parameters Selected for the Analysis

TS

Table 3-4 Sensitivity Studies for Multi-jets

TS



Table 3-5 Summary of the results of the simplified steam explosion cases (50, 100 and 150)

TS

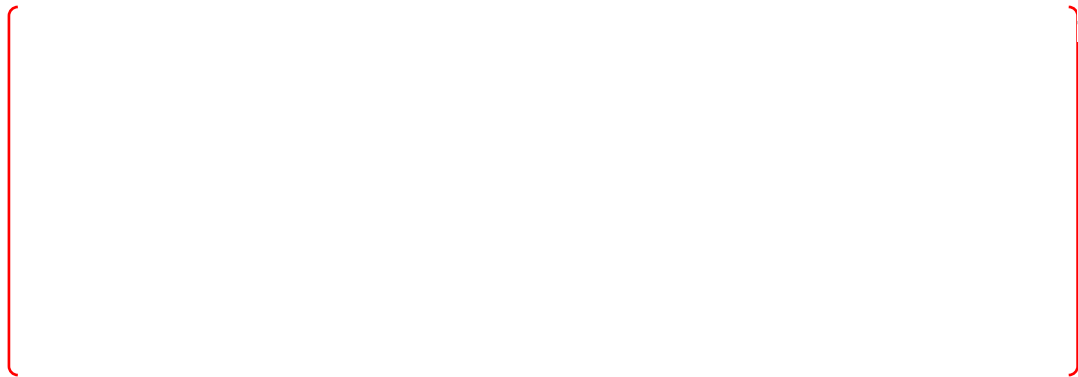




Figure 3-1 **TEXAS-V Nodalization for the In-Vessel Steam Explosion in the APR1400 RPV**



Figure 3-2 Corium Jet Penetration (a) and Axial Distribution of Void and Fragmented Melt Fraction at the time of Triggering (b)



Figure 3-3 **Void Fractions along the Axial Direction during Mixing Phase**



Figure 3-4 **Fragmented Melt Fractions along the Axial Direction during Mixing Phase**



Figure 3-5 **Void Fractions and Fragmented Melt Fraction History during Mixing Phase**



Figure 3-6 Pressures Calculated for the Base Case in terms of Variation of the User-Specific Mixing Diameter with respect to the Corium Jet Diameter



Figure 3-7 **Void Fractions along the Axial Direction during Explosion Phase**

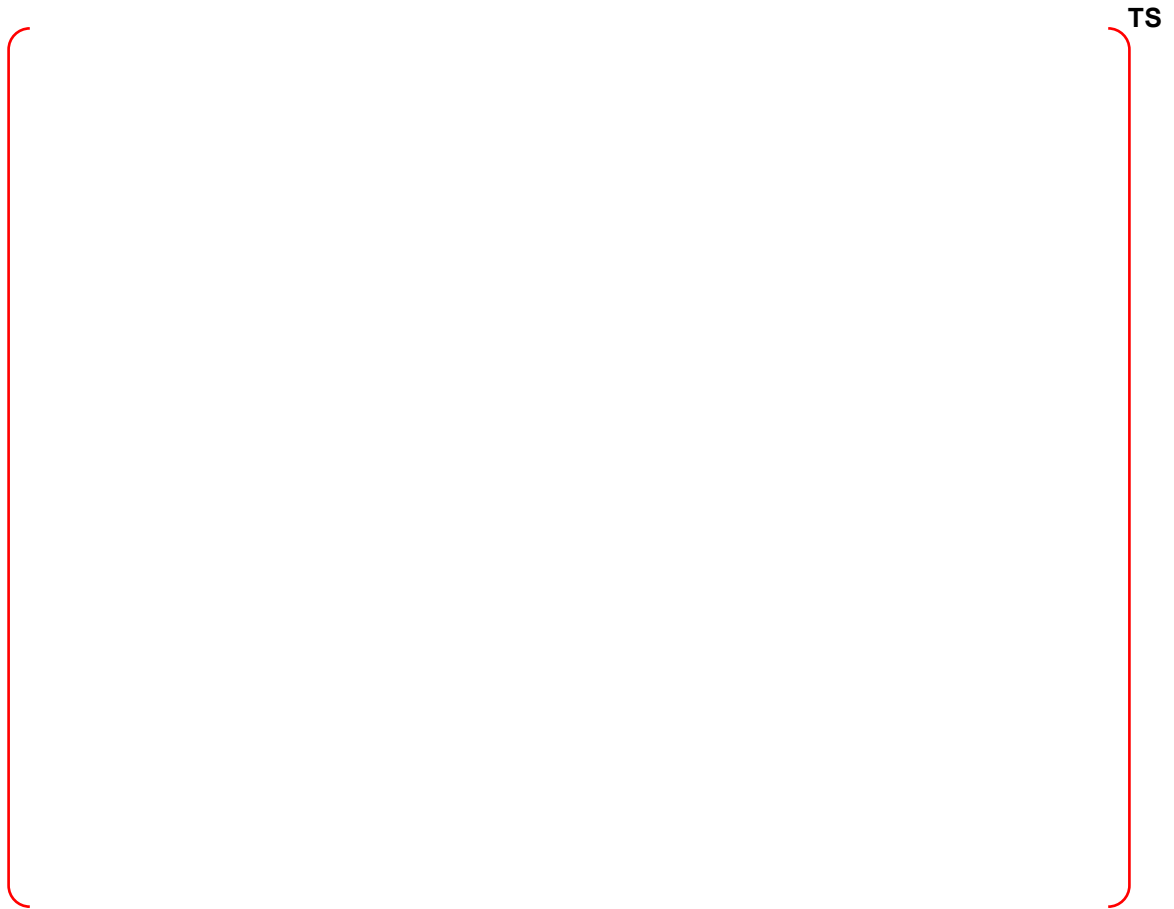


Figure 3-8 Impulses, Energy Transfer to Coolant, maximum Kinetic Energies of Coolant and the Conversion Ratio calculated for the Base Case



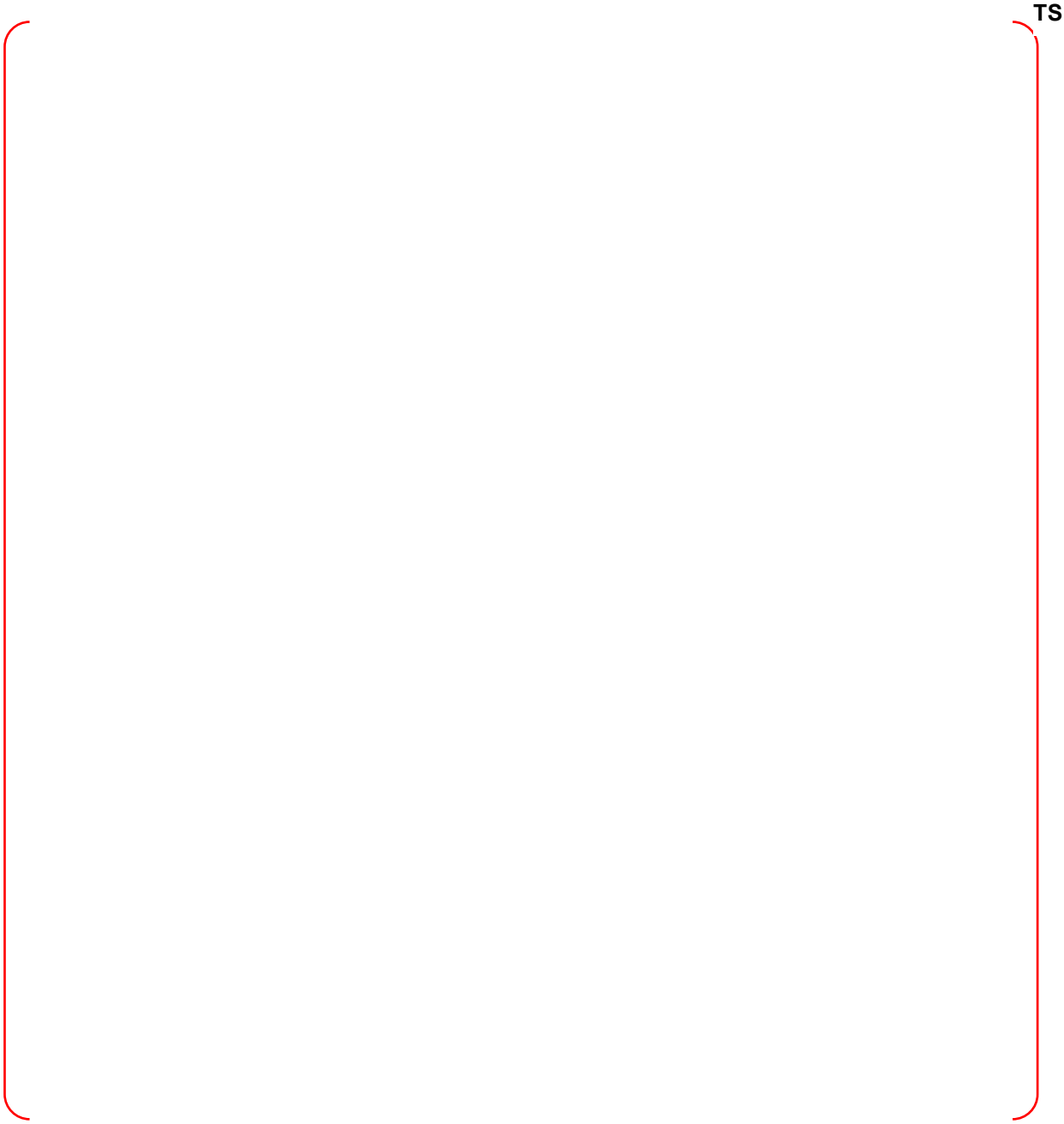
Figure 3-9 Pressure and Void Fractions History during Mixing Phase



Figure 3-10 **Models for the Reactor Case Analysis in the SERENA-I Project**



Figure 3-11 **Simplified Steam Explosion Pressure Profile for the Structure Analysis**



TS

Figure 3-12 Axisymmetric Sketch of Reactor Vessel: (a) Geometry, (b) Grid and (c) Boundary Conditions

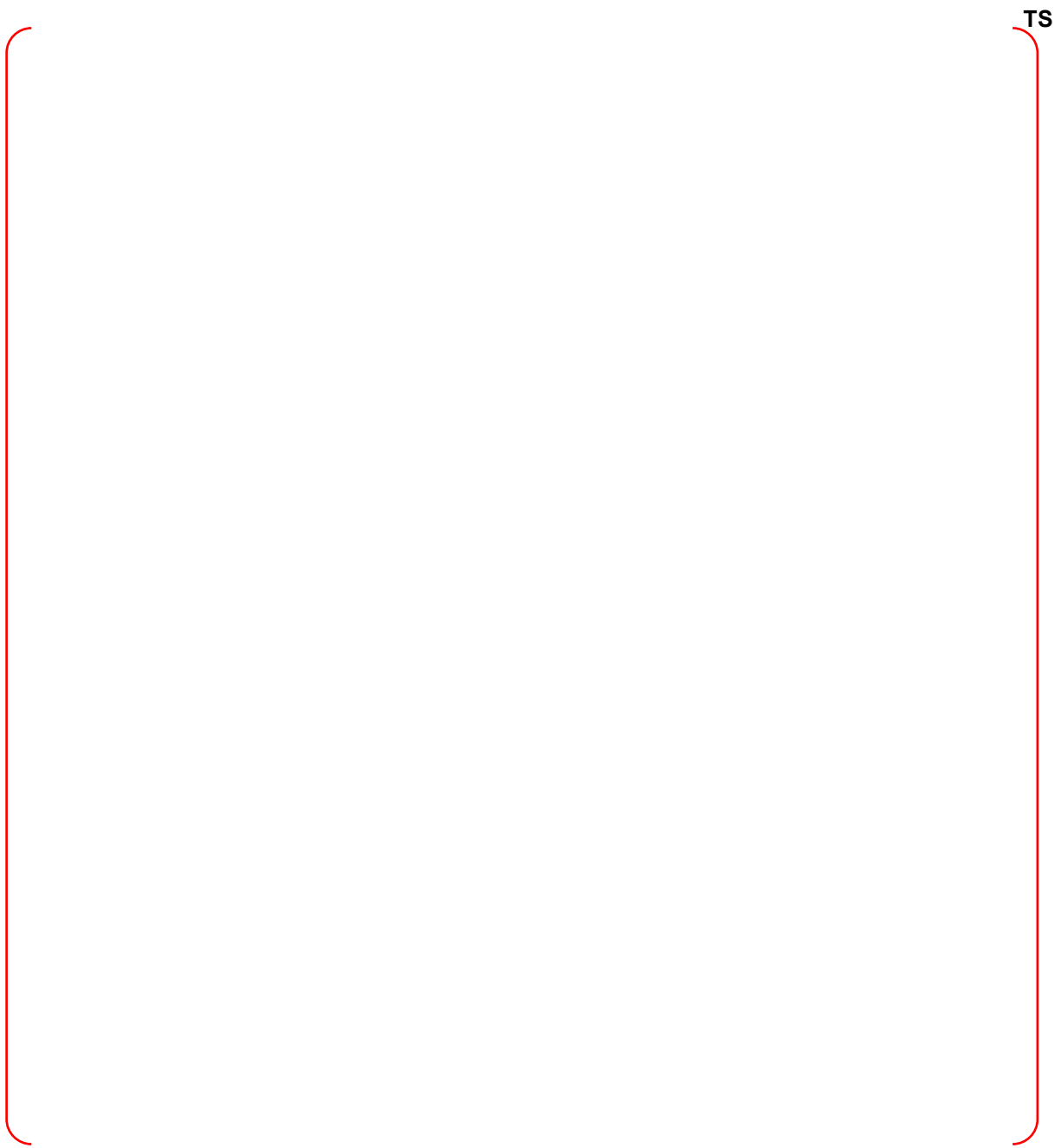


Figure 3-13 Results for the Maximum Pressure of 50 MPa: (a) Maximum Equivalent Plastic Strain, (b) Equivalent Plastic Strain at the Maximum Strain Node, and (c) Von Mises Stress at the Maximum Strain Node



Figure 3-14 Results of Stress Analysis: (a) Von Mises Stress and (2) Equivalent Plastic Strain

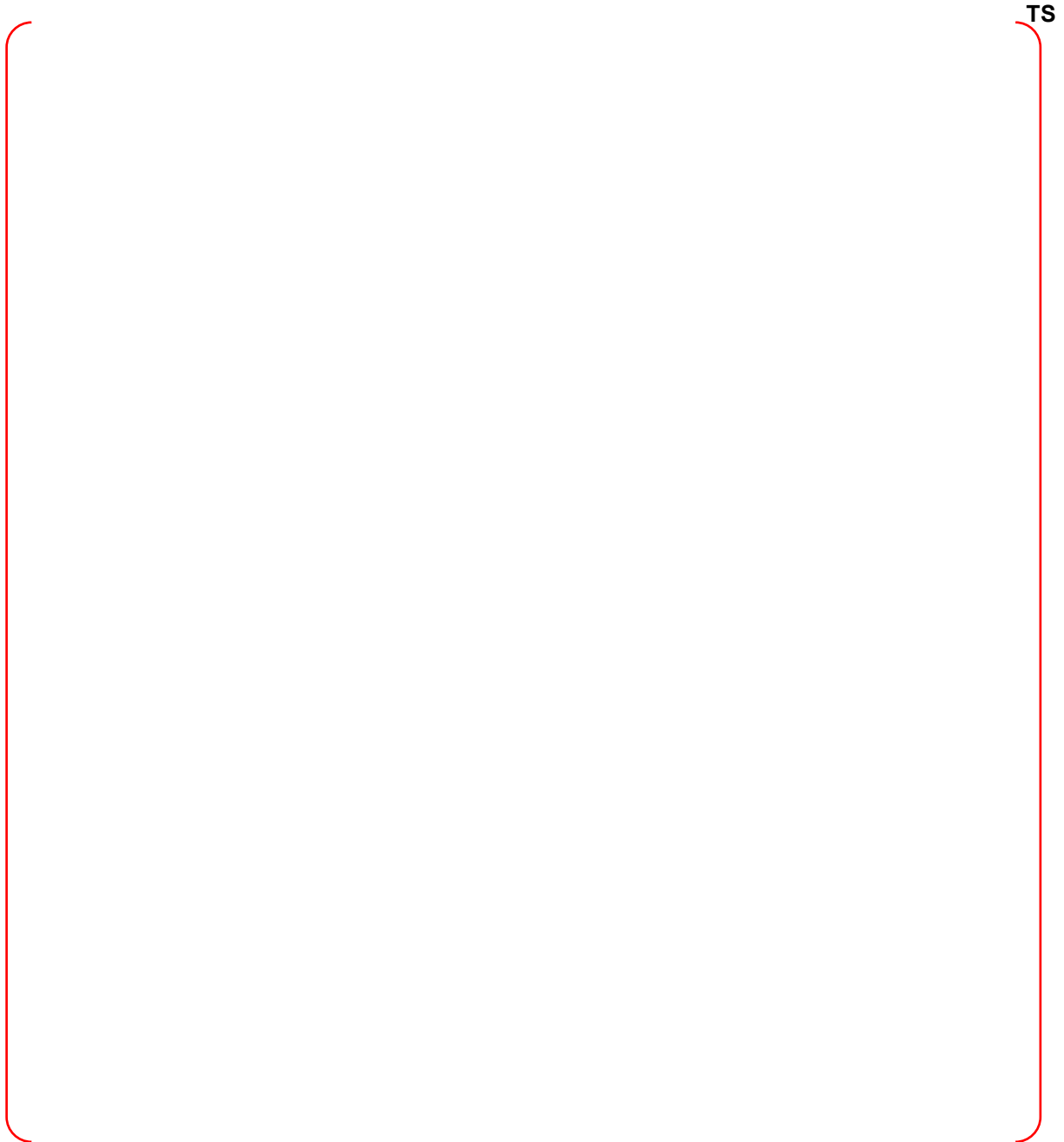


Figure 3-15 Results for the Maximum Pressure of 100 MPa: (a) Maximum Equivalent Plastic Strain, (b) Equivalent Plastic Strain at the Maximum Strain Node, and (c) Von Mises Stress at the Maximum Strain Node.

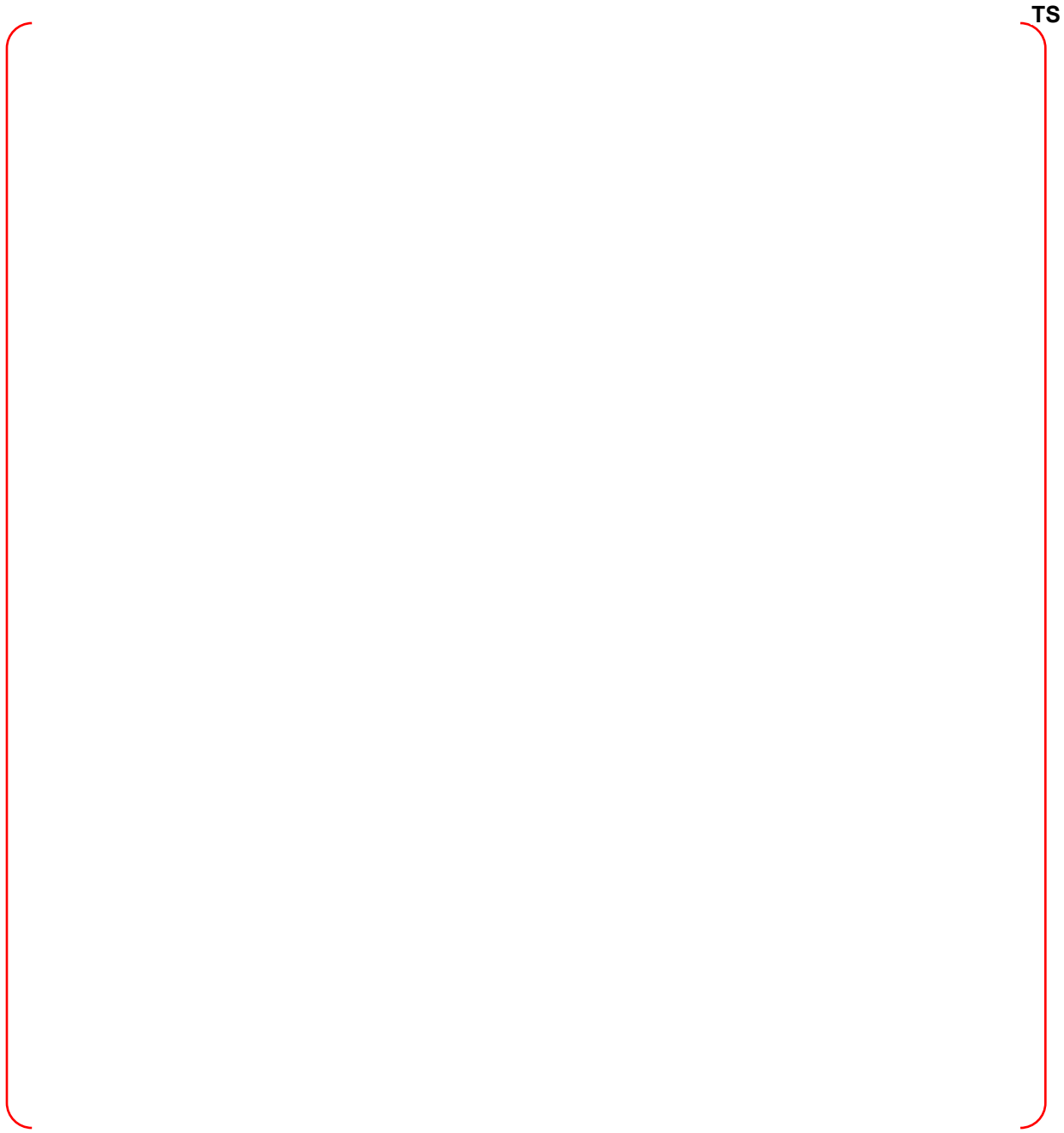


Figure 3-16 Results for the Maximum Pressure of 150 MPa: (a) Maximum Equivalent Plastic Strain, (b) Equivalent Plastic Strain at the Maximum Strain Node, and (c) Von Mises Stress at the Maximum Strain Node.



Figure 3-17 Maximum Hoop Strain in terms of Explosion Impulse



Figure 3-18 **Maximum Plastic Equivalent Strains in terms of Explosion Impulse for the comparison with the Failure Criteria.**

4 EX-VESSEL STEAM EXPLOSION ANALYSIS RESULTS FOR APR1400

4.1 Introductions

In this chapter, the APR1400 design specific analysis for the evaluation of ex-vessel steam explosion (EVSE) risk is discussed. The analysis consists of (a) determination of initial and boundary conditions for EVSE, (b) the evaluation of EVSE energetics, (c) the sensitivity analysis for key parameters that vary with the consideration of severe accident scenarios, measures and progression, and (d) finally, the analysis results is discussed to assess the EVSE risk in the APR1400 design.

4.2 Initial and Boundary Conditions of EVSE Analysis

In the EVSE analysis, it is of essence that vessel failure mode is identified to define the initial conditions of the EVSE analysis. However, the vessel failure mode is one of the most uncertain phenomena in the severe accidents since it requires understanding of the in-vessel severe accident progression as well as complex corium-vessel interaction. Therefore, the degree of uncertainty involved in the prediction of EVSE is determined by the sensitivity of those key uncertain parameters to the EVSE energetics. Minimizing the uncertainty associated with the determination of initial conditions for the EVSE analysis, the results from comprehensive system code analysis such as SCDAP/RELAP, MELCOR or MAAP in terms of risk-significant severe accident scenarios are often used. For instance, SCDAP/RELAP analysis for APR1400 plant [Reference 31] provides detailed quantitative prediction on the thermo-physical conditions of corium at vessel failure in terms of accident scenarios such as Total LOFW, SBO, and LOCA as shown in Table 4-1. In this analysis, the configuration of the melt components such as oxide and metal layers allows to evaluate the vessel failure location, corium composition, corium break velocity as well as the thermal conditions. However, the size of the vessel failure spot is still largely unknown although the size determines one of the most influential parameters, the corium jet diameter.

Recently, the MAAP analysis [Reference 32] is used to investigate the corium conditions when the reactor vessel fails for APR1400 plant considering several accident scenarios listed in Table 4-2. They employed MAAP4.0.8 to simulate a set of selected sequences in order to characterize the corium flow at vessel failure to provide initial conditions for ex-vessel steam explosion calculations as shown in Tables 4-3 to 4-5 for APR1400 design. The summary of the corium flow characteristics at vessel failure had been estimated in Table 4-6.

In this section, the initial and boundary conditions for the EVSE analysis will be determined by considering those analysis results as well as other experimental evidences.

In order to determine the initial and boundary conditions a few general assumptions related to FCI risk significant events of severe accident sequences are given below and further detailed assumptions for selecting a base case of the analysis are also given in the following sections.

- Ex-vessel steam explosion occurs at the partially flooded cavity with which the reactor pressure vessel is unable to be covered for ex-vessel cooling. This assumption was justified in the case of the complete station black-out event in when a passive cavity flooding is only available by opening a manual valve of the HVT tank connected to IRSWT. In the sensitivity analysis, the effects of the cavity water level on steam explosion loadings are examined.
- The late in-vessel phase with a complete generation of a liquid corium pool in the RPV lower plenum is assumed. The internal corium pool thermal conditions at a vessel failure are provided by the SCDAP/RELAP-5 analysis [Reference 31, 43]
- Global RPV failure is assumed to be unphysical and thereby excluded when discharged corium from RPV is directly relocated to the flooded cavity without temporal accumulation near RPV.

- The main mode of vessel failure without adequate cooling mechanisms is assumed to be a side RPV break due to so-called focusing effect resulted from an overlying thick metallic corium layer. In the case, 100% metallic corium is assumed to be poured into a flooded cavity for steam explosions. In the sensitivity analysis, the bottom RPV failure with 100% oxide release through a break hole generated by a 2-4 ICI tubes.

4.2.1 Corium Characteristics

4.2.1.1. Corium composition and thermal properties

The reference corium composition 90%UO₂-10%ZrO₂ with its thermal and transport properties as shown in Table 3-1 is chosen as for the in-vessel steam explosion analysis. Table 4-7 indicates also the properties of corium composition of 80%UO₂-20%ZrO₂ that often used in experiments that most of thermo-physical properties are similar and no significant effects of those difference on the steam explosion energetics.

4.2.1.2. Corium temperature

The corium temperature of 3000 K that corresponds to the superheat of 150 K is selected for the base case EVSE analysis. In the MAAP analysis the mean corium temperature of 2705 K was obtained due to the complex composition of materials that lowers the melt eutectic temperature. However, it is important to note that the melt superheat of 151 K similar to other analyses, the SCDAP/RELAP 5 analysis [Reference 31, 5, 19]. For the AP1000 analysis [Reference 19], for instance, the oxidic layer corium temperature of 3150 K was used as a conservatively bounding case. In addition, it is difficult to use the MAAP analysis results on corium conditions (temperature, composition etc.) because the corium formed in the RPV lower head prior to vessel breach were assumed to be a mixture of oxide and metal components of corium. In this case, the corium temperature may be low due to the eutectic process as well as its properties may also differ from the oxide or the metal components that may form as separate layers during the corium relocation from reactor core to the RPV lower head. Therefore, the corium composition with the known thermo-physical properties (90%-10% corium) but with keeping the same corium melt superheat of 150 K suggested the initial corium temperature of 3000 K for this EVSE analysis. Since the corium temperature is one of the most significant parameters that influences to the EVSE energetics, sensitivity analyses cover the corium temperatures from 2900 (50 K superheat) up to 3150 K (300 K superheat).

For the metallic layer of the corium, there is a few analysis for reactor applications; the AP1000 analysis used the metallic corium temperature of 2060K. Therefore in this analysis, the ranges of the metallic corium temperatures from 1700 up to 2300 K were chosen and the base case temperature of 2100K was selected.

4.2.2 Corium Discharge Characteristics

The reactor vessel failure will be inevitable consequence if a large molten corium pool generated in the lower plenum of the reactor vessel due to the corium relocation has no sufficient cooling from the vessel outside. Under the circumstances, the vessel steel experiences large degradation of its strength, resulting creep behavior due to the high temperature corium pool and pressure loading on the wall.

Some relevant information can be drawn from existing literatures [Reference 44, 45];

- Vessel steel creep accelerates when the wall temperature reaches more than 800 °C, much lower than corium melt pool temperature.
- The highest wall temperature on the vessel wall occurs at the location of the highest temperature of the melt pool established by a melt-pool convection.

- Molten corium pool produces multi-composition layer; top metallic layer, middle oxide layer and bottom metallic layer.
- Vessel failure experiments from the OECD-LHF and OLHF projects without a melt pool and the RIT-FOREVER with a melt pool shows a localized vessel failure at the hot spot of the wall temperature. In the FOREVER tests, the vessel failure always occurred at the hot spot, about 70° angle from the lower center of the vessel, on the wall produced by the melt pool convection.
- The creep rupture of the vessel occurs at a strain of 13~16% in the FOREVER test. It is worth to note that a vessel failure occurs at the location of the hot spot of the wall, not at the location of the largest strain or at the location of penetration which is usually located at near bottom of the vessel.
- Crack of the vessel similar to a fish mouth travels along the azimuthal direction to less than 30% of the vessel circumference.

Melt discharge rate due to the vessel failure depends on the vessel rupture characteristics originated from the vessel material properties. Amount of melt discharge due to a gradual rupture of the vessel results much less melt discharge than one with rapid rupture. Even in a moderate pressurized vessel (~ 20 bar), not all the melt was discharged at the time of failure.

4.2.2.1. Corium jet diameter (RPV Failure Size)

The vessel failure sizes depend largely on the thermo-mechanical interactions between the corium melt pool convections and the reactor vessel walls. Assuming no external cooling by cavity water is unavailable prior to the reactor vessel failure as a conservative ex-vessel scenario; the vessel failure is anticipated at the side of the vessel wall due to the focusing effect based upon the SCDAP/RELAP in-vessel analysis [Reference 31].

However, the estimation of vessel failure modes including the location, size and shape is hardly achievable in any certain degree. Based upon information above, the following postulations can be made for the estimation of a vessel breach size. This breach size will be considered as a corium jet diameter for the TEXAS analysis.

For the case of the side failure,

- (a) the vessel fails at the interface at the top metallic layer,
- (b) the global failure is remote,
- (c) the crack shape of the vessel is a fish mouth

Under the assumptions, the maximum breach size can be obtained by assuming the breach hole diameter equal to the metallic melt layer thickness, ranging from 0.54-0.63m. The practical minimum size of the vessel breach size can be estimated by assuming the fish mouth failure observed in experiments and considered to be 0.1 m.

For the case of the bottom failure,

- (a) localized failure of the 1-4 vessel penetration tubes is most likely and
- (b) the global bottom rupture due to combined failure of adjacent penetration tubes are unlikely.

The MAAP analysis also suggested that RPV with penetration results mostly in the penetration failure than the creep rupture and the mean vessel failure diameter is suggested to 0.56 m with the standard deviation of 0.14m.

In general, however, for the penetration failure, the vessel breach size, or the initial corium diameter, of 0.3 m is used [Reference 5] and the corium diameter of 0.5 m is used to represent the typical vessel failure size due to the creep rupture. In the MAAP analysis, no evidence of global vessel failure results in much larger corium jet diameter to be considered.

Based on the information, the initial corium diameter for the base case ex-vessel steam explosion is set to 0.3 m and the corium jet diameters from 0.1 to 0.6 m are considered for the sensitivity analysis.

4.2.2.2. Corium jet velocity

The corium jet velocity of 4 m/s is selected for the base case EVSE analysis considering the MAAP analysis results (see Table 4-8). For the sensitivity analysis, the initial corium jet velocities from 1 to 6 m/s were considered.

4.2.2.3. Water in Cavity

The cavity flooding system (CFS) is one of the main safety measures followed by the SAMG (Severe Accident Management Guideline) with which subcooled water floods the cavity and partially submerges the RPV as shown in Figure 4-1. The measure aims to prevent severe accidents progression beyond in-vessel scenarios by providing ex-vessel cooling. In the case of failing in-vessel retention of corium, the flooded cavity provides long-term cooling of corium debris discharged from the failed RPV.

4.2.2.4. Containment ambient pressure

The containment ambient pressure increases during the severe accident progress. Typical 0.2 MPa containment pressure is selected. In general, since the effect of the ambient pressure in the ranges of order of few bars has little effect on the steam explosion energetics, the sensitivity analysis for this parameter is not considered.

4.2.2.5. Cavity water level

The CFS provides water from the IRSWT in two separate operations; (a) passive flooding by manual opening of HVT valves and (b) active flooding by operating External Reactor Vessel Cooling System. The first passive flooding operation fills water up to 6.4 m from the cavity floor within 1350 s from the HVT valve opening and the second active operation floods water up to 13.2 m for additional 2400 to 3000 s, covering approximately a half of RPV for ex-vessel cooling. The present base case analysis considered the risk of steam explosions as the IVR/ERVC measure is not provided. However, in the sensitivity analysis, fully flooded cavity water level that covers the RPV lower head to provide the IVR/ERVC measure is considered.

4.2.2.6. Cavity water subcooling

The water subcooling in the cavity is selected from the various analysis results to be ranged from 20 to 90 K at the estimated containment pressure, considering various analyses for the ex-vessel steam explosions. The base case condition of 42 K subcooling is selected by the consideration of the lower subcooling of coolant estimated by the MAAP analysis. However, the sensitivity analysis is performed for the subcooling ranges.

4.2.3 Summary

In summary, Table 4-8 lists the initial and boundary conditions for the base case of EVSE analysis and their minimum and maximum ranges. The base case is assumed to be the EVSE due to the bottom vessel failure with the partially flooded cavity. The side vessel failure case can be considered as a sensitivity study if the vessel failure occurs due to the focusing effect.

4.3 TEXAS-V Modeling

The plant geometry for the TEXAS-V analysis is shown in Figure 4-2(a). The computational nodalization for the TEXAS analysis for the RPV is built as shown in Figure 4-2(b).

The first nodalization group that represents the RPV water has 16 nodes that have the thickness of 0.4 m. The second nodalization that represents the gas buffer region has 12 nodes with the same node thickness of 0.4 m, because of the consideration of water level swelling during the mixing phase. Lastly, the third nodalization has seven nodes with the thickness of 1 m. The location of corium introduction is at 6.5 m. At the bottom of the nodes, trigger cell is located to provide the trigger pressure. The diameter of the first and second nodes are the user input parameter, ARIY, that should be determined to let the 1-D TEXAS-V code produce the maximum energetics for given initial and boundary conditions. The diameter of the gas buffer zone is set for 50 m² sufficiently large.

4.4 Evaluation of Dynamic Loads of EVSE – Base Case

4.4.1 Mixing Phase of EVSE

Figure 4-3 illustrate the void fraction generated by corium jet penetration into cavity water during the mixing phase of the base case. The corium reached to the bottom of the RPV about 1.4 s when the explosion starts. The corium jet penetrates and breaks up into small particles. Figure 4-3 shows typical void generation where the larger amount of vapor void on the top of the cavity water, reaching up to 2% average void fraction. Figure 4-4 shows the fraction of melt along the axial direction in the cavity water. The void fractions in the lower region were very low although the corium jet fragmented. Therefore, it is expected that steam explosion can likely occur at the bottom and propagates upward, triggering subsequent explosions.

4.4.2 Explosion Phase of EVSE

Figures 4.5 and 4.8(a) show the steam explosion pressure profiles in terms of the explosion time. The maximum pressure and impulse of 60.519 MPa and 179.93 kPa-s, respectively. The pressure profiles show the typical shock characteristics as the rapid build-up of pressure front and a long tail with respect to time. The explosion pressure front traveled up and dissipated in the upper axial location due to the presence of a volume of steam as shown in the mixing phase.

Figures 4.6 shows the void fraction profiles during the explosion phase. The lower part of the lower head where steam explosion was triggered builds up steam due to the explosion during the period the explosion phase. The upper region however where the steam generated in the mixing phase shows the rapid condensation during the explosion phase period, 20 ms.

The impulse asserted to the surrounding structure was estimated by the integration of the explosion shock pressure during the explosion period. The evaluated impulses at each node are shown in Figure 4-7(a). The impulse at the node of cavity floor reached 179.93 kPa-s. The maximum possible energetics of steam explosion in this case estimated by the 1-D TEXAS-V analysis will travel (and be attenuated) to the surrounding cavity structure. The dissipation of shock pressure from a mixing zone to the cavity walls along the single phase cavity water is discussed in the next section. Figure 4-9 show the top view of the cavity structure. In this figure, seven locations at the cavity wall to evaluate the explosion shock attenuation at those cavity wall surface. The distances from the RPV center to the seven locations ranges from 2.159 to 5.744 m.

Figures 4.7(b), (c) and (d) show more insights of the explosion phase of the steam explosions in RPV that include the energy partitioning, the coolant kinetic energy and the conversion ratio history during the explosion phase. In particular, the conversion ratio of the steam explosion reaches its maximum of near 1.8% after the triggering of explosion.

4.4.2.1. Evaluation of Dynamic Loads of EVSE at the Cavity Walls

Shock pressure generated from the steam explosion in the reactor cavity pool propagates. In the TEXAS code, however, due to its one-dimensionality of computational domain, the pressure generated at one location, $x(z)$, can be tractable only in the vertical z -direction. Therefore, the impulse acts to the cavity wall in the radial direction requires additional analysis. The most recent version of the TEXAS-V code encompassed with the ANSYS CFD packages to analyze the radial shock propagation. On the other hand, the underwater shock propagation studied by Cole [Reference 46] known as a TNT method has been well applied for this purpose.

Figure 4-9 illustrates the reactor cavity arrangement in the APR1400 plant. The distances from the center axis of the RPV centerline to the near cavity walls are listed in Table 4-11. It is noted that the closest wall from the center has a distance of 2.159 m.

If the maximum explosion pressure at a known distance, for instance, $r=R_{mix}$, is ΔP_{mix} , the distance-dependent maximum explosion pressure, $\Delta P_m(r)$ becomes,

$$\Delta P_m = \Delta P_{max} \left(\frac{1}{r} \right)^\alpha \quad (\text{Eq. 4.1})$$

where, $\alpha=1.13$ and all units are the British units, ie., P [psia] and r [ft]. For instance, in the TEXAS-V analysis, it is difficult to evaluate the exact mixing zone for the steam explosion although the one-dimensional characteristic parameter, ARIY, was at to 7 m^2 that is the diameter of approximately 3 m. By assuming this diameter be the mixing zone and considering the distance from the outer mixing boundary to the near cavity wall, the maximum pressure propagation along the lateral direction to the cavity wall can be estimated by Eq. (4.1) using $\Delta P_{max}=60.51 \text{ MPa}$. Table 4-11 shows the estimated maximum pressures at the cavity walls that significantly attenuated from the EVSE maximum pressure. These estimated values can be used for the structure analysis of cavity integrity due to the EVSE loadings.

4.5 Sensitivity Study

For the sensitivity study, additional cases for issues associated with (a) vessel failure modes such as bottom failure due to penetration tube failure, and side vessel failure due to metallic layer focusing effect, (b) severe accident management strategies, and (c) key corium characteristics including the corium temperature, the velocity and diameter and the cavity water temperature are examined. Tables 4-12 to 16 show the result of the analyses in comparison to the base case. The details are discussed in the following sub-sections.

4.5.1 Reactor Vessel Failure Mode Issues

For the side vessel failure, the vessel failure location and break size are important parameters that determine the energetics of EVSE because it determines the mass of corium participated during EVSE and the distance between the mixing zone of steam explosion and the nearest cavity wall. In the case of a potential vessel failure due to the metallic corium layer focusing effect with assumption of the side vessel failure without IVR-ERVC (In-Vessel Core Melt Retention-External Reactor Vessel Cooling) SAM strategy, RPV is exposed to atmosphere and the location of side vessel failure occurs at 8.05 m above the cavity floor ($\sim 80^\circ$) as shown in Figure 4-2(A).

The analysis shows that the peak pressure and corresponding impulse of 60.35 MPa and 194.07 kPa-s,

as shown in Table 4-12, are estimated. The results are similar to those from the base case. As described in Table 4-8, the initial conditions for the SVF case assume that the corium is 100% metallic composition with high superheat of corium but lower temperature. In addition, the corium injection velocity at the vessel breach location is low due to the small gravitational head of corium in the reactor vessel. Comparing to the base case, the peak pressure due to steam explosion is similar but the impulse generated by the steam explosion is higher. The steam explosion loadings to the cavity wall will be higher than that of the base case due to the location of the vessel failure.

4.5.2 SAMG Related Issues: In-Vessel Corium Melt Retention (IVR)

For the case of IVR/ERVC, the RPV is in a stage of submersion in the fully flooded cavity water up to EL114'-4" from the plant ground level, or 13.8 m from the plant cavity floor (see Figure 4-2), to provide the external cooling when the core meltdown and relocation to the bottom of the reactor vessel occurs. In this situation, there is two potential vessel failure modes; bottom and side vessel failures at the locations assumed to be 6.5 and 8.05 m, respectively.

Table 4-12 shows that the peak pressures and maximum impulses for both bottom and side vessel failures with IVR-ERVC are 69.79 MPa, 217.33 kPa-s and 48.84 MPa, 226.16 kPa-s. It is noted that for the bottom vessel failure in the case of fully-flooded (FF) case, the explosion peak pressure is slightly higher but the impulse becomes about 20% higher. For the side vessel failure, however, it was observed that the tendency of explosion pressure profile was opposite to one for the bottom vessel failure, resulting in about 20% lower peak pressure but 26% higher impulse. The result indicates that the energetics of the side vessel failure is slightly higher than one of the bottom vessel failure.

4.5.3 Effects of Key Physical Parameters on EVSE Energetics

In this sensitivity analysis, some of key parameters pertaining to the thermal and dynamic properties of corium and the conditions of cavity water are examined to investigate their uncertainties on the energetics of EVSE in the APR1400 design. In this sensitivity analysis, it is worth to note that the mixing area defined by the model parameter, ARYI value of 7 m², is maintained in most of cases (except corium jet diameter effects).

4.5.3.1 Corium Temperature Effects

The effect of the initial corium temperatures on the EVSE energetics with the minimum and the maximum temperatures of 2900 and 3150 K is analyzed as shown in Table 4-13. Those temperatures correspond to the corium superheats of 50 and 300 K respectively. The results show that the energetics of EVSE in terms of pressure impulse increases with the corium temperature; 168.27 and 216.69 kPa-s for 50 K and 300 K superheat of corium, respectively. However, it also shows that the peak pressures for three cases; minimum, base, and maximum, are in a similar range of approximately 57-67 MPa. It indicates that the increase of thermal contents of corium enhances the explosion pressure peaks and profiles.

4.5.3.2 Corium Ejection Velocity Effects

The corium ejection velocity influences directly to the mixing phase of steam explosion process, mainly to corium jet breakup. In general, jet breakup length depends on the Froude number, and the ratio of density ratios between jet and coolant as shown in Eq. (4-2) below, showing the linear increase of the jet breakup length with the jet velocity,

$$\frac{L}{D_j} \propto \left(\frac{\rho_j}{\rho_c}\right)^{0.5} (Fr)^{0.5} \quad (\text{Eq. 4.2})$$

where,

$$\text{Fr} \propto \frac{V_j^2}{gD_j} \quad (\text{Eq. 4.3})$$

The jet breakup diameter during the breakup process in the TEXAS-V code is calculated based upon the Weber number in terms of the relative velocity between jet and coolant. Therefore, as the corium jet velocity increases the jet breakup occurs in a deeper penetration length and the diameter of fragmented jet becomes exponentially decreases. This process provides the finer mixing particle diameters, resulting more energetic steam explosion. Table 4-14 shows that the peak pressures and the impulses of steam explosion increases from 48.3 to 83.4 MPa and from 83.1 to 181.9 kPa-s as the jet velocity increases from 1 to 6 m/s.

4.5.3.3. Corium Jet Diameter

The corium jet diameter directly influences on the corium mass participation in the EVSE process. For the computational stability, the ARIY parameter is adjusted. As shown in Table 4-15, the effect of the corium jet diameter significantly influences on the EVSE energetics. For the jet diameter of 0.1 and 0.6, the resulting peak pressures and the maximum impulses become 12.34 to 86.42 MPa and 35.74 to 250.12 kPa-s.

4.5.3.4. Corium Temperature

Table 4-16 shows that the effect of coolant temperature, the degree of water subcooling in the cavity show no significant effect on the EVSE energetics comparing to those from other parameters.

4.6 Corium Material Effects on EVSE Energetics

It is worth noting that the analysis was performed with the 1-D TEXAS-V code that potentially provides the conservative maximum energetics for the given initial and boundary conditions. In addition, the TEXAS-V model has been validated for the KROTOS-alumina tests that provided the high energetics. However, recent experimental results with corium suggested that the energetics of steam explosion with the corium composition is very limited. To verify this issue, TEXAS-V analysis for the recent TROI TS-4 test has been performed. As shown in Figure 4-10 the TEXAS-V significantly over-predict the corium experimental pressure, explain the conservatism associated with the present TEXAS-V model and results of potential conservatism in the reactor case analysis like in this work.

4.7 Reactor Cavity Structural Integrity Assessment

4.7.1 Introduction

The ex-vessel steam explosion (EVSE) is a severe accident condition that occurs in the reactor cavity. During this severe accident event, the reactor pressure vessel (RPV) fails allowing molten core to pour into the water under the RPV. The formation of shock waves from an EVSE may cause damage to the reactor cavity structure that supports the RPV and the shield wall.

The structural assessment of reactor cavity EVSE loading performed in SKN 3&4 project. As the geometries and reinforcement re-bar layout are same between SKN 3&4 and APR1400, the results of reactor cavity structural assessment of APR1400 will be same SKN 3&4 evaluation results if EVSE pressure time history is not changed.

As shown in the Figure 4-11, the EVSE pressure time history curve obtained from APR 1400 shows the almost identical values compared with that from SKN 3&4 with small perturbation after peak pressure. The difference is negligible because the dynamic structural response depends on the peak value and its time.

Therefore, the reactor cavity assessment of SKN 3&4 EVSE loading is acceptable instead of using APR1400 EVSE loading. The results of reactor cavity assessment of SKN 3&4 provided in following sections.

4.7.2 SKN 3&4 Reactor Cavity Structural Assessment on EVSE loading

4.7.2.1. Model Description

The finite element model of the reactor cavity wall are shown and highlighted in Figure 4-12 and Figure 4-13 respectively. Figure 4-12 displays a side view and Figure 4-13 the top view of the reactor cavity. The model includes the reactor cavity between elevations 66 ft and 130 ft. Steel reinforcement, liner plates, RPV, and the piping between the RPV and the two steam generators were included in the model. The steam generators and the Reactor Coolant Pumps (RCP) were partially included in the model to predict the motion of the piping more accurately. The model was composed of solid elements, shell elements and beam elements.

4.7.2.2. Finite Element Model

The finite element model (Figure 4-13 ~ 4-16) generated to perform the integrity assessment can be described in five modularized models:

- Reactor cavity
- Steel liner plates
- Horizontal rebars
- Vertical rebars
- RPV, Reactor Coolant System (RCS), and its support system

The reactor cavity is modeled using 3D solid elements. The concrete material is modeled using the Winfrith concrete material model available in LS-DYNA. Steel liners are modeled using shell elements and they are merged with the concrete; in other words, they have common nodes with the concrete underneath. Two types of liner plates are used in the model: Stainless steel liner plates (SS liner) and Carbon steel liner plates (CS Liner) as illustrated in the related figures. The reinforcement steel bars are modeled using beam elements.

The RCS are modeled as elastic-plastic shell elements. The support legs are modeled as solid elements. The Steam Generator (SG) and the Reactor Coolant Pump (RCP) are modeled as beam elements with elastic properties to represent their stiffness contribution. The top end of the SG and RCP are connected to the RCS using constrained interpolation option in LS-DYNA. By using this constraint, the motion of a dependent node (nodes on SG and RCP) is interpolated from the motion of a set of independent nodes (nodes on hot leg and cold leg pipes).

4.7.2.3. EVSE Locations and Pressure Time History

The pressure distribution is calculated using the following equation:

$$\Delta P_m(r) = k \left(\frac{1}{r} \right)^{1.13} \quad (\text{Eq. 4.4})$$

where k is the pressure at the explosion location, r is the distance of the segment to the explosion location and ΔP_m is the pressure at corresponding segment.

The pressure distribution zones and time-history are calculated based on Eq. (4.4) and shown in Figure 4-17 & 4-18. The pressure distribution for Zone 2 and Zone 3 along the elevation is tabulated in Table 3-4. The pressure distribution for Zone 1 is assumed to be constant in horizontal direction with a scale factor of 0.0297 based on the distance from the explosion location to the wall of Zone 1.

4.7.2.4. Analysis Results

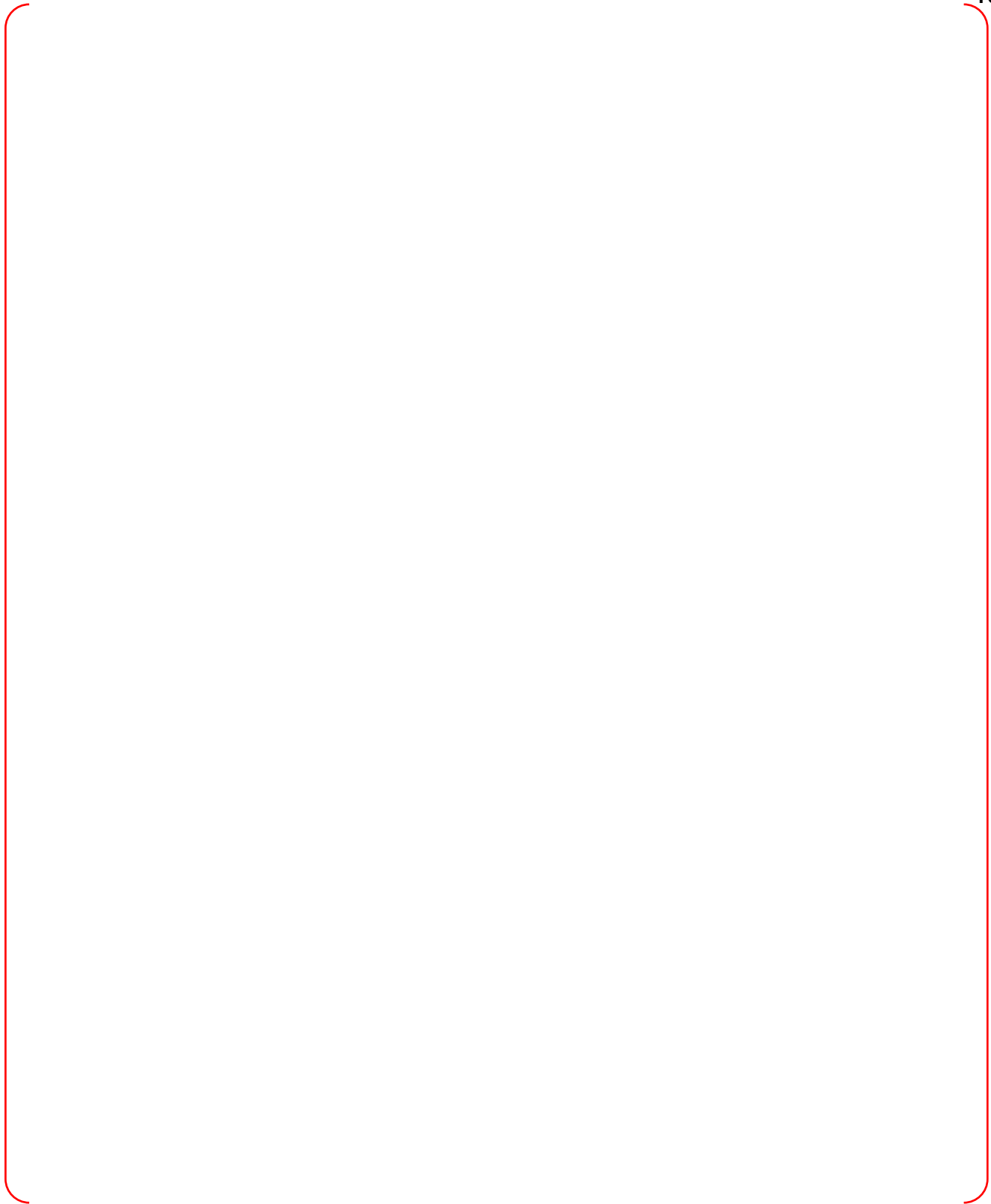
The maximum resultant displacement of the concrete cavity wall is 0.48 inch at 4 ms. The cracks are formed in the concrete and the pattern is shown in Figures. As can be seen, base slab, Zone 1, Zone 2, Zone 3 and Zone 4 are cracked. Also, cracks are formed in the concrete supporting the RPV. The induced maximum effective plastic strain is around 1.1% and it occurs in the bottom liner plate. The effective plastic strains induced in the rebars are around 1.7% for the horizontal rebars and around 0.7% for the vertical rebars. The maximum strain occurs in the base slab rebars. The rebars in the concrete region where RPV supports are anchored remain elastic. The maximum vertical displacement of the RPV is around 0.073 inch. The displacement is measured at the lower dome section of the RPV.

The least vertical gap between the penetrations sleeve of primary shield wall and the hot and cold leg pipes is 19 in. The maximum vertical displacement of the hot and cold leg pipes is observed to be around 0.043 inch. The displacement is small and will not lead to interaction between the hot and cold leg pipes and the penetration sleeve of reactor cavity wall. These displacements are measured at the top end of steam generator and RCP supports where RCS is connected.

The maximum axial load acting in the RPV column support anchor bolts is approximately 380 kips. This corresponds to a stress of 21.5 ksi in each anchor bolt. Hence, the anchor bolts remain elastic.

The maximum displacements, concrete cracks, liner plate stresses, reinforcement re-bar stresses, RPV column support anchor bolt stresses and strains for EVSE loading to reactor cavity are summarized in Table 4-17 and analysis result are shown in Figures 4-19 to 4-24.

Table 4-1 Corium Pool Configuration and Thermal Loads with respect to Accident Scenarios
(Reference 31, Table 3.1.6 and 3.1.7)



TS



TS

Table 4-2 Accident Scenarios Considered in the MAAP Analysis [Reference 32]

TS

A large, empty rectangular area enclosed by a red bracket, indicating that the content of Table 4-2 is missing or redacted from the document.

Table 4-3 Melt Conditions at Vessel Failure with Penetrations (IOXIDHT=0) [Reference 32]

TS



TS

Table 4-4 Melt Conditions at Vessel Failure without Penetration (IOXIDHT=0) [Reference 32]

TS



Table 4-5 Melt Conditions at Vessel Failure with Penetrations (IOXIDHT=1) [Reference 32]

TS



TS

Table 4-6 Mean and Standard Deviation of Corium Flow Results at Vessel Failure [Reference 32]



TS

Table 4-7 Corium Material Properties

TS

Table 4-8 Initial and Boundary Conditions for EVSE Analysis

TS



Table 4-9 The TEXAS-V Model Parameters Selected for the Analysis

TS



Table 4-10 Results of the TEXAS-V Analyses for the Base Cases

TS

A large red bracket is drawn on the page, spanning the vertical space where Table 4-10 would be located. The bracket is open at the top and bottom, and its ends are curved inward. It indicates that the content of this table is missing or redacted.

Table 4-11 Predicted Pressure at the Cavity Wall based on the TEXAS-V Analyses

TS

A large red bracket is drawn on the page, spanning the vertical space where Table 4-11 would be located. The bracket is open at the top and bottom, and its ends are curved inward. It indicates that the content of this table is missing or redacted.

Table 4-12 Effect of Accident Progression Scenarios



A large red bracket on the right side of the page, spanning from the level of Table 4-12 down to the level of Table 4-13, indicating that the content of these tables is redacted or withheld.

Table 4-13 Effect of Corium Temperature



A large red bracket on the right side of the page, spanning from the level of Table 4-13 down to the level of the footer, indicating that the content of this table is redacted or withheld.

Table 4-14 Effect of Corium Ejection Velocity

	TS
--	-----------

Table 4-15 Effect of Corium Jet Diameter

	TS
--	-----------

Table 4-16 Effect of Cavity Water Temperature

	TS
--	-----------

Table 4-17 Summary of Cavity Structural Integrity Analysis Result



The table area is currently empty, indicated by large red brackets on the left and right sides.

TS

TS



Figure 4-1 Schematic Diagram of the Cavity Flooding System of APR1400

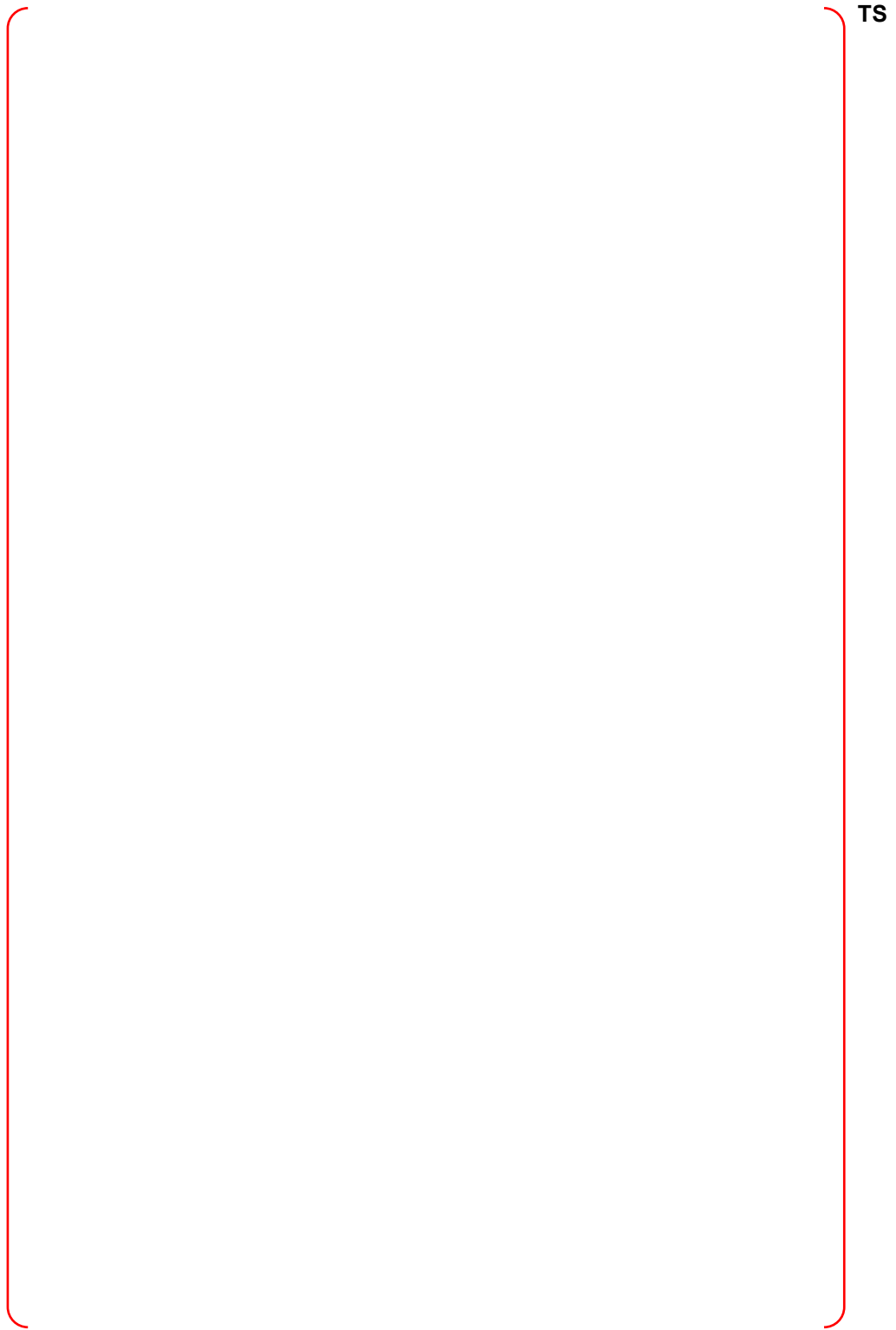


Figure 4-2 Nodalization for the Ex-Vessel Steam Explosion in the APR1400 Cavity

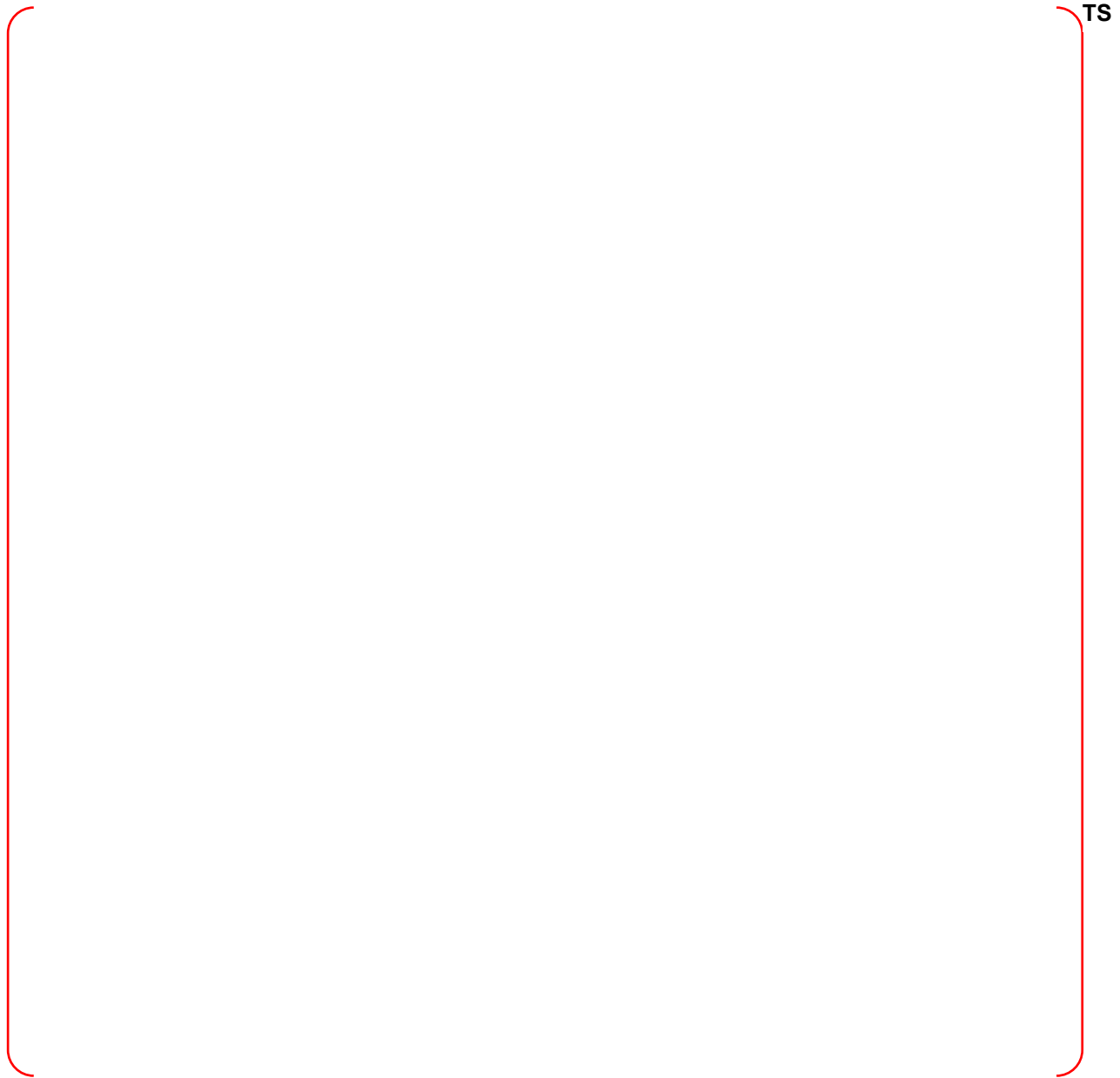


Figure 4-3 Void Fractions Calculated for the Base Case during Mixing Phase



Figure 4-4 Melt Fractions Calculated for the Base Case during Mixing Phase



Figure 4-5 Pressures Calculated for the Base Case

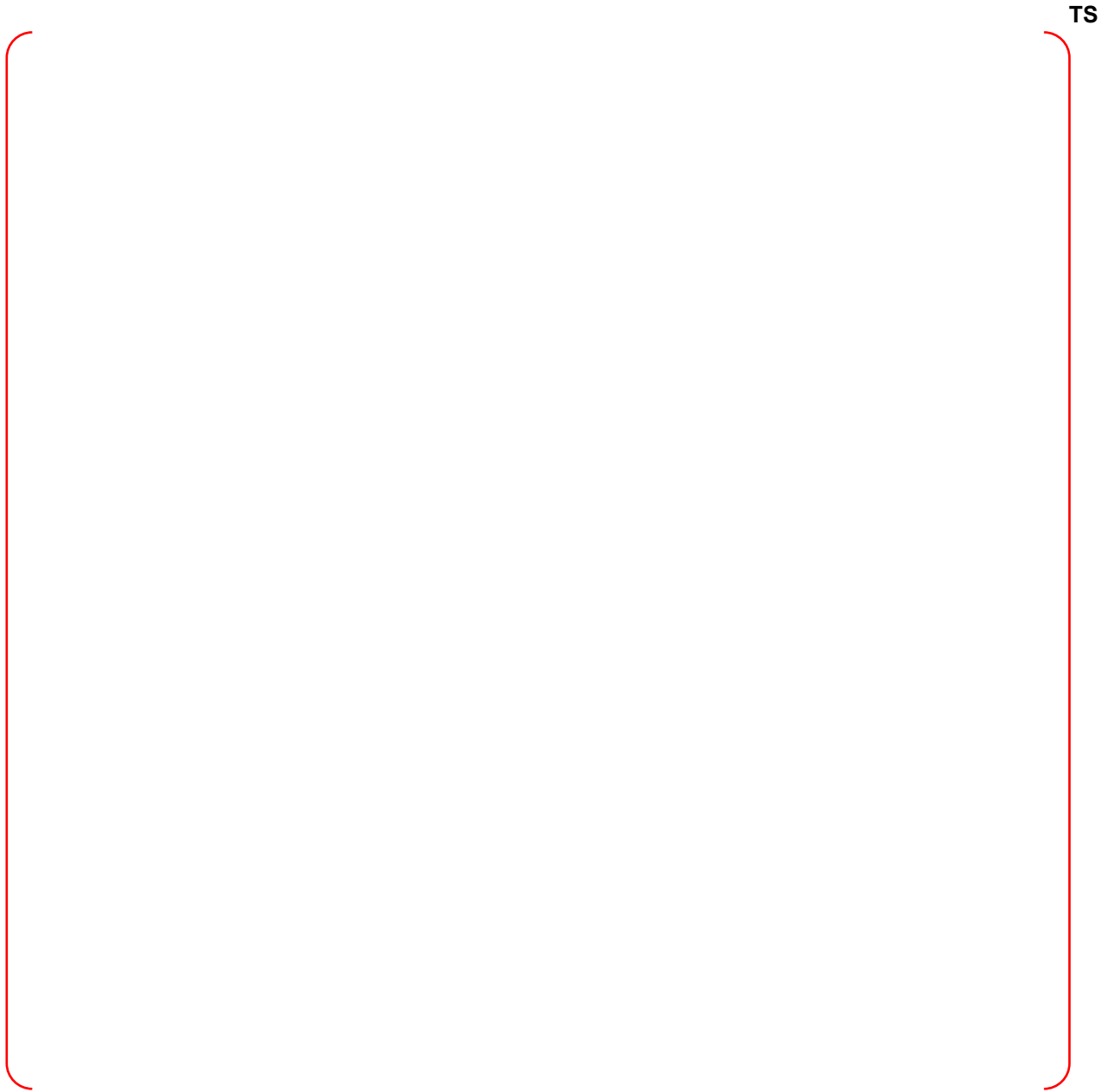


Figure 4-6 Void Fractions Calculated for the Base Case during Explosion Phase

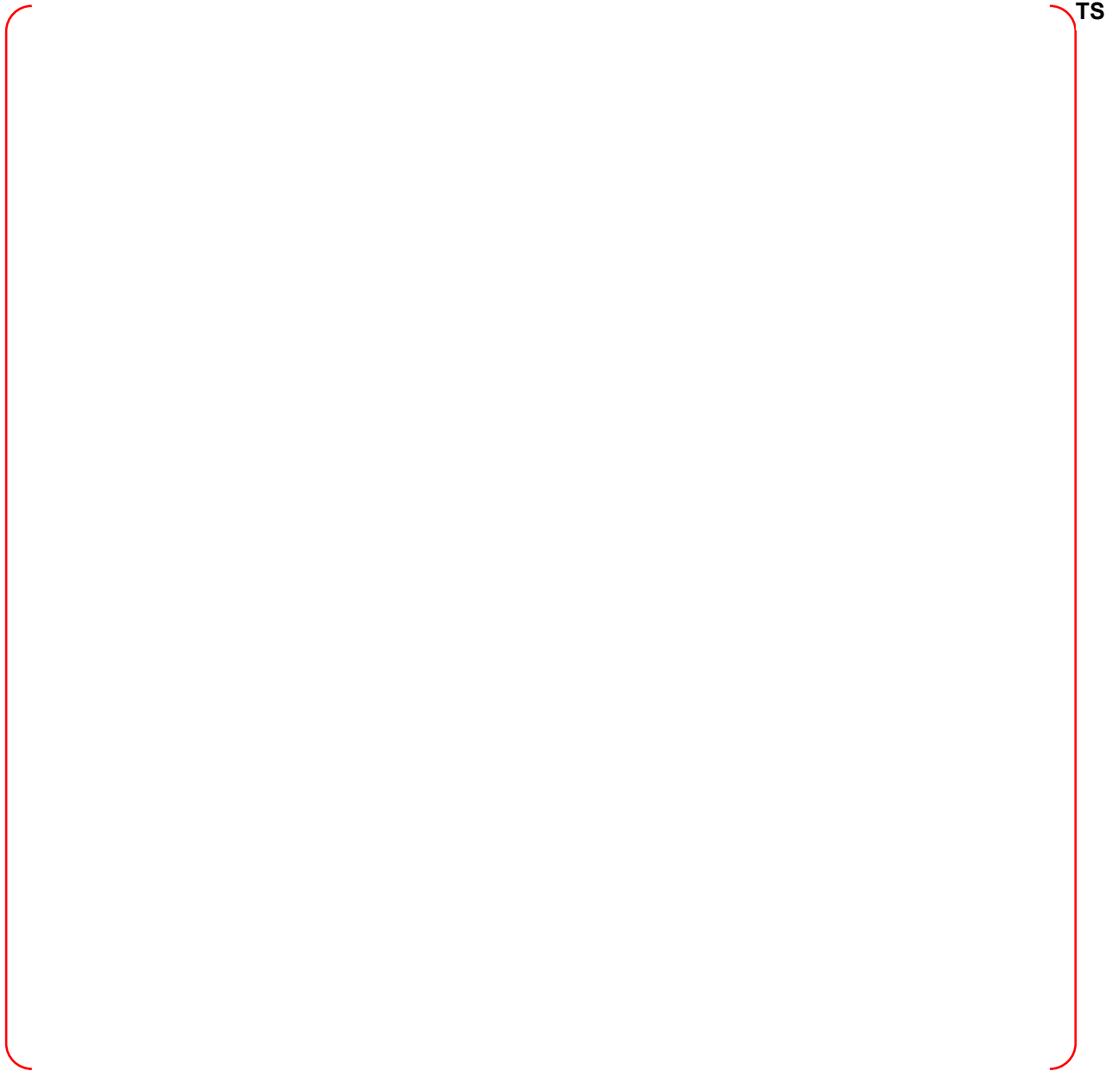


Figure 4-7 Impulses, Conversion Ratio, Energy Transfer to Coolant, Kinetic Energies of Coolant calculated for the Base Case



TS

Figure 4-8 Pressures and Impulses Calculated for the Base Case



Figure 4-9 Schematic Drawing of APR1400 Reactor Cavity



Figure 4-10 Comparison of TEXAS-V Calculation for TROI TS-4 Experimental Pressure Data



Figure 4-11 Comparison of Ex-Vessel Steam Explosion Pressure



Figure 4-12 **Side View of the General Arrangement of the Reactor Cavity**



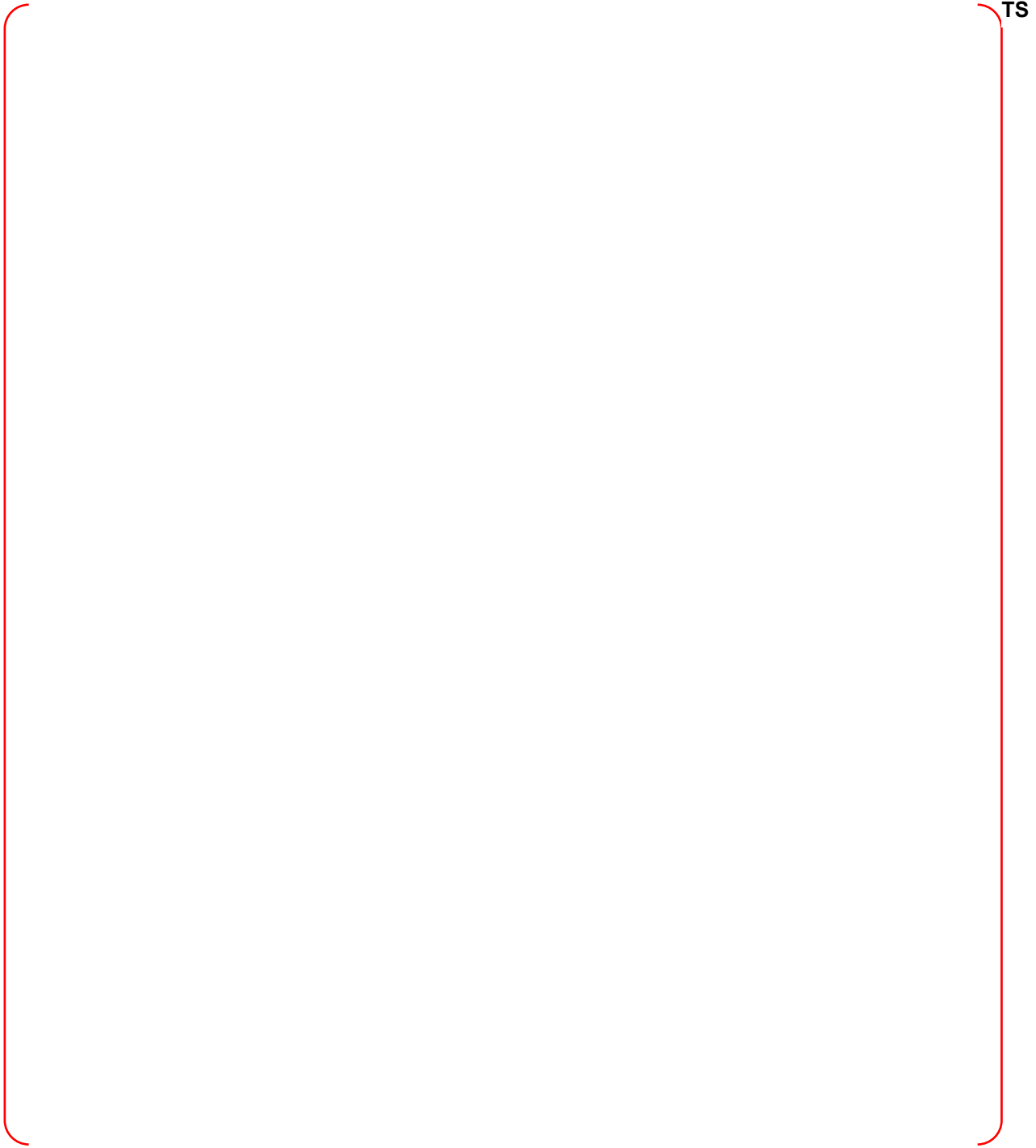
Figure 4-13 Top View of the General Arrangement of the Reactor Cavity



Figure 4-14 **Isometric View of all Reinforcement Bars in the Reactor Cavity**



Figure 4-15 **Isometric View of the RPV Model**



TS

Figure 4-16 Isometric View of the Global Model

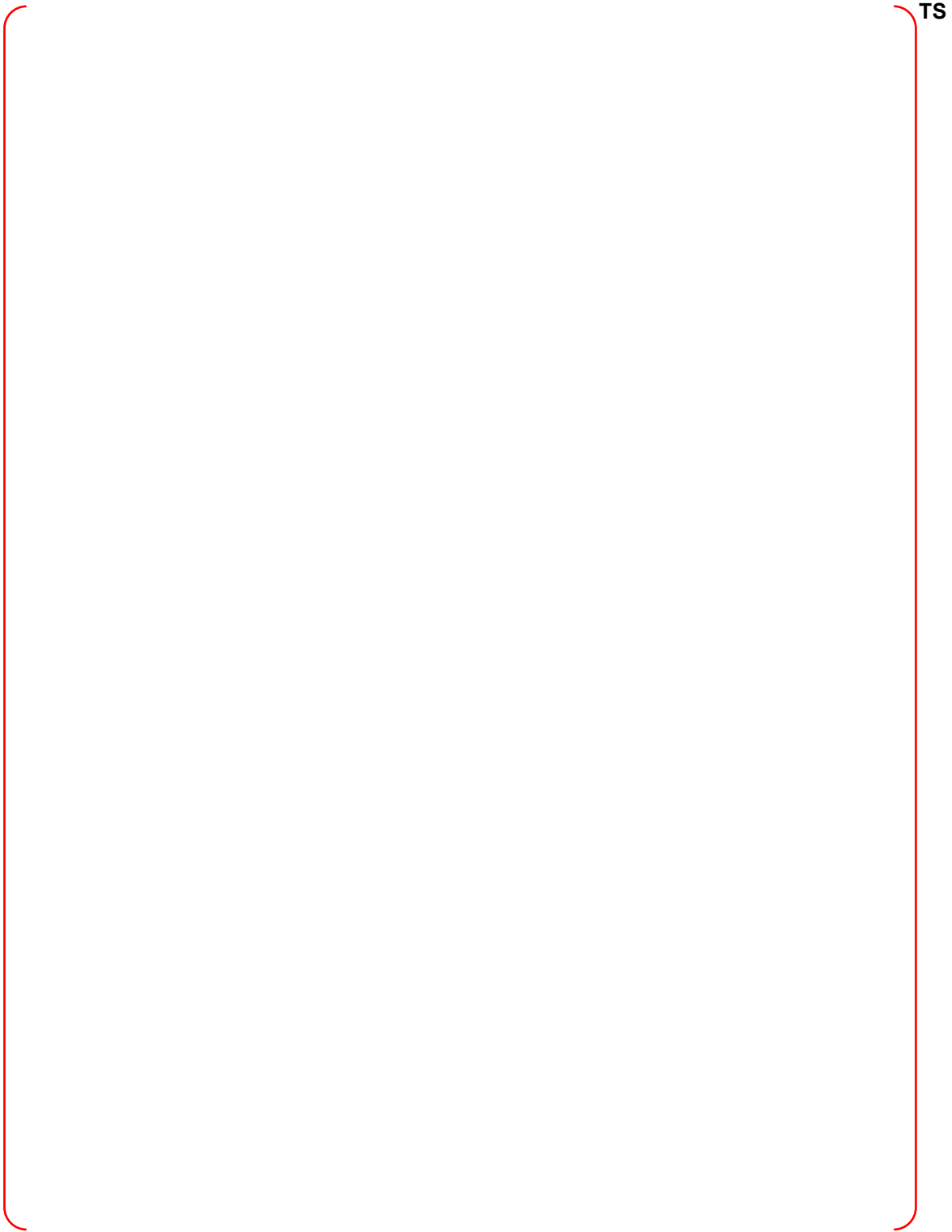
TS



Figure 4-17 Pressure Time Histories for the Zones



Figure 4-19 Maximum Resultant Displacement Contours for the Concrete Cavity



TS

Figure 4-20 Crack Pattern of the Reactor Cavity

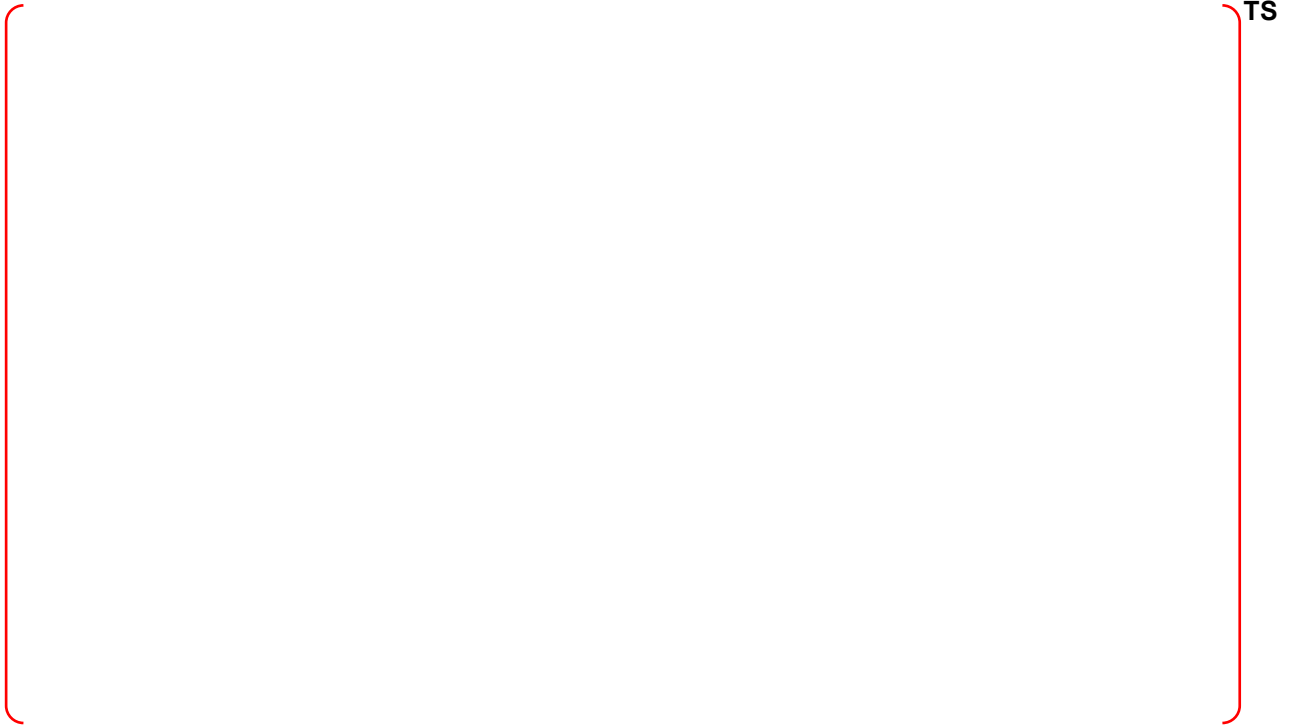


Figure 4-21 Plastic Strain Contours for Liner Plates

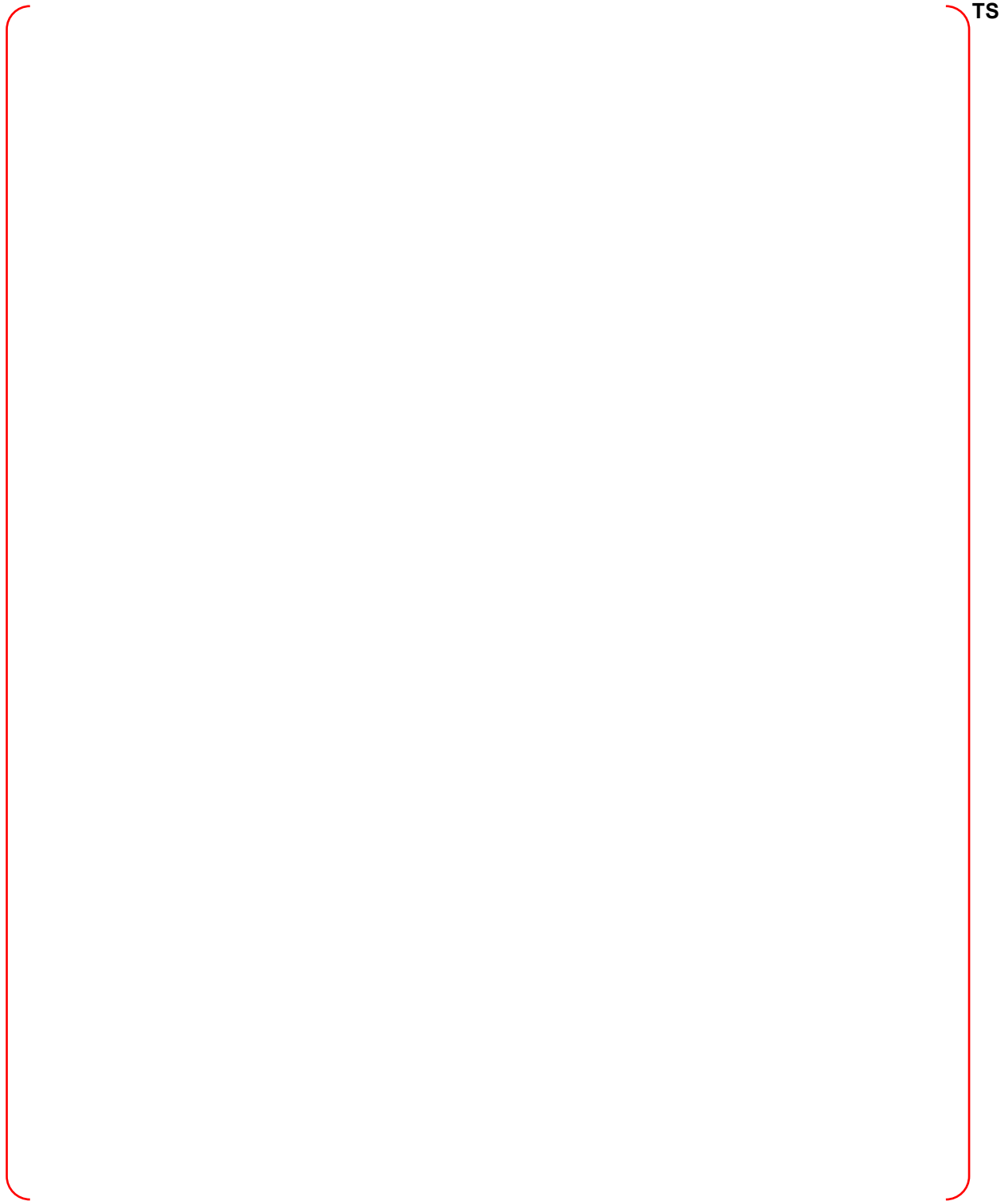
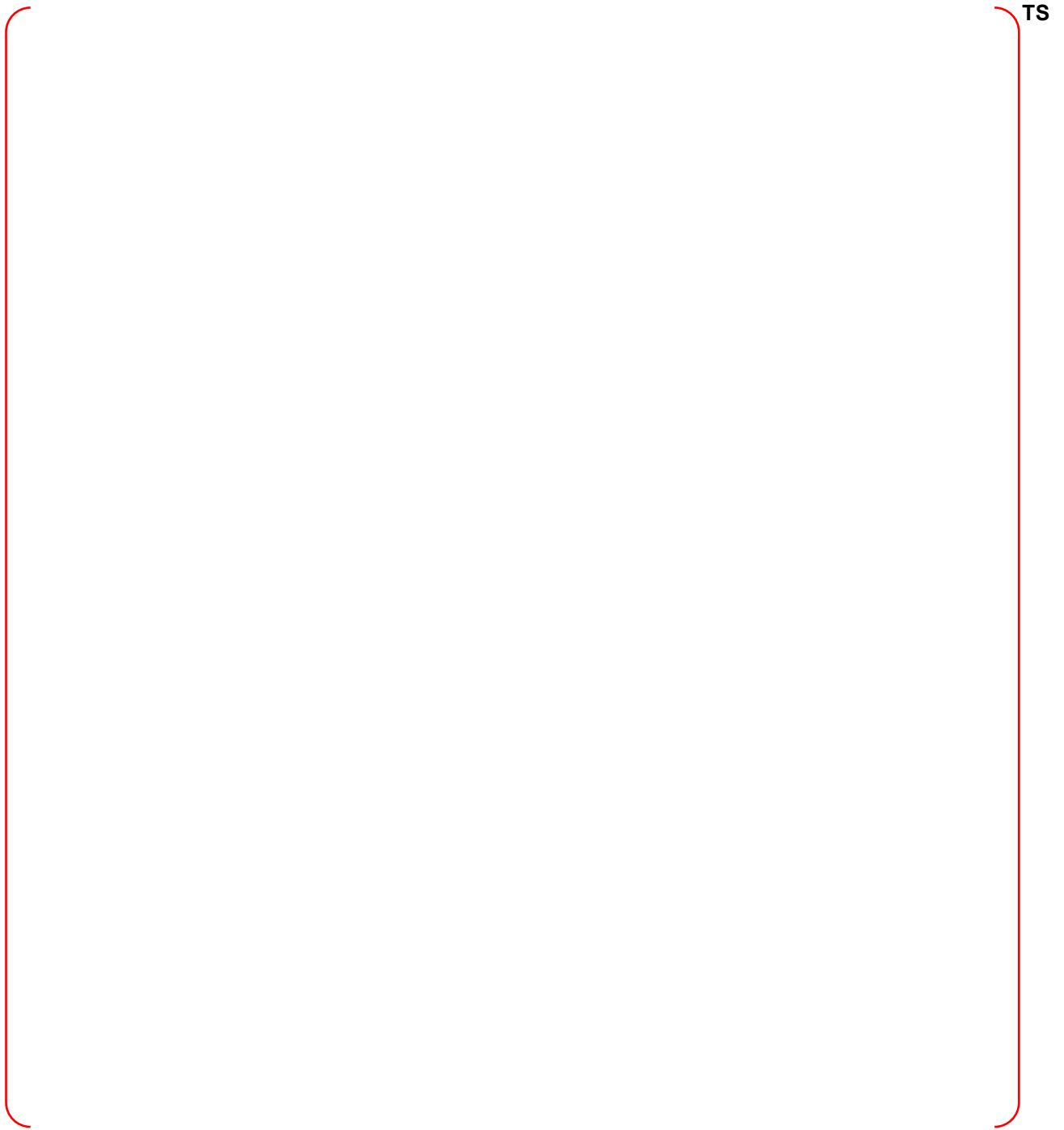


Figure 4-22 Plastic Strain Contours in Vertical Rebars



TS

Figure 4-23 Vertical Displacement and Anchor Bolt Reaction of RPV

TS

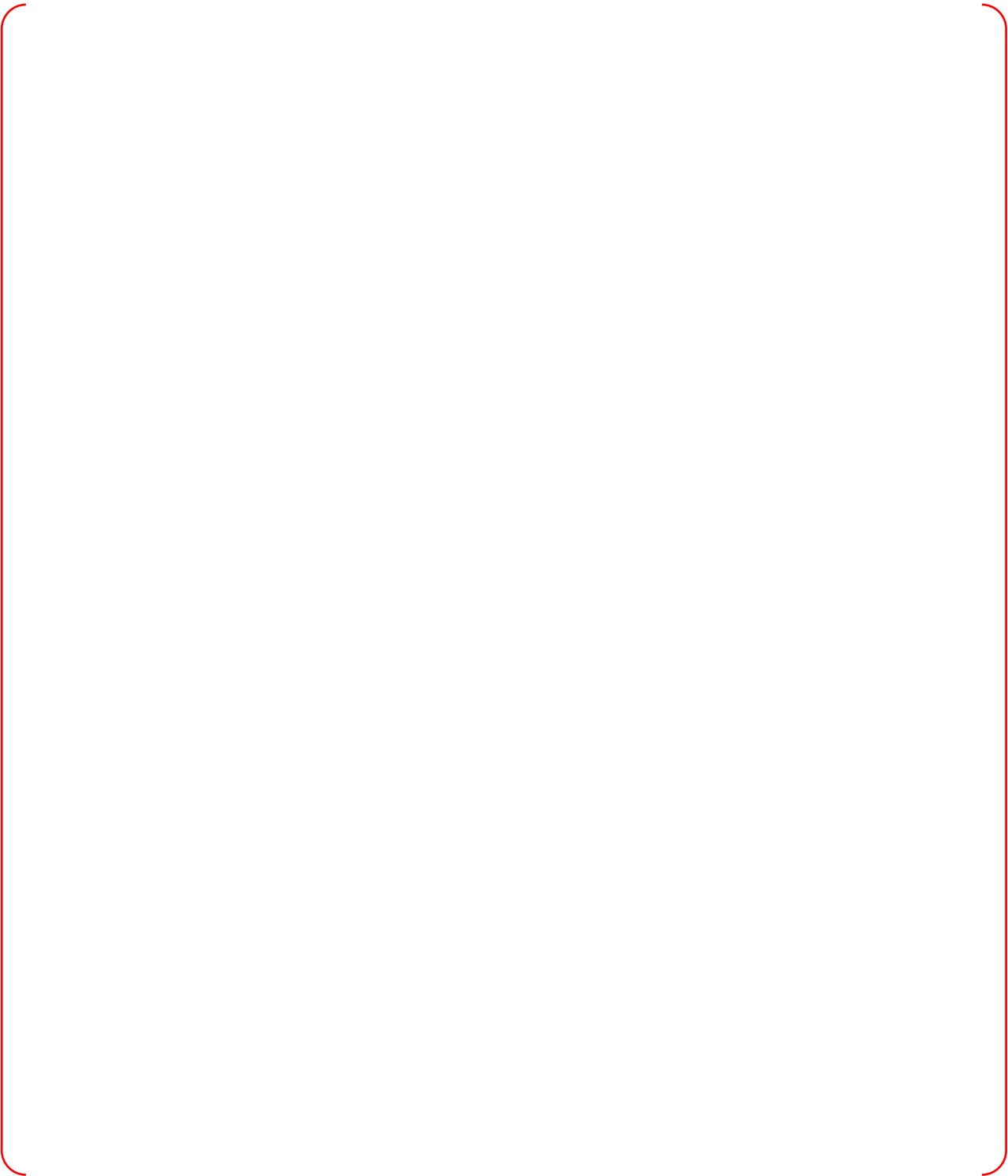


Figure 4-24 Vertical Displacements of Cold Leg and Hot Leg Pipes

5 CONCLUSIONS

Steam explosion is a remaining risk-significant issue in nuclear power plant due to the threatening of integrity of the defense-in-depth barriers by explosive dynamic loadings that could lead to release radioactive fission product to public.

Therefore, it is needed to evaluate steam explosion risk when a new design reactor like APR1400 is considered. The steam explosion risk can be categorized into two groups in terms of the locations of steam explosion initiation, that is, in-vessel and ex-vessel.

In this report, comprehensive analyses on both in-vessel and ex-vessel steam explosion were conducted and the most updated technical information on the phenomena, risk evaluation, and analysis methodology were collected and utilized for the assessment of steam explosion risk in the APR1400 design.

The report describes the analysis efforts by selecting the base case adequate to the APR1400 design and examining the ranges of key parameters and their uncertainties. The analysis results can be used for the evaluation of structure integrity relevant to the steam explosion issue in the APR1400 design, especially in the case of ex-vessel severe accident progression.

Table 5-1 summarizes the results of the analysis for the IVSE and EVSE energetics in the APR1400 plant. This analysis concluded that IVSE provided no threat to fail RPV. For the EVSE analysis, reactor cavity structure with EVSE pressure loading is evaluated using LS-DYNA and the maximum displacements, concrete cracks, liner plate stresses, reinforcement re-bar stresses, RPV column support anchor bolt stresses and strains for EVSE loading to reactor cavity are summarized in Table 4-17.

Table 5-1 Summary of the IVSE and EVSE Analysis for the APR1400

TS



6 REFERENCES

1. NUREG-75/0114 (WASH-1400), "Reactor Safety Study; An Assessment of Accident Risks in U.S. Commercial Nuclear Power Plants," U.S. Nuclear Regulatory Commission, October, 1975.
2. NUREG-1116, "A Review of Current Understanding of the Potential for Containment Failure Arising from In-Vessel Steam Explosion," U.S. Nuclear Regulatory Commission, Steam Explosion Review Group, 1985.
3. NUREG-1524, "A reassessment of the potential for an Alpha-Mode containment failure and a review of the current understanding of broader fuel-coolant interaction (FCI) issues," U.S. Nuclear Regulatory Commission, Steam Explosion Review Group-2, 1995.
4. OECD, "OECD/CSNI Specialist Meeting on Fuel Coolant Interactions, Summary and Conclusions", NEA/CSNI/R(97)30, JAERI, Tokai-Mura, Japan, 1997.
5. Magallon, D., "OECD Research Programme on Fuel-Coolant Interaction: Steam Explosion Resolution for Nuclear Applications (SERENA)," Final Report, NEA/CSNI/R(2007)11, OECD/NEA, France, 2006.
6. Hong, S.W., et al., "Status of SERENA-2," presentation slide at the Cooperative Severe Accident Research Program (CSARP) meeting, September 14-16, Nuclear Regulatory Commission, Residence Inn Bethesda, Bethesda, Maryland, USA, 2010.
7. Chen, R. H., Corradini, M. L., and Su, G. H., "Simulation of FARO Corium Coolant Interaction Experiment with TEXAS-VI," Proc. American Nuclear Society Meeting, Chicago, USA, Paper No. 1029, USA, 2012.
8. Theofanuous, T. G., Najafi, B., and Rumble, E., "An Assessment of Steam-Explosion-Induced Containment Failure, Part I-IV," Nuclear Science and Engineering, 97 (1989), pp. 259~326.
9. Turland, B. D., Fletcher, D. F., Hodges, K. I., Attwood, G. J., "Quantification of the Probability of Containment failure Caused by an In-Vessel Steam explosion For the Sizewell B PWR," Proc. Of the CSNI Specialists Meeting on Fuel-Coolant Interactions, Santa Barbara, California, USA, NUREG/CP-0127, NEA/CSNI/R(93)8, pp. 309-321 , 1993.
10. Theofanous, T. G. and Yuen W. W., "The Probability of ALPHA-Mode Containment Failure Updated," Proceedings of the CSNI Specialists Meeting on Fuel-Coolant Interactions, NUREG/CP-0127, Santa Barbara, CA, USA, pp. 330~342, 1993.
11. Amarasooriya, W. H. and Theofanous, T. G., "Scaling Considerations in Steam Explosions," ANS Proceedings of National Heat Transfer Conference, Vol. 2 (1987), pp. 58~67.
12. Theofanous, T.G., et al., "Lower head integrity under steam explosion loads," Nuclear Engineering and Design 189 (1999), p. 7~57.
13. Chu, C. C., Sienicki, J. J., Spencer, B. W., Frid, W., Lowenhielm, G., "Ex-Vessel Melt-Coolant Interactions in Deep Water Pool; Studies and Accident Management for Swedish BWRs, Nuclear Engineering and Design, Vol. 155, Issue 1-2(1995), pp. 159-213.
14. Zuchuat, O., Schmocker, U., Esmaili, H., et al., "Steam explosions-induced containment failure studies for Swiss nuclear power plants," Proc. OECD/CSNI Specialists Meeting on Fuel-Coolant Interactions, Tokai-mura, Japan, JAERI-Conf 97-011, NEA/CSNI/R(97)26 (Part I), pp. 36~61, 1997.

15. Moriyama, K., et al., "Evaluation of Containment Failure Probability by Ex-Vessel Steam Explosion in Japanese LWR Plants," J. of Nuclear Science and Technology, Vol. 43, No. 7(2006), p. 774-784.
16. Cizelj, L., Koncar, B., and Leskovar, M., "Vulnerability of a Partially Flooded PWR Reactor Cavity to a Steam Explosion," Nuclear Engineering and Design, 236(2006), pp1617-1627.
17. Murphy, J. and Corradini, M. L., "An Assessment of Ex-Vessel FCI Energetics for Advanced Light Water Reactors," Nuclear Technology, Vol. 117(1997), p 49~63.
18. U.S. Nuclear Regulatory Commission, "Final Safety Evaluation Report; Related to the Certification of the AP600 Standard Design, Vol.2," U.S. Nuclear Regulatory Commission, 1998.
19. NUREG/CR-6849, Esmaili, H., et. al., "Analysis of In-Vessel Retention and Ex-Vessel Fuel Coolant Interaction for AP1000," Energy Research Inc., U.S. NRC, Washington, USA, 2004.
20. Aya K. D., and Corradini, M. L., "Ex-Vessel Vapor Explosion Simulations for Postulated Severe Accident Conditions," Proc. Of the ASME 2011 Pressure Vessels and Piping Division Conference, PVP2011, July 17-21, Baltimore, Maryland, USA, 2011.
21. Moriyama, K., and Nakamura, H., "A Strategy for the Application of Steam Explosion Codes to Reactor Analysis," Technical Meeting on Severe Accident and Accident Management, Toranomon Pastoral, Minato-ku, Tokyo, Japan, March 14-16, 2006.
22. U.S. Nuclear Regulatory Commission, "Final Safety Evaluation Report; Related to the Certification of the Advanced Boiling Water reactor Design, Main Report," U.S. Nuclear Regulatory Commission, 1994.
23. U.S. Nuclear Regulatory Commission, "Design Control Document for US-APWR, Chapter 19 Probabilistic Risk Assessment and Severe Accident Evaluation," MUAP-DC0019, Rev. 2, Mitsubishi Heavy Industries, Ltd, 2009.
24. Hwang, M. K., et al., "Assessment of Steam Explosion Impact on KNGR Plant," KAERI/TR-1303/99, Korea Atomic Energy Research Institute, Daejeon, Korea, (In Korean), 1999.
25. Bang, K. H., Cho, Jong-Rae, and Park, S. Y., "An Assessment of Reactor Vessel Integrity under In-Vessel Vapor Explosion Loads," J. of the Korean Nuclear Society, Vol. 32, No. 4(2000), pp. 299-308.
26. Berman, M., Swenson, D. V., and Eickett, A. J., "An Uncertainty Study of PWR Steam Explosions," SAND83-1438, NUREG/CR-3369, Sandia National Laboratories, USA, 1984.
27. Bohl, W. R. and Bulter, T. A., "Comments on Proposed Research Contributing to the Relation of Residual Steam Explosion Issues," Letter Report in "Review of Current Understanding Failure Arising from In-Vessel Steam Explosion," NUREG-1116, U.S. Nuclear Regulatory Commission, 1985.
28. Shockey, D. A., Seaman, L., Dao, K. C., and Curran, D. R., "Kinetics of Void Development in Fracturing A533B Tensile Bars," J. Pressure Vessel Technology, 102(1980), pp14-21.
29. Bang, K.H., Park, I.G., and Park, G.C., "TRACER-II: A Complete Computational Model for Mixing and Propagation of Vapor Explosions," Proc. Of OECD/CSNI FCI Specialists Meeting, Tokia-Miura, Japan, pp.804-816, May, 1997.
30. Corradini, M. L., Blanchard, J. P., and Martin, C. J., "Evaluation of Dynamic Pressures from Steam Explosions applied to Advanced LWRs," submitted to Nuclear Science and Engineering, 2012.

31. Kim S. B., et al., "Development of Optimal Severe Accident Management Strategy and Engineering Safety Features: Optimization of the Severe Accident Management for Domestic Plants and Validation Experiments," KAERI/RR-2528/2004, Korea Atomic Energy Research Institute, Daejeon, Korea (In Korean), 2004.
32. Paik, C. Y., "Corium Flow Characteristics delivered from a Failed Vessel for Steam Explosion Calculations," Draft Report No. FAI/12-0395, Fauske Associates, LLC, USA, 2012.
33. Chu, C. C., "One-Dimensional Transient Fluid Model for Fuel-Coolant Interactions," Ph.D. Thesis, University of Wisconsin-Madison, Madison, Wisconsin, 1986.
34. Tang, J., "Modeling of the Complete Process of One-Dimensional Steam explosions," Ph.D. Thesis, University of Wisconsin-Madison, Madison, Wisconsin, USA, 1993.
35. Young, M. F., "The TEXAS Code for Fuel-Coolant Interaction Analysis," Proc. ANS/ENS Fast Reactor Safety Conference, July, Lyon, France, 1982.
36. Chu, C. C., Corradini, M. L., "One-Dimensional Transient Fluid Model for Fuel/Coolant Interaction Analysis," Nuclear Science and Engineering, V 101(1989), No 1, p 48-72 (Jan.).
37. Pilch, M., "Acceleration Induced Fragmentation of Liquid Drops," Ph.D. Thesis of University of Virginia, 1981.
38. Kim, B. J., "Heat Transfer and Fluid Flow Aspects of Small-Scale Single Droplet Fuel-Coolant Interactions," Ph.D. Thesis, University of Wisconsin-Madison, Madison, Wisconsin, 1985.
39. Huhtiniemi, I., Magallon, D., and Hohmann. H., "Results of recent KROTOS FCI tests: Alumina versus Corium melts," Nuclear Engineering and Design, 189(1999):379-389.
40. Nelson, L. S. and Duda, P., M., "Steam Explosions of Molten Iron Oxide Drops: easier Initiation at Small Pressurizations, Nature, 296(1982), pp. 844-846.
41. Corradini, M., et al, A Users' Manual for TEXAS-V: A One-Dimensional Transient Fluid Model for Fuel-Coolant Interaction Analysis, UW Nuclear Engineering and Engineering Physics (Aug.), 2000.
42. ASME Boiler & Pressure Vessel Design Code Section III, ASME, 2004.
43. Knudson, D.L., Rempea, J.L., Condiea, K.G., Suh, K.Y., Cheung, F.-B., Kim, S.-B., "Late-phase melt conditions affecting the potential for in-vessel retention in high power reactors," Nuclear Engineering and Design, Vol. 230, Issues 1-3(2004), pp.133-150.
44. Humphries, L.L., et al., OECD Lower Head Failure Project Final Report, Sandia National Laboratories, Albuquerque, NM, 2002.
45. Sehgal, B. R. et al., "Assessment of Reactor Vessel Integrity (ARVI)," Nuclear Engineering and Design, 221(2003), pp. 23-53.
46. Cole, R. H., Underwater Explosions, Princeton-New Jersey, Princeton University Press, 1948.
47. Khatib-Rahbar, M., Cassoli, E., Lee, M, Nourbakhsh, R. Davis, and Schmidt E., "A probabilistic approach to quantifying uncertainties in the progression of severe accidents," Nuclear Science and Engineering, 102(1989), 219.
48. Iman, R. L., Davenport, J. M., and Zeigler, D. K., "Latin Hypercube Sampling (A Program User's

Guide),” Technical Report SAND79-1473, Sandia Laboratories, Albuquerque (1980).

49. Corradini, M. L. and Swenson, D. V., “Probability of Containment Failure Due to Steam Explosions Following a Postulated Core meltdown in an LWR,” Report SAND 80-2132, 1981.

Appendix-E

**Severe Accident Analysis Report for
Containment Performance**

TABLE OF CONTENTS

1	INTRODUCTION	E-4
2	REVIEW OF CONTAINMENT FAILURE PHENOMENOLOGY AND EXPERIMENTS.....	E-5
2.1	Containment Failure Phenomenology	E-5
2.1.1	Controlling Physical Processes	E-5
2.1.2	Containment Failure Mechanisms and Modes.....	E-5
2.1.3	Relationship to Source Term	E-6
2.2	Containment Failure Experiments	E-7
2.2.1	Sandia 1:6 Scale Model Containment Pressure Test Program.....	E-7
2.2.2	Sandia/CBI Personnel Airlock Testing.....	E-9
2.2.3	EG&G Containment Penetration System Testing.....	E-10
2.2.4	Sandia Electrical Penetration Assemblies (EPA) Program	E-10
2.2.5	NUPEC/NRC Pre-stressed Concrete Containment Vessel (PCCV) Model Test.....	E-10
2.3	Past Analytical Studies of Containment Failure	E-17
2.3.1	Large Dry Containment Types.....	E-17
2.3.2	Finite Element Analysis of the PCCV Model Test.....	E-17
3	APR1400 Containment Performance Criteria	E-22
3.1	Description of the Containment.....	E-22
3.2	Containment Performance Criteria regarding FLC requirement.....	E-22
4	APR1400 CONTAINMENT PERFORMANCE ANALYSIS	E-23
5	CONCLUSION	E-25
6	REFERENCE	E-26

LIST OF FIGURES

Figure 2-1	Sandia 1:6 Scale Reinforced Concrete Containment Model	E-8
Figure 2-2	Sandia 1:6 Scale Model Liner Stretchout Showing Leakage.....	E-9
Figure 2-3	PCCV Model Elevation and Cross-Section.....	E-12
Figure 2-4	Completed PCCV Model.....	E-13
Figure 2-5	Images of the Eventual Rupture of the PCCV Model	E-14
Figure 2-6	Image of the PCCV Model After the SFMT.....	E-15
Figure 2-7	Images of the Equipment Hatch where Liner Tear Occurred in the PCCV Test.....	E-16
Figure 2-8	Axisymmetric Model of 1:4-scale PCCV	E-19
Figure 2-9	Local Model of PCCV Equipment Hatch.....	E-20
Figure 2-10	PCCV Three-Dimensional Cylinder Mid-Height Model.....	E-21
Figure 4-1	Containment Pressure for Large Break LOCA with ECSBS Actuated 24 hours after Onset of Core Damage.....	E-24

1 INTRODUCTION

The potential failure of a nuclear power plant containment due to pressurization caused by the generation of steam and non-condensable gases has been recognized as a possibility by the nuclear regulatory agencies and the nuclear industry worldwide. The concern is that decay heat generated in the core may not be able to be transferred to the Ultimate Heat Sink and may be deposited in containment. If containment heat removal is unavailable, the containment atmosphere will be heated and pressurized. The increased temperature and pressure can challenge the ability of containment to act as a barrier against the release of fission products.

United States Nuclear Regulatory Commission (USNRC) regulations establish requirements for containment performance as listed below:

Title 10 of the United States Code of Federal Regulations (CFR) Part 50 Appendix A General Design Criterion 50 states that the containment structure should accommodate “without exceeding the design leakage rate and with sufficient margin, the calculated pressure and temperature conditions resulting from any loss-of-coolant accident.” Containment structures designed in accordance with American Society of Mechanical Engineers (ASME) Code requirements have margin above the design pressure. Revision 3 of the Standard Review Plan (NUREG-0800) Sections 3.8.1 and 3.8.2 specify that for a license application to be accepted for review, it must include an explicit demonstration that the containment internal pressure capacity significantly exceeds the design-basis accident pressure.

The USNRC has established performance goals for containments under severe accident conditions. The Staff Requirements Memorandum (SRM) to SECY-90-16 (Reference 1) approved the use of a conditional containment failure probability of 0.1 as a basis for regulatory guidance on containment performance. Subsequently, the SRM to SECY-93-087 (Reference 2) stated:

The containment should maintain its role as a reliable, leak-tight barrier (for example, by ensuring that containment stresses do not exceed ASME Service Level C limits for metal containments, or Factored Load Category for concrete containments) for approximately 24 hours following the onset of core damage under the more likely severe accident challenges and, following this period, the containment should continue to provide a barrier against the uncontrolled release of fission products.

USNRC Regulatory Guide (RG) 1.216 (Reference 3) specifies the methodology for determining “more likely severe accident challenges” as selecting sequences or plant damage states that represent 90 percent or more of the core damage frequency and determining bounding pressure and temperature loadings based on the pressures and temperatures identified for these sequences. These pressure and temperature loadings can then be used to analyze the containment to determine whether the acceptance criteria have been met. Taken together, this imposes the requirement that concrete containments should meet the Factored Load Category requirements of ASME Code, Section III, Division 2.

The objective of this report is to determine if the APR1400 plant will satisfy the requirements related to the containment performance under the more likely severe accident challenges. Section 2 presents a review of past experimental and analytical investigations of the failure modes of large dry containment structures. Section 3 describes the containment performance criteria for the APR1400 containment. Section 4 presents the containment performance analyses during severe accidents. Section 5 presents the conclusions drawn in this report.

2 REVIEW OF CONTAINMENT FAILURE PHENOMENOLOGY AND EXPERIMENTS

2.1 Containment Failure Phenomenology

Containment overpressurization is a postulated event in which the pressure loads applied to the containment boundary during a severe accident eventually exceed the boundary's ultimate strength at its most vulnerable point(s). This event has been hypothesized as a means of containment failure through one or more of several potential physical mechanisms. The extent of pressurization, its timing, and the pressurization rate all depend on a number of factors, including the accident sequence characteristics involved, the containment geometric configuration, etc. At the heart of the matter however, are the needs to define the containment's pressure limits and determine how much pressure the containment will undergo during severe accidents.

2.1.1 Controlling Physical Processes

Several controlling physical processes have been postulated that can be considered relevant to containment overpressurization in severe accidents. Such processes result in either heating the gas and/or vapor mass in the containment's finite volume, or increasing the gas/vapor mass existing in the finite volume. These processes, or pressure sources, include potential ex-vessel vapor (steam) explosions, combustion, core-concrete interaction, direct containment heating (DCH) and steaming of primary system and water in the reactor cavity. Processes that exclusively involve heating of the existing containment volume include gas combustion and direct heating of the containment atmosphere by finely fragmented core debris. Over the course of a severe accident, pressure sources may participate individually or in combination.

Steam produced within or external to the primary system is another potentially influential pressure source in some severe accidents. Steam addition to the containment occurs due to either flashing of effluent from primary system ruptures or rapid vaporization of water in the reactor cavity by interactions with core debris ejected from the vessel. This phenomenon and ex-vessel steam explosions are pressurization mechanisms that originate as containment mass addition processes only. Following these initial stages, steam added to the containment through these sources becomes a containment volume heating mechanism. Concrete attack by molten core debris represents a situation where heat and mass are more or less simultaneously added to the containment volume. Chemical reactions that may occur in such cases directly release heat as well as contribute significant masses of aerosols and non-condensable gases, which in their turn also become containment volume heating mechanisms.

2.1.2 Containment Failure Mechanisms and Modes

Containment overpressurization can potentially result in early or late failure modes. Depending on the specific accident sequence characteristics, overpressurization failures may be observed across a wide range of event times, either substantially before or substantially after vessel failure. Apart from direct bypass or failure to isolate events (where containment pressure retention capability is assumed to fail by definition), the potential for containment overpressure failures exists in most severe accident scenarios where pressure suppression facilities, namely the normal containment sprays and/or the Emergency Containment Spray Backup System (ECSBS), are disabled.

The failure mechanism associated with overpressure of the containment is due to exceeding the ultimate strength of certain structural components or attachments. Efforts to precisely and confidently characterize this mechanism can be (and have been) extraordinarily complicated for severe accident purposes. There are four fundamental considerations; 1) failure flow sizes (areas), 2) failure locations, 3) failure timing, and 4) the pressure levels at which failures may occur. As discussed below, some aspects of the containment failure modes do not depend, to an important degree, on the physical process (or combination of processes) that causes overpressurization. Failure location and the pressure levels at which failure may occur depend upon the containment design, construction and materials, but not on the

process creating the pressurization. Containment failure timing, i.e., early or late, and failure size, on the other hand, do depend on the physical process and the rapidity of the pressurization.

Regarding failure sizes, the ultimate strength of involved structures may be achieved rapidly in some postulated sequences, and the total energy delivered (to the containment) may be sufficient to result in large rupture areas. Conversely, this limit may be approached gradually, and the energy delivered may only be enough to induce relatively small rupture areas unlikely to become any larger than what is necessary to stabilize the containment pressure (i.e., create a choked flow condition). Based on the results of the APR1400 for DCH, steam explosions, and combustion, cases in this category are generally considered to be significantly more likely than rapid loading, high energy cases. Potential examples may include concrete attack events or steaming to the containment.

Although there are innumerable containment details that could fail under over-pressurization conditions, there are only a few possible overpressure failure locations that need consideration with respect to source term estimates. For a large dry containment, a failure location creates a flowpath to either the auxiliary building, the atmosphere or into the soil beneath the basemat. Each of these flowpaths has different fission product retention mechanisms, which results in varying source terms. For a direct release to the atmosphere, fission product retention occurs in the containment. In this case, most of the noble gases and some of the volatile fission products would escape into the environment. Some amount of fission product retention can be credited to the auxiliary building, depending upon its configuration and at what elevation the containment failure occurs. A failure of the containment that would result in a release into the soil (i.e., basemat failure) would have to consider soil retention mechanisms as well as effects of the failure occurring below the containment water line.

Factors that control overpressure failure timing are somewhat more defined than factors associated with size and location variables. In this area, the pressurization rates occurring in the containment regions during a severe accident exert the greatest influence on the time when a failure can be expected. Pressurization rates are themselves controlled by the pressure source phenomena characteristics, the containment boundary conditions when the phenomena originate, and containment physical characteristics (region geometry in particular). A wide variety of efforts have been accomplished to analytically model the physical bases for how the phenomena actually generate pressure. For the most part, these models are sensitive to crucial boundary conditions and plant characteristics. Furthermore, the pressurization rates revealed in development of these models appear to fall within a relatively low range regardless of pressure source phenomena distinctions. This strongly suggests that loading of the containment shell and other pressure boundary components can be considered essentially static rather than dynamic. On this basis, overpressure failure timing is reduced to a matter of the rapidity at which actual pressures reach the pressure retention capacities (i.e., the pressure point corresponding to ultimate strength stress levels) of containment boundary components.

2.1.3 Relationship to Source Term

The three characteristics of containment overpressurization failures which most strongly influence the fission product source term are, 1) failure timing, 2) failure location, and 3) failure size.

A late containment failure provides ample time for natural fission product settling mechanisms to take effect, thus reducing the airborne fission product concentration and the source term.

The effect of different failure locations has been discussed in the previous section. Since the cylinder-basemat junction is located below ground level and would be submerged by water during a severe accident, fission product releases resulting from a failure at this location or in the base slab would be inhibited. The very effective soil and water pool scrubbing mechanisms which would be encountered along these failure paths would significantly reduce the fission product source term.

The remaining failure locations would not have the benefit of fission product retention in overlying water

pools and soil beds but would be influenced by several other factors. For instance, failures at the access ways would create a path to the auxiliary building which would then act as an additional fission product barrier. Failures of the reinforced concrete cylinder, on the other hand, may not lead to the auxiliary building but directly to the environment. A failure path directly to the environment would have a minimal number of fission product retention mechanisms and an increased source term. Finally, fission product releases would be different depending on whether the containment failure occurred in the upper compartment wall or the annular compartment wall. Due to the containment gas circulation paths, the airborne fission product concentration would be larger in the upper compartment than it would be in the lower compartment. Thus, the most conservative containment failure location which can be postulated is one in the upper compartment leading directly to the environment.

Regardless of failure location, the failure size is based on "leak before break" considerations. Experimental results show that concrete containments subjected to slow pressurization will leak before they break. Thus, as a containment pressurizes, it is most likely that a leak will develop of sufficient magnitude to prevent further pressurization.

2.2 Containment Failure Experiments

A few experimental results relevant to containment overpressurization in large, dry PWR containments like Zion are highlighted here. Many of the experimental conclusions are applicable to the APR1400 because both Zion and the APR1400 have pre-stressed concrete containments. The Zion containment has a failure pressure of 150 psia and the APR1400 containment has a volume approximately 10% larger than that of Zion. Experimental programs that tested the overall response of 1:6 reinforced concrete containment model and the response of individual containment details (personnel airlocks, mechanical penetrations, etc.) are considered below.

2.2.1 Sandia 1:6 Scale Model Containment Pressure Test Program

This 1987 test (Reference 4) involved destructive testing of a 1:6 scale reinforced concrete model considered representative of large, dry PWR containment designs (see Figure 2-1). Conventional materials were used for the concrete aggregate and the #4 (1/2" dia.) primary rebar. Containment details such as a liner, equipment hatches, personnel airlocks and penetrations were represented in the model, which was built to ASME/ACI code. An integral basemat was included but the dead load internal to the containment was not. Tests were conducted at ambient, as opposed to elevated, temperatures, but this does not present a limitation for a large, reinforced concrete containment, because severe accident temperatures will not be high enough to affect material properties for this containment type. In brief, the test objectives were to determine the failure pressure and location for the device, and produce a wide spectrum of structural failure data for further analysis. The test was conducted by pressurizing the facility in 10 psi steps early on and 2 to 3 psi pressure steps at the end. Final test pressure was 145 psig.

A small leakage was noted near equipment hatch "A" at 125 psig and in equipment hatch "B" at 138 psig. Equipment hatch "A" began to ovalize at 128 psig, as the horizontal diameter increased nearly 1/2". Leakage could not be quantified at this point. At 140 psig, however, leakage was measured to be 13% mass/day. Leakage became very large (over 200% mass/day) between 140 and 145 psig, suggesting that liner tears occur at these pressure levels. Leakage occurred due to strain concentrations in the vicinity of containment penetrations as shown by Figure 2-2.

Two important conclusions of the work are: (1) pre-test analyses gave good results for cylinder displacements, rebar strains, etc., and, (2) pre-test analyses of the bending areas of the containment, namely the cylinder-basemat junction, were not in good agreement with test results. Post-test analysis was performed on the cylinder basemat junction to make use of test results and improve on the original predictions. Revised predictions for liner tearing at basemat-cylinder junction show failure at 152 to 154 psig.

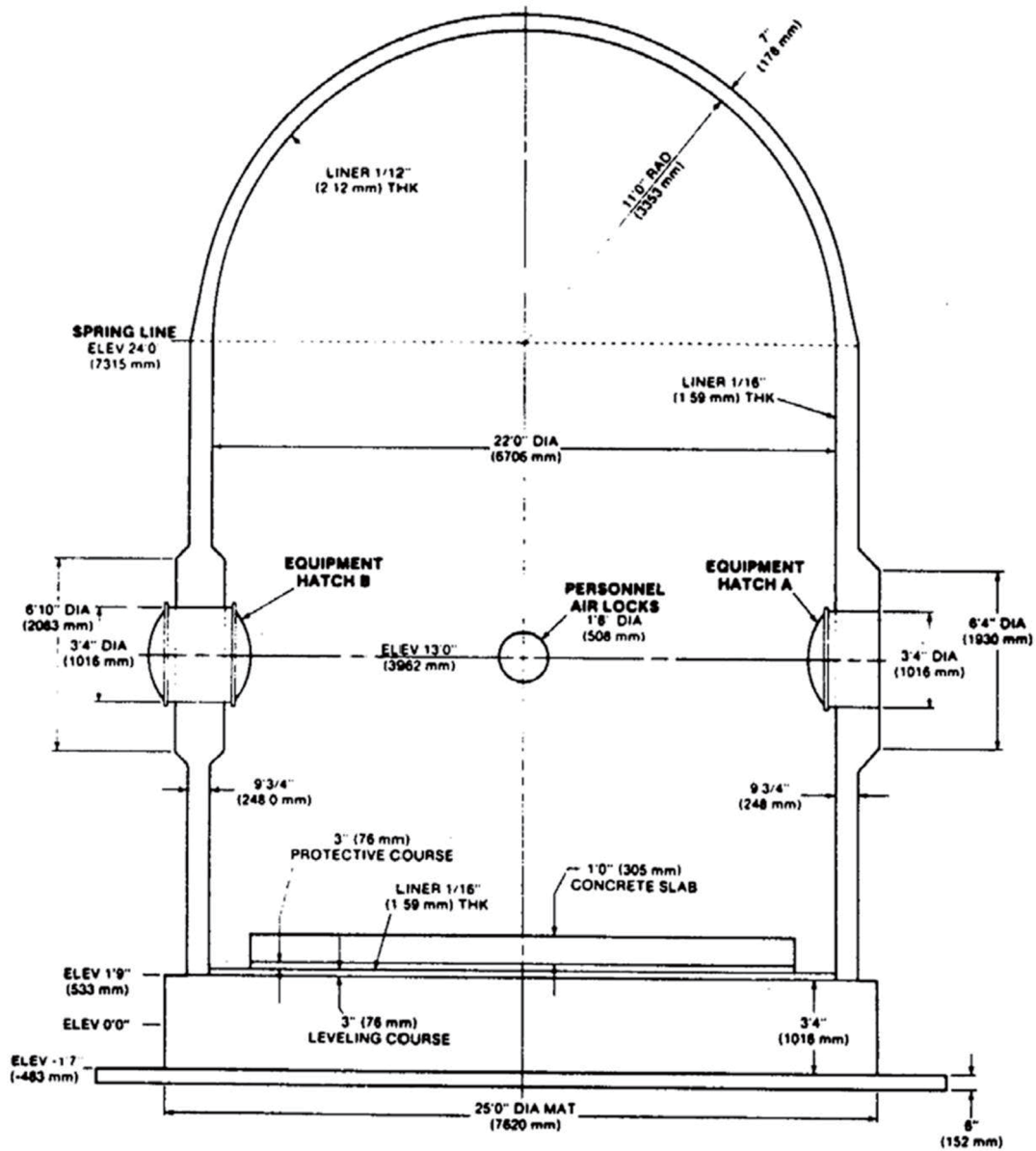
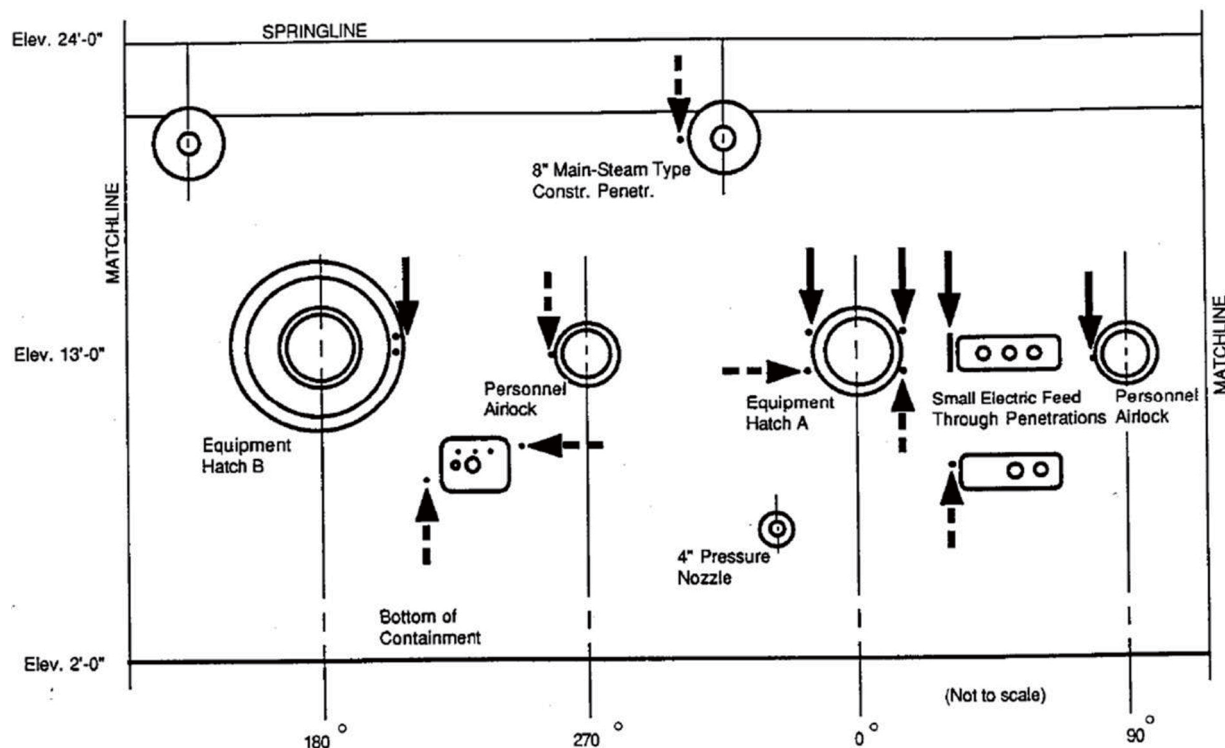


Figure 2-1 Sandia 1:6 Scale Reinforced Concrete Containment Model (Reference 5)



Locations (Arrows with Solid Lines Had Measurable Leakage; Arrows with Dashed Lines Showed 'Distress,' but Leakage Could not be Confirmed)

Figure 2-2 Sandia 1:6 Scale Model Liner Stretchout Showing Leakage (Reference 5)

2.2.2 Sandia/CBI Personnel Airlock Testing

In this test program, an actual full-scale airlock assembly (surplus from a canceled PWR; Callaway Unit 2) was subjected to environmental conditions considered applicable to certain design basis (LOCA) and severe accident events. In general terms, the overall objective of the program was to study potential adverse impacts on the pressure integrity of such devices attributable to these conditions. The conduct and results of these efforts are detailed in Reference 6. Test pressures as high as 300 psig were applied during this program.

In most of the individual tests performed, no pressure boundary integrity losses whatsoever were detected, structural response notwithstanding. For one case however, the test conditions did yield a significant degree of inner door seal leakage. In this specific case, the airlock inner door temperature was held at 650 °F while the atmosphere (air) temperature inside this door was raised to 800 °F. Pressure inside the door (i.e., corresponding to the containment side) was then increased from ambient to 150 psig, and at this point the leakage referred to was detected. Note that even at these elevated temperatures, which cannot be expected in a large, dry containment, the airlock would not begin to leak on overpressure until after other containment details, namely the equipment hatch and hoop rebar, (as demonstrated by the 1:6 scale test) had already failed.

2.2.3 EG&G Containment Penetration System Testing

Idaho National Engineering Laboratory performed a series of full-scale tests to determine the performance of mechanical, or piping, penetrations systems under design basis and severe accident conditions (Reference 7). In particular, three separate piping systems complete with valves, penetrations, supports, and piping were subjected to design basis conditions of 280 °F and 120 psig without any signs of failure for the duration of the test. These piping systems modeled the containment spray system (an 8" gate valve), the containment purge and vent system (an 8" butterfly valve), and a nominal small diameter (2") globe valve piping system. These three systems were configured so that results "would be applicable to a high percentage of plants."

Results indicate that there was significant plastic strain in the piping sections and many of the piping supports were badly deformed, but there was no buckling of the piping sections and the penetration assemblies showed no damage. The tested systems performed well and the program conclusion was that leak integrity and valve operability will most likely be maintained during severe accidents which challenge light water containments.

2.2.4 Sandia Electrical Penetration Assemblies (EPA) Program

The EPA program (Reference 8) tested electrical penetrations from three manufacturers: Conax, D. G. O'Brien, and Westinghouse. For a large, dry PWR containment, D. G. O'Brien assemblies were tested under a severe accident profile. This profile consisted of: (1) ramping the temperature and pressure from ambient to 293 °F and 60 psia, (2) then to 361 °F and 155 psia in 12 hours using saturated steam, and, (3) holding these conditions for the remainder of a 10 day test. There were no detectable leaks through the EPA during the severe accident test.

2.2.5 NUPEC/NRC Pre-stressed Concrete Containment Vessel (PCCV) Model Test

As part of a Cooperative Containment Research Program that was co-sponsored and jointly funded by the Nuclear Power Engineering Corporation (NUPEC) of Japan and the U.S. Nuclear Regulatory Commission (NRC), Sandia National Laboratories (SNL) conducted a test of a 1:4 scale model of a large dry PWR pre-stressed concrete containment vessel. The PCCV model was a 1:4-scale model of the pre-stressed concrete containment vessel (PCCV) of an actual nuclear power plant in Japan, Ohi-3. Ohi-3 is an 1,127 MWe Pressurized Water Reactor (PWR) unit, one of four units comprising the Ohi Nuclear Power station located in Fukui Prefecture, owned and operated by Kansai Electric Power Company.

The design pressure for the model was 0.39 MPa (56.6 psig). The features and scale of the PCCV model were chosen so that the response of the model would mimic the global behavior of the prototype and local details, particularly those around penetrations, would be represented. The model included a steel liner anchored to the concrete shell by semi-continuous structural shapes (T's). Conventional reinforcing ratios match the prototype and pre-stressing tendons match 1-to-1 with the prototype. The un-bonded pre-stressing system consisted of three, seven-wire strands per hairpin tendon, anchored in the basemat and identical, 360° hoop tendons anchored in opposing vertical buttresses. Figure 2-3 shows a cross-section of the model and Figure 2-4 shows an image of the completed model. Details of the design, including the design drawings, and construction are reported in the PCCV test report (Reference 9).

A Limit State Test (LST) was carried out to pressurize the model beyond design basis accident loads and to compare that data against calculations. During the test an audible event occurred and the subsequent leak test showed that the model had failed functionality between 2.4 and 2.5 times the design pressure. It was concluded that a leak path opened most likely due to a liner tear in the vicinity of the equipment hatch. The model was then further pressurized to collect data on the inelastic response of the structure and to observe, if possible, a structural failure mode. At a pressure of 3.3 times the design pressure

large local liner strains (6.5%) were measured and the liner was torn in several locations. However, the remainder of the structure appeared to have suffered little damage. There was no indication of tendon or rebar failure and the tendon strains stayed within the elastic limit (1%). Since a structural failure mode was not seen it was decided to depressurize the system and seal the inside with an elastomeric membrane. The model was filled to 97% with water and the remaining gas space was pressurized with nitrogen for the Structural Failure Mode Test (SFMT). After exceeding 3.3 times the design pressure a high noise level event was registered, which was interpreted as the breaking of a tendon. Shortly thereafter, at a peak pressure of 3.63 times the design pressure (1.42 MPa or 206.4 psig), the model ruptured violently near the mid-height of the cylinder. Figure 2-5 and Figure 2-6 depict the rupture of the PCCV model during the SFMT.

The dominant containment failure mode in the PCCV test is leakage induced by tearing of the containment liner. Images of these failures are shown in Figure 2-7. These failures are caused by large local liner strains in the vicinity of containment penetrations and terminations of rebar patterns. Finite element analysis (FEA) of the PCCV model is discussed in Section 2.3.2.

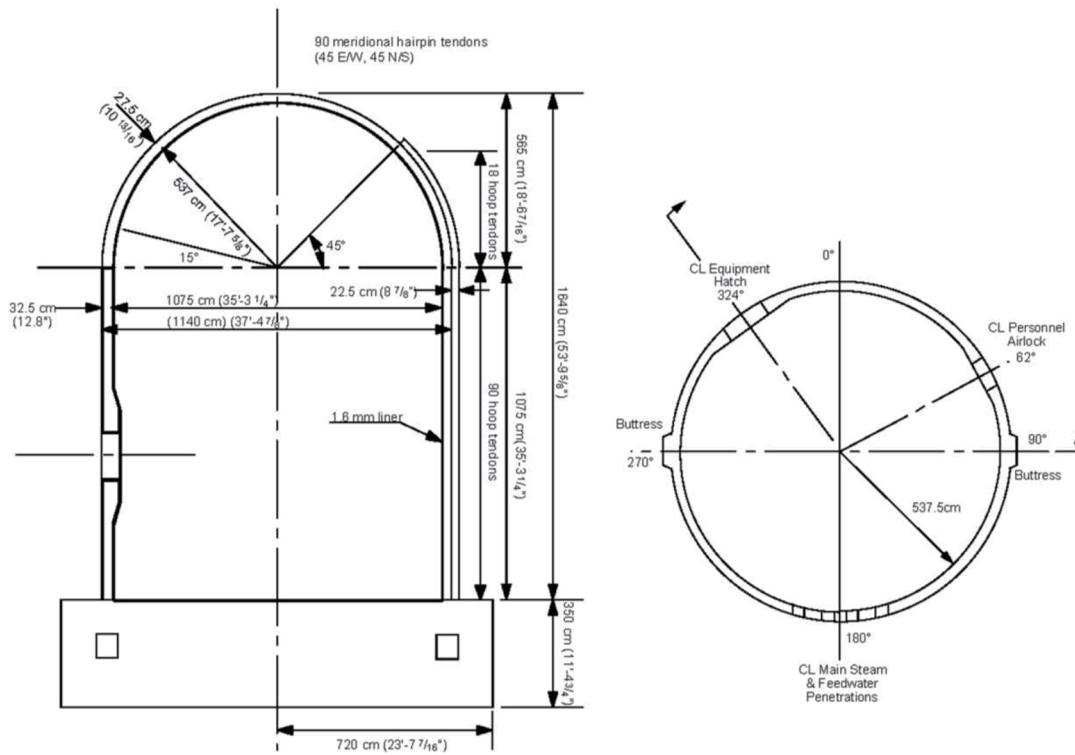


Figure 2-3 PCCV Model Elevation and Cross-Section (Reference 5)



Figure 2-4 **Completed PCCV Model (Reference 5)**

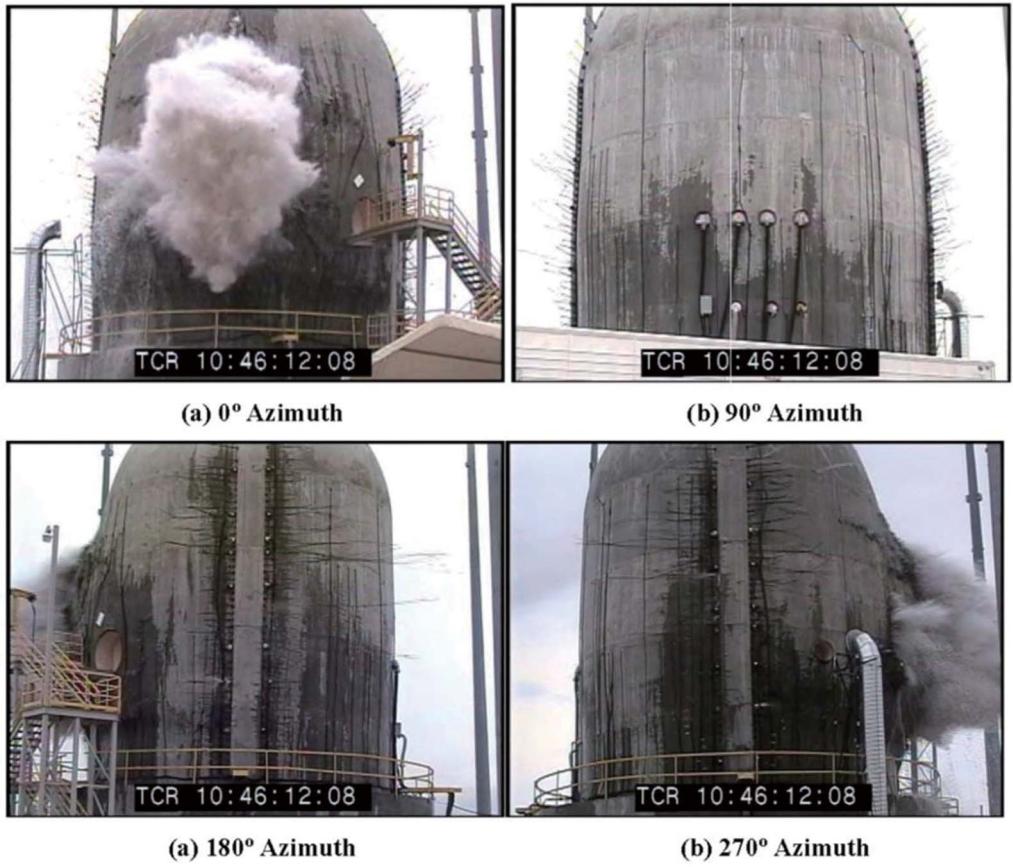


Figure 2-5 Images of the Eventual Rupture of the PCCV Model (Reference 5)



Figure 2-6 **Image of the PCCV Model After the SFMT (Reference 5)**



Figure 2-7 Images of the Equipment Hatch where Liner Tear Occurred in the PCCV Test (Reference 5)

2.3 Past Analytical Studies of Containment Failure

2.3.1 Large Dry Containment Types

Three structural assessments of the Zion containment have been performed by: Sargent & Lundy (S&L) for the IDCOR program (Reference 10), Brookhaven National Laboratory (BNL) for the NRC (Reference 11), and Los Alamos National Laboratory for the NRC (Reference 12). Because of the similarities between the APR1400 and Zion containment types, some of the analyses' conclusions are applicable to the APR1400. For this reason, the Zion analyses will be reviewed briefly below.

A 1983, S&L study utilized equilibrium hand calculations for membrane stresses in the Zion cylinder and dome, and a non-linear finite element analysis for overall response of the containment building, i.e., the stresses and strains in the post-tensioning tendons, steel reinforcement, concrete, steel liner and the soil. Both the hand calculations and the finite element analysis were in excellent agreement predicting failure at the hoop tendons near 134 psig.

Conclusions from this study which are pertinent to the current APR1400 analysis are that the ultimate containment failure pressure and location are not affected by the physical process that causes the pressurization. That is, the containment failure pressure and location will be the same regardless of whether the pressurization is caused by DCH, steaming, combustion, etc.

A 1985 BNL study using the NFAP computer code stands in contrast to the S&L study in that it predicted a shear failure at the basemat-cylinder intersection at 111 psig. To obtain this result, a finite element model with 268 elements and 954 nodes was used. To model the containment wall thickness with the liner and various rebars and tendons, six layers of elements were used. A more refined grid was used at the basemat-cylinder intersection.

One of the major conclusions of the study is that although hoop yielding can be calculated accurately even by hand, shear failure must be handled with complicated FEA models that capture the influence of rebars and tendons. BNL concluded that the S&L finite element model overestimated shear capacity in the basemat because the shell elements used were inadequate. BNL's report states that "models in which the steel members are lumped on the inside and outside faces of the containment wall, overestimate the shear capacity of the containment structures." This is precisely the model used by S&L for its study. However, the results of Sandia's 1:6 scale model test contradict the findings of the BNL study. In the scale model tests, failure occurred in the equipment hatch and the hoops tendons at roughly the same time rather than in the basemat-cylinder junction. There is no mention of modeling the load bearing capability of the soil in the BNL study, which might also explain some of the differences between the BNL and S&L study.

Los Alamos work performed in 1982 predicts shear failure near the basemat- cylinder intersection at 125 psig. However, since analysis above 125 psig could not be carried out due to numerical instabilities, this value seems dubious. This work also predicts hoop tendon yielding at 136 psig, which is in good agreement with the S&L study and the 1:6 scale model test.

2.3.2 Finite Element Analysis of the PCCV Model Test

The PCCV Model Test described in Section 2.2.5 consisted of three phases: pretest analysis, testing, and posttest analysis. These phases are described in NUREG/CR-6906 (Reference 5) and the analysis phases are discussed in this section.

The pretest analysis was completed several months prior to the execution of the Limit State Test so that analysis predictions could be published ahead of test results. The purpose of the pretest analysis was to validate structural models of pre-stressed concrete containments, gain insight into probable failure modes, and support planning of test procedures. The bulk of the analysis was performed using several finite

element models which covered both global structural response as well as local response around key containment details, some of these are shown in Figure 2-8 through Figure 2-10. Analysis was performed using the ABAQUS and ANACAP-U computer programs.

The key results of the pretest analysis were:

- The largest hoop expansion occurs at the Equipment Hatch, and the "free-field displacement" (displacement at 0° and 180°) are slightly less and are approximately equal to each other.
- There is significant local circumferential bending adjacent to each buttress.
- There are significant strain concentrations at terminations or step-downs in rebar patterns.
- There are significant strain concentrations near hatches and near the edges of wall embossments.
- Using a strain-based failure criteria which considers the triaxiality of stress and a reduction in ductility in the vicinity of a weld, the liner failure strain was 0.16. The failure pressure at which a local analysis computed effective plastic strain that reached the failure strain, was 3.2 times the design pressure or 1.3 MPa (188.5 psi). The location for this liner-tearing failure was near the Equipment Hatch (E/H), adjacent to a vertical liner anchor that terminated near the liner insert plate transition.

These results show good general agreement between analysis and experiment, but show that the pretest analysis overpredicted the experimentally determined pressure capacity somewhat.

The final phase of the PCCV Model Test involved a posttest analysis with a goal toward improving the analytical methods for predicting the structural response of a pre-stressed concrete containment and analysis of any phenomena or failure mode observed during the test that had not been predicted by analysis. The posttest analysis involved performing several additional studies using the models developed for the pretest analysis to identify where key model assumptions deviated from experimental results.

One key result of the posttest analysis was that the representation of friction in the tendon modeling of the analytical model was not in good agreement with the experiment. Because of this, liner strains in the vicinity of the Equipment Hatch penetration collar measured in the experiment had been found to be significantly lower than those determined in the pretest model. Since this was the failure location in the experiment, this difference was analyzed more closely. It was determined that preventing slip between the liner and concrete prevented prediction of the erroneously high strains around Equipment Hatch collar while leaving the results of the rest of the model relatively unchanged.

In addition to the change in slip modeling, a new model was also created for the liner "rat-hole" detail. Analysis of this detail showed that the elevated strain in this location was sufficient to cause liner tearing at as early as 2.8 times the design pressure. This prediction is in fairly good agreement with the experimental result.

Overall, the posttest analysis showed that a main factor in determining the limit state of the vessel was the radial expansion of the containment cylinder. This response must be predicted correctly in order to approximate the local mechanisms of liner tearing and penetration ovalization. The posttest analysis confirmed that the analytical model developed in the pretest analysis was able to predict the strain and radial expansion of the cylinder very accurately. Based on this, it is determined that the minimum requirement for a containment overpressurization evaluation is an accurate representation of the structural elements and material properties in a numerically-stable nonlinear finite element model that is insensitive to numerical solution strategy and control parameters.

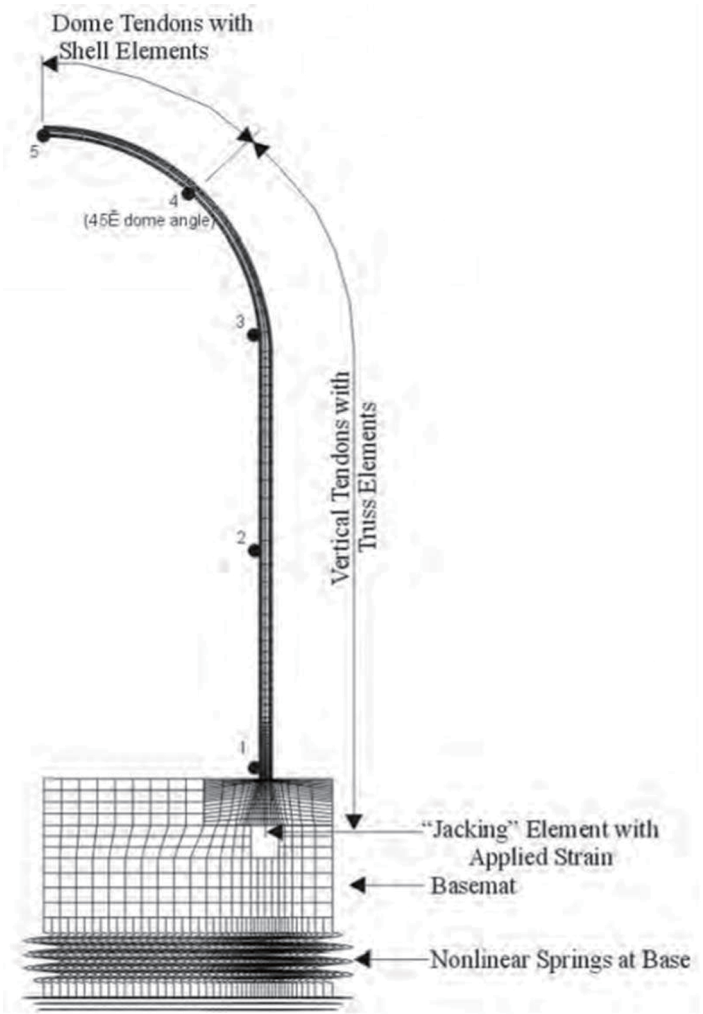


Figure 2-8 Axisymmetric Model of 1:4-scale PCCV (Reference 5)

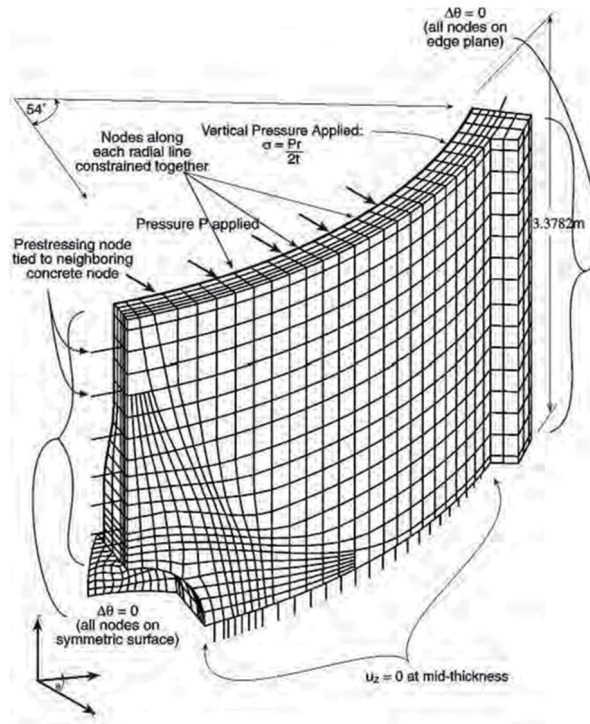


Figure 2-9 Local Model of PCCV Equipment Hatch (Reference 5)

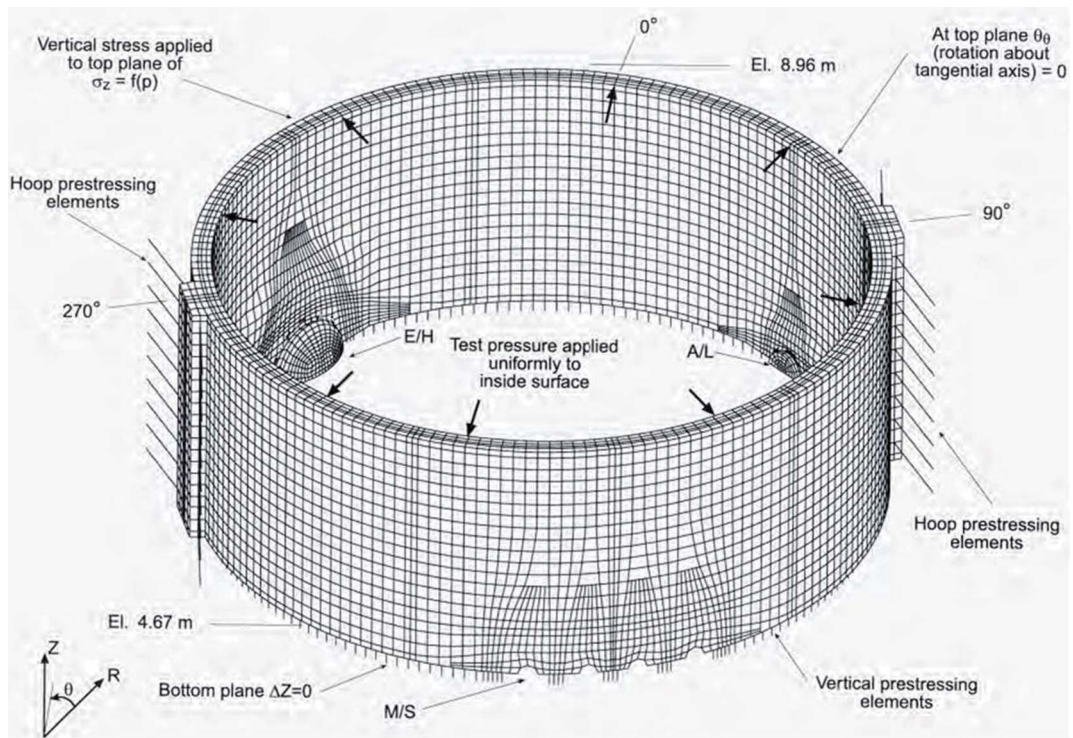


Figure 2-10 PCCV Three-Dimensional Cylinder Mid-Height Model (Reference 5)

3 APR1400 Containment Performance Criteria

This section contains the description of the containment design for the APR1400 and determination of containment performance criteria. Containment performance criteria are the criteria used to judge if the containment would maintain its role as an effective fission product barrier in the analyses presented in Section 0.

3.1 Description of the Containment

The APR1400 containment is a prestressed concrete structure composed of a right circular cylinder with a hemispherical dome and is founded on safety-related common basemat. The APR1400 containment encloses the reactor vessel, steam generators, reactor coolant loops, and portions of the auxiliary and engineered safety features systems. The containment provides reasonable assurance that leakage of radioactive material to the environment does not exceed the acceptable dose limit as defined in 10 CFR 50.34 even if a loss of coolant accident (LOCA) occurred.

The cylindrical containment shell has a constant thickness of (^{TS}) from the top of the foundation basemat to the springline. The shell is thickened locally around the equipment hatch, two personnel airlocks, feedwater, and main steam line penetrations. The containment reinforcing consists primarily of hoop and meridional steel. Prestressing tendons are also arranged in hoop and meridional directions.

The roof of the containment is a hemispherical dome. The inside of the dome is lined with a steel liner plate to provide leak-tightness. The buttresses are extended up to 48 degrees into the dome to provide anchorage for the dome hoop tendons.

The containment provides a minimum net free volume of 0.088 million cubic meters (3.128 million cubic feet) with its internal structures arranged in a manner to (1) protect the inner containment from missile threats, (2) promote mixing throughout the containment atmosphere, and (3) accommodate condensable and non-condensable gas releases from design basis and severe accidents. The internal structures, which are made of reinforced concrete, enclose the reactor vessel and other reactor coolant system (RCS) components. The internal structures provide radiation shielding for the containment interior and missile protection for the reactor vessel and containment shell.

3.2 Containment Performance Criteria regarding FLC requirement

As stated in SECY 93-087, the containment stress should not exceed Factored Load Category (FLC) presented in ASME Code, Section III, Division 2, Subarticle CC-3720, approximately 24 hours following the onset of core damage. In addition, USNRC RG 1.216 requires the containment integrity analysis to consider the FLC requirement presented in regulatory position 5 of USNRC RG 1.7.

[^{TS}]

4 APR1400 CONTAINMENT PERFORMANCE ANALYSIS

The response of the APR1400 containment to gradual pressurization under severe accident conditions was investigated by using the MAAP 4.0.8 code for a range of possible sequences. The containment pressurization sequences considered in the analysis included the overpressurization by steam and non-condensable gases.

The sequences analyzed covered the most likely severe accident initiators for the APR1400. In accordance with the design of the APR1400, Cavity Flooding System (CFS) and ECSBS were included in the sequences. The ECSBS is designed to protect the containment integrity against overpressure and prevent the uncontrollable release of radioactive materials into the environment. The ECSBS flow path is from external water sources (the reactor makeup water tank, demineralized water storage tank, fresh water tank, or the raw water tank), through the fire protection system line via the diesel-driven fire pump, to the ECSBS line emergency connection located at ground level near the auxiliary building. The

TS

Among the sequences, a large break LOCA resulted in the highest pressure in containment at 24 hours following the onset of core damage. The break was approximately equivalent to a 0.24 m (9.5 inch) diameter hole in one of the hot legs. Four safety injection tanks (SITs) and motor-driven auxiliary feed water (AFW) pumps were available. Safety injection pumps (SIPs), charging pumps (CPs) and containment spray pumps (CSPs) were assumed to be unavailable. RCS depressurization using the POSRV was not assumed for this sequence. The CFS actuation and alignment of the three-way valves to the steam generator compartment were assumed to start 30 minutes after the onset of core damage.

Due to the break, RCS pressure rapidly drops and causes the reactor to scram. The break flow from the RCS rapidly pressurizes containment and the core is quickly uncovered. Due to the low RCS pressure, the coolant in SITs is injected temporarily recovering and cooling the core. Once the inventory in SITs has been depleted, the core uncovers again and begins to heat up. Core exit temperature soon reaches 922.04 K (1,200°F), signaling the onset of core damage.

It is assumed that operators align the three-way valves to the steam generator compartment 30 minutes after the onset of core damage. At the same time, the actuation of the CFS, which allows the gravity-driven water flow from the IRWST into the reactor cavity, is assumed. The core begins to melt and relocate to the reactor vessel lower plenum. This produces a momentary pressure spike in the RCS due to the rapid steaming of the water pool that exists in the lower plenum.

The molten corium in the reactor vessel lower plenum eventually caused the vessel to fail at low pressure. The core debris slumped into the flooded reactor cavity. The corium caused the water pool in containment to heat up and boil. The core debris slumps into the flooded reactor cavity. The corium causes the water pool in containment to heat up and boil. Due to the gradual steam generation in the cavity and non-condensable gas generation during MCCI, containment pressure steadily increases. Heat removal by the overlying water pool quenches the corium and eventually halts concrete ablation. At the time of complete quenching of the corium, the concrete ablation depth is much less than the depth of the steel containment liner in the reactor cavity.

TS

It begins to cool and depressurize the containment atmosphere as shown in Figure 4-1. The result shows that the ECSBS is capable of controlling containment pressure for a period of 48 hours after 24 hours following the onset of core damage. The maximum pressure and temperature following the initial 24 hour period are enveloped by the maximum pressure and temperature during the initial 24 hour period.



**Figure 4-1 Containment Pressure for Large Break LOCA with ECSBS
Actuated 24 hours after Onset of Core Damage**

In summary, the most likely severe accident initiators for the APR1400 were analyzed in the analysis.

It can be concluded that the APR1400 containment is prevented from the uncontrolled release of fission products into the environment.

5 CONCLUSION

Based on the containment performance criteria established in Section 3 and the severe accident analyses discussed in Section 4, it is confirmed that that the APR1400 containment design satisfies the regulatory criteria established by the USNRC such as SECY 93-087 and RG 1.216. Therefore, APR1400 containment can maintain its role as a reliable, leak-tight barrier for approximately 24 hours following the onset of core damage under the more likely severe accident challenges and, following this period, the containment can continue to provide a barrier against the uncontrolled release of fission products.

6 REFERENCE

1. SECY-90-016, "Evolutionary Light-Water Reactor (LWR) Certification Issues and Their Relationship to Current Regulatory Requirements," U.S. Nuclear Regulatory Commission, Washington, DC, June 1990.
2. SECY-93-087, "Policy, Technical, and Licensing Issues Pertaining to Evolutionary and Advanced Light-Water Reactor (ALWR) Designs," U.S. Nuclear Regulatory Commission, Washington, DC, April 1993.
3. Regulatory Guide 1.216, "Containment Structural Integrity Evaluation for Internal Pressure Loadings above Design Basis Pressure," NRC U.S.NRC, August 2010.
4. NUREG/CR-5121, Horschel, D. S. "Experimental Results from Pressure Testing a 1:6-Scale Nuclear Power Plant Containment". Sandia National Laboratories. Albuquerque NM : s.n., SAND88-0906, 1992.
5. NUREG/CR-6906, Hessheimer, M. F. and Dameron, R. A. "Containment Integrity Research at Sandia National Laboratories. Sandia National Laboratories". Albuquerque NM : s.n., SAND2006-2274P, 2006.
6. NUREG/CR-5118, Julien, J. T. and Peters, S. W. "Leak and Structural Test of Personnel Airlock for LWR Containments Subjected to Pressures and Temperatures Beyond Design Limits", CBI Research Corporation. Plainfield IL : s.n., SAND88-7155, 1989.
7. MacDonald, P. E. "Containment Penetration System Behavior During Design Basis and Severe Accidents", Idaho National Engineering Laboratory. Idaho Falls ID : s.n.
8. NUREG/CR-5334, Clauss, D. B. "Severe Accident Testing of Electrical Penetration Assemblies", Sandia National Laboratories. Albuquerque NM : s.n., SAND89-0327, 1989.
9. NUREG/CR-6810, Hessheimer, M. F., et al. "Overpressurization Test of a 1:4-Scale Prestressed Concrete Containment Vessel Model", Sandia National Laboratories. Albuquerque NM : s.n., SAND2003-0840P, 2003.
10. IDCOR. "Containment Capability of Light Water Nuclear Power Plants", Technical Report 10.1., 1983.
11. NUREG/CR-4149, Sharma, S. et. al. Ultimate Pressure Capacity of Reinforced and Prestressed Concrete Containments. Brookhaven National Laboratory. BNL-NUREG-51857, 1985.
12. NUREG/CR-2569, Butler, T. A. and Fugelso, L. E. Response of the Zion and Indian Point Containment Buildings to Severe Accident Pressures. Los Alamos Scientific Laboratory. LA-9301-MS., 1982.

Appendix-F

**Severe Accident Analysis Report for
Equipment Survivability Evaluation**

TABLE OF CONTENTS

1	INTRODUCTION	F-10
2	APPLICABLE REGULATIONS AND CRITERIA	F-11
2.1	SECY-90-016.....	F-11
2.2	SECY-93-087	F-12
2.3	Severe Accident Resolution	F-13
3	IDENTIFICATION OF REQUIRED EQUIPMENT AND INSTRUMENTATION FOR EQUIPMENT SURVIVABILITY ASSESSMENT.....	F-15
3.1	High Level Actions to Achieve a Controlled, Stable State in Plant	F-15
3.2	Severe Accident Time Frames	F-15
3.2.1	Time Frame 0 – Pre-Core Uncovery	F-15
3.2.2	Time Frame 1 – Core Heatup Phase.....	F-16
3.2.3	Time Frame 2 – In-Vessel Severe Accident Phase	F-16
3.2.4	Time Frame 3 - Ex-Vessel Severe Accident Phase	F-17
3.3	Equipment and Instrumentation that Require Equipment Survivability Assessment	F-18
4	SEVERE ACCIDENT ENVIRONMENTS.....	F-20
4.1	Method Discussion	F-20
4.1.1	Description of the MAAP 4.0.8 Code.....	F-20
4.1.2	MAAP Model of APR1400.....	F-21
4.1.3	Description of MAAP4-DOSE Code	F-21
4.1.4	MAAP4-DOSE Model of APR1400.....	F-21
4.1.5	Hydrogen Generation Equivalent to a 100% Fuel-Clad Metal Water Reaction for Equipment Survivability Assessment	F-21
4.1.6	Ex-Vessel Hydrogen Generation Due to MCCI	F-23
4.1.7	Construction of ES Profiles	F-27
4.1.8	Bounding Radiation Environment.....	F-28
4.2	Selection of Severe Accident Sequences.....	F-30
4.3	Assumptions and Uncertainties	F-32
4.4	Thermal-Hydraulics and Radiation Envelopes	F-33
4.4.1	Containment Gas Temperatures.....	F-33
4.4.2	Containment Pressure.....	F-34
4.4.3	Radiation	F-34
5	ASSESSMENT OF EQUIPMENT SURVIVABILITY	F-42
5.1	Hydrogen Igniters	F-43
5.2	Passive Autocatalytic Recombiners (PARs)	F-43

5.3	Cavity Flooding System (CFS) Motor Operated Valves (MOVs).....	F-43
5.4	Post-Accident Sampling System (PASS)	F-43
5.5	Containment Hydrogen Monitoring System	F-43
5.6	Containment Atmospheric Temperature Sensors.....	F-44
5.7	Containment Radiation Monitor System (RMS).....	F-44
5.8	Equipment Hatch and Personnel Air Lock.....	F-44
5.9	Electrical Penetration Assembly (EPA)	F-45
5.10	Mechanical Penetrations	F-45
5.11	Safety Depressurization and Vent System (SDVS)	F-45
5.12	Reactor Vessel Level Monitoring System (RVLMS).....	F-46
5.13	Core Exit Thermocouples (CETs) and Resistance Temperature Detectors (RTDs)	F-46
5.14	Pressurizer Pressure Sensors and SG Level Monitors	F-46
5.15	Class 1E Power, Control, and Instrumentation Cables.....	F-46
5.16	Equipment Located Outside Containment.....	F-46
5.17	Radiation Dose ES Results.....	F-47
6	SUMMARY AND CONCLUSION.....	F-49
7	REFERENCES	F-50
	ATTACHMENT A:CONTAINMENT NODALIZATION	F-A-1
	ATTACHMENT B:TEMPERATURE HISTORIES IN EACH CONTAINMENT NODE	F-B-1

LIST OF TABLES

Table 3-1	Systems and Equipment/Instrumentation Requiring Equipment Survivability Assessments.....	F-19
Table 4-1	Parameters Selected for In-Vessel Hydrogen Generation.....	F-22
Table 4-2	Parameter Values that Match COREQUENCH MCCI Results: MAAP Input File Name with Suffix "MCCI" Uses These Values	F-23
Table 4-3	Parameter Values that Match Steam/Hydrogen Generation from Molten Jet-Water Interaction: MAAP Input File Name with Suffix "CP" Uses These Values	F-23
Table 4-4	Dominant PRA Sequences	F-30
Table 4-5	Deterministic Sequences for ES Curves.....	F-31
Table 4-6	Summary of Temperature Envelopes for Equipment Survivability Assessment	F-35
Table 4-7	Maximum Containment Pressure.....	F-36
Table 5-1	Tested Radiation Dose	F-48
Table A-1	APR1400 Containment Node Description	F-A-2

LIST OF FIGURES

Figure 4-1	Geometric Model for Dose Analysis.....	F-24
Figure 4-2	TMI-2 Generated Hydrogen Mass History	F-25
Figure 4-3	Comparison of PHEBUS FPT0 Results with MAAP	F-26
Figure 4-4	Essential Aspects of an Equipment Survivability Curve	F-29
Figure 4-5	ES Curve for Nominally Challenging Environments	F-38
Figure 4-6	ES Curve for Moderately Challenging Environments	F-38
Figure 4-7	ES Curve for Quite Challenging Environments.....	F-39
Figure 4-8	ES Curve for Highly Challenging Environments	F-39
Figure 4-9	ES Curve for Severely Challenging Environments	F-40
Figure 4-10	Cumulative Dose in Containment for Large Break LOCA Sequence	F-40
Figure 4-11	Cumulative Dose in Containment for LOFW Sequence	F-41
Figure 4-12	Cumulative Dose in Containment for SBO Sequence	F-41
Figure A-1	Containment Nodalization Diagram for APR1400	F-A-3
Figure A-2	Containment Nodes in Section A-A	F-A-3
Figure A-3	Containment Nodes in Section B-B.....	F-A-5
Figure A-4	Containment Nodes at EL. 78' – 0".....	F-A-6
Figure A-5	Containment Nodes at EL. 100' 0".....	F-A-7
Figure A-6	Containment Nodes at EL. 114' – 0".....	F-A-8
Figure A-7	Containment Nodes at EL. 136' – 0".....	F-A-9
Figure A-8	Containment Nodes at EL. 156' – 0".....	F-A-10
Figure B-1	Node 1, Reactor Cavity – PRA Sequences	F-B-2
Figure B-2	Node 1, Reactor Cavity – Bounding Sequences – MCCI	F-B-3
Figure B-3	Node 1, Reactor Cavity – Bounding Sequences – CP	F-B-4
Figure B-4	Node 1, Reactor Cavity – Bounding Sequences – DF.....	F-B-4
Figure B-5	Node 2, ICI Chase - PRA Sequences.....	F-B-6
Figure B-6	Node 2, ICI Chase - Bounding Sequences – MCCI.....	F-B-7
Figure B-7	Node 2, ICI Chase - Bounding Sequences – CP	F-B-8
Figure B-8	Node 2, ICI Chase - Bounding Sequences – DF	F-B-9
Figure B-9	Node 3, Corium Chamber Room - PRA Sequences.....	F-B-10
Figure B-10	Node 3, Corium Chamber Room - Bounding Sequences – MCCI	F-B-11
Figure B-11	Node 3, Corium Chamber Room - Bounding Sequences – CP.....	F-B-12
Figure B-12	Node 3, Corium Chamber Room - Bounding Sequences – DF	F-B-13
Figure B-13	Node 4, Reactor Cavity Access Area - PRA Sequences.....	F-B-14
Figure B-14	Node 4, Reactor Cavity Access Area - Bounding Sequences – MCCI.....	F-B-15
Figure B-15	Node 4, Reactor Cavity Access Area - Bounding Sequences – CP.....	F-B-15

Figure B-16	Node 4, Reactor Cavity Access Area - Bounding Sequences - DF	F-B-17
Figure B-17	Node 5, Holdup Volume Tank - - PRA Sequences	F-B-18
Figure B-18	Node 5, Holdup Volume Tank - Bounding Sequences – MCCI	F-B-19
Figure B-19	Node 5, Holdup Volume Tank - Bounding Sequences – CP	F-B-20
Figure B-20	Node 5, Holdup Volume Tank - Bounding Sequences – DF	F-B-21
Figure B-21	Node 6, S/G Compartment #2 at Elev 100' - PRA Sequences	F-B-22
Figure B-22	Node 6, S/G Compartment #2 at Elev 100' - Bounding Sequences – MCCI	F-B-23
Figure B-23	Node 6, S/G Compartment #2 at Elev 100' - Bounding Sequences – CP	F-B-24
Figure B-24	Node 6, S/G Compartment #2 at Elev 100' - Bounding Sequences – DF	F-B-25
Figure B-25	Node 7, S/G Compartment #2 at Elev 136.5' - PRA Sequences	F-B-26
Figure B-26	Node 7, S/G Compartment #2 at Elev 136.5' - Bounding Sequences – MCCI	F-B-27
Figure B-27	Node 7, S/G Compartment #2 at Elev 136.5' - Bounding Sequences – CP	F-B-28
Figure B-28	Node 7, S/G Compartment #2 at Elev 136.5' - Bounding Sequences – DF	F-B-29
Figure B-29	Node 8, S/G Compartment #1 at Elev 100' - PRA Sequences	F-B-30
Figure B-30	Node 8, S/G Compartment #1 at Elev 100' - Bounding Sequences – MCCI	F-B-31
Figure B-31	Node 8, S/G Compartment #1 at Elev 100' - Bounding Sequences – CP	F-B-32
Figure B-32	Node 8, S/G Compartment #1 at Elev 100' - Bounding Sequences – DF	F-B-33
Figure B-33	Node 9, S/G Compartment #1 at Elev 136.5' - PRA Sequences	F-B-34
Figure B-34	Node 9, S/G Compartment #1 at Elev 136.5' - Bounding Sequences – MCCI	F-B-35
Figure B-35	Node 9, S/G Compartment #1 at Elev 136.5' - Bounding Sequences – CP	F-B-36
Figure B-36	Node 9, S/G Compartment #1 at Elev 136.5' - Bounding Sequences – DF	F-B-37
Figure B-37	Node 10, NW Annular Compartment at Elev 100' - PRA Sequences	F-B-38
Figure B-38	Node 10, NW Annular Compartment at Elev 100' - Bounding Sequences –MCCI ...	F-B-39
Figure B-39	Node 10, NW Annular Compartment at Elev 100' - Bounding Sequences – CP	F-B-40
Figure B-40	Node 10, NW Annular Compartment at Elev 100' - Bounding Sequences – DF	F-B-41
Figure B-41	Node 11, SW Annular Compartment at Elev 100' - PRA Sequences	F-B-42
Figure B-42	Node 11, SW Annular Compartment at Elev 100' - Bounding Sequences – MCCI...	F-B-43
Figure B-43	Node 11, SW Annular Compartment at Elev 100' - Bounding Sequences – CP	F-B-44
Figure B-44	Node 11, SW Annular Compartment at Elev 100' - Bounding Sequences – DF	F-B-45
Figure B-45	Node 12, NW Annular Compartment at Elev 114' - PRA Sequences	F-B-46
Figure B-46	Node 12, NW Annular Compartment at Elev 114' - Bounding Sequences – MCCI ..	F-B-47
Figure B-47	Node 12, NW Annular Compartment at Elev 114' - Bounding Sequences – CP	F-B-48
Figure B-48	Node 12, NW Annular Compartment at Elev 114' - Bounding Sequences – DF	F-B-49
Figure B-49	Node 13, SW Annular Compartment at Elev 114' - PRA Sequences	F-B-50
Figure B-50	Node 13, SW Annular Compartment at Elev 114' - Bounding Sequences – MCCI...	F-B-51
Figure B-51	Node 13, SW Annular Compartment at Elev 114' - Bounding Sequences – CP	F-B-52

Figure B-52	Node 13, SW Annular Compartment at Elev 114' - Bounding Sequences – DF	F-B-53
Figure B-53	Node 14, NW Annular Compartment at Elev 136.5' - PRA Sequences	F-B-54
Figure B-54	Node 14, NW Annular Compartment at Elev 136.5' - Bounding Sequences – MCCIF-B-55	
Figure B-55	Node 14, NW Annular Compartment at Elev 136.5' - Bounding Sequences – CP....	F-B-56
Figure B-56	Node 14, NW Annular Compartment at Elev 136.5' - Bounding Sequences – DF	F-B-57
Figure B-57	Node 15, SW Annular Compartment at Elev 136.5' - PRA Sequences.....	F-B-58
Figure B-58	Node 15, SW Annular Compartment at Elev 136.5' - Bounding Sequences – MCCI F-B-59	
Figure B-59	Node 15, SW Annular Compartment at Elev 136.5' - Bounding Sequences – CP....	F-B-60
Figure B-60	Node 15, SW Annular Compartment at Elev 136.5' - Bounding Sequences– DF	F-B-61
Figure B-61	Node 16, Refueling Pool - PRA Sequences	F-B-62
Figure B-62	Node 16, Refueling Pool - Bounding Sequences – MCCI	F-B-63
Figure B-63	Node 16, Refueling Pool - Bounding Sequences – CP	F-B-64
Figure B-64	Node 16, Refueling Pool - Bounding Sequences – DF.....	F-B-65
Figure B-65	Node 17, Containment Dome at Elev 254.5' - PRA Sequences.....	F-B-66
Figure B-66	Node 17, Containment Dome at Elev 254.5' - Bounding Sequences – MCCI.....	F-B-67
Figure B-67	Node 17, Containment Dome at Elev 254.5' - Bounding Sequences – CP.....	F-B-68
Figure B-68	Node 17, Containment Dome at Elev 254.5' - Bounding Sequences – DF	F-B-69
Figure B-69	Node 18, Upper Containment #2 - PRA Sequences	F-B-70
Figure B-70	Node 18, Upper Containment #2 - Bounding Sequences – MCCI	F-B-71
Figure B-71	Node 18, Upper Containment #2 - Bounding Sequences – CP	F-B-72
Figure B-72	Node 18, Upper Containment #2 - Bounding Sequences – DF.....	F-B-73
Figure B-73	Node 19, Upper Containment #1 - PRA Sequences	F-B-74
Figure B-74	Node 19, Upper Containment #1 - Bounding Sequences – MCCI	F-B-75
Figure B-75	Node 19, Upper Containment #1 - Bounding Sequences – CP	F-B-76
Figure B-76	Node 19, Upper Containment #1 - Bounding Sequences – DF.....	F-B-77
Figure B-77	Node 20, Reactor Drain Tank Room - PRA Sequences.....	F-B-78
Figure B-78	Node 20, Reactor Drain Tank Room - Bounding Sequences – MCCI.....	F-B-79
Figure B-79	Node 20, Reactor Drain Tank Room - Bounding Sequences – CP.....	F-B-80
Figure B-80	Node 20, Reactor Drain Tank Room - Bounding Sequences – DF	F-B-81
Figure B-81	Node 21, Letdown Heat Exchanger Room - PRA Sequences	F-B-82
Figure B-82	Node 21, Letdown Heat Exchanger Room - Bounding Sequences – MCCI	F-B-83
Figure B-83	Node 21, Letdown Heat Exchanger Room - Bounding Sequences – CP.....	F-B-84
Figure B-84	Node 21, Letdown Heat Exchanger Room - Bounding Sequences – DF.....	F-B-85
Figure B-85	Node 22, Regenerative Heat Exchanger Room - PRA Sequences.....	F-B-86
Figure B-86	Node 22, Regenerative Heat Exchanger Room - Bounding Sequences – MCCI	F-B-87
Figure B-87	Node 22, Regenerative Heat Exchanger Room - Bounding Sequences – CP.....	F-B-88

Figure B-88	Node 22, Regenerative Heat Exchanger Room - Bounding Sequences – DF	F-B-89
Figure B-89	Node 23, NE IRWST - PRA Sequences	F-B-90
Figure B-90	Node 23, NE IRWST - Bounding Sequences – MCCI	F-B-91
Figure B-91	Node 23, NE IRWST - Bounding Sequences – CP.....	F-B-92
Figure B-92	Node 23, NE IRWST - Bounding Sequences – DF.....	F-B-93
Figure B-93	Node 24, Pressurizer Compartment - PRA Sequences.....	F-B-94
Figure B-94	Node 24, Pressurizer Compartment - Bounding Sequences – MCCI	F-B-95
Figure B-95	Node 24, Pressurizer Compartment - Bounding Sequences – CP.....	F-B-96
Figure B-96	Node 24, Pressurizer Compartment - Bounding Sequences – DF.....	F-B-97
Figure B-97	Node 25, Valve Rooms - PRA Sequences	F-B-98
Figure B-98	Node 25, Valve Rooms - Bounding Sequences – MCCI	F-B-99
Figure B-99	Node 25, Valve Rooms - Bounding Sequences – CP	F-B-100
Figure B-100	Node 25, Valve Rooms - Bounding Sequences - DF	F-B-101
Figure B-101	Node 26, NW IRWST with Spargers - PRA Sequences	F-B-102
Figure B-102	Node 26, NW IRWST with Spargers - Bounding Sequences – MCCI.....	F-B-103
Figure B-103	Node 26, NW IRWST with Spargers - Bounding Sequences – CP	F-B-104
Figure B-104	Node 26, NW IRWST with Spargers - Bounding Sequences – DF	F-B-105
Figure B-105	Node 27, Containment Dome at Elev 291.5' - PRA Sequences.....	F-B-106
Figure B-106	Node 27, Containment Dome at Elev 291.5' - Bounding Sequences – MCCI.....	F-B-107
Figure B-107	Node 27, Containment Dome at Elev 291.5' - Bounding Sequences – CP.....	F-B-108
Figure B-108	Node 27, Containment Dome at Elev 291.5' - Bounding Sequences – DF	F-B-109
Figure B-109	Node 28, SW IRWST with Spargers - PRA Sequences	F-B-110
Figure B-110	Node 28, SW IRWST with Spargers - Bounding Sequences – MCCI.....	F-B-111
Figure B-111	Node 28, SW IRWST with Spargers - Bounding Sequences – CP	F-B-112
Figure B-112	Node 28, SW IRWST with Spargers - Bounding Sequences - DF	F-B-112
Figure B-113	Node 29, SE IRWST - PRA Sequences	F-B-114
Figure B-114	Node 29, SE IRWST - Bounding Sequences – MCCI	F-B-115
Figure B-115	Node 29, SE IRWST - Bounding Sequences – CP	F-B-116
Figure B-116	Node 29, SE IRWST - Bounding Sequences – DF.....	F-B-116
Figure B-117	Node 30, NE Annular Compartment at Elev 100' - PRA Sequences	F-B-118
Figure B-118	Node 30, NE Annular Compartment at Elev 100' - Bounding Sequences – MCCI .	F-B-119
Figure B-119	Node 30, NE Annular Compartment at Elev 100' - Bounding Sequences – CP.....	F-B-120
Figure B-120	Node 30, NE Annular Compartment at Elev 100' - Bounding Sequences – DF.....	F-B-121
Figure B-121	Node 31, SE Annular Compartment at Elev 100' - PRA Sequences.....	F-B-122
Figure B-122	Node 31, SE Annular Compartment at Elev 100' - Bounding Sequences – MCCI	F-B-122

Figure B-123	Node 31, SE Annular Compartment at Elev 100' - Bounding Sequences – CP.....	F-B-124
Figure B-124	Node 31, SE Annular Compartment at Elev 100' - Bounding Sequences – DF	F-B-125
Figure B-125	Node 32, NE Annular Compartment at Elev 114' - PRA Sequences	F-B-126
Figure B-126	Node 32, NE Annular Compartment at Elev 114' - Bounding Sequences – MCCI .	F-B-127
Figure B-127	Node 32, NE Annular Compartment at Elev 114' - Bounding Sequences – CP.....	F-B-128
Figure B-128	Node 32, NE Annular Compartment at Elev 114' - Bounding Sequences – DF	F-B-129
Figure B-129	Node 33, SE Annular Compartment at Elev 114' - PRA Sequences.....	F-B-130
Figure B-130	Node 33, SE Annular Compartment at Elev 114' - Bounding Sequences – MCCI..	F-B-131
Figure B-131	Node 33, SE Annular Compartment at Elev 114' - Bounding Sequences – CP.....	F-B-132
Figure B-132	Node 33, SE Annular Compartment at Elev 114' - Bounding Sequences – DF	F-B-133
Figure B-133	Node 34, NE Annular Compartment at Elev 136.5' - PRA Sequences	F-B-134
Figure B-134	Node 34, NE Annular Compartment at Elev 136.5' - Bounding Sequences – MCCIF-B-135	
Figure B-135	Node 34, NE Annular Compartment at Elev 136.5' - Bounding Sequences – CP... F-B-136	
Figure B-136	Node 34, NE Annular Compartment at Elev 136.5' - Bounding Sequences – DF... F-B-137	
Figure B-137	Node 35, SE Annular Compartment at Elev 136.5' - PRA Sequences.....	F-B-138
Figure B-138	Node 35, SE Annular Compartment at Elev 136.5' - Bounding Sequences – MCCIF-B-139	
Figure B-139	Node 35, SE Annular Compartment at Elev 136.5' - Bounding Sequences – CP... F-B-140	
Figure B-140	Node 35, SE Annular Compartment at Elev 136.5' - Bounding Sequences – DF... F-B-141	
Figure B-141	Node 36, Upper Reactor Vessel Annulus - PRA Sequences	F-B-142
Figure B-142	Node 36, Upper Reactor Vessel Annulus - Bounding Sequences – MCCI	F-B-143
Figure B-143	Node 36, Upper Reactor Vessel Annulus - Bounding Sequences – CP	F-B-144
Figure B-144	Node 36, Upper Reactor Vessel Annulus - Bounding Sequences – DF.....	F-B-145

1 INTRODUCTION

Severe accidents, in which the reactor core is damaged, can lead to elevated temperatures and pressures in the containment, with significant concentrations of combustible hydrogen. In order to achieve a safe stable state, even in the event of vessel failure, it is necessary that certain equipment and instrumentation continue to function under these extreme conditions. The purpose of this Equipment Survivability (ES) assessment is to show that there is reasonable assurance that the equipment and instrumentation used to mitigate and monitor severe accident progression will perform their intended functions under the harsh environmental conditions of severe accidents.

The approach used in the APR1400 certification to demonstrate equipment survivability includes several steps:

- Identify the high level actions used to achieve a controlled, stable state,
- Define the accident time frames,
- Determine the equipment and instrumentation used to diagnose, perform and verify high level actions in each timeframe,
- Determine the bounding environment, and
- Demonstrate with reasonable assurance that the equipment will survive to perform its function in the severe environment.

Chapter 2 presents the applicable regulations and criteria for equipment survivability analysis. In Chapter 3, the equipment and instrumentation that require equipment survivability analysis are determined. In Chapter 4, the bounding thermal-hydraulic and radiation conditions during a severe accident are determined in each containment node. In Chapter 5, equipment survivability is evaluated for essential equipment and instrumentation.

2 APPLICABLE REGULATIONS AND CRITERIA

Under design-basis accident conditions, without core damage, the ability of safety-related equipment to perform their required function is demonstrated through “equipment qualification.” Under severe accident conditions (beyond design basis) the environmental conditions are generally more challenging. The Nuclear Regulatory Commission (NRC) has developed criteria, described below, to provide reasonable assurance that necessary equipment will continue to function (i.e., survive) for the required time period during a severe accident. Thus these criteria are used to demonstrate “equipment survivability.”

2.1 SECY-90-016

On January 12, 1990, the NRC staff issued SECY-90-016 which requested Commission approval for the staff’s recommendations concerning proposed departures from current regulations for the evolutionary light-water reactors (LWRs). The issues in SECY-90-016 were significant to reactor safety and fundamental to the NRC decision on the acceptability of evolutionary LWR designs. The positions in SECY-90-016 were developed as a result of the following activities:

- NRC reviews of current-generation reactor design and evolutionary LWRs,
- Consideration of operating experience, including the TMI-2 accident,
- Results of PRAs of current-generation reactor designs and the evolutionary LWRs,
- Early efforts conducted in support of severe accident rulemaking, and
- Research to address previously identified safety issues.

The Commission approved some of the positions stated in SECY-90-016 and provided additional guidance regarding others in a Staff Requirements Memorandum (SRM) dated June 26, 1990. Section III (Mitigative Feature Issues) Part F (Equipment Survivability) of SECY-90-016 provides the following regulatory guidance.

F. Equipment Survivability

With regard to the Commission’s request concerning “The measures to ensure that systems and equipment required only to mitigate severe accidents are available to perform their intended function (e.g., environmental qualifications),” the staff believes that features provided for severe-accident protection (prevention and mitigation) only (not required for design basis accidents) need not be subject to (a) the 10 CFR 50.49 environmental qualification requirements (b) all aspects of 10 CFR Part 50, Appendix B quality assurance requirements, or (c) 10 CFR Part 50, Appendix A redundancy/ diversity requirements. The reason for this judgment is that the staff does not believe that severe core damage accidents should be design basis accident (DBA) in the transitional sense that DBAs have been treated in the past.

Notwithstanding that judgment, however, mitigation features must be designed so there is reasonable assurance that they will operate in the severe-accident environment for which they are intended and over the time span for which they are needed. In instances where safety related equipment, (which is provided for design basis accidents) is relied upon to cope with severe accidents situations; there should also be a high confidence that this equipment will survive severe accident conditions for the period that is needed to perform its intended function. However, it is not necessary for redundant trains to be qualified to meet this goal.

During the review of the credible severe accident scenarios for specific ALWR designs, the

equipment needed to perform mitigative functions, and the conditions under which the mitigative systems must function, will be identified. Equipment survivability expectations under severe accident conditions should include consideration of the circumstances of applicable initiating events (e.g., station blackout, earthquakes) and the environment (e.g., pressure, temperature, radiation) in which the equipment is relied upon to function. The required system performance criteria will be based on the results of these design-specific reviews. In addition, the staff concludes that severe-accident mitigation equipment for evolutionary ALWRs should be capable of being powered from an alternate power supply as well as from the normal Class 1E onsite systems. Appendices A and B to Regulatory Guide 1.155, "Station Blackout", provide guidance on the type of quality assurance activities and specifications which the staff concludes are appropriate for equipment utilized to prevent and mitigate the consequences of severe accidents.

2.2 SECY-93-087

On April 3, 1993, the NRC staff issued SECY-93-087 which sought Commission approval for the staff's positions pertaining to evolutionary and passive LWR design certification policy issues. This paper evolved from SECY-90-16. SECY-93-087 addresses various preventive features and issues, as well as mitigative features including Equipment Survivability.

The Commission approved some of the staff positions stated in SECY-93-087 and provided additional guidance regarding others in the SRM dated July 21, 1993. Section I (SECY-90-016 Issues), Part L (Equipment Survivability) of SECY-93-087 provides the following regulatory guidance.

In SECY-90-016, the staff recommended that the Commission approve the position that features provided only for severe-accident protection need not be subject to the environmental qualification requirements of 10 CFR 50.49; quality assurance requirements of 10 CFR Part 50, Appendix B; or redundancy/diversity requirements 10 CFR Part 50, Appendix A. The reason for this judgment is that the staff does not believe that severe core damage accidents should be treated in the same manner traditionally used for design-basis accident (DBAs) because of significant differences in their likelihood of occurrence. However, SECY-90-016 further stated that mitigation features must be designed to provide reasonable assurance that they will operate in the severe-accident environment for which they are intended and over the time span for which they are needed. In instances where safety-related equipment provided for DBAs is relied upon to cope with severe-accident situations, there should also be a high confidence that this equipment will survive severe-accident conditions for the period that is needed to perform its intended function.

During the review of the credible severe-accident scenarios for ALWR designs, the staff will evaluate the ALWR vendors identification of the equipment needed to perform mitigative functions and the conditions under which the mitigative systems must operate. Equipment survivability expectations under severe-accident conditions should consider the circumstances of applicable initiating events (such as station blackout or earth quakes) and the environment (including pressure, temperature, and radiation) in which the equipment is relied upon to function. The required system performance criteria will be based on the results of these design-specific reviews.

In its SRM of June 26, 1990, the Commission approved the staff's position. In its letter of May 6, 1991, the staff clarified its position that these criteria would be applied to features provided only for severe accident mitigation.

The EPRI requirements document and the evolutionary ALWR designers have indicated that their submittals are consistent with these criteria. The passive ALWR vendors have indicated that their designs will comply with the applicable EPRI requirements document. In its letter of

August 17, 1992, ACRS agreed with the staff position discussed above.

2.3 Severe Accident Resolution

The basis for resolving the severe accident issues associated with the APR1400 design are the requirements of 10 CFR Part 52, as well as the NRC guidance in SECY-93-087, SECY-96-128, and SECY-97-044, as approved by the Commission.

As noted above, equipment that is classified as safety-related must perform its intended function under the environmental conditions associated with design-basis accidents; the level of assurance is demonstrated through "equipment qualification" and is governed by the requirements in 10 CFR 50.49. Severe accident environmental conditions are generally expected to be more extreme than conditions from design-basis events, so the NRC has established criteria to provide a reasonable level of assurance that necessary equipment will survive a severe accident for the time period it is required. This is referred to as "equipment survivability" and it is fundamentally different from equipment qualification.

The NRC requires the plant designer to perform analyses to demonstrate reasonable assurance of equipment survivability. The Commission approved the position that for the review of the credible severe-accident scenarios for ALWRs they will evaluate the design certification applicant's identification of equipment needed to perform mitigative functions as well as conditions under which the mitigative system must operate.

Beyond design basis events can generally be categorized into in-vessel and ex-vessel severe accidents, depending upon whether or not core damage leads to vessel failure. The environmental conditions resulting from these events are generally more limiting than those from design basis events. The applicable criteria for mechanical and electrical equipment and instrumentation required for recovery from in-vessel severe accidents are provided in 10 CFR 50.34(f) and are summarized below:

- Part 50.34(f)(2)(ix)(c) states that equipment necessary for achieving and maintaining safe shutdown of the plant and maintaining containment integrity will perform its safety function during and after being exposed to the environmental conditions attendant with the release of hydrogen generated by the equivalent of a 100 percent fuel-clad metal-water reaction including the environmental conditions created by activation of the hydrogen control system.
- Part 50.34(f)(3)(v) states that systems necessary to ensure containment integrity shall be demonstrated to perform their function under conditions associated with an accident that releases hydrogen generated from 100 percent fuel-clad metal-water reaction.
- Part 50.34(f)(2)(xvii) requires instrumentation to measure containment pressure, containment water level, containment hydrogen concentration, containment radiation intensity, and noble gas effluents at all potential accident release points.
- Part 50.34(f)(2)(xix) requires instrumentation adequate to monitoring plant conditions following an accident that includes core damage.

The applicable criteria for mechanical and electrical equipment and instrumentation required to mitigate the consequences of ex-vessel severe accidents are discussed in the "Equipment Survivability" section of SECY-90-016 (Section III Part F, see above) and its SRM and are summarized as follows:

- Features provided only for severe-accident protection (prevention and mitigation) need not be subject to the 10 CFR 50.49 environmental qualification requirements,

- 10 CFR Part 50, Appendix B quality assurance requirements, and 10 CFR Part 50, Appendix A redundancy/diversity requirements.
- Mitigation features must be designed to provide reasonable assurance that they will operate in the severe accident environment for which they are intended and over the time span for which they are needed. In cases where safety related equipment (provided for DBAs) is relied upon to cope with severe accident situations, there should be reasonable assurance that this equipment will survive accident conditions for the period that is needed to perform its intended function.
 - Severe accident mitigation equipment should be capable of being powered from an alternate power supply as well as from the normal Class 1D onsite systems. Appendices A and B to Regulatory Guide 1.155, "Station Blackout," provide guidance on the type of quality assurance activities and specifications which are appropriate for equipment utilized to prevent and mitigate the consequences of severe accidents.

3 IDENTIFICATION OF REQUIRED EQUIPMENT AND INSTRUMENTATION FOR EQUIPMENT SURVIVABILITY ASSESSMENT

In order to identify the required equipment and instrumentation for assessment of equipment survivability under severe accident conditions, the high level actions needed to achieve a controlled, stable state in the plant are first determined. Then, the severe accident progression is divided into accident time frames. Lastly, the equipment and instrumentation used to diagnose, perform and verify high level actions in each time frame are identified.

3.1 High Level Actions to Achieve a Controlled, Stable State in Plant

During a core damage accident, operators are confronted with multiple failures of essential safety equipment and/or operator errors. For operators to effectively cope with this plant condition, they must make use of the available equipment and instrumentation with the ultimate goal of achieving safe shutdown of the plant and maintaining containment integrity. These equipment and instrumentation can be grouped according to their general function: RCS inventory control, RCS heat removal, reactivity control, and containment integrity.

RCS inventory control is primarily provided by the safety injection (SI) system. Should the SI system not be available, and if the RCS has depressurized below about 200 psia, then inventory control can also be provided via realignment of the containment spray or shutdown cooling (SC) system pumps to operate in injection mode.

RCS heat removal following a severe accident will be accomplished by establishing the auxiliary feedwater (AFW) system to at least one steam generator, or using "Feed and Bleed Operation", where the operator feeds liquid inventory into the RCS via SI and bleeds off steam and/or water. Once a sufficiently low pressure is established in the RCS, long-term heat removal can be established via Shutdown Cooling (SC) functions using either the SC system or containment spray (CS) pumps, with associated heat exchangers.

Reactivity control is provided by insertion of control rods (typically done early in the transient) and by assuring the delivery of sufficiently borated water into the RCS.

Given the highly reliable containment isolation systems, containment integrity for the APR1400 depends on restoration of the containment heat removal function and the successful performance of seals in the Electric Penetration Assemblies (EPAs), Personnel Air Lock (PAL), and equipment hatch. If the reactor vessel fails and molten corium relocates into the containment, the cavity flooding system minimizes the Molten Core-Concrete Interaction (MCCI) and resulting non-condensable gas generation. Containment integrity also depends on hydrogen control and mitigation because hydrogen burns can create short but extreme temperature conditions in the containment.

3.2 Severe Accident Time Frames

Severe accident progression is divided into four time frames (identified here as Time Frames 0 through 3) to categorize the high level actions required and the corresponding equipment and instrumentation used. Also, the environmental conditions inside the reactor vessel and in the containment are related to these specific time frames.

3.2.1 Time Frame 0 – Pre-Core Uncovery

Time Frame 0 is the period from the initiation of an accident to the time of core uncovery. The high level action in this phase is to recover the reactor coolant system inventory and to remove heat so as to maintain reactor vessel integrity. The equipment and instrumentation used in this phase are:

- Auxiliary Feedwater System (AFWS),
- Safety Injection System (SIS),
- Chemical and Volume Control System (CVCS) via charging pumps,
- Shutdown Cooling System (SCS),
- RCS/Pressurizer Pressure Indicators, and
- Reactor Vessel Level Measurement System (RVLMS).

Equipment survivability during Time Frame 0 is covered under the design basis equipment qualification (EQ).

3.2.2 Time Frame 1 – Core Heatup Phase

Time Frame 1 is the period from core uncover to the onset of significant core damage. The onset of significant core damage is typically identified by a core-exit gas temperature measurement exceeding 1,200 °F. Core overheating is accompanied by rapid fuel-clad metal-water reaction, producing hydrogen. The high level action in this phase is to recover the reactor coolant system inventory and to remove heat so as to maintain reactor vessel integrity.

The equipment and instrumentation used in this phase are:

- Auxiliary Feedwater System (AFWS),
- Safety Injection System (SIS),
- Chemical and Volume Control System (CVCS) via charging pumps,
- Shutdown Cooling System (SCS),
- RCS/Pressurizer Pressure Indicators,
- Reactor Vessel Level Measurement System (RVLMS), and
- Core Exit Thermocouples (CETs).

Equipment survivability during Time Frame 1 is covered under the design basis equipment qualification except for equipment and instrumentation inside the RCS.

3.2.3 Time Frame 2 – In-Vessel Severe Accident Phase

Time Frame 2 is the period from the onset of significant core damage to reactor vessel failure. A significant amount of hydrogen is generated in the reactor vessel during this phase. The core melts and relocates to the lower plenum.

The high level action in this time frame is to recover the reactor coolant system inventory and heat removal, and to maintain containment integrity. To this end, the operator will open the POSRVs to depressurize the reactor vessel to allow SCS pumps to inject water into the RCS and to thereby minimize the possibility of Direct Containment Heating (DCH) if the reactor vessel fails. In addition, the operator will align the 3-way valves on POSRVs to direct the hydrogen-rich effluent to the steam generator

compartment and containment dome, instead of the IRWST and annular compartment. The operator will turn on the igniters. The operator will also actuate the Cavity Flooding System (CFS) in anticipation of vessel failure and subsequent relocation of corium to the reactor cavity floor.

The equipment and instrumentation used to maintain reactor vessel integrity are:

- Auxiliary Feedwater System (AFWS),
- Safety Injection System (SIS),
- Chemical and Volume Control System (CVCS) via charging pumps,
- Shutdown Cooling System (SCS),
- RCS/Pressurizer Pressure Indicators,
- Reactor Vessel Level Measurement System (RVLMS),
- Core Exit Thermocouples (CETs), and
- Rapid Depressurization and Vent System (RDVS) and 3-way Valves.

The equipment and instrumentation needed to maintain containment integrity are:

- Hydrogen Mitigation System (HMS) – PARs and igniters,
- Cavity Flooding System (CFS),
- Containment penetrations – equipment hatch, personnel air lock, electrical penetration assemblies, and mechanical penetrations,
- Hydrogen monitors,
- Post Accident Sampling System (PASS),
- High level radiation monitors, and
- Containment temperature RTDs.

3.2.4 Time Frame 3 - Ex-Vessel Severe Accident Phase

Time Frame 3 is the period from reactor vessel failure to the establishment of a controlled, stable state. The high level actions in this phase are to re-establish a coolable corium configuration on the containment floor, maintain containment integrity, and monitor the accident progression. To this end the operator will turn on the Emergency Containment Spray Backup System (ECSBS) if the controlled, stable state is not achieved 24 hours after the onset of core damage. The ECSBS is designed to protect the containment integrity against challenge due to overpressure and prevent the uncontrollable release of radioactive material into the environment. It accomplishes this by removing heat for a period of approximately 48 hours in duration following the first 24-hour period after the onset of core damage.

The equipment and instrumentation needed to maintain containment integrity are:

- Hydrogen Mitigation System (HMS) – PARs and igniters,

- Containment Spray System (CSS),
- SCS pumps as a backup to containment spray pumps,
- Emergency Containment Spray Backup System (ECSBS),
- Containment penetrations – equipment hatch, personnel air lock, electrical penetration assembly, and mechanical penetrations,
- Hydrogen monitors, and
- Post Accident Sampling System (PASS).

3.3 Equipment and Instrumentation that Require Equipment Survivability Assessment

The list of equipment and instrumentation that require equipment survivability assessment are summarized in Table 3-1.

Table 3-1 Systems and Equipment/Instrumentation Requiring Equipment Survivability Assessments

System	Equipment and Instrumentation
Hydrogen Mitigation System	Hydrogen Igniters
	PARs
Cavity Flooding System	MOVs and Position Transmitters
Post-Accident Sampling System	MOVs and Position Transmitters
Containment Monitoring System	Containment Hydrogen Monitoring Inlet Valves
	Containment Temperature Elements
Radiation Monitoring System	High Level Radiation Monitors
Containment Penetrations	Personnel Air Locks
	Equipment Hatch
	Electrical Penetration Assembly
Safety Depressurization and Vent System	POSRVs
	Motor Operated 3-Way Valves
Reactor Coolant System	RVLMS (HJTCs)
	CETs
	RTD
	Pressurizer PIs
	S/G Wide Range LT
Safety Injection and Shutdown Cooling System	Cavity Injection Line Valve
	IRWST Recirculation Line Valve
Chemical and Volume Control System	Cavity Injection Line Valve
	IRWST Injection Line Valve

4 SEVERE ACCIDENT ENVIRONMENTS

4.1 Method Discussion

In order to determine the environmental conditions expected during a severe accident, the MAAP 4.0.8 code is used to analyze a range of possible sequences. The equipment survivability (ES) profile in each containment node is constructed by selecting appropriate accident scenarios, determining the resulting environmental conditions in the node during each scenario, aggregating the results, and simplifying the curves in a conservative manner.

4.1.1 Description of the MAAP 4.0.8 Code

MAAP 4.0.8 (Modular Accident Analysis Program version 4.0.8) is a computer code that simulates the response of LWR power plants during accidents (Ref.1). Given a set of initiating events and operator actions, MAAP predicts the plant's response as the accident progresses. MAAP4 has been benchmarked against major experiments and plant transient experiences.

MAAP is an integral code which treats the full spectrum of important phenomena that could occur during a severe accident, simultaneously modeling those that relate to the thermal- hydraulics and to fission products. It simultaneously models the primary system and the containment and reactor/auxiliary building. MAAP is designed to account for plant signals, signal delays and component strokes, and for equipment opening or actuation times.

The PWR primary system model calculates the thermal-hydraulic conditions in the reactor pressure vessel, the hot legs, the cold legs, the cross-over (intermediate) legs, and the primary side of the steam generators. (The pressurizer is treated in a separate model.) The primary system is modeled as two conceptual loops, referred to as the broken loop and the unbroken loop. The user specifies how many actual primary system loops are incorporated into each MAAP4 loop, and which loop contains the surge line to the pressurizer. (The terms broken and unbroken are misnomers, as breaks can be modeled in either or both of the loops. These terms are carryovers from earlier, more restricted versions of the code.)

There are 14 gas control volumes in the primary system model: core, upper plenum, broken and unbroken hot legs, broken and unbroken hot and cold leg tubes (hot and cold sides of the tubes) for U tube steam generators, broken and unbroken cross-over (intermediate) legs, broken and unbroken cold legs, downcomer, and reactor vessel dome. There are six water pools: the core (includes the upper plenum, the reactor vessel dome, the hot legs, and the hot side of U-tubes), broken and unbroken cold tubes (the cold side of U-tubes), broken and unbroken cross-over legs (includes the steam generator outlet plenum through to the outlet of the pumps), and downcomer (includes the horizontal portion of the cold legs). In addition, there are 19 primary system structural heat sinks, which are modeled as two-dimensional slabs. Because the number of gas volumes is larger than the number of water pools, a pool can occupy several gas volumes.

The pressurizer is modeled as a single control volume, with one water pool and one gas node. The water and gas can be at different temperatures (which are also distinct from the primary system fluid temperatures). Calculations of the TH (thermal-hydraulic) conditions in the pressurizer account for evaporation, condensation, steam stripping due to steam and non-condensable gases sparging through the water pool, and water and gas exchange (co-current and countercurrent), with the primary system through the surge line, and with the containment through relief valves and safety valves via the quench tank. Mass and energy contributions from pressurizer sprays and heaters, as well as heat transfer to structures, are also included in the pressurizer model.

The core model predicts the TH behavior of the core, including the water and gas contained within the core boundary, and the response of core components during all phases of a sequence. The calculations

are performed on a nodal basis. Users can specify up to 50 axial rows and 7 radial rings (channels). The code tracks the mass, energy, and temperature of the following constituents in each node:

- Fuel (UO_2)
- Cladding (Zr, ZrO_2 , stainless steel, steel oxide, and U-Zr-O)
- Control rod or water rod (Ag-In-Cd or B_4C , stainless steel, steel oxide, Zr, and ZrO_2)
- Structural materials (Zr, ZrO_2 , stainless steel, and steel oxide)

The MAAP steam generator model calculates the heat transfer, from the primary side water or condensing steam, to the secondary side water and/or uncovered portion of the tubes. The calculations start with the masses and energies of the secondary side water and gas. The pressure, the temperature of each phase, the water levels, and the rates of change of the mass and energy terms are then determined. The two-region model calculates individual water levels in each region. It also has a tube bundle heat transfer model that tracks the subcooled length, and includes a fully imposed fluid momentum model, a two-phase swell model, and a structural heat sink model. Both equilibrium and non-equilibrium thermodynamics between the gas and the water are included.

4.1.2 MAAP Model of APR1400

The environmental conditions in the containment during a severe accident, including hydrogen burns, are obtained by running the MAAP 4.0.8 code. The MAAP model for APR1400 is specified in the parameter file SKN34-408-X.par. The sequence definitions are specified in individual input files. The MAAP model for the APR1400 containment consists of 36 nodes and 88 junctions. The APR1400 nodalization diagrams can be found in Attachment A.

4.1.3 Description of MAAP4-DOSE Code

MAAP4-DOSE (Ref.2) is a radiation dose calculation code that reads input from MAAP4 output.

4.1.4 MAAP4-DOSE Model of APR1400

The MAAP4-DOSE geometry model for calculating radiation doses in the containment is constructed based on the assumption that the individual containment regions can be approximated by a rectangular box whose dimensions are shown in Figure 4-1. There are 13 containment regions represented by 13 boxes in the dose parameter file. Some regions, such as the steam generator compartments (nodes 6 to 9), are assumed to have a square base, while other regions are assumed to have a rectangular base. For example, the annulus region node 10 is modeled as a rectangular box with base dimensions of 6.7 m \times 32.5 m and a height of 4.3 m. The width and the height of the box are same as the actual width and height of the annulus. The 32.5 m length of the box is obtained from dividing the floor area by the width. For steam generator compartment nodes 6 to 9, the base of the region is assumed to be a square whose length is equal to the square root of the floor area. The height of the box is the same as the height of the node (already defined in the MAAP4 parameter file).

Dose parameter files DOSE_LLOCA-ES-0HF0P0-MCCI.PAR, DOSE_LOFW-ES-0HF0DP3-MCCI.PAR, and DOSE_SBO-ES-0HF0DP3-MCCI.PAR, were prepared and used for the analysis. They define the geometry of the containment regions, the dose points, and the control parameters needed for running the code.

4.1.5 Hydrogen Generation Equivalent to a 100% Fuel-Clad Metal Water Reaction for Equipment Survivability Assessment

According to the regulatory requirements (10 CFR 50.34(f)), it must be demonstrated that equipment necessary for achieving and maintaining safe shutdown of the plant, or maintaining containment integrity, will perform its safety function during and after being exposed to the environmental conditions attendant with the release of hydrogen generated by the equivalent of 100% fuel-clad metal-water reaction, including the environmental conditions created by activation of the hydrogen control system. The NRC position on the accident scenarios and methodologies to produce an amount of hydrogen equivalent to a 100% metal-water reaction is provided in the Safety Evaluation Report that was issued in support of the Hydrogen Control Owner Group (HCOG). The HCOG submittal noted that 100% fuel-clad oxidation could be achieved by an extended simulation that imposed a source of water/steam for the metal-water reaction. For the HCOG submittal, the Grand Gulf plant (BWR) was assessed and found to require an artificially extended steam generation rate of approximately 0.1 lb/sec to achieve 100% fuel-clad oxidation. The Grand Gulf reactor is rated at 3830 MW (thermal). This is the same order of magnitude as the APR1400 power rating. The method applied in the ALWR certifications followed this NRC approved general guidance of extending the steam/water inventory availability (if needed) until the hydrogen equivalent of 100% active fuel-clad oxidation was achieved.

To conservatively calculate the in-vessel hydrogen generation, the following model parameters related to oxidation are selected and changed from the default values:

Table 4-1 Parameters Selected for In-Vessel Hydrogen Generation

	TS
--	----

FAOX is the multiplier for the cladding external surface area available for oxidation. This parameter is set greater than one to account for steam ingress inside the cladding after cladding rupture. The oxidation rate is increased when the oxidation surface area is increased. FGBYPA is a parameter to divert gas flows in the core to the bypass channel. When FGBYPA is equal to 1, all channel flows are diverted to the bypass channel if the whole core is blocked for a given elevation, such that steam is unavailable for oxidation and heat transfer for nodes above these blocked nodes. When FGBYPA is equal to 0, all channel flow will “reappear” above the blocked nodes and thus be available for oxidation and heat transfer.

	TS
--	----

4.1.6 Ex-Vessel Hydrogen Generation Due to MCCI

All analyzed sequences consider ex-vessel hydrogen generation by MCCI. Following vessel failure, MCCI is controlled by two model parameters FCHF and ENT0C.

FCHF, a “Kutateladze number” multiplier to the flat plate critical heat flux, is the controlling input parameter for molten debris heat transfer to overlying water following vessel failure. ENT0C is a parameter controlling the corium-water interactions as the molten jet falls into a flooded reactor cavity. Appropriate values for FCHF and ENT0C have been studied in the technical report appendix B. In that report, one pair of values was chosen to match the results of more sophisticated MCCI codes, COREQUENCH 3.2 and MAAP5.01.1146, while ignoring hydrogen generation from molten jet-water interactions. A second pair of values was chosen to better represent hydrogen generation from molten jet-water interactions.

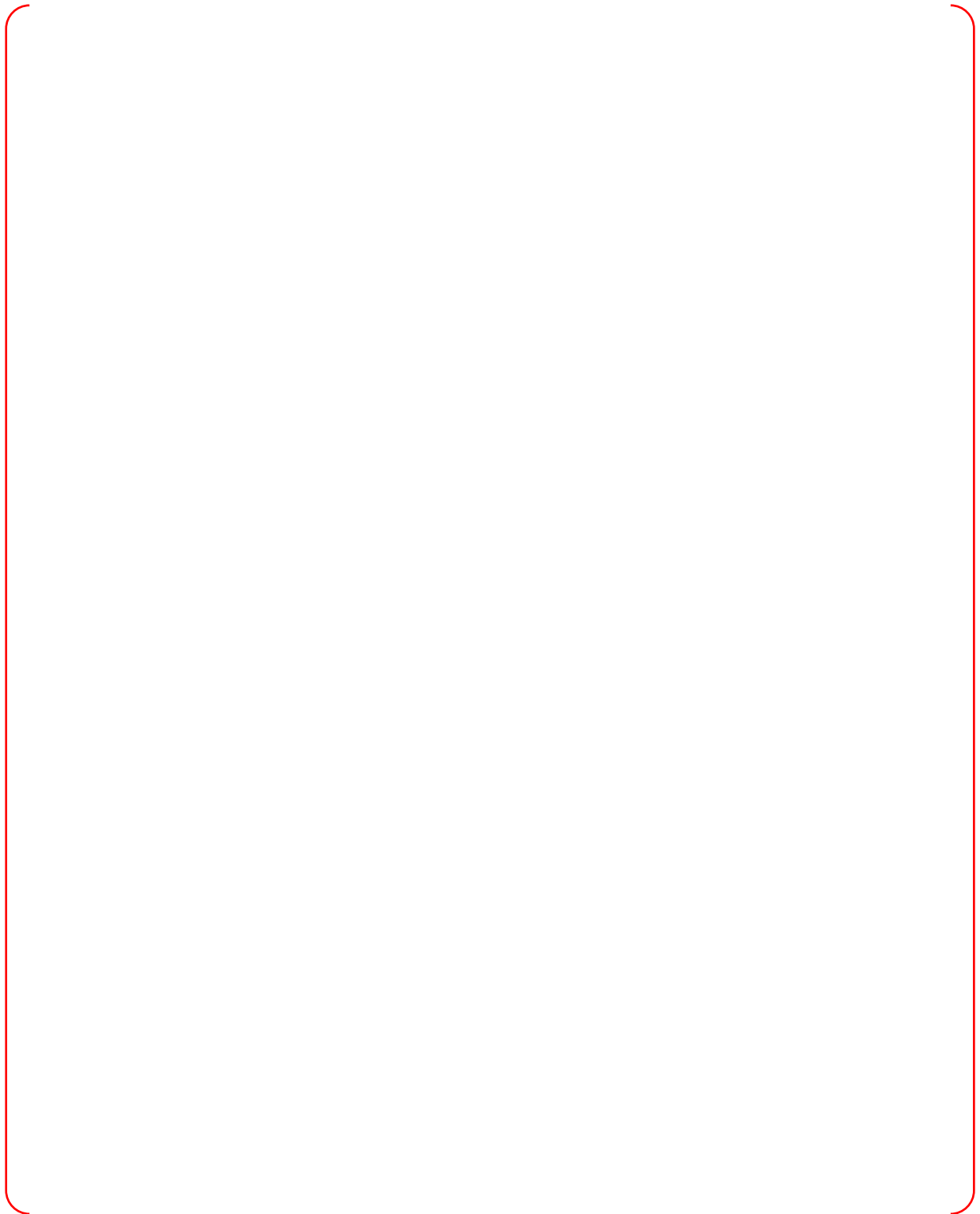
Each sequence in this analysis was analyzed with the two sets of parameters. Table 4-2 summarizes the set of values for FCHF and ENT0C that matches sophisticated MCCI code results. Those values are used in MAAP runs whose input file name has an “-MCCI” suffix. Table 4-3 summarizes the set of values for FCHF and ENT0C that have a more realistic hydrogen generation during molten jet-water interactions. Those values are used in MAAP runs whose input file name has an “-CP” suffix.

Table 4-2 Parameter Values that Match COREQUENCH MCCI Results: MAAP Input File Name with Suffix “MCCI” Uses These Values

	TS
--	----

Table 4-3 Parameter Values that Match Steam/Hydrogen Generation from Molten Jet-Water Interaction: MAAP Input File Name with Suffix “CP” Uses These Values

	TS
--	----



TS

Figure 4-1 Geometric Model for Dose Analysis

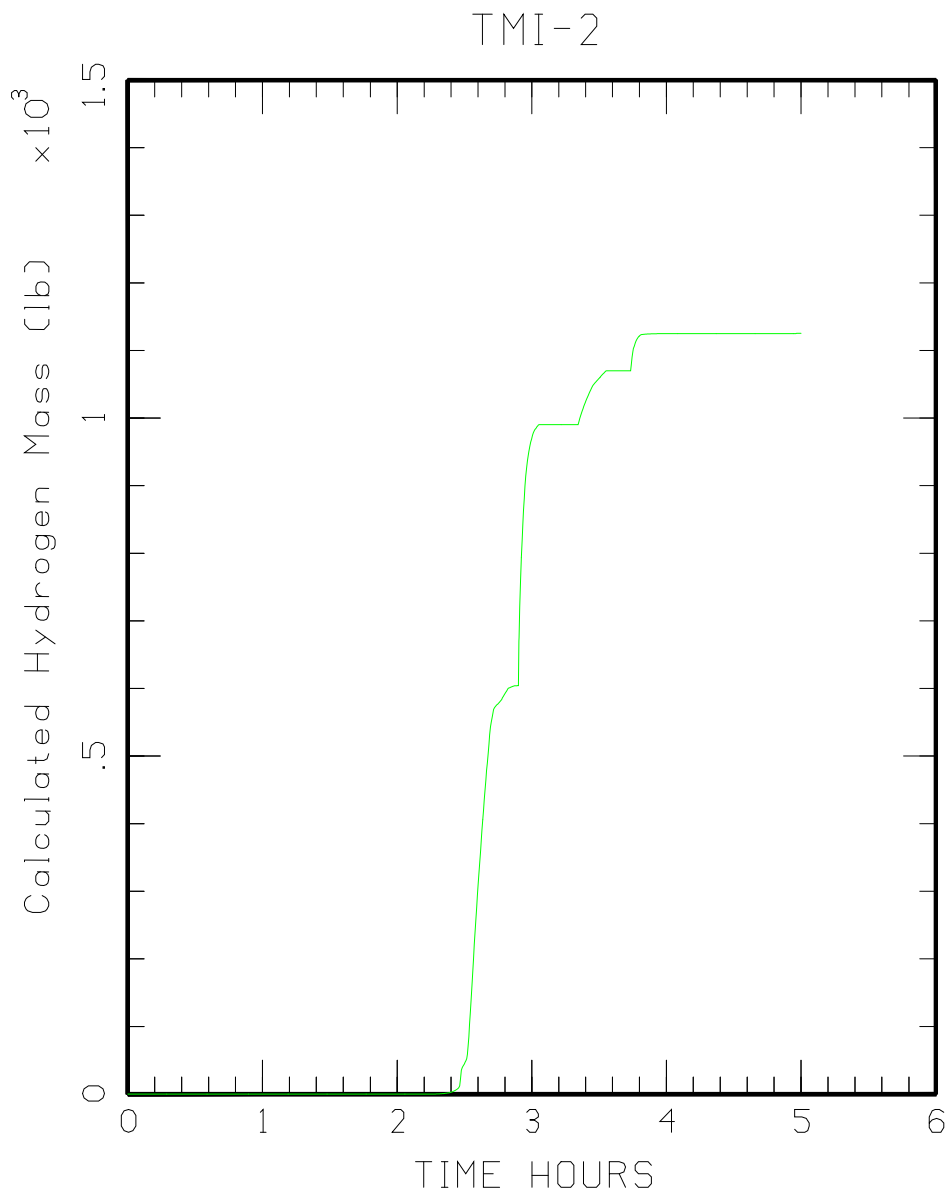


Figure 4-2 TMI-2 Generated Hydrogen Mass History

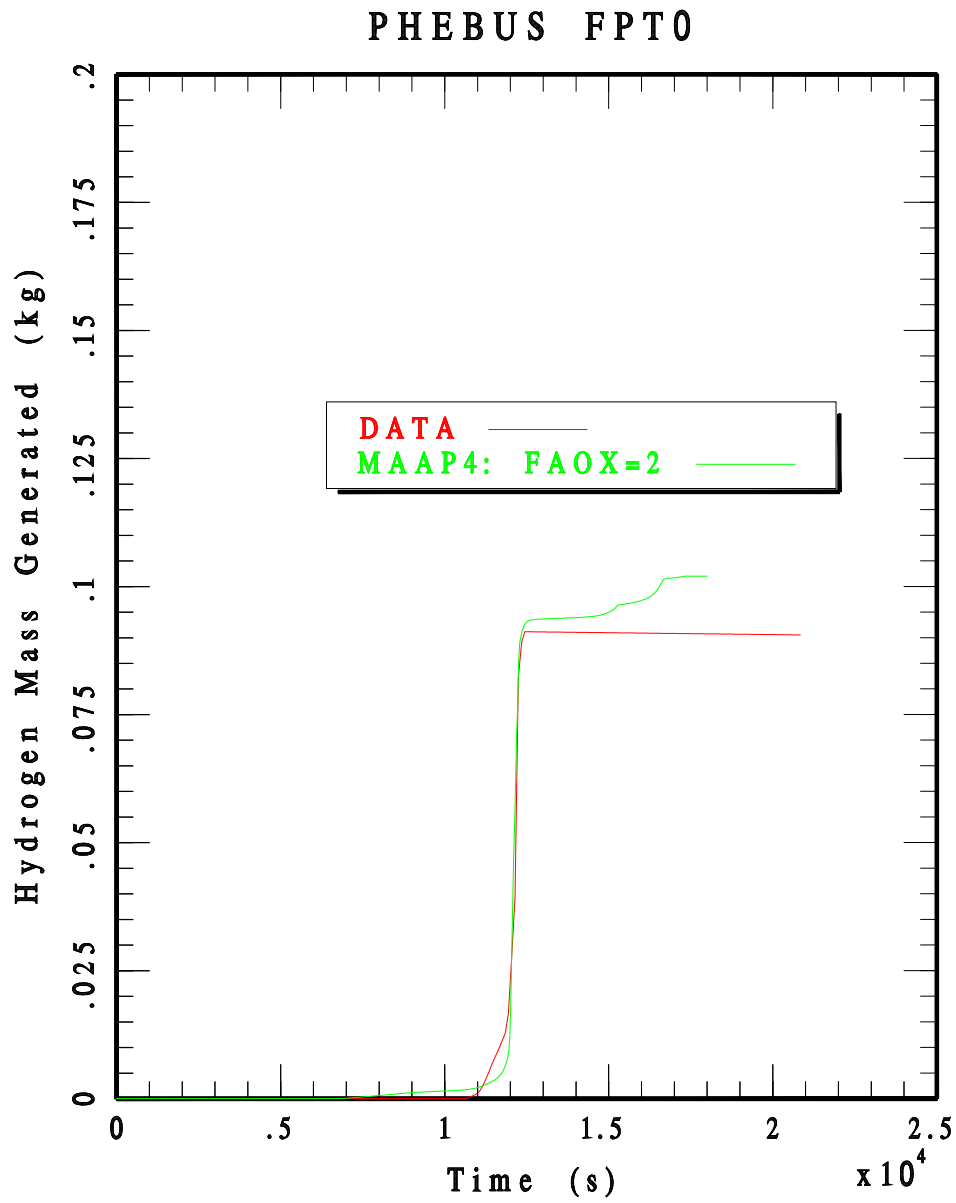


Figure 4-3 Comparison of PHEBUS FPT0 Results with MAAP

4.1.7 Construction of ES Profiles

Each accident sequence was analyzed with MAAP 4.0.8 to produce time-temperature histories for various locations in the containment (i.e. for the different MAAP containment nodes) over the 24 hours after onset of core damage. All severe accident mitigation features, including the Emergency Containment Spray Backup System (ECSBS), are assumed to be available for the purpose of evaluating equipment survivability. ECSBS is actuated 24 hours after the onset of core damage. The spray begins to cool and depressurize the containment atmosphere, removing the harsh environmental conditions that essential equipment and instrumentation were exposed to up to that point. Therefore, it is only necessary to evaluate equipment survivability during the first 24 hours after the onset of core damage.

Due to variability in the timing of severe accident phenomena, the option for bounding the entire set of results with a single curve is unnecessarily conservative. For example, a hydrogen burn subjects a compartment to extreme temperatures for a short duration. The time at which a hydrogen burn occurs varies with each scenario. Therefore, a simple curve which bounds all scenarios would model a compartment as experiencing extreme temperatures for an excessively long duration.

The temperature history of a compartment can be discretized and treated as a histogram. The bins in this histogram can then be reordered, not by time but by decreasing order of temperature magnitude, to create a monotonically decreasing characterization of compartment temperature which reproduces the same integrated value of temperature vs. time. This preserves the duration and the magnitude of high-temperature conditions, while minimizing the effect of uncertainty in phenomena timing. This reordering is conservative, since it maximizes the duration at extreme conditions. For example, two hydrogen burn events, each of 10 second duration, would be represented as a single high temperature event of 20 second duration. By reordering scenario results in this manner, the results of different sequences can be easily compared, and a simple bounding curve for all results may be constructed. This method of constructing ES curves accounts for the varied progression of accident sequences while maintaining conservatism.

A FORTRAN program was written to convert a temperature history to an equivalent reordered temperature histogram. The program also generates the time-temperature integrals before and after reordering, to verify that the appropriate integral value of temperature with time is preserved.

Except for the reactor cavity and the IRWST, where massive hydrogen burns cause extreme conditions, the temperatures in containment can be bounded by superposition of a long term elevated temperature of 460 K and short term temperature transients due to hydrogen burn, which can rise to as high as 900 K. Peak temperatures may last up to 10 seconds. Then, the temperatures decrease to 460 K over several hundred seconds. A bounding equipment survivability curve may consist of up to four regions as shown in Figure 4-4. Region I is a rapid initial temperature rise, indicated by the region from t_0 to t_1 . This region corresponds to a rapid increase in compartment temperature, typically due to gas combustion or reactor coolant release. Equipment is initially at a normal operating temperature (T_{normal}) and experiences a rapid temperature increase to T_{max} over a short duration ($t_1 - t_0$). Note that the sorted histogram method described previously obscures the rate of temperature rise. Therefore an alternate method is used to create this region of an ES curve.

Regions II, III, and IV are conservatively constructed based on the sorted histogram method to bound the aggregate MAAP results.

Region II represents a sustained application of high temperature, typically associated with gas combustion or reactor coolant release. This is shown in Figure 4-4 in the time period from t_1 to t_2 , where equipment is subject to a constant temperature T_{max} over an interval on the order of 10-100 seconds.

Region III is a cooling period, representing a compartment temperature decrease from its high value to a steady-state temperature (T_{steady}) over an extended interval (from t_2 to t_3) on the order of 1000 seconds.

The temperature decrease rate in this region may vary.

Region IV is an extended interval of elevated temperature, representing accident conditions which have approached a steady state (T_{steady}) above normal operating conditions. This is shown in the region after t_3 ; this period lasts on the order of 1,000 to 100,000 seconds.

4.1.8 Bounding Radiation Environment

This analysis provides the cumulative radiation dose in selected containment regions during severe accidents for the purpose of equipment survivability assessment. The severe accident sequences selected for this analysis include large LOCA, loss of feedwater, and station blackout. The analysis was performed using the MAAP4-DOSE code. Necessary input information for the MAAP4-DOSE analysis can be obtained directly from the output files of the MAAP4 runs.

For each dose node, dose points are defined where cumulative radiation doses are calculated and reported. Note that in Figure 4-1 the MAAP containment node numbers (shown inside squares) are different from the dose node numbers (which are shown inside circles). For most nodes, the dose point is assigned to be the central point of the box. For nodes adjacent to the containment floor, such as the lower SG and lower annular regions (containment nodes 6, 8, 10 and 11), long-term radiation dose is expected to be highest near the floor, due to the deposition of airborne fission products. For these nodes, the dose point is located 0.5 m above the floor center to yield a higher dose reading than the node center.

TS



TS

Figure 4-4 Essential Aspects of an Equipment Survivability Curve

4.2 Selection of Severe Accident Sequences

Accident scenarios were selected both by deterministic and probabilistic means. The ten most likely core damage scenarios were selected from the PRA results as shown in Table 4-4, representing 87.6% of core damage frequency.

Deterministic sequences were selected for their severity and coverage. They include large, medium, and small loss of coolant accidents (LLOCA, MLOCA, and SLOCA), station blackout (SBO), and loss of feedwater (LOFW) scenarios. Table 4-5 shows the deterministic sequences analyzed by MAAP. For each base sequence, several sensitivity cases, with and without accumulators and containment spray, were analyzed to produce bounding environmental conditions.

Table 4-4 Dominant PRA Sequences

TS

Table 4-5 Deterministic Sequences for ES Curves

TS

4.3 Assumptions and Uncertainties

The thermal-hydraulic results produced by the selected sequences are expected to cover all credible environmental conditions that essential equipment and instruments could be exposed to during a severe accident. Additional sensitivity cases address uncertainties in operator actions (i.e. delay time for actuation of the safety depressurization and vent system) and in phenomena (i.e. burns with and without a diffusion flame). In all sequences, the severe accident mitigation features are assumed to be available as follows.

- Hydrogen Igniters are available – Igniters are placed near hydrogen release points to control rapid hydrogen releases during a severe accident. The igniters require AC power. Therefore, the igniters are not available during a station blackout.
- Passive Autocatalytic Recombiners (PARs) are available - PARs are a passive system effective in removing long-term hydrogen evolved from core-concrete interactions. A PAR efficiency of 50% is conservatively assumed.
- The Safety Depressurization and Vent System (SDVS) is available. Also, the Three-Way Valves are available. For loss of feedwater or station blackout sequences, the operator is supposed to open the POSRVs and align the Three-Way Valves to the steam generator compartment in order to depressurize the RPV after the onset of significant core damage. Without depressurization, massive release of hydrogen to the steam generator compartment will occur during a hot leg creep rupture event. Extreme temperatures of up to 1,600 K are expected in the steam generator compartment due to a continuous hydrogen burn. Hence, with SDVS available, hot leg creep rupture is not considered. However, uncertainty in the delay time in the operator action is considered by running the sequences with both 5 minutes and 30 minutes delay time between core damage and actuation of the SDVS and Three-Way Valves. For station blackout sequences, the SDVS is actuated and Three-Way Valves are aligned to the SG compartment after the first opening of the POSRVs or one hour before battery depletion, whichever occurs first.
- In station blackout sequences, POSRV opening, due to high primary system pressure while significant water remains in the steam generators, are not used as a cue for the actuation of SDVS or the alignment of the Three-Way Valves to the SG compartment. "Significant water" is defined as a collapsed water level in the steam generator downcomers above the set point to generate an Auxiliary Feedwater Actuation Signal (3.317 m). This is done because primary system pressure is not expected to climb high enough to cause the POSRVs to lift while secondary side heat removal is still available, which delays the time at which SDVS initiation and Three-Way Valve alignment occur.
- The Cavity Flooding System (CFS) is available – The cavity flooding system is assumed to be actuated 30 minutes after the onset of significant core damage (i.e. core exit temperature is greater than 1,200°F).
- The Emergency Containment Spray Backup System (ECSBS) is available – ECSBS is an alternate means of providing containment spray during a beyond design basis accident when both the Containment Spray (CS) and Shutdown Cooling (SC) pumps, and/or the IRWST, are not available. This system is actuated 24 hours after the onset of significant core damage (i.e. core-exit gas temperature increases above 1,200°F). The harsh environmental condition in the containment is removed once the spray is turned on and cools the containment atmosphere. Therefore, equipment

survivability assessment needs to be done only for the first 24 hours following the onset of significant core damage.

4.4 Thermal-Hydraulics and Radiation Envelopes

4.4.1 Containment Gas Temperatures

The temperature results for the thirty six compartments are compiled in Attachment B. For each compartment a figure with two temperature plots is provided. The temperature histories for all the various sequences are shown in the top plot. The corresponding sorted histograms are shown in the bottom plot. Time (x-axis variable) in the re-ordered temperature histories is plotted on a log scale so that the rapid temperature transients during hydrogen burns can be viewed.

Because of the sheer number of sequences analyzed, the analyzed sequences are divided into five groups:

- PRA sequences,
- Bounding sequences with model parameters FCHF and ENT0C tuned to match concrete erosion results of more sophisticated MCCI codes (case names have “-MCCI” suffix),
- Bounding sequences with model parameters FCHF and ENT0C tuned to give more realistic hydrogen generation rate during molten jet-water interactions (case names have “-CP” suffix),
- Bounding sequences with diffusion flame assumed on the SDVS 3-way valves (case names have “-DF” suffix),
- Bounding sequences with a 5 minutes delay time between core damage and actuation of the SDVS and 3-way valve (normally a 30 minutes delay time is assumed; case names have “-5M” suffix).

Severe accident temperature environments can be classified (in decreasing order of severity) as severely challenging, highly challenging, quite challenging, moderately challenging, or nominally challenging, depending on the magnitude and duration of extreme conditions. Severely challenging environments are characterized by highly-confined extreme conditions for a relatively long duration, such as in the reactor cavity and the IRWST. Highly challenging environments are areas close to a combustible gas source such as the steam generator compartments or the annular compartment above the IRWST. Quite challenging and moderately challenging environments are areas where combustible gas may accumulate such as the containment dome. Nominally challenging environments are compartments where the containment atmosphere can be considered well-mixed and is inerted by a high steam concentration. The equipment survivability curves constructed for each of the five types of environments are shown in Figure 4-5 through Figure 4-9. They are also shown with the sorted histograms in Attachment B.

As described in Section 3.3, all severe accident mitigation features are assumed to be available for the purpose of constructing the bounding temperature environment for equipment survivability assessment. The cavity flooding system (CFS) insures the presence of water in the reactor cavity when the vessel fails and core debris is relocated to containment. The water pool formed in the reactor cavity following CFS actuation reaches the top of reactor cavity ceiling; the gas spaces in the corium chamber room, ICI chase, and reactor cavity access area are isolated from the gas space below the reactor vessel. Consequently, the environmental conditions in these areas are relatively benign whereas severe conditions are predicted in the reactor cavity and upper RPV annulus.

The bounding temperature profile expected in each containment node during a severe accident is summarized in Table 4-6.

4.4.2 Containment Pressure

[] TS

4.4.3 Radiation

[] TS

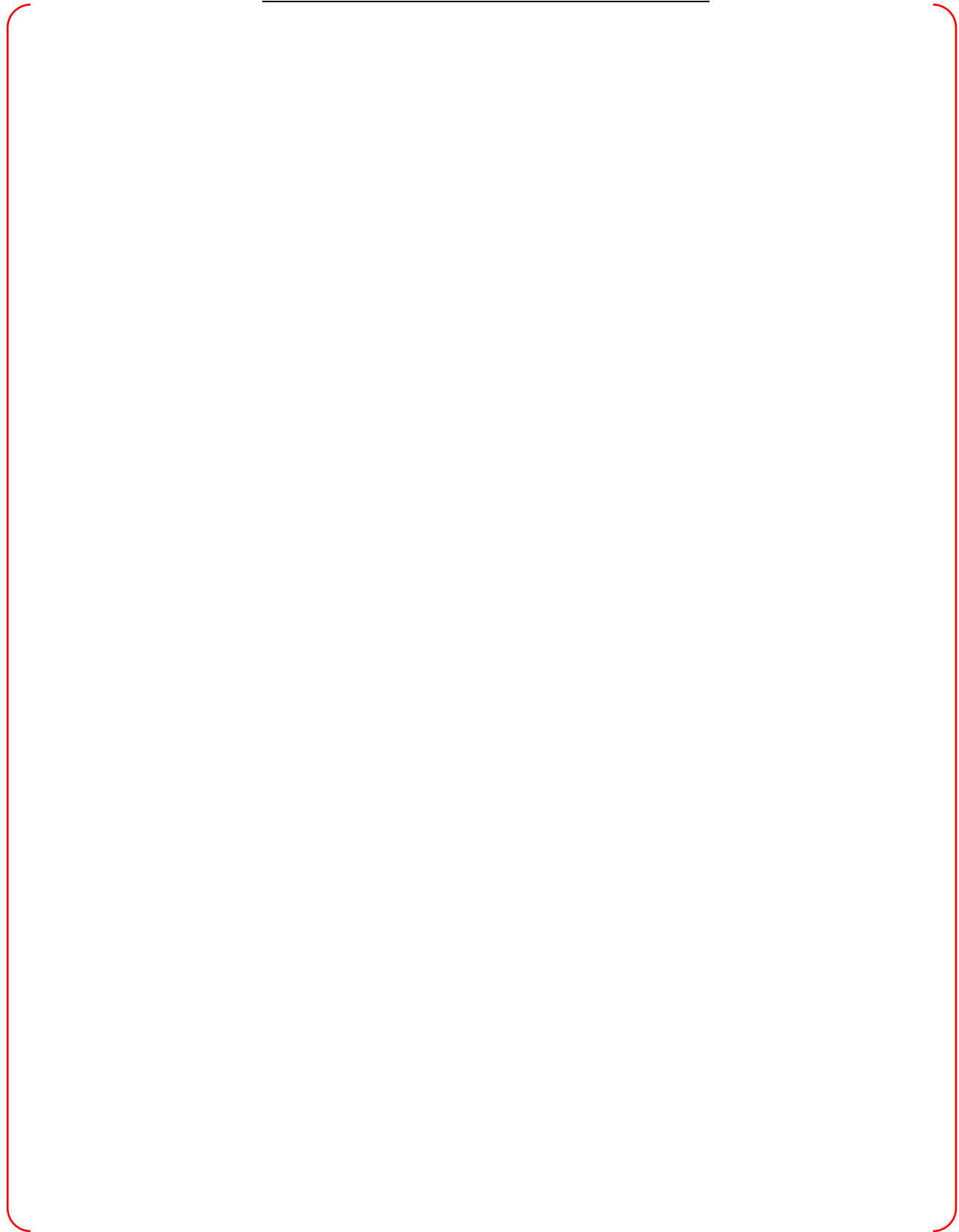
Table 4-6 Summary of Temperature Envelopes for Equipment Survivability Assessment

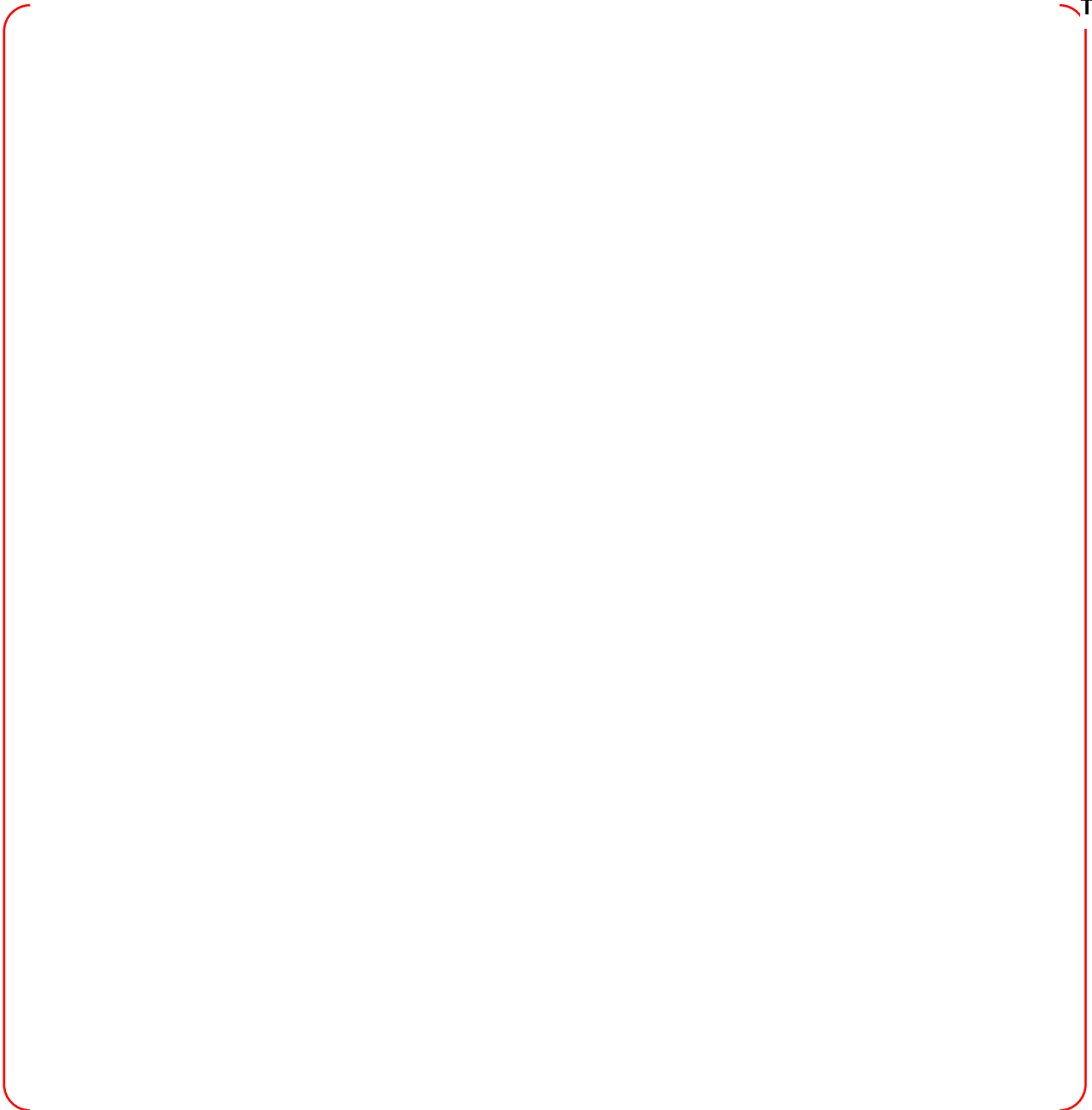
TS



Table 4-7 Maximum Containment Pressure

TS





TS

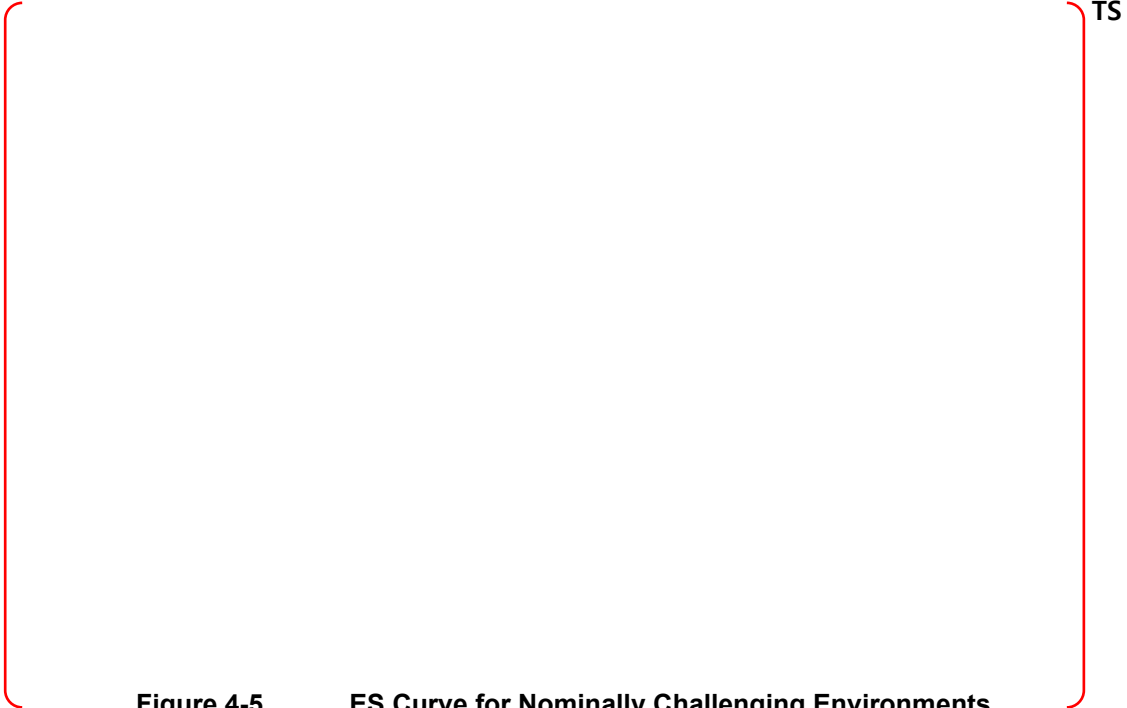


Figure 4-5 ES Curve for Nominally Challenging Environments

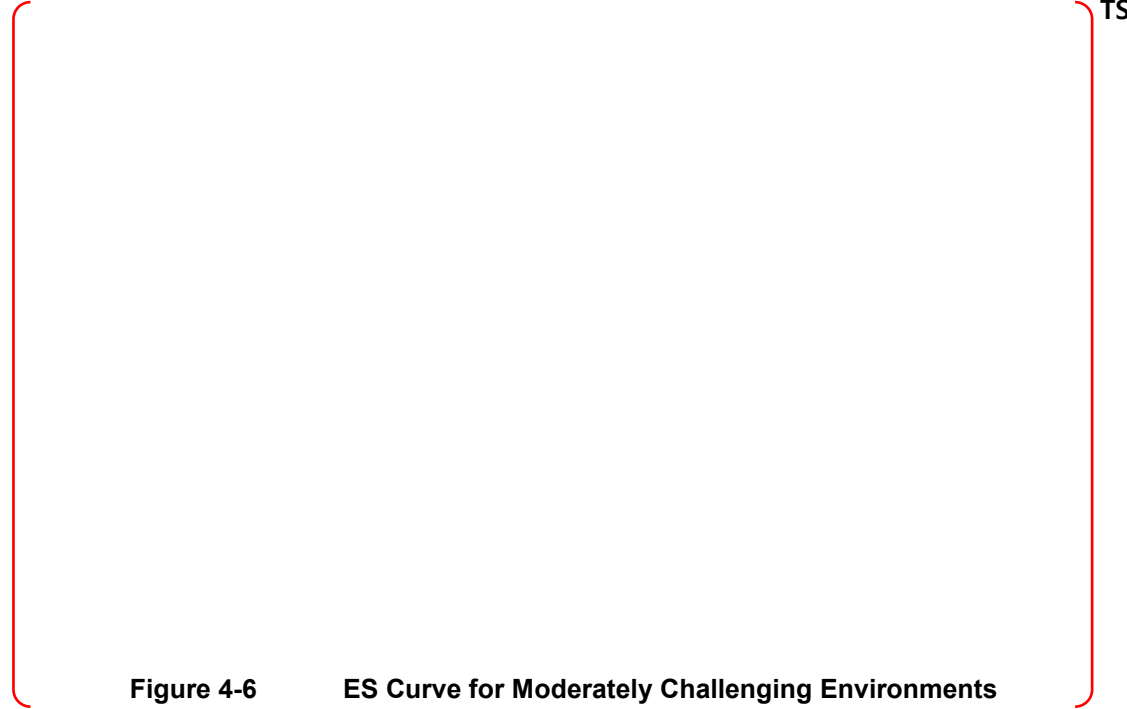


Figure 4-6 ES Curve for Moderately Challenging Environments



Figure 4-7 ES Curve for Quite Challenging Environments



Figure 4-8 ES Curve for Highly Challenging Environments



Figure 4-9 ES Curve for Severely Challenging Environments



Figure 4-10 Cumulative Dose in Containment for Large Break LOCA Sequence



Figure 4-11 Cumulative Dose in Containment for LOFW Sequence



Figure 4-12 Cumulative Dose in Containment for SBO Sequence

5 ASSESSMENT EQUIPMENT SURVIVABILITY

Equipment survivability is assessed by comparing reliable equipment qualification information such as equipment suppliers' documents, research results and experimental data with severe accident environmental conditions at the locations where the equipment is installed.

The principal cause for environments that are harsher than design basis events is hydrogen combustion. Severe accidents may produce significant quantities of hydrogen which can burn locally, globally, and either continuously or intermittently in different regions of the containment. Due to this potential for hydrogen burns it is necessary to assess the additional thermal loading on equipment that needs to survive for severe accident mitigation. This can be done by comparing the plant specific simulations of the thermal environments imposed by hydrogen burns against the available experimental basis.

The primary source of performance expectations of similar equipment in severe accident environments is an EPRI report (Achenbach, 1985) and supplemental information in NUREG/CR-5344 (SAND89-0327) (Clauss, 1989) and NUREG/CR-6530 (Blanchat, 1997). These reports describe programs which tested equipment types that have previously been qualified for design basis event environmental conditions. The temperature range in the test chamber for the EPRI program was 700 to 800°F for 10-20 minutes during a continuous hydrogen injection test. Additionally, the equipment in the EPRI program was exposed to significant hydrogen burns. The same equipment was exposed to and survived several events, both pre-mixed and continuous hydrogen injection, which provides confidence in the equipment's ability to survive a severe accident. The second program tested containment penetrations to high temperatures for long durations. Thus, reasonable assurance is achieved by applying available experimental databases to the expected containment conditions induced by hydrogen burns for the selected instrumentation and required functional intervals. Additionally, plant design features such as redundancy, separation of redundant capabilities and containment internal structures that shield equipment from burns can be used to construct arguments that provide reasonable assurance of the survivability of the designated equipment.

For the comparison with equipment supplier's documents, related documents are reviewed and the location of equipment is identified. The assessment of survivability is performed by comparing the equipment data to the ES profile, which defines the accident conditions the equipment will potentially be exposed to. If the equipment data cannot support survivability under the specified severe accident environmental conditions, survivability will be confirmed by consulting the equipment vendors.

A key input for the assessment of each individual piece of equipment or instrumentation is identification of its location within the containment. Furthermore, for each component on the equipment and instrumentation ES list, one may need to identify the thermally limiting (non-metallic) subcomponent. This identification is typically also performed as part of the design basis equipment qualification (EQ) activity. Usually equipment placed on the ES list is also included in the plant as part of design basis instrumentation such that the thermally limiting component for those items may already have been determined

Examples of non-metallic components and materials include compression seals, gaskets, cables (electrical power, control and instrumentation), and motor winding insulation. Non-metallic materials often encountered in these components include ethylene propylene (EPDM), silicone rubber, and neoprene.

Thermal lag analysis may be used for equipment survivability assessments. For example, even though the local atmospheric condition could momentarily rise to an extreme temperature during hydrogen combustion, the temperature at the surface of the equipment may remain much lower than that in the gas space. Hence, equipment survivability can be assessed using simplified thermal lag analysis based on

the temperature difference between the containment atmosphere and the equipment surface and/or internal components.

5.1 Hydrogen Igniters

Eight hydrogen igniters are distributed near expected hydrogen release points throughout the containment: reactor cavity access area, generative heat exchanger room, steam generator compartments, and pressurizer compartment. Of these, the harshest environment is expected to be the steam generator compartment. The ES profile in this area is characterized by a constant 900 K for 10 seconds, decreasing to 460 K at 600 seconds, and then staying constant.

The hydrogen igniters are protected with E-5A-3 fire wrap from 3M Corporation. The igniters can thus survive an accident environment temperature of 1,073 K for four hours and still perform their intended function.

5.2 Passive Autocatalytic Recombiners (PARs)

The PARs are made of Pt or Pd catalyst in a stainless steel casing. They do not contain any organic material components which could be susceptible to thermal degradation. Therefore, they are expected to survive the harsh environment of a severe accident and continue to perform their intended function of hydrogen removal.

5.3 Cavity Flooding System (CFS) Motor Operated Valves (MOVs)

The CFS consists of two spillways between the IRWST and the Hold-up Volume Tank (HVT), two spillways between the HVT and the reactor cavity, and related valves. Four MOVs are installed in the Hold-up Volume Tank. The goal of the CFS is to pre-flood the reactor cavity prior to vessel failure so as to possibly prevent vessel failure or, in the event of vessel failure, to cool core debris which would accumulate on the reactor cavity floor. The MOVs need to operate only prior to vessel failure, under a relatively mild environment. In that case the cavity conditions should be bounded by the DBA EQ peak temperature of 455 K. Therefore, the CFS MOVs are expected to perform their intended function of opening the valves for cavity flooding.

5.4 Post-Accident Sampling System (PASS)

PASS is designed to collect and deliver representative samples of liquids and gases in various process system to sample stations for chemical and radiological analysis. The RCS hot-leg sample isolation MOVs and their position transmitters are located in the steam generator compartment. The containment air sample isolation MOVs and their position transmitters are located in the annular compartment at the 121'-6" elevation. The bounding ES profile in the steam generator compartments is characterized by a constant 700 K for 100 seconds, decreasing to 500 K at 1,000 seconds, and staying constant thereafter. The ES profile in the annular compartment is characterized by a constant 700 K for 10 seconds, decreasing to 460 K at 600 seconds, and staying constant thereafter. MOVs were included in the EPRI hydrogen burn experiments (EPRI NP-4354) and survived many transients.

5.5 Containment Hydrogen Monitoring System

The containment and IRWST hydrogen monitoring system contains hydrogen monitor inlet valves, hydrogen analyzers and piping. This system samples the containment atmosphere and measures the hydrogen concentration, employing sensing devices outside containment. The hydrogen analyzers and discharge valve are not subject to the harsh environment of a severe accident because they are located outside containment. However, the inlet valves are potentially subjected to a harsh environment because they are located inside containment. They are located in the dome, in the annular compartment, and in the IRWST.

The environmental condition in the containment dome is quite challenging. The environmental condition in the annular compartment is highly challenging. The environmental condition in the IRWST is severely challenging, with a peak temperature of 1,200 K for 10 seconds, decreasing to 700 K at 2,000 seconds, and staying at a constant 600 K thereafter. If the inlet valves fail during a severe accident, the Post-Accident Sampling System can be used to determine representative hydrogen concentrations since a relatively uniform hydrogen concentration is expected throughout the containment.

5.6 Containment Atmospheric Temperature Sensors

Thirteen temperature sensors are distributed throughout the containment: dome, steam generator compartments, pressurizer room, annular compartment above the operating deck, annular compartment below the operating deck, and reactor cavity. The sensor located in the reactor cavity will be exposed to a severely challenging environmental condition, with a peak temperature of 1,200 K for 10 seconds, decreasing to 700 K at 2,000 seconds, and staying at constant 600 K thereafter.

The sensor located in the steam generator compartments will be exposed to a highly challenging environmental condition, with a peak temperature of 900 K for 10 seconds, decreasing to 460 K at 600 seconds, and staying constant thereafter. In addition, sensors in the path of a diffusion flame on the IRWST vent stack and on the SDVS 3-way valves will likely not survive.

Although the EQ data conditions provided by the equipment vendor are less than the harsh environmental conditions expected during a severe accident in some locations, there are enough temperature sensors distributed throughout the containment to provide redundancy. Also, installation of fire wrap around these sensors would minimize the effect of high temperatures and shield against diffusion flames.

5.7 Containment Radiation Monitor System (RMS)

Two radiation monitoring systems are located in the south side of the upper operating area. The ES curve in this area is characterized by a constant 900 K for 10 seconds, decreasing to 460K at 600 seconds and staying constant thereafter.

The thermally limiting components in the radiation monitor system are PEEK insulators in the chamber and cable connectors. Based on the "Percentage retention of elongation at break after aging" test data for PEEK material, it is determined to have qualified life of 50 hours at 583 K. The test temperature is higher than the long term severe accident environmental temperature of 460 K. Due to thermal lag, short temperature transients due to hydrogen burns should not affect the insulators. Therefore, the PEEK insulators in the RMS are expected to maintain their integrity during a severe accident.

5.8 Equipment Hatch and Personnel Air Lock

The equipment hatch and personnel air locks are located in the annular compartment, two at the operating deck and one above the IRWST. The environmental conditions at the operating deck during a severe accident will be highly challenging, while those above the IRWST will be less harsh. The highly challenging ES curve is characterized by a constant 900K for 10 seconds, decreasing to 460 K at 600 seconds, and staying constant thereafter.

Thermally limiting components in the equipment hatch and personnel air lock are EPDM O-rings, compression seals, and gaskets. In the Sandia/CBI Personnel Airlock Testing, an actual full-scale airlock assembly was subjected to environmental conditions corresponding to severe accident events. In particular, Test 2C consisted of three thermal and pressure cycles. In the second cycle, the air temperature was raised to 700 K. Then, the pressure was increased to 300 psig. There was no measurable leakage of the inner door seal. In the tests, it was determined that the temperature at which the material deteriorates is approximately 600 K. Indeed, the peak temperature recorded on the door surface when the seal failed during the third cycle was 633 K. Results of Test 2C demonstrated that the

EPDM seal material will survive the ambient temperature of 485 K over 24 hours, the long term bounding temperature of the highly challenging ES curve. When a thermal-lag calculation was done on the door seal, the short 900 K temperature spike in the atmosphere was not transmitted to the door seal. Hence, the seal and gaskets in the Equipment Hatch and Personnel Air Locks are expected to maintain their integrity during a severe accident.

5.9 Electrical Penetration Assembly (EPA)

The Electrical Penetration Assemblies (EPAs) are installed on the containment pressure boundary and are sealed with double O-rings. The EPAs are located in the annular compartment at various elevations above the operating deck. The environmental conditions in the annular compartment where EPAs are installed are bounded by the highly challenging ES curve. The highly challenging ES curve is characterized by a constant 900 K for 10 seconds, decreasing to 460 K at 600 seconds and staying constant thereafter.

The thermally limiting components in EPAs are Viton O-rings, polysulfone module conductor sealant, and polyimide film conductor insulation. A Conax EPA was tested under severe accident conditions by Sandia National Laboratories. The EPA was a lower voltage penetration assembly with a typical cable mix for power, control, and instrumentation functions. The EPA was first irradiated and then thermally aged. Then, the EPA was exposed to steam at 135 psia and 644 K for 8 days. The temperature in the test chamber reached the maximum value, 644 K, about 45 minutes into the test. Temperature in the junction box reached a steady-state temperature of about 561 K at about 4 hours into the test. Temperature on the header plate reached the steady-state temperature of about 444 K at about 4 hours into the test. The leak integrity of the Conax EPA was maintained during the entire 10 day period of the severe accident test. Clearly the test condition of 644 K exceeds the long term ES curve. Thermal-lag calculations show that the short temperature spike of 900 K in the ambient is not transmitted to the air inside the termination box, and certainly not to the sealant. Hence, the seal in the EPA is expected to maintain its integrity during a severe accident.

5.10 Mechanical Penetrations

Mechanical penetrations include the Main Steam (MS) and Feedwater (FW) flow penetrations and hot/cold process piping. These penetrations have no organic material and are designed to remain sealed under severe accident environmental conditions.

5.11 Safety Depressurization and Vent System (SDVS)

The POSRVs in the pressurizer compartment, and 3-way valves located in the steam generator compartment, are manually operated to rapidly depressurize the RCS following onset of core damage. The goal of the system is to depressurize the RCS from 2,500 to 250 psia prior to vessel failure, thereby preventing high pressure melt ejection. The essential components of the system that need to be assessed for a harsh environment include:

- POSRVs and actuation circuitry
- POSRV position transmitters and indicators
- POSRV discharge branch line isolation valves and position transmitters, and indicators
- MOVs for 3-Way Valves

The system is not needed during a LOCA because the break will depressurize the RCS. Therefore, the essential components are not subject to the harsh environment of design basis accidents. Also, prior to

actuation of SDVS the essential components will not be subjected to the harsh environment of a hydrogen burn or to the long term elevated temperatures following vessel breach. Hence, the SDVS equipment is expected to survive and perform its intended function during a severe accident. _

5.12 Reactor Vessel Level Monitoring System (RVLMS)

The RVLMS consists of two probes with heated and unheated junction thermocouples. The heated junction thermocouple (HJTC) probes monitor the liquid inventory above the fuel alignment plate. The temperature difference between the heated and unheated junction thermocouples is a direct indication of the presence of liquid inventory. RVLMS provides useful information as the core uncovers and it provides confirmation of core recovery. Individual unheated junction thermocouples may also trend the progression of core degradation by monitoring the reactor vessel upper plenum gas temperature.

The HJTC probes utilize heated and unheated junction Type K thermocouples. Unlike the core exit thermocouple, the RVLMS thermocouple string is top mounted and it does not pass through the core. These thermocouples are calibrated to operate up to 1,255 K, in accordance with the RVLMS design requirements. Hence, these instruments are expected to function well after the start of core degradation

5.13 Core Exit Thermocouples (CETs) and Resistance Temperature Detectors (RTDs)

The CETs and RTDs used to monitor RCS inventory are relatively robust. They can survive well past design basis conditions and provide useful information until their temperature limits are exceeded. These temperature limits are about 1,533 K for Type K thermocouples procured for "in-vessel" application and about 673 K for RTDs.

5.14 Pressurizer Pressure Sensors and SG Level Monitors

RCS pressure monitoring is necessary to trend RCS depressurization following operator actions taken to either establish "feed and bleed" operation or to confirm sufficiently low pressure to enter shutdown cooling (SDC) operation. In the event the operator has to depressurize the RCS via the steam generator (SG), the water level in the SG must be monitored to assure sufficient SG secondary-side inventory.

All pressure transmitting devices are located outside the secondary shield wall. A long, small diameter tube connects the RCS to the high pressure side of the pressure transmitter. The sensor tap of these pressure transmitting devices is typically filled with low viscosity fluid. The long length of the tube provides sufficient heat loss and thermal capacity to maintain the fluid temperature closer to the ambient. Therefore, the "in-vessel" environment will not influence the operation of these pressure transmitting devices.

All transducers, cables, and associated signal conditioning equipment inside the containment have been tested by Duke Power Company, and have shown to withstand a combined LOCA and hydrogen burn environmental condition.

5.15 Class 1E Power, Control, and Instrumentation Cables

Power, control, and instrumentation cables are distributed throughout the containment including the annular compartment, steam generator compartments, pressurizer compartment, holdup volume tank, and reactor cavity. They are exposed to a harsh environment of long- term elevated temperature as well as short-term temperature transients due to hydrogen burn. Except for the reactor cavity, the cables can be protected from the harsh environment using the E-54 series Fire Wrap made by 3M Company.

5.16 Equipment Located Outside Containment

The active components of the following equipment, required for severe accident mitigation and monitoring,

are located outside containment. They are not subjected to the harsh environment of a severe accident.

- Safety Injection System (SIS)
- Auxiliary Feedwater System (AFWS)
- Containment Spray System (CSS)
- Emergency Containment Spray Backup System (ECSBS)
- Shutdown Cooling System (SCS)
- Containment hydrogen monitors
- Containment pressure sensor
- IRWST water level sensors

The check valve on the ECSBS spray headers is located inside containment, but it contains no organic material susceptible to thermal degradation.

5.17 Radiation Dose ES Results

The environment qualification report for safety related equipment usually contains radiation test data. Table 5-1 summarizes the radiation dose test data for essential equipment and instrumentation. All equipment was tested under at least five times the bounding radiation dose in the containment during a severe accident.

For most equipment and instrumentation, it is concluded there is reasonable assurance that instrumentation and equipment required to mitigate a severe accident and achieve a safe stable state perform their function as intended under severe accident environmental conditions.

Table 5-1 Tested Radiation Dose



TS

6 SUMMARY AND CONCLUSION

The applicable regulations and criteria for equipment survivability assessment are reviewed. The required equipment and instrumentation for equipment survivability assessment are identified. Bounding radiation and thermal-hydraulic environmental conditions during a severe accident are determined. Each piece of essential equipment and instrumentation is assessed for equipment survivability.

Several potential design modifications may be considered if the equipment survivability of a given item cannot be demonstrated by analysis or use of existing test data. Typically localized high temperature conditions due to hydrogen burns within containment during postulated severe accident sequences constitute the greatest challenge to the component's survivability. Thus, detailed knowledge of the containment's response for a variety of bounding severe accident sequences can identify locations within the containment that have the least challenging thermal conditions. The relocation of some components to a position with less severe thermal conditions may better ensure their survivability.

Some devices, such as hydrogen igniters, must be appropriately located to ensure the successful operation of the system. Thus, relocating igniters may not be a useful approach given that they are intended to control the hydrogen in the regions of the containment where they are placed. These cases may require the use of redundancy or an understanding of the functional interval required for their operation.

Other design modifications include adding a thermal shield or wall to provide protection against the local severe accident environment, and modifying the component (replacing non-metallic material or changing its configuration).

7 REFERENCES

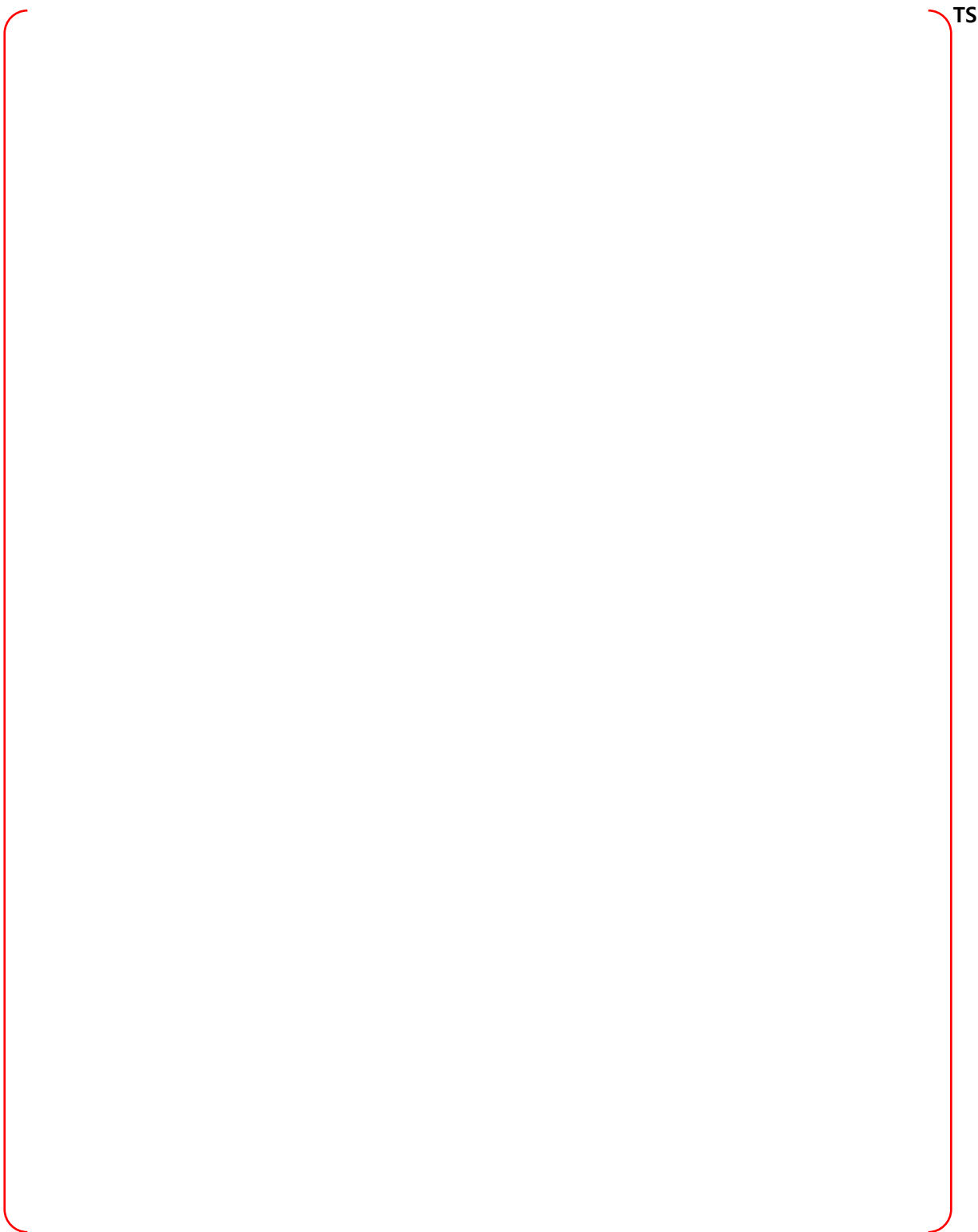
1. FAI, 2012, FAI/12-0005, "MAAP 4.0.8 Transmittal Document," EPRI, Palo Alto, CA, Feb 15.
2. FAI, 1994, "MAAP4-DOSE User's Manual, Modular Accident Analysis Program User's Manual," Vol. 4, EPRI, Palo Alto, CA, May.
3. ANSI/ANS-6.1.1, "American National Standard for Neutron and Gamma-Ray Fluence-to-Dose Factor," ANSI/ANS-6.1.1-1991, American Nuclear Society.
4. O'Brien et.al., 1976, "The Distribution of Absorbed Dose-Rates in Humans from Exposure to Environmental Gamma Rays," Health Physics Journal, Vol. 30, pp. 71-80, January.
5. Boerner et.al., 2007, "An Evaluation of Direct Gamma Dose at Site Boundary of the Vermont Yankee Nuclear Power Station," Oak Ridge Associated Universities, January.

ATTACHMENT A: Containment Nodalization

Table A-1 APR1400 Containment Node Description

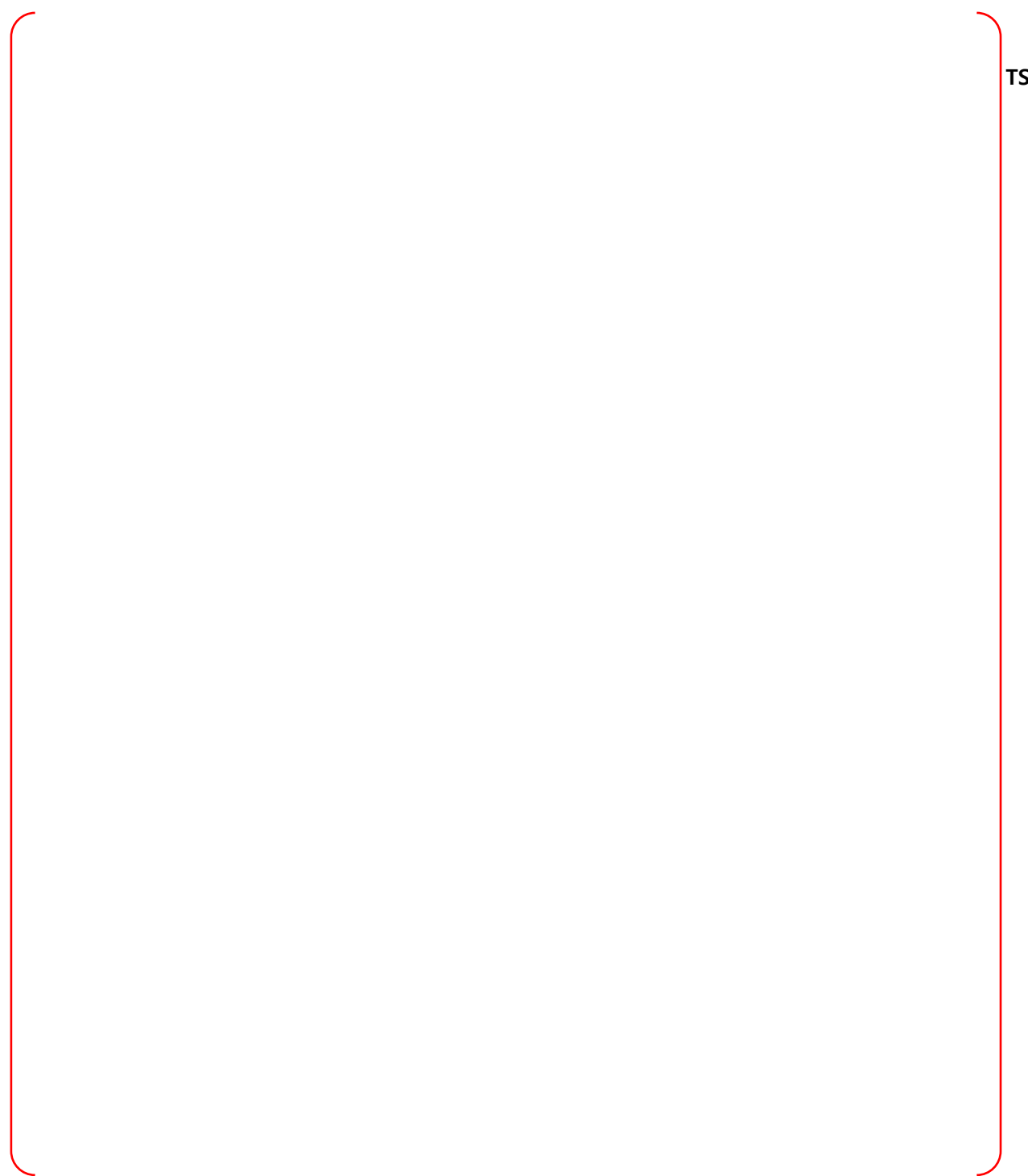
TS

The table content is missing from the page. A large red bracketed area is present, indicating that the table content is missing or redacted.



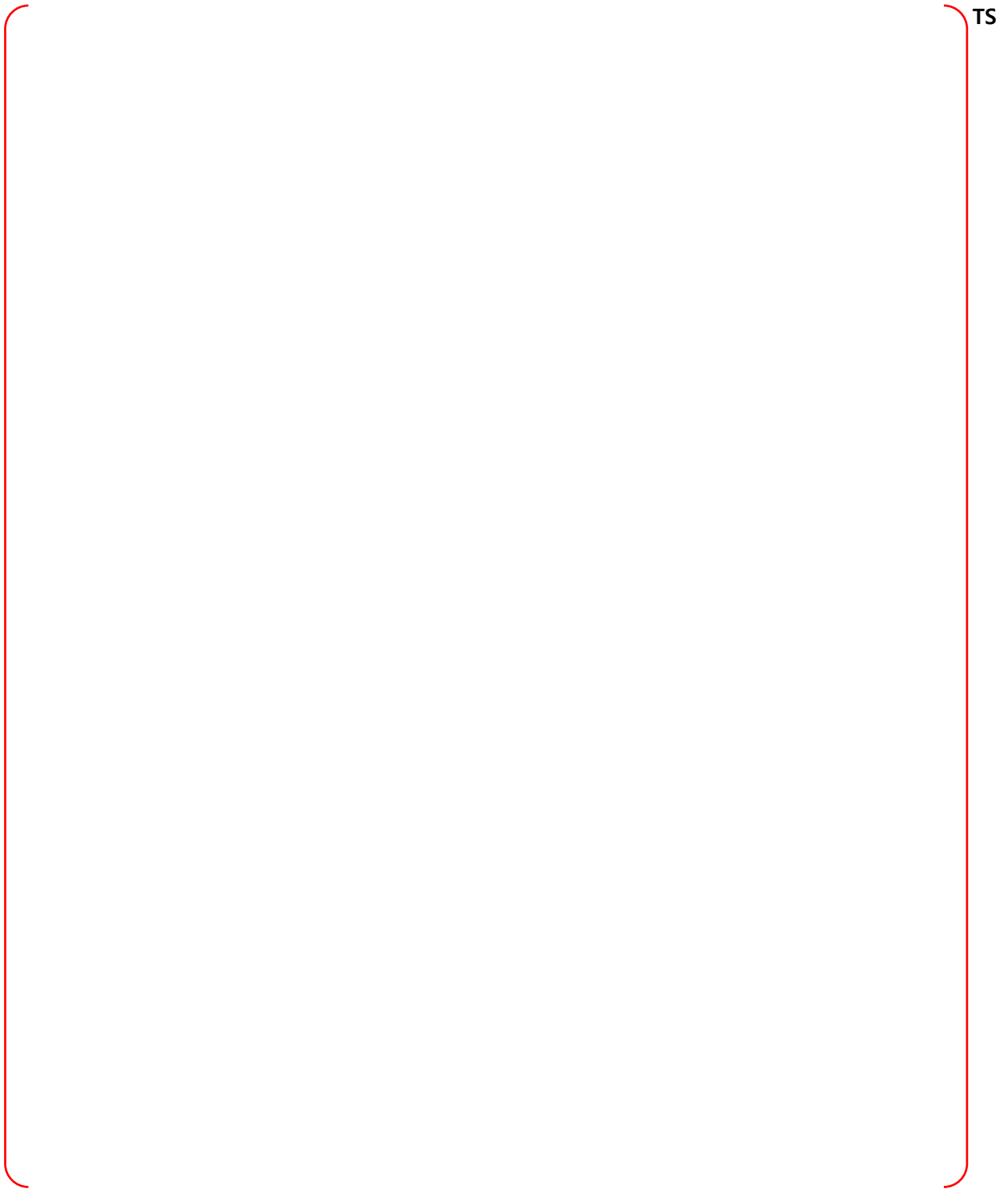
TS

Figure A-1 Containment Nodalization Diagram for APR1400



TS

Figure A-2 Containment Nodes in Section A-A



TS

Figure A-3 Containment Nodes in Section B-B



Figure A-4 Containment Nodes at EL. 78' – 0"



TS

Figure A-5 Containment Nodes at EL. 100' 0"



Figure A-6 Containment Nodes at EL. 114' – 0"



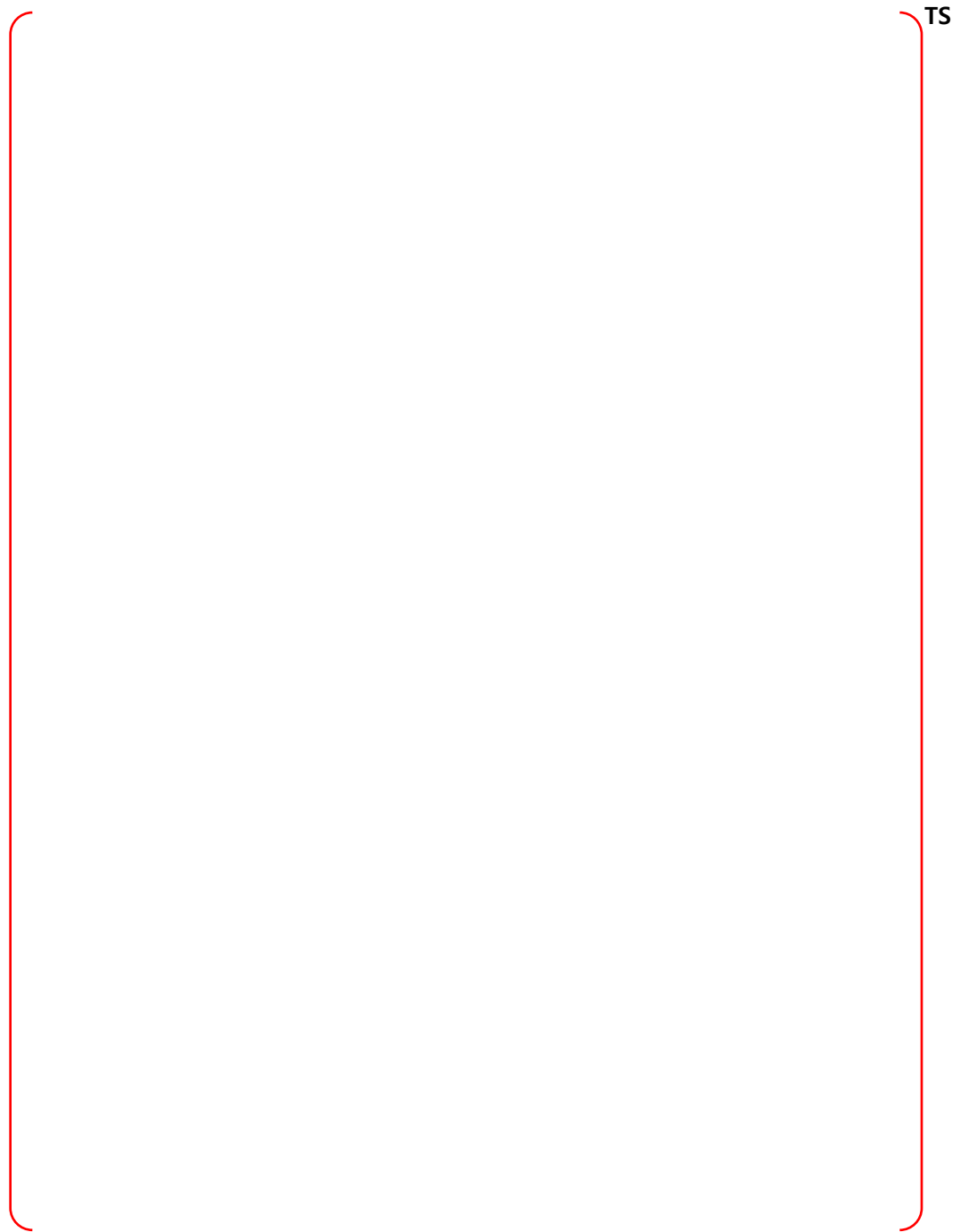
TS

Figure A-7 Containment Nodes at EL. 136' – 0"



Figure A-8 Containment Nodes at EL. 156' – 0"

ATTACHMENT B: Temperature Histories in Each Node



TS

Figure B-1 Node 1, Reactor Cavity – PRA Sequences

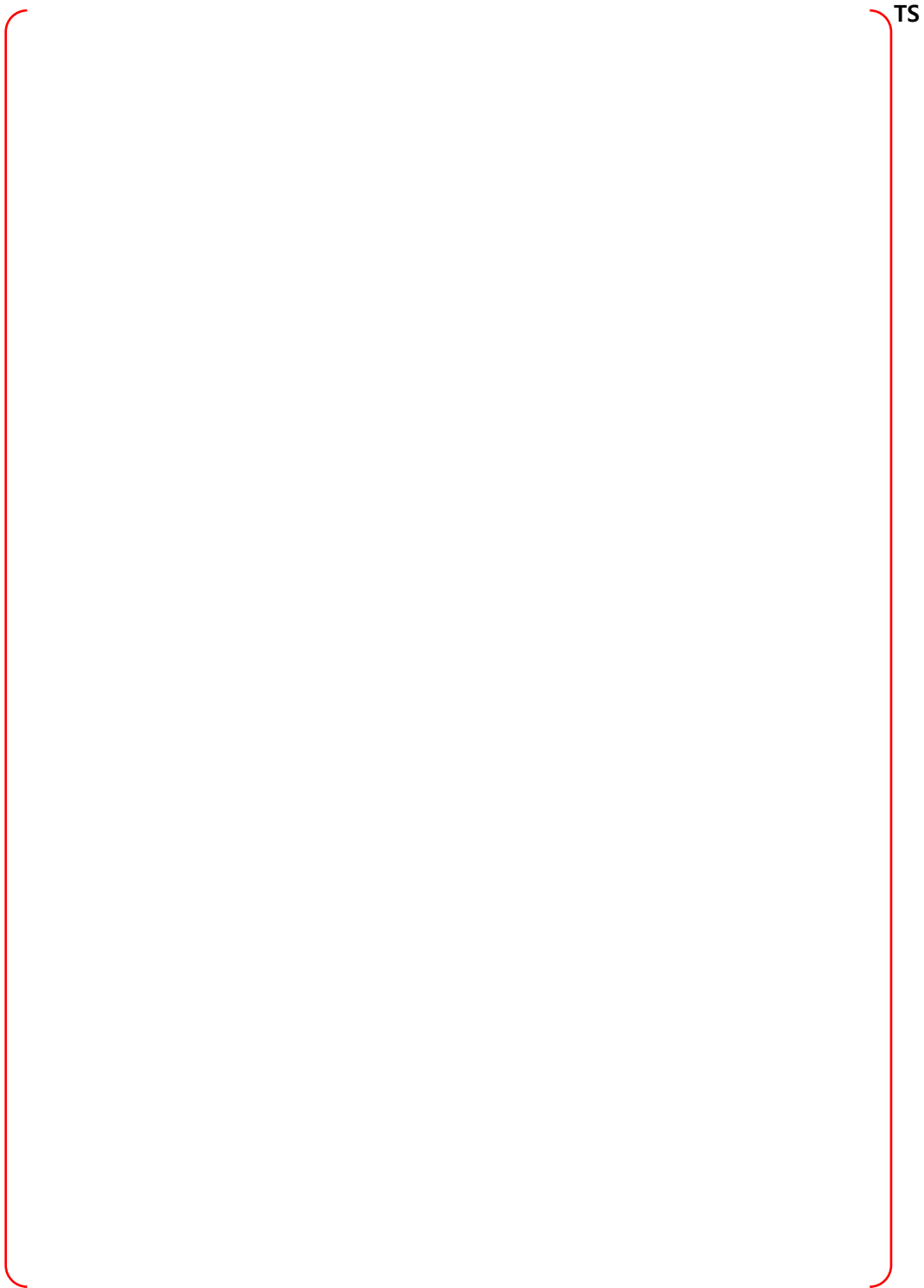


Figure B-2 Node 1, Reactor Cavity – Bounding Sequences – MCCI

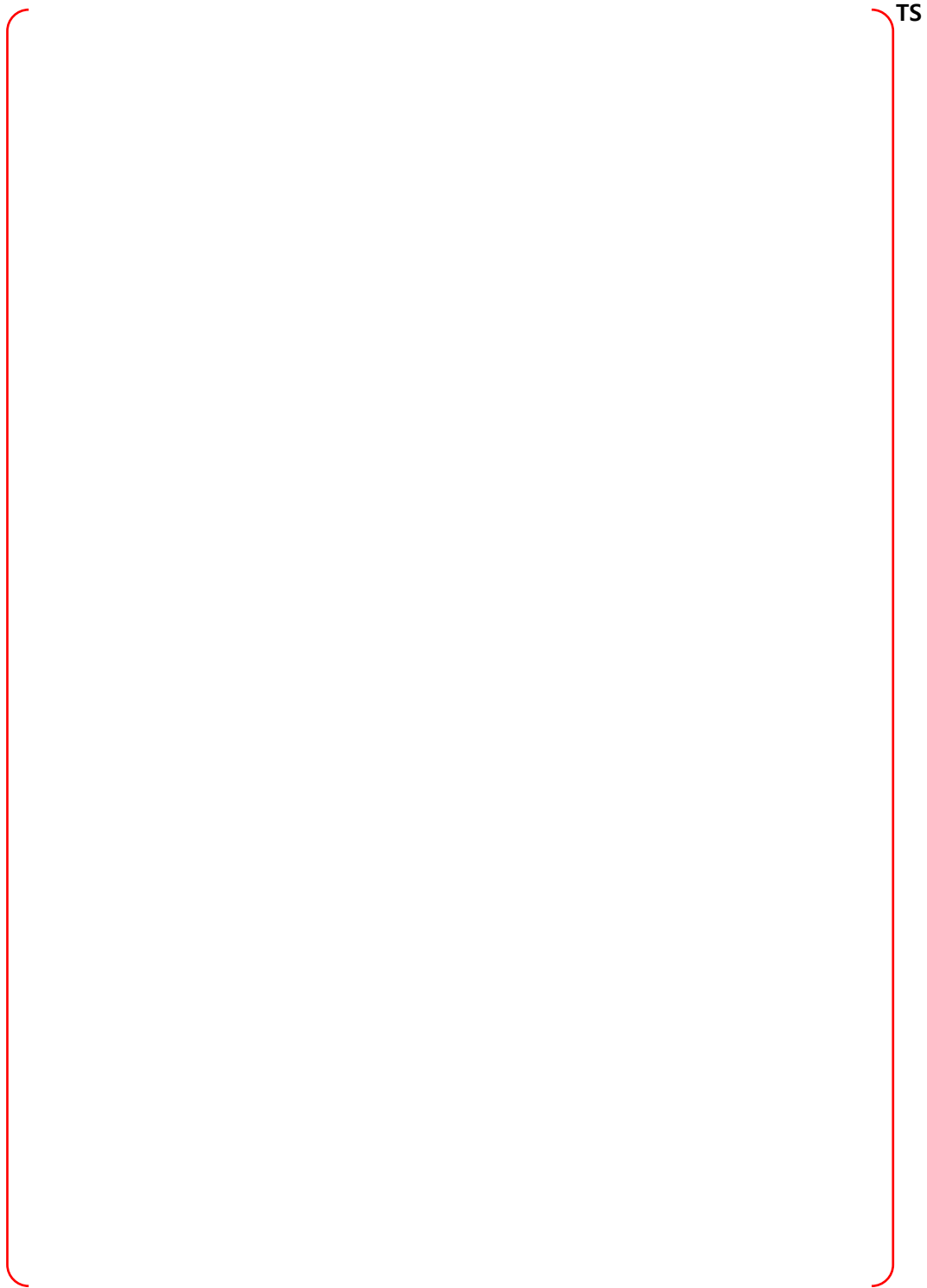


Figure B-3 Node 1, Reactor Cavity – Bounding Sequences – CP

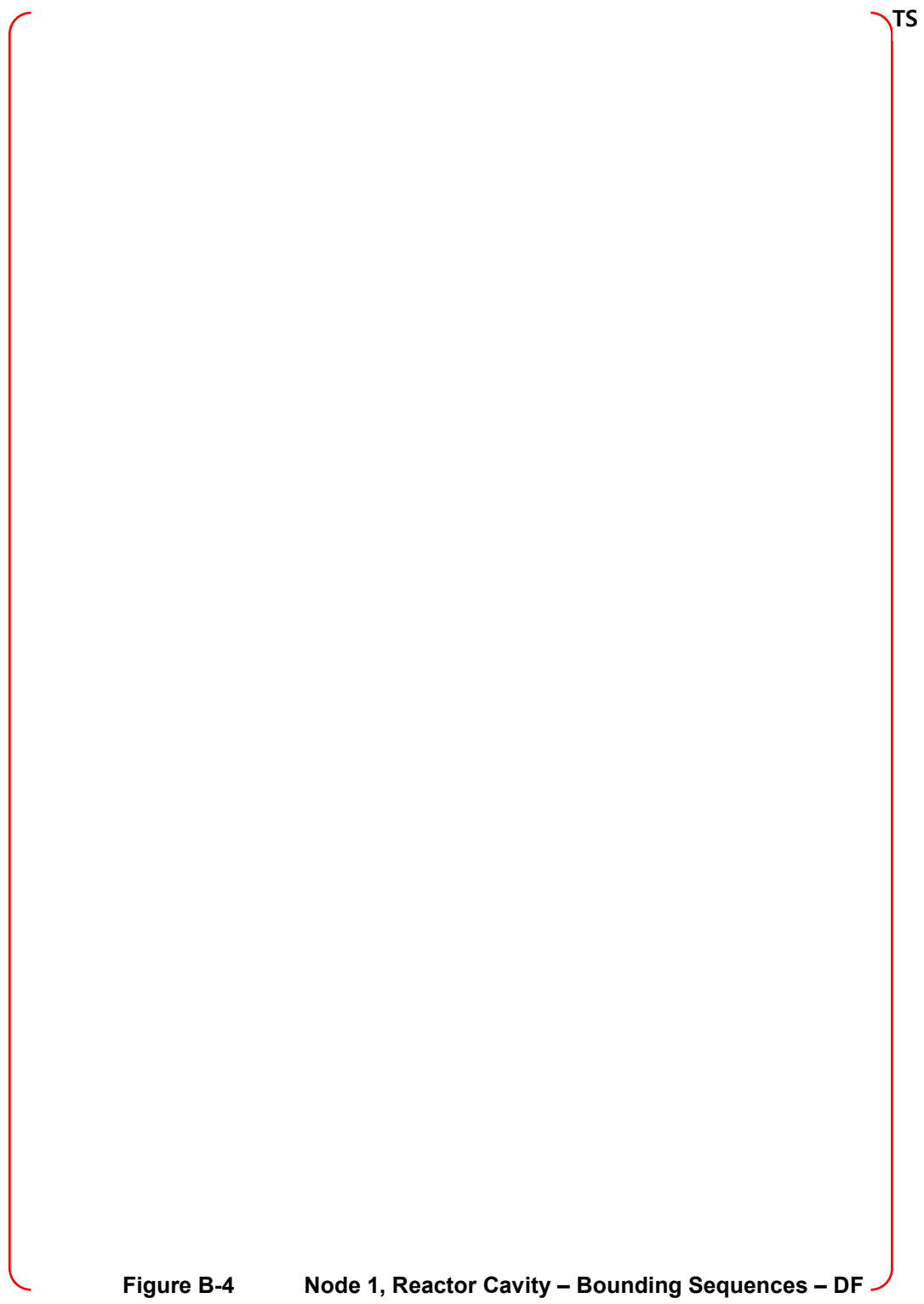


Figure B-4 Node 1, Reactor Cavity – Bounding Sequences – DF

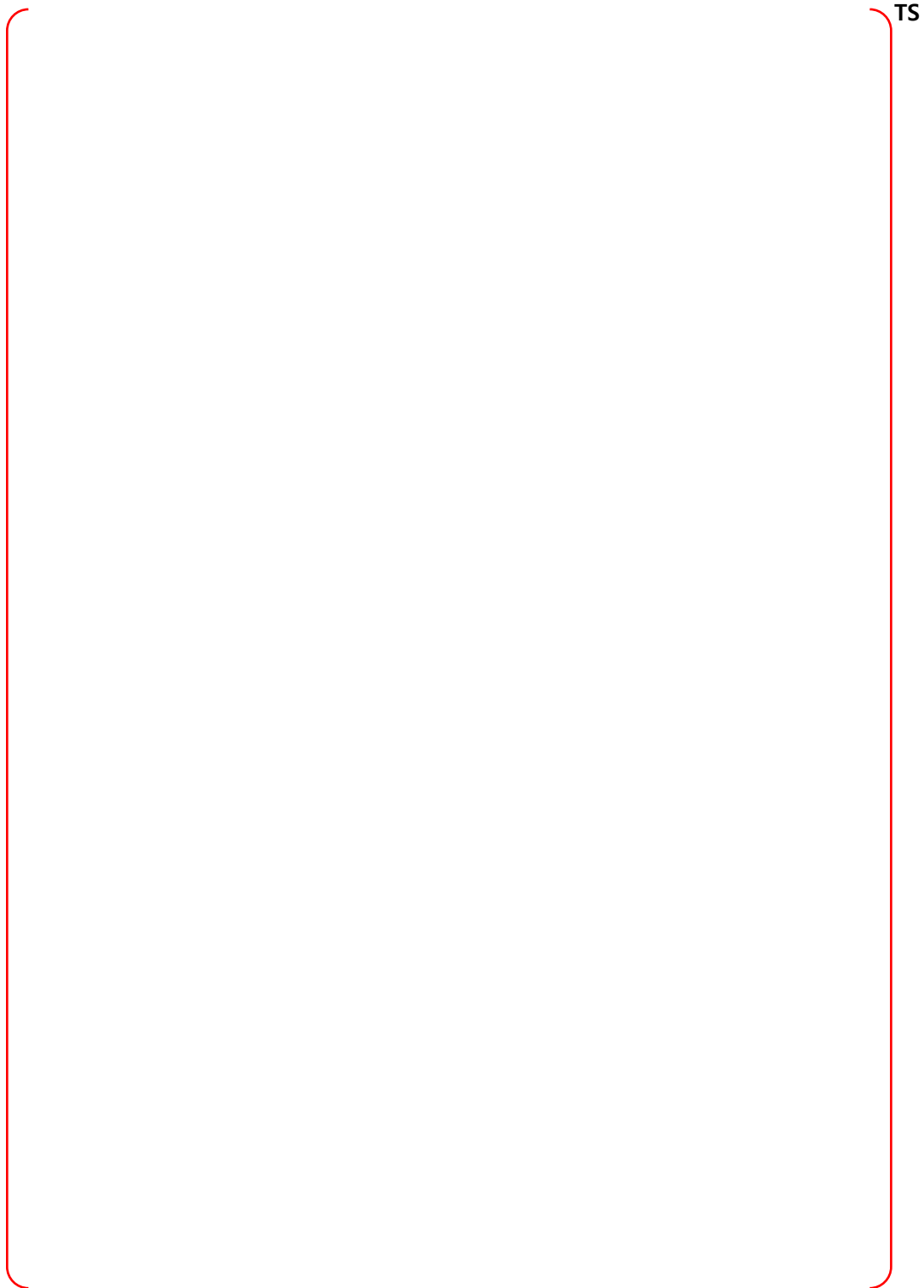


Figure B-5 Node 2, ICI Chase - PRA Sequences

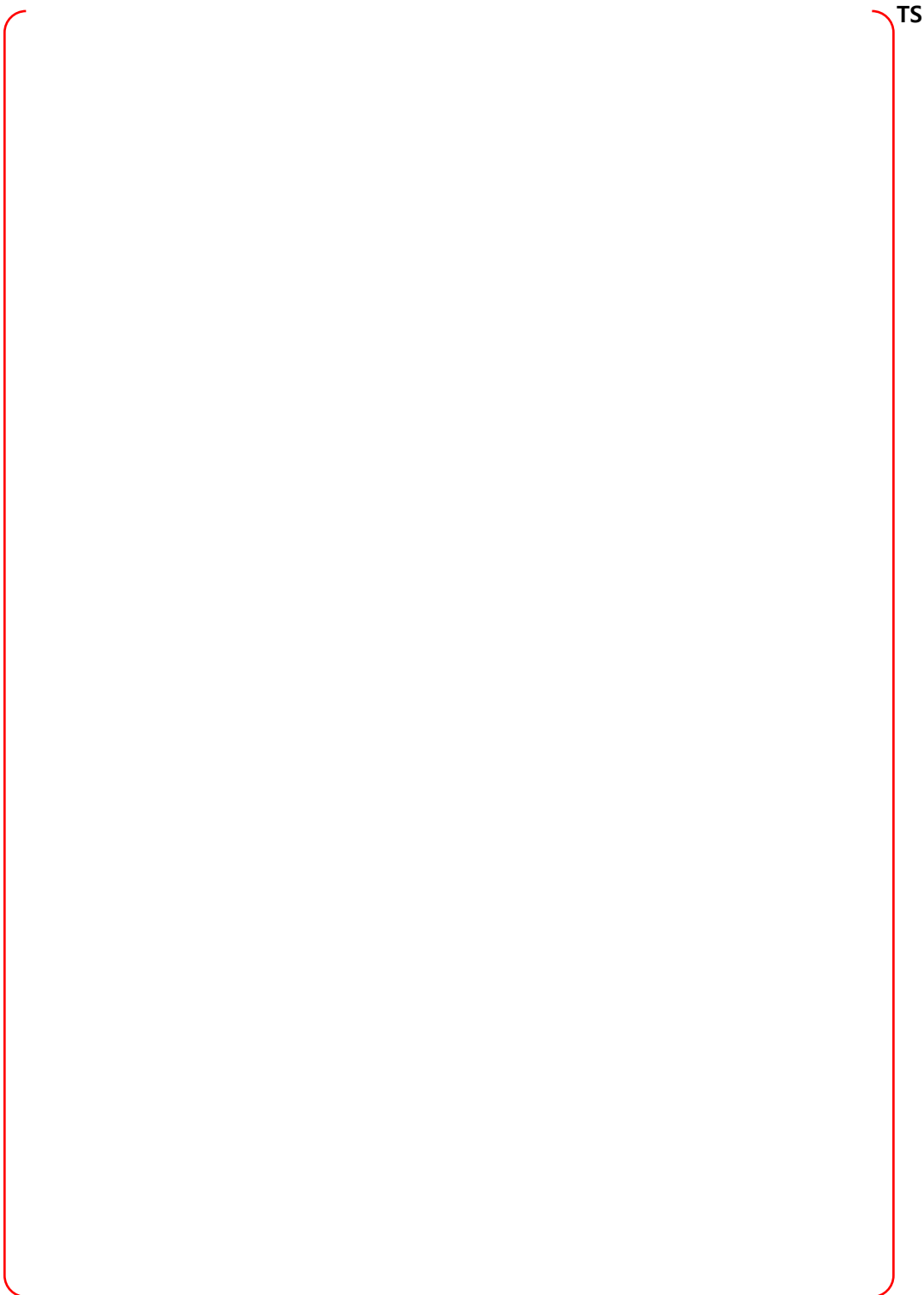


Figure B-6 Node 2, ICI Chase - Bounding Sequences – MCCI

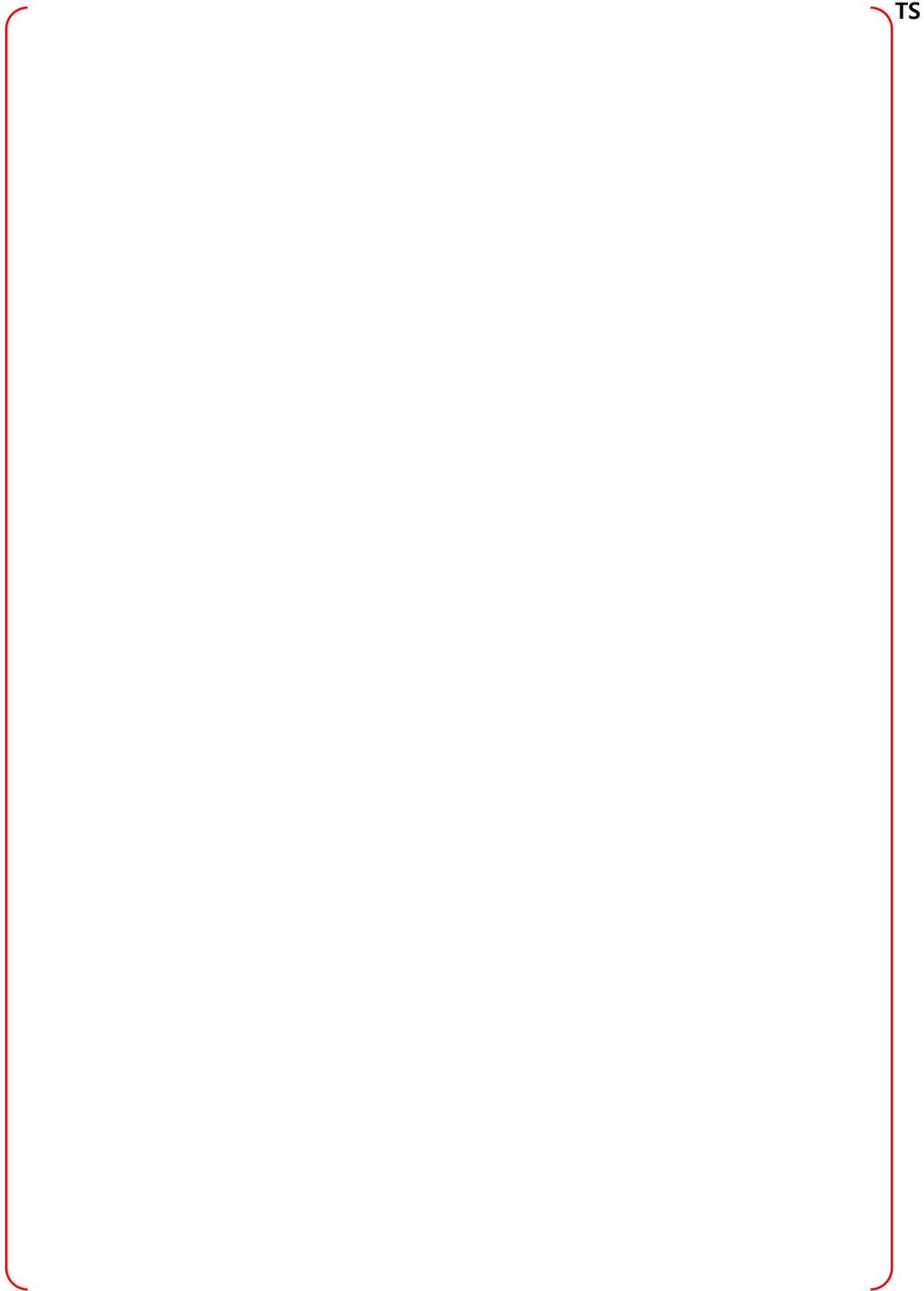


Figure B-7 Node 2, ICI Chase - Bounding Sequences – CP

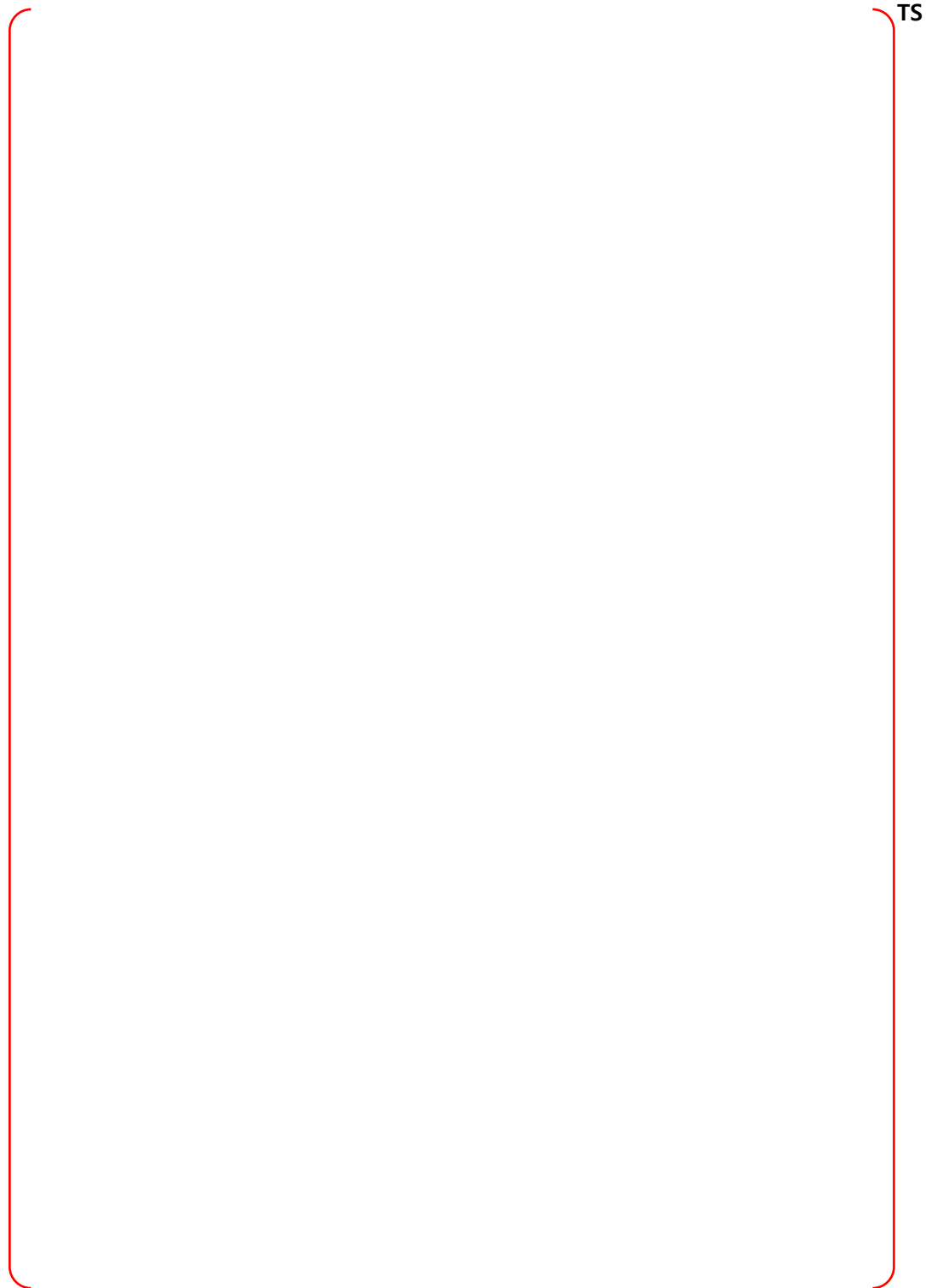


Figure B-8 Node 2, ICI Chase - Bounding Sequences – DF

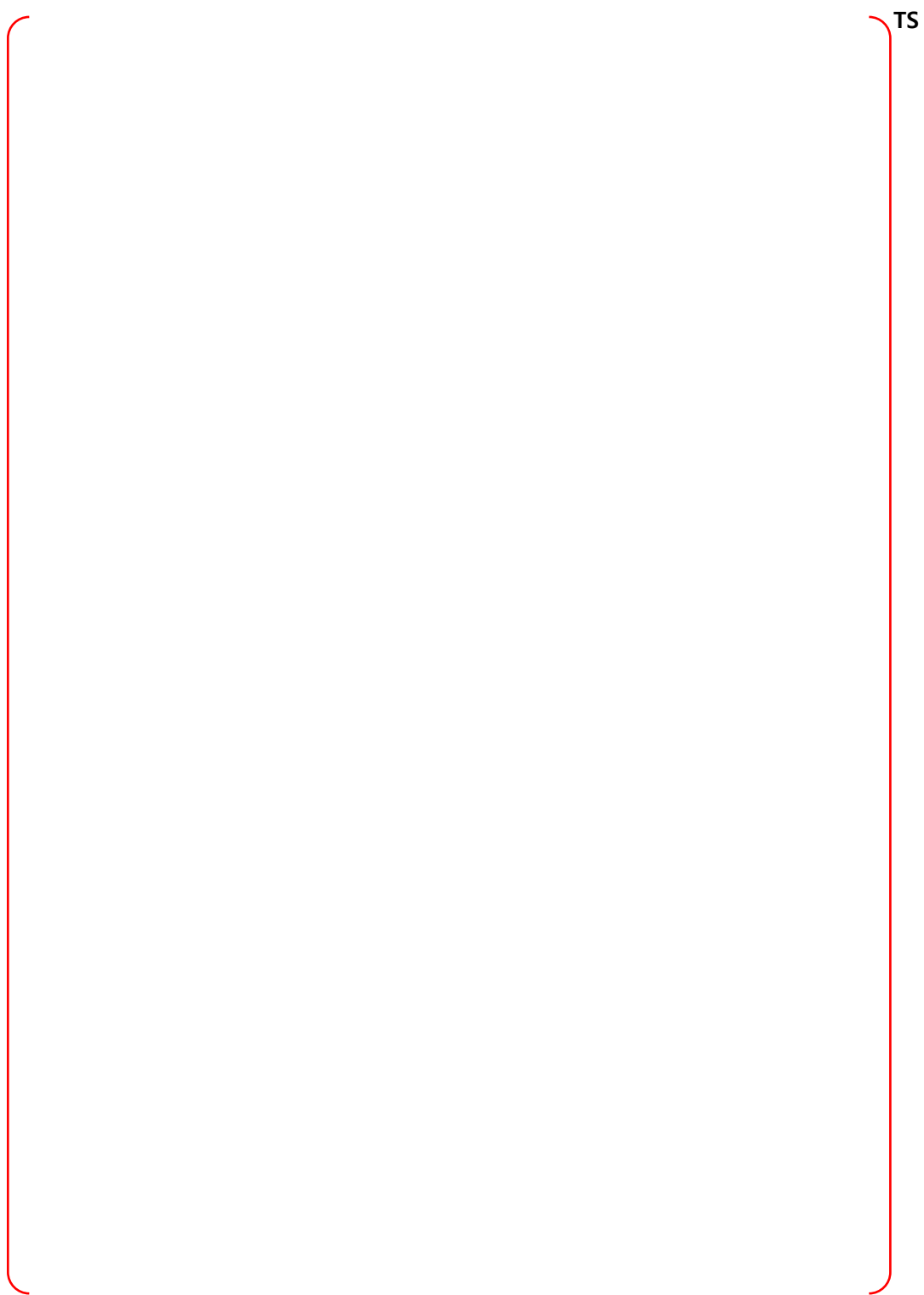


Figure B 9 Node 3, Corium Chamber Room - PRA Sequences

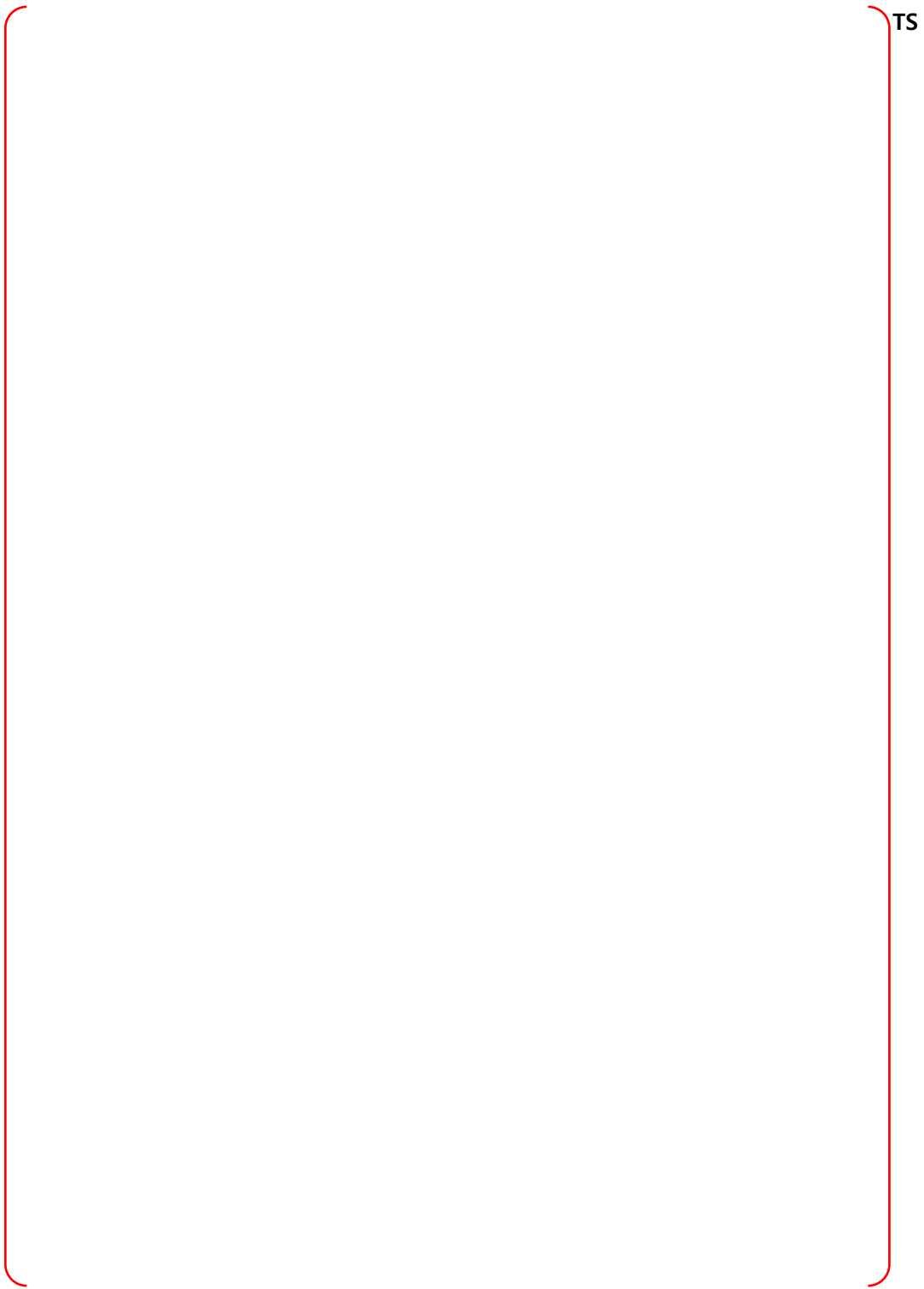


Figure B-9 Node 3, Corium Chamber Room - Bounding Sequences – MCCI

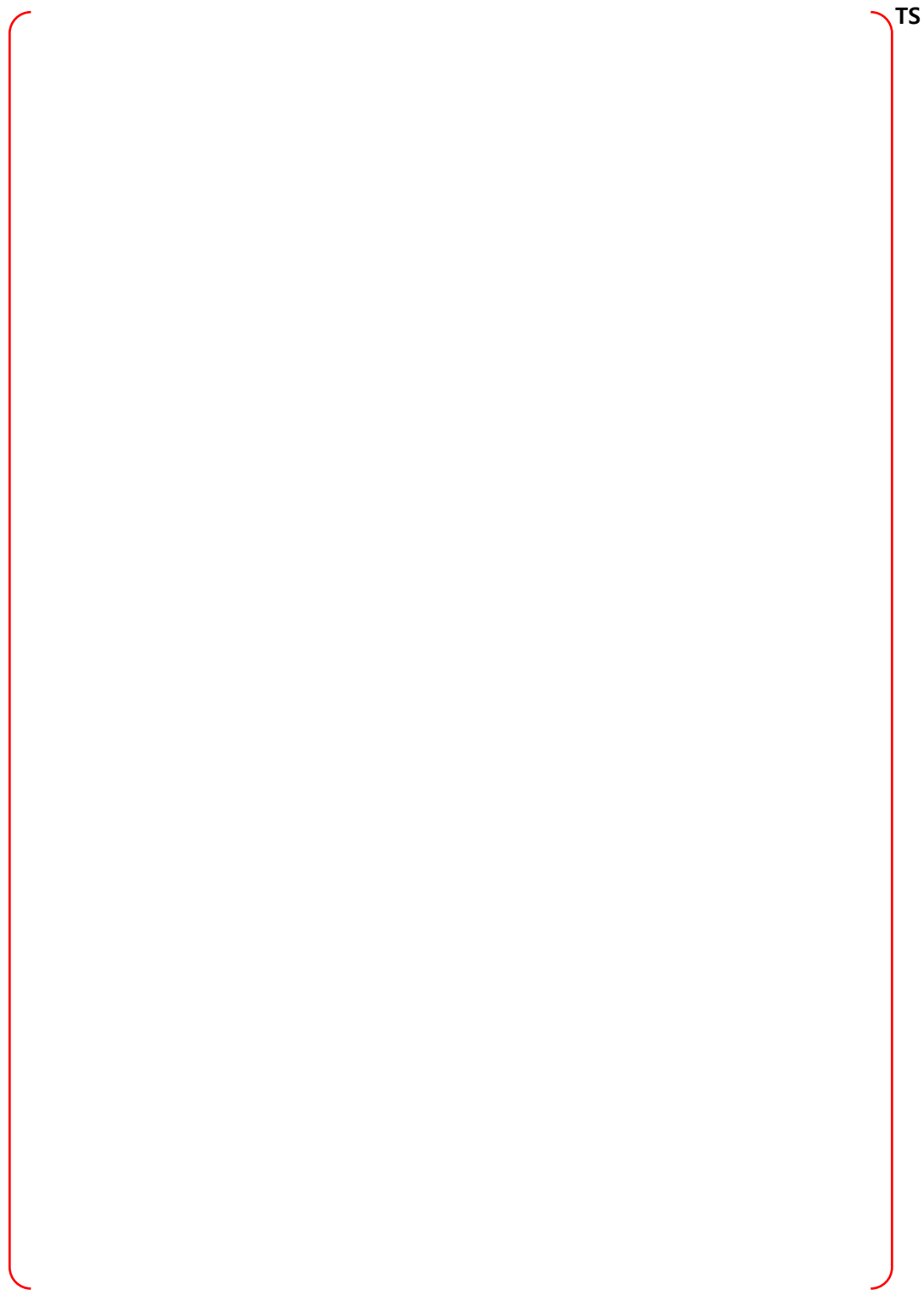


Figure B-10 Node 3, Corium Chamber Room - Bounding Sequences – CP

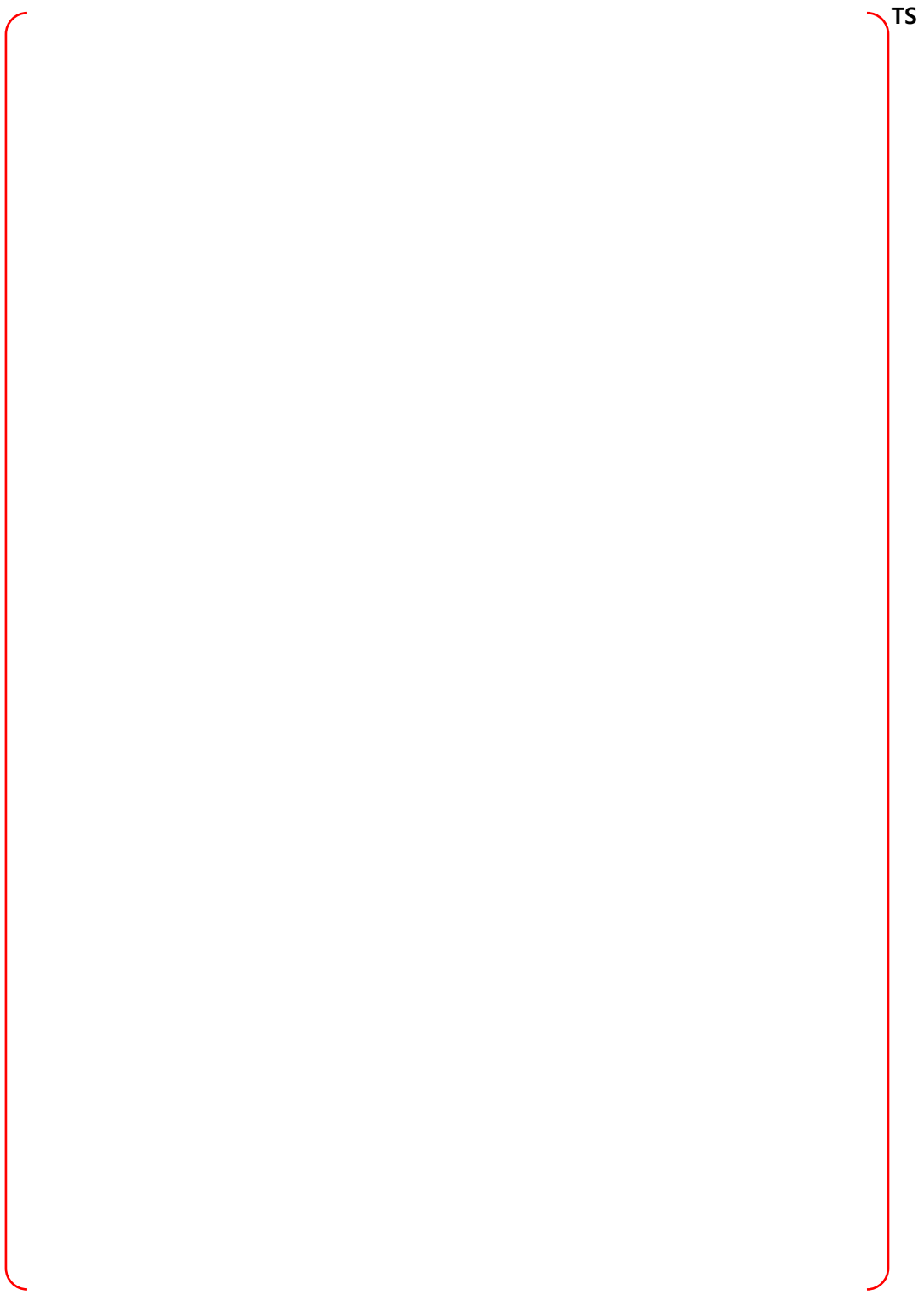


Figure B-11 Node 3, Corium Chamber Room - Bounding Sequences – DF

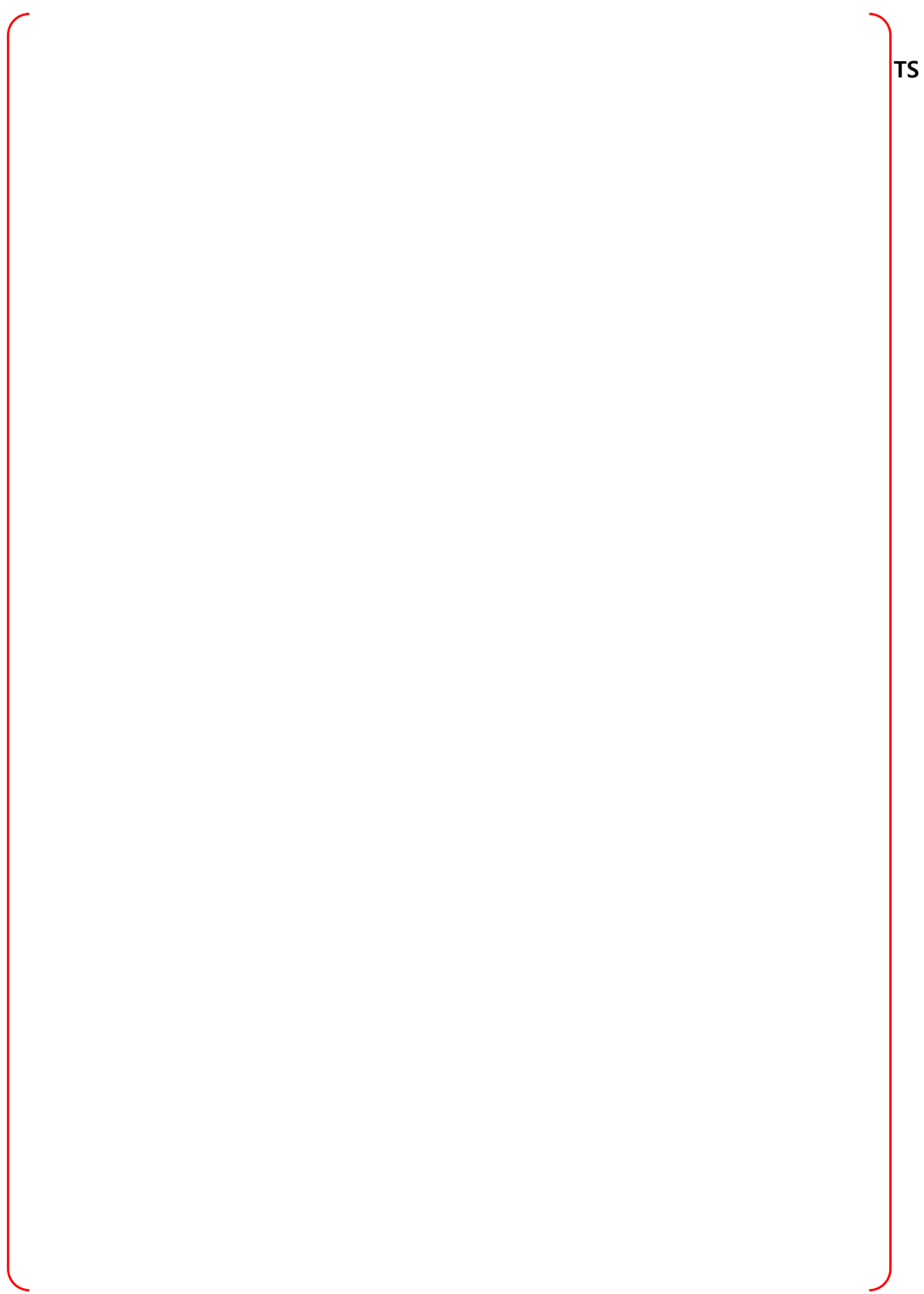


Figure B-12 Node 4, Reactor Cavity Access Area - PRA Sequences

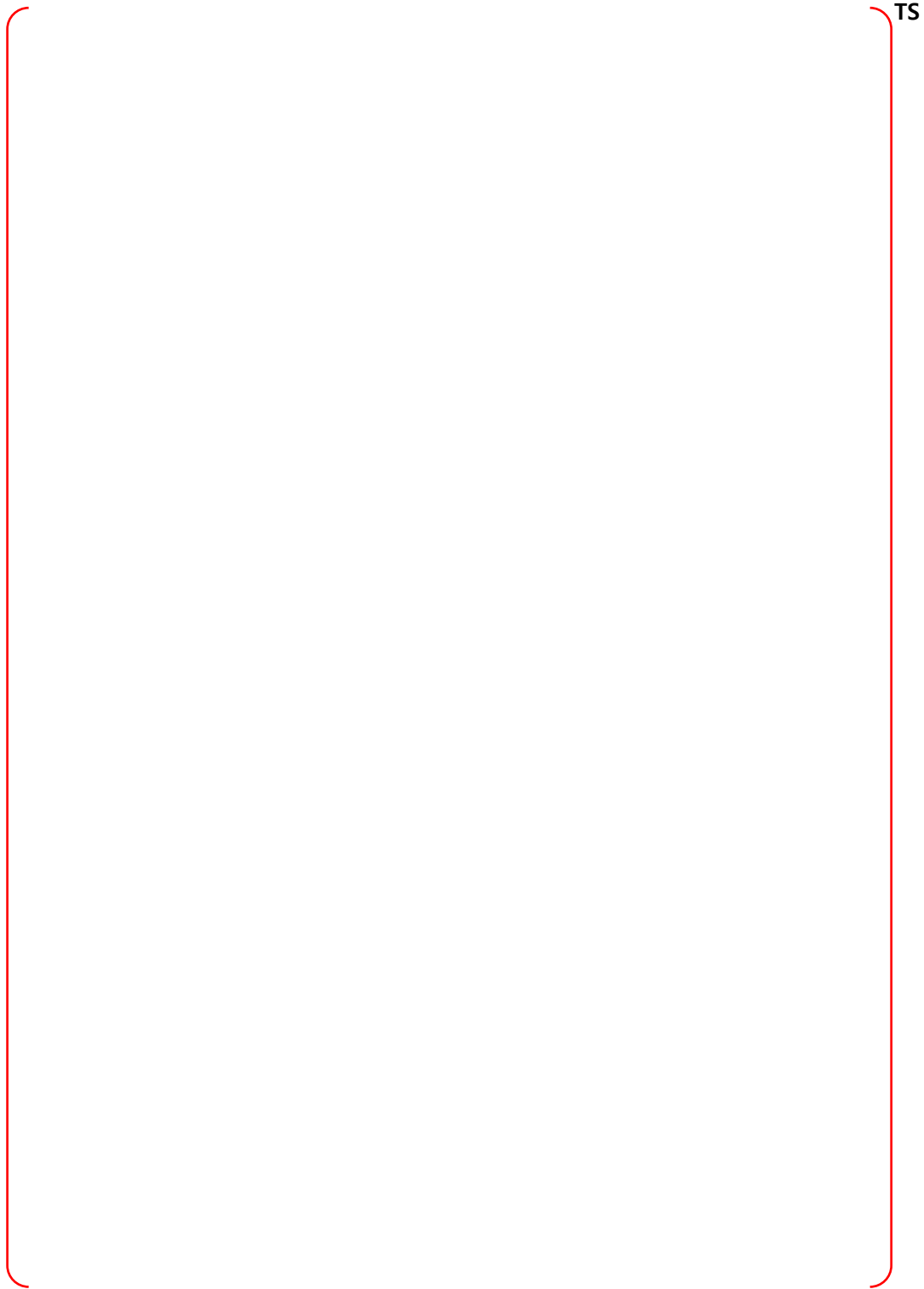
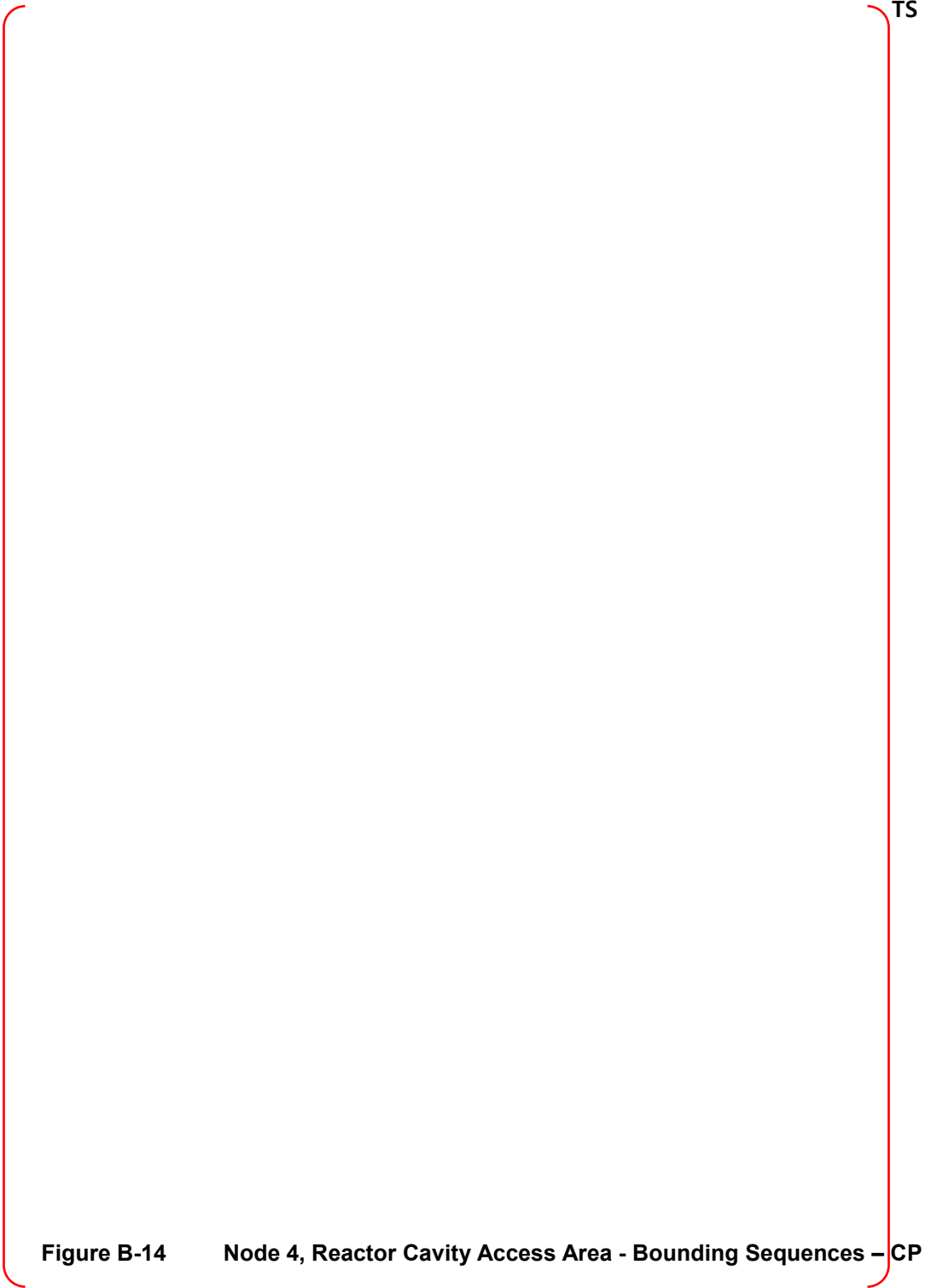


Figure B-13 Node 4, Reactor Cavity Access Area - Bounding Sequences – MCCI



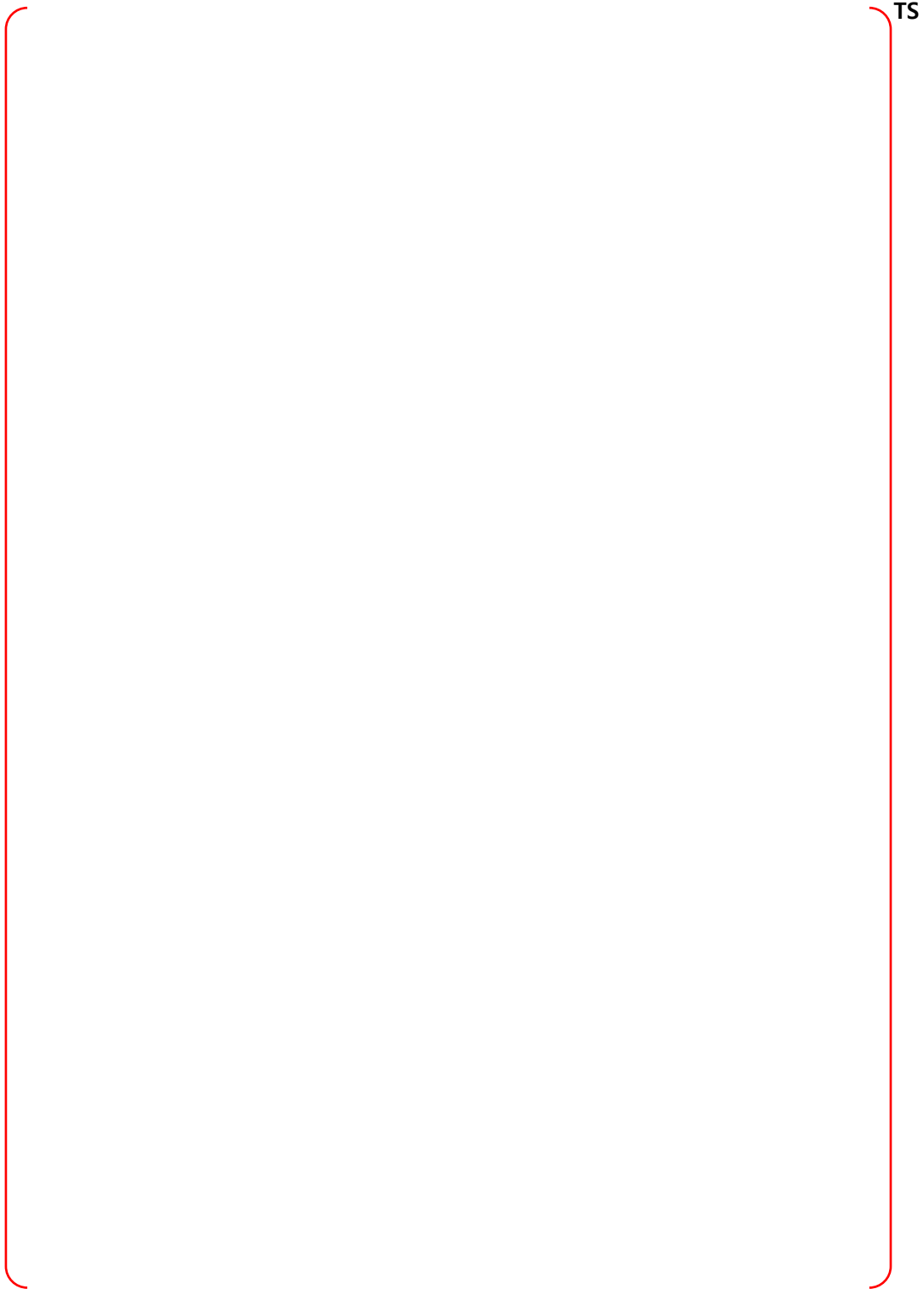


Figure B-15 Node 4, Reactor Cavity Access Area - Bounding Sequences – DF

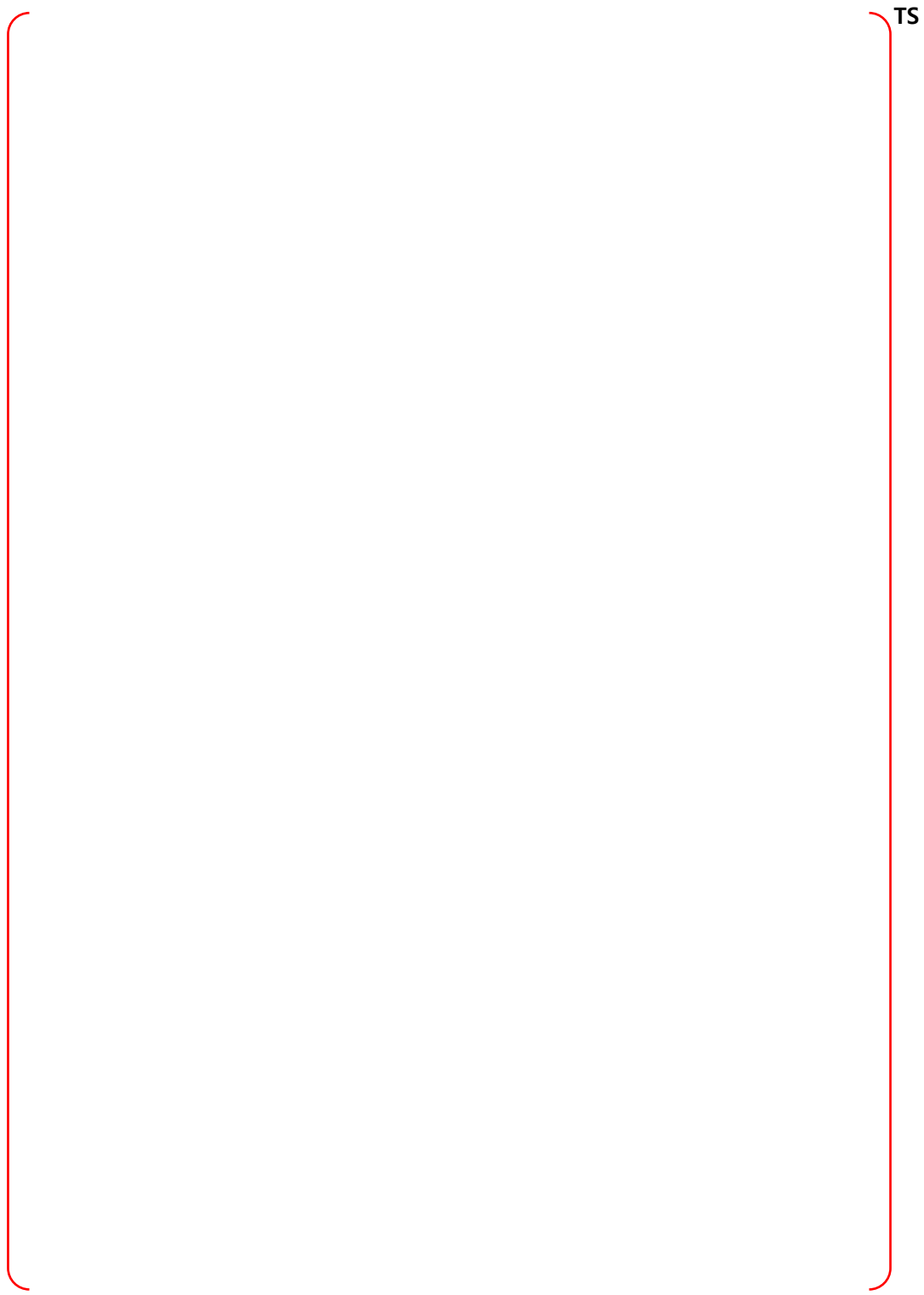


Figure B-16 Node 5, Holdup Volume Tank - - PRA Sequences

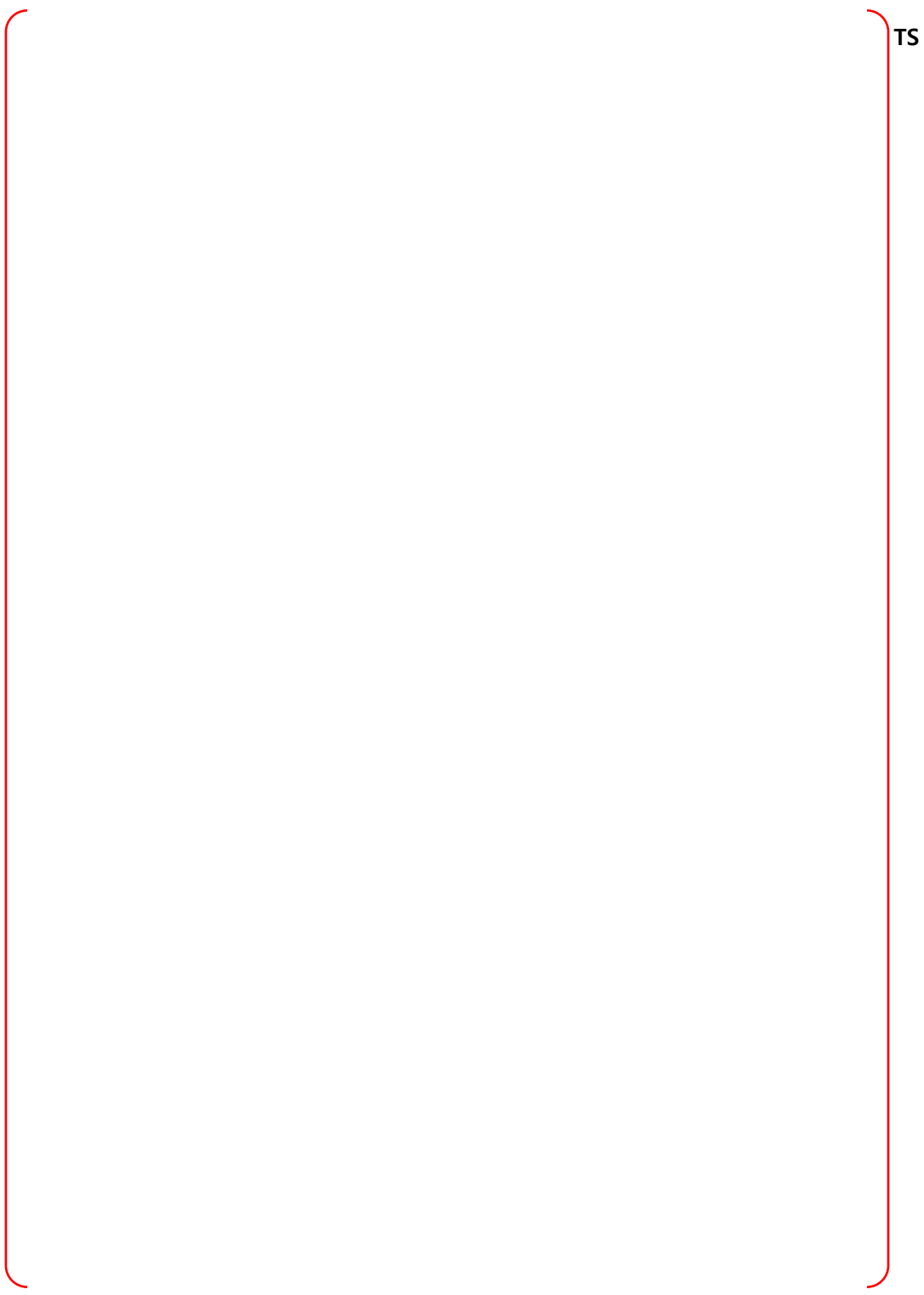


Figure B-17 Node 5, Holdup Volume Tank - Bounding Sequences – MCCI

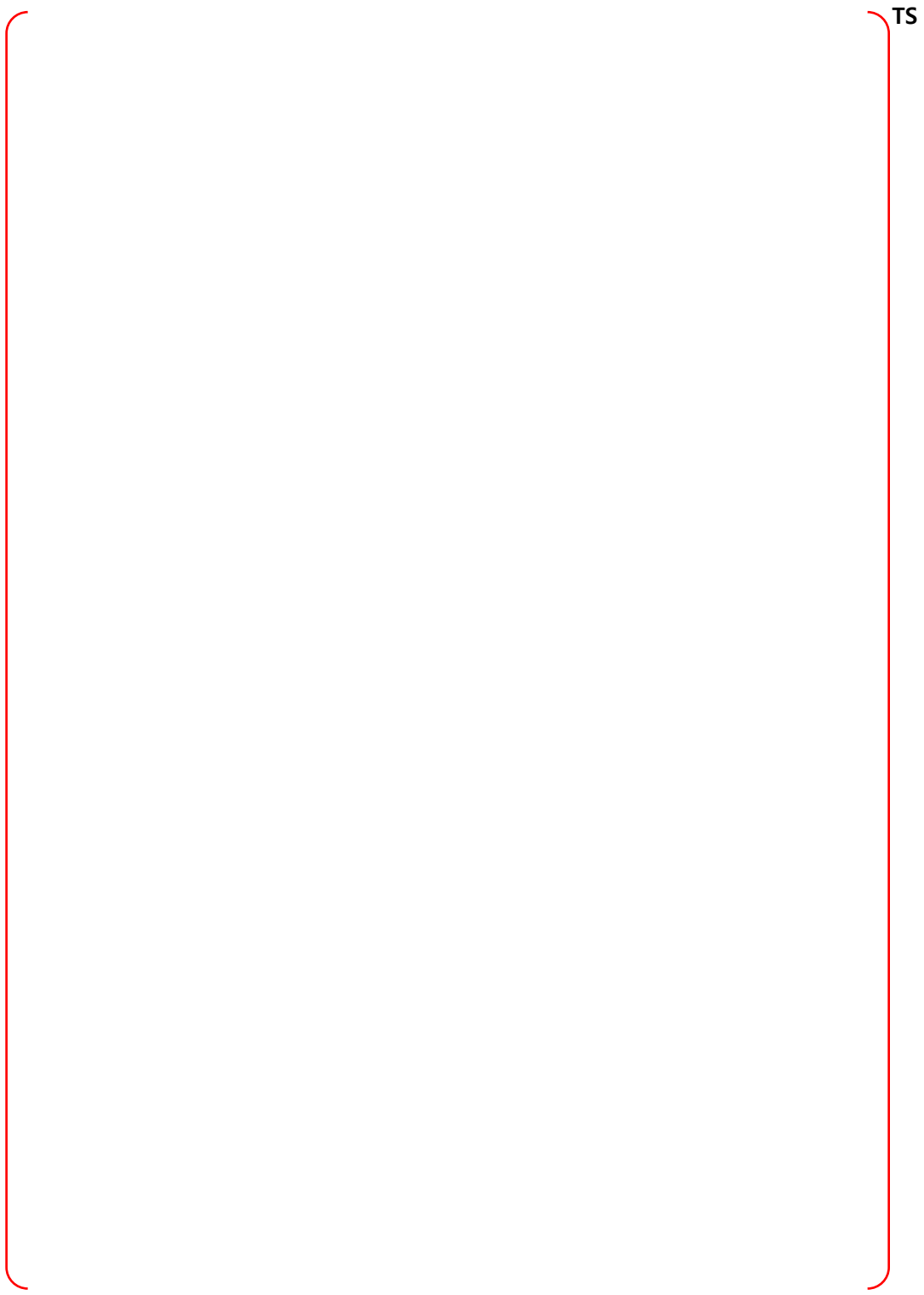


Figure B-18 Node 5, Holdup Volume Tank - Bounding Sequences – CP

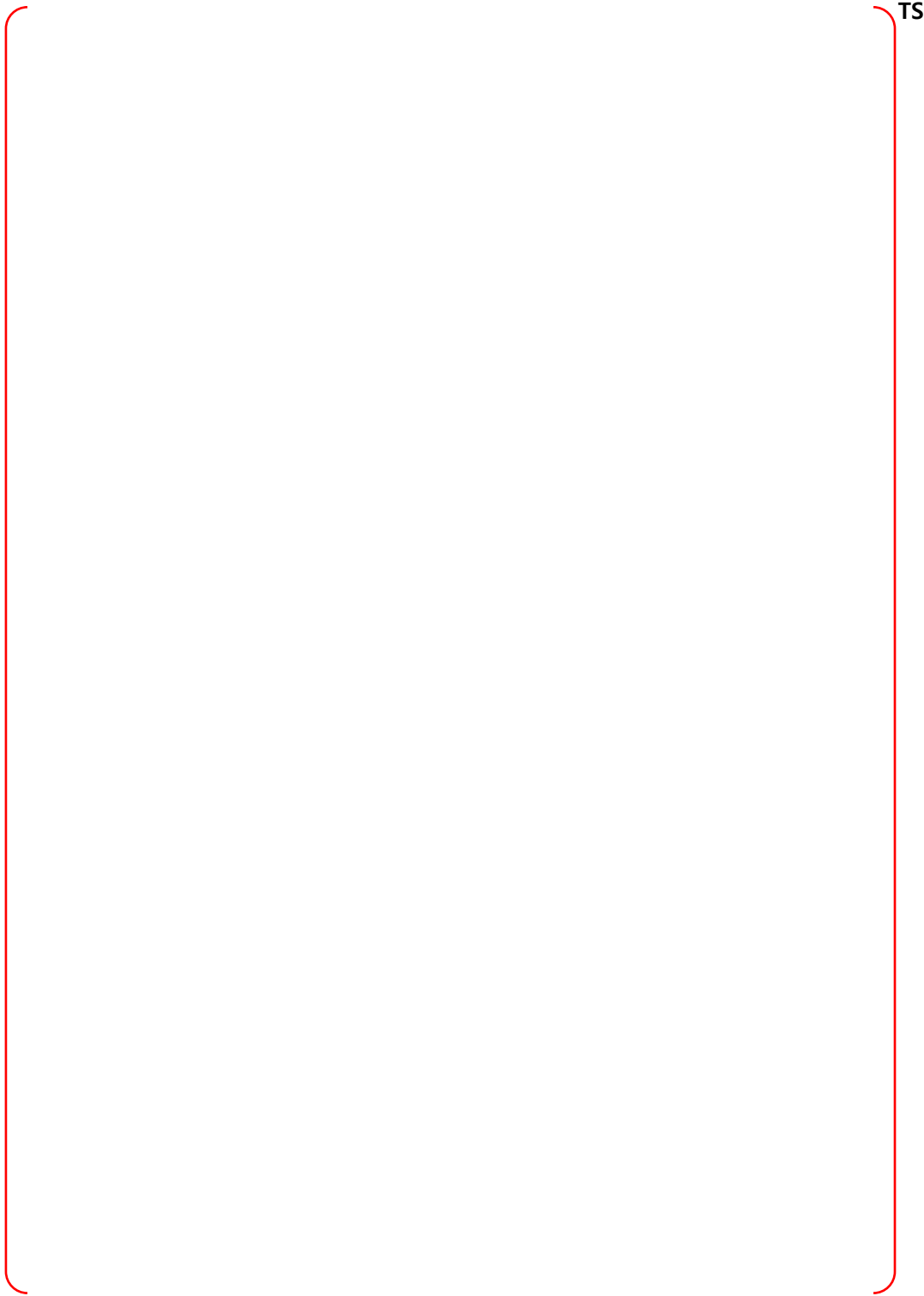


Figure B-19 Node 5, Holdup Volume Tank - Bounding Sequences – DF

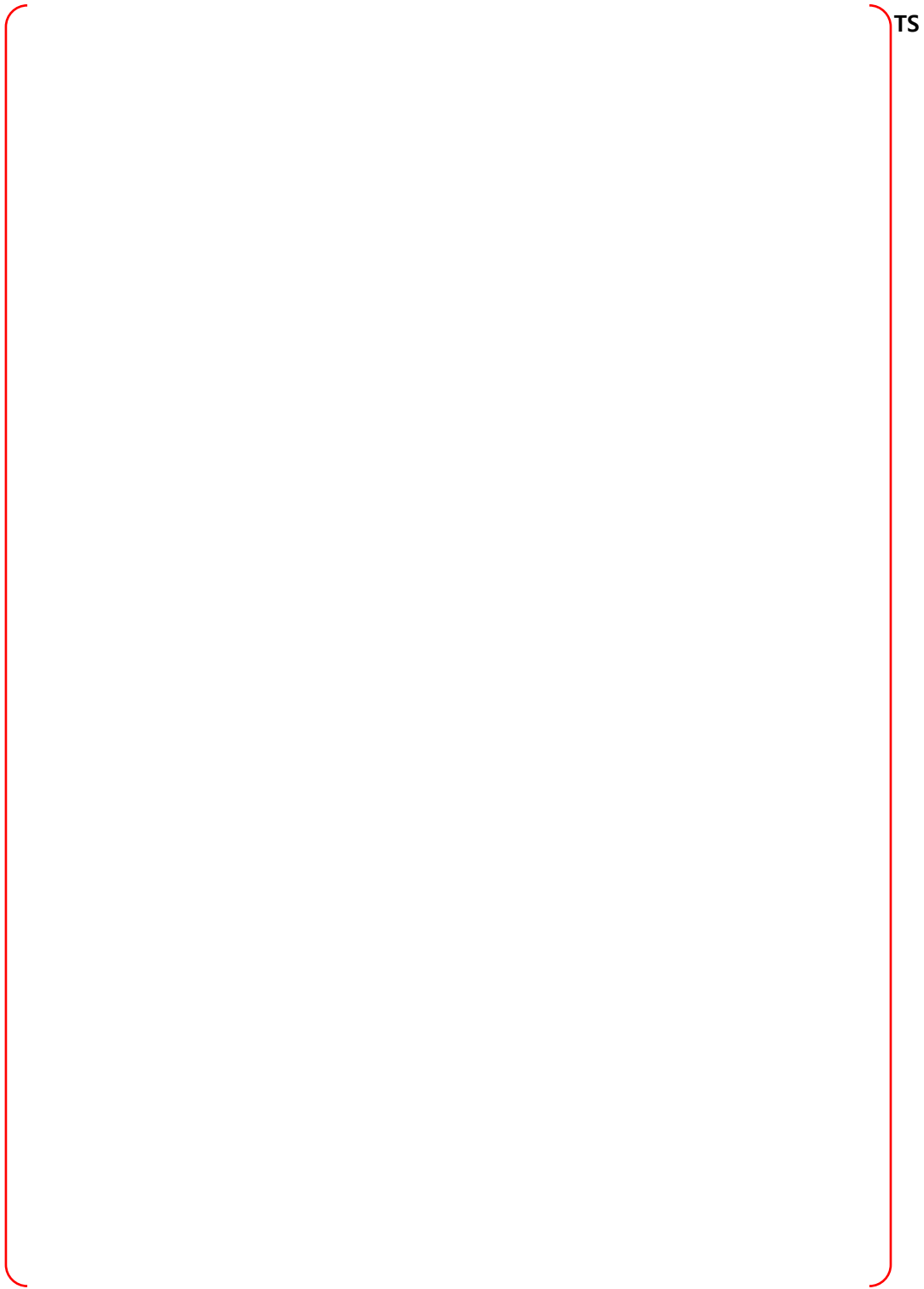


Figure B-20 Node 6, S/G Compartment #2 at Elev 100' - PRA Sequences

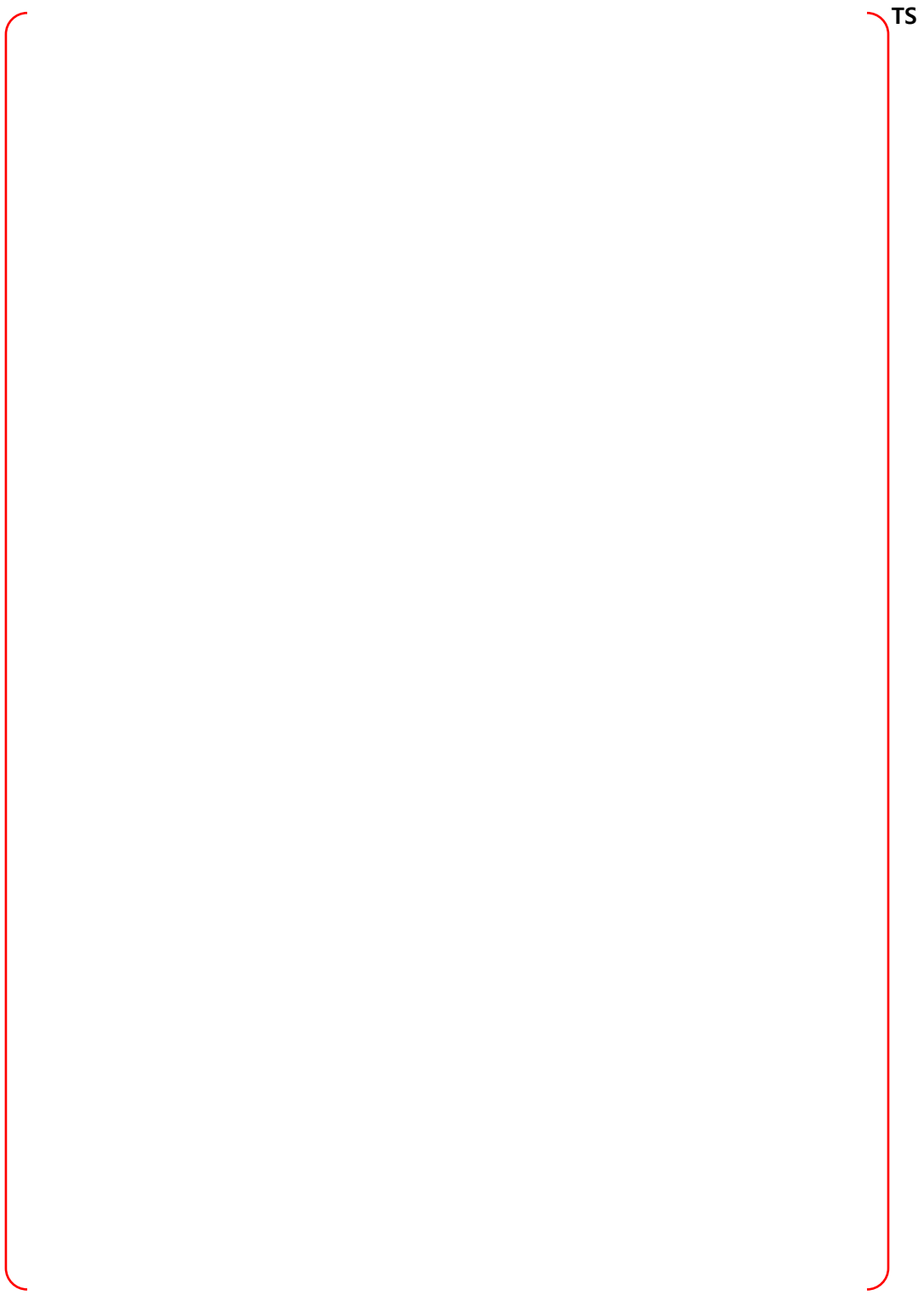


Figure B-21 Node 6, S/G Compartment #2 at Elev 100' - Bounding Sequences – MCCI

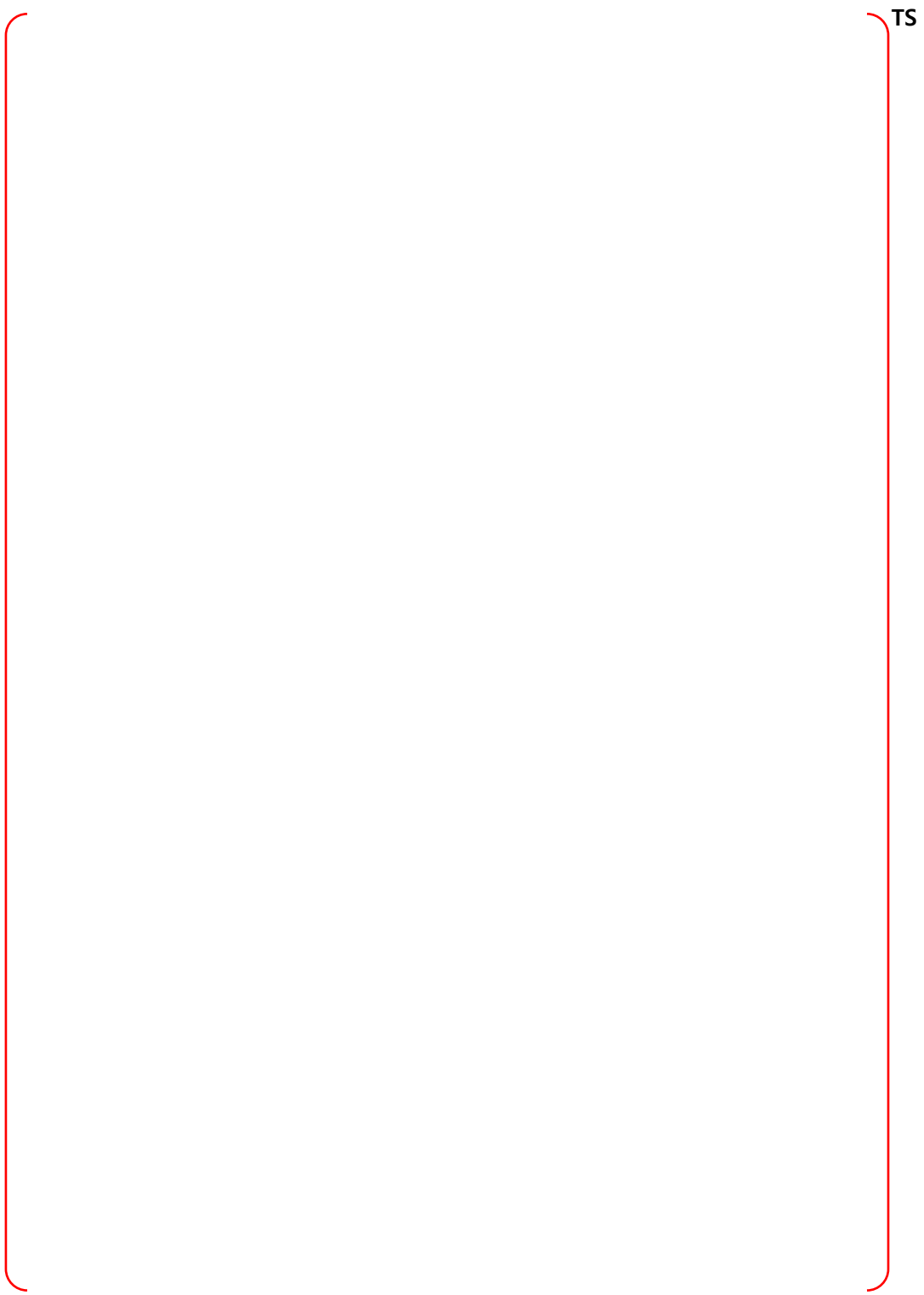


Figure B-22 Node 6, S/G Compartment #2 at Elev 100' - Bounding Sequences – CP

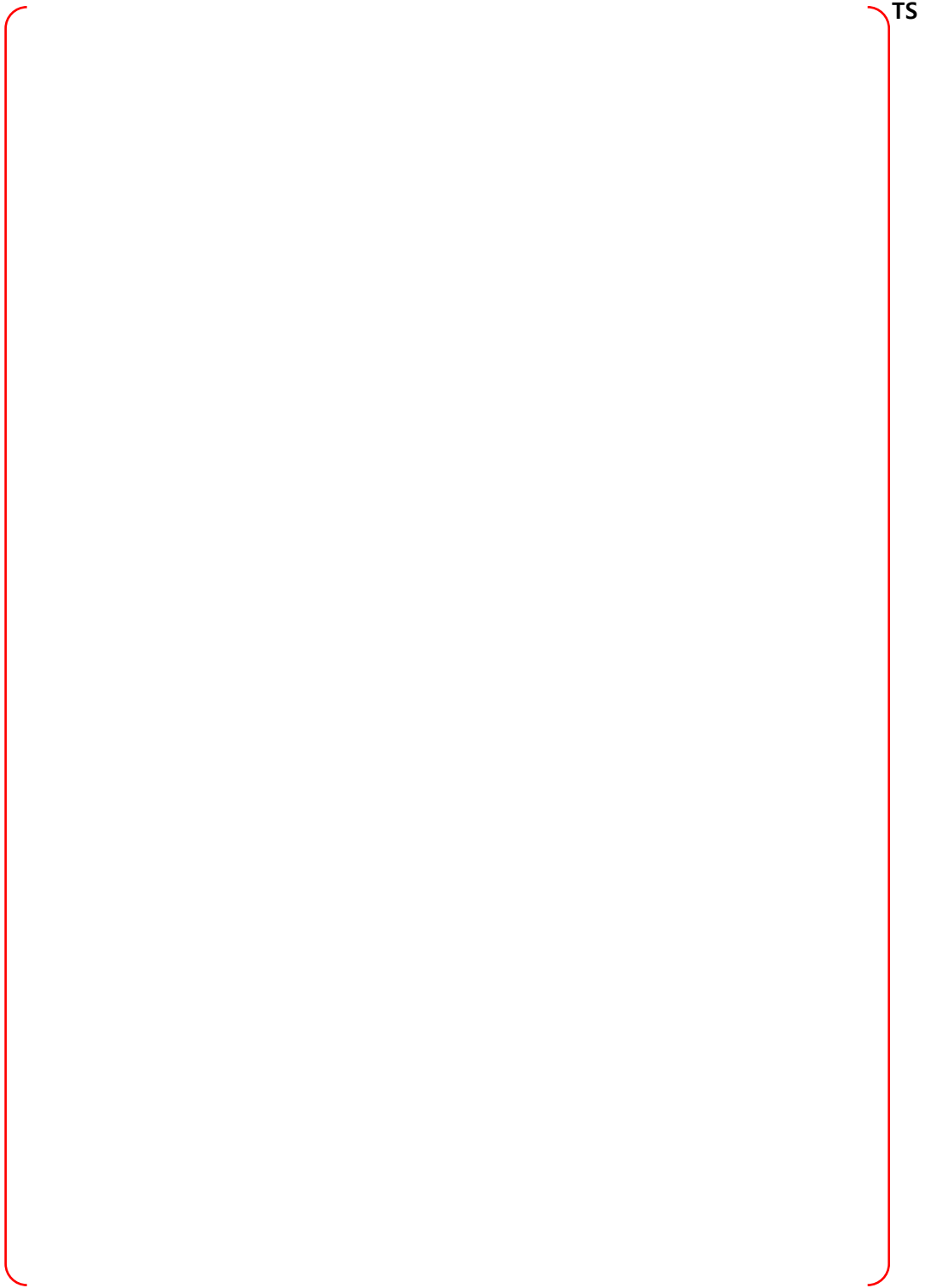


Figure B-23 Node 6, S/G Compartment #2 at Elev 100' - Bounding Sequences – DF

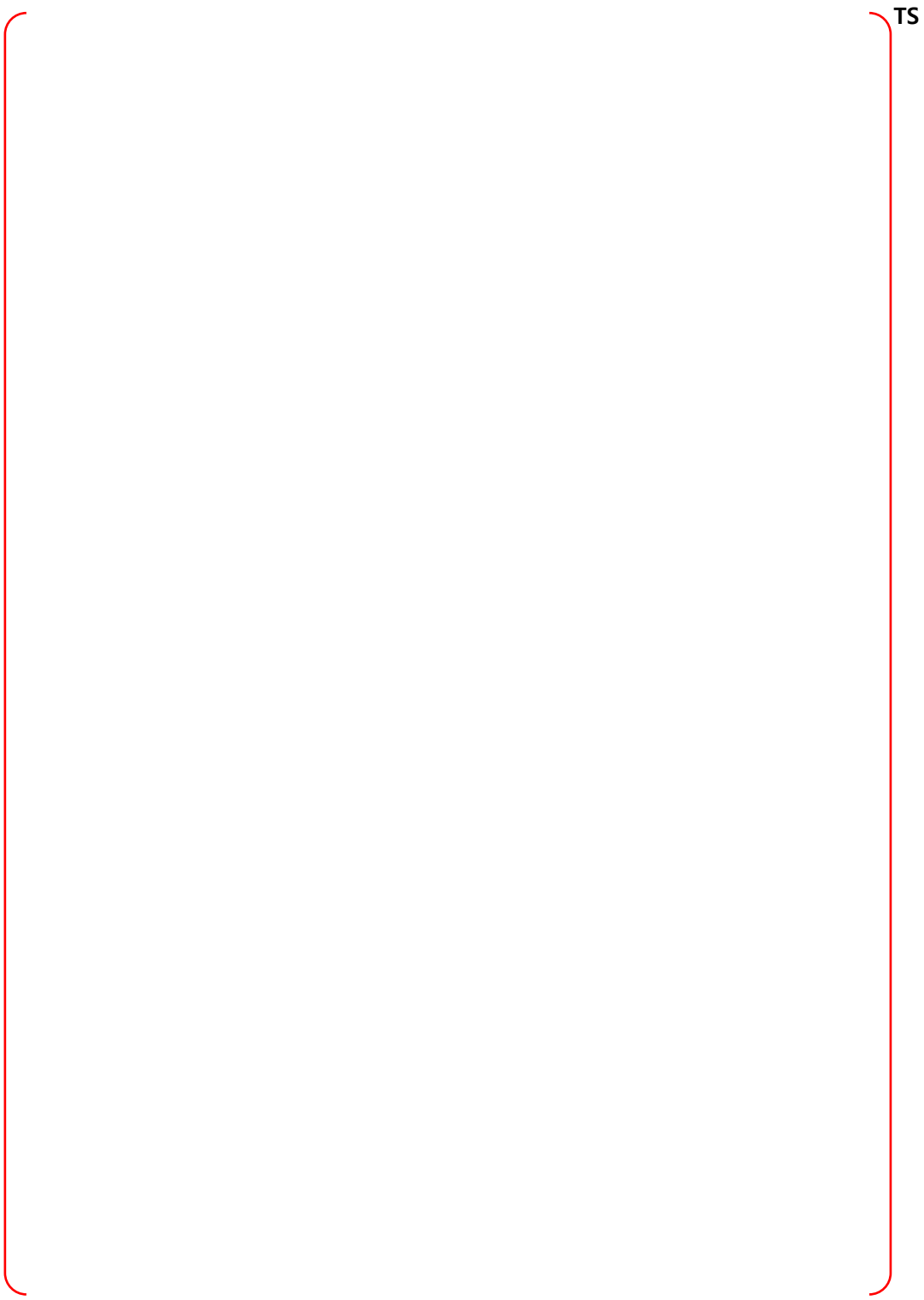
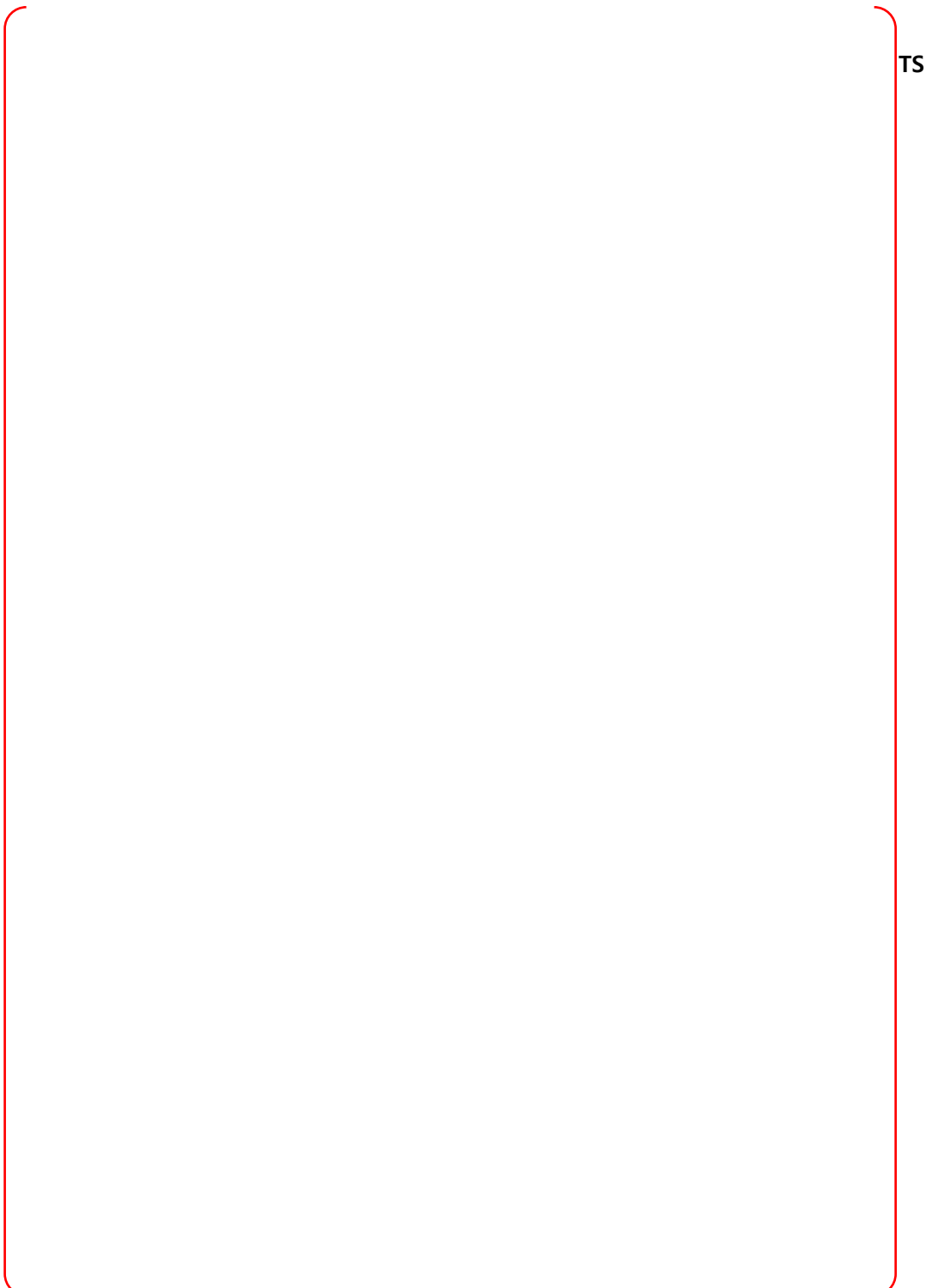


Figure B-24 Node 7, S/G Compartment #2 at Elev 136.5' - PRA Sequences



TS

Figure B-25 Node 7, S/G Compartment #2 at Elev 136.5' - Bounding Sequences – MCCI

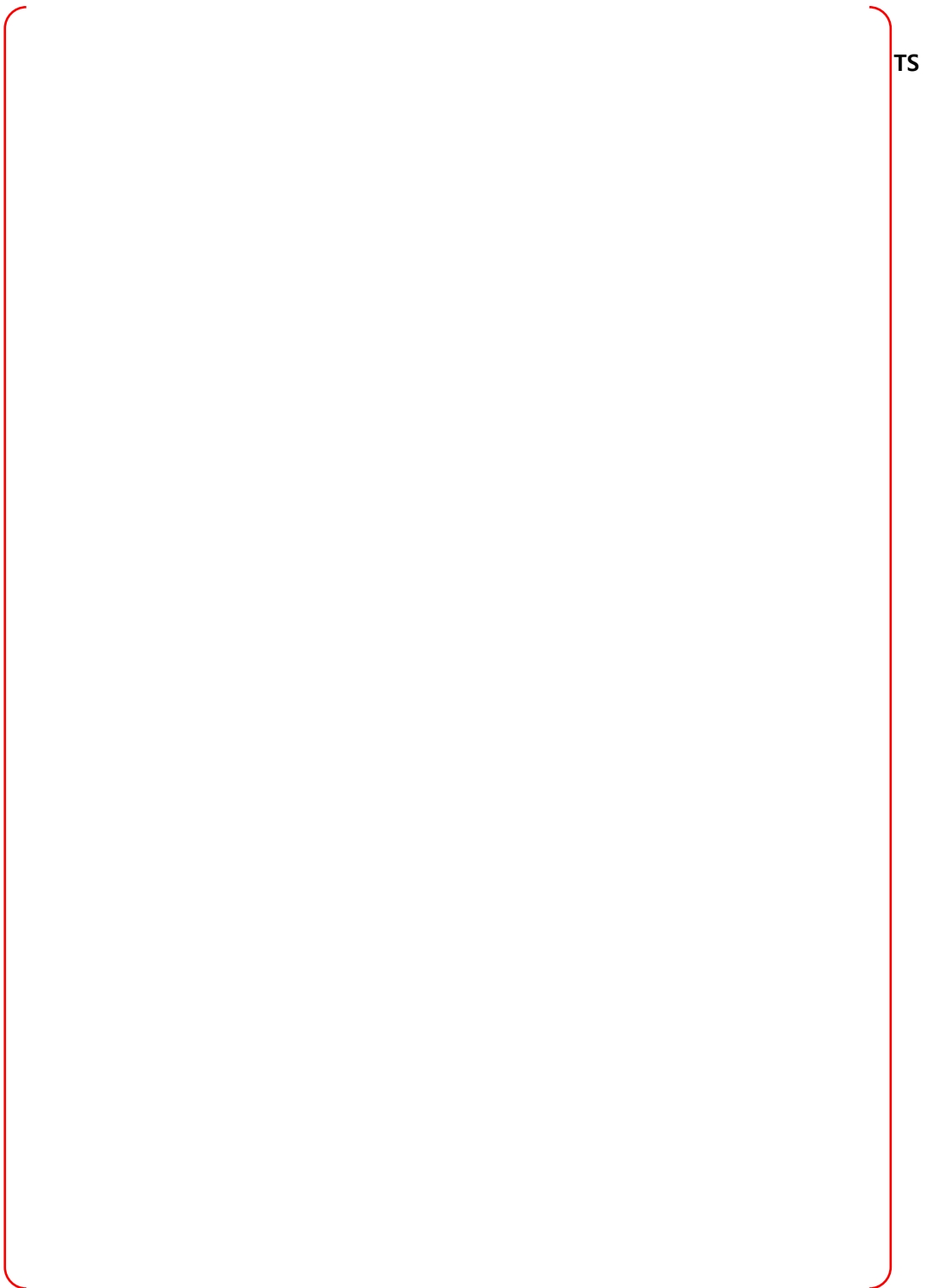


Figure B-26 Node 7, S/G Compartment #2 at Elev 136.5' - Bounding Sequences – CP

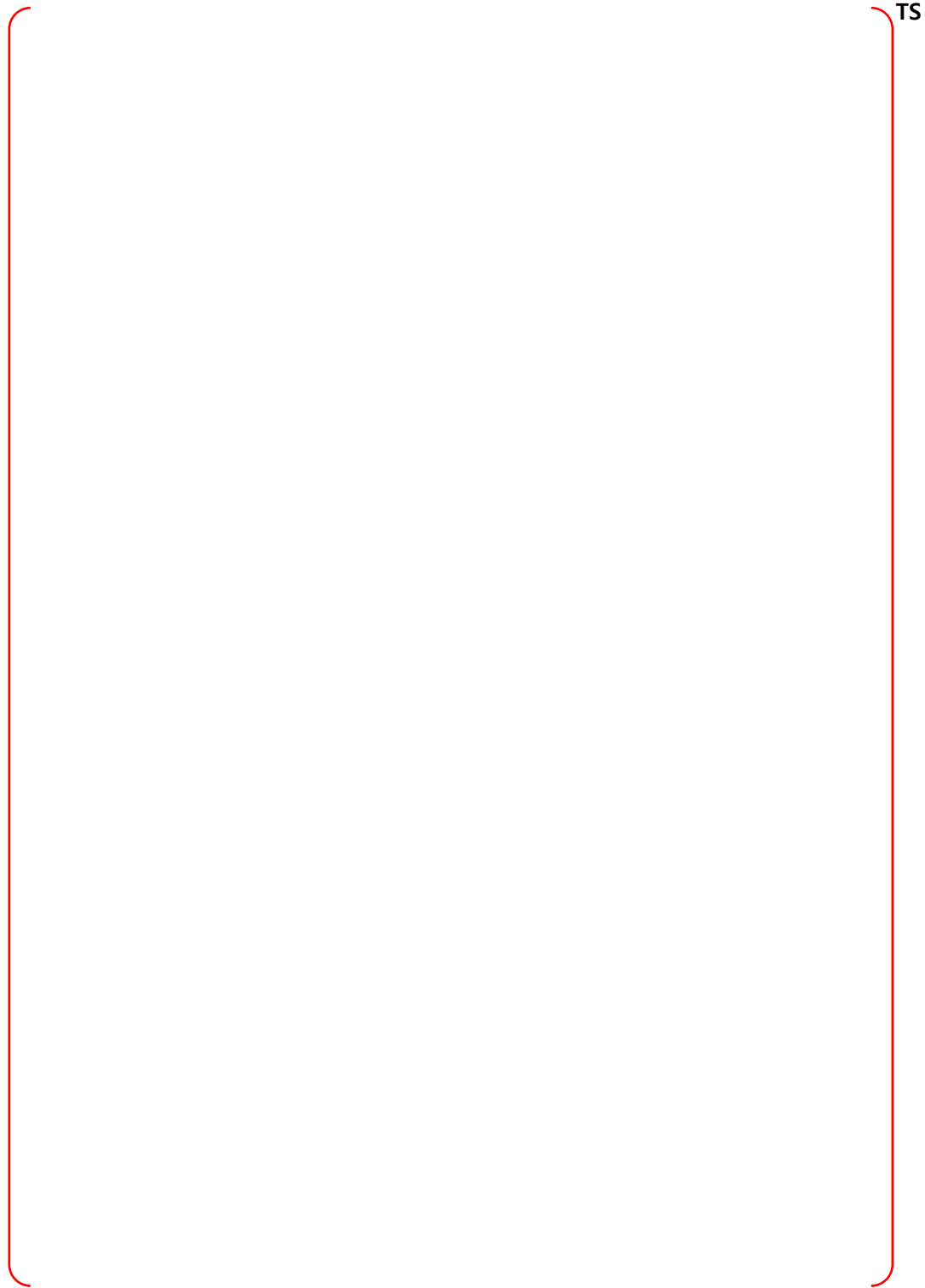


Figure B-27 Node 7, S/G Compartment #2 at Elev 136.5' - Bounding Sequences – DF

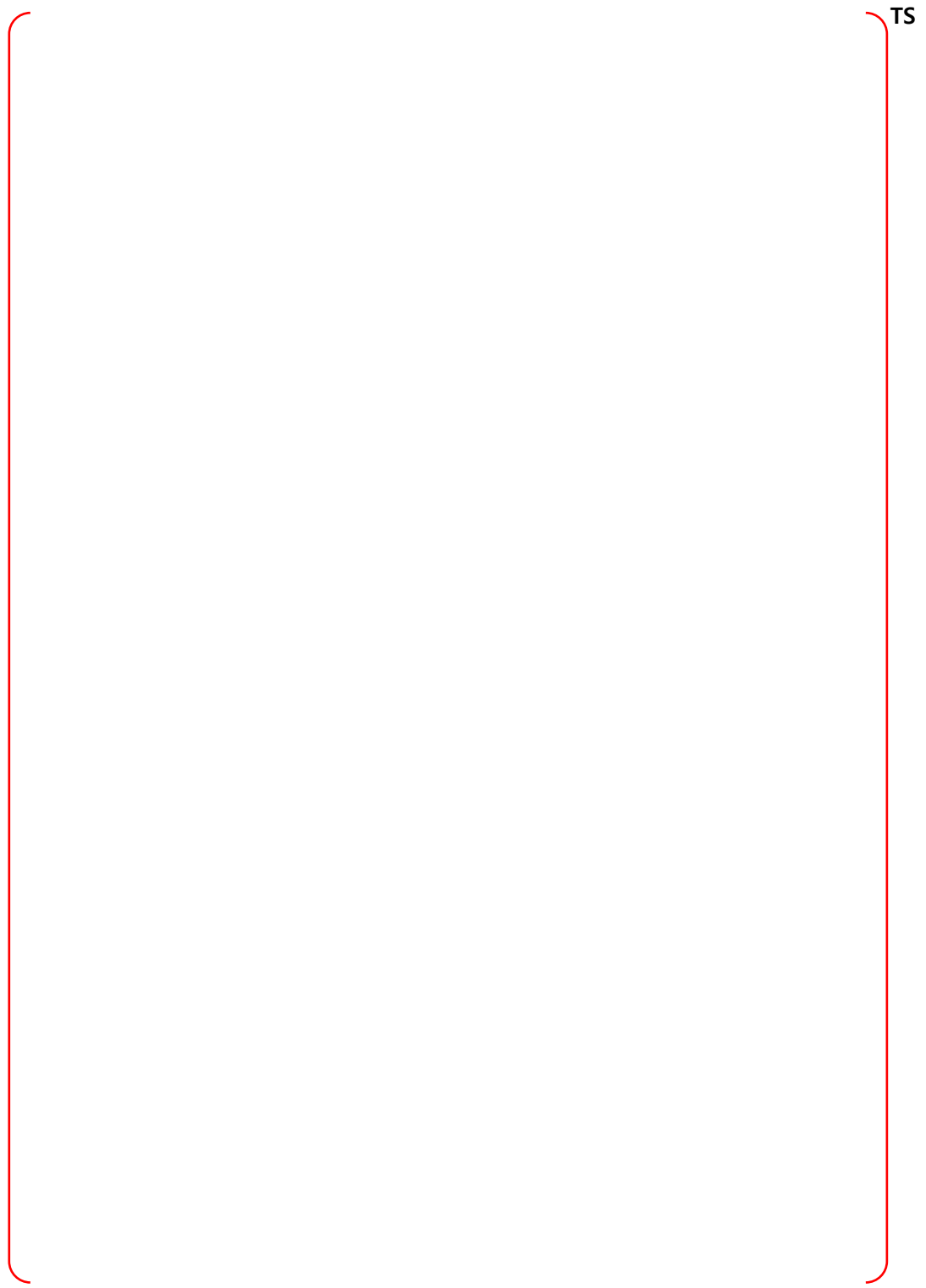


Figure B-28 Node 8, S/G Compartment #1 at Elev 100' - PRA Sequences

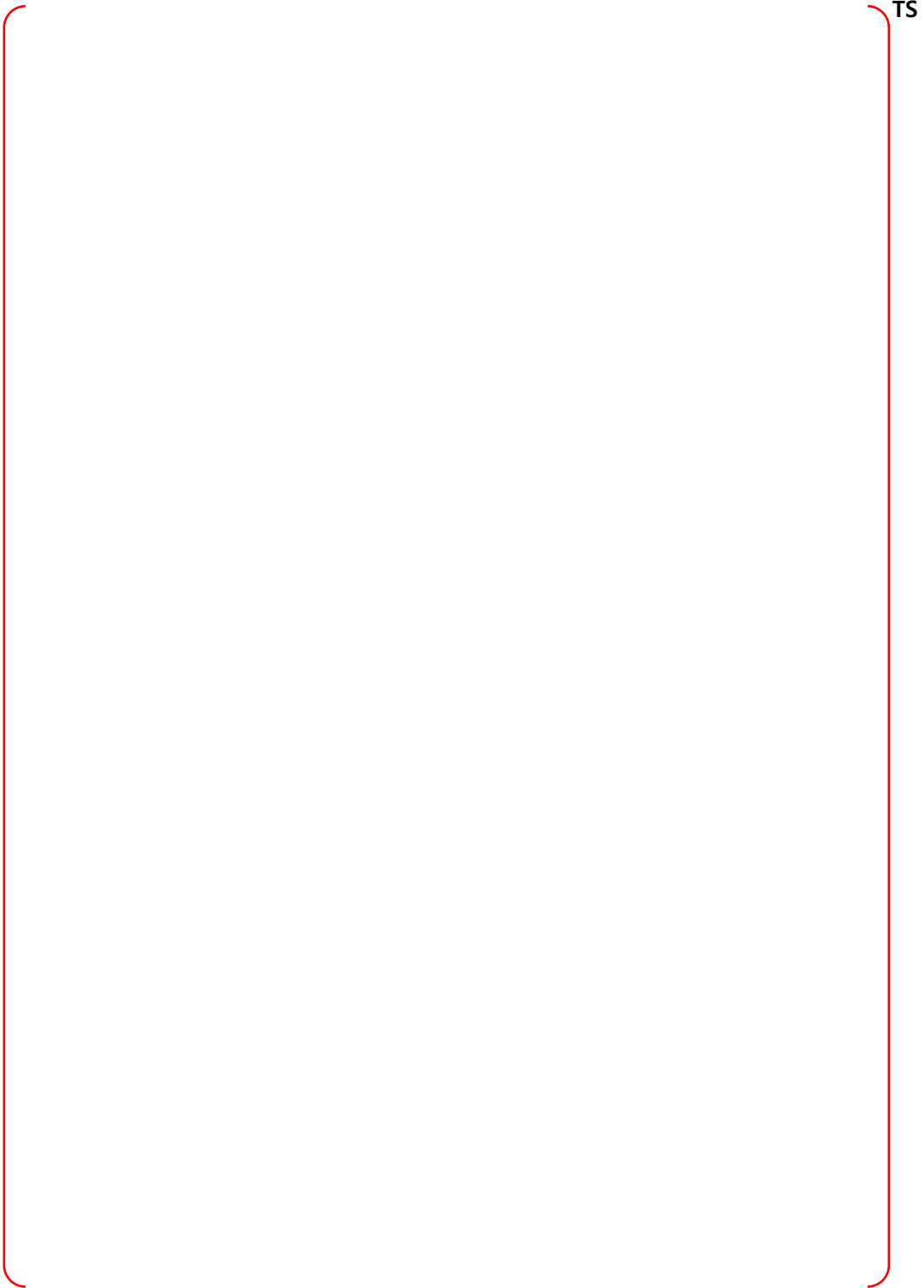


Figure B-29 Node 8, S/G Compartment #1 at Elev 100' - Bounding Sequences – MCCI

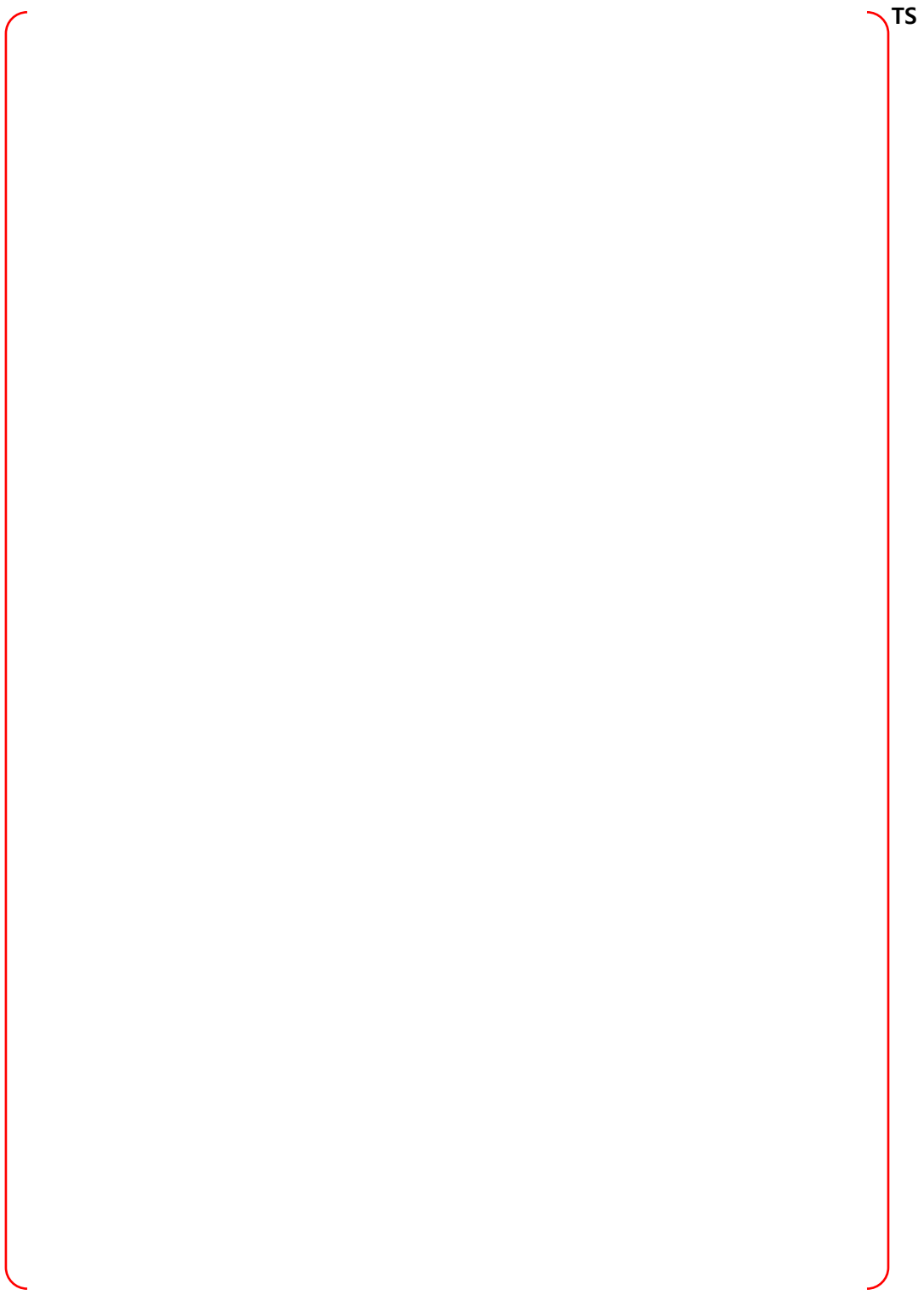


Figure B-30 Node 8, S/G Compartment #1 at Elev 100' - Bounding Sequences – CP

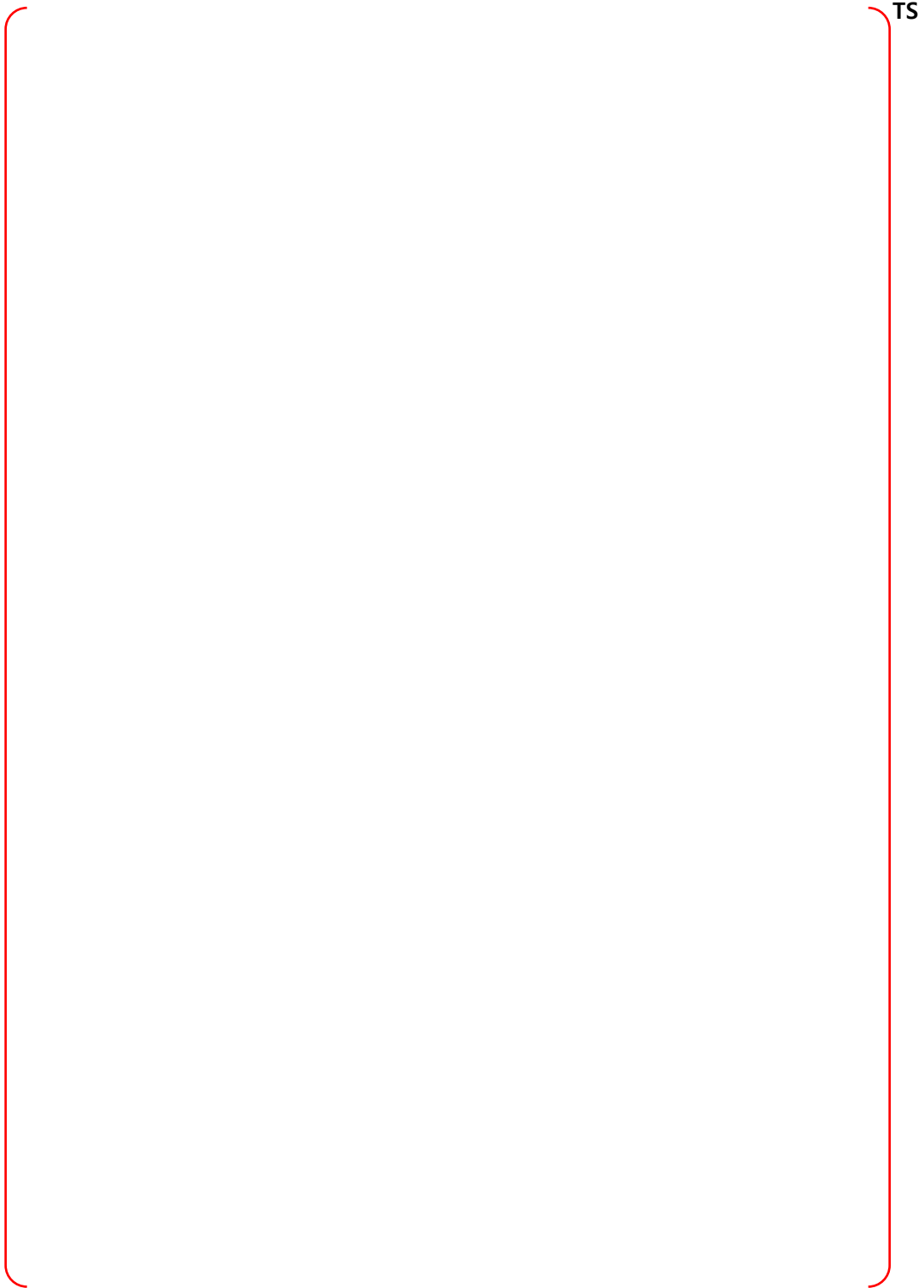
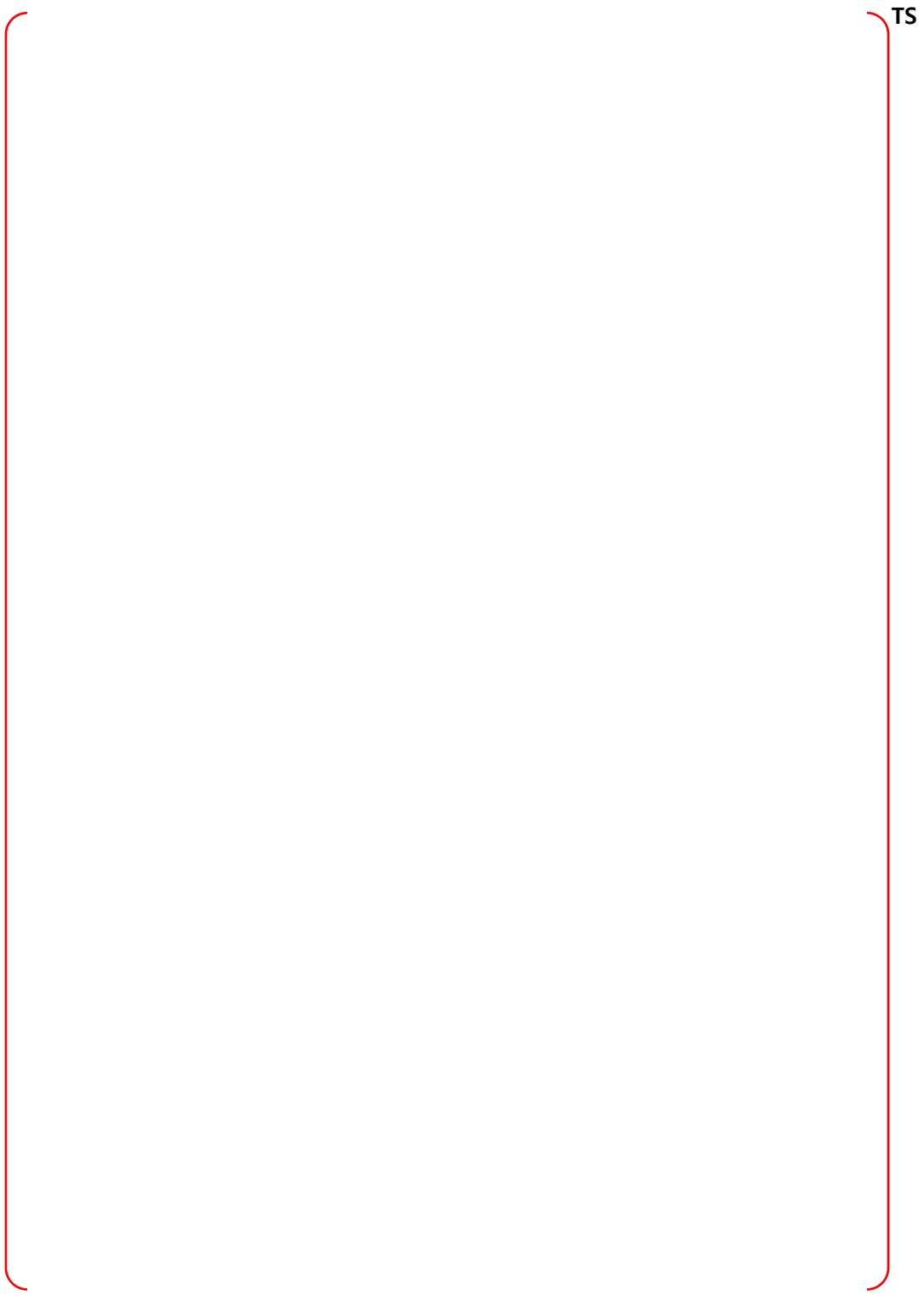
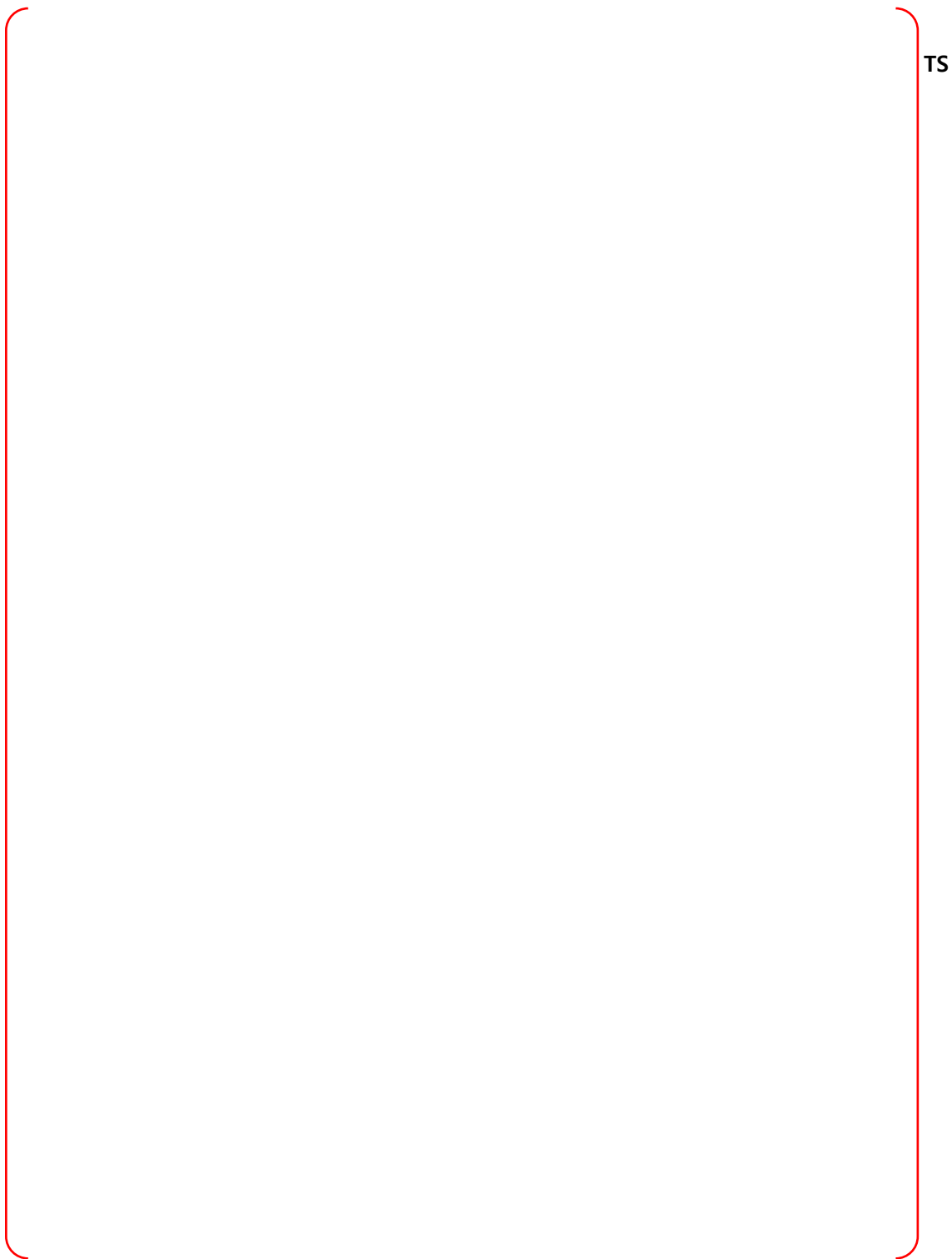


Figure B-31 Node 8, S/G Compartment #1 at Elev 100' - Bounding Sequences – DF



TS

Figure B-32 Node 9, S/G Compartment #1 at Elev 136.5' - PRA Sequences



TS

Figure B-33 Node 9, S/G Compartment #1 at Elev 136.5' - Bounding Sequences – MCCI

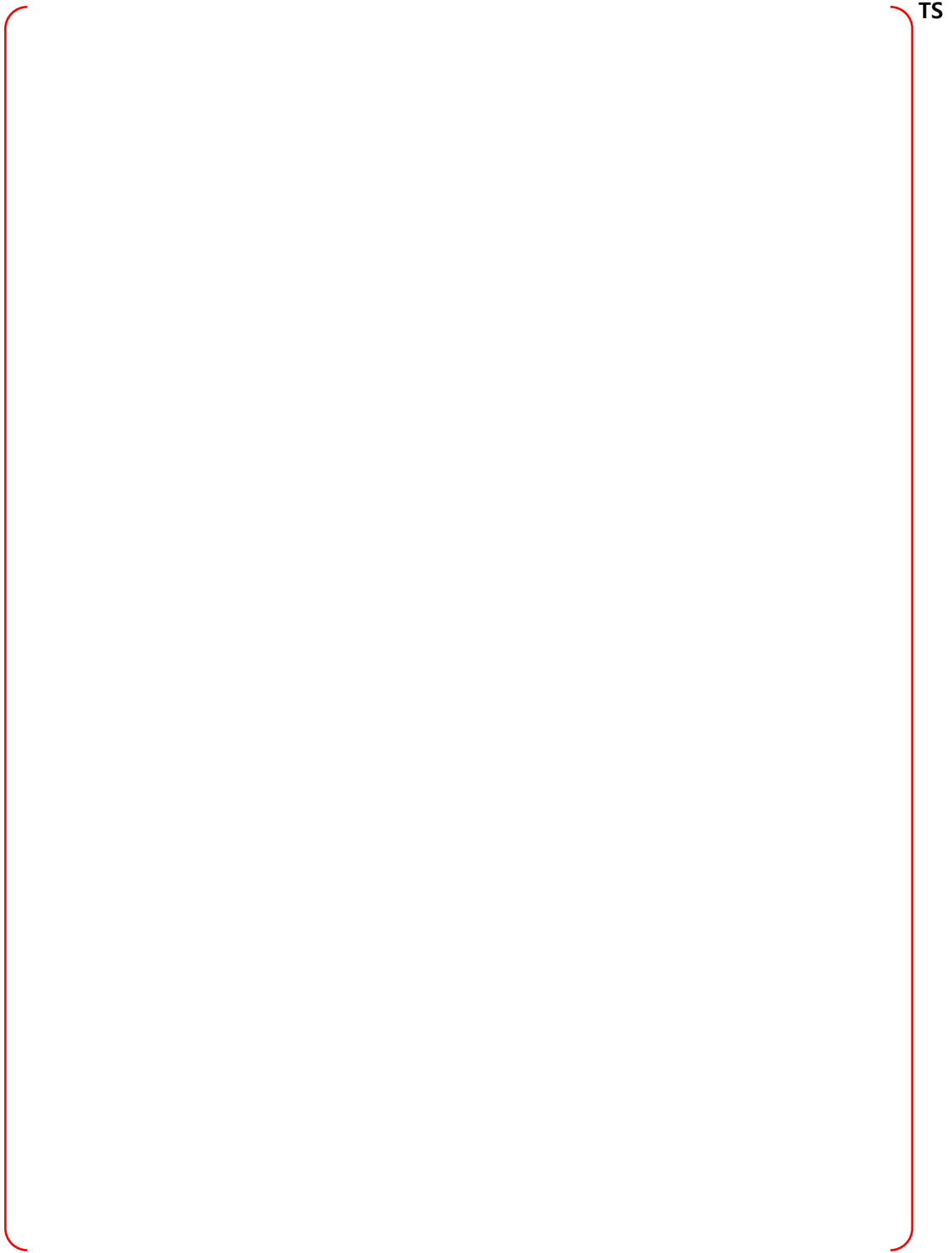


Figure B-34 Node 9, S/G Compartment #1 at Elev 136.5' - Bounding Sequences – CP

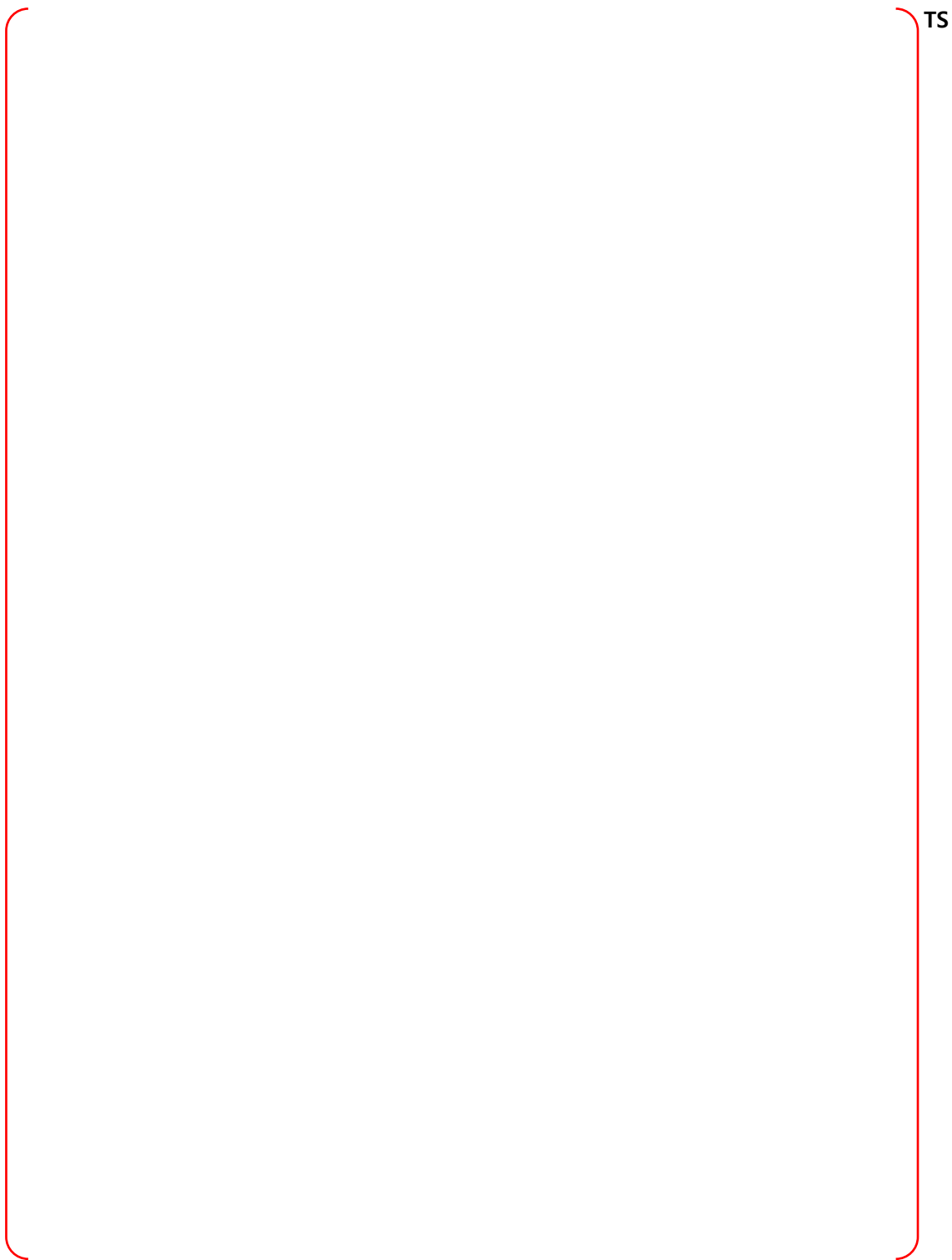


Figure B-35 Node 9, S/G Compartment #1 at Elev 136.5' - Bounding Sequences – DF

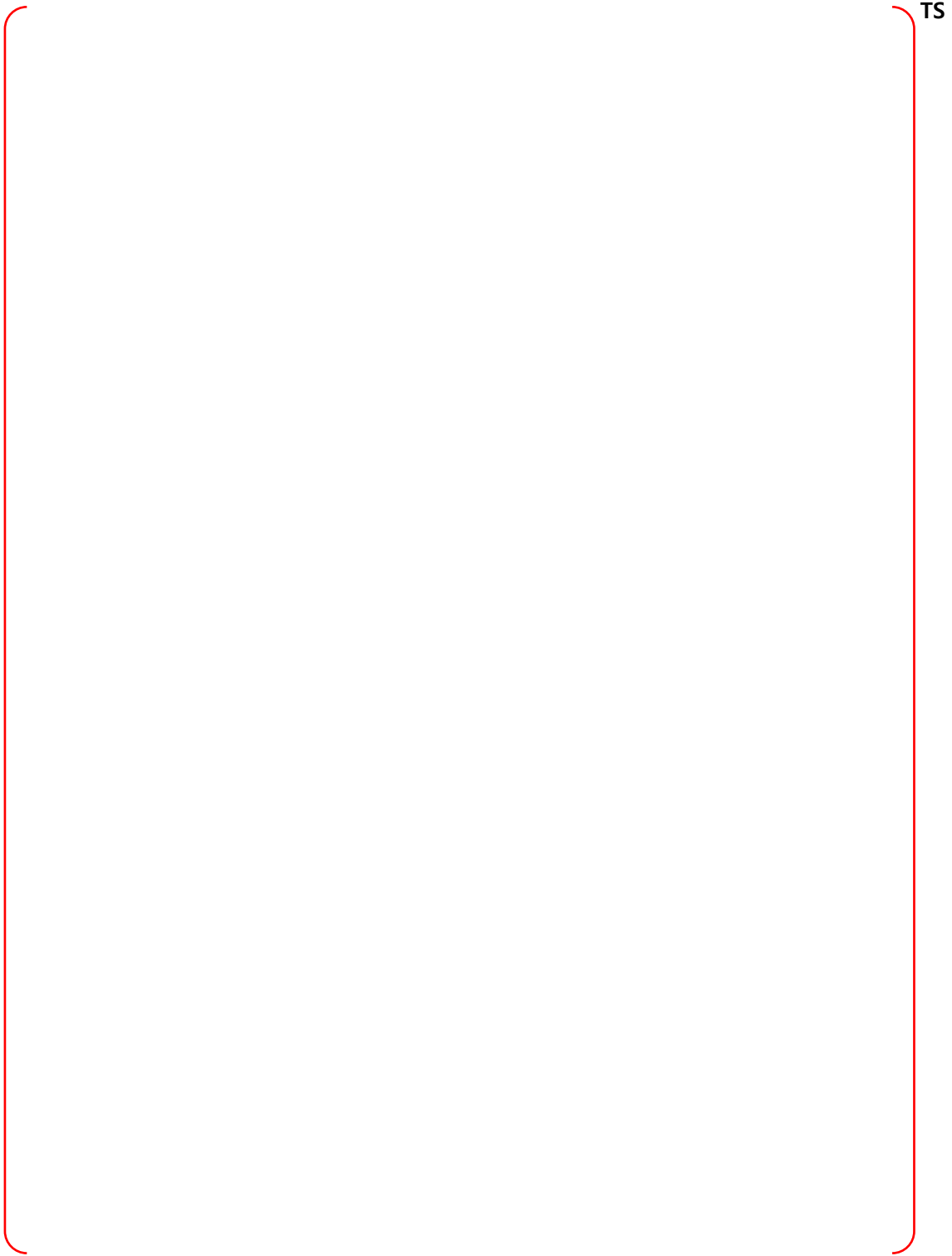


Figure B-36 Node 10, NW Annular Compartment at Elev 100' - PRA Sequences

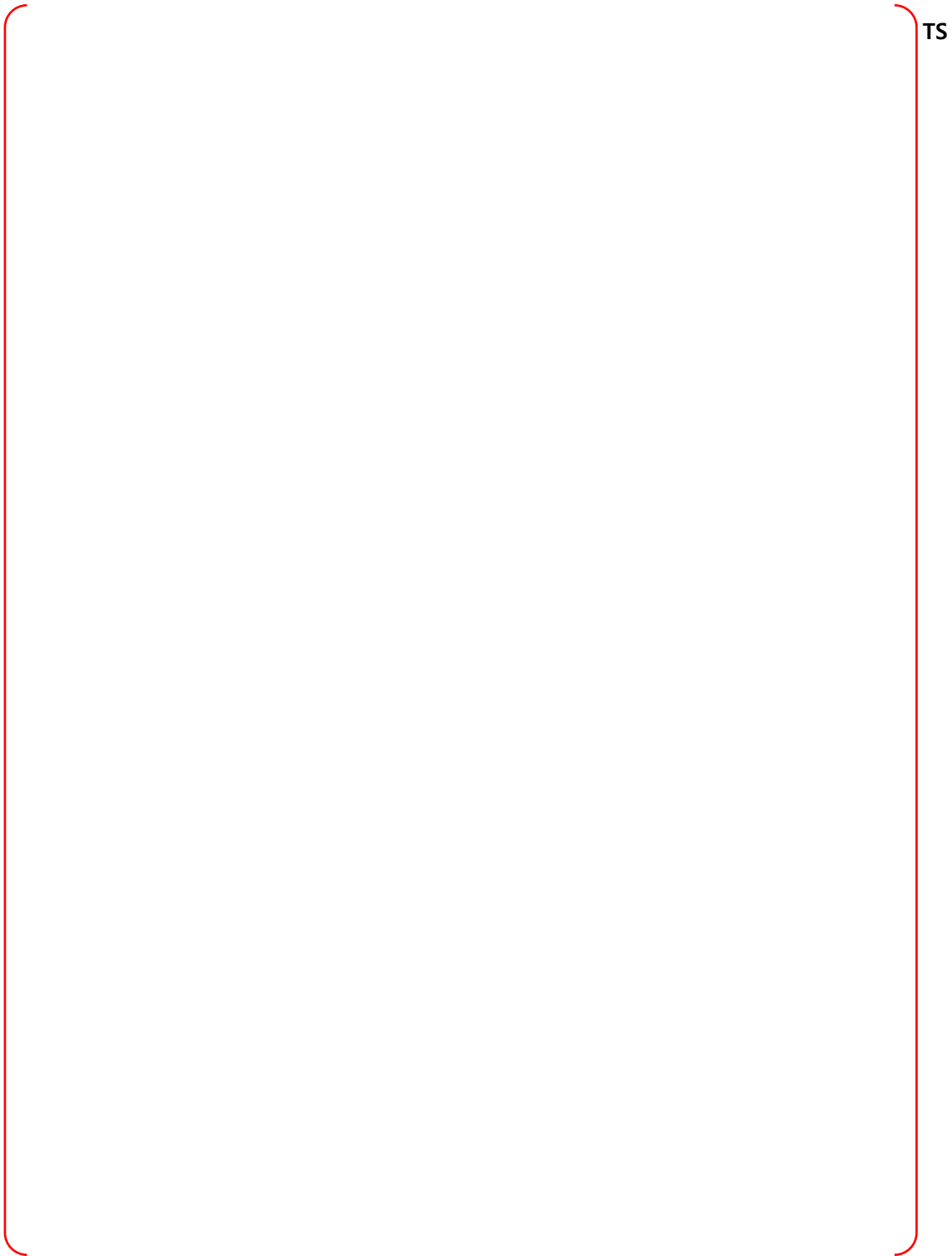


Figure B-37 Node 10, NW Annular Compartment at Elev 100' - Bounding Sequences – MCCI

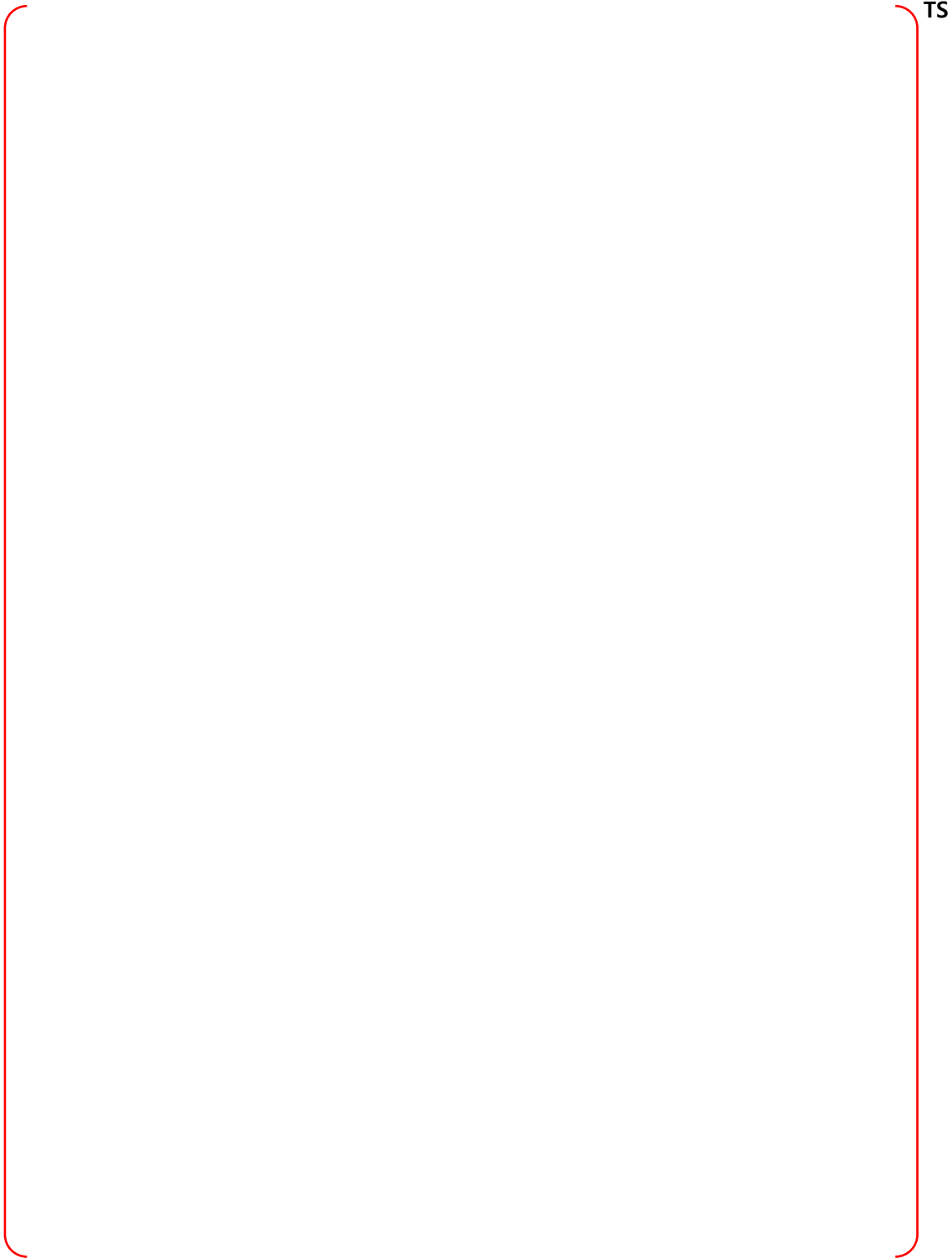
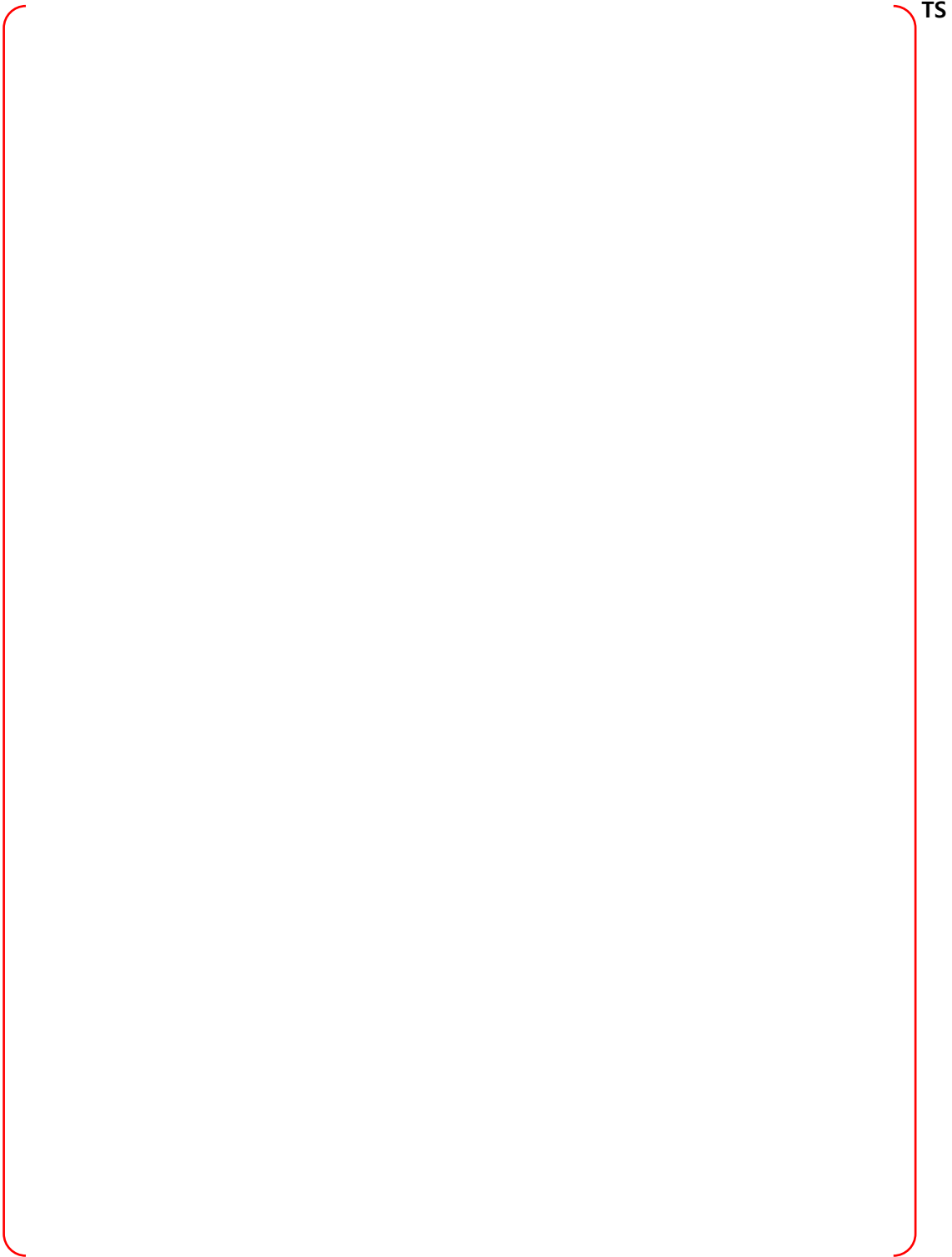


Figure B-38 Node 10, NW Annular Compartment at Elev 100' - Bounding Sequences – CP



TS

Figure B-39 Node 10, NW Annular Compartment at Elev 100' - Bounding Sequences - DF

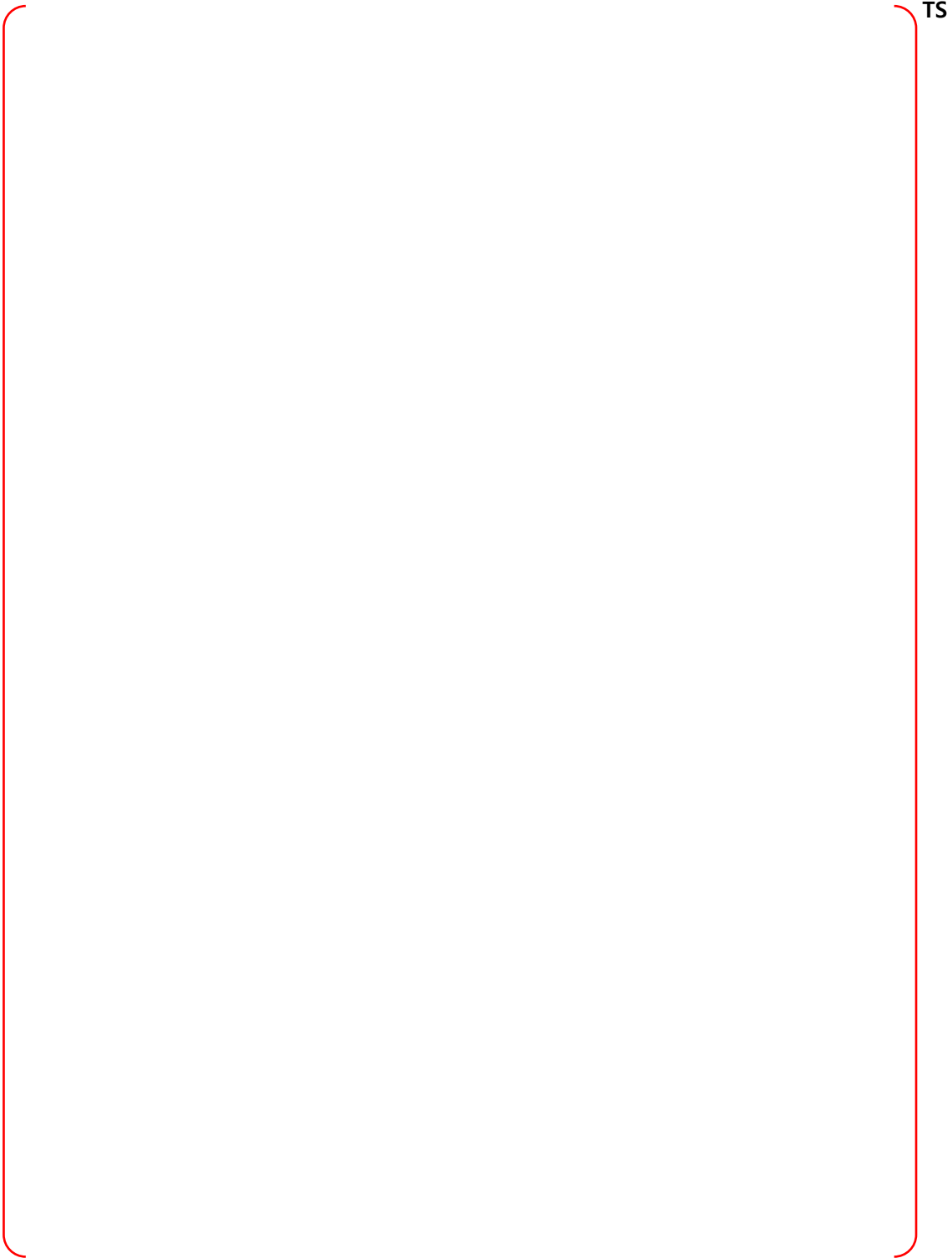


Figure B-40 Node 11, SW Annular Compartment at Elev 100' - PRA Sequences

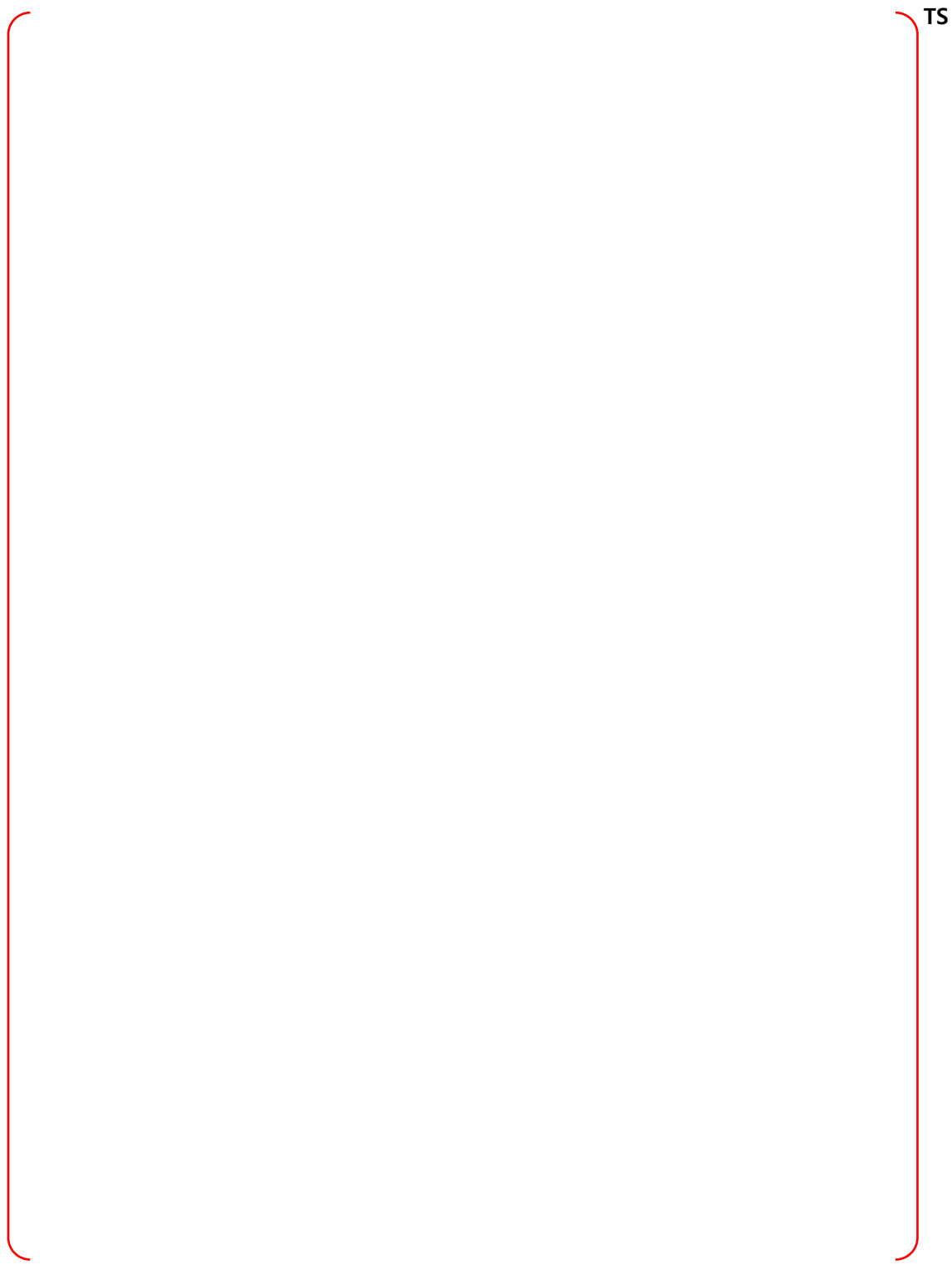


Figure B-41 Node 11, SW Annular Compartment at Elev 100' - Bounding Sequences – MCCI

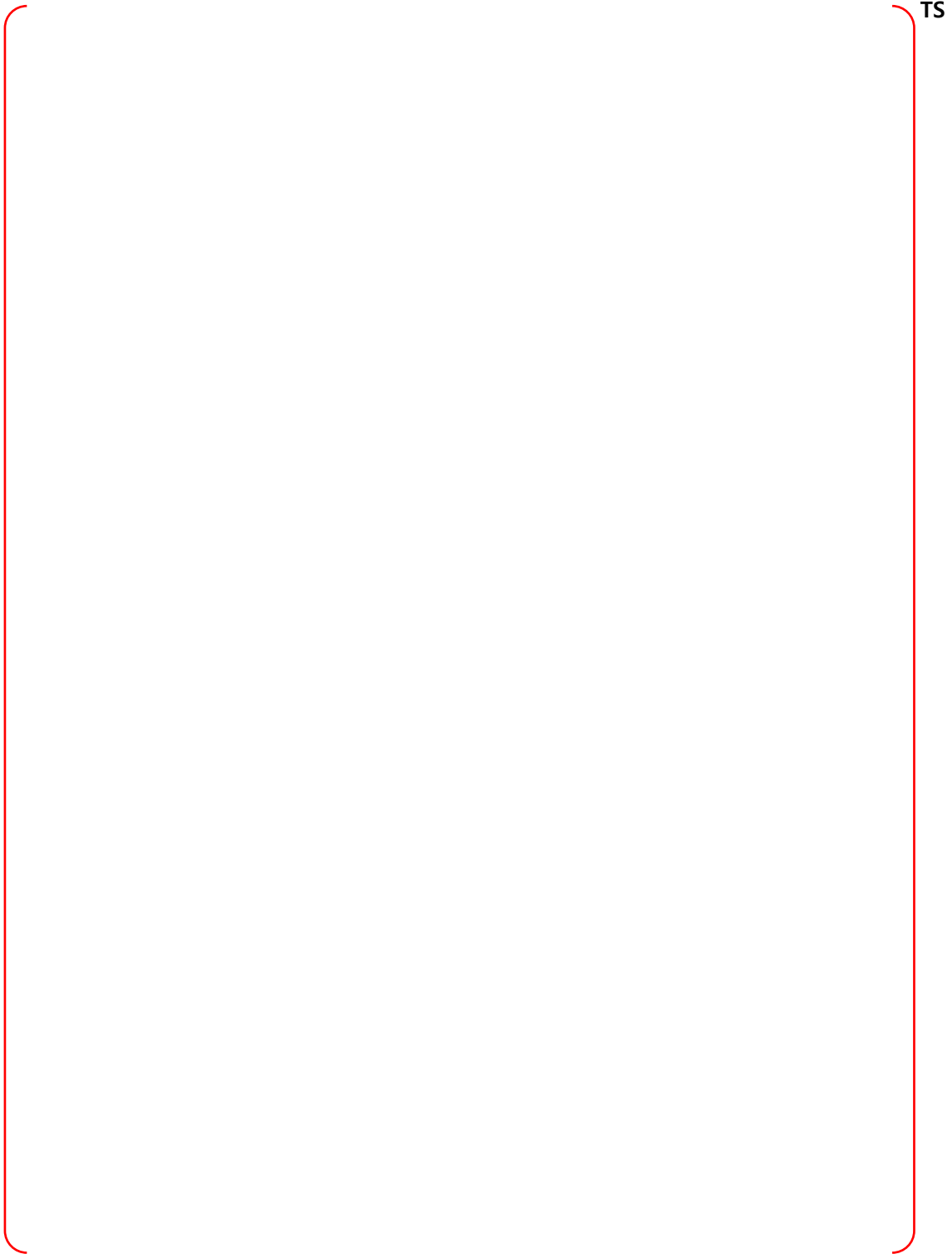


Figure B-42 Node 11, SW Annular Compartment at Elev 100' - Bounding Sequences – CP

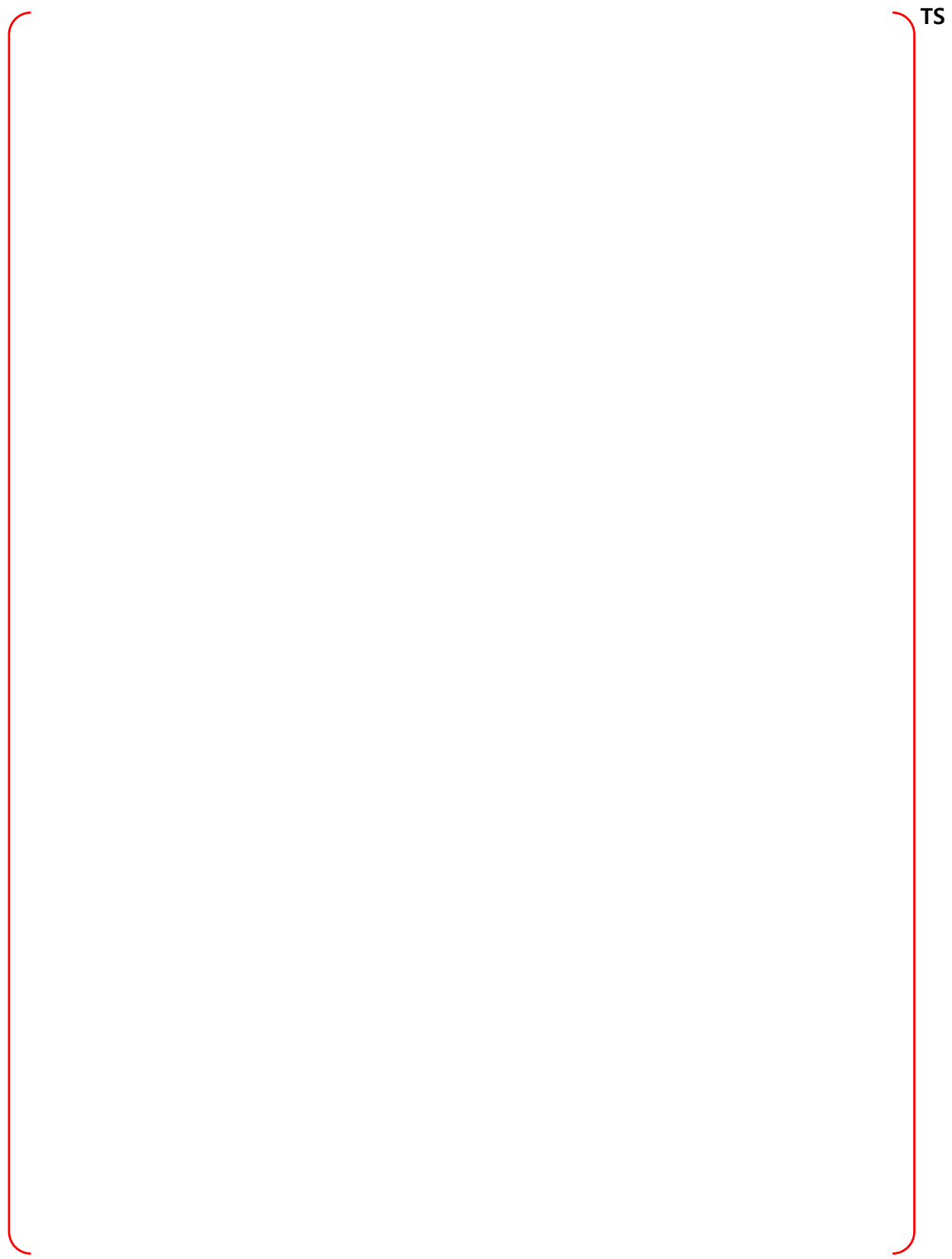


Figure B-43 Node 11, SW Annular Compartment at Elev 100' - Bounding Sequences - DF

TS

Figure B-44 Node 12, NW Annular Compartment at Elev 114' - PRA Sequences

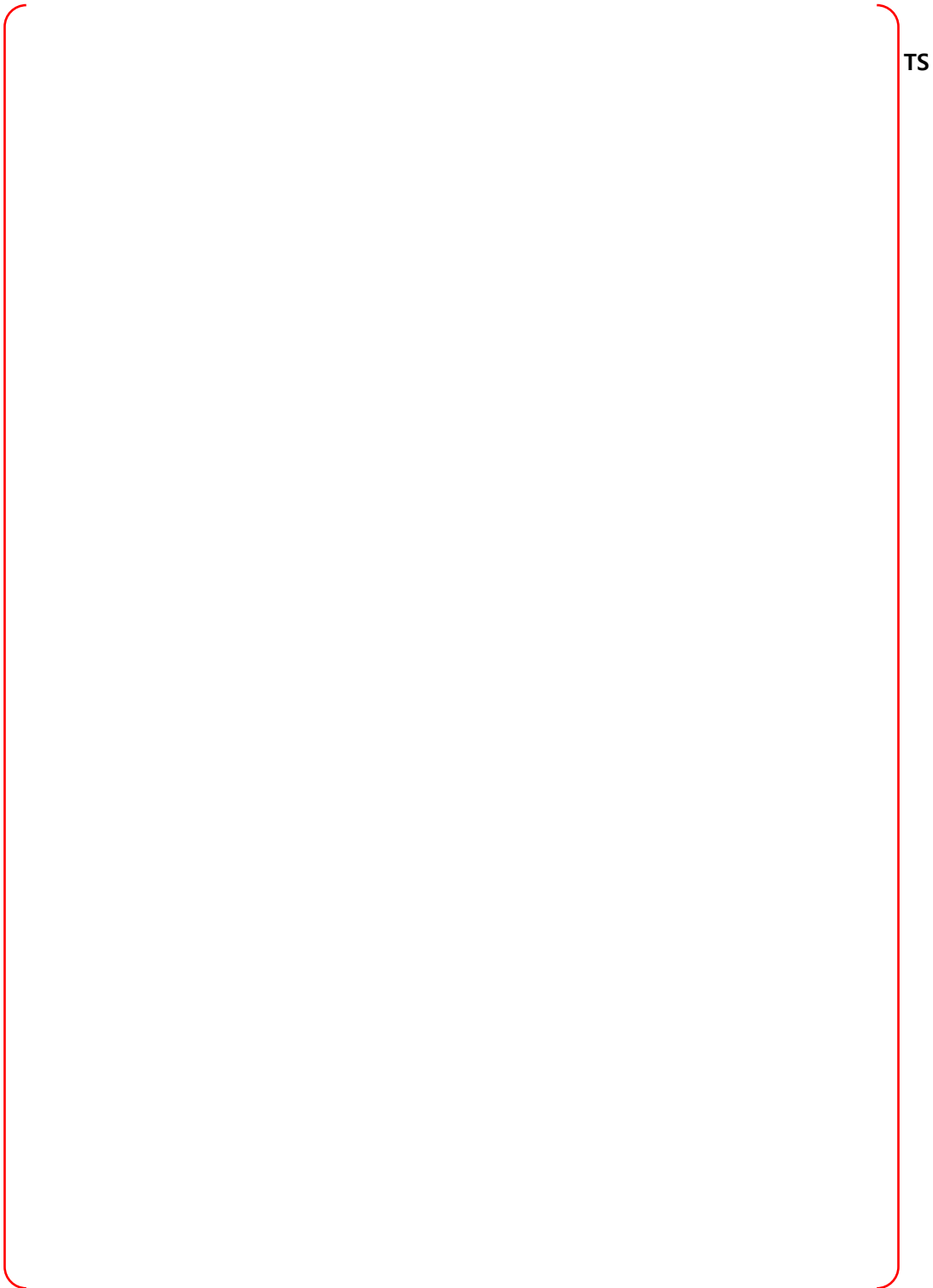


Figure B-45 **Node 12, NW Annular Compartment at Elev 114' - Bounding Sequences – MCCI**

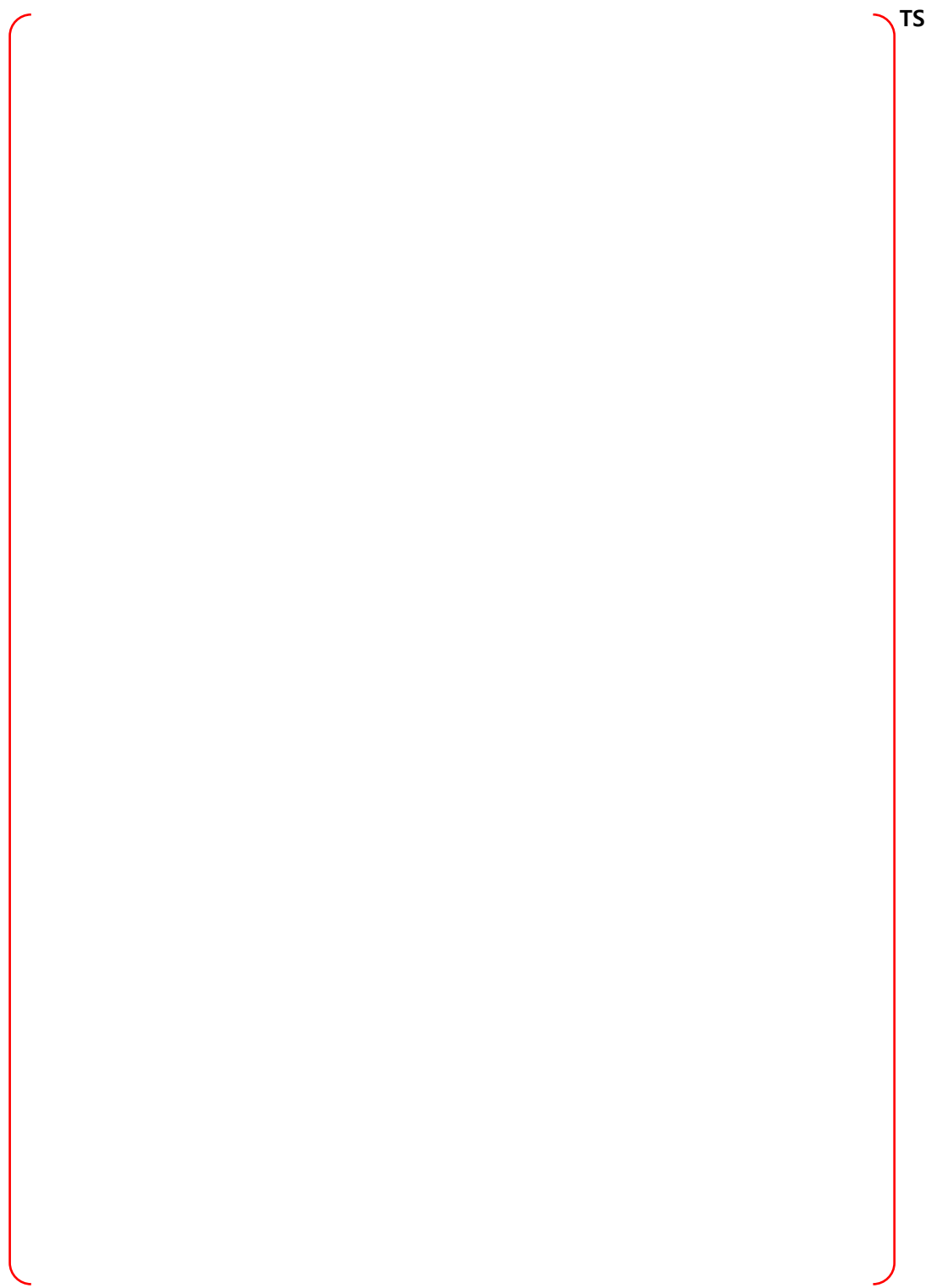


Figure B-46 Node 12, NW Annular Compartment at Elev 114' - Bounding Sequences – CP

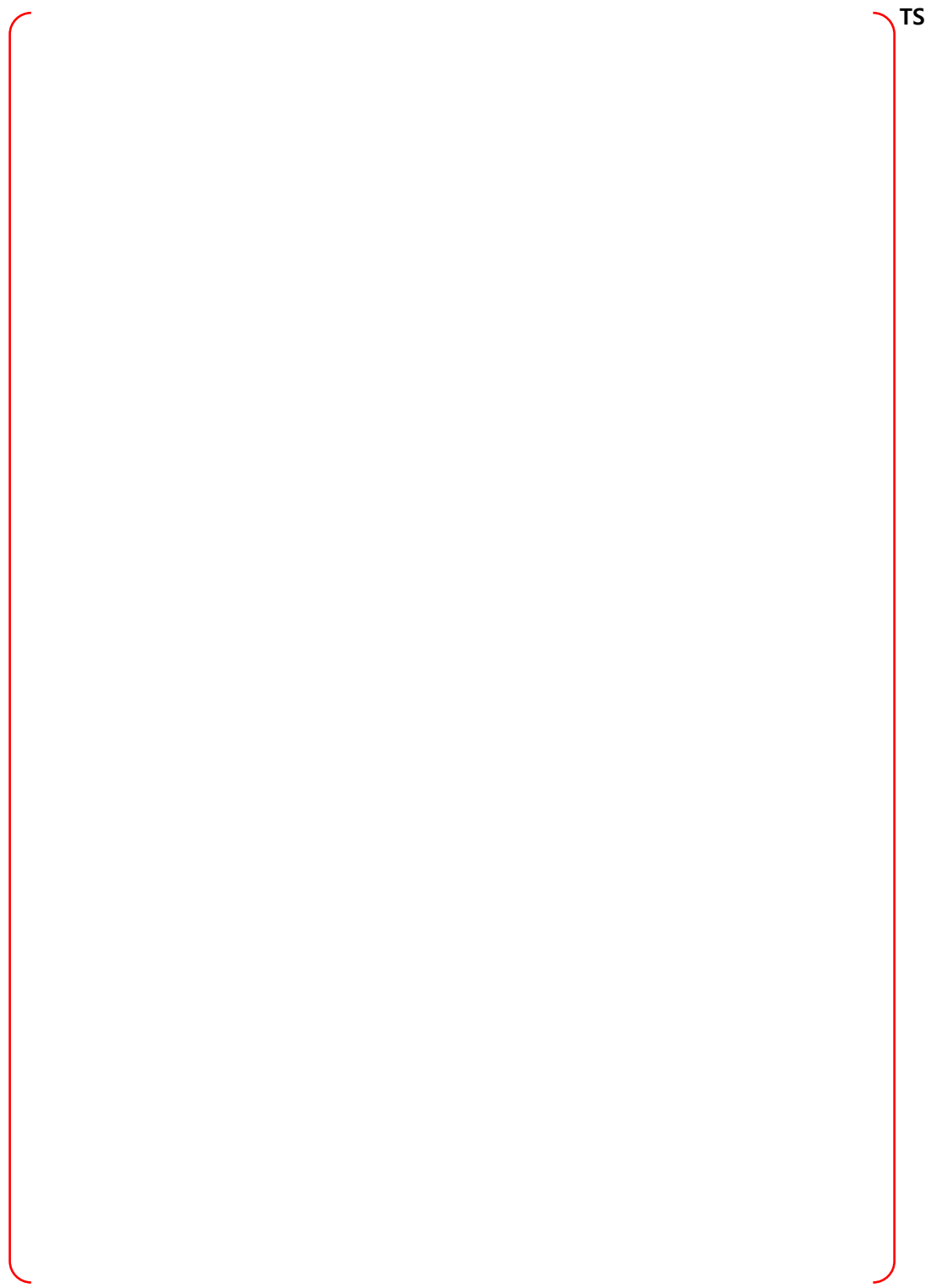


Figure B-47 Node 12, NW Annular Compartment at Elev 114' - Bounding Sequences - DF

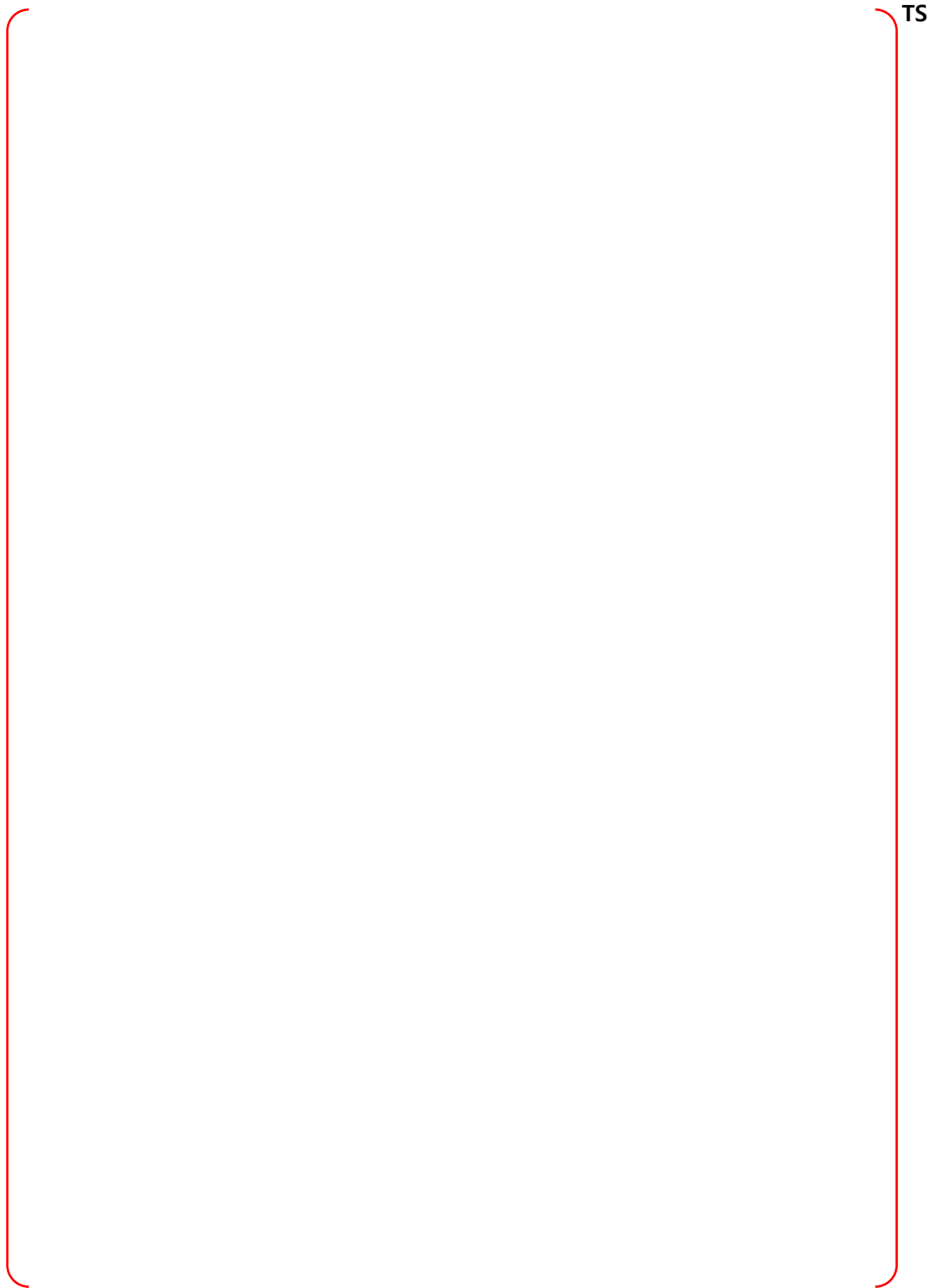


Figure B-48 Node 13, SW Annular Compartment at Elev 114' - PRA Sequences

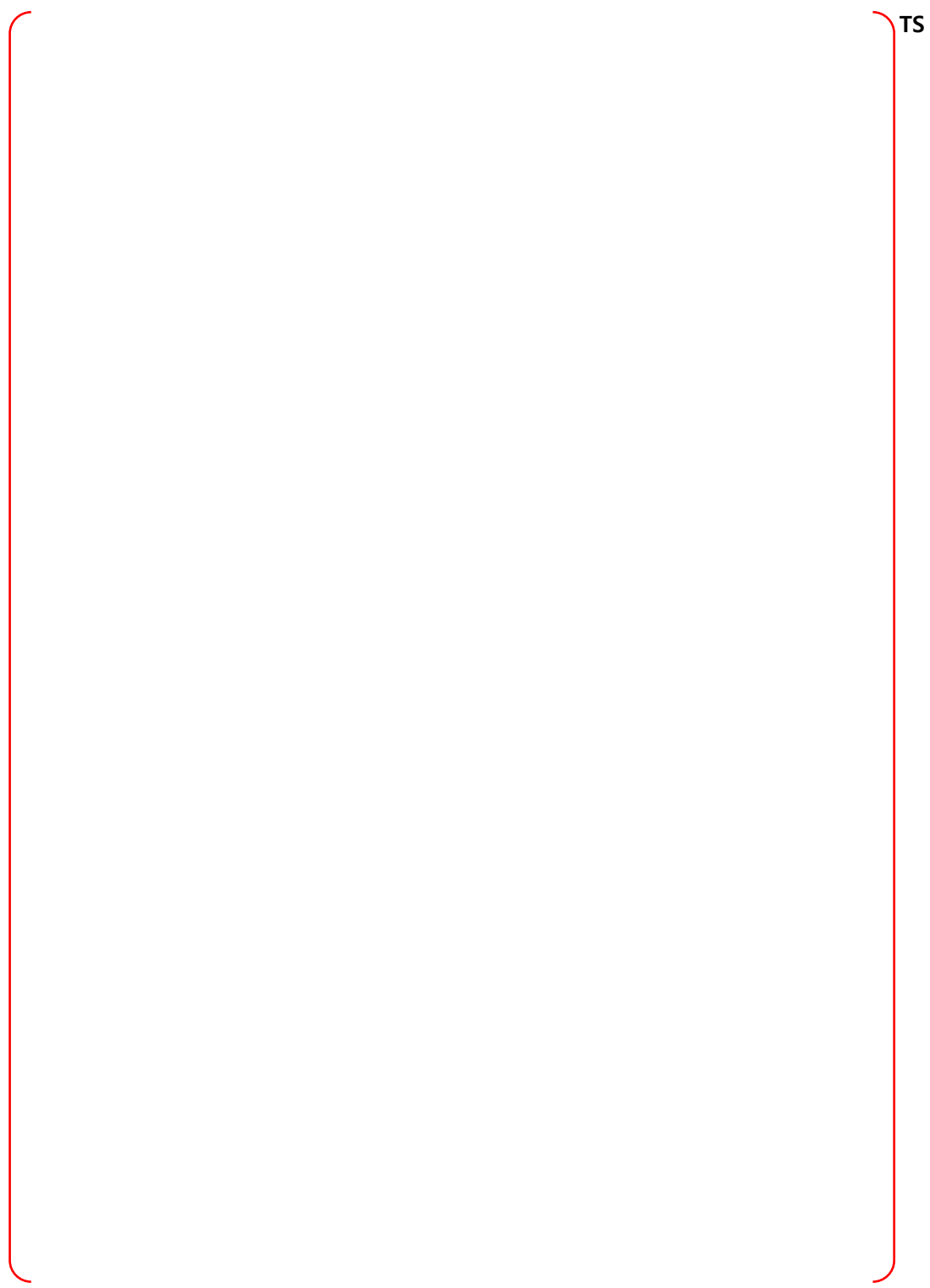
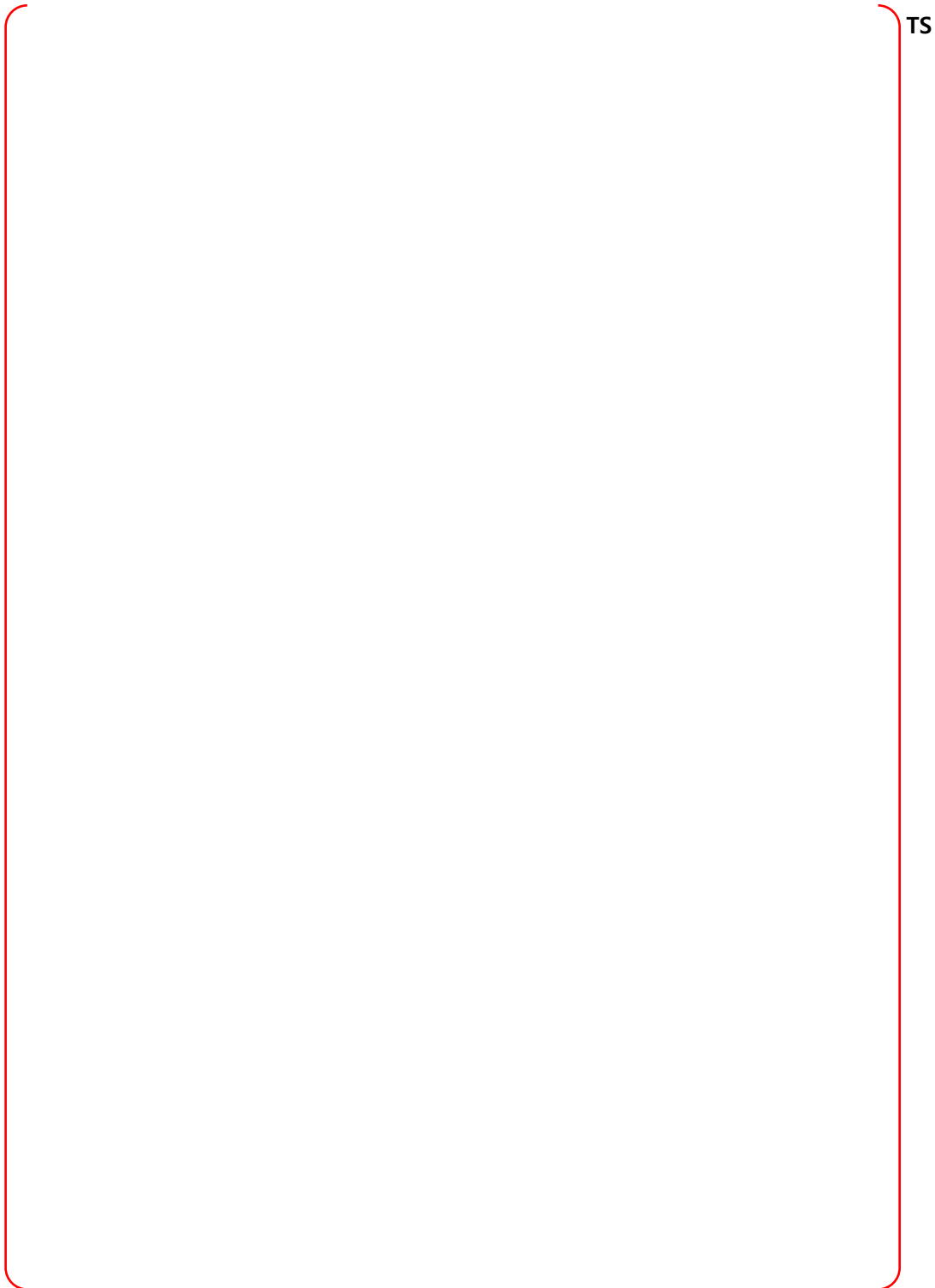


Figure B-49 Node 13, SW Annular Compartment at Elev 114' - Bounding Sequences – MCCI



TS

Figure B-50 Node 13, SW Annular Compartment at Elev 114' - Bounding Sequences – CP

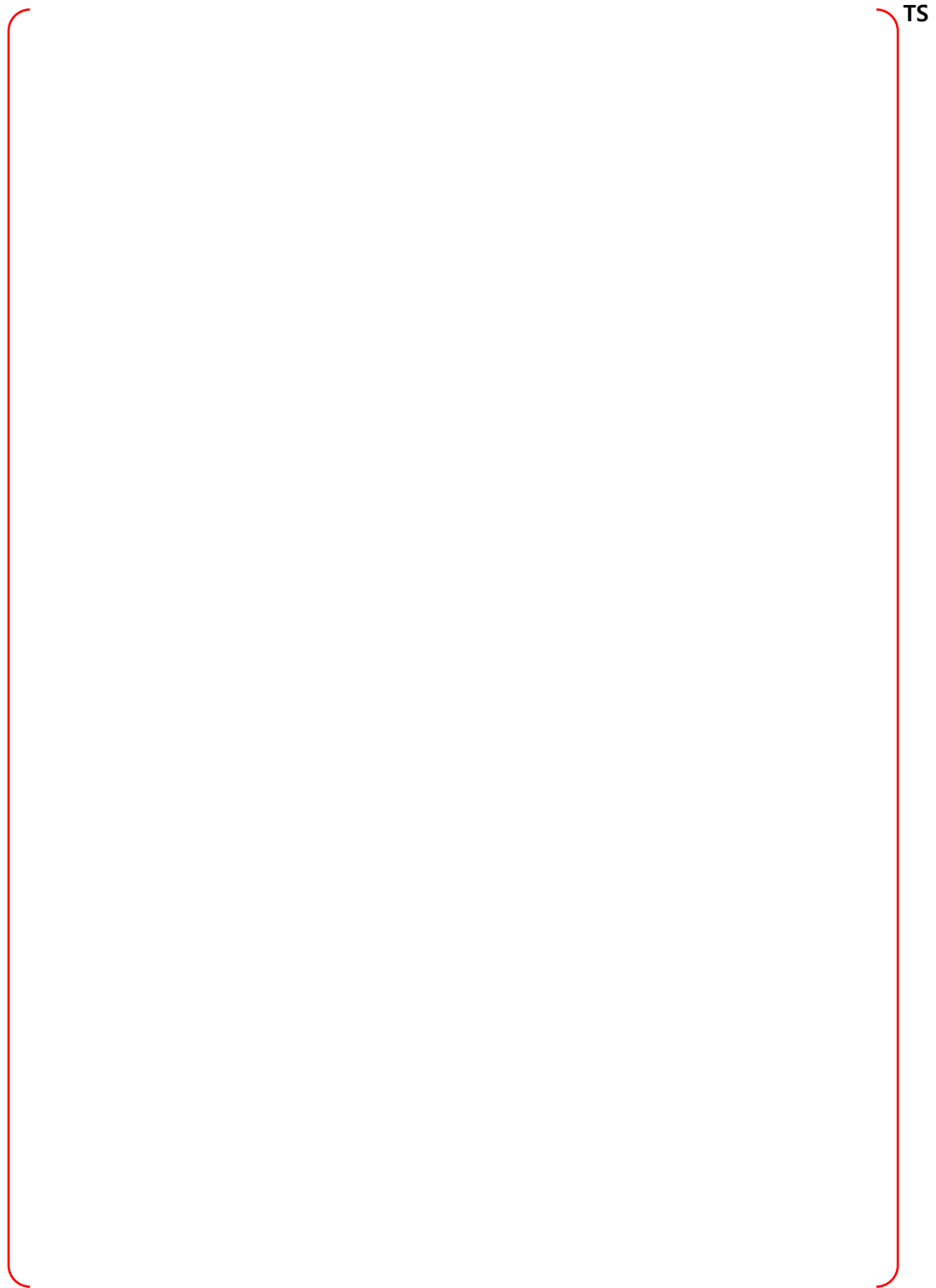


Figure B-51 Node 13, SW Annular Compartment at Elev 114' - Bounding Sequences - DF

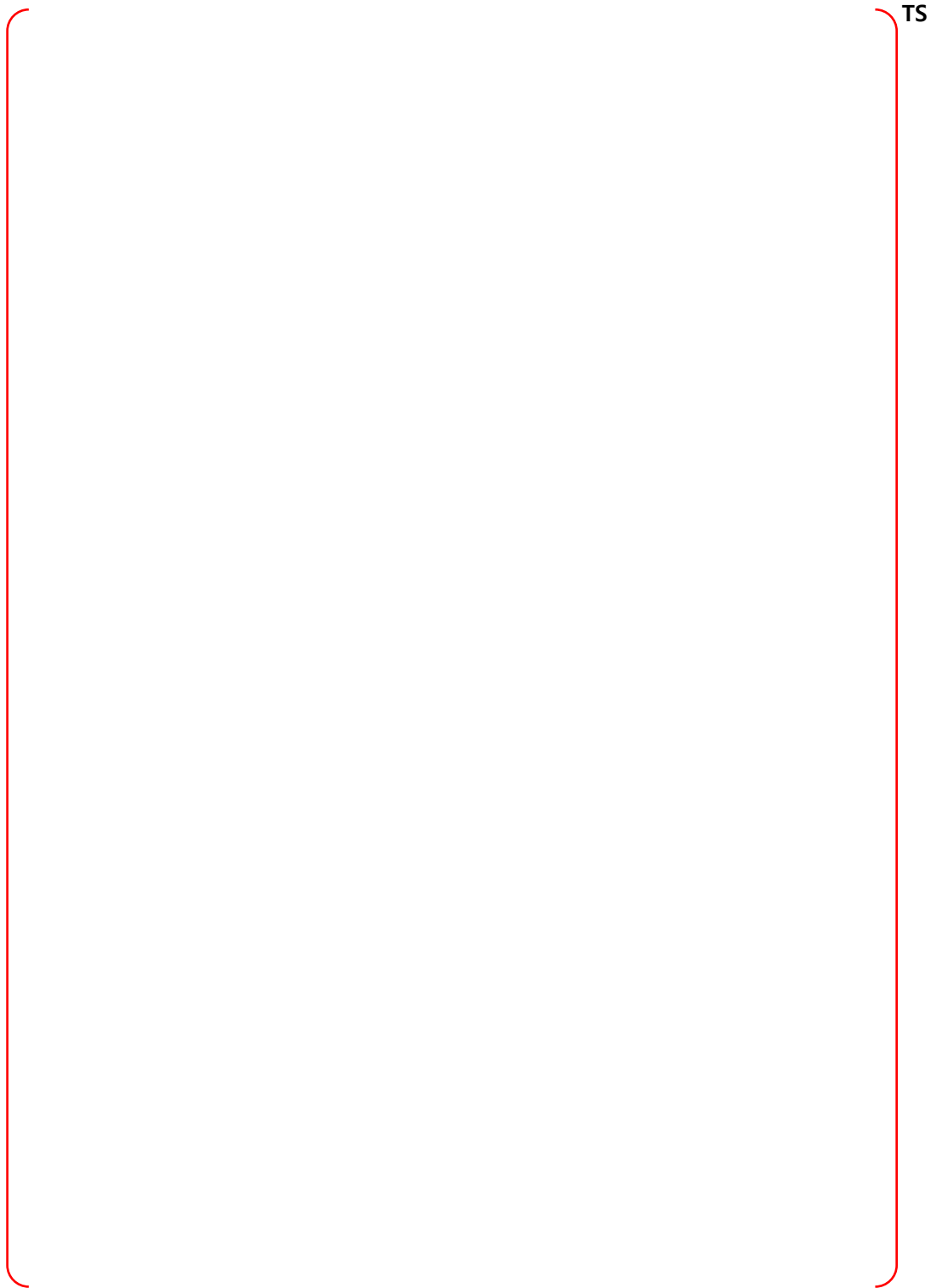


Figure B-52 Node 14, NW Annular Compartment at Elev 136.5' - PRA Sequences

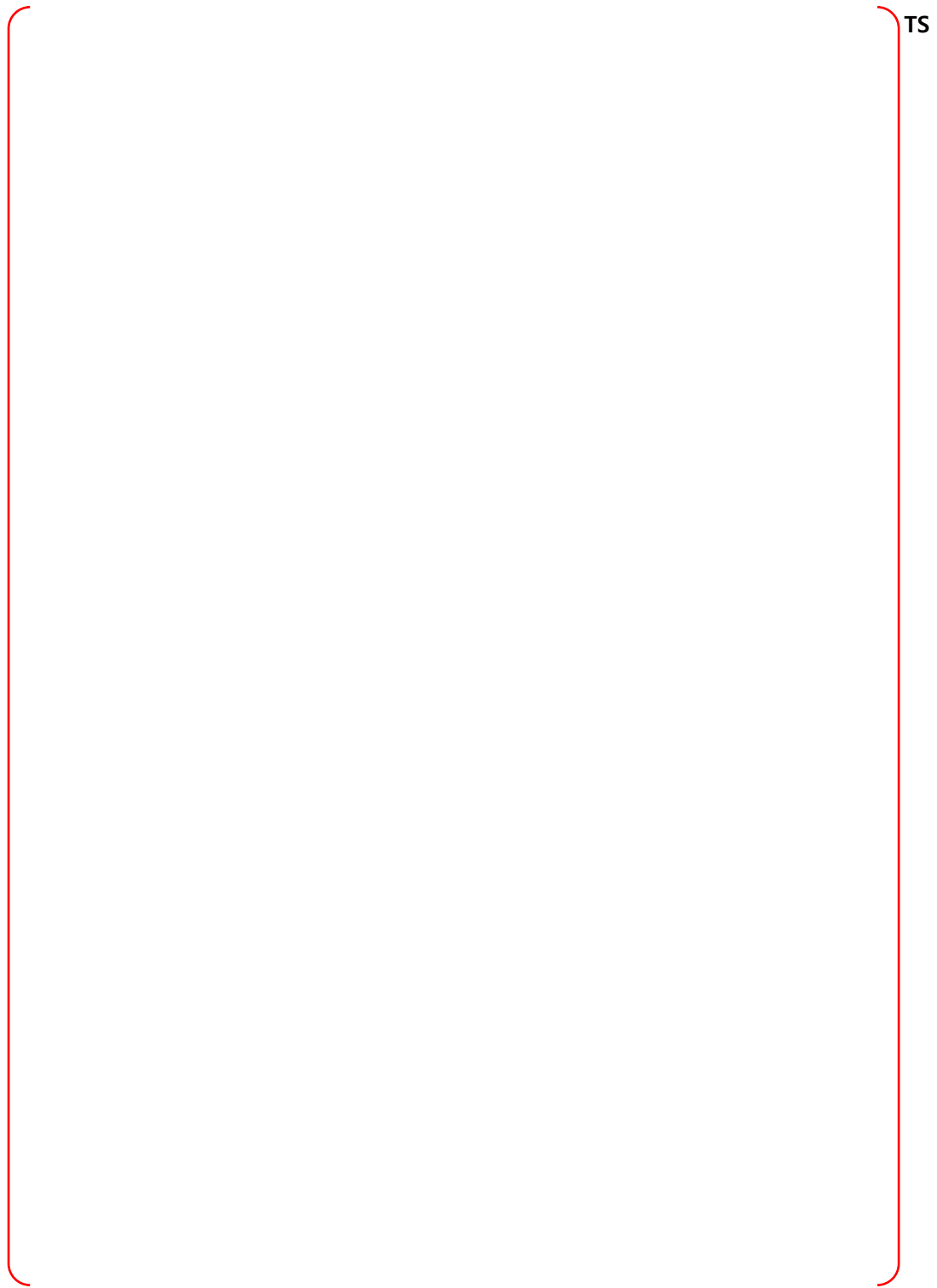


Figure B-53 Node 14, NW Annular Compartment at Elev 136.5' - Bounding Sequences – MCCI

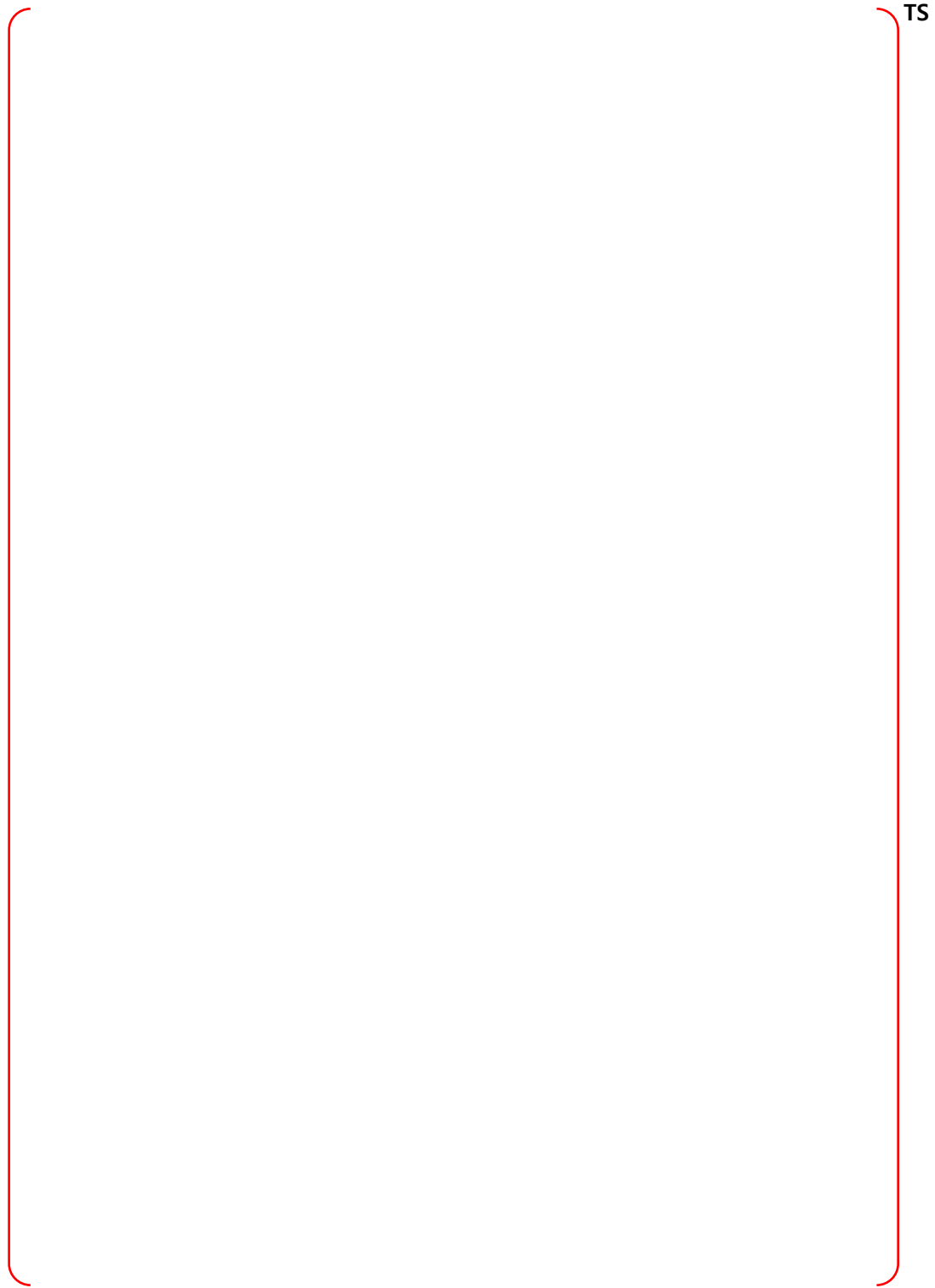


Figure B-54 Node 14, NW Annular Compartment at Elev 136.5' - Bounding Sequences – CP

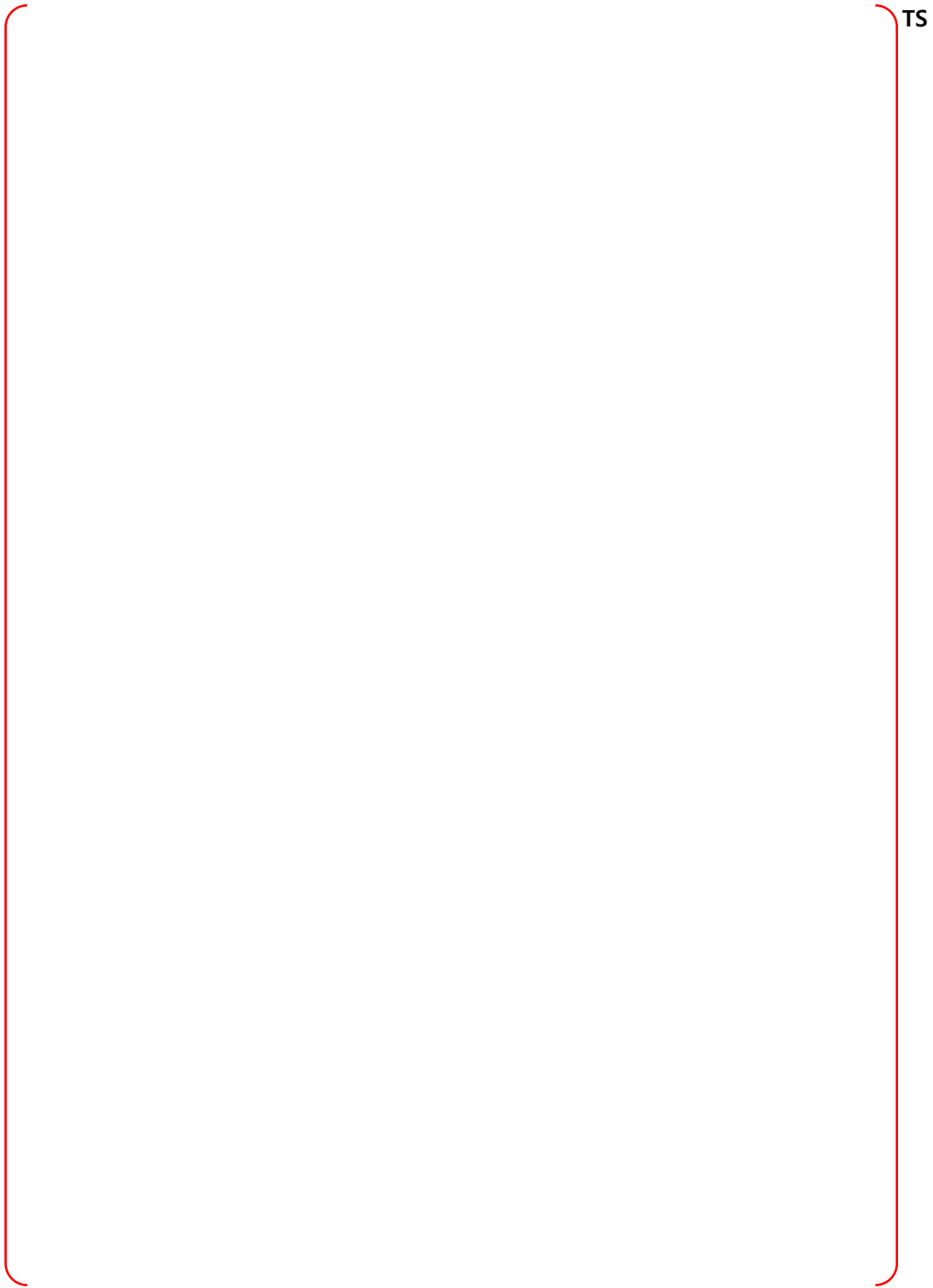


Figure B-55 Node 14, NW Annular Compartment at Elev 136.5' - Bounding Sequences – DF

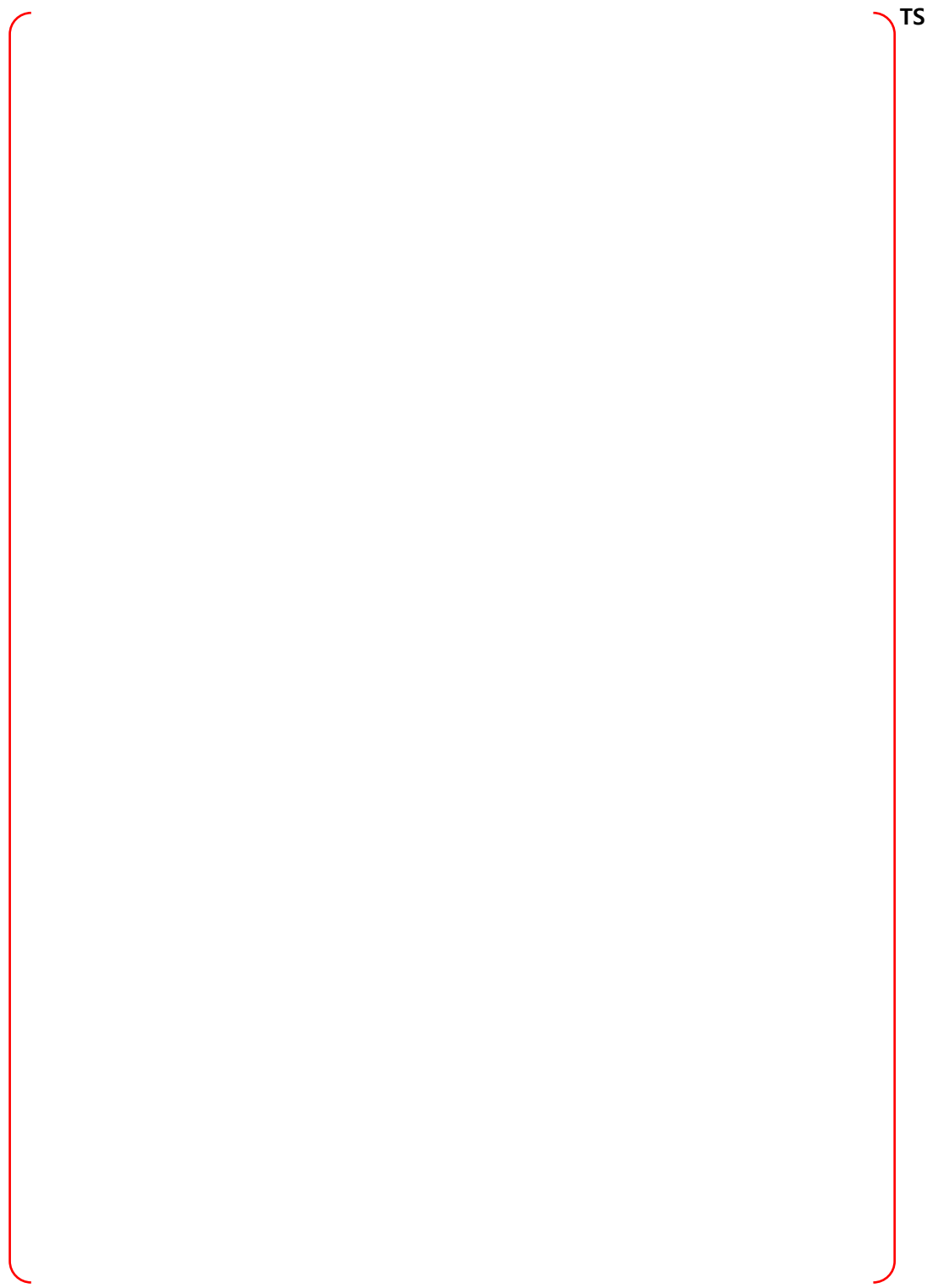


Figure B-56 Node 15, SW Annular Compartment at Elev 136.5' - PRA Sequences

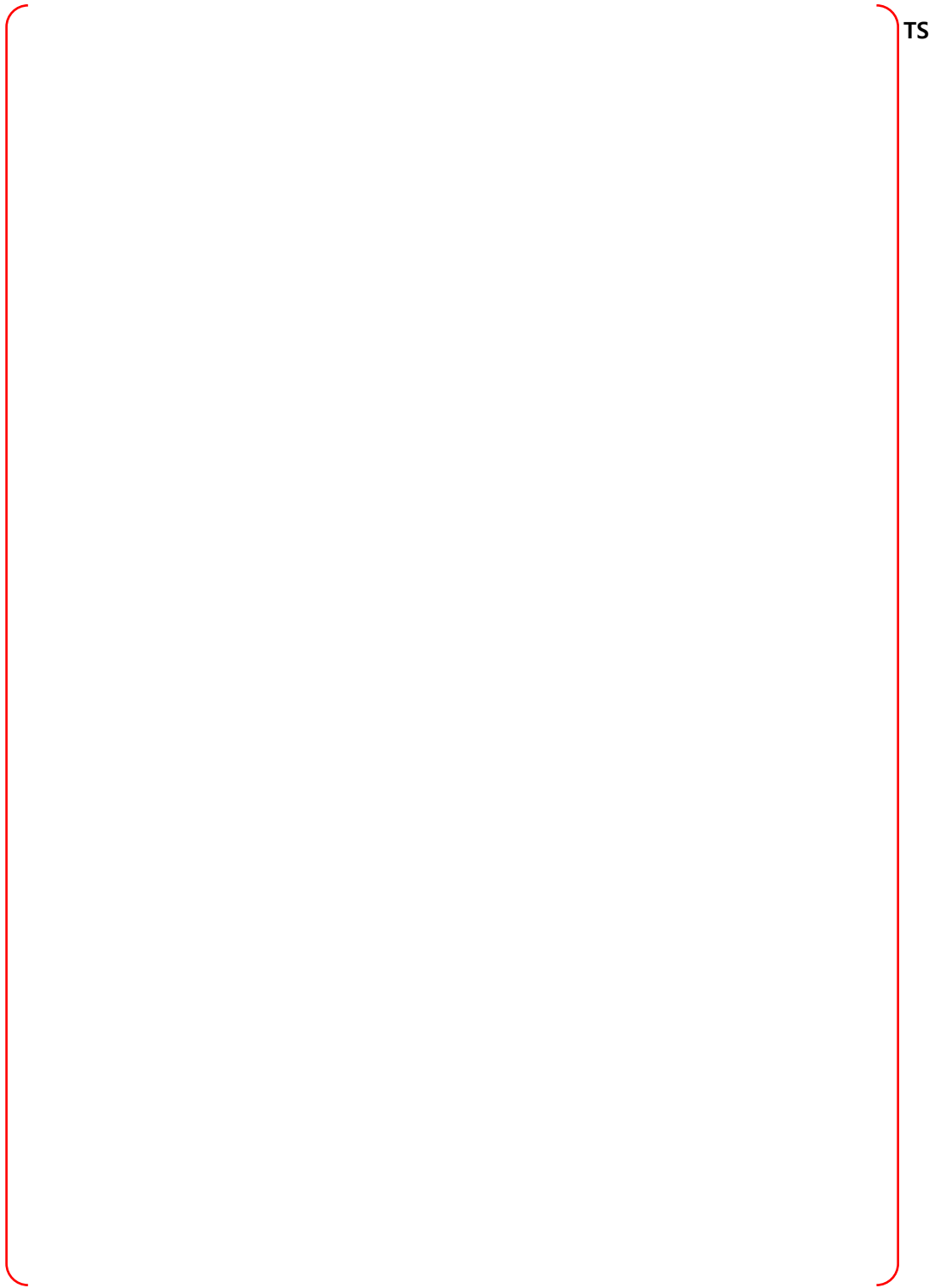


Figure B-57 Node 15, SW Annular Compartment at Elev 136.5' - Bounding Sequences – MCCI

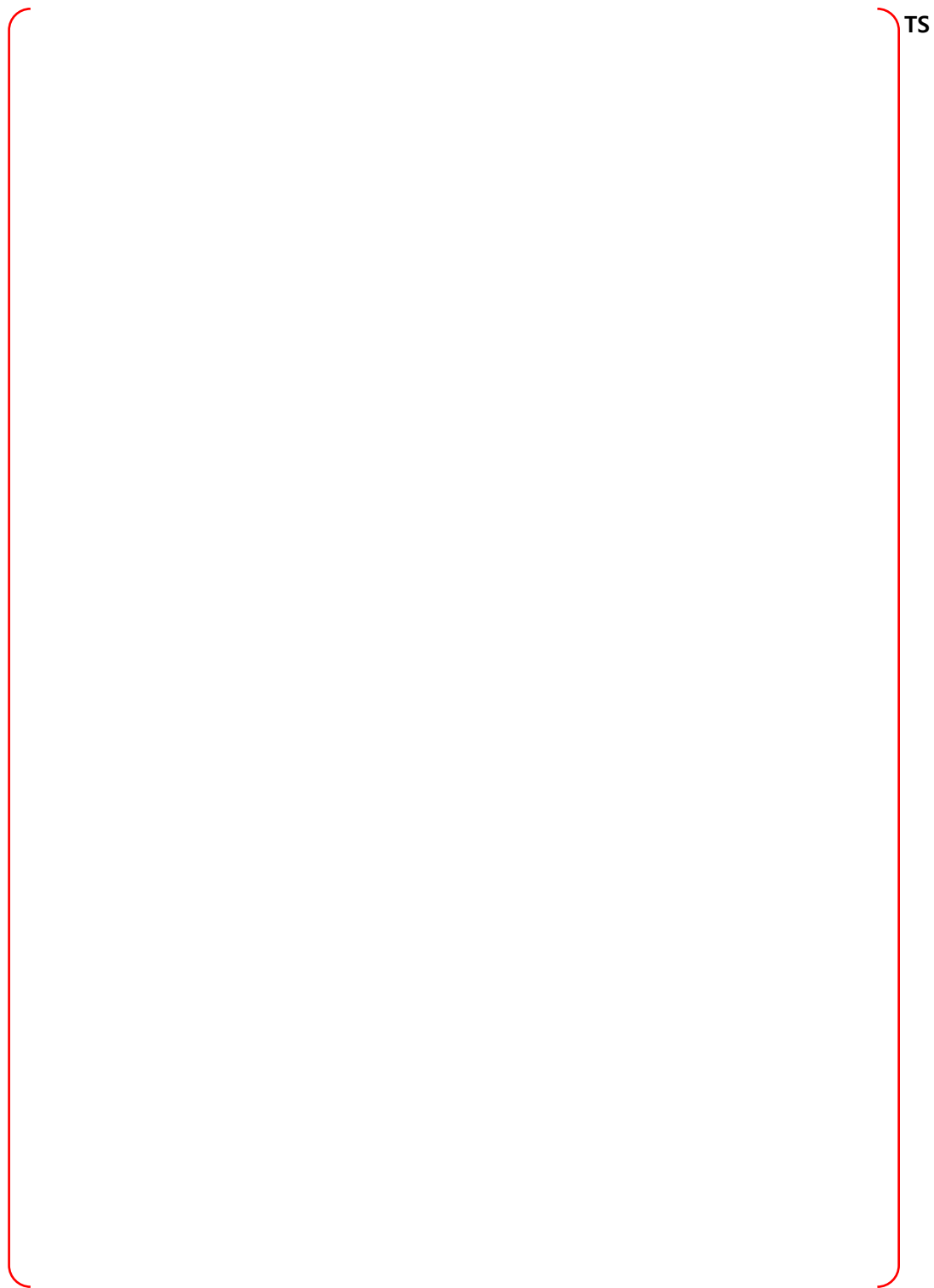


Figure B-58 Node 15, SW Annular Compartment at Elev 136.5' - Bounding Sequences – CP

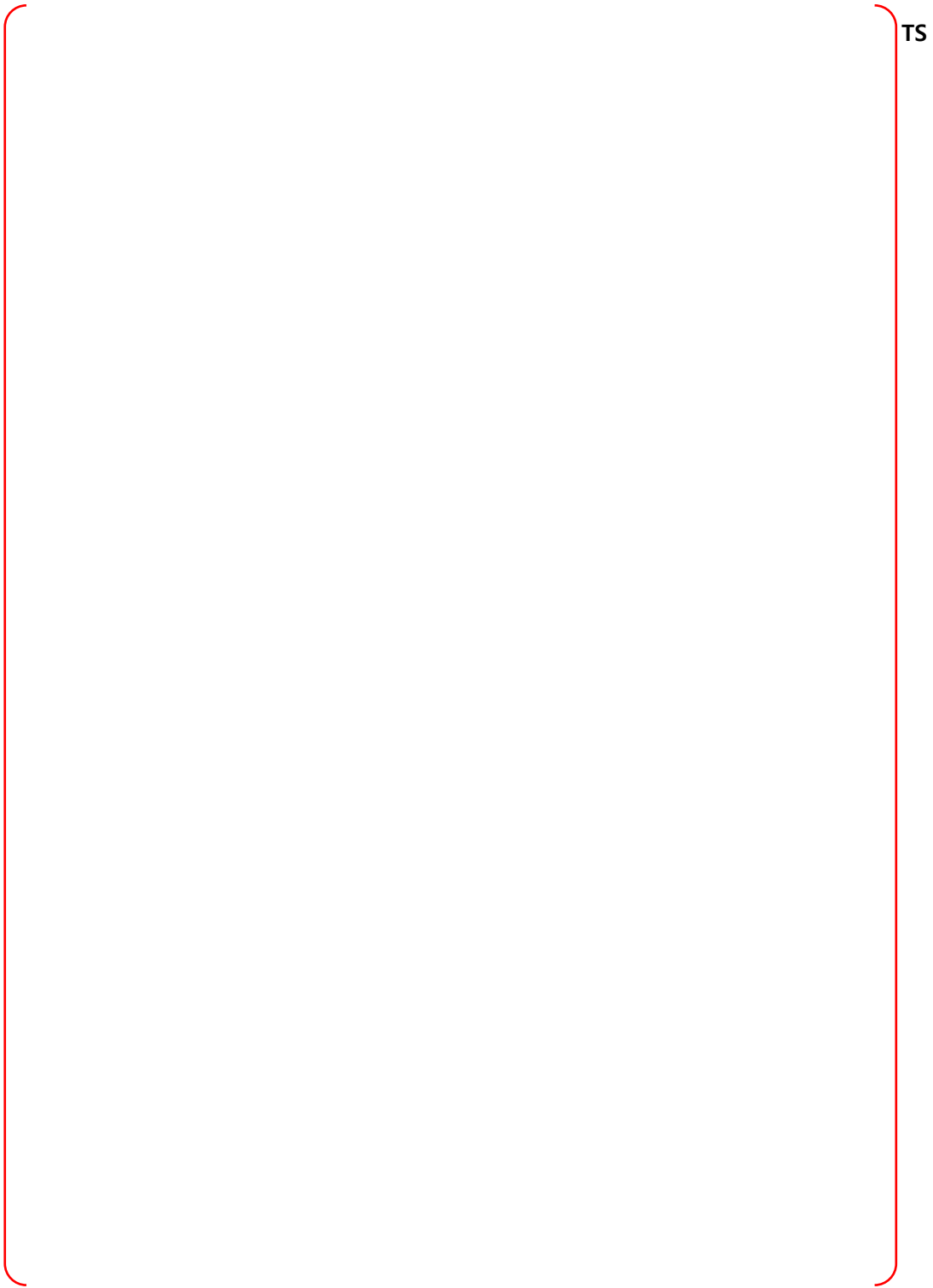


Figure B-59 Node 15, SW Annular Compartment at Elev 136.5' - Bounding Sequences – DF

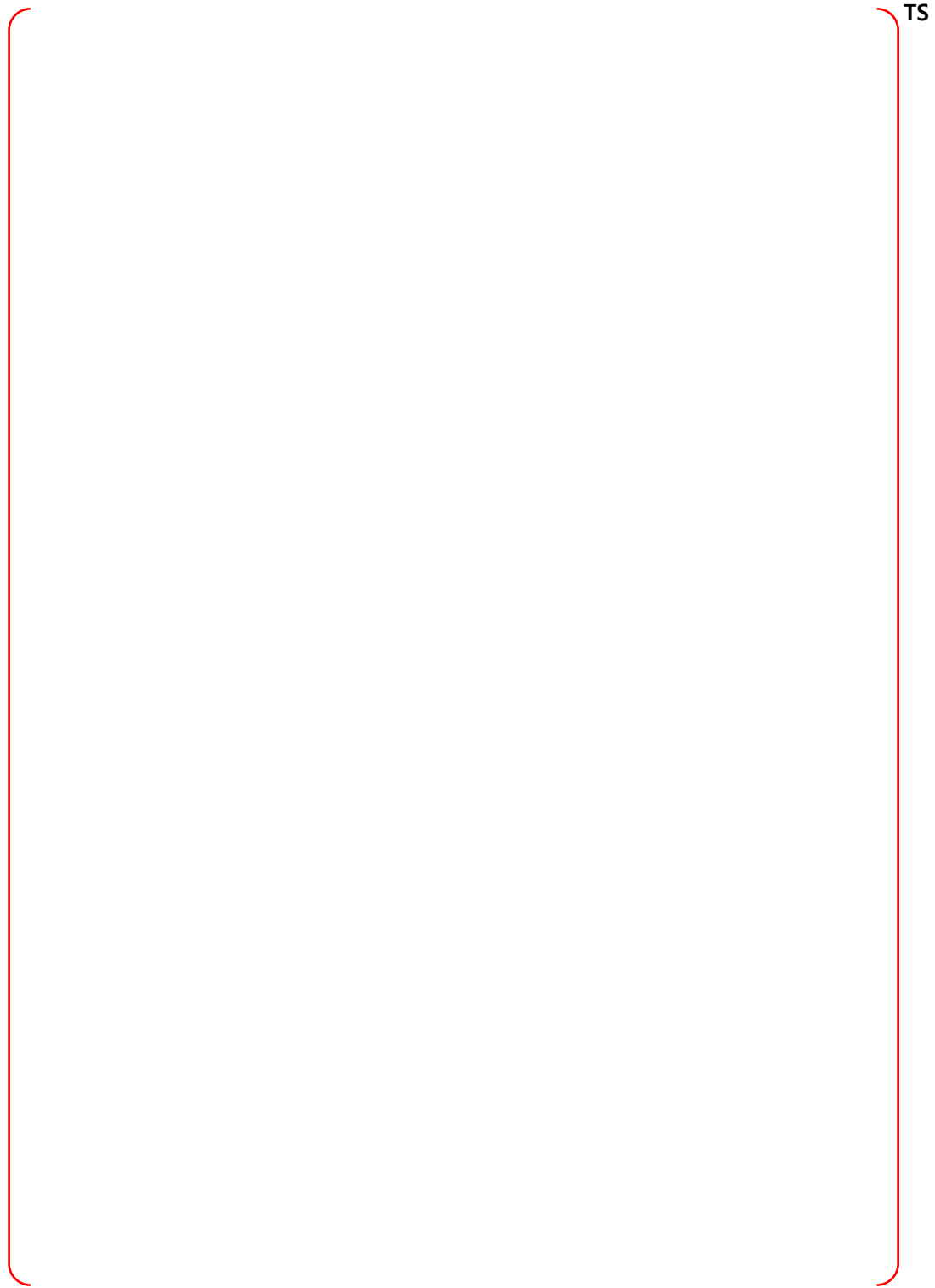


Figure B-60 Node 16, Refueling Pool - PRA Sequences

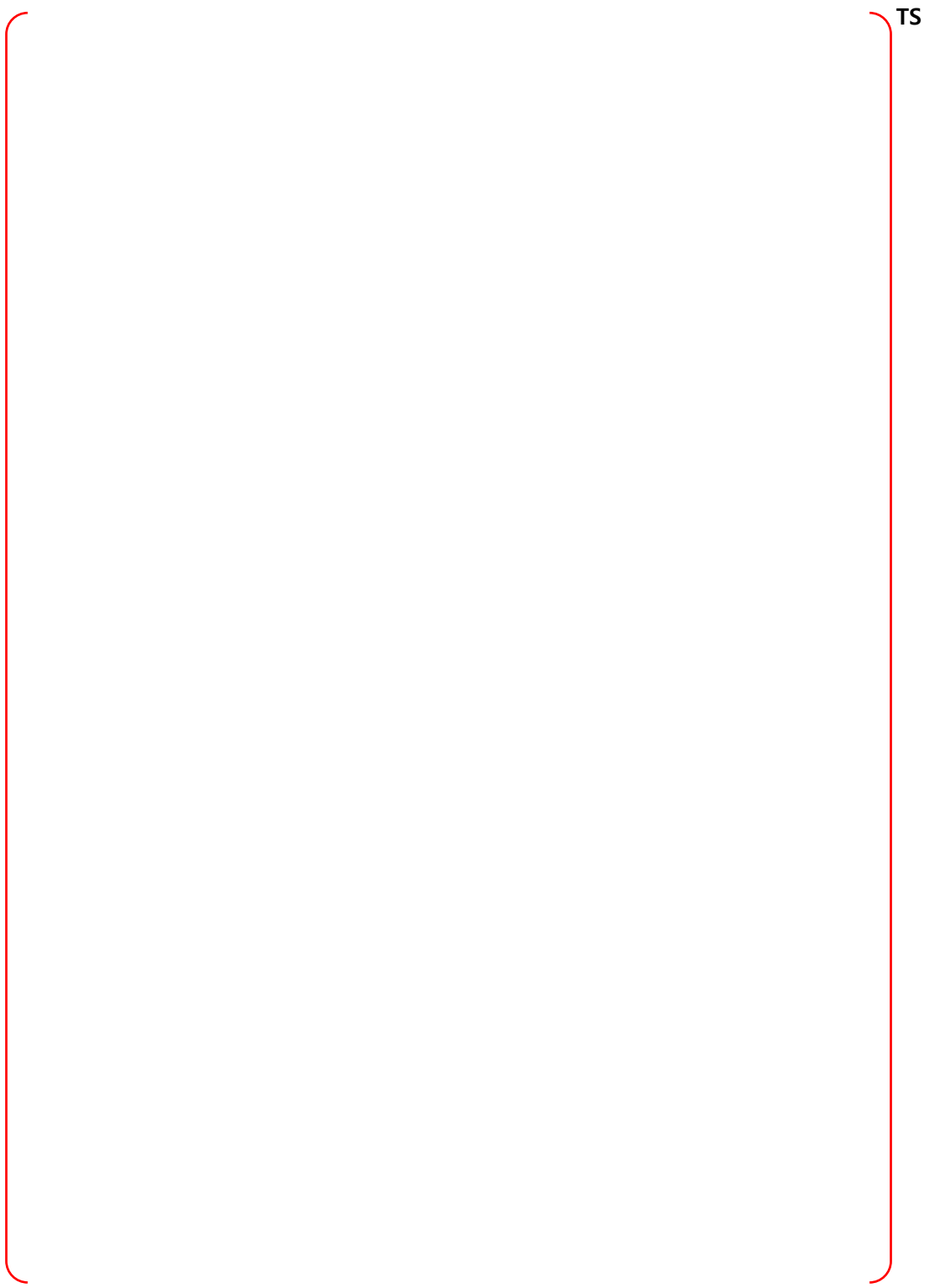


Figure B-61 Node 16, Refueling Pool - Bounding Sequences – MCCI

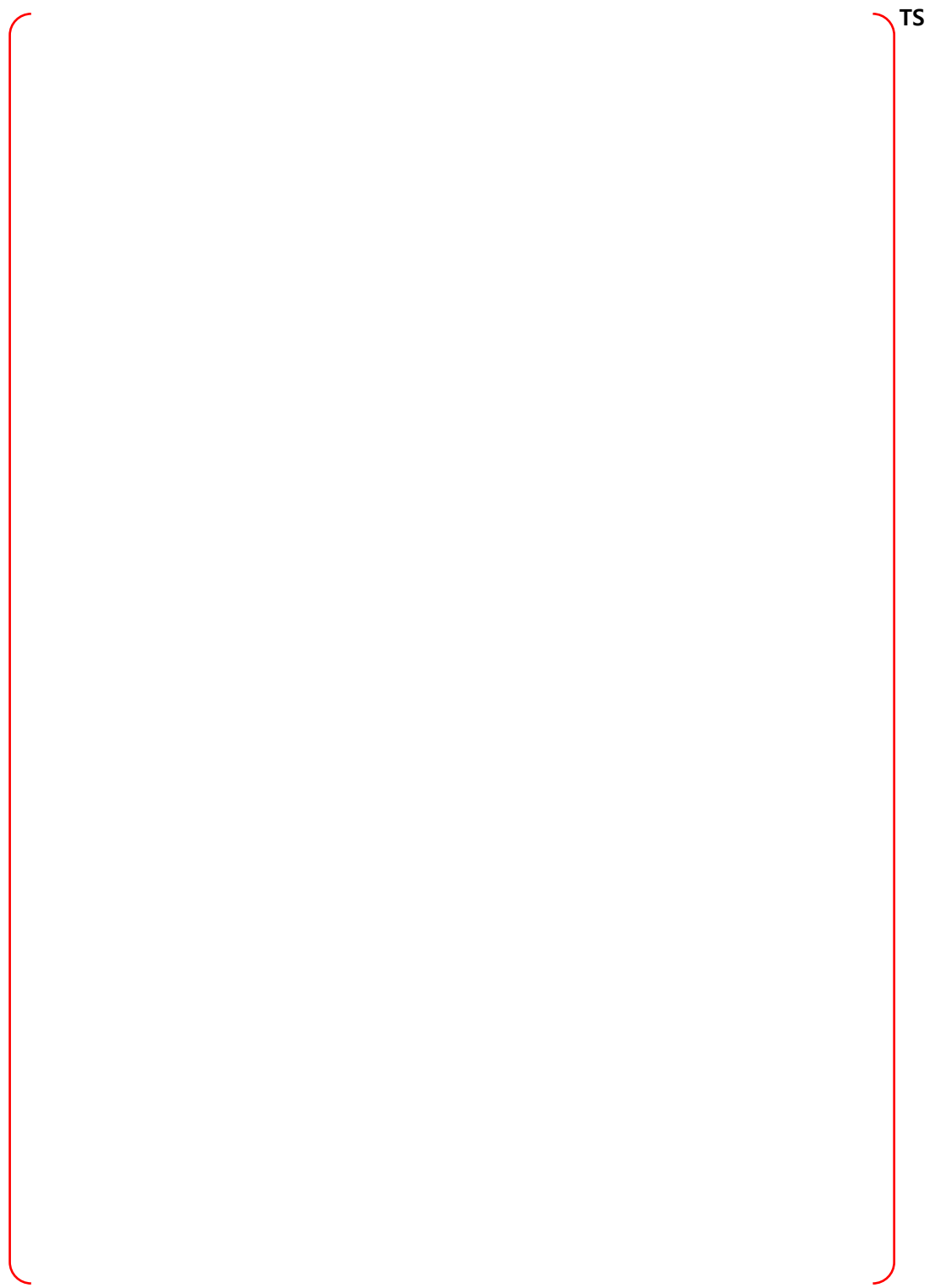


Figure B-62 Node 16, Refueling Pool - Bounding Sequences – CP

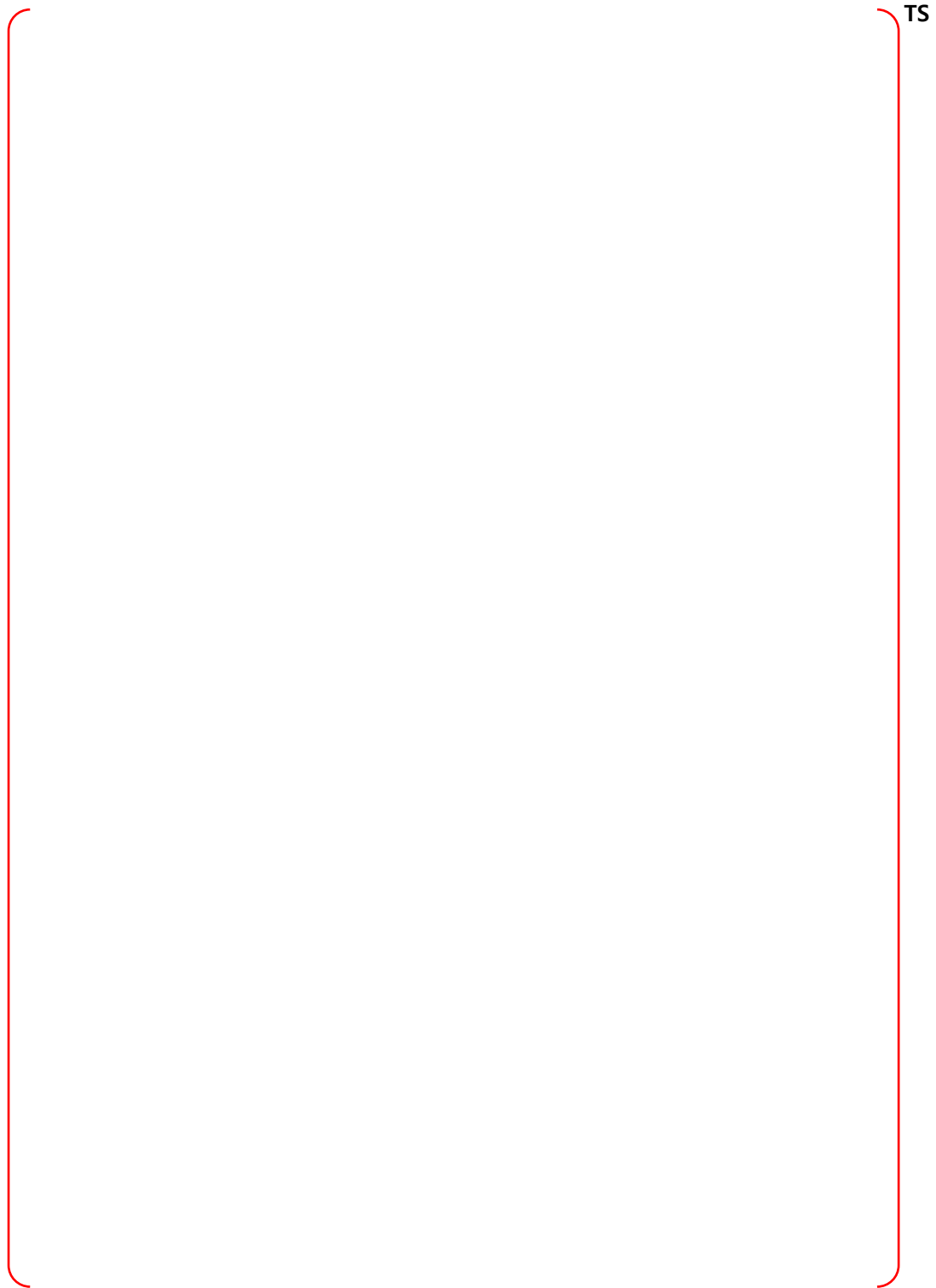


Figure B-63 Node 16, Refueling Pool - Bounding Sequences – DF

TS

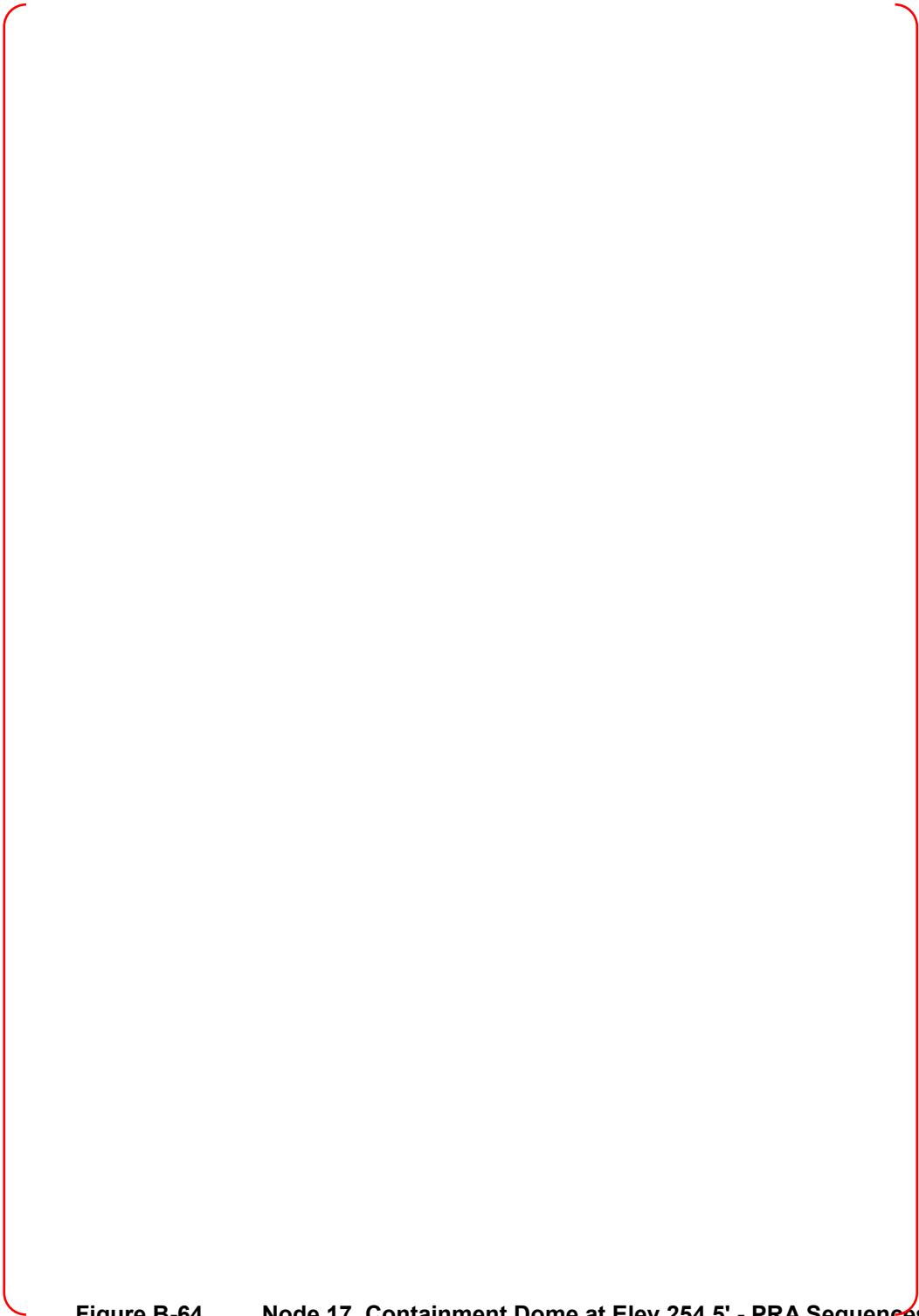


Figure B-64 Node 17, Containment Dome at Elev 254.5' - PRA Sequences

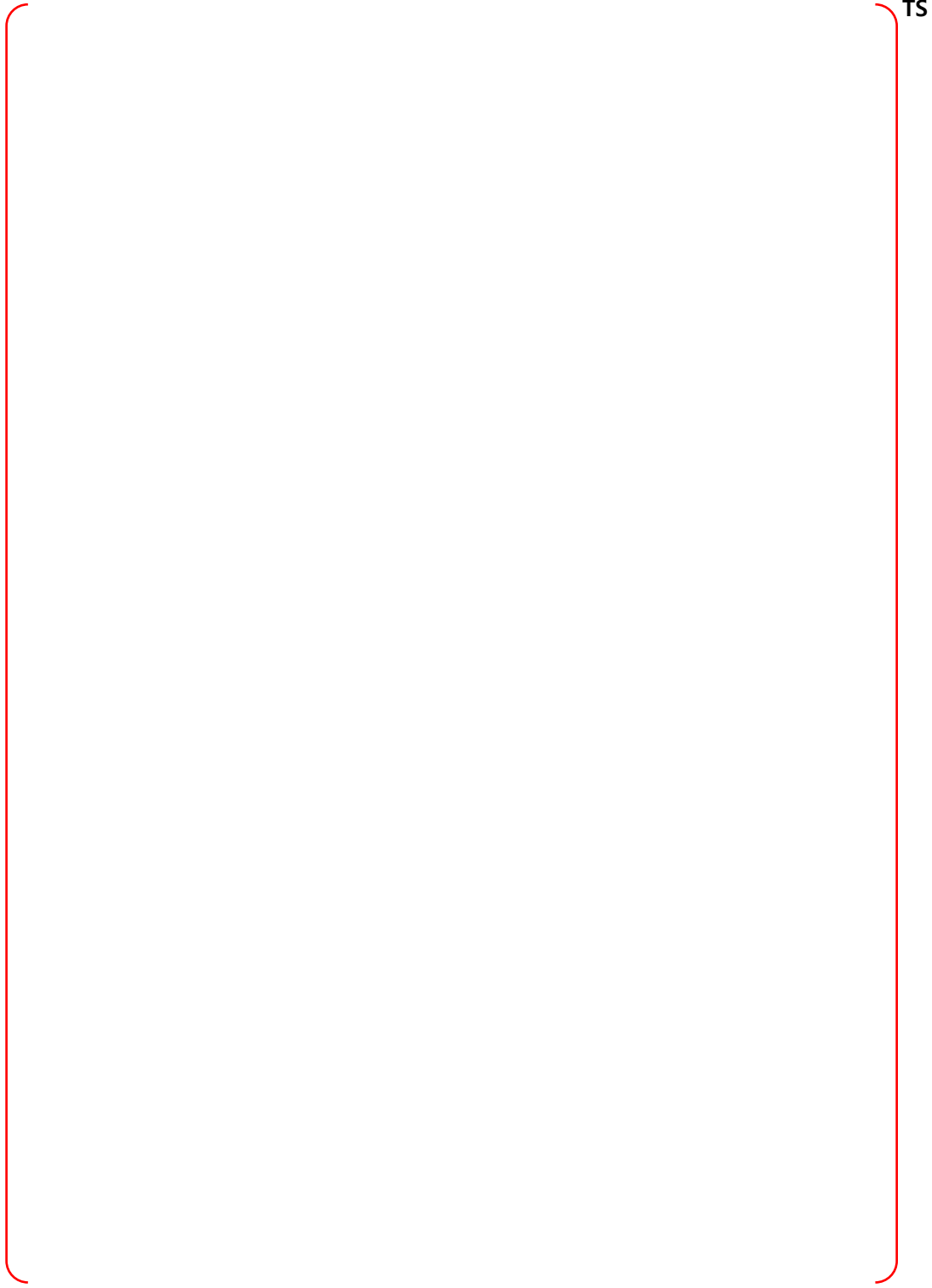


Figure B-65 Node 17, Containment Dome at Elev 254.5' - Bounding Sequences – MCCI

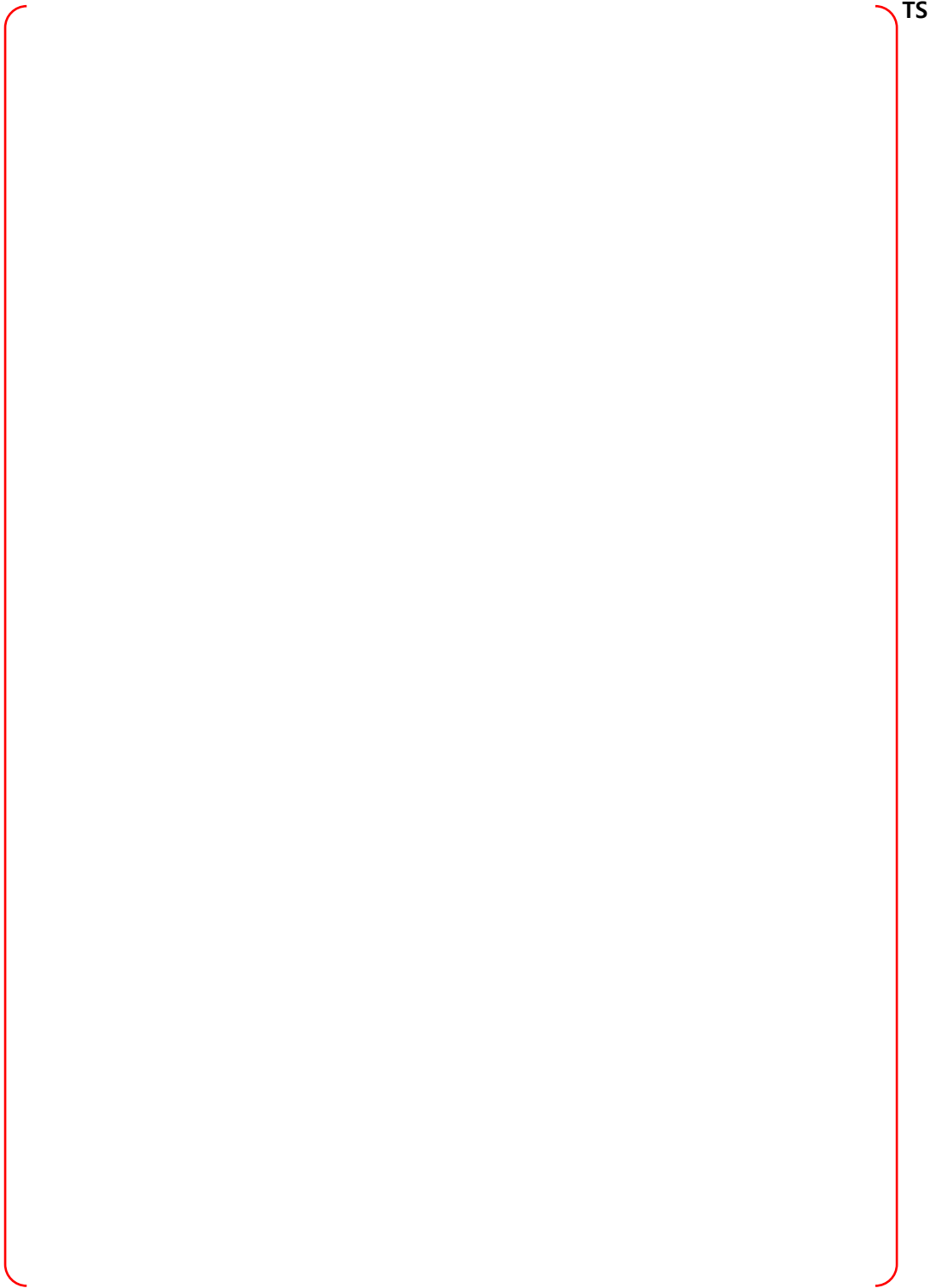


Figure B-66 Node 17, Containment Dome at Elev 254.5' - Bounding Sequences – CP

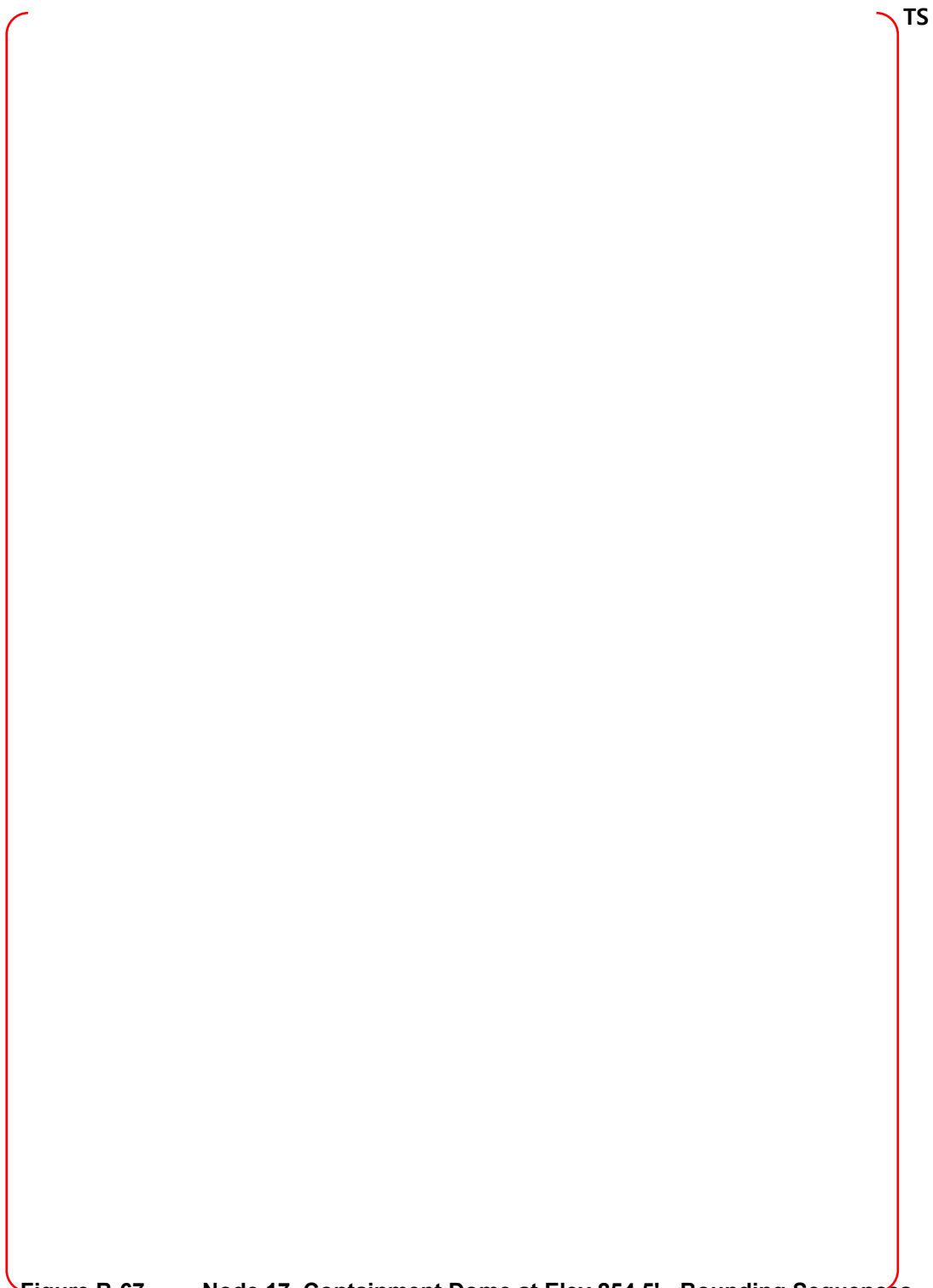


Figure B-67 Node 17, Containment Dome at Elev 254.5' - Bounding Sequences – DF

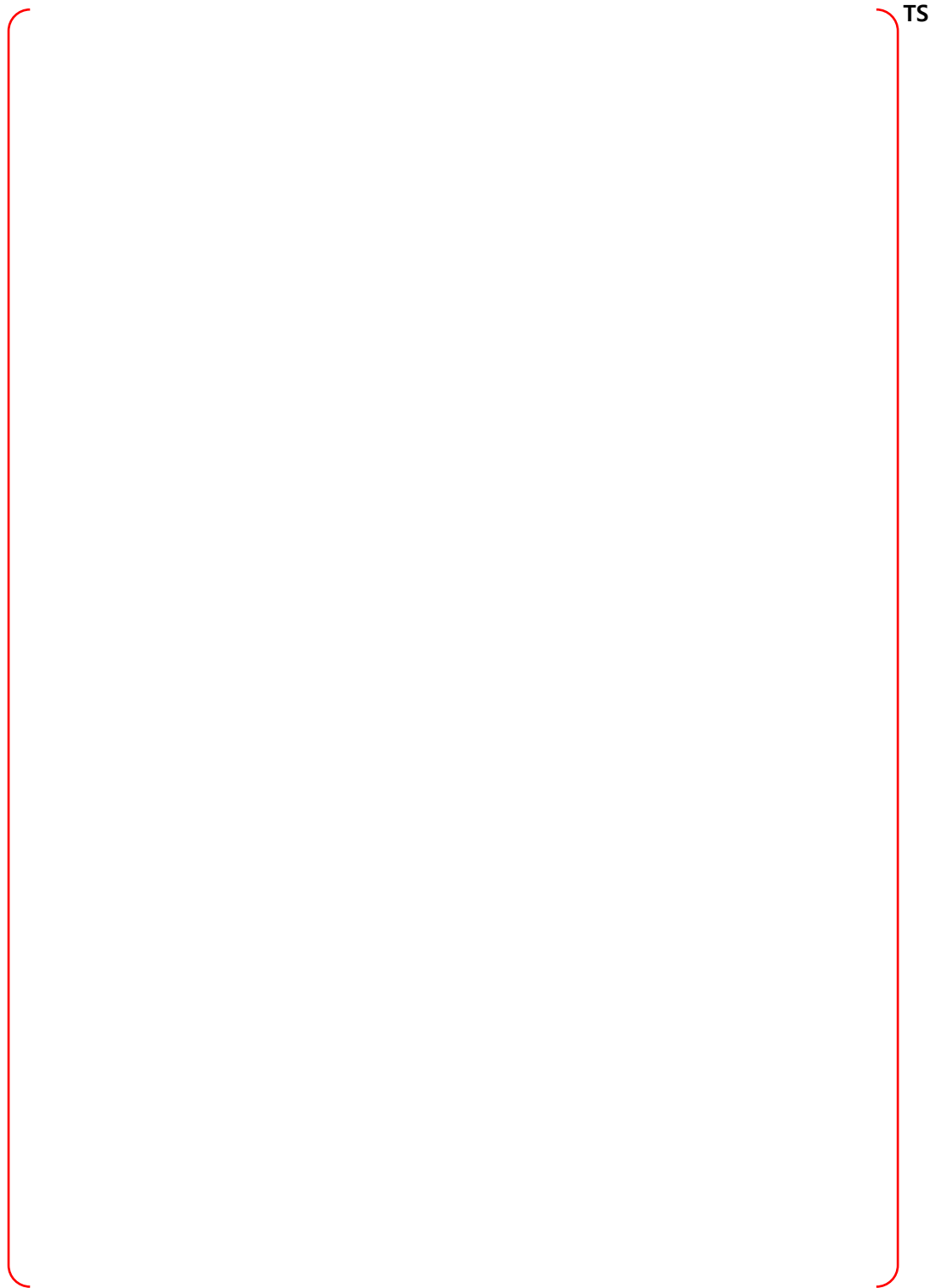


Figure B-68 Node 18, Upper Containment #2 - PRA Sequences

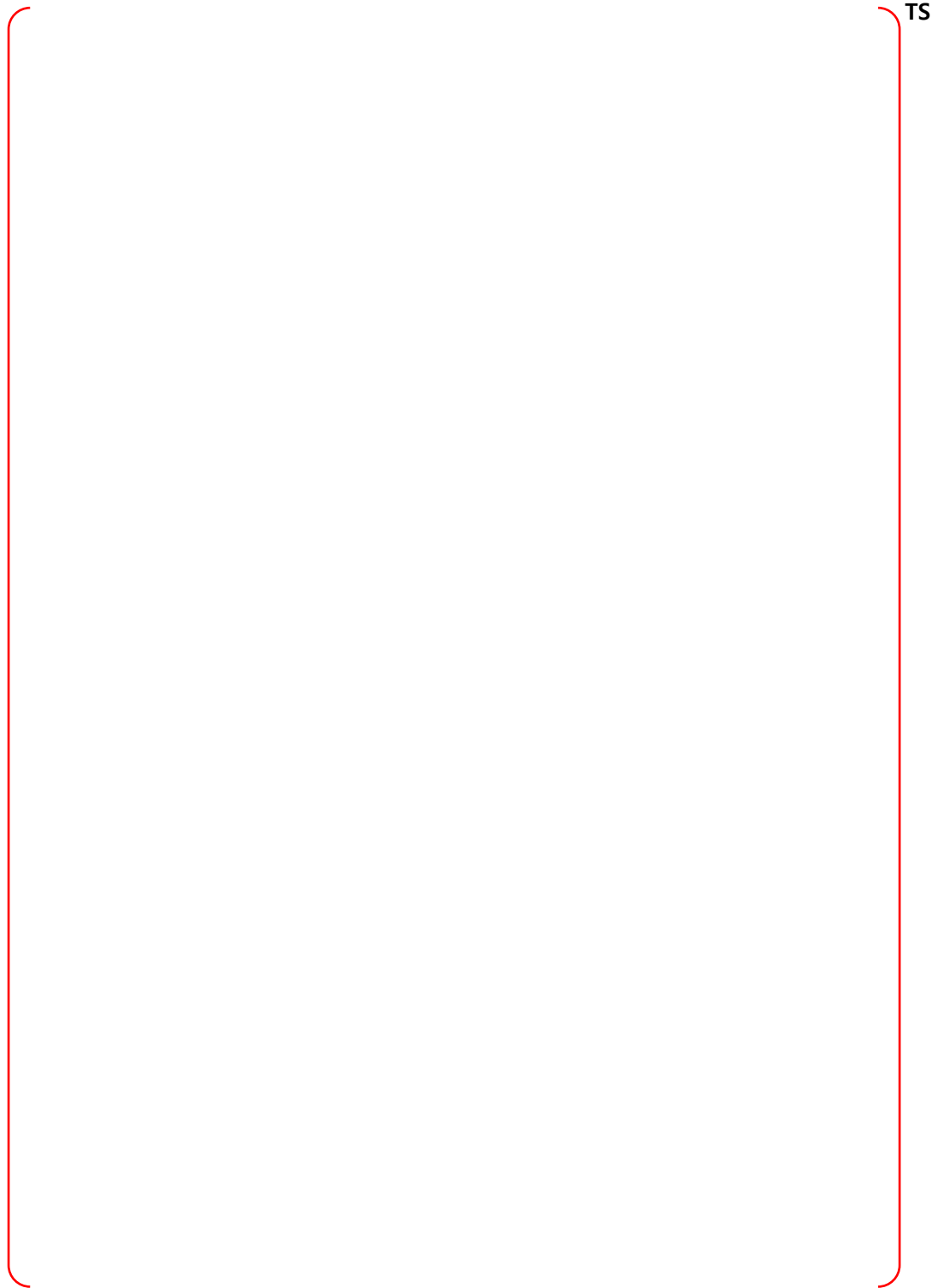


Figure B-69 Node 18, Upper Containment #2 - Bounding Sequences – MCCI

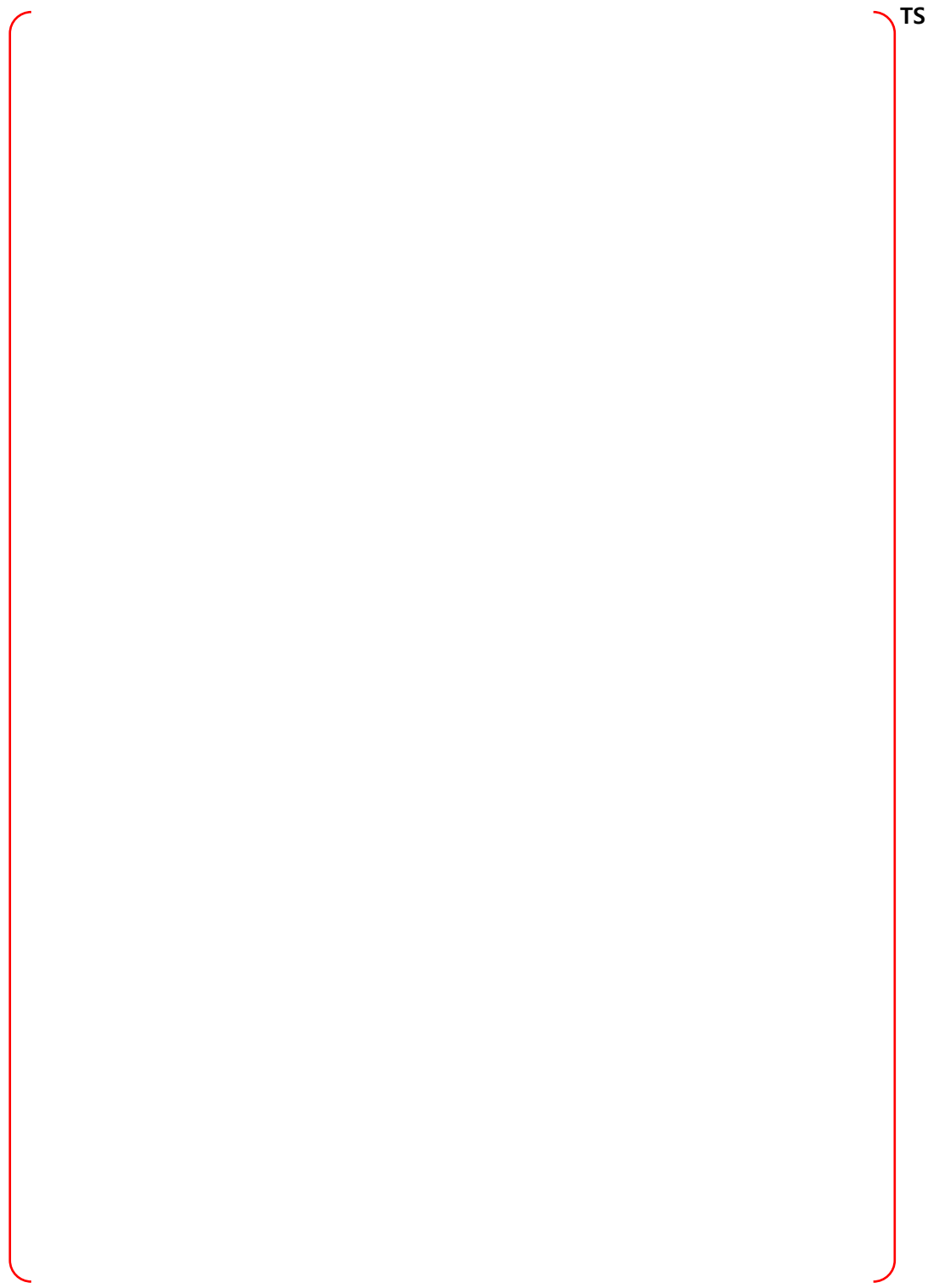


Figure B-70 Node 18, Upper Containment #2 - Bounding Sequences – CP

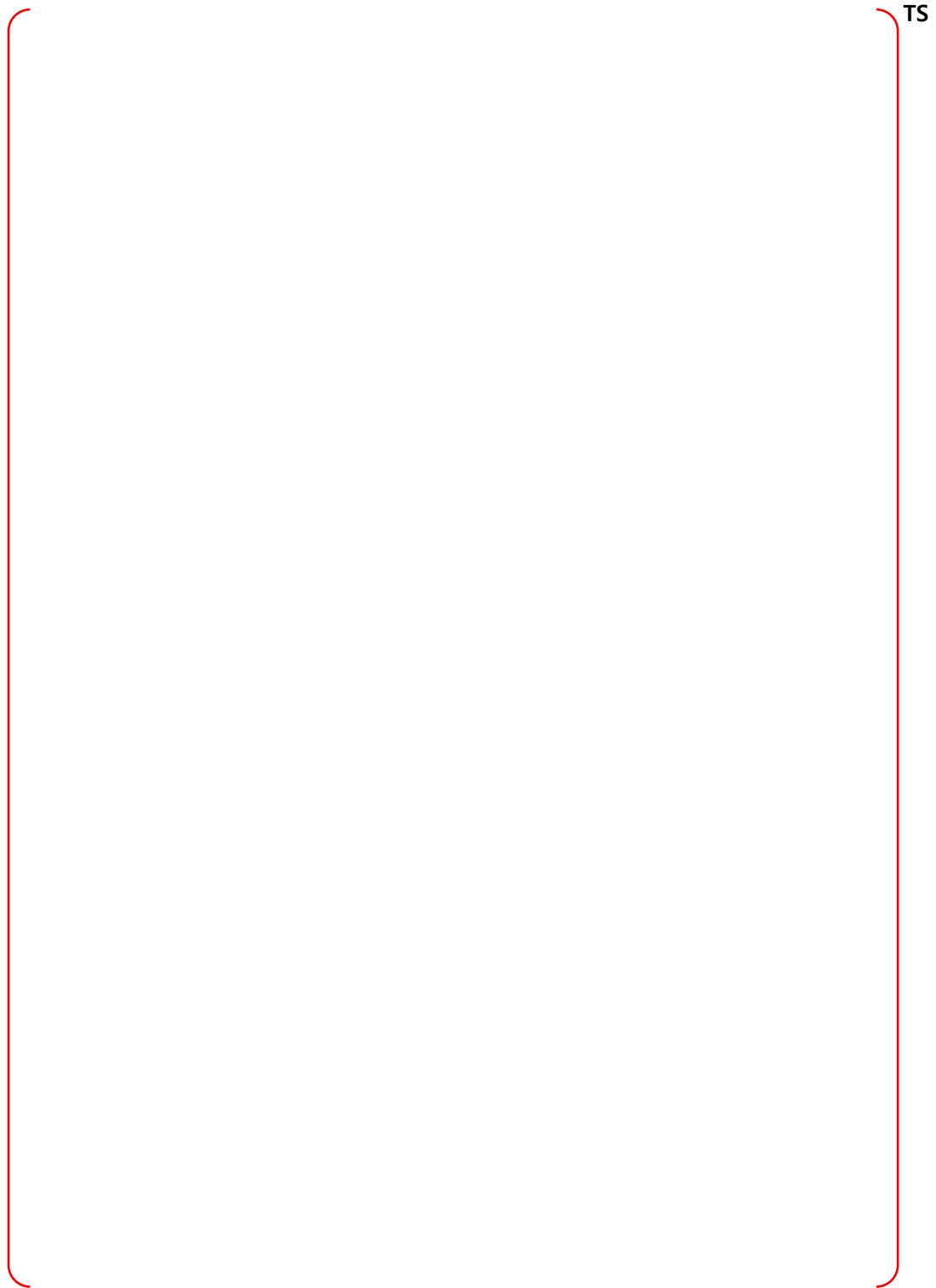


Figure B-71 Node 18, Upper Containment #2 - Bounding Sequences – DF

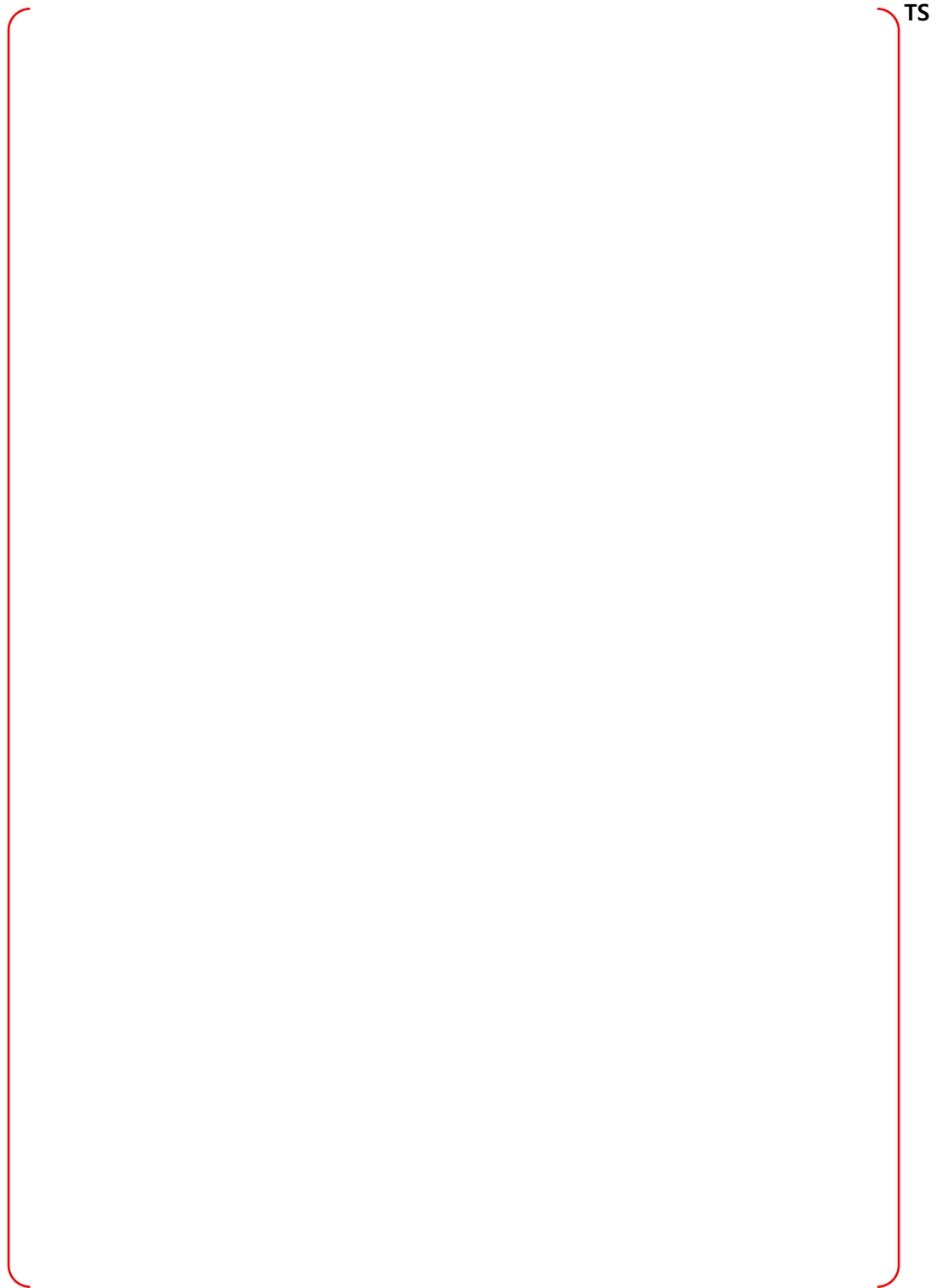


Figure B-72 Node 19, Upper Containment #1 - PRA Sequences

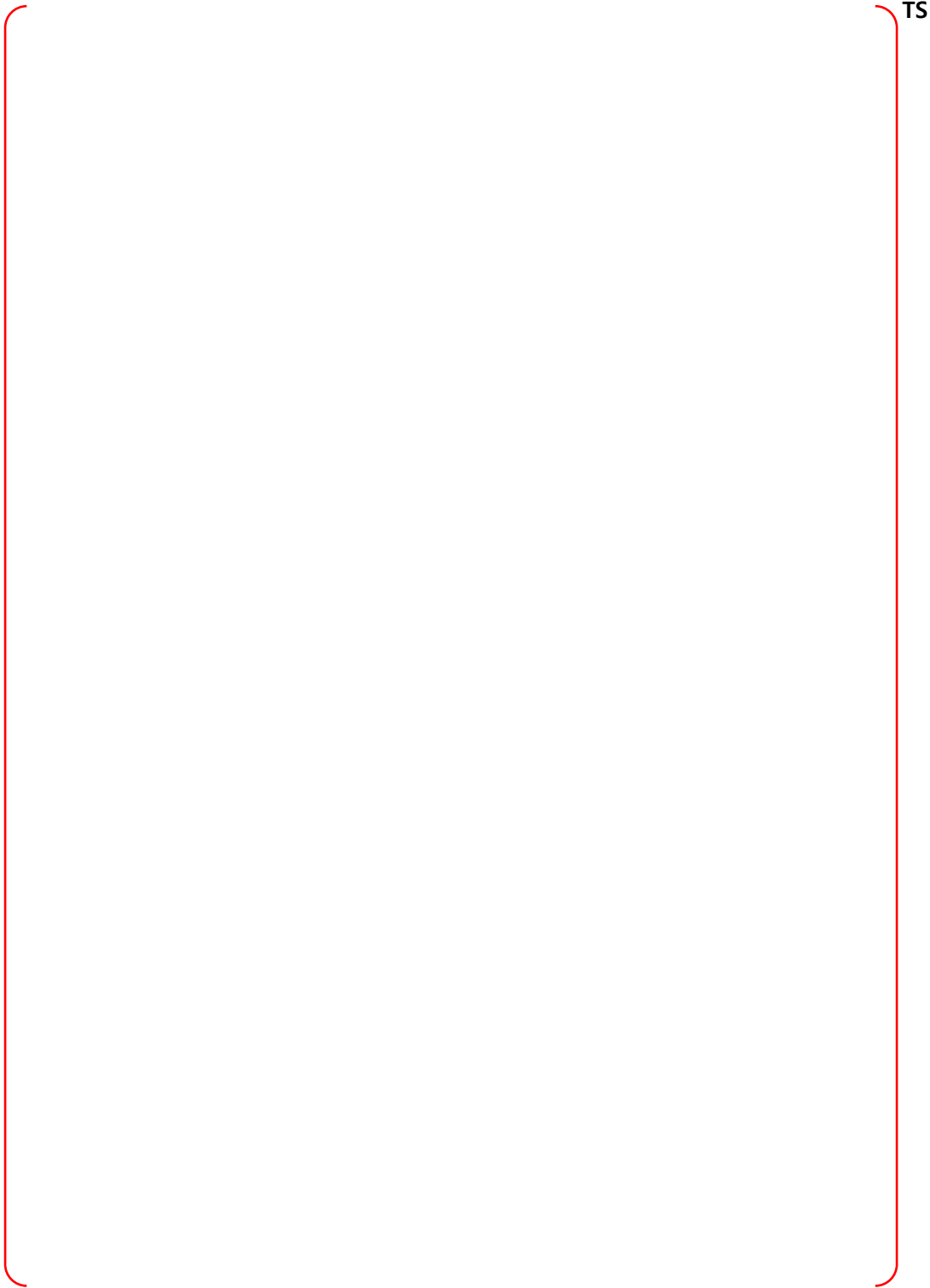


Figure B-73 Node 19, Upper Containment #1 - Bounding Sequences – MCCI

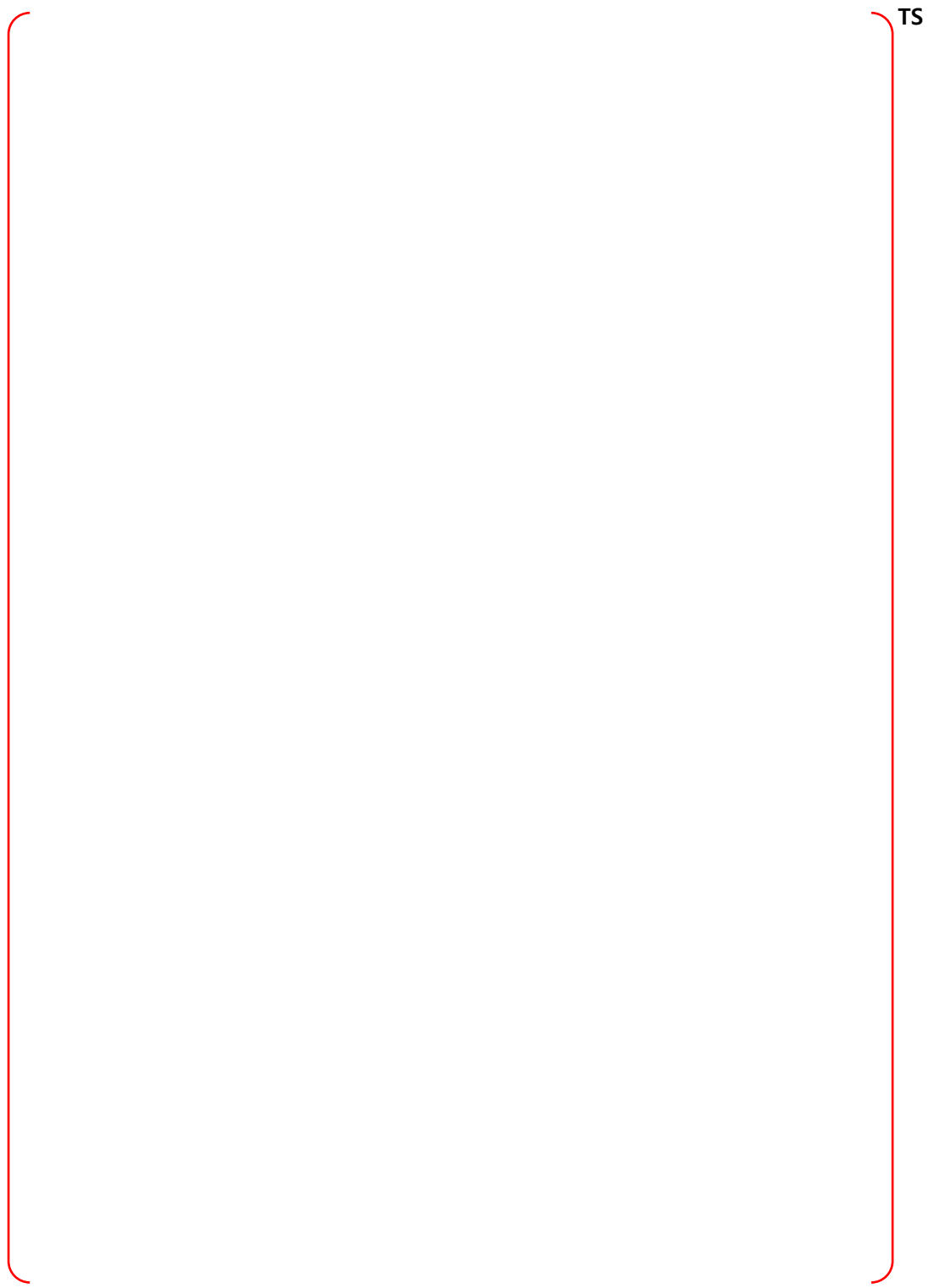


Figure B-74 Node 19, Upper Containment #1 - Bounding Sequences – CP

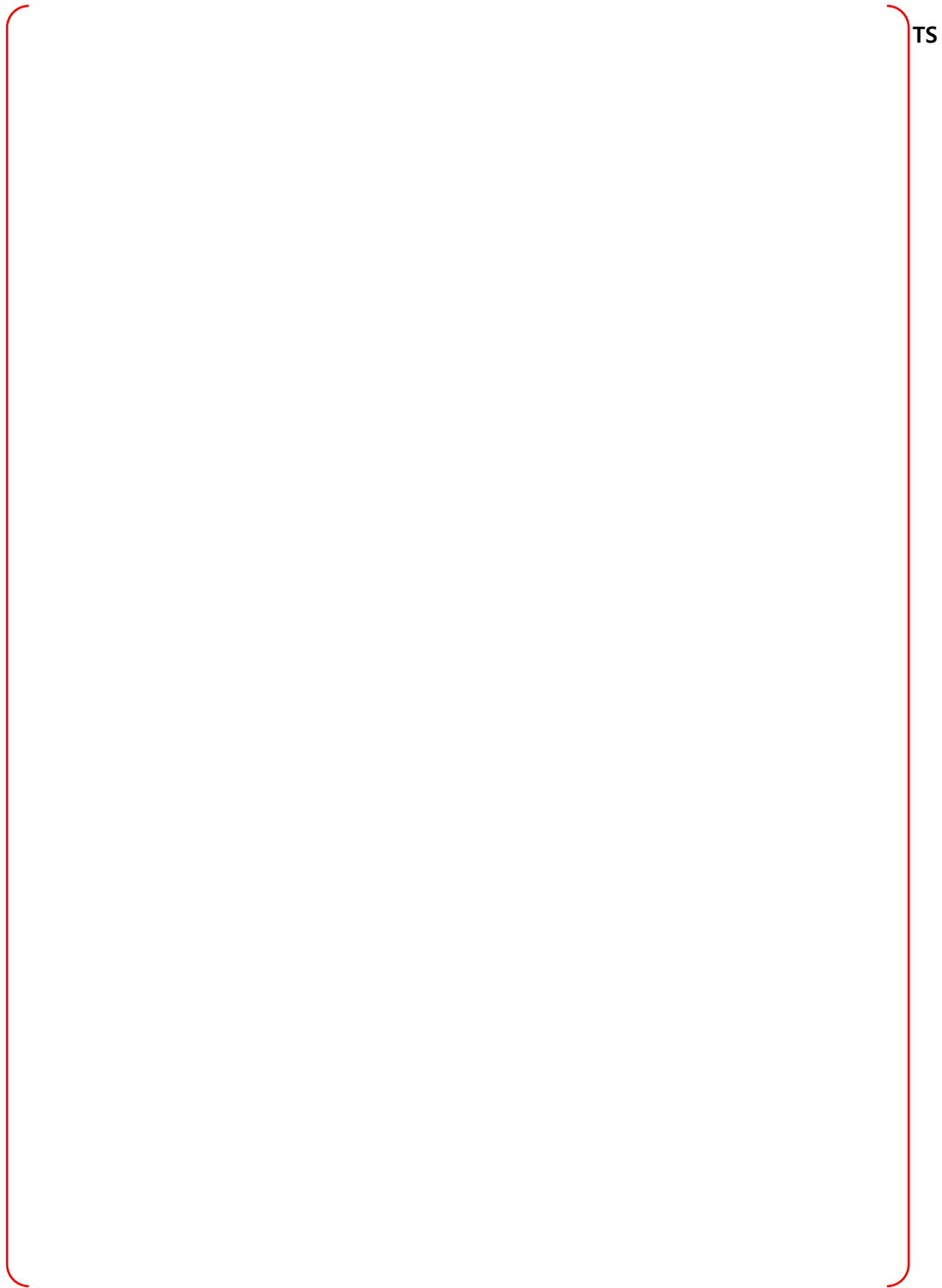


Figure B-75 Node 19, Upper Containment #1 - Bounding Sequences – DF

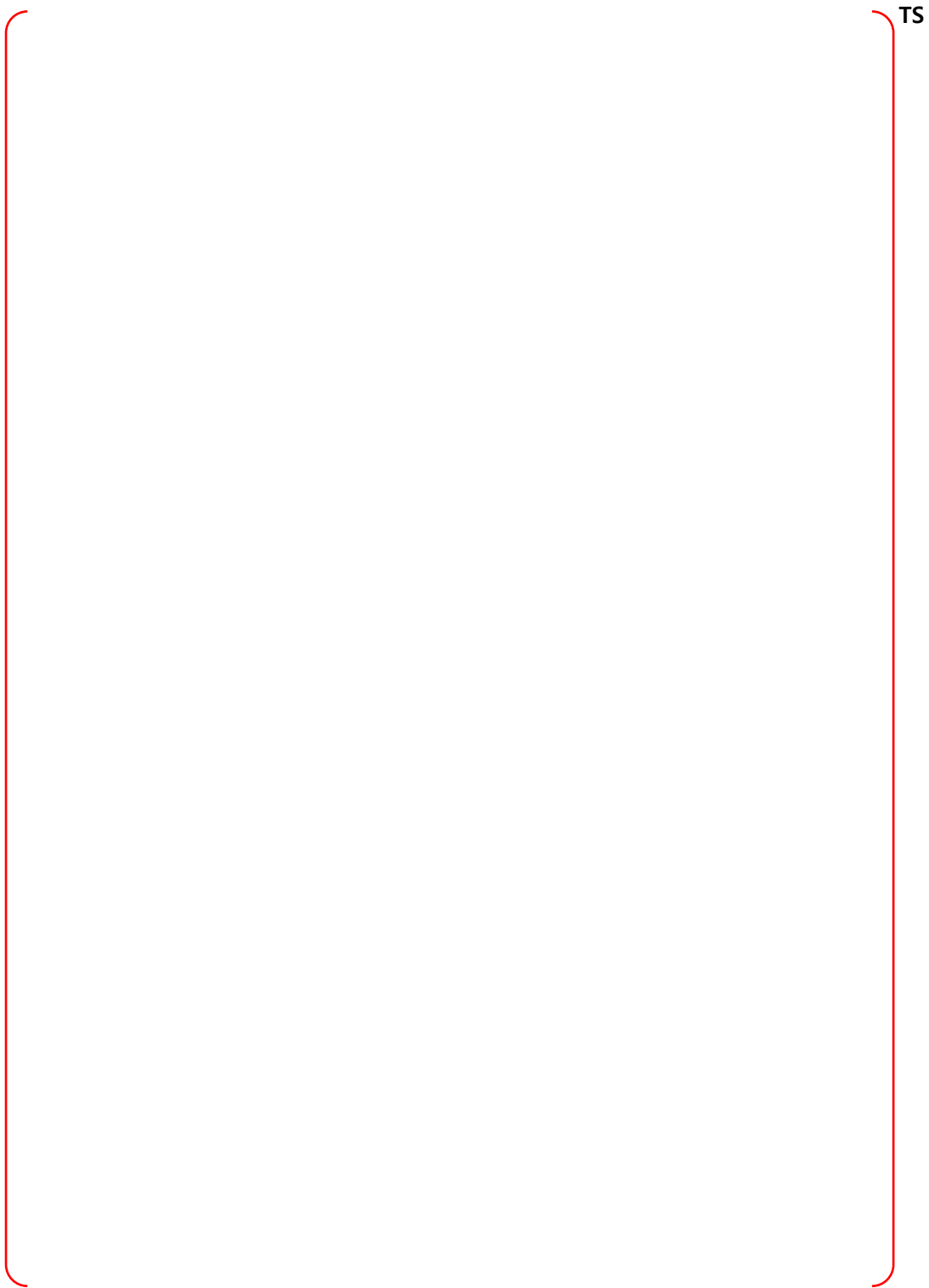


Figure B-76 Node 20, Reactor Drain Tank Room - PRA Sequences

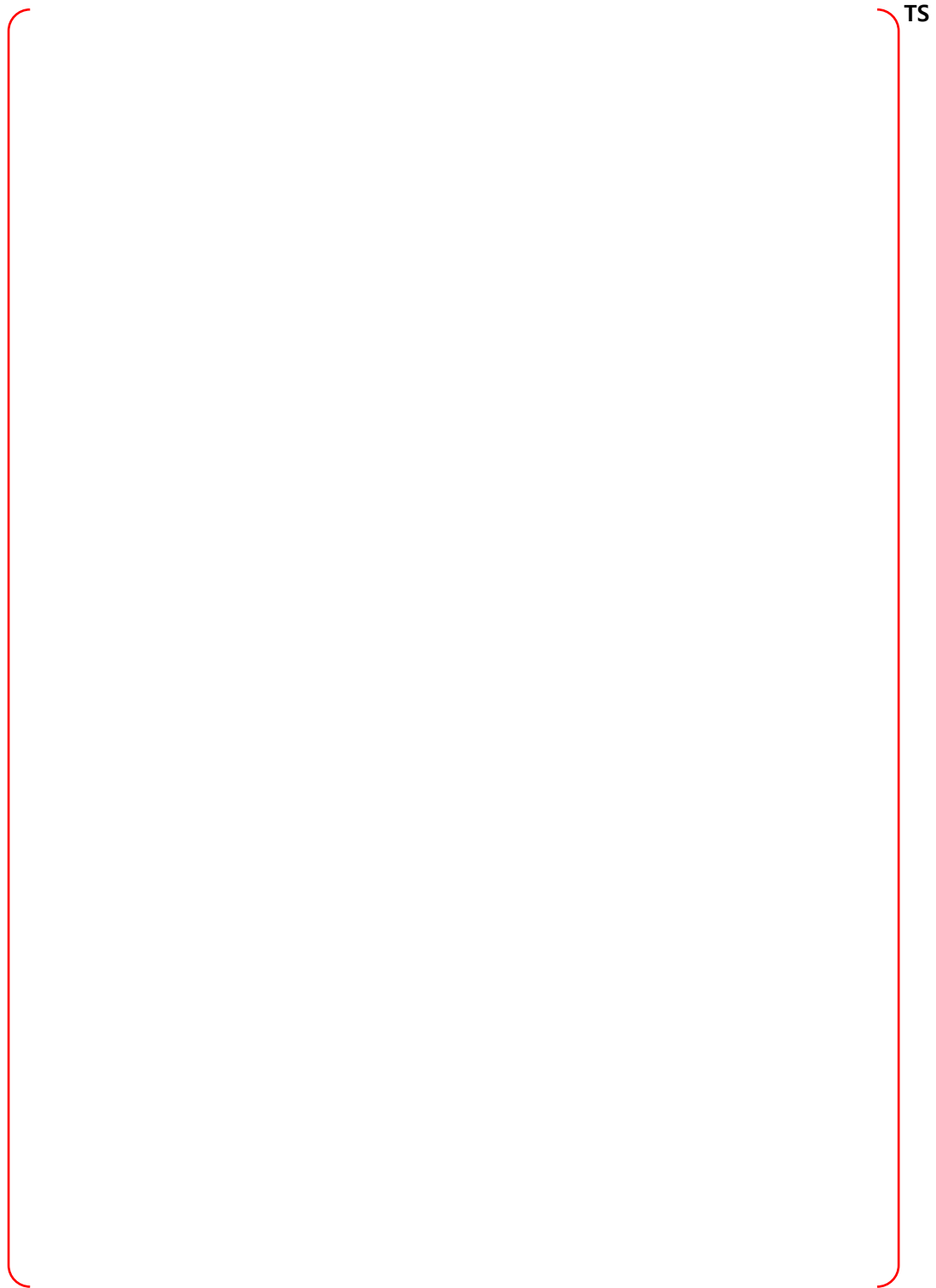


Figure B-77 Node 20, Reactor Drain Tank Room - Bounding Sequences – MCCI

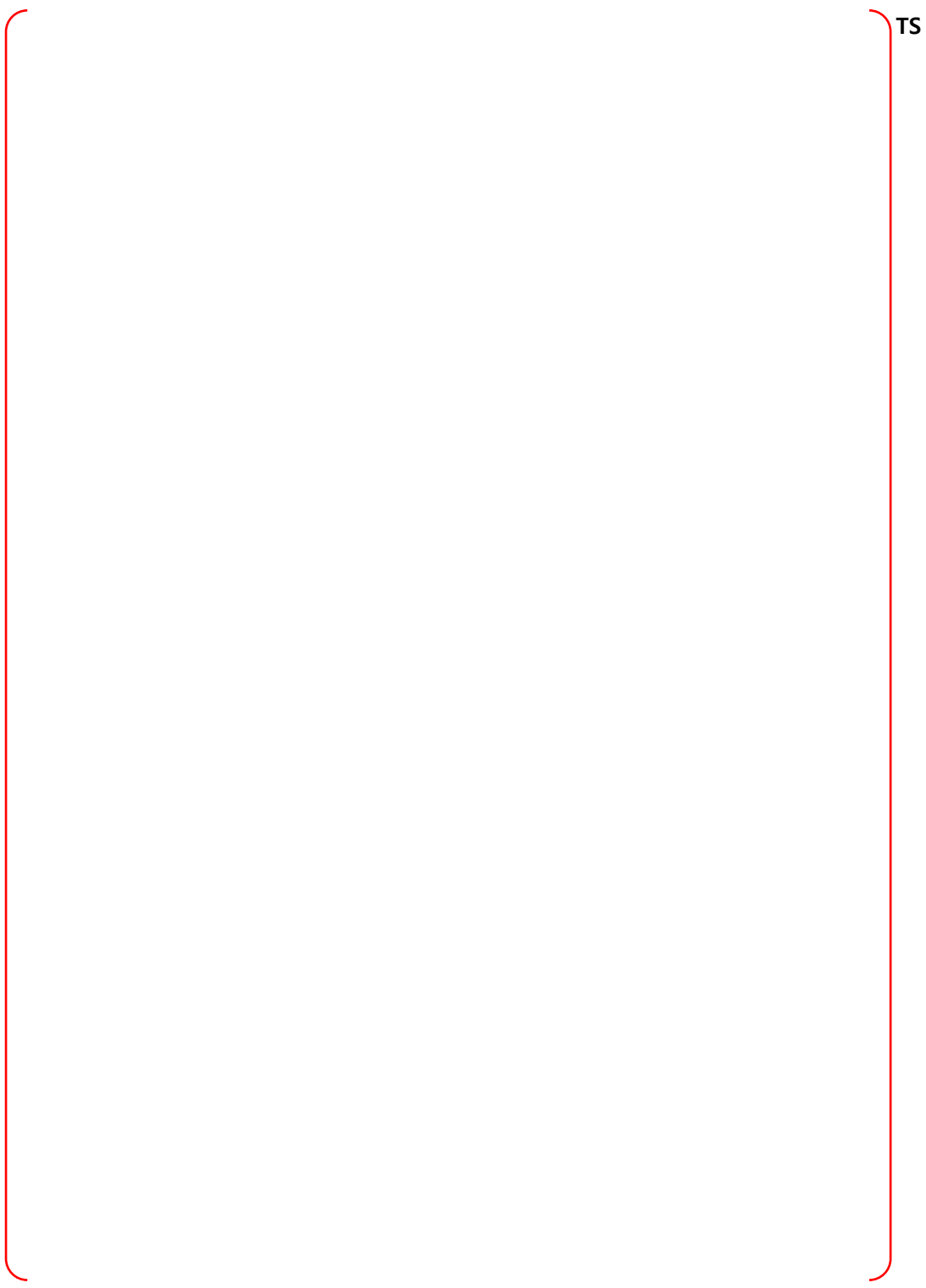


Figure B-78 Node 20, Reactor Drain Tank Room - Bounding Sequences – CP

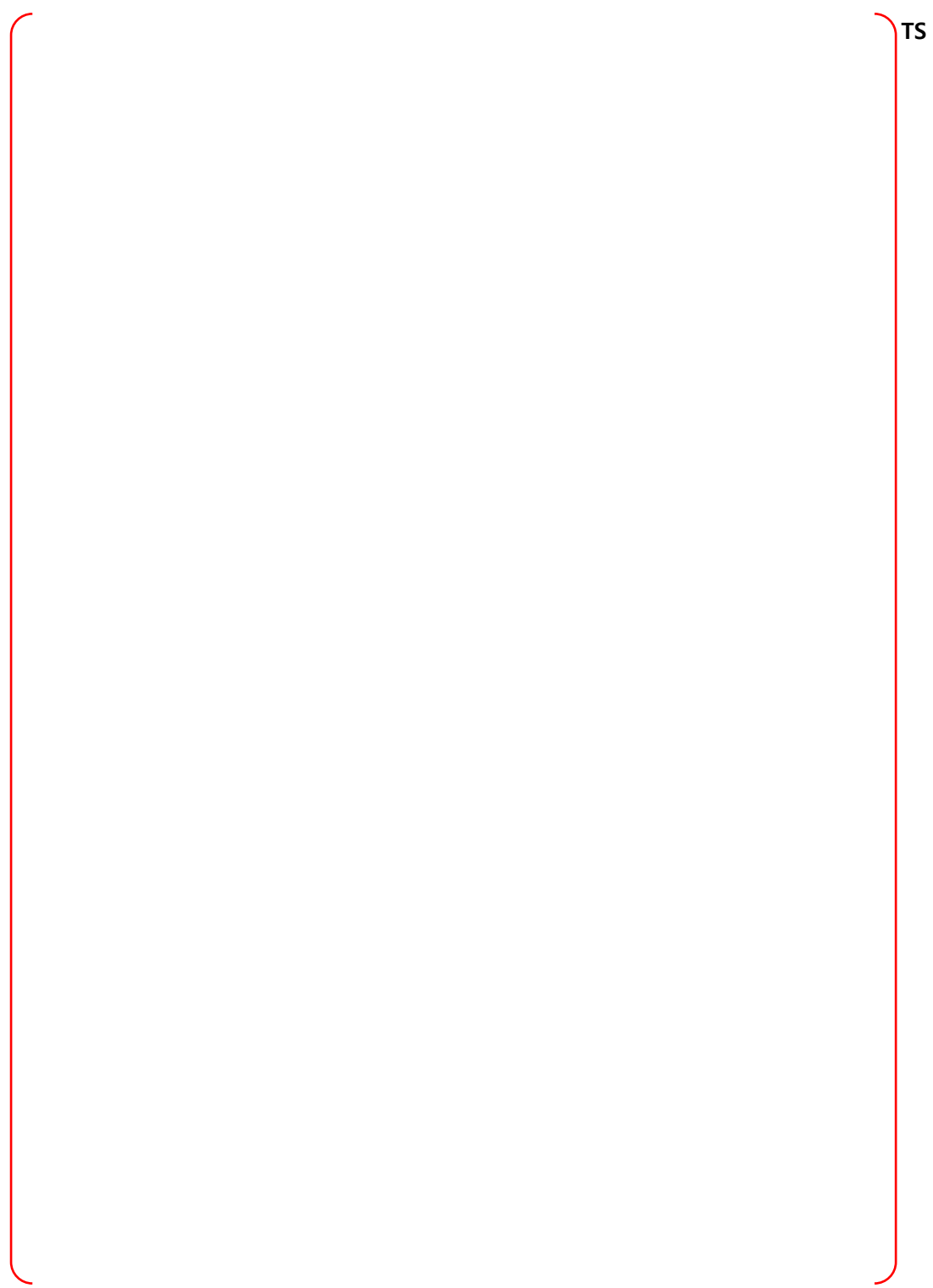


Figure B-79 Node 20, Reactor Drain Tank Room - Bounding Sequences – DF

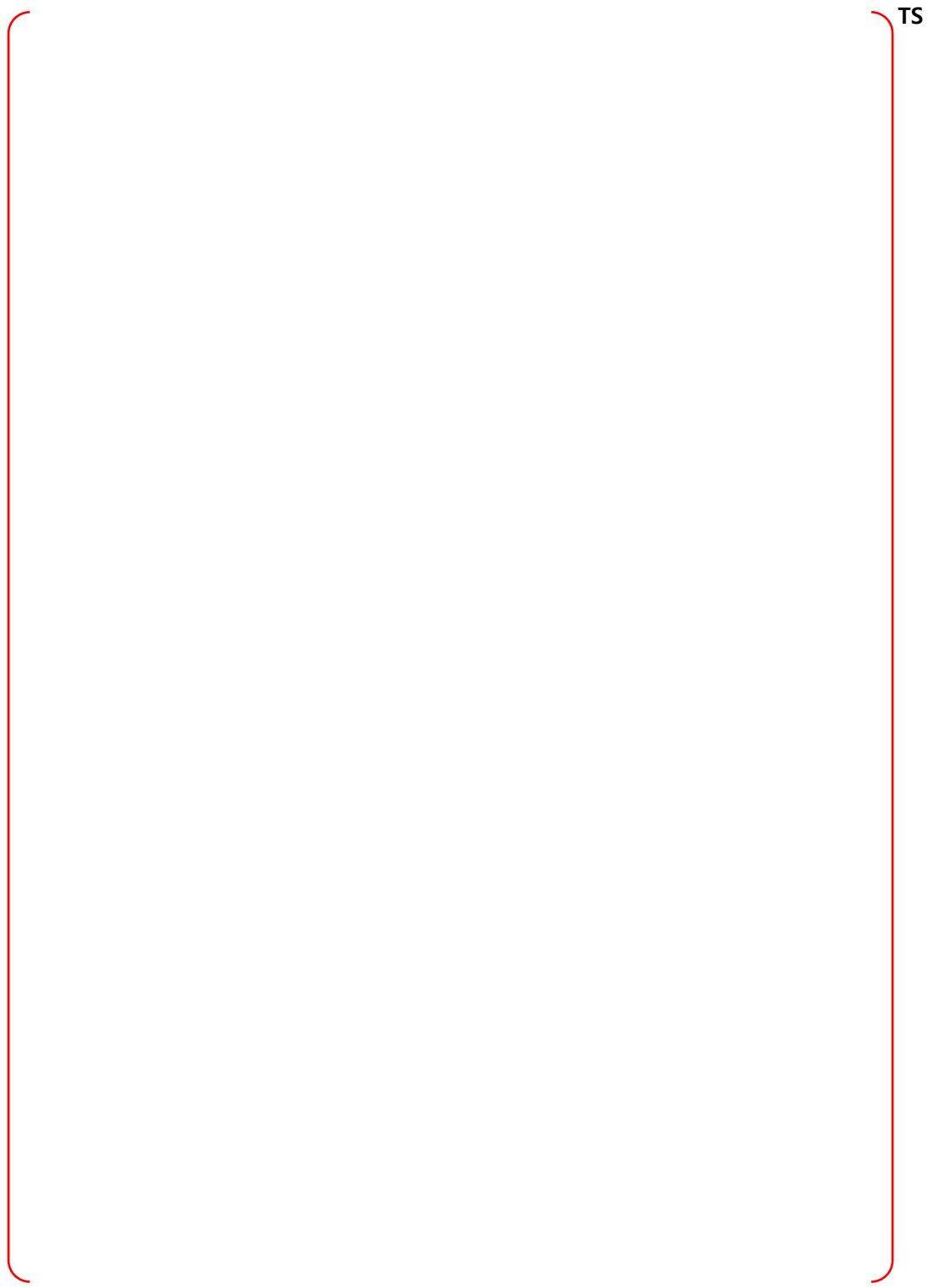


Figure B-80 Node 21, Letdown Heat Exchanger Room - PRA Sequences

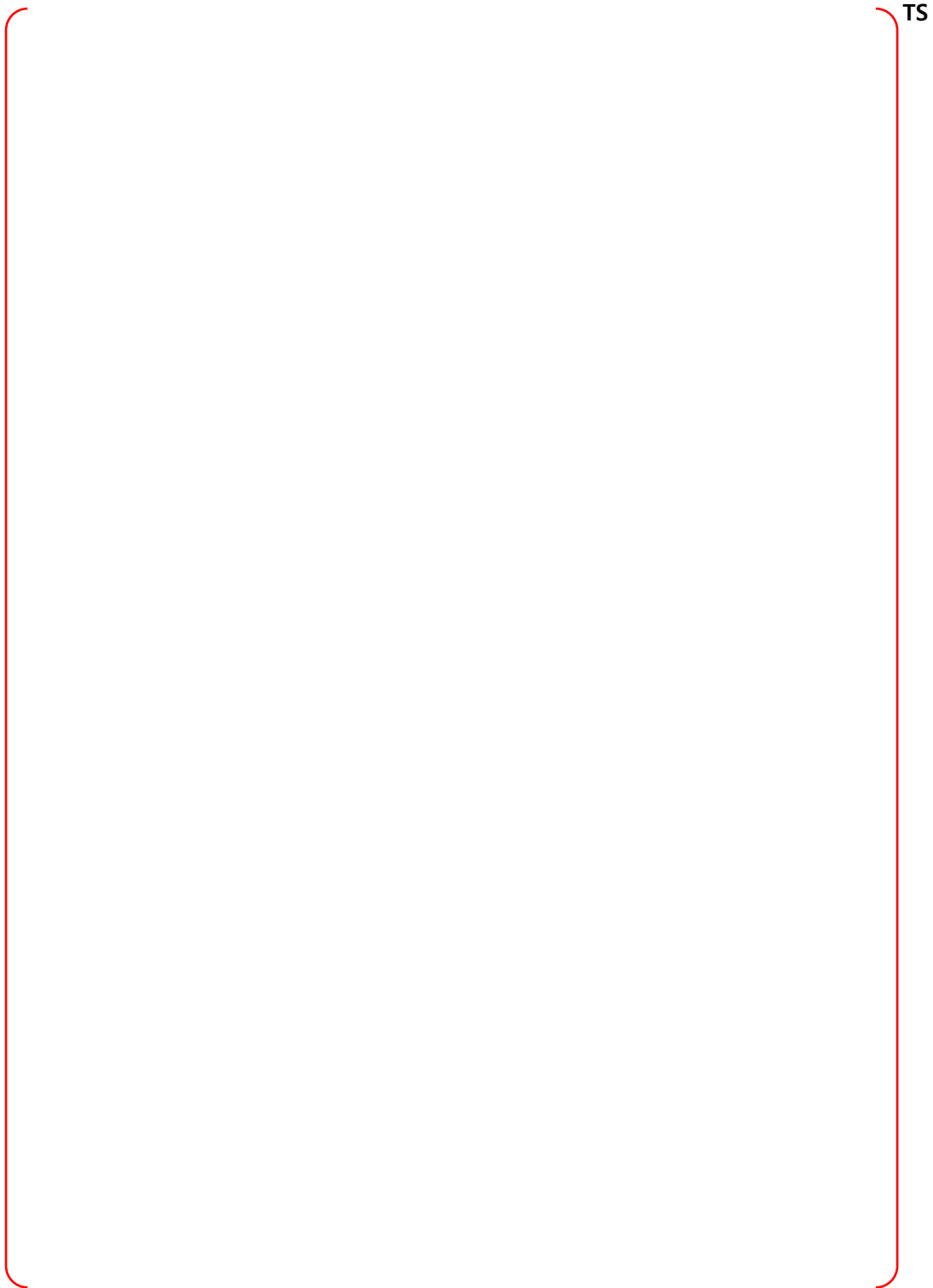


Figure B-81 Node 21, Letdown Heat Exchanger Room - Bounding Sequences – MCCI

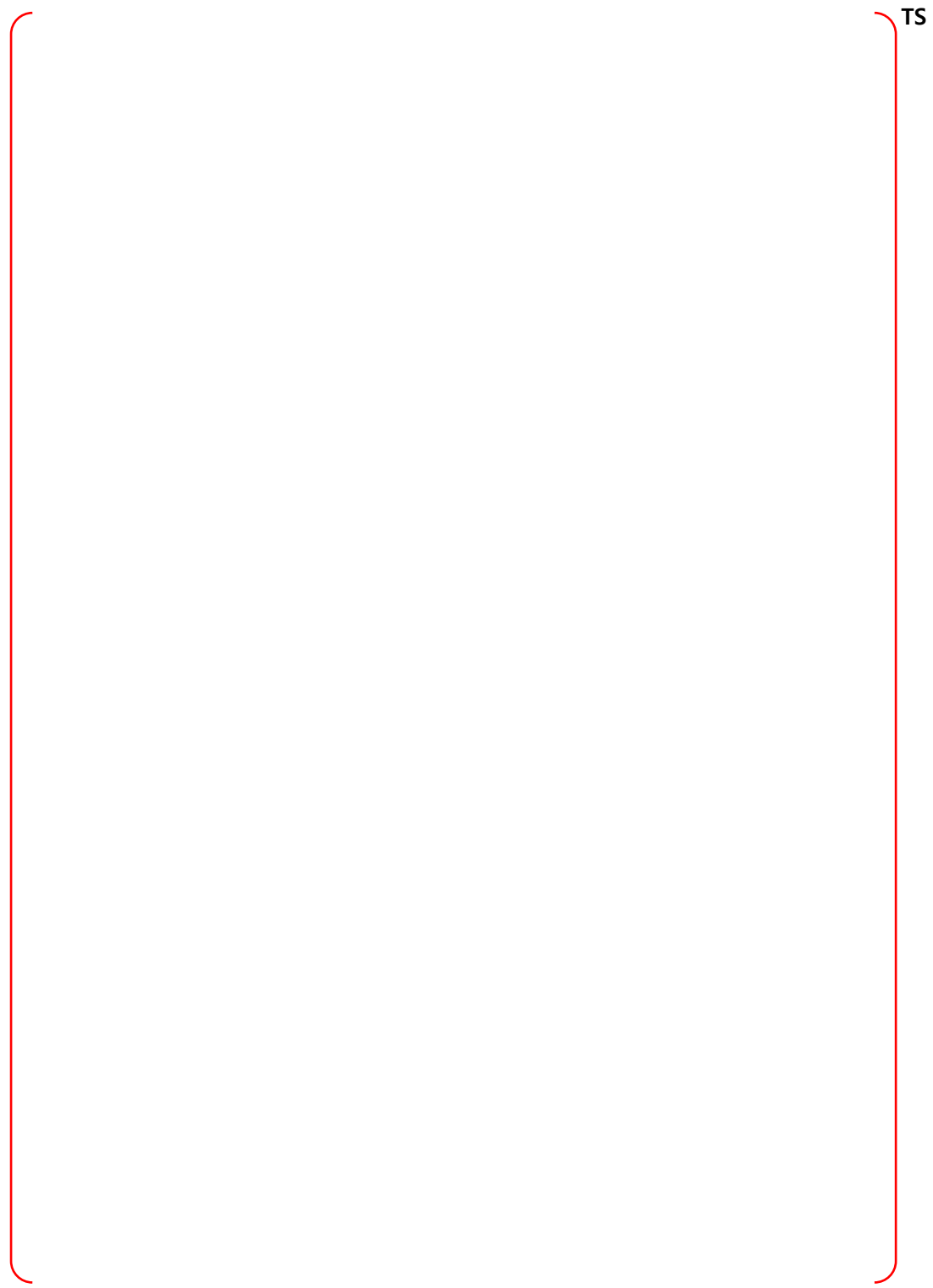


Figure B-82 Node 21, Letdown Heat Exchanger Room - Bounding Sequences – CP

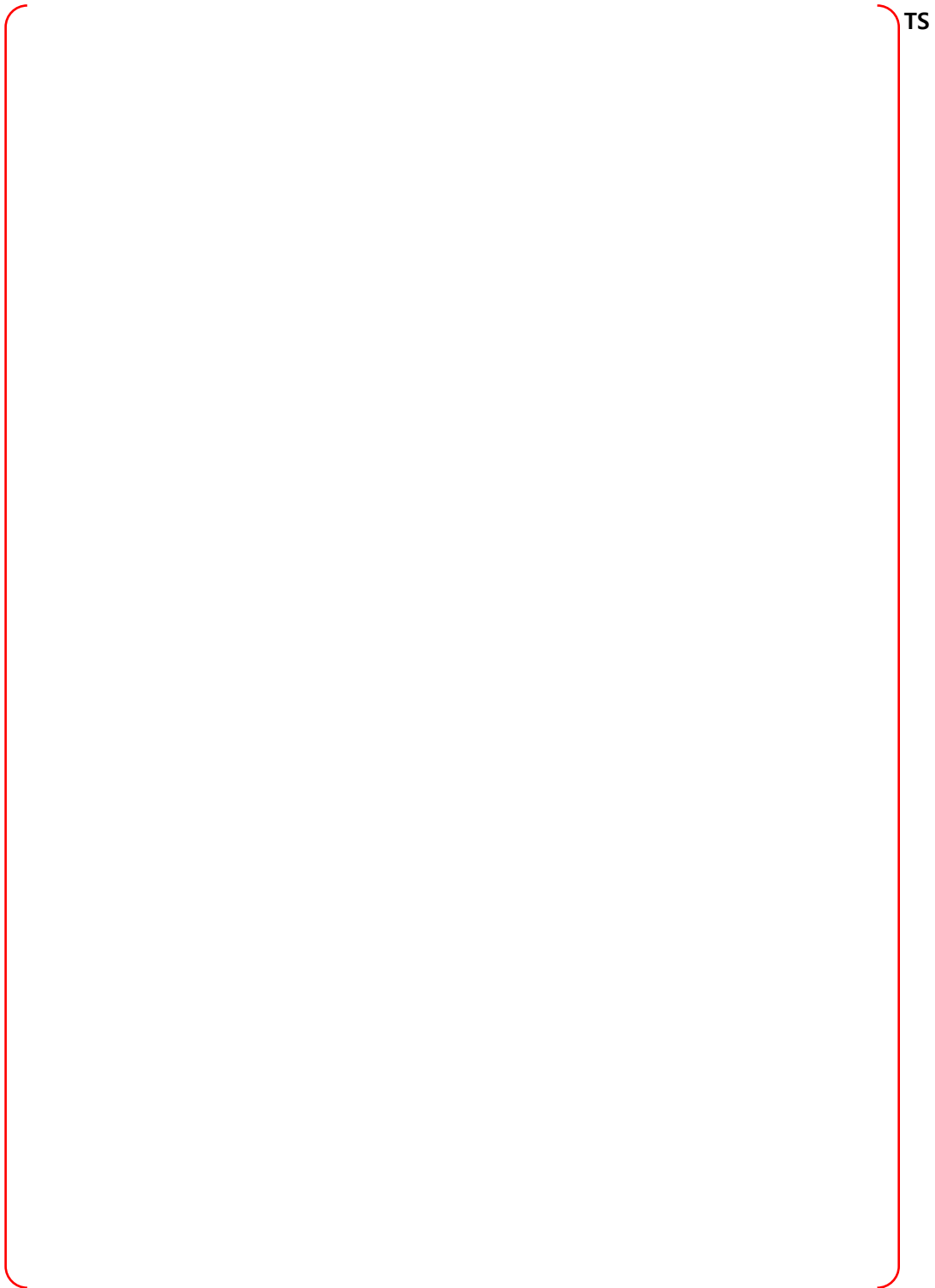
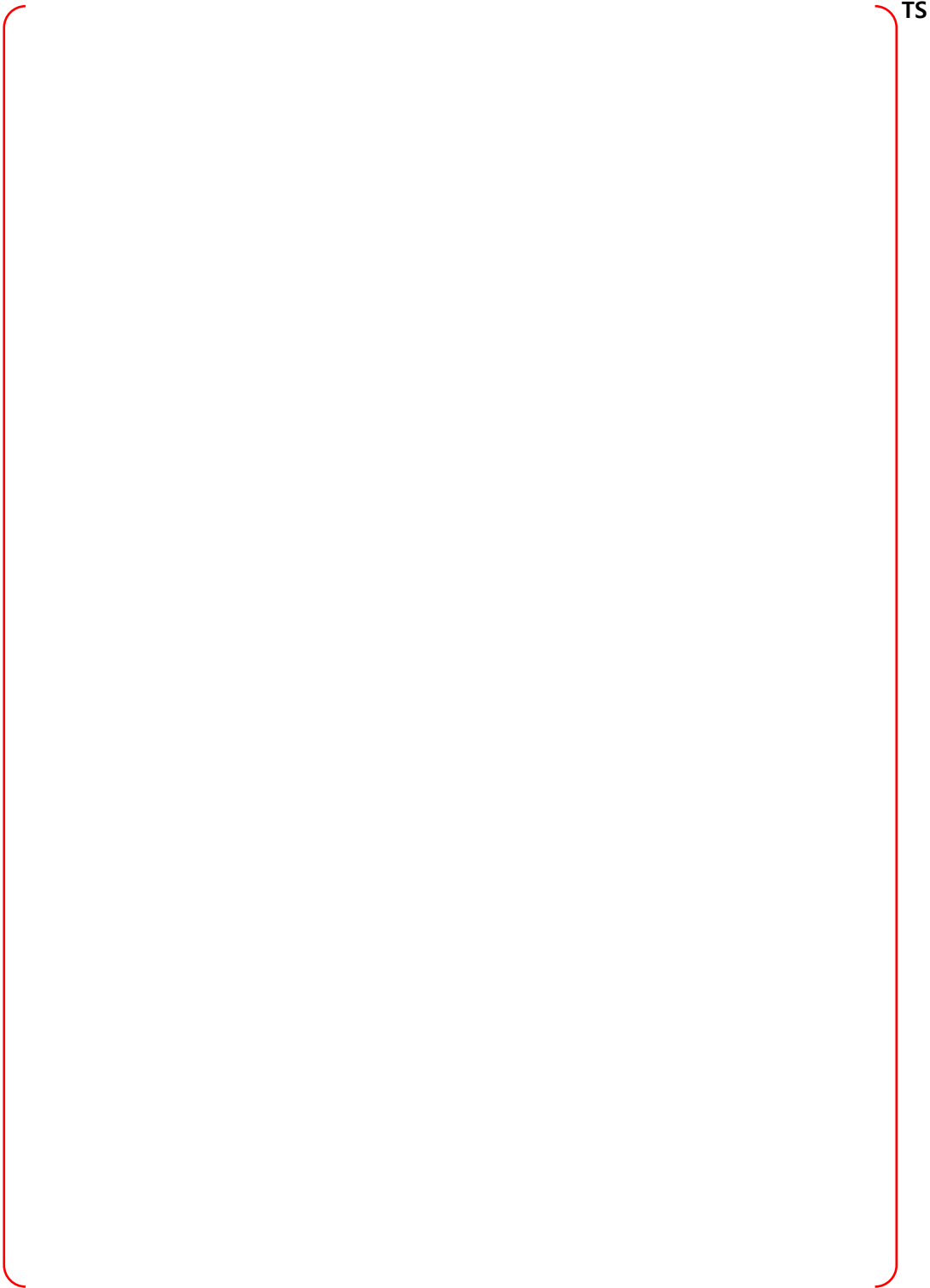


Figure B-83 Node 21, Letdown Heat Exchanger Room - Bounding Sequences – DF



TS

Figure B-84 Node 22, Regenerative Heat Exchanger Room - PRA Sequences

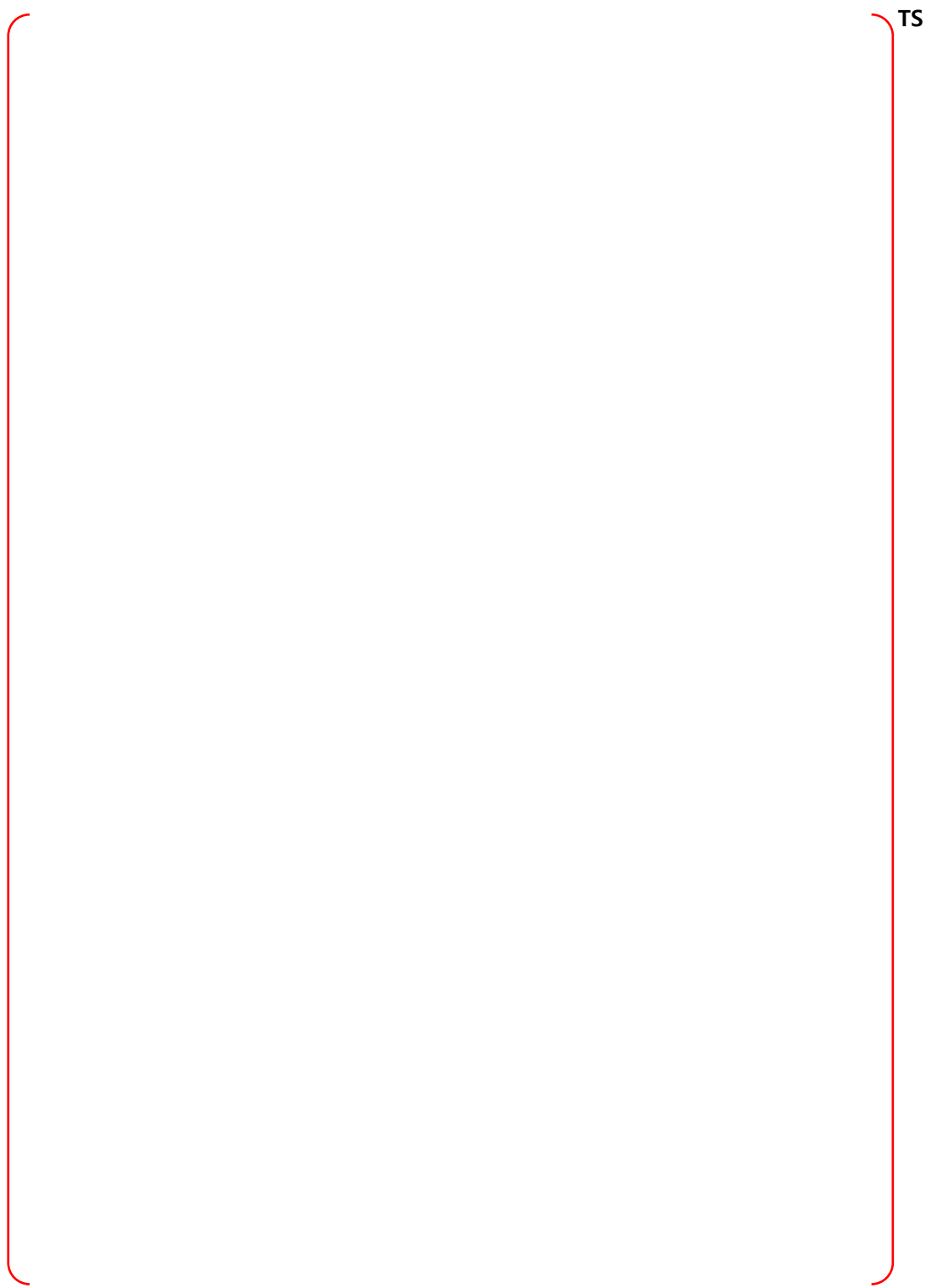


Figure B-85 Node 22, Regenerative Heat Exchanger Room - Bounding Sequences – MCCI

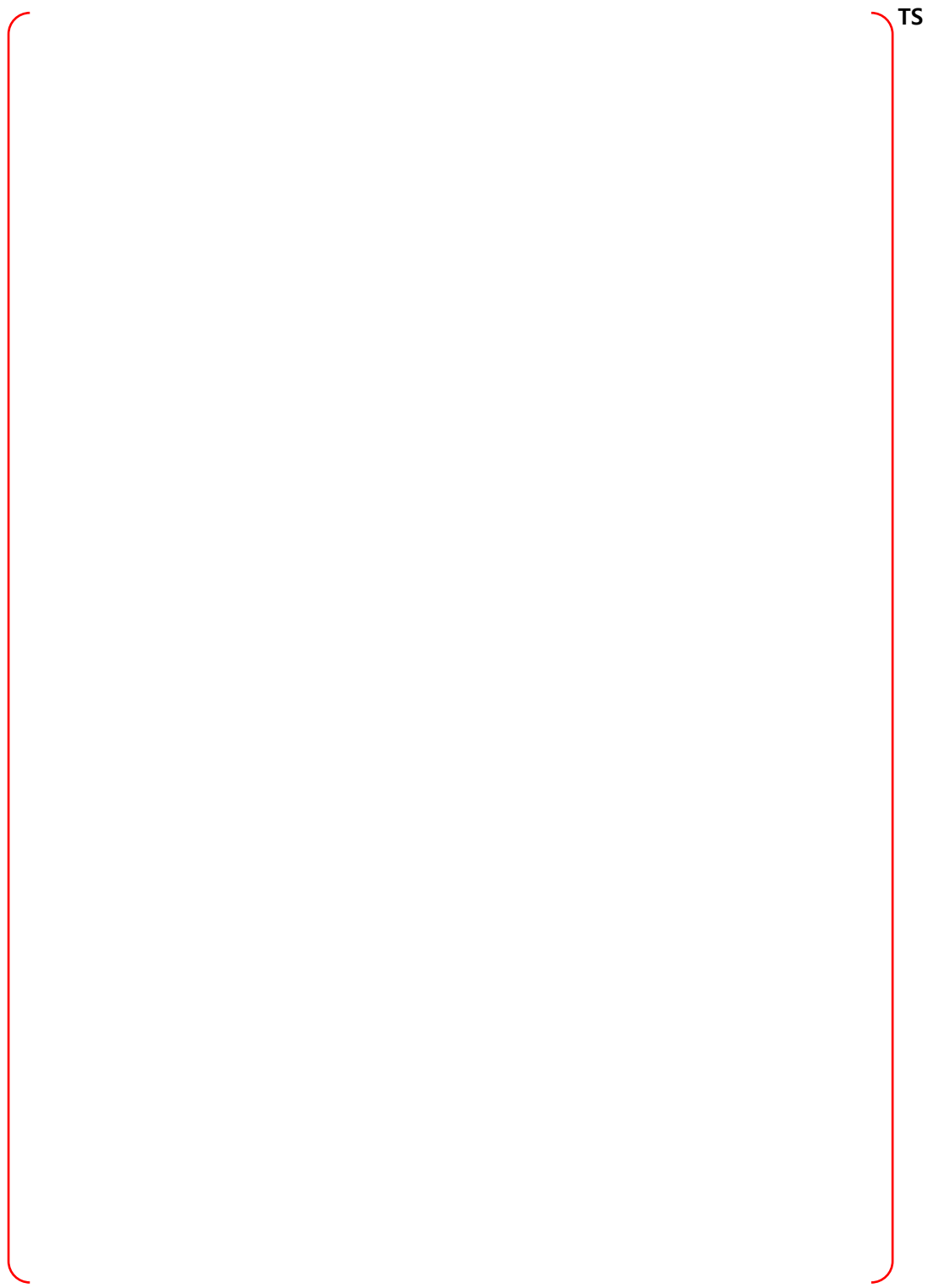


Figure B-86 Node 22, Regenerative Heat Exchanger Room - Bounding Sequences – CP

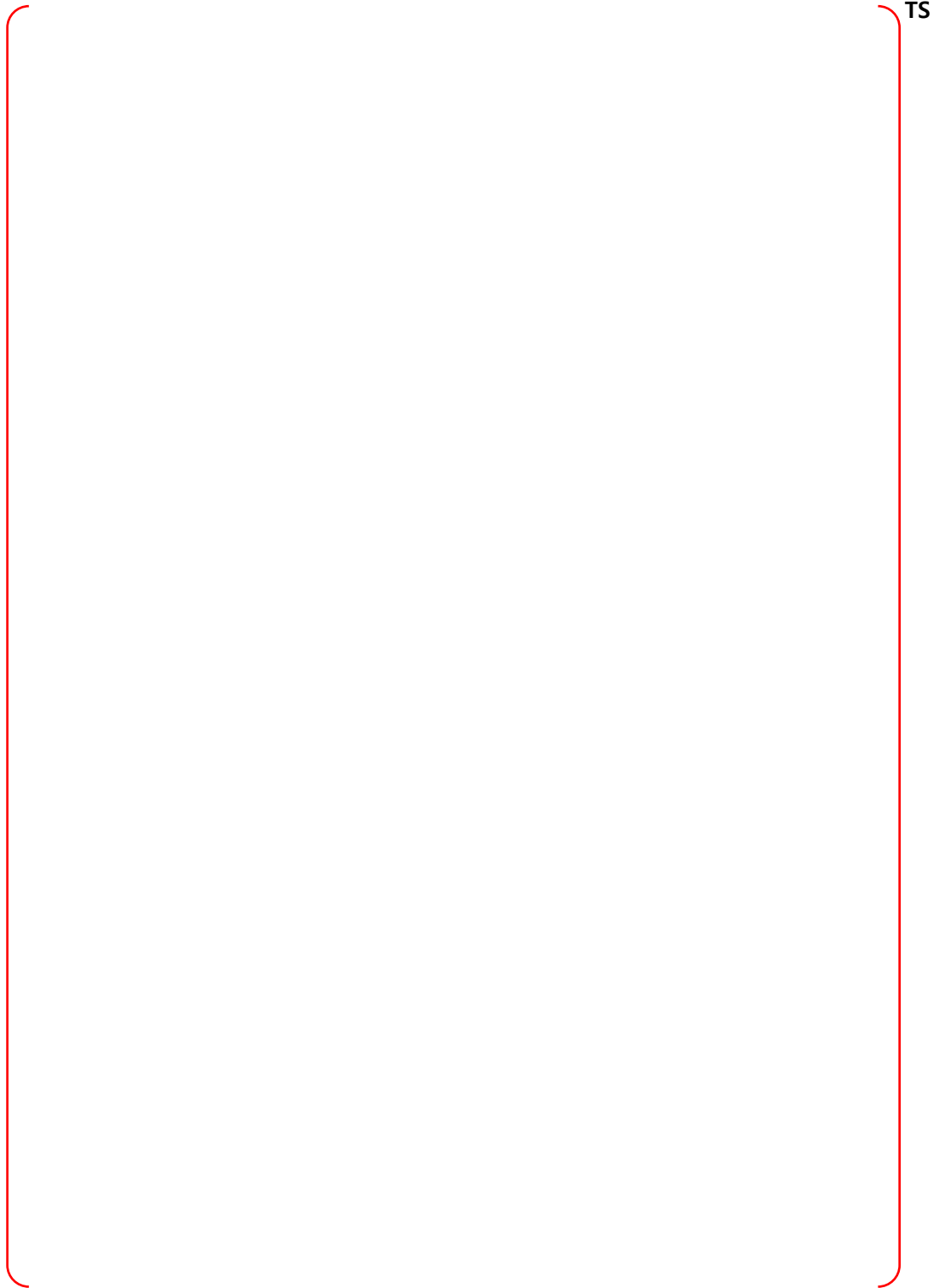


Figure B-87 Node 22, Regenerative Heat Exchanger Room - Bounding Sequences – DF

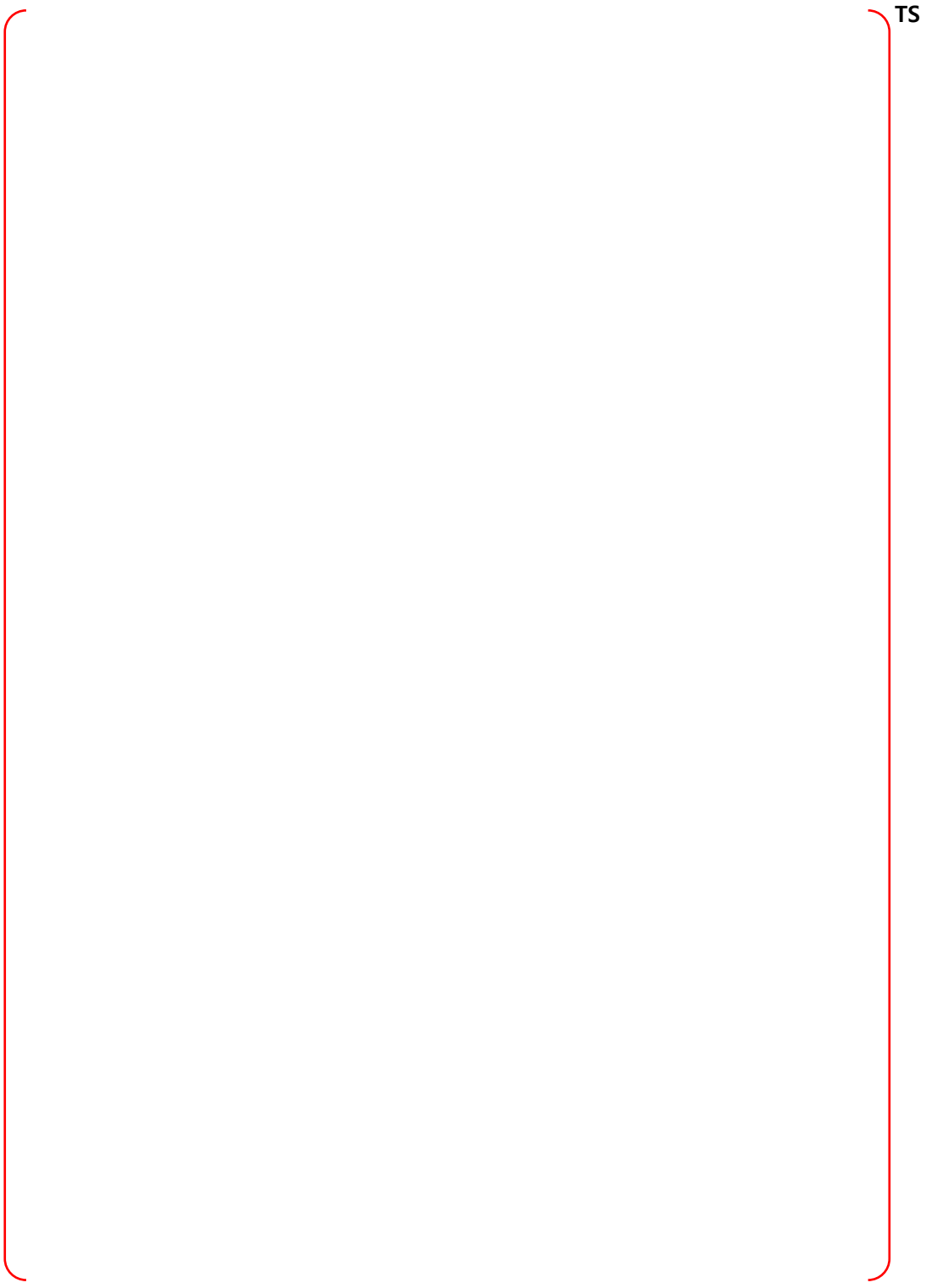


Figure B-88 Node 23, NE IRWST - PRA Sequences

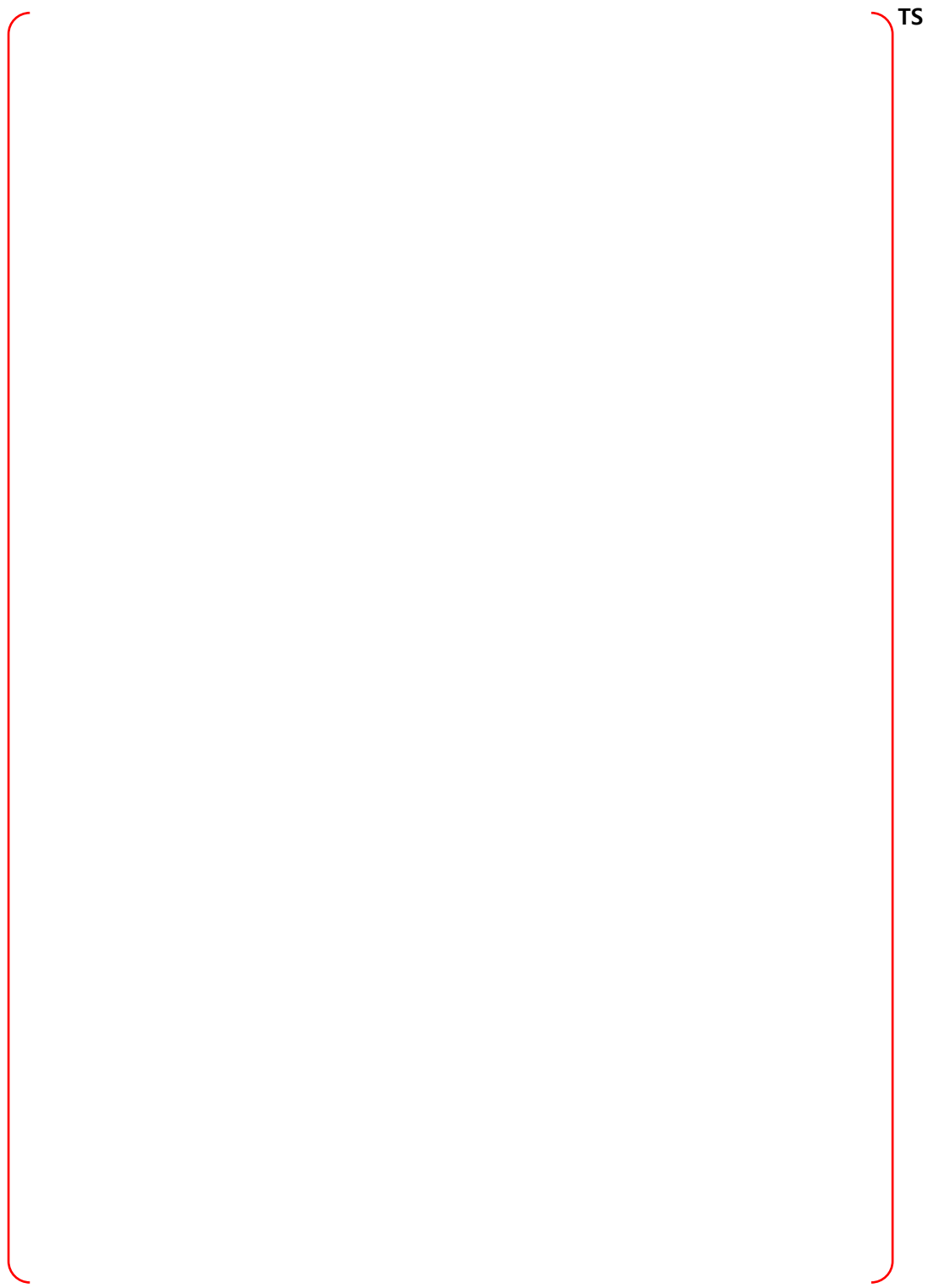


Figure B-89 Node 23, NE IRWST - Bounding Sequences – MCCI

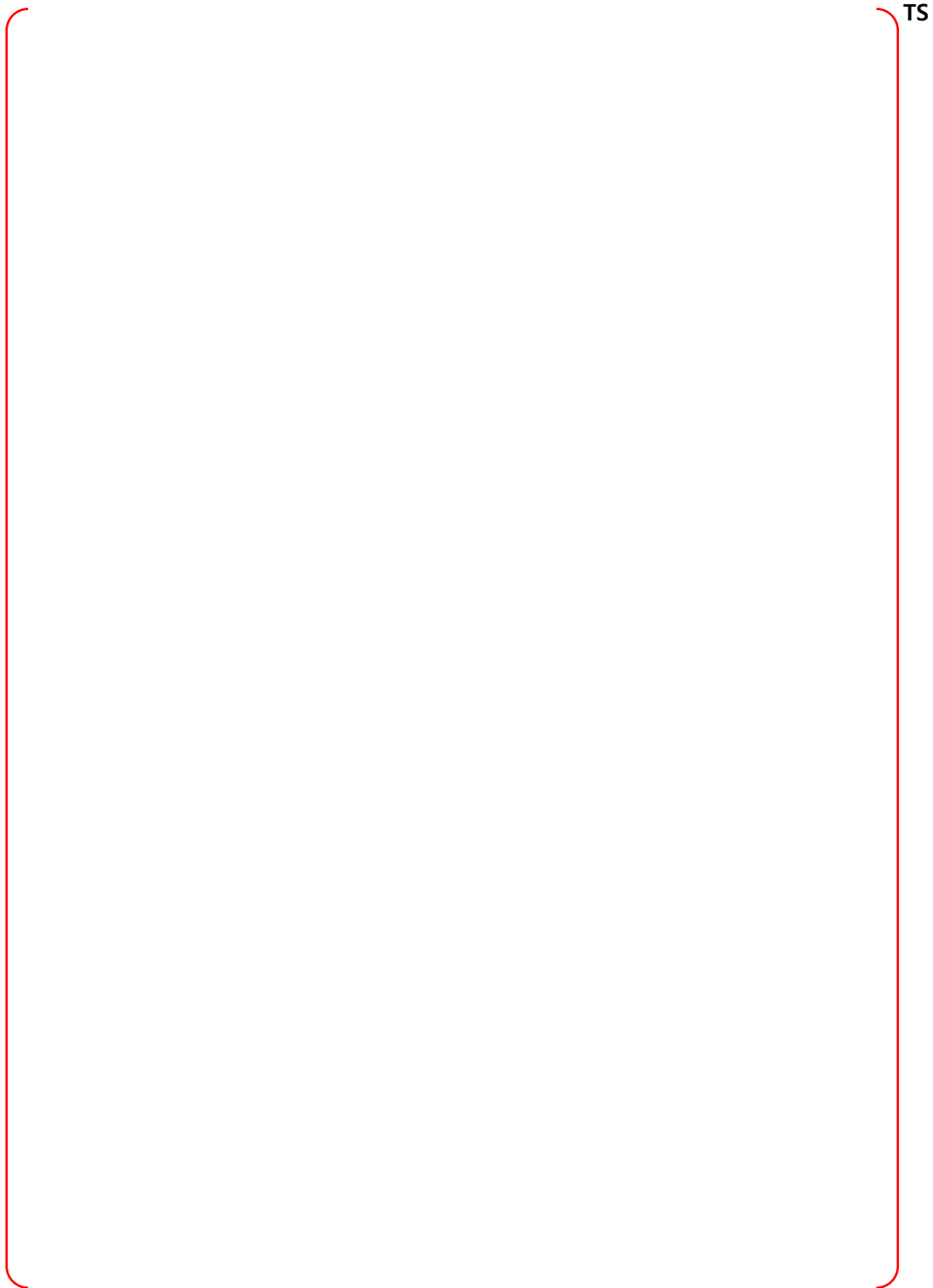


Figure B-90 Node 23, NE IRWST - Bounding Sequences – CP

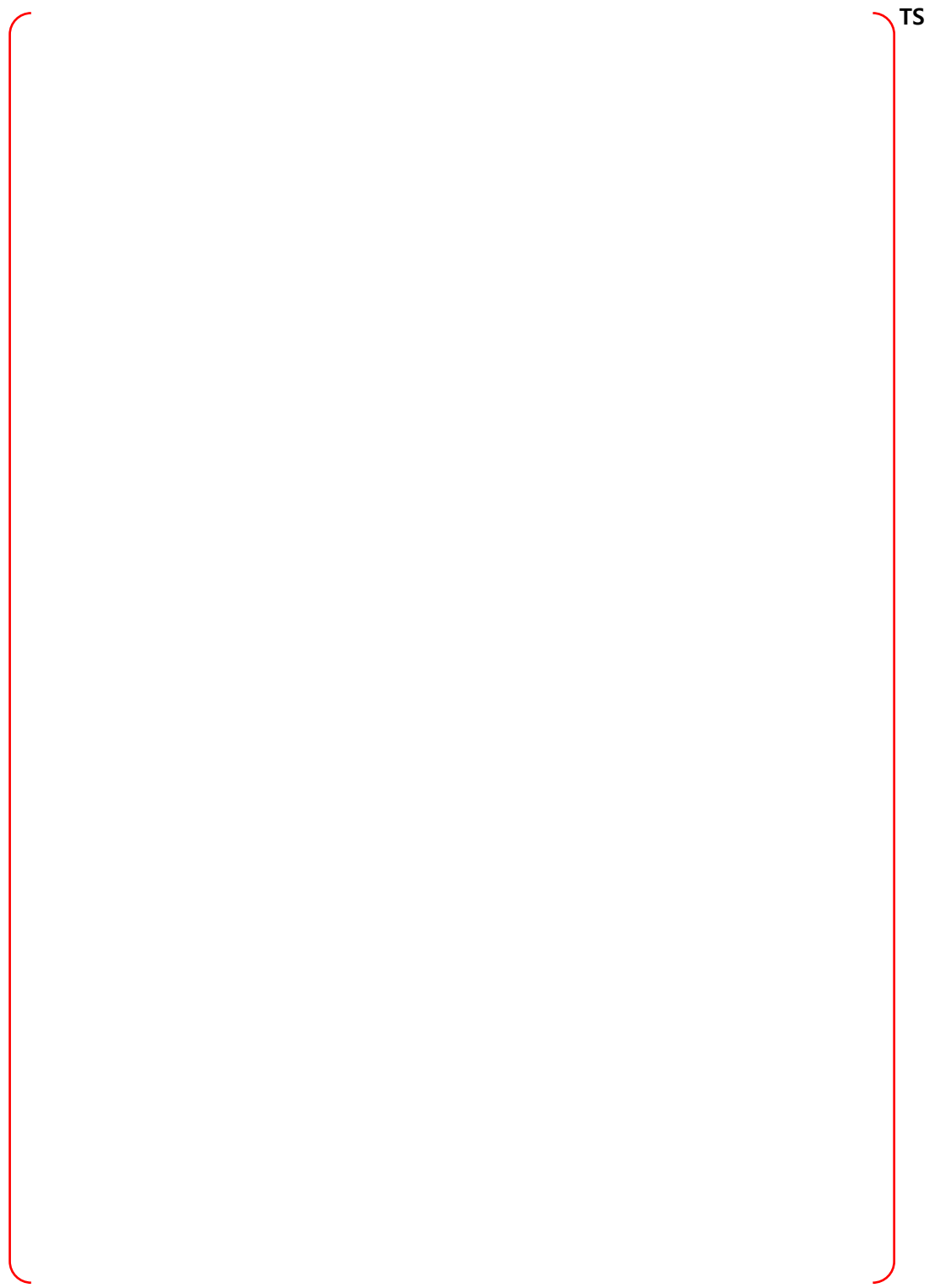


Figure B-91 Node 23, NE IRWST - Bounding Sequences – DF

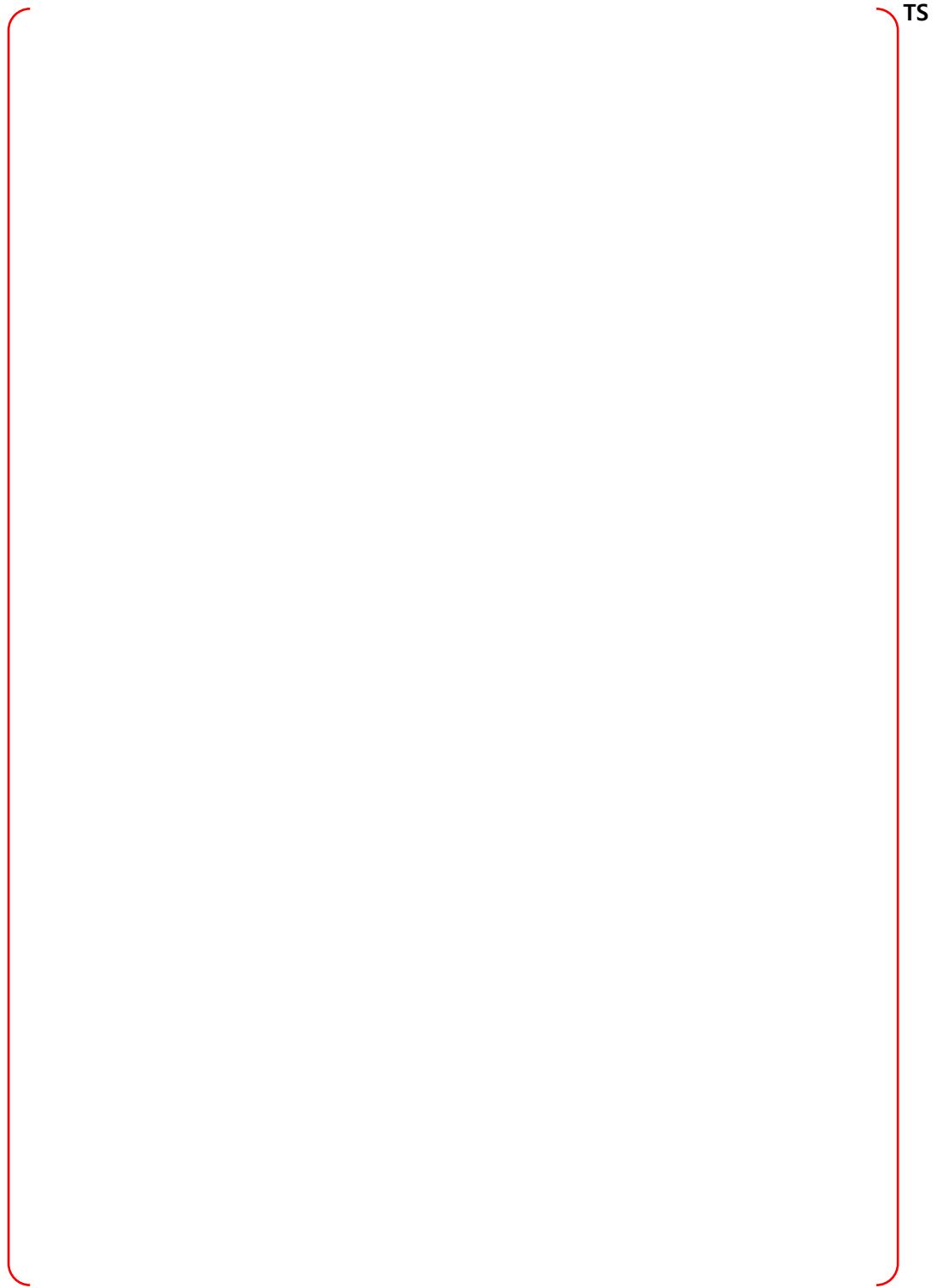


Figure B-92 Node 24, Pressurizer Compartment - PRA Sequences

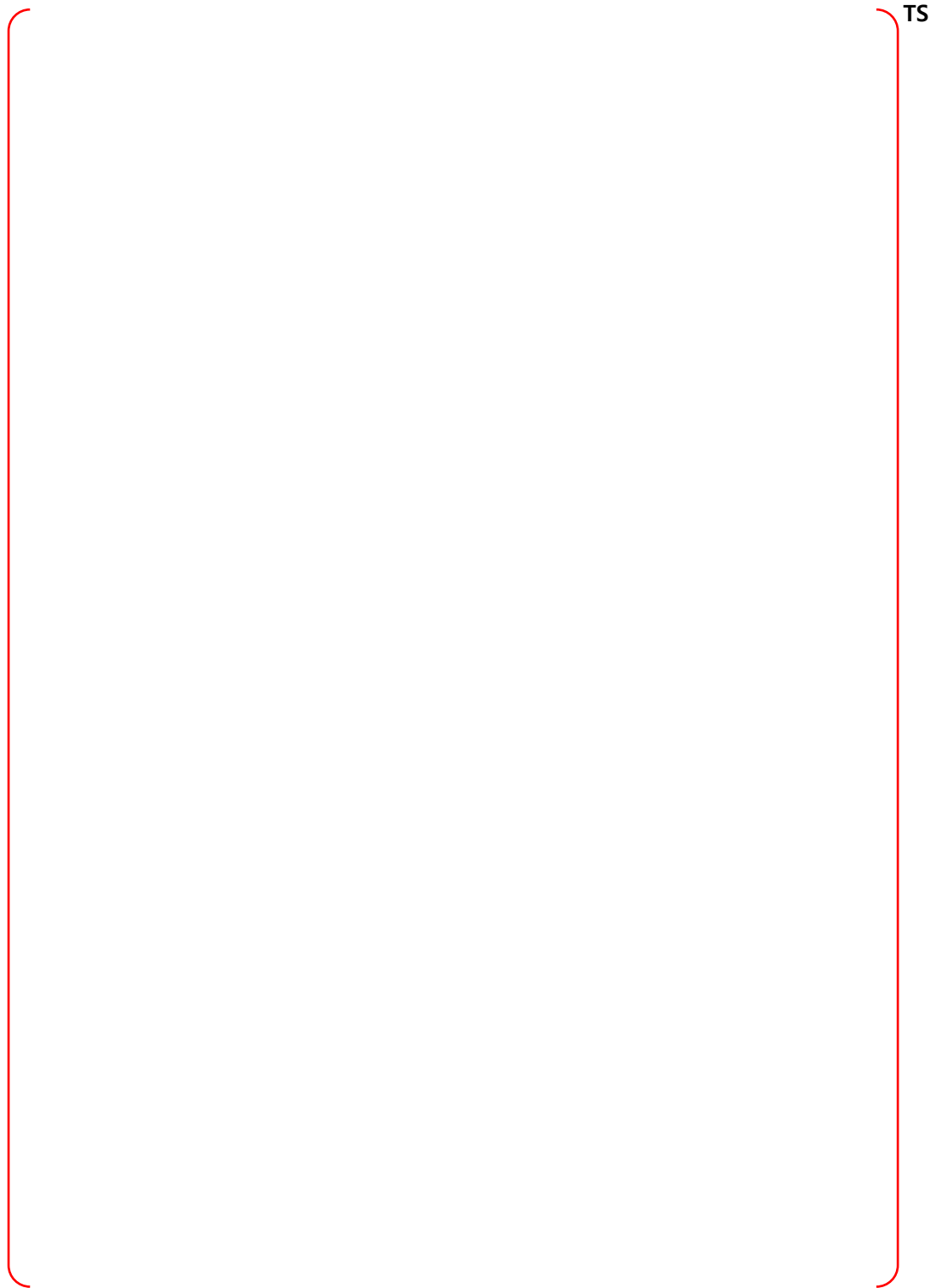


Figure B-93 Node 24, Pressurizer Compartment - Bounding Sequences – MCCI

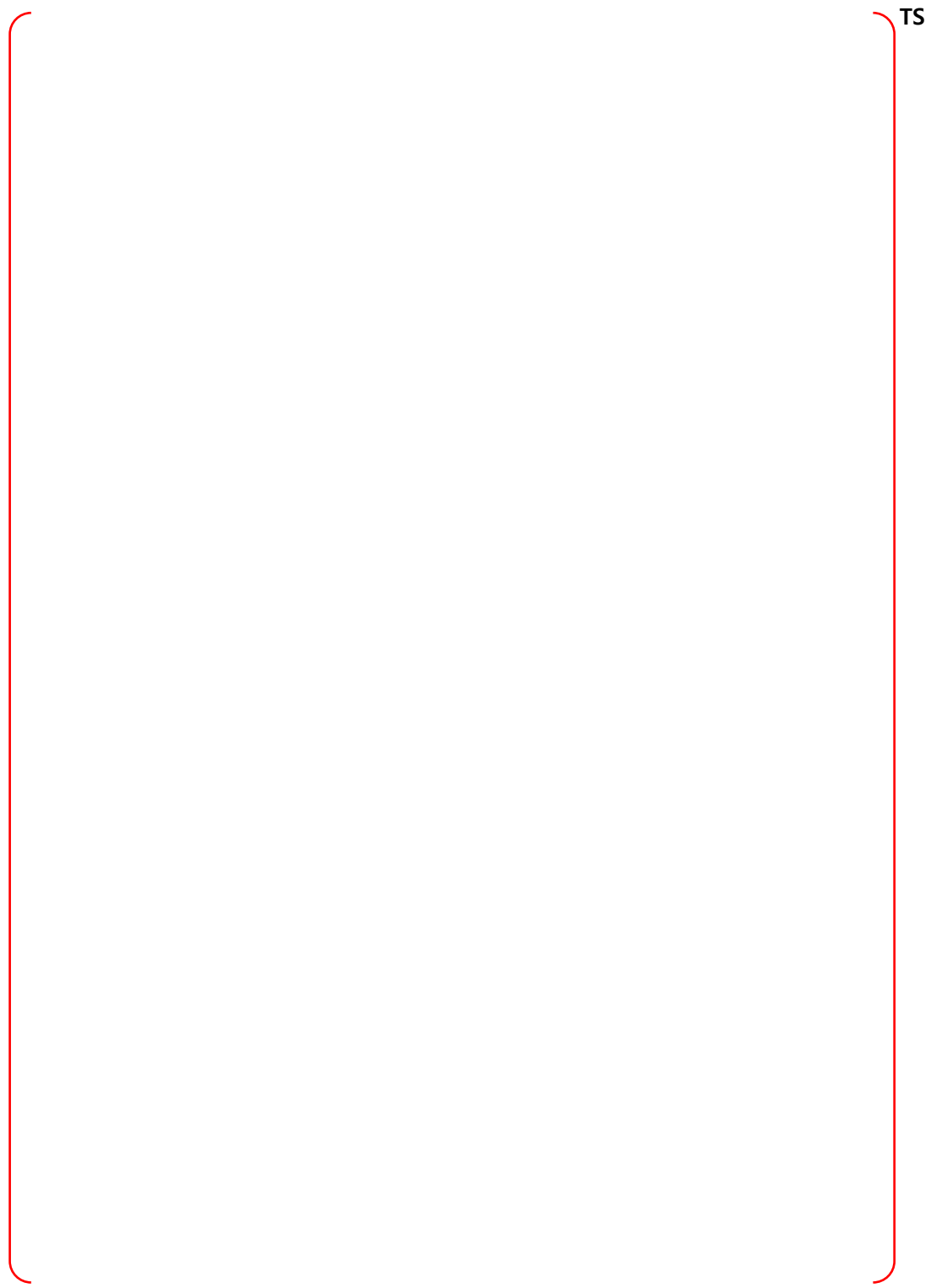
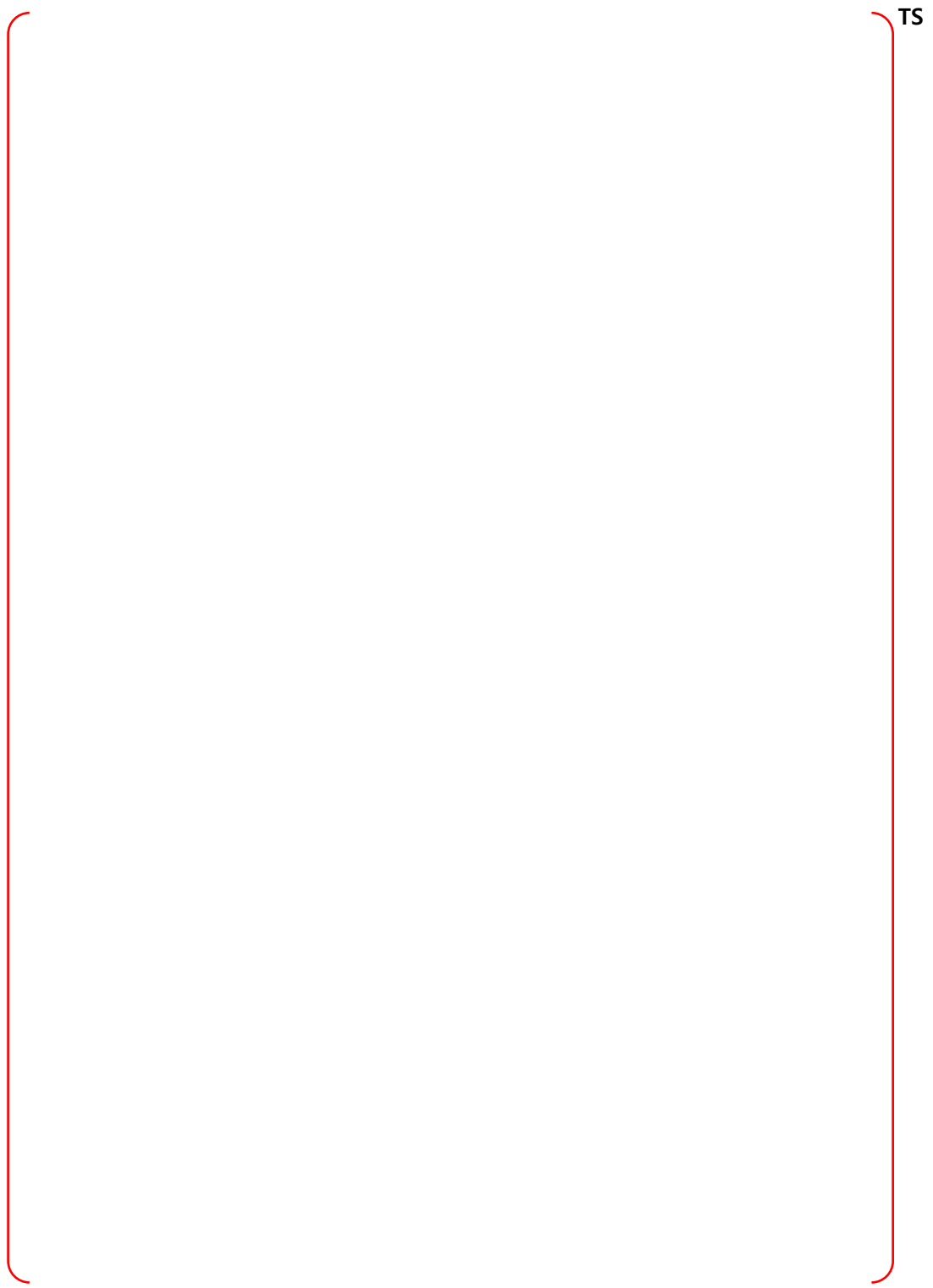


Figure B-94 Node 24, Pressurizer Compartment - Bounding Sequences – CP



TS

Figure B-95 Node 24, Pressurizer Compartment - Bounding Sequences – DF

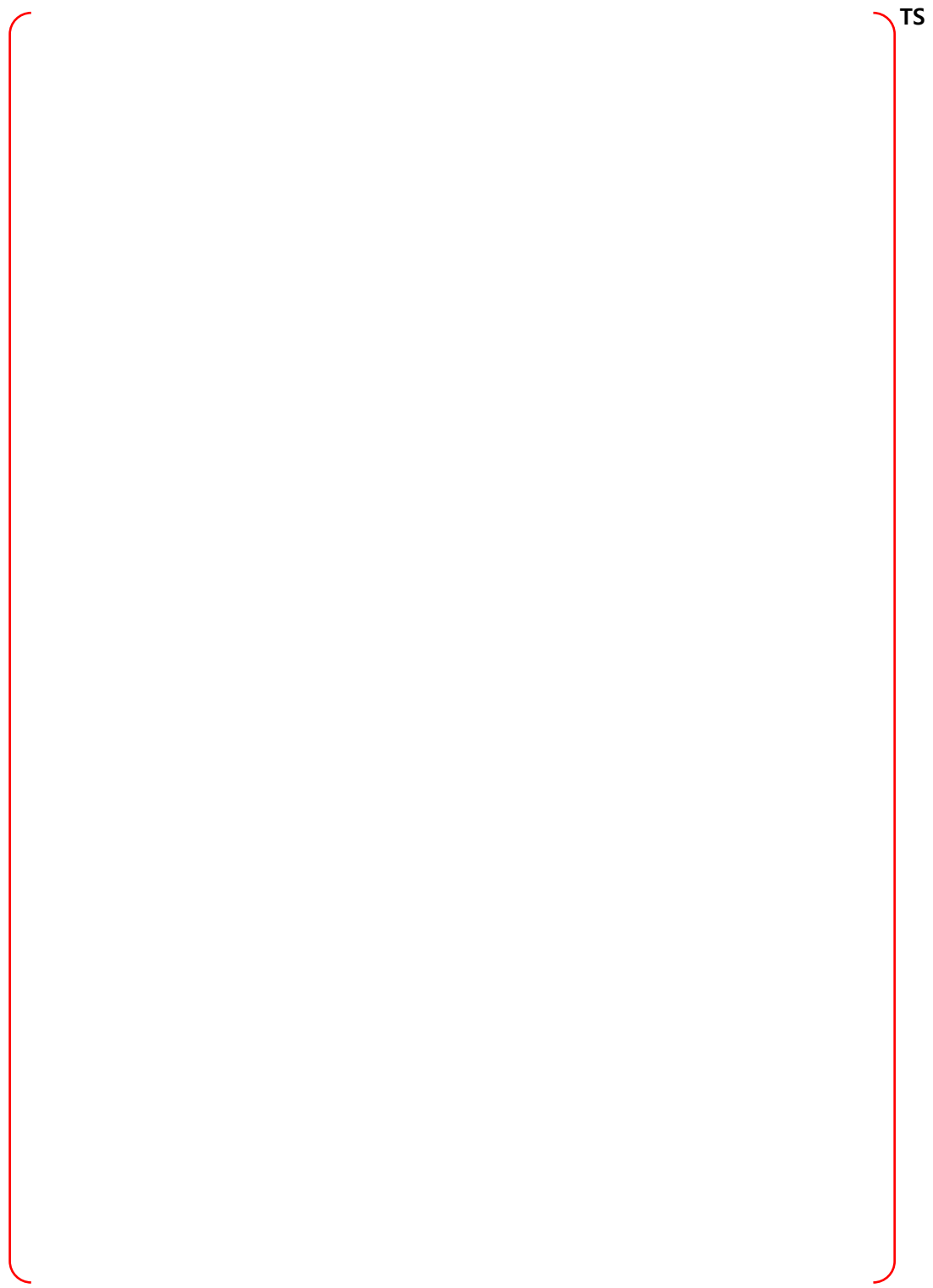


Figure B-96 Node 25, Valve Rooms - PRA Sequences

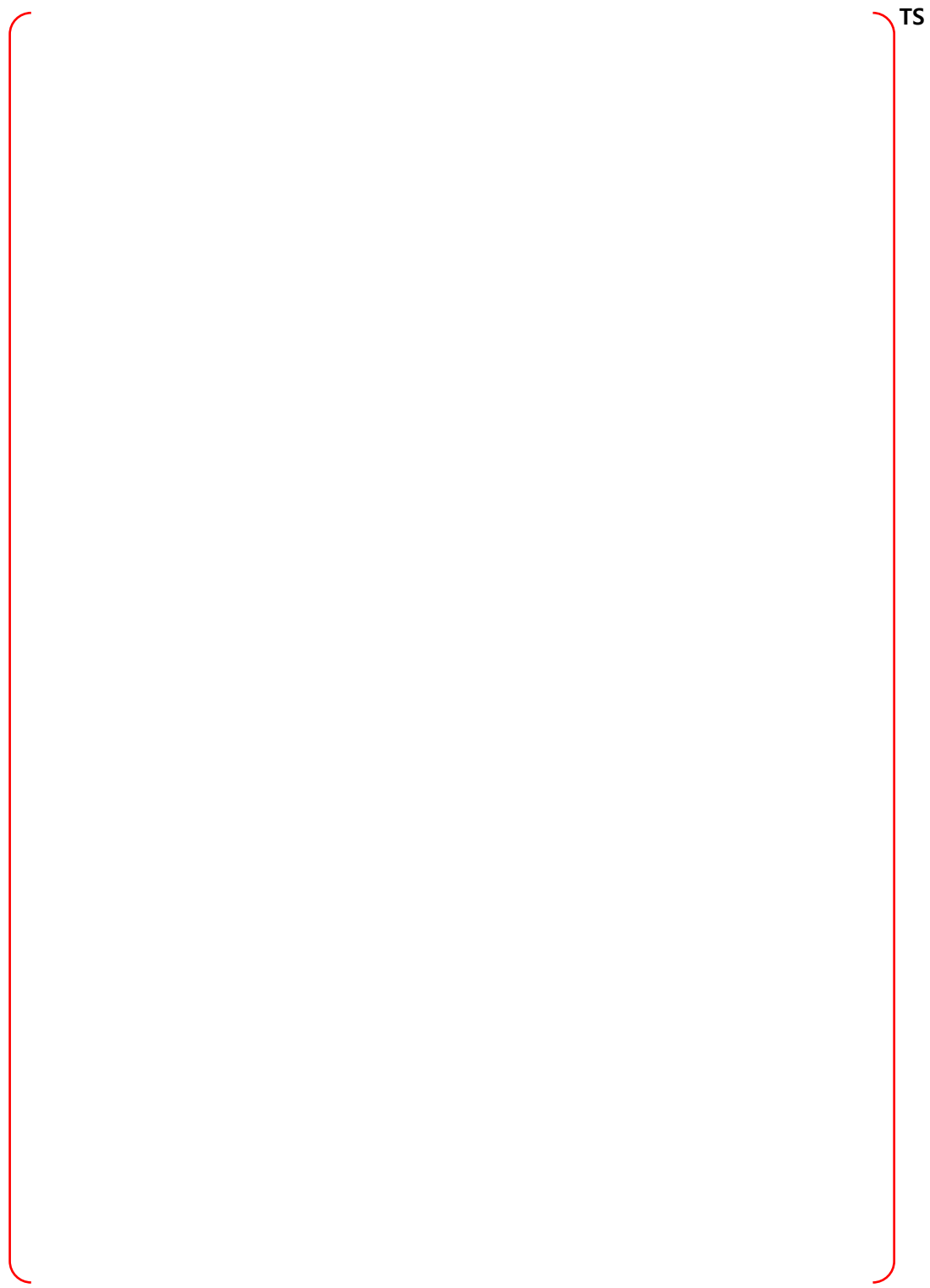


Figure B-97 Node 25, Valve Rooms - Bounding Sequences – MCCI

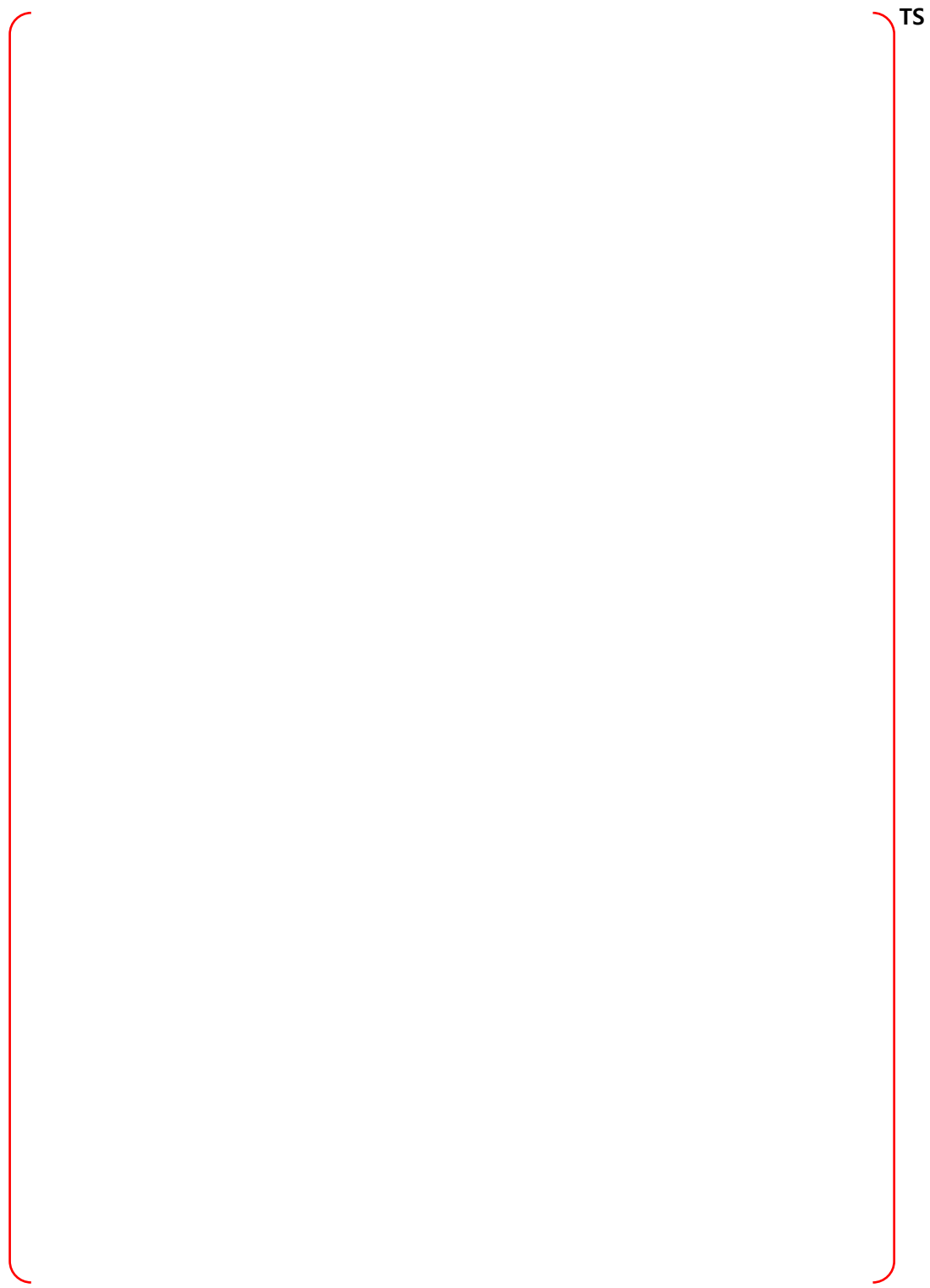


Figure B-98 Node 25, Valve Rooms - Bounding Sequences – CP

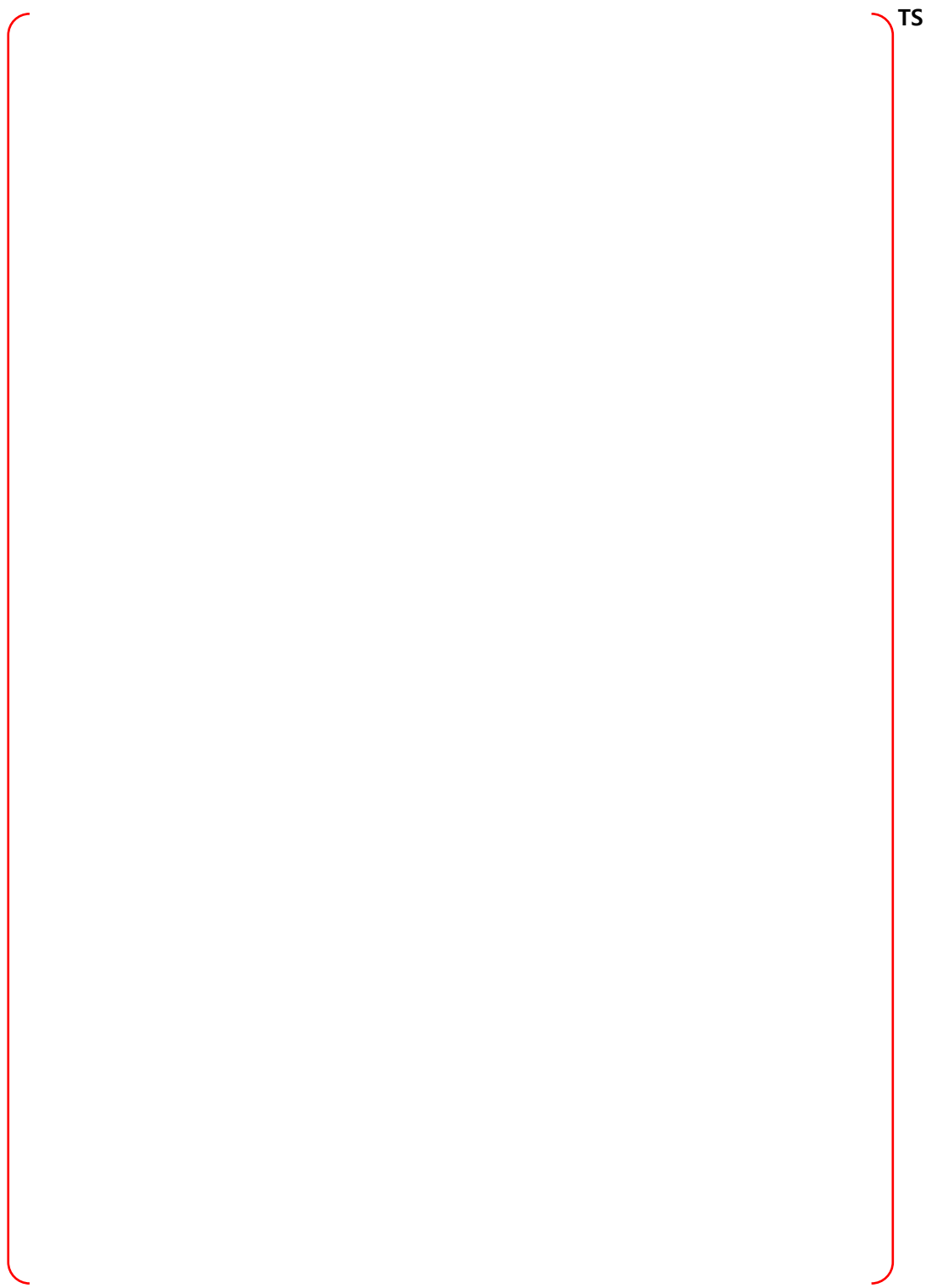


Figure B-99 Node 25, Valve Rooms - Bounding Sequences – DF

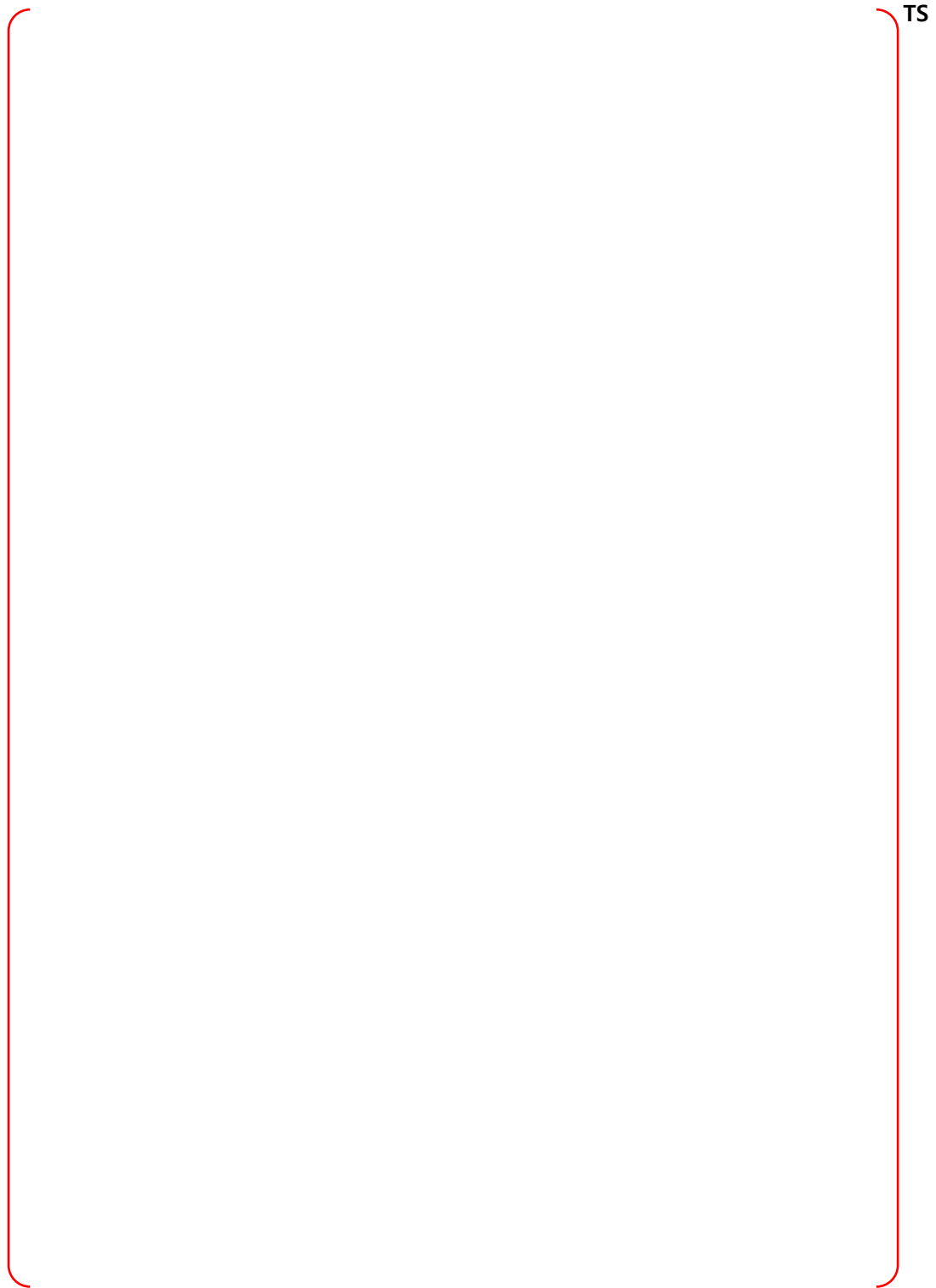


Figure B-100 Node 26, NW IRWST with Spargers - PRA Sequences

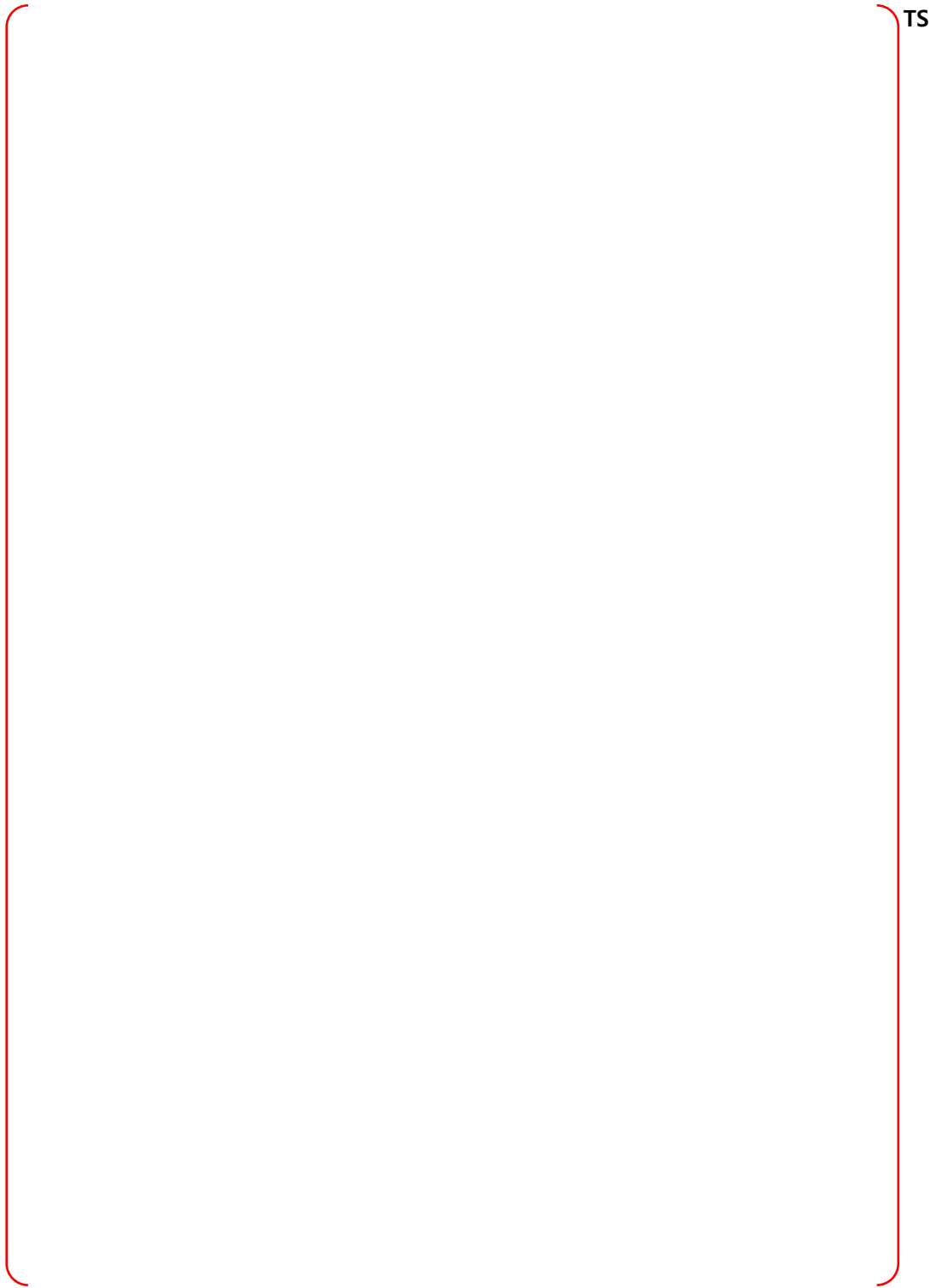


Figure B-101 Node 26, NW IRWST with Spargers - Bounding Sequences – MCCI

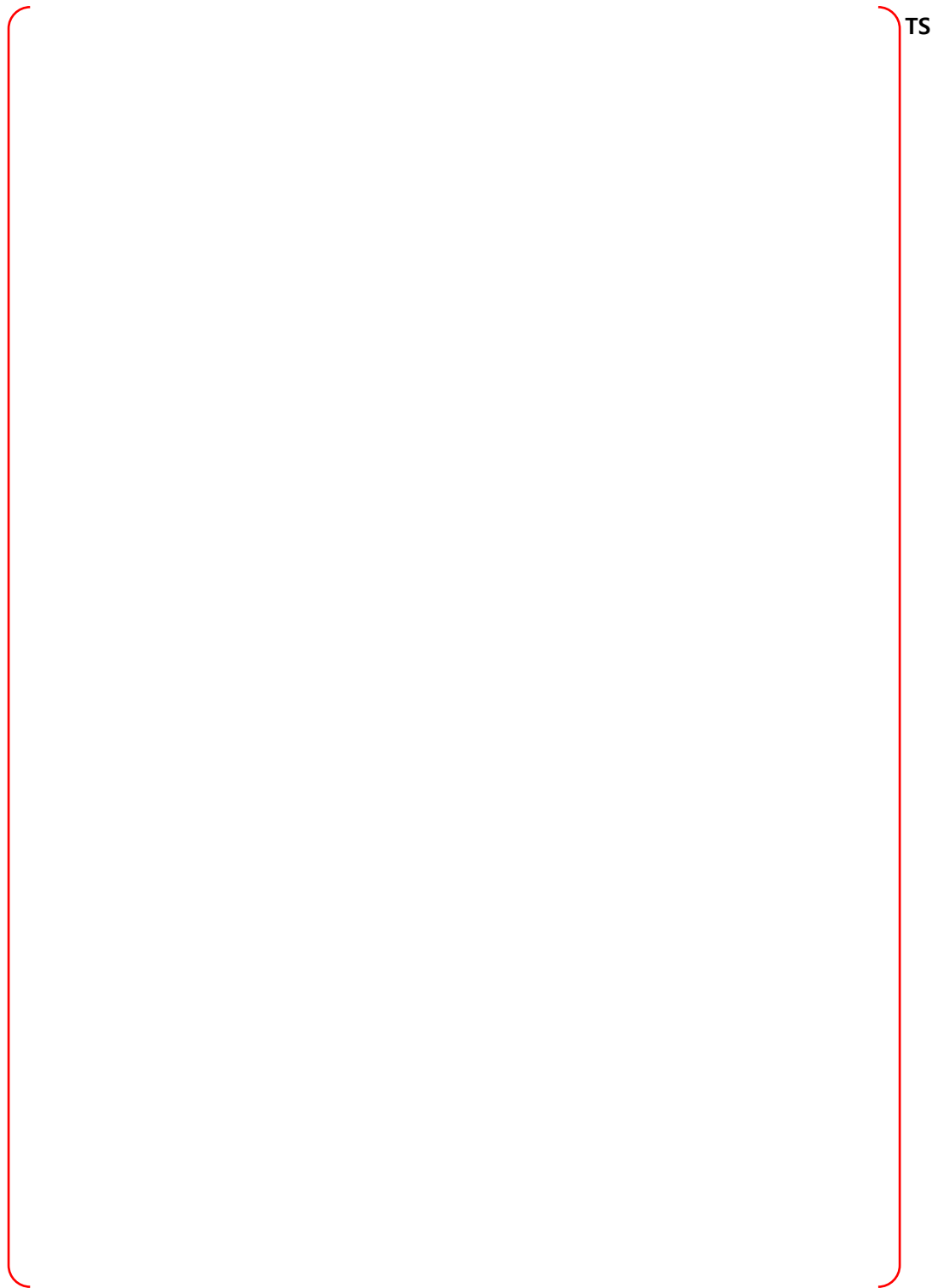


Figure B-102 Node 26, NW IRWST with Spargers - Bounding Sequences – CP

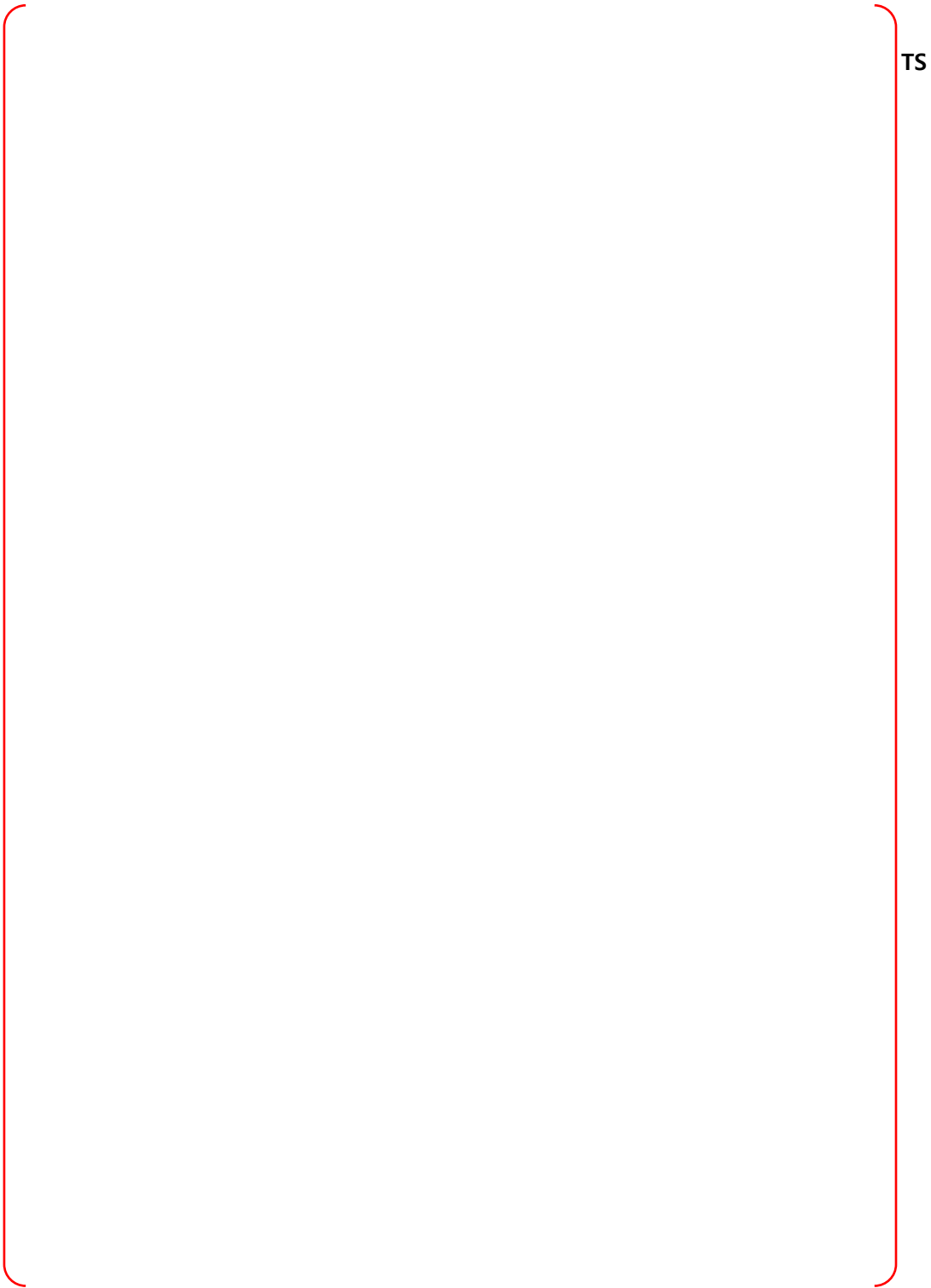


Figure B-103 Node 26, NW IRWST with Spargers - Bounding Sequences – DF

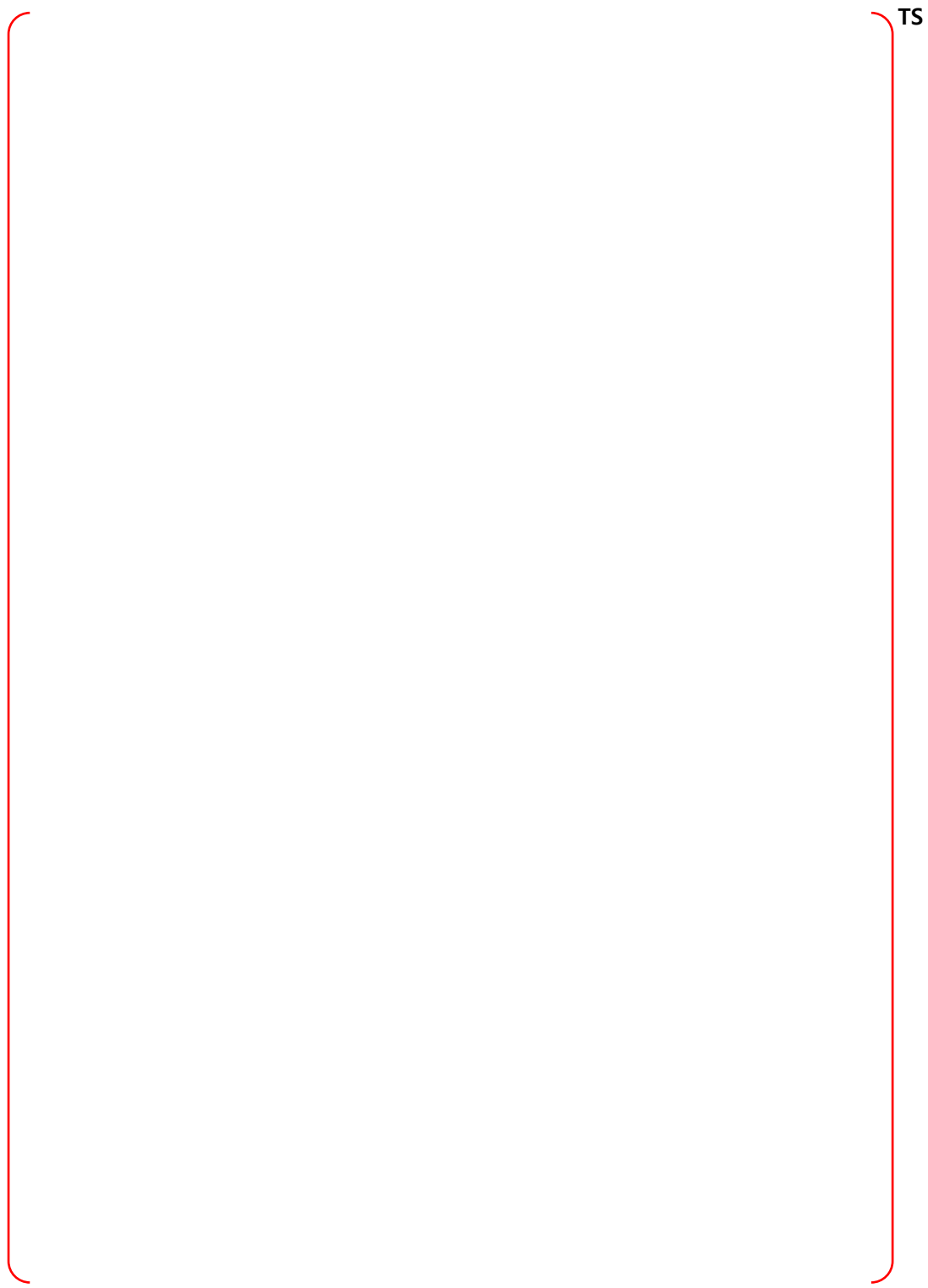


Figure B-104 Node 27, Containment Dome at Elev 291.5' - PRA Sequences

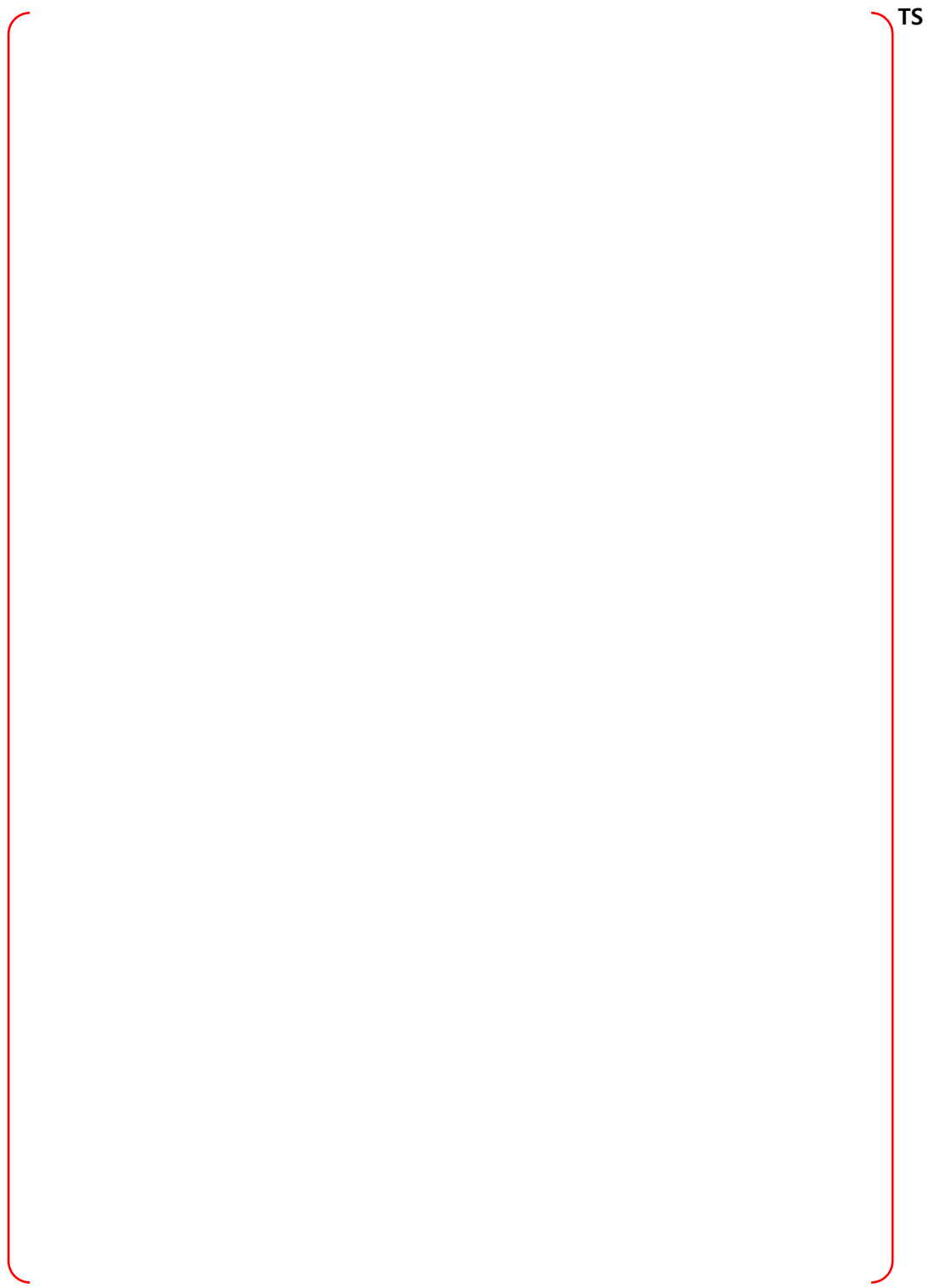


Figure B-105 Node 27, Containment Dome at Elev 291.5' - Bounding Sequences – MCCI

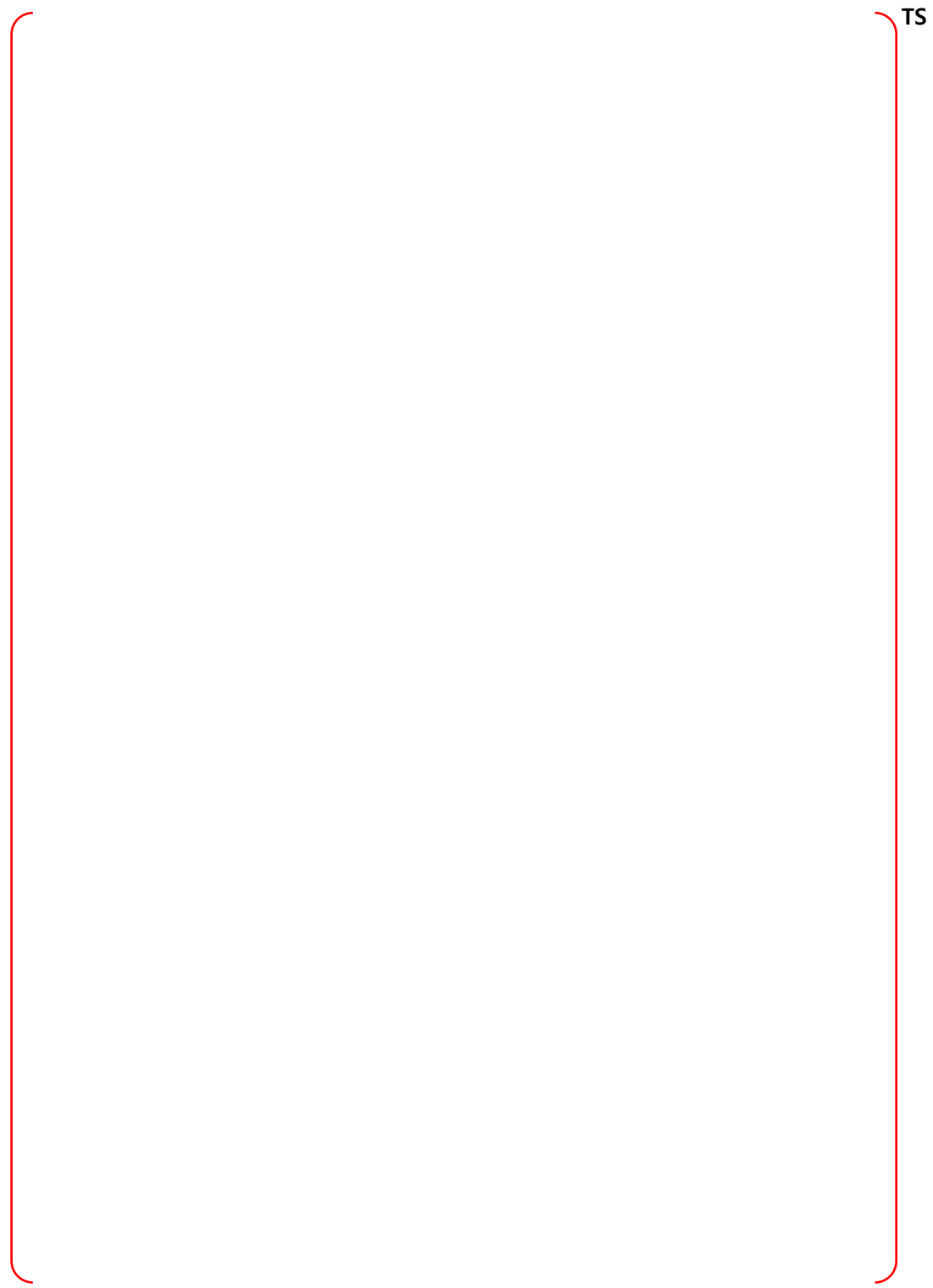


Figure B-106 Node 27, Containment Dome at Elev 291.5' - Bounding Sequences – CP

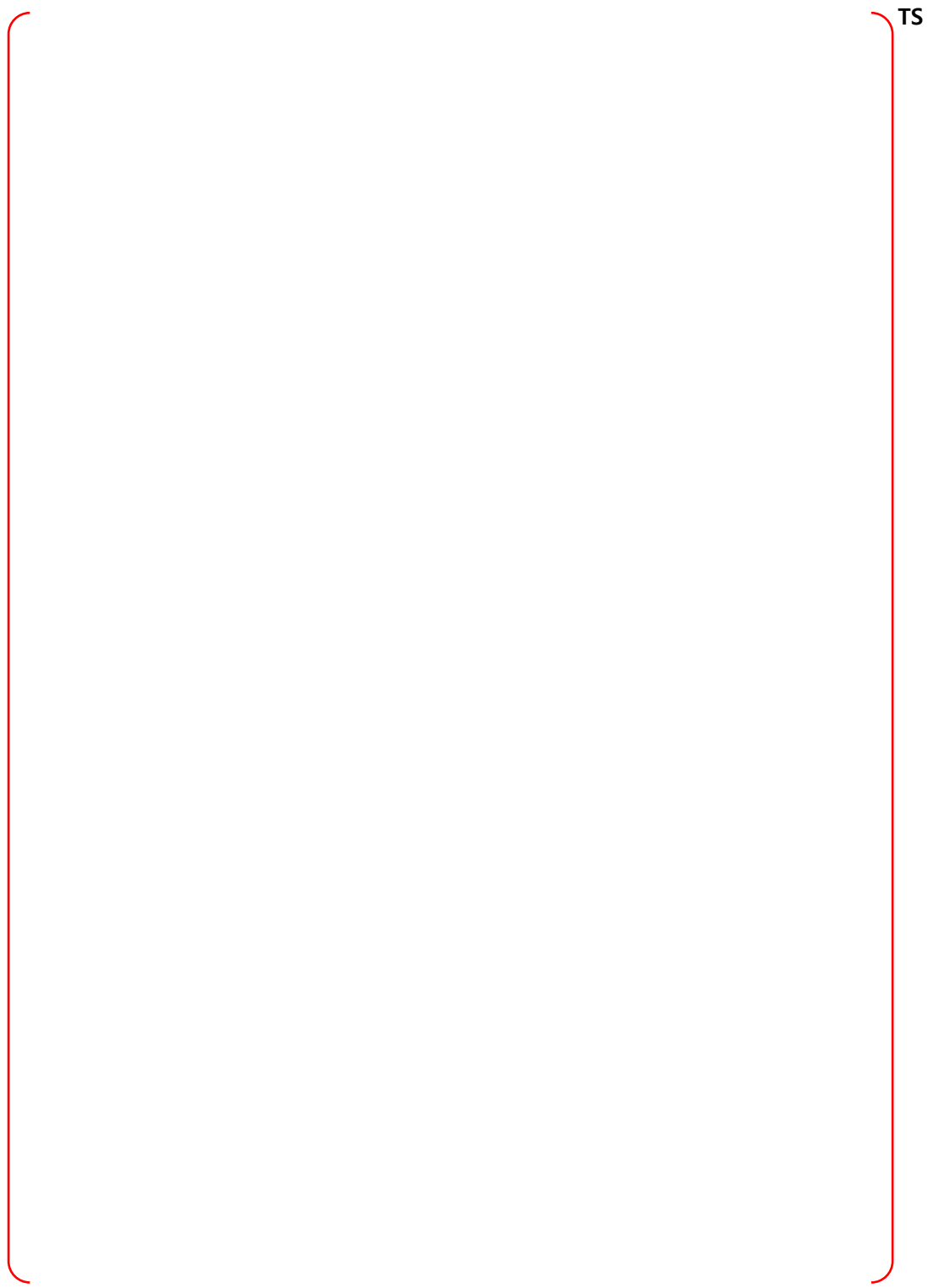


Figure B-107 Node 27, Containment Dome at Elev 291.5' - Bounding Sequences – DF

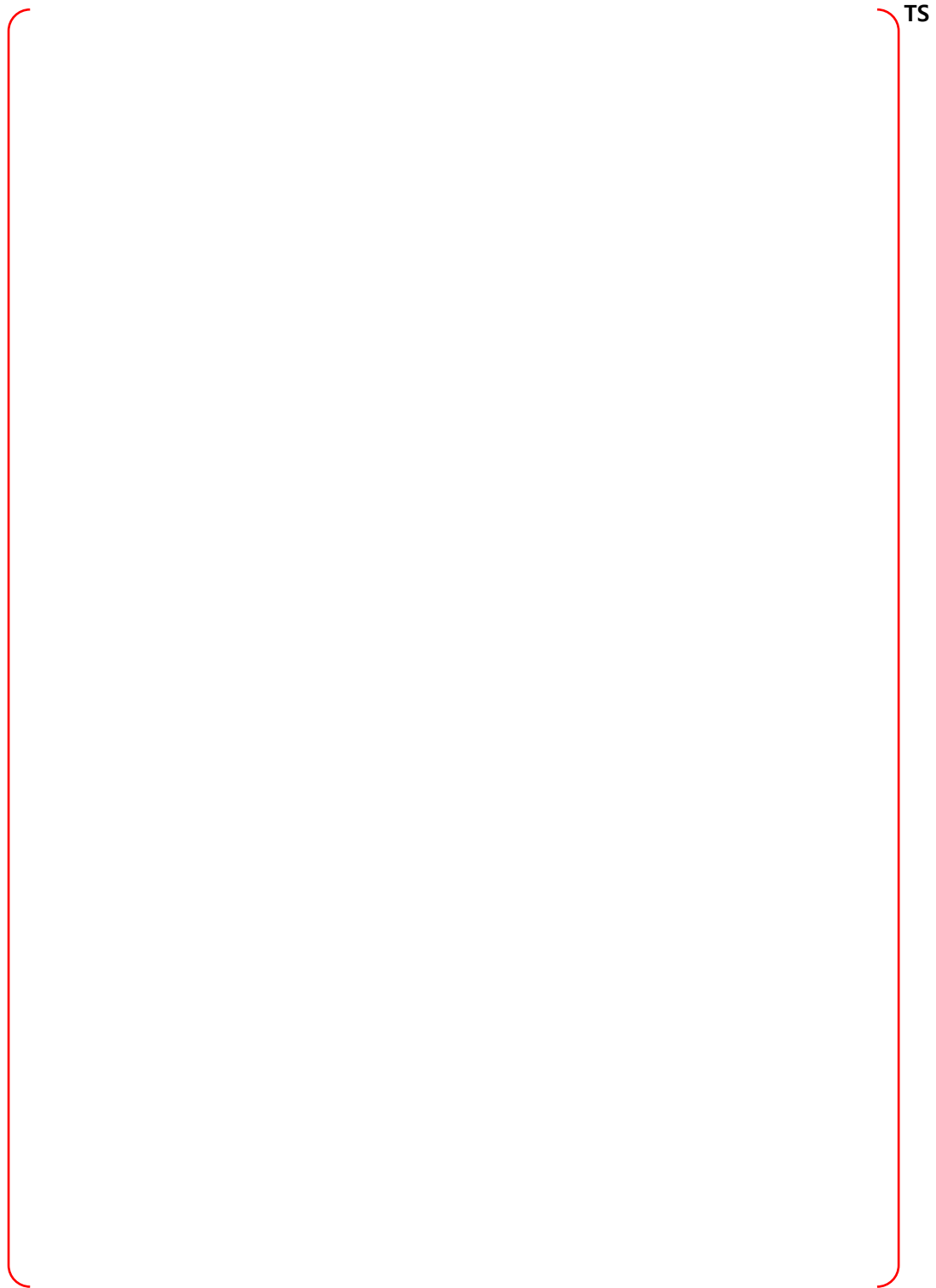


Figure B-108 Node 28, SW IRWST with Spargers - PRA Sequences

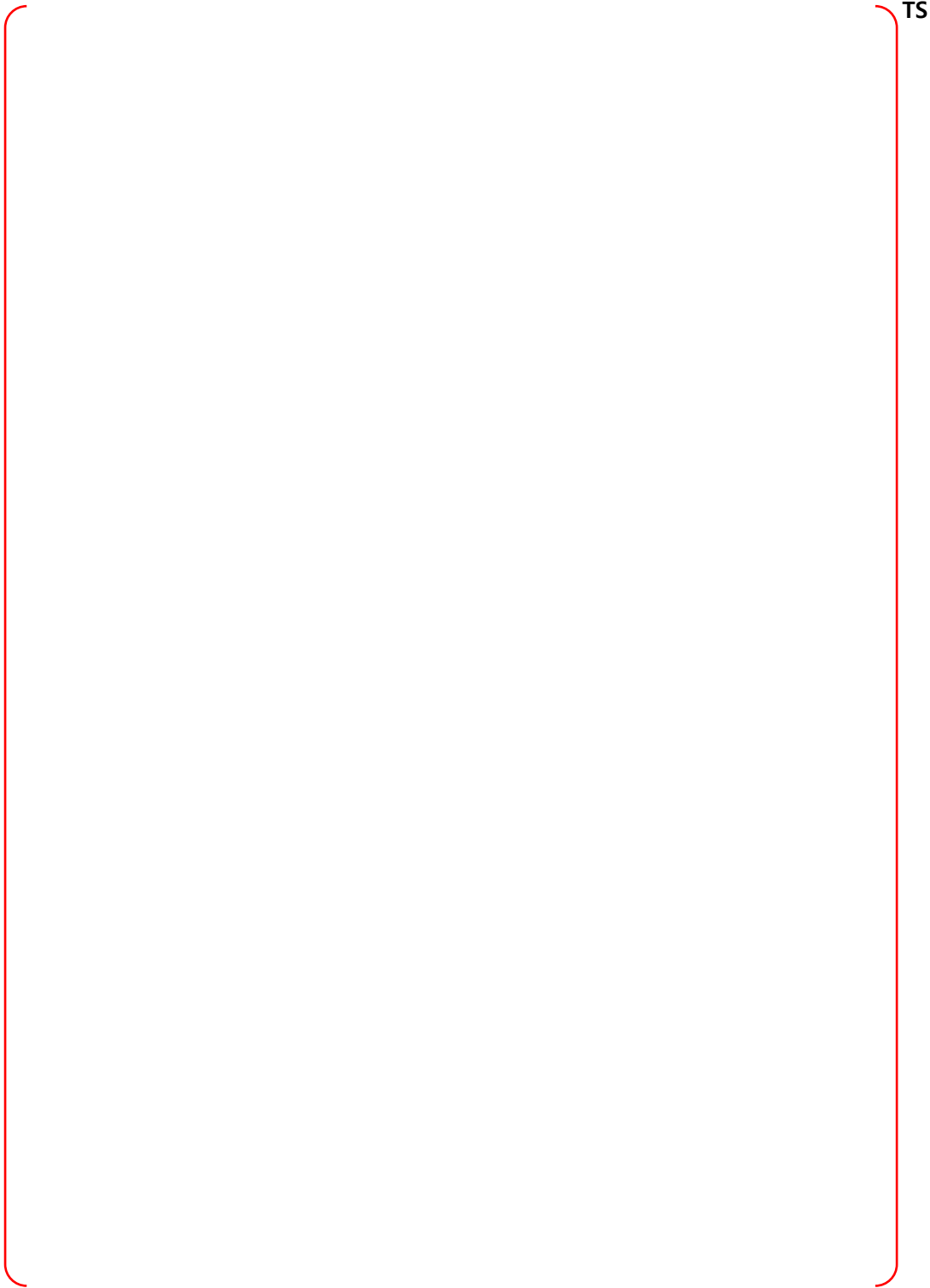


Figure B-109 Node 28, SW IRWST with Spargers - Bounding Sequences – MCCI

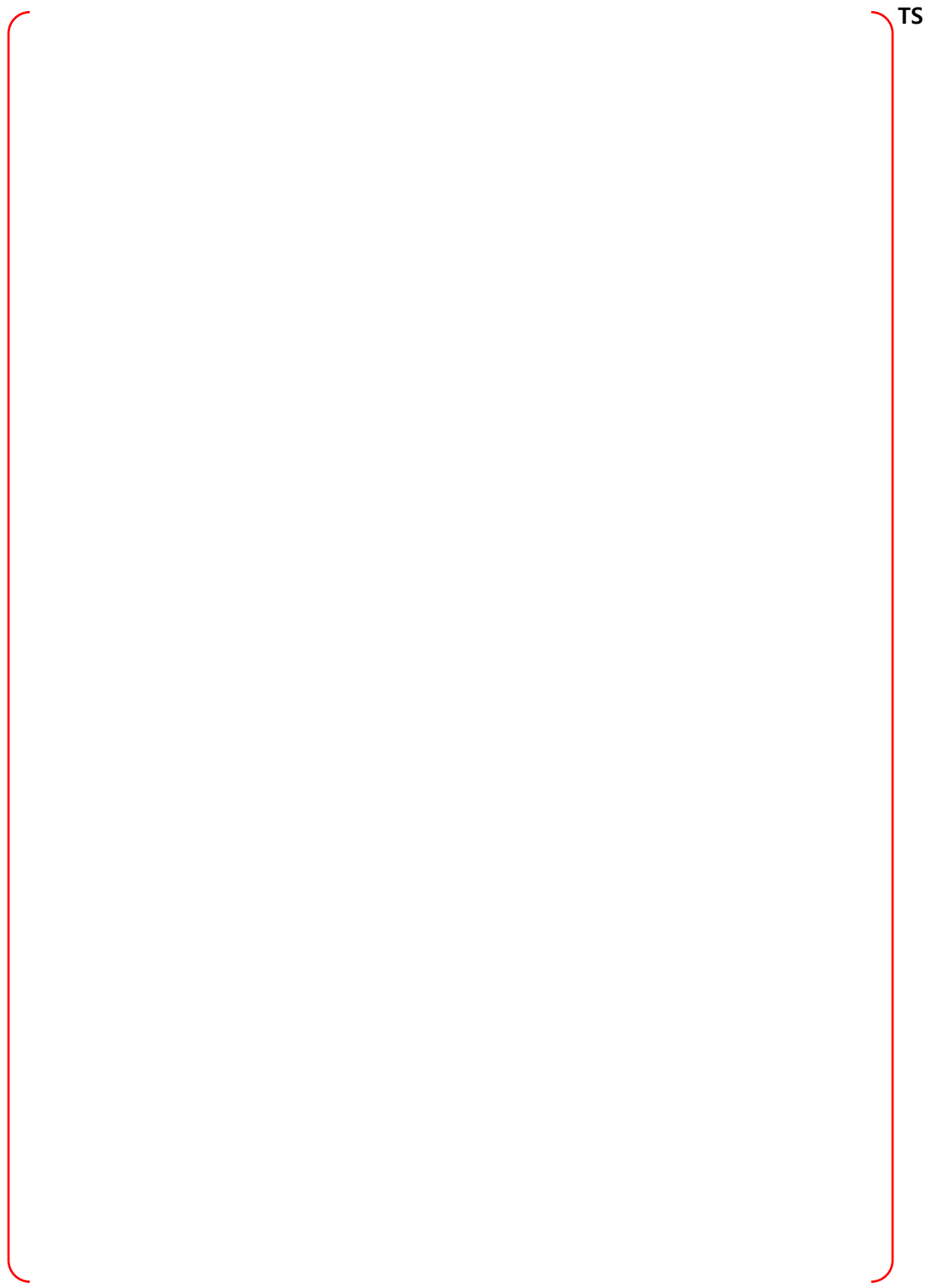


Figure B-110 Node 28, SW IRWST with Spargers - Bounding Sequences – CP

TS

Figure B-111 Node 28, SW IRWST with Spargers - Bounding Sequences – DF

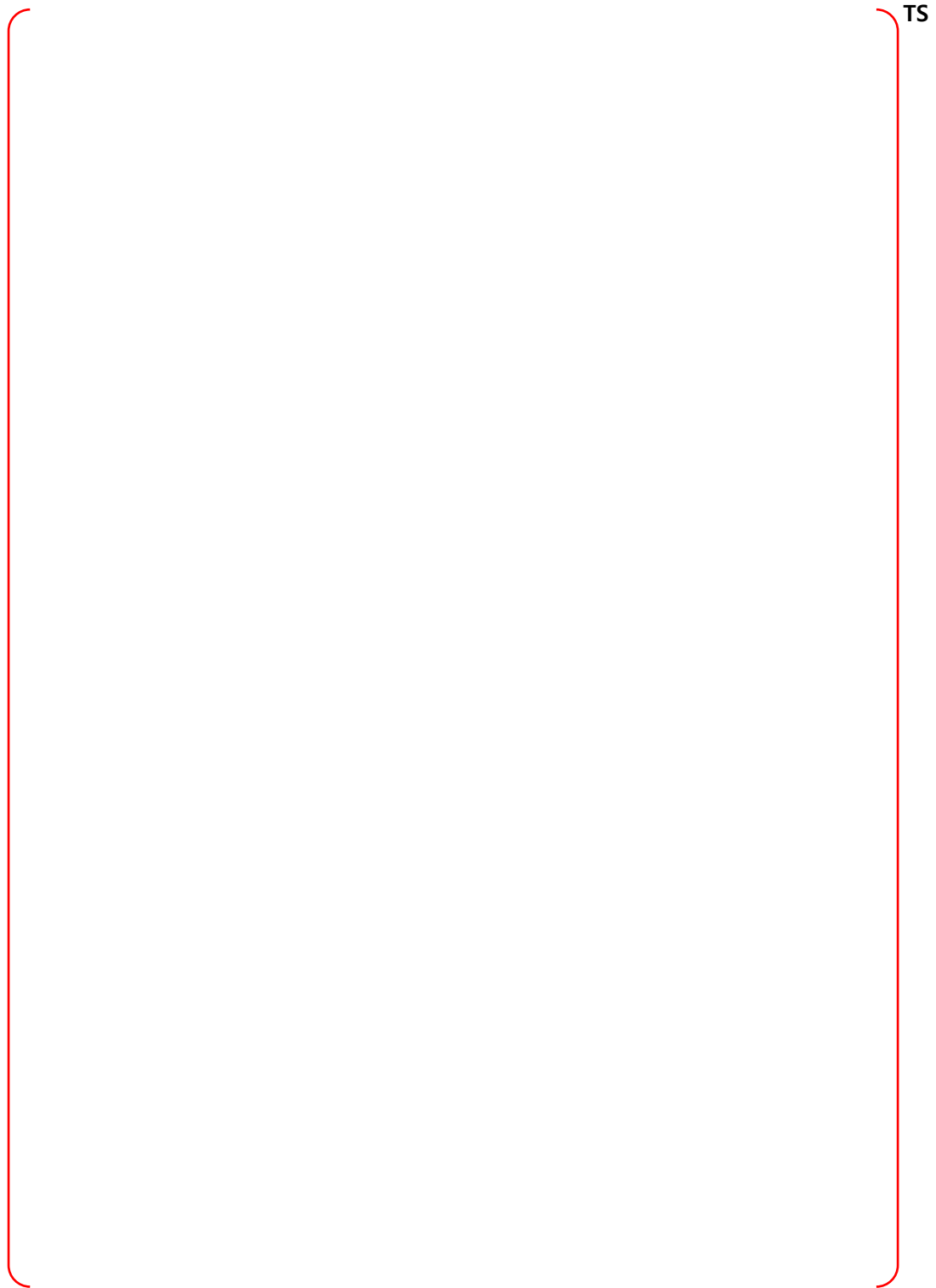


Figure B-112 Node 29, SE IRWST - PRA Sequences

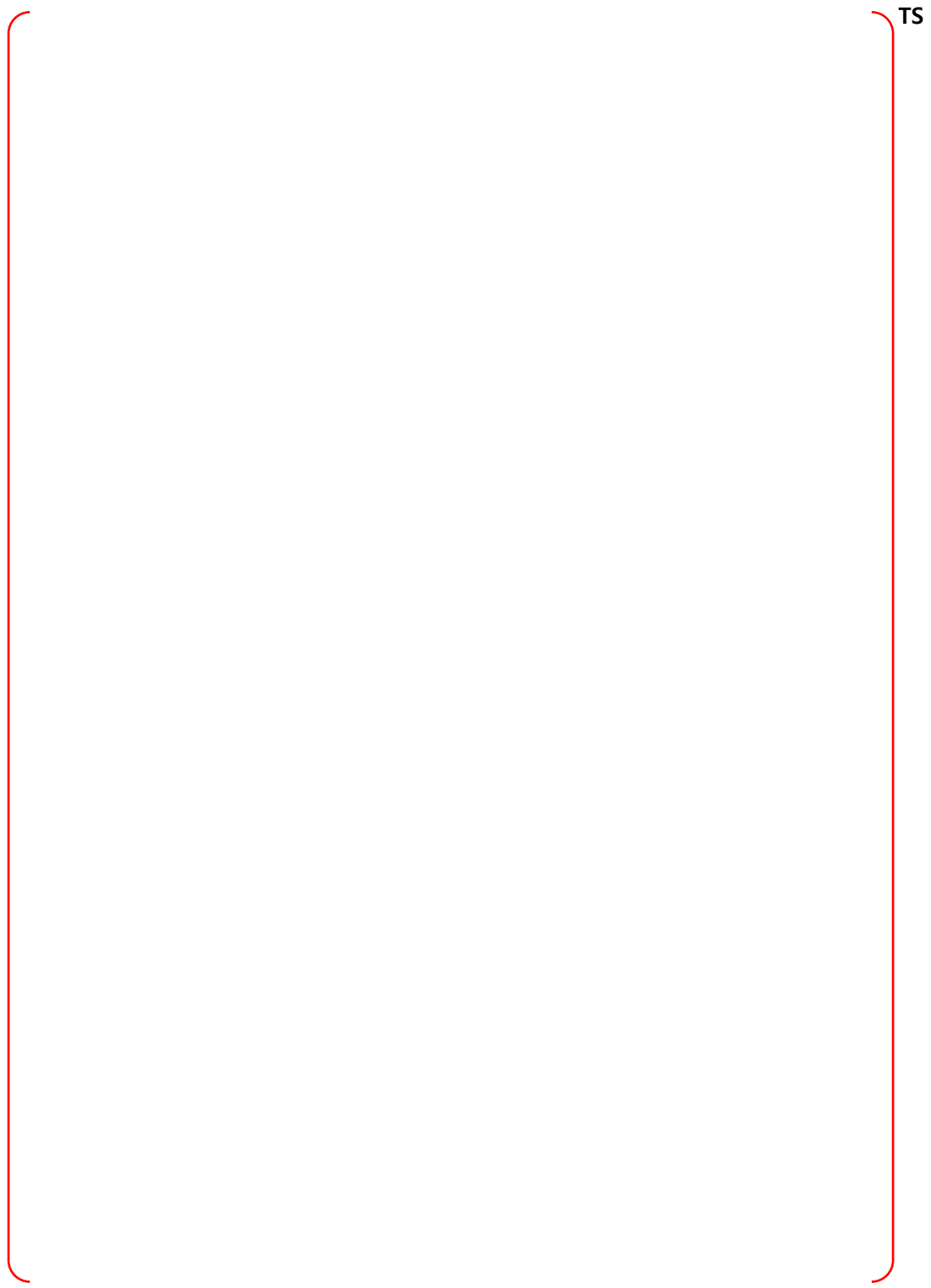


Figure B-113 Node 29, SE IRWST - Bounding Sequences – MCCI

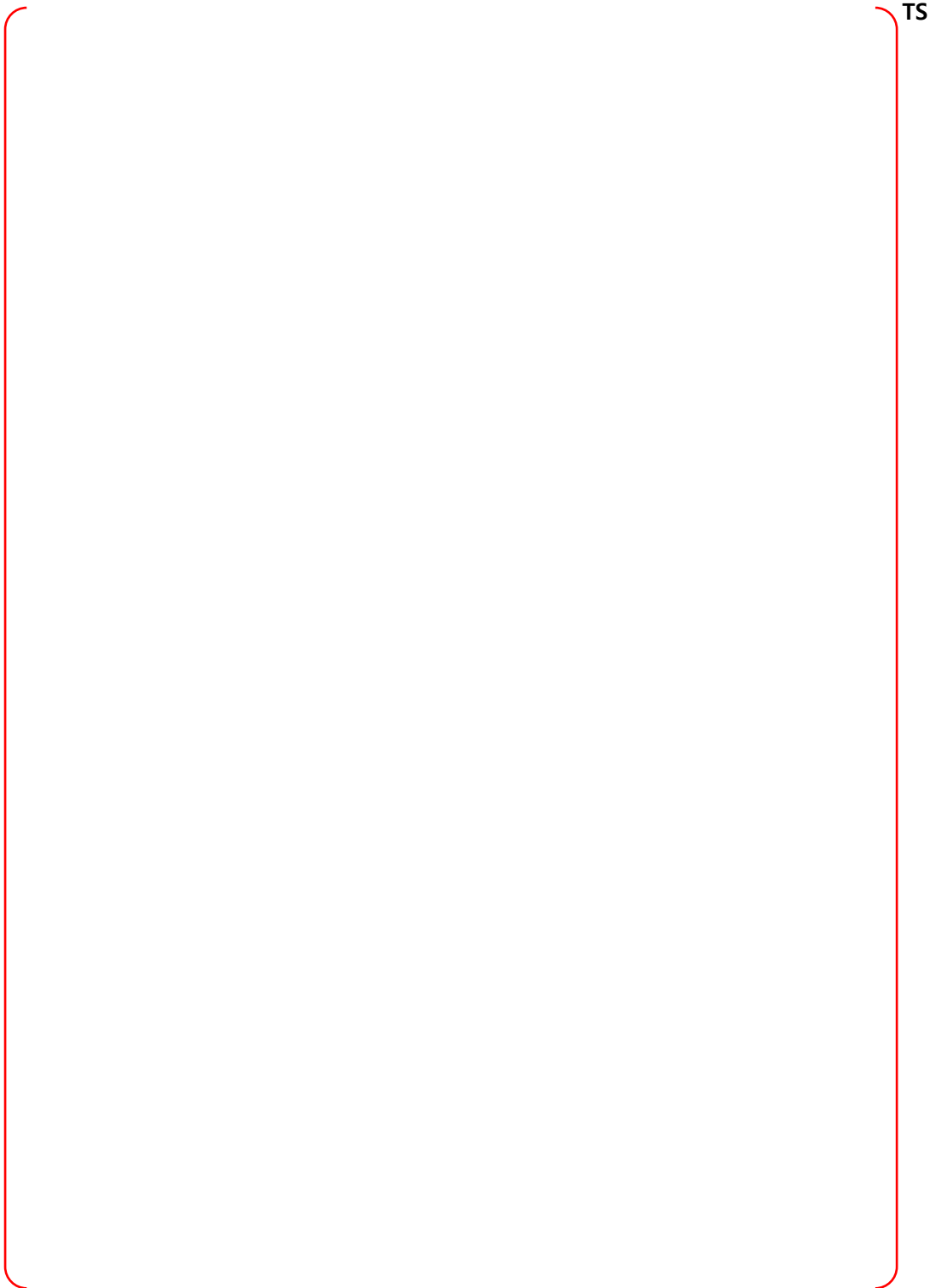


Figure B-114 Node 29, SE IRWST - Bounding Sequences – CP

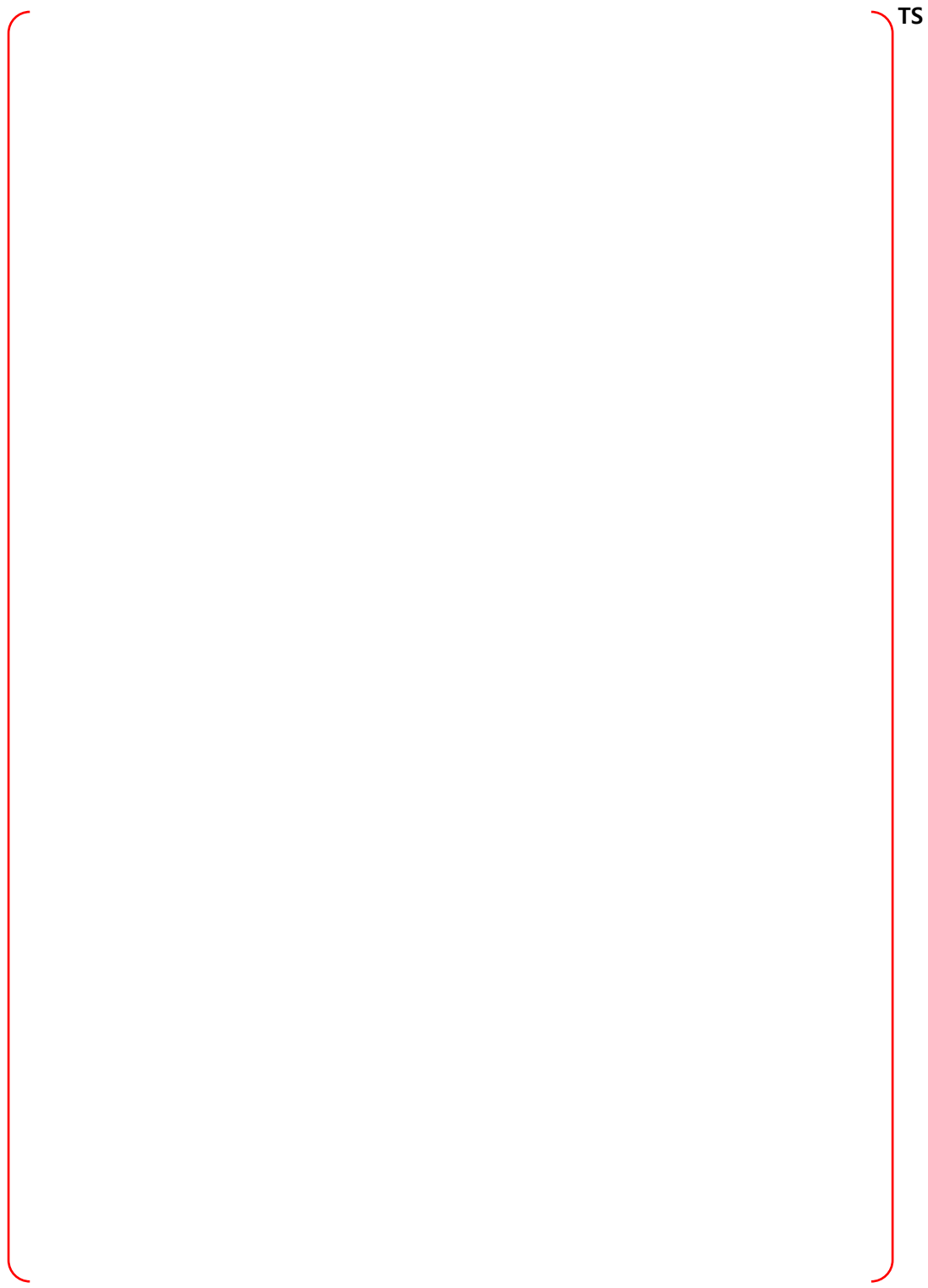


Figure B-115 Node 29, SE IRWST - Bounding Sequences – DF

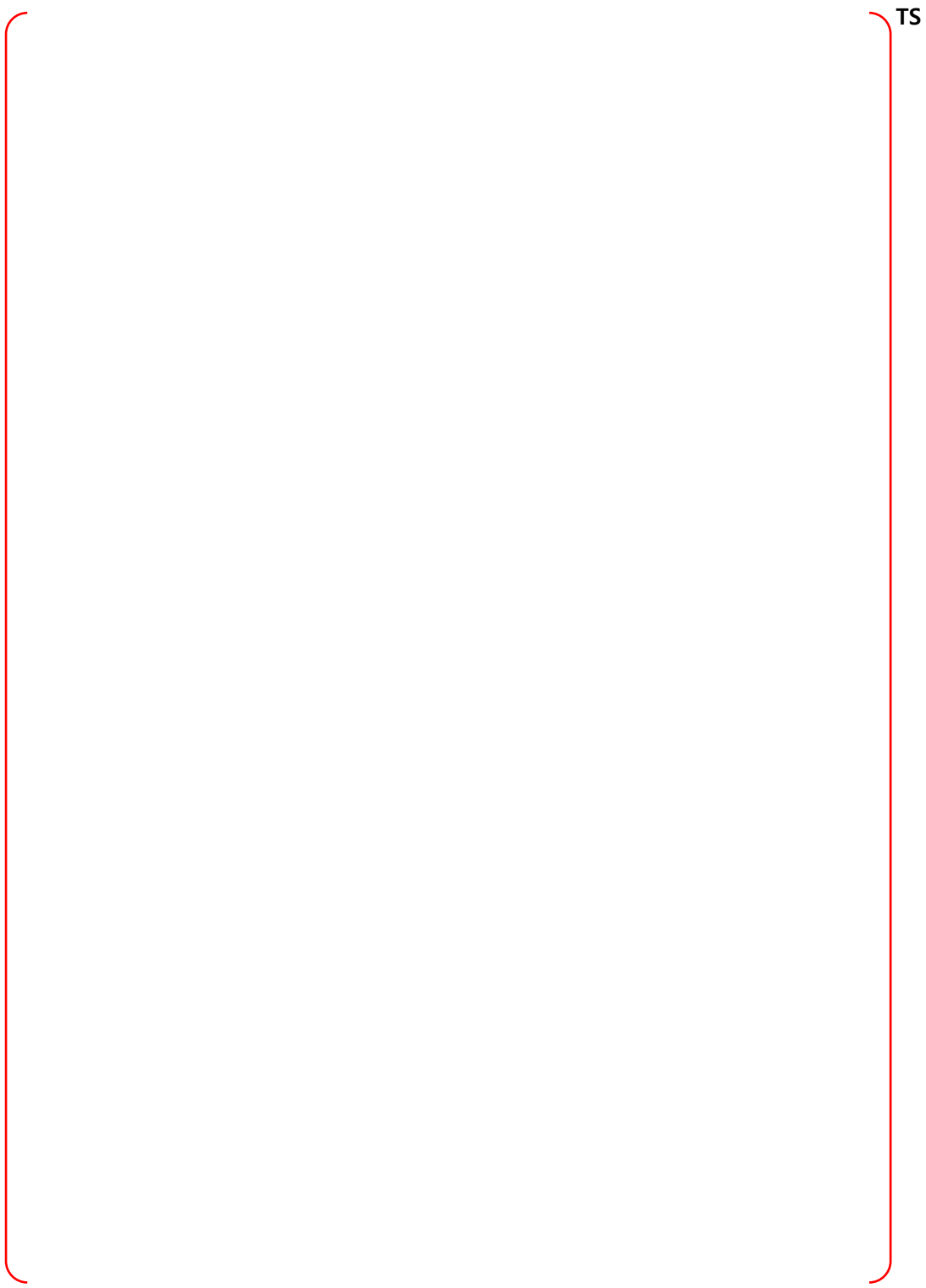


Figure B-116 Node 30, NE Annular Compartment at Elev 100' - PRA Sequences

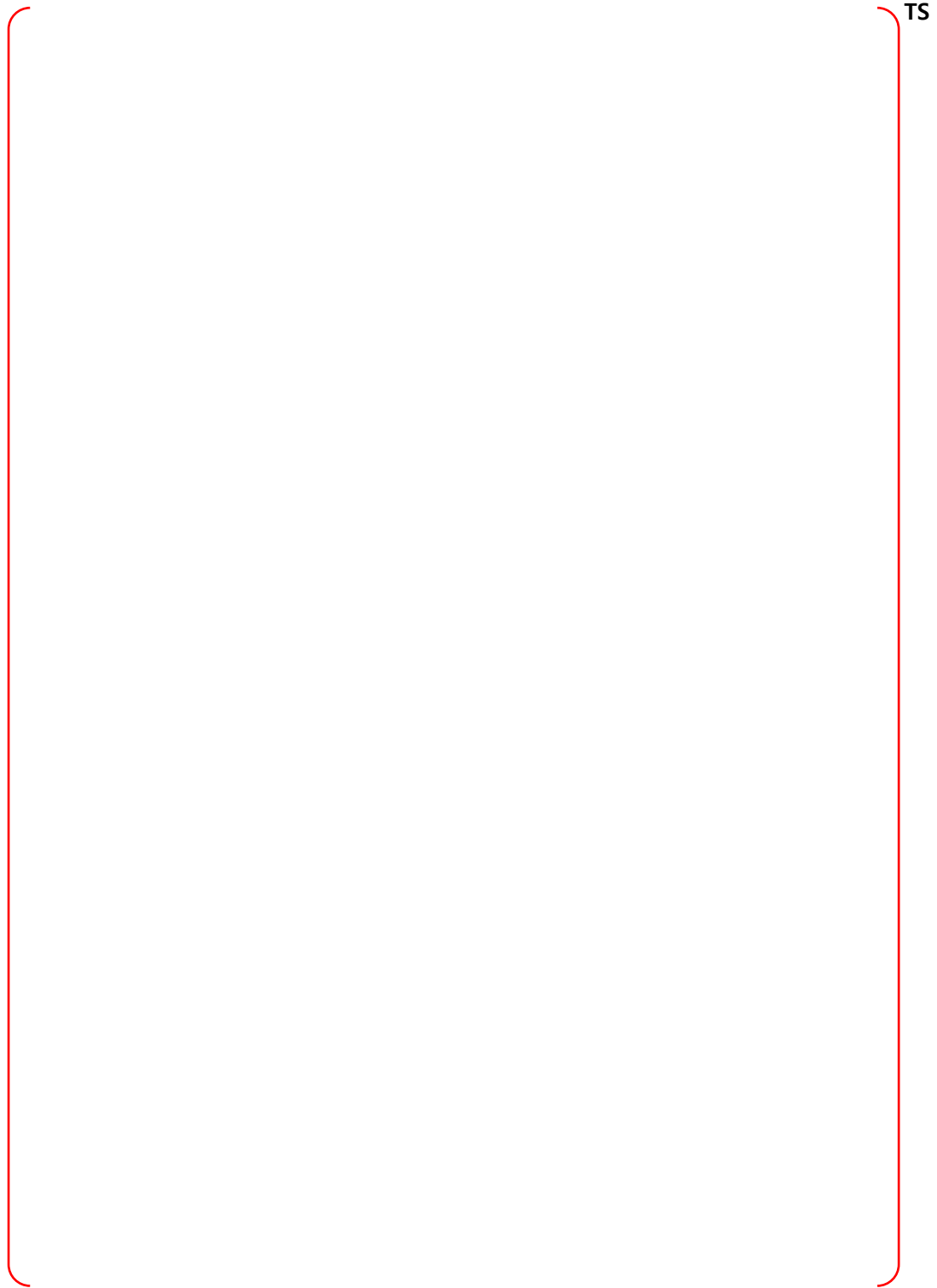


Figure B-117 Node 30, NE Annular Compartment at Elev 100' - Bounding Sequences – MCCI

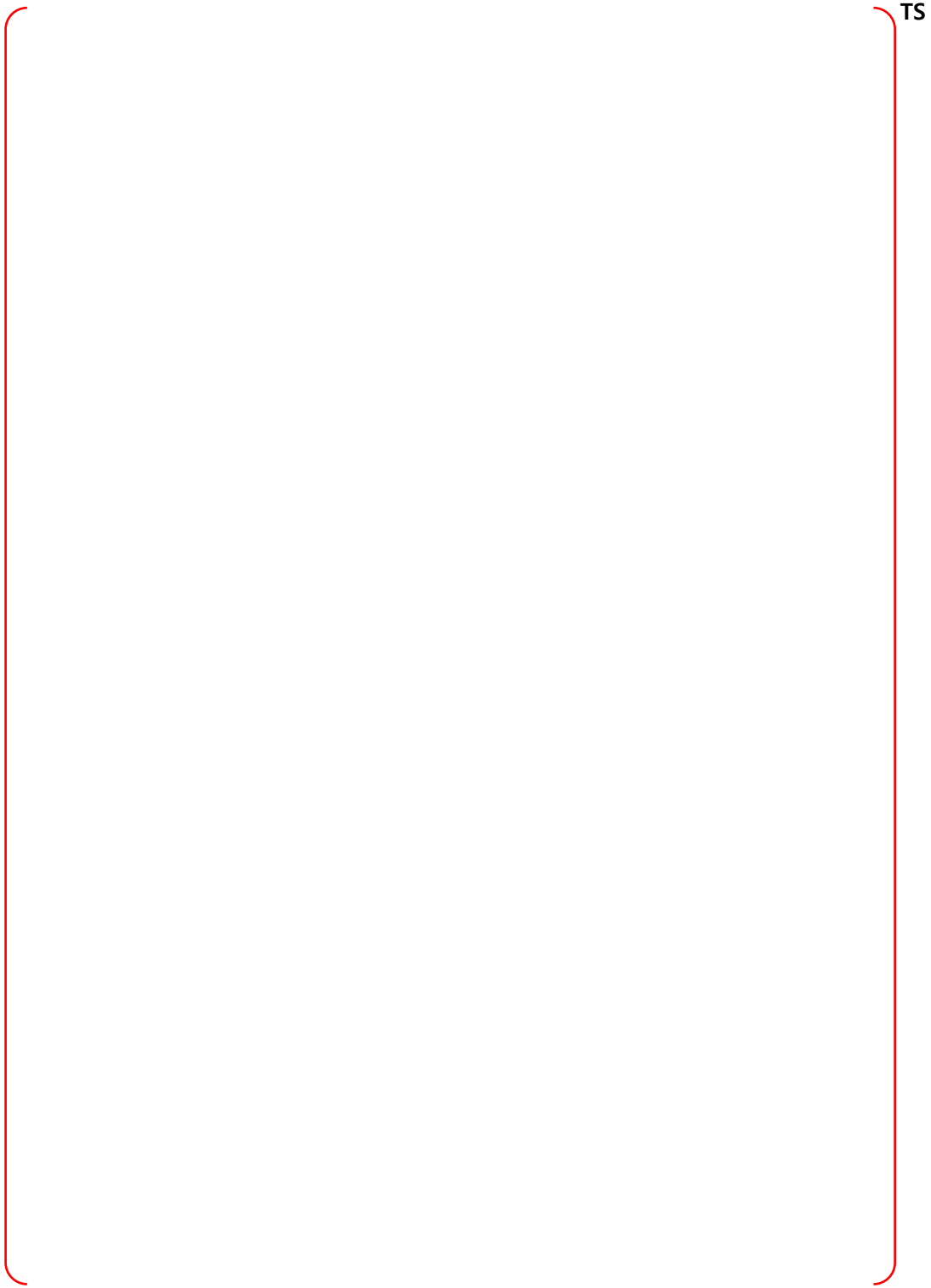


Figure B-118 Node 30, NE Annular Compartment at Elev 100' - Bounding Sequences – CP

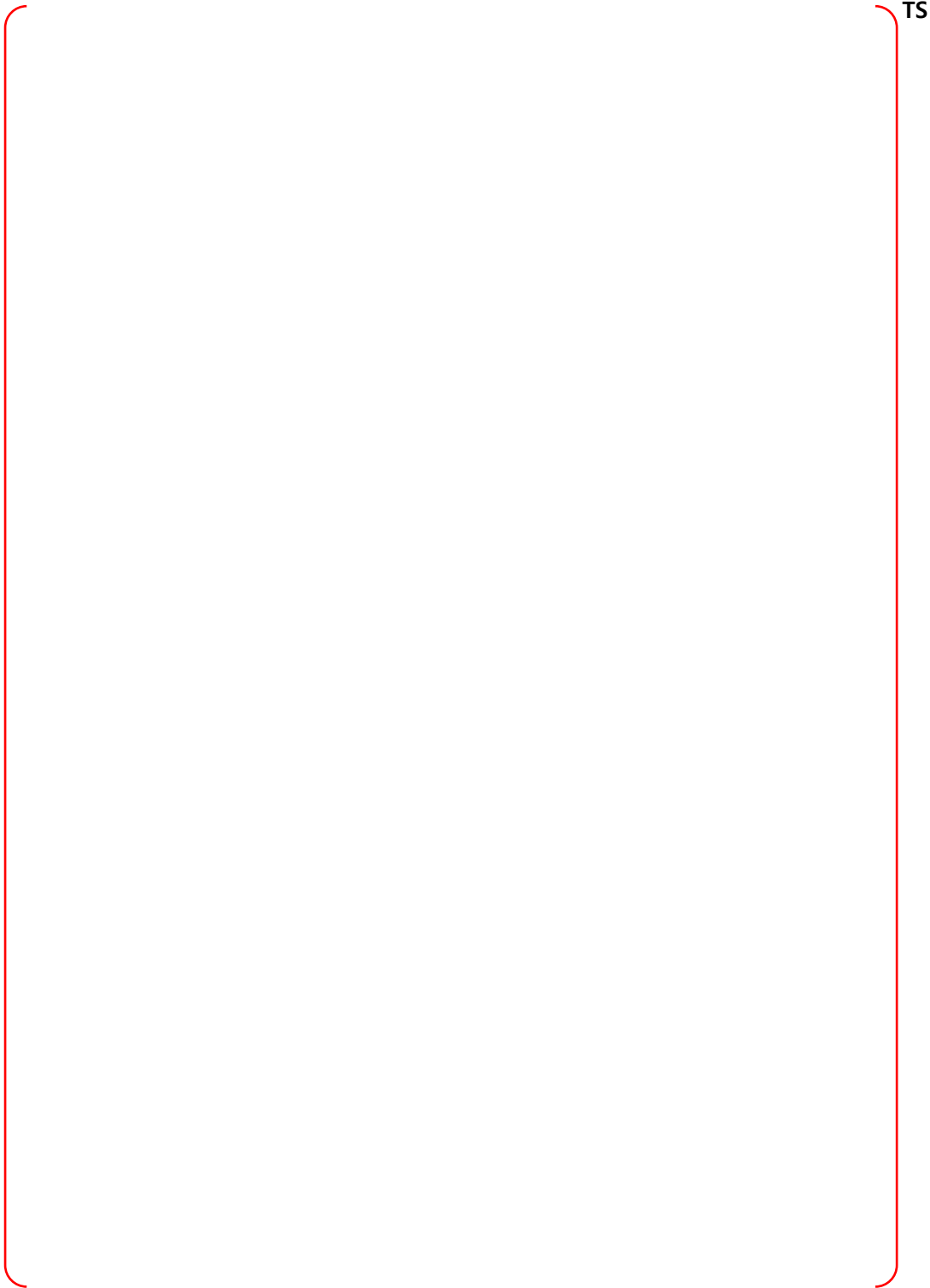


Figure B-119 Node 30, NE Annular Compartment at Elev 100' - Bounding Sequences - DF

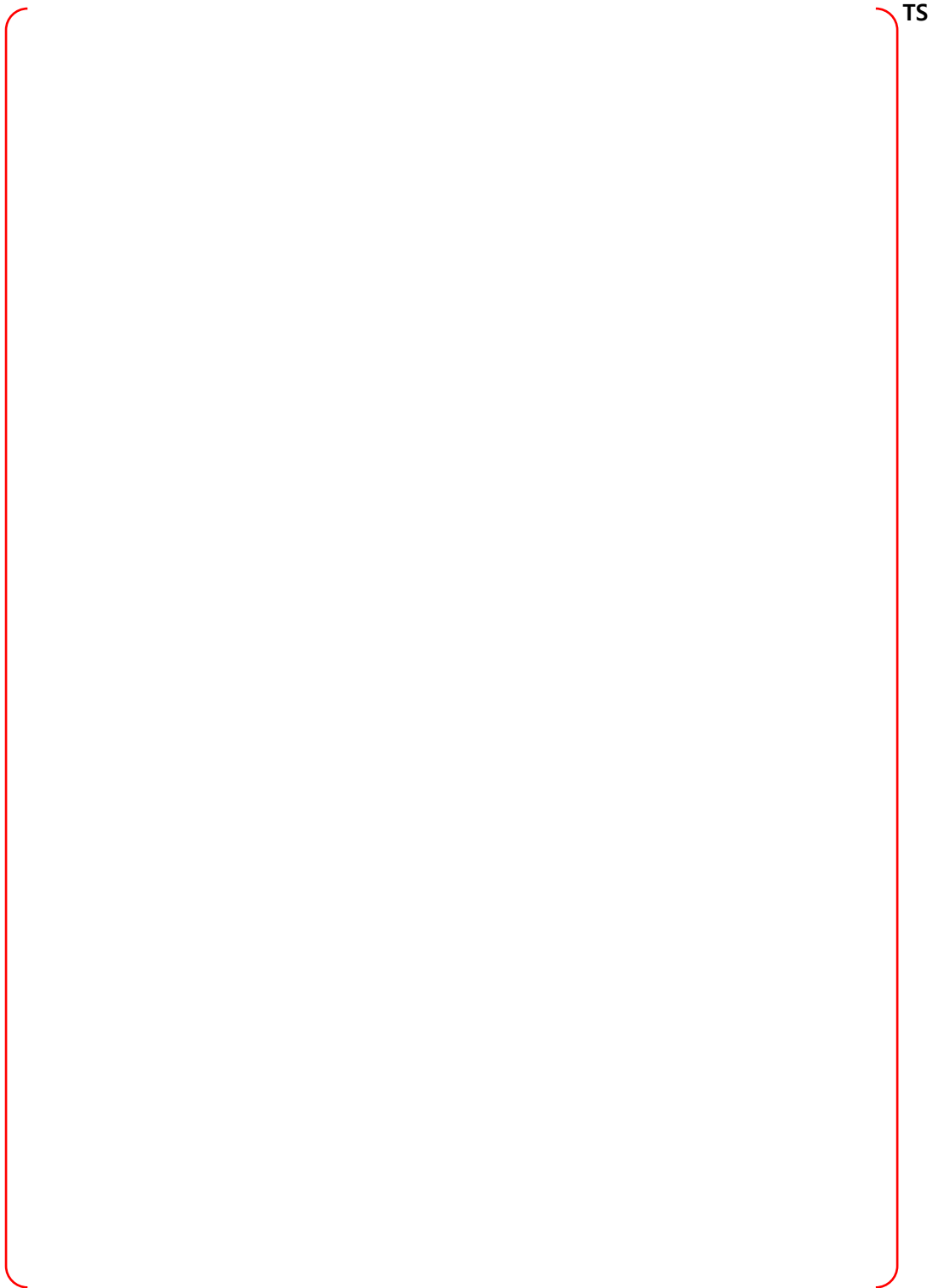


Figure B-120 Node 31, SE Annular Compartment at Elev 100' - PRA Sequences

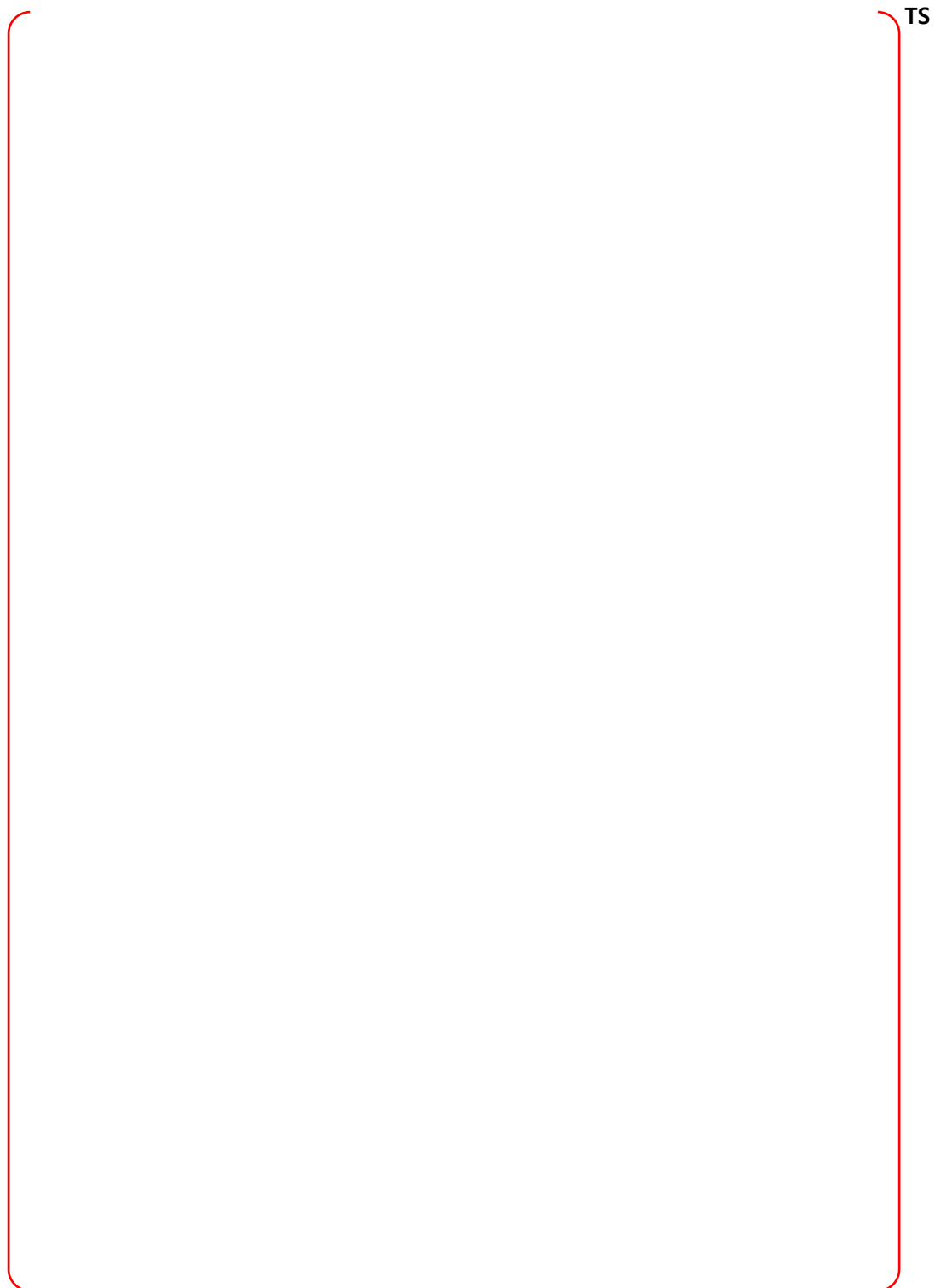


Figure B-121 Node 31, SE Annular Compartment at Elev 100' - Bounding Sequences – MCCI

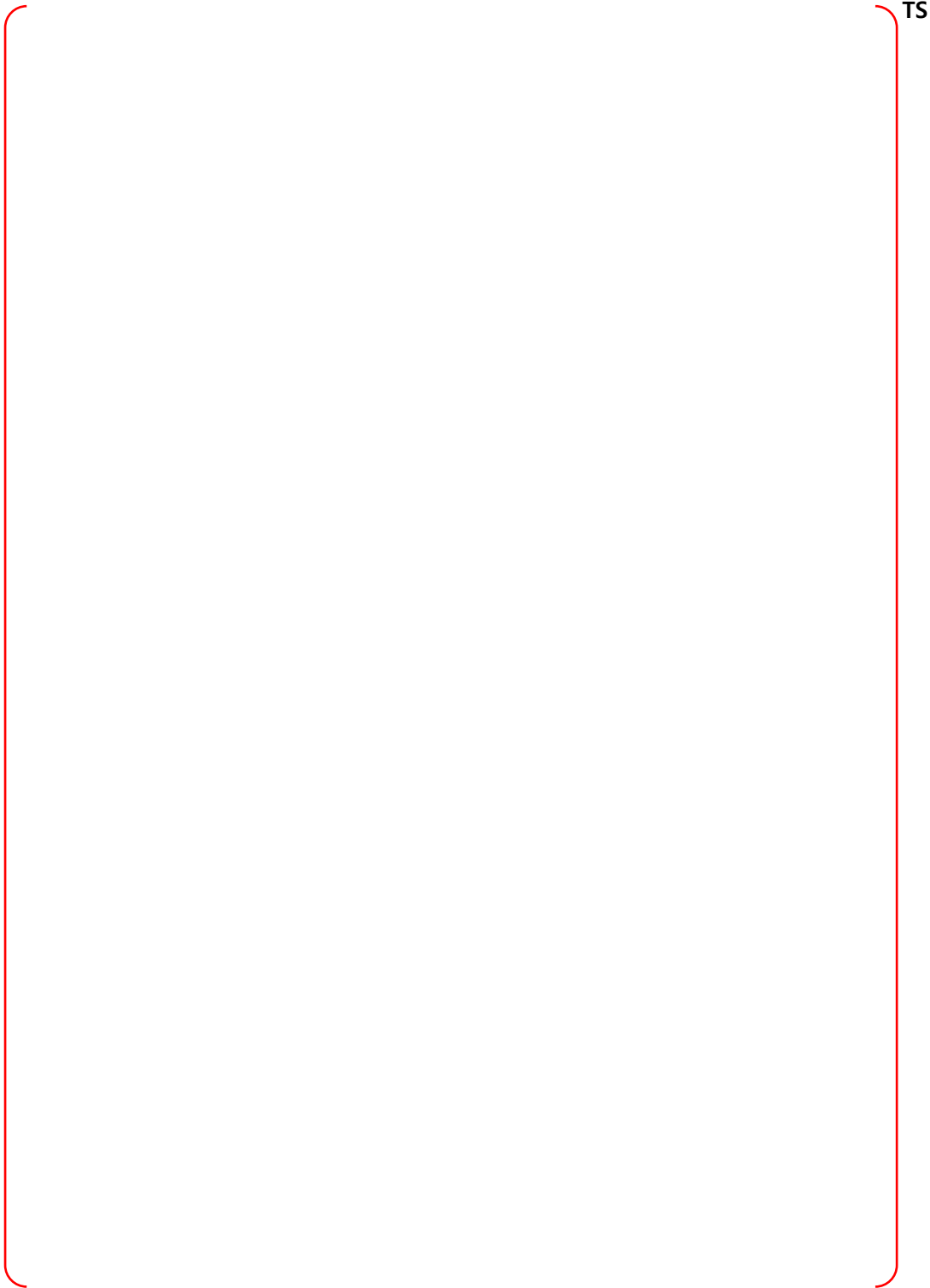


Figure B-122 Node 31, SE Annular Compartment at Elev 100' - Bounding Sequences – CP

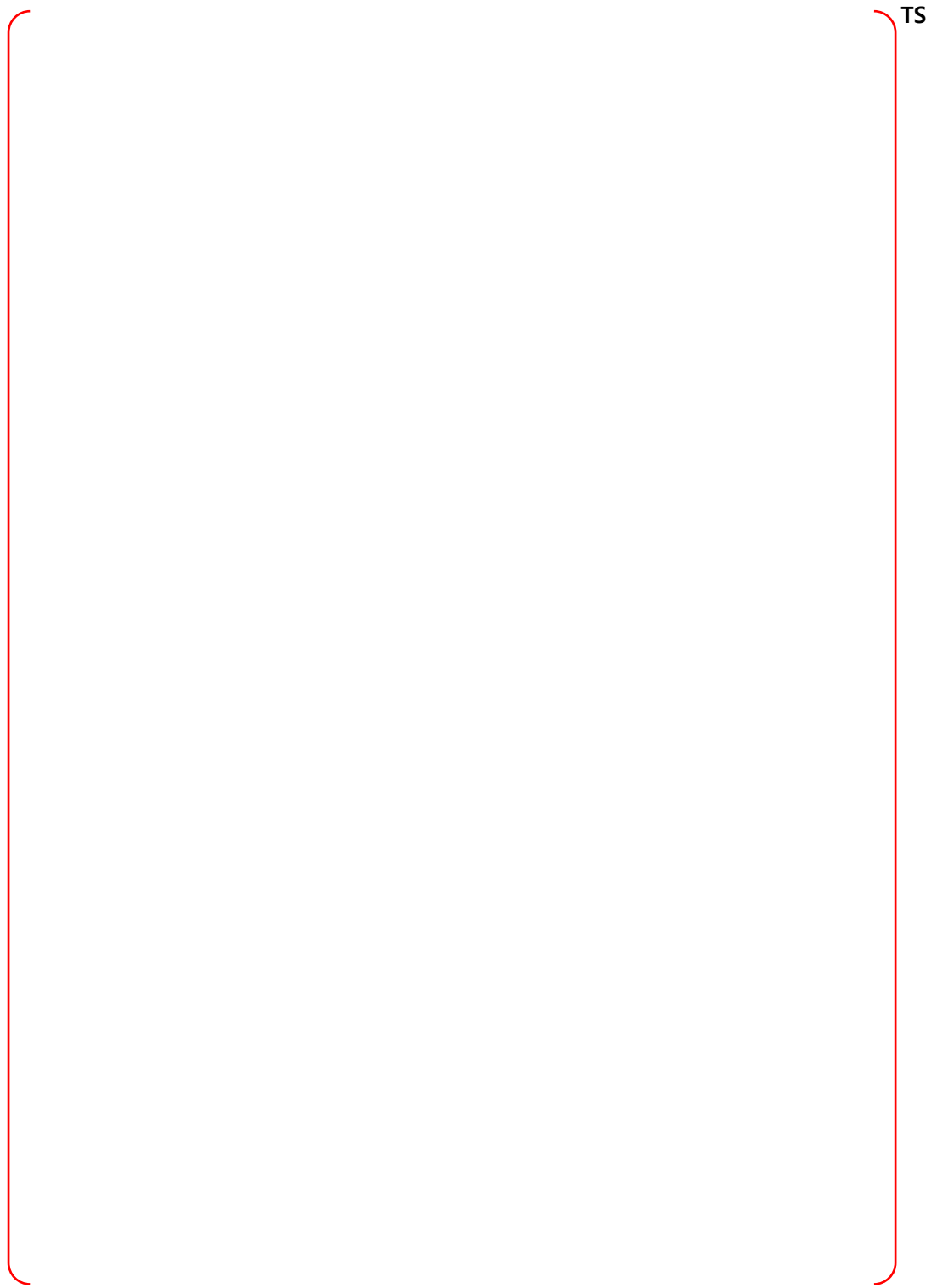


Figure B-123 Node 31, SE Annular Compartment at Elev 100' - Bounding Sequences - DF

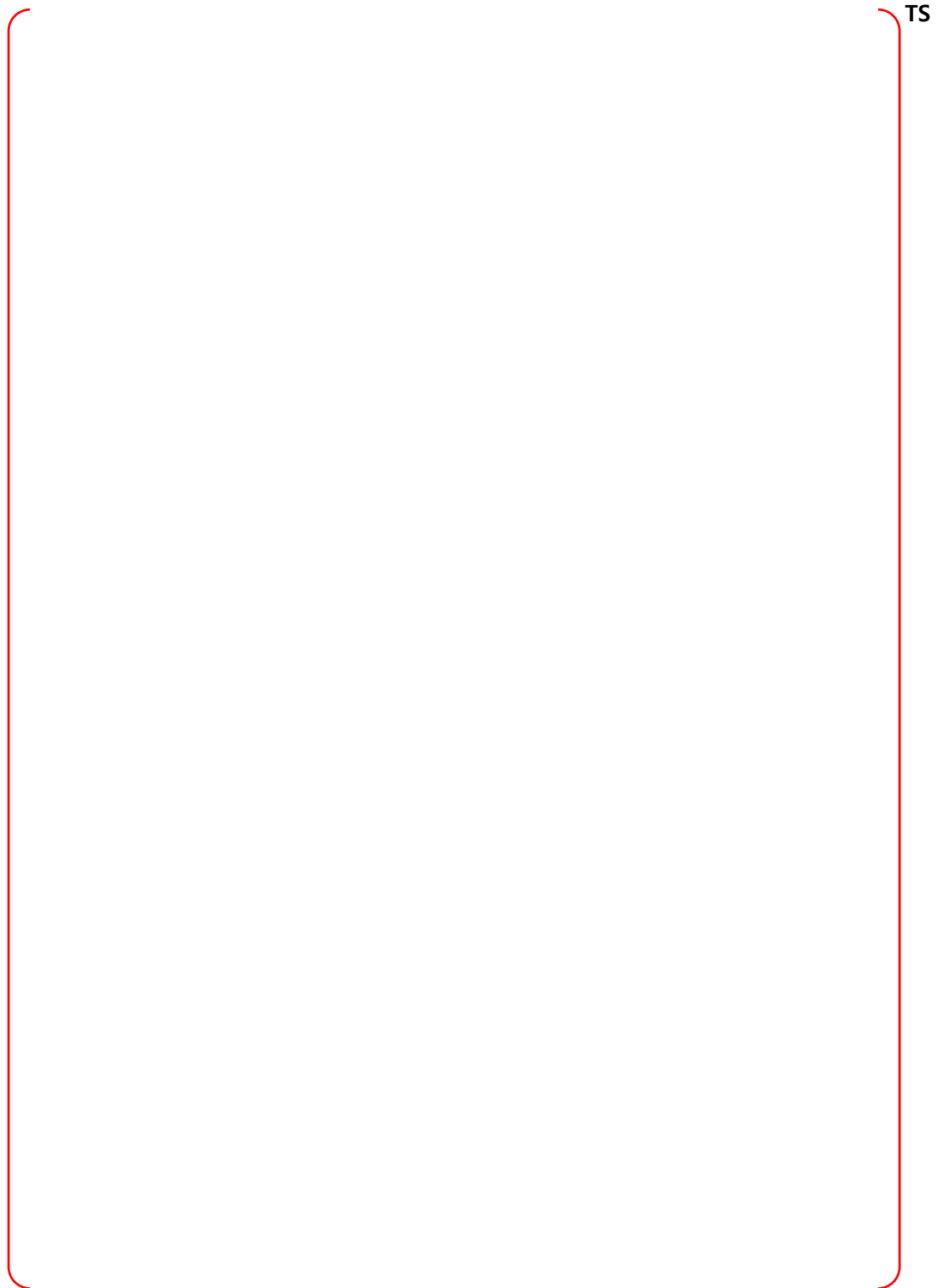


Figure B-124 Node 32, NE Annular Compartment at Elev 114' - PRA Sequences

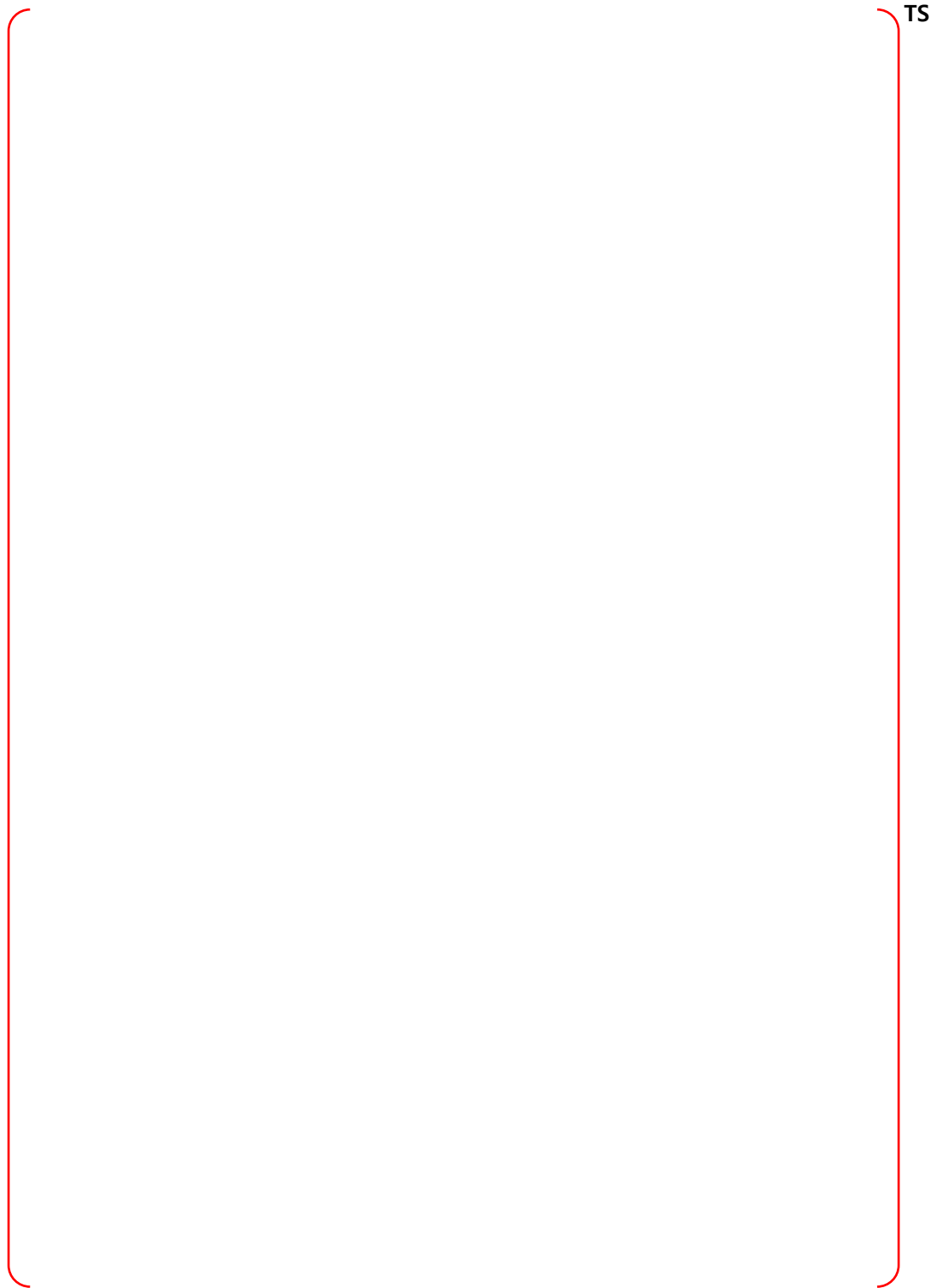


Figure B-125 Node 32, NE Annular Compartment at Elev 114' - Bounding Sequences – MCCI

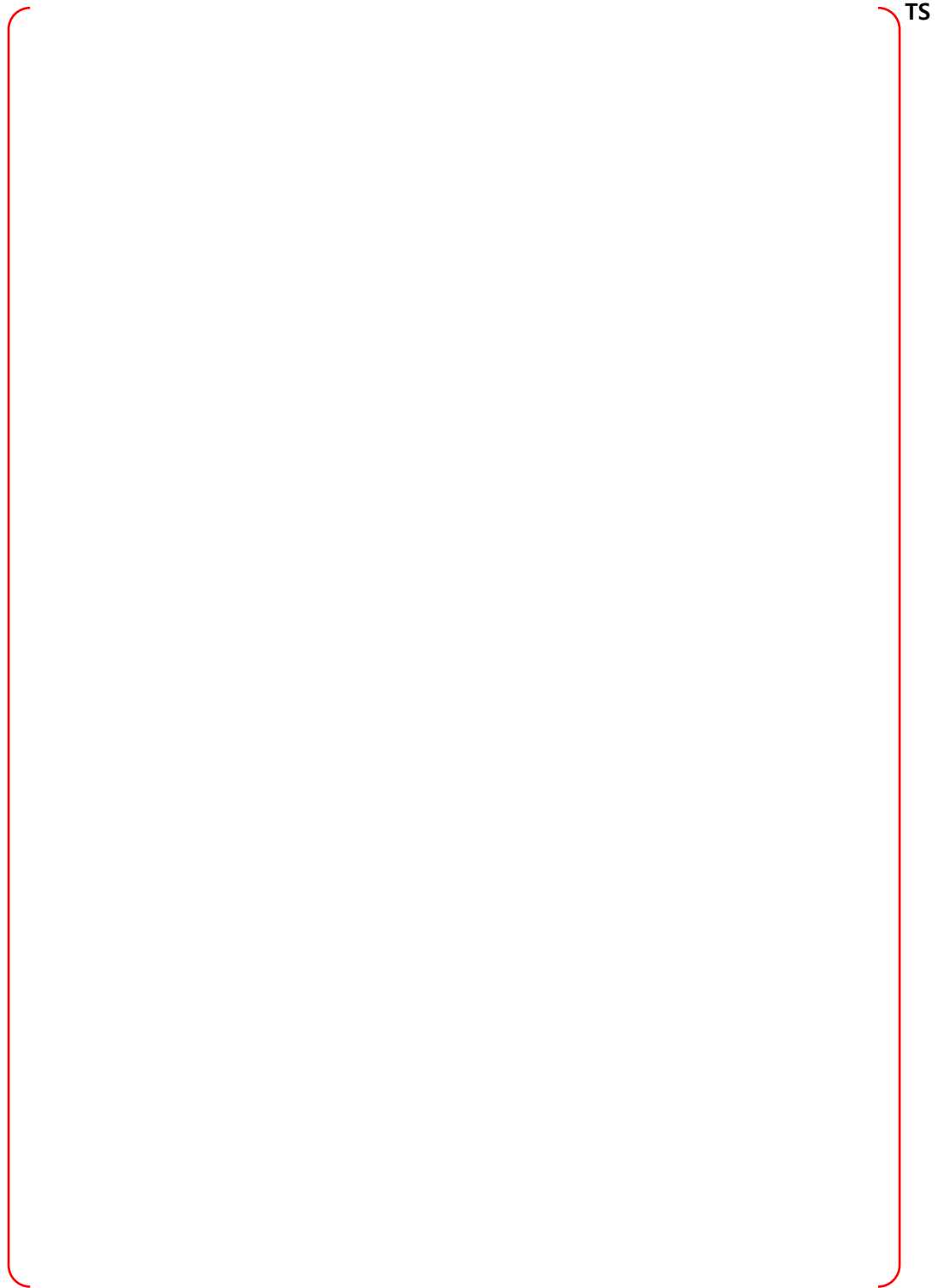


Figure B-126 Node 32, NE Annular Compartment at Elev 114' - Bounding Sequences – CP

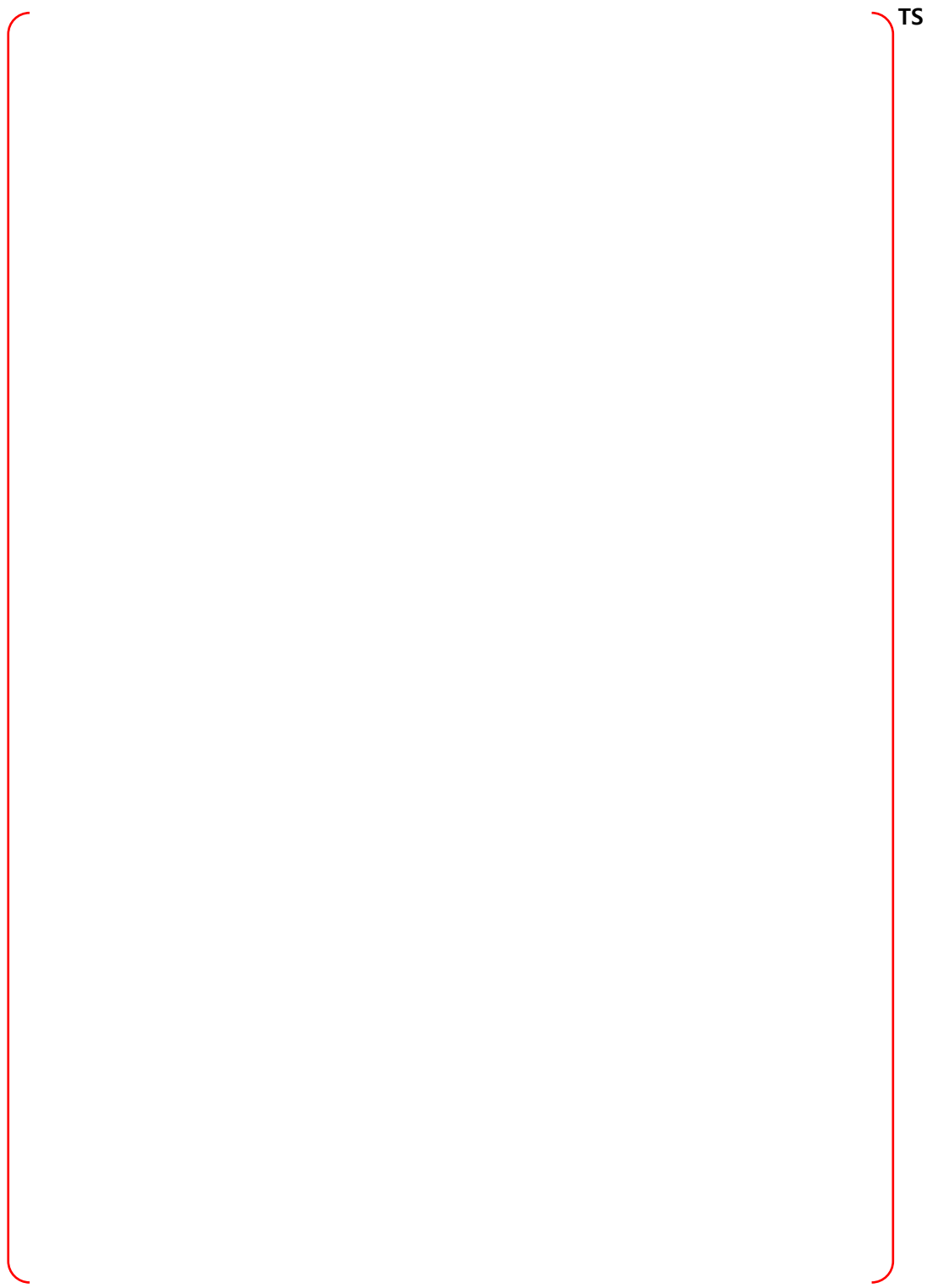


Figure B-127 Node 32, NE Annular Compartment at Elev 114' - Bounding Sequences - DF

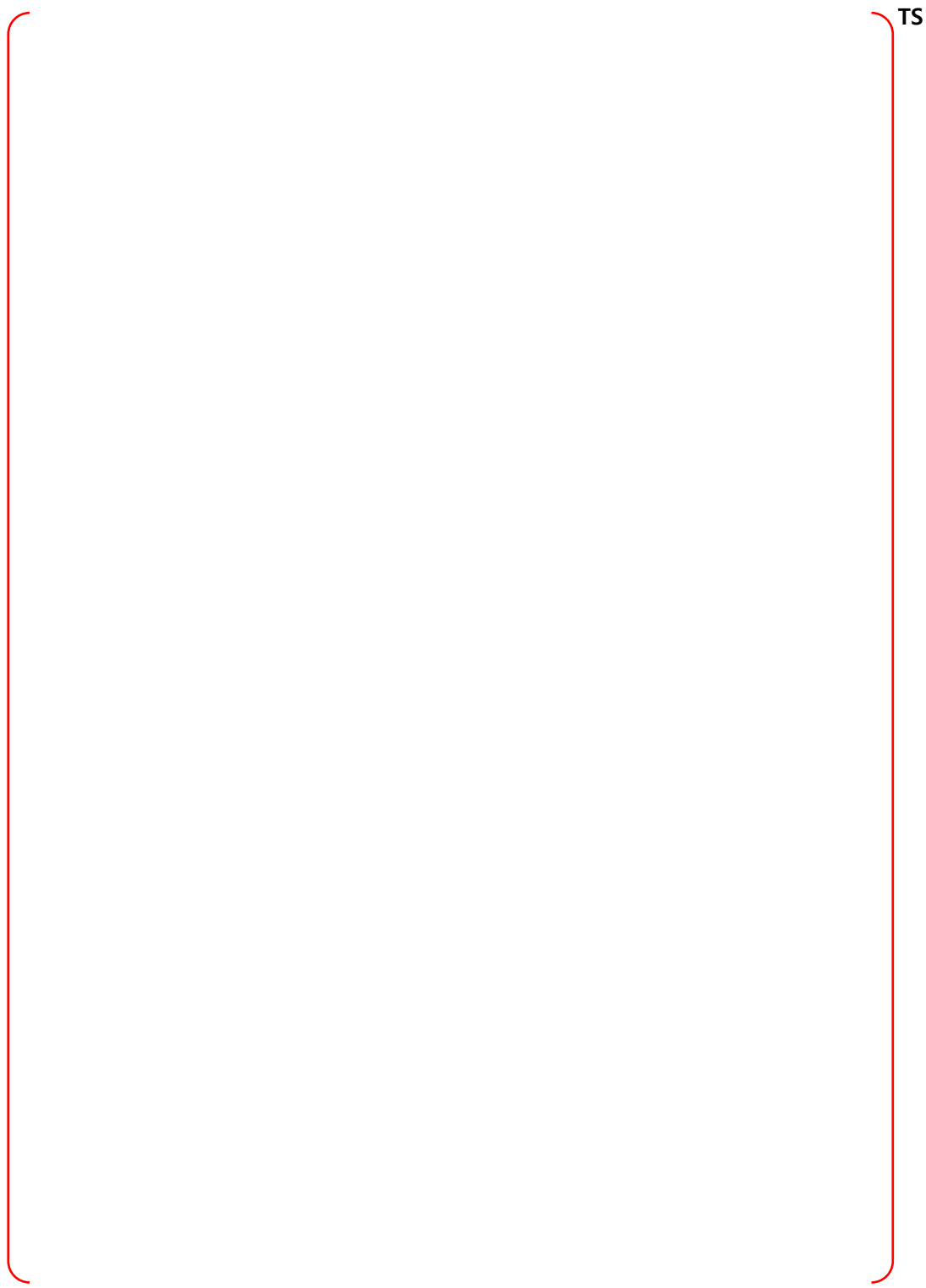


Figure B-128 Node 33, SE Annular Compartment at Elev 114' - PRA Sequences

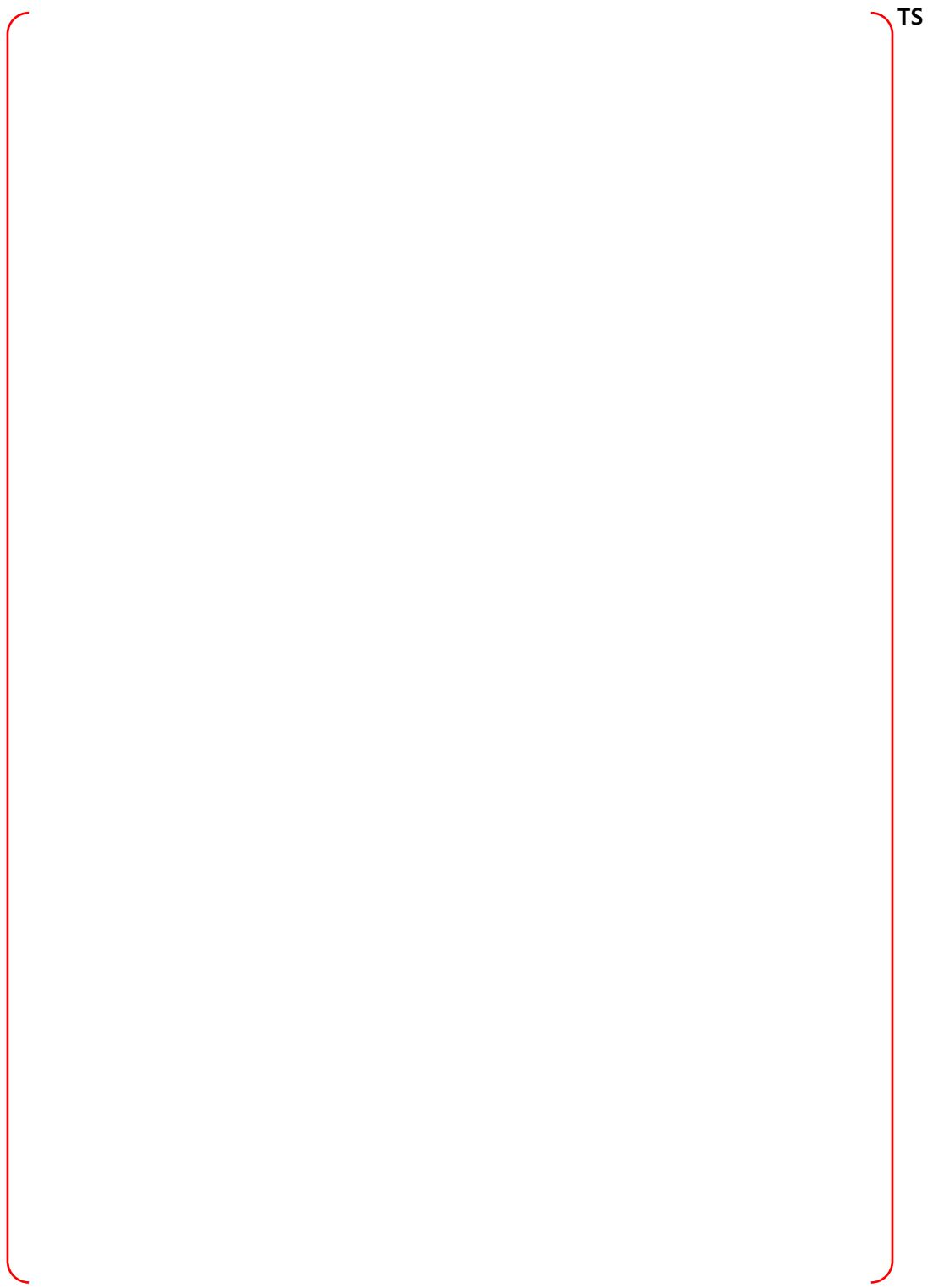


Figure B-129 Node 33, SE Annular Compartment at Elev 114' - Bounding Sequences – MCCI

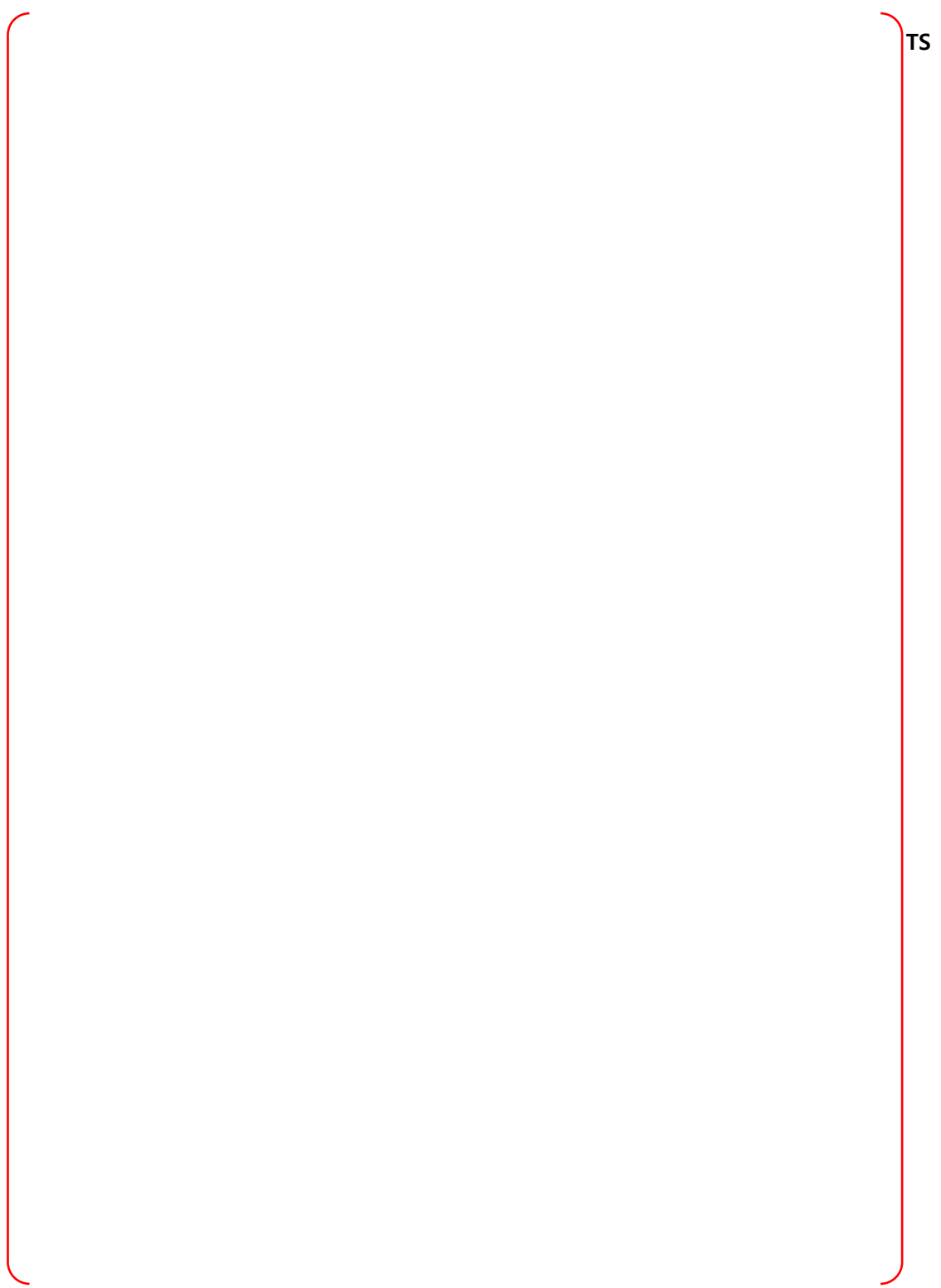


Figure B-130 Node 33, SE Annular Compartment at Elev 114' - Bounding Sequences – CP

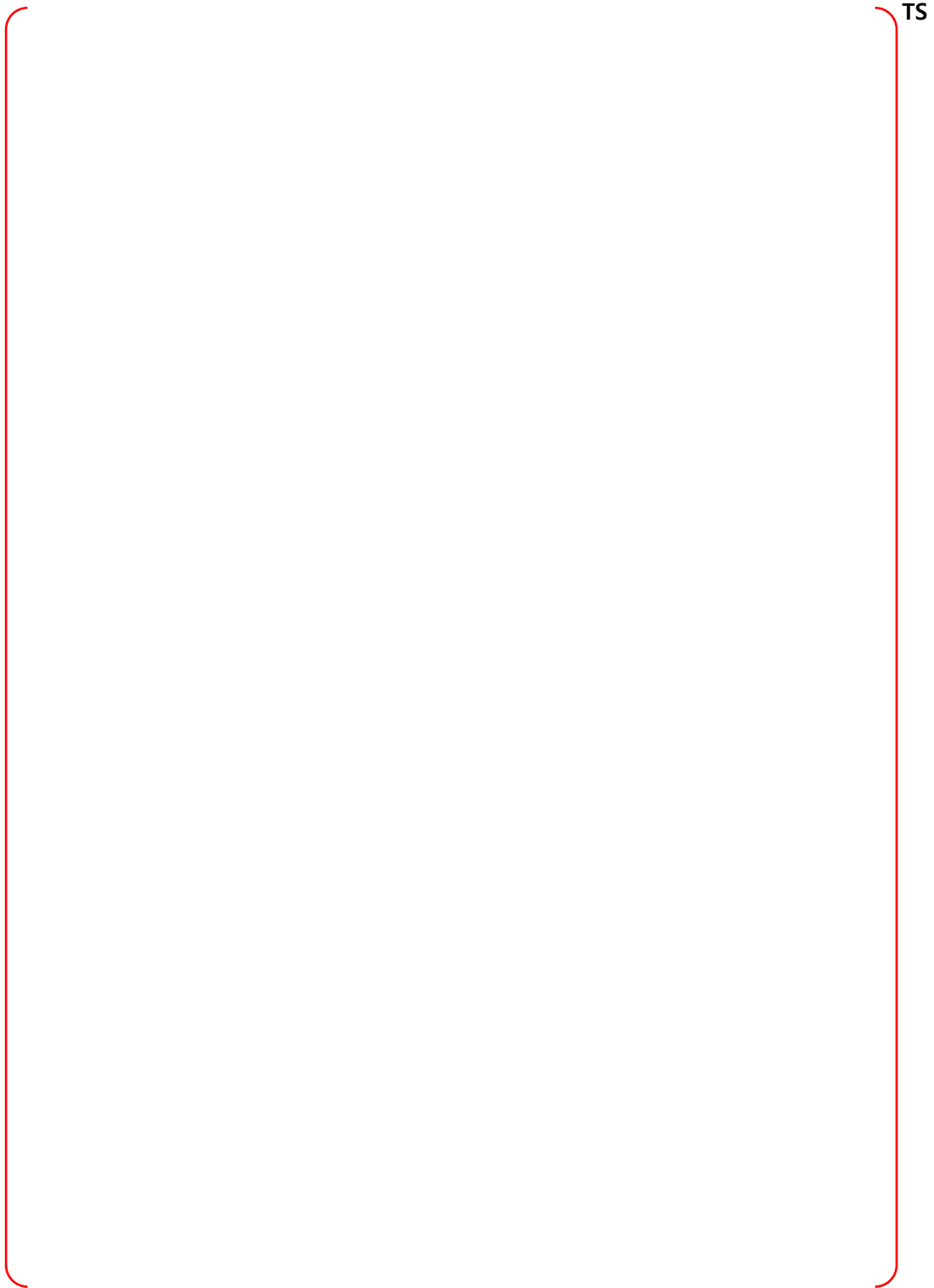


Figure B-131 Node 33, SE Annular Compartment at Elev 114' - Bounding Sequences - DF

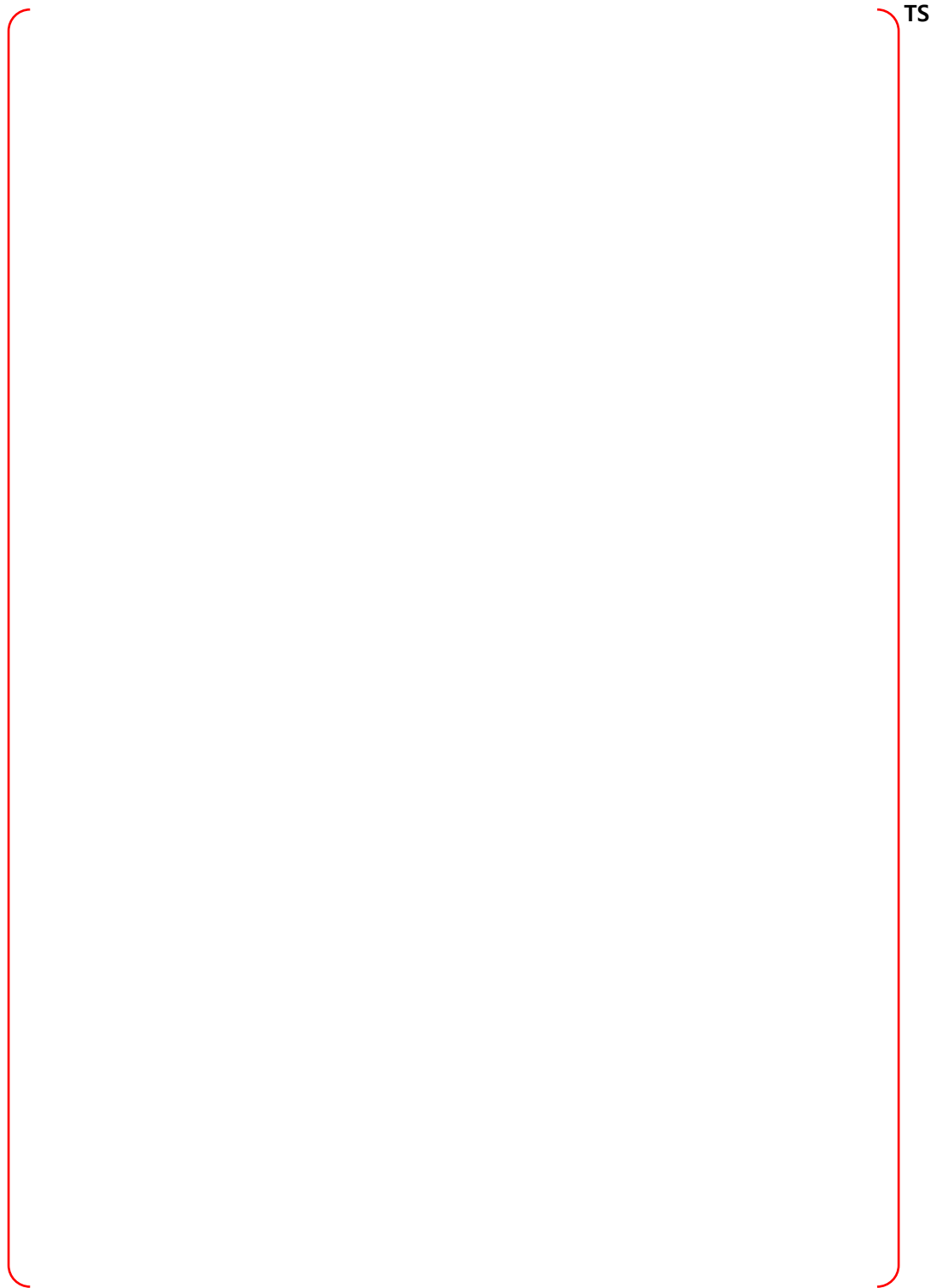


Figure B-132 Node 34, NE Annular Compartment at Elev 136.5' - PRA Sequences

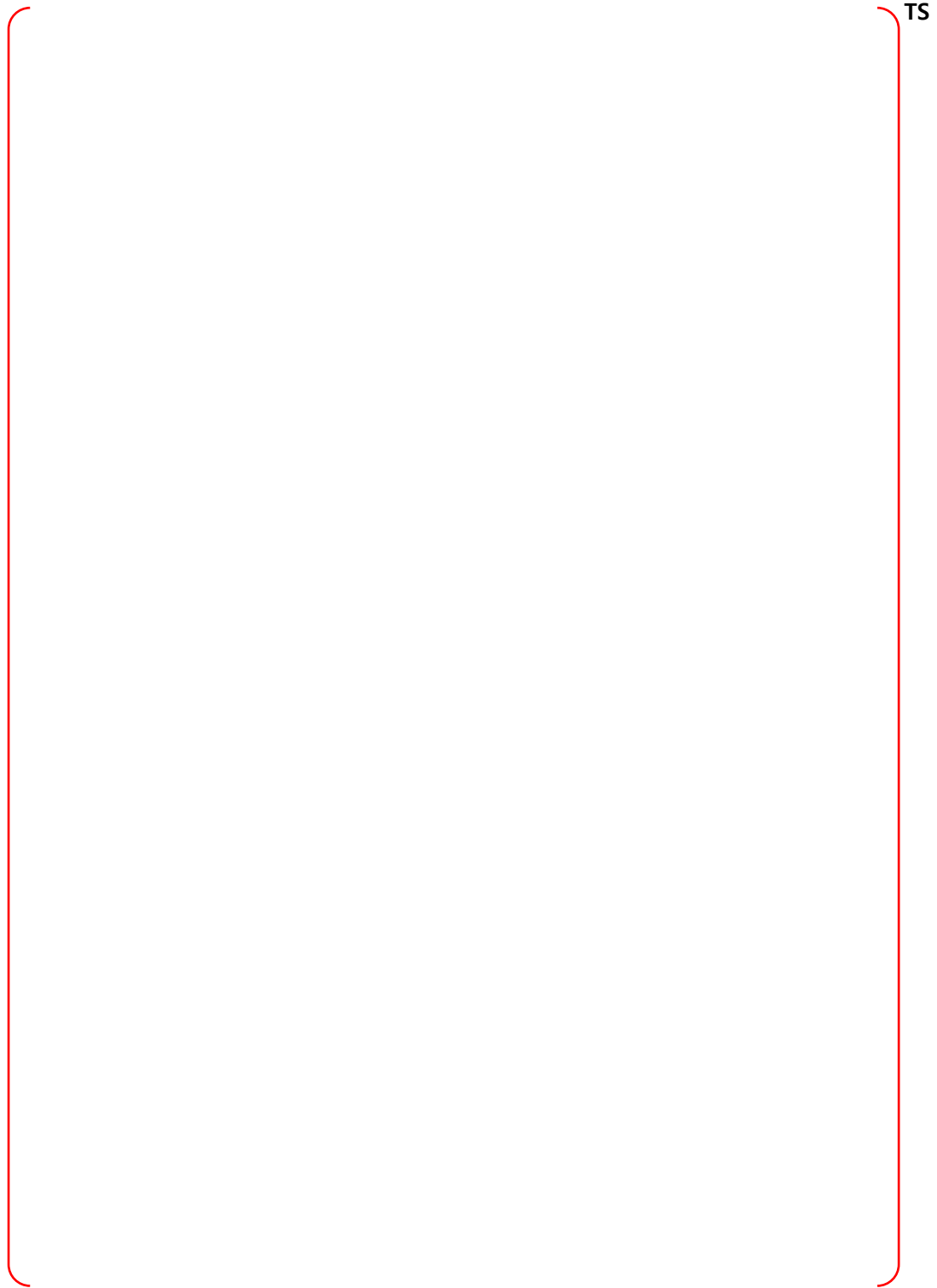


Figure B-133 Node 34, NE Annular Compartment at Elev 136.5' - Bounding Sequences – MCCI

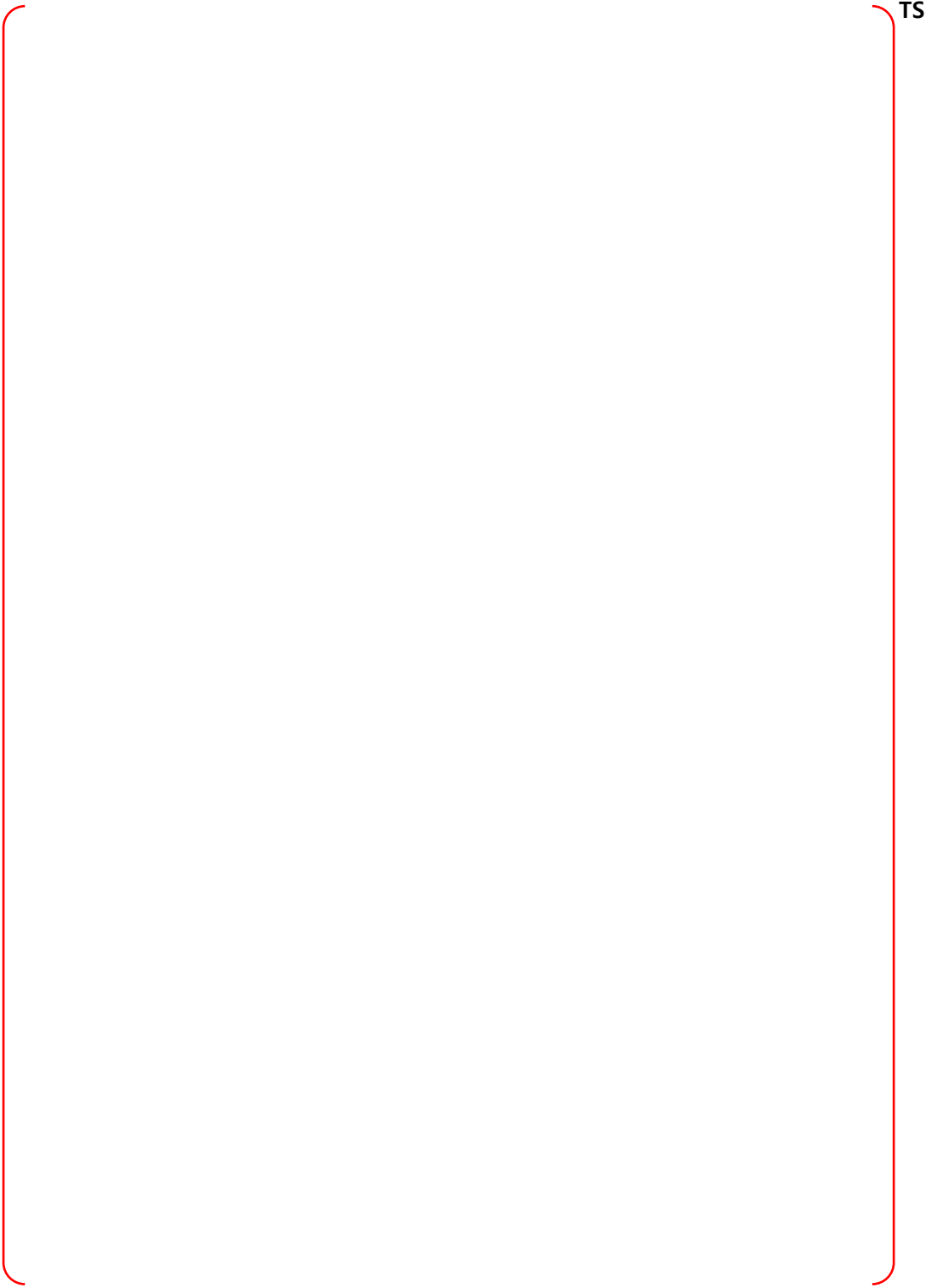


Figure B-134 Node 34, NE Annular Compartment at Elev 136.5' - Bounding Sequences – CP

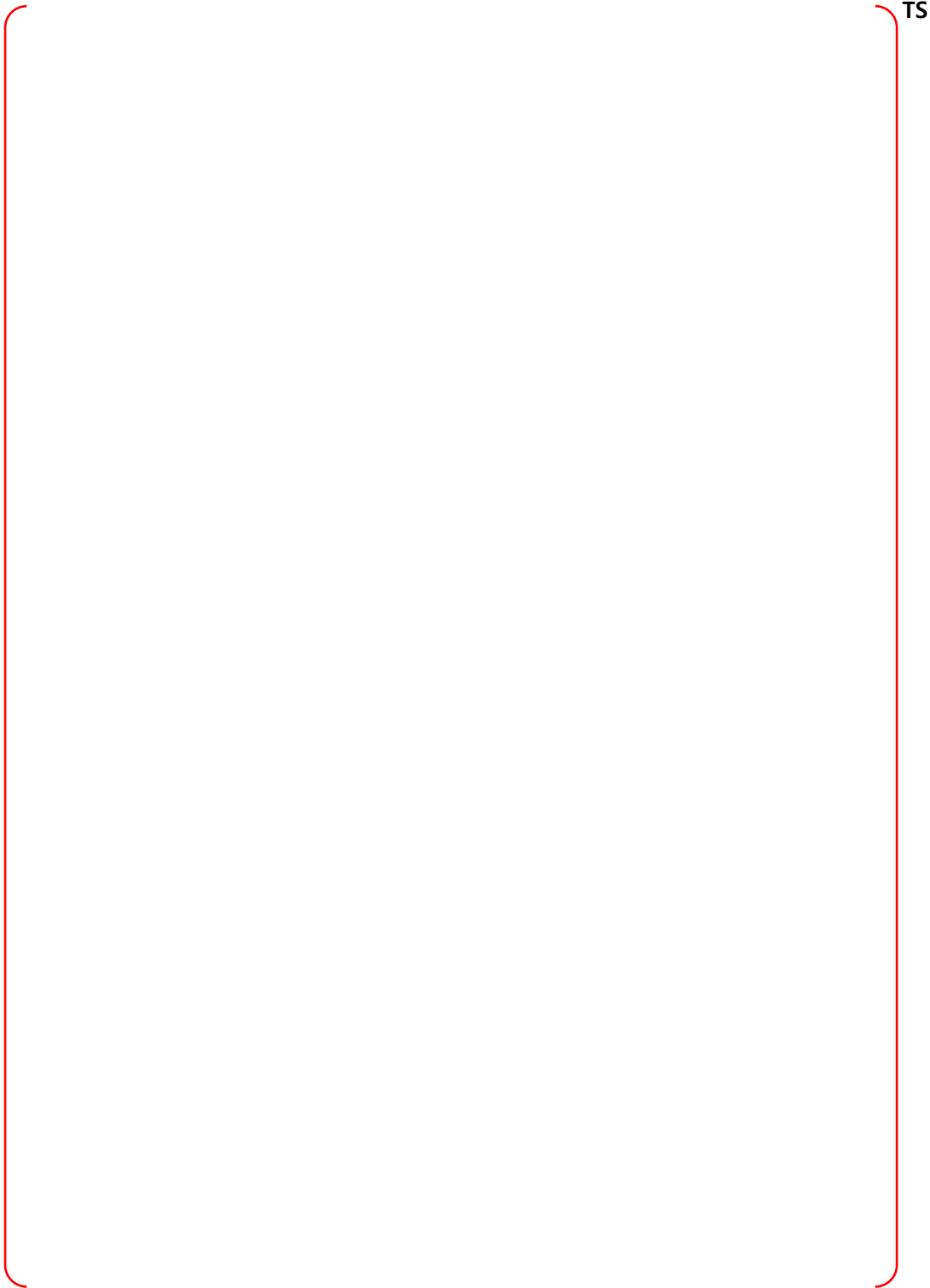


Figure B-135 Node 34, NE Annular Compartment at Elev 136.5' - Bounding Sequences – DF

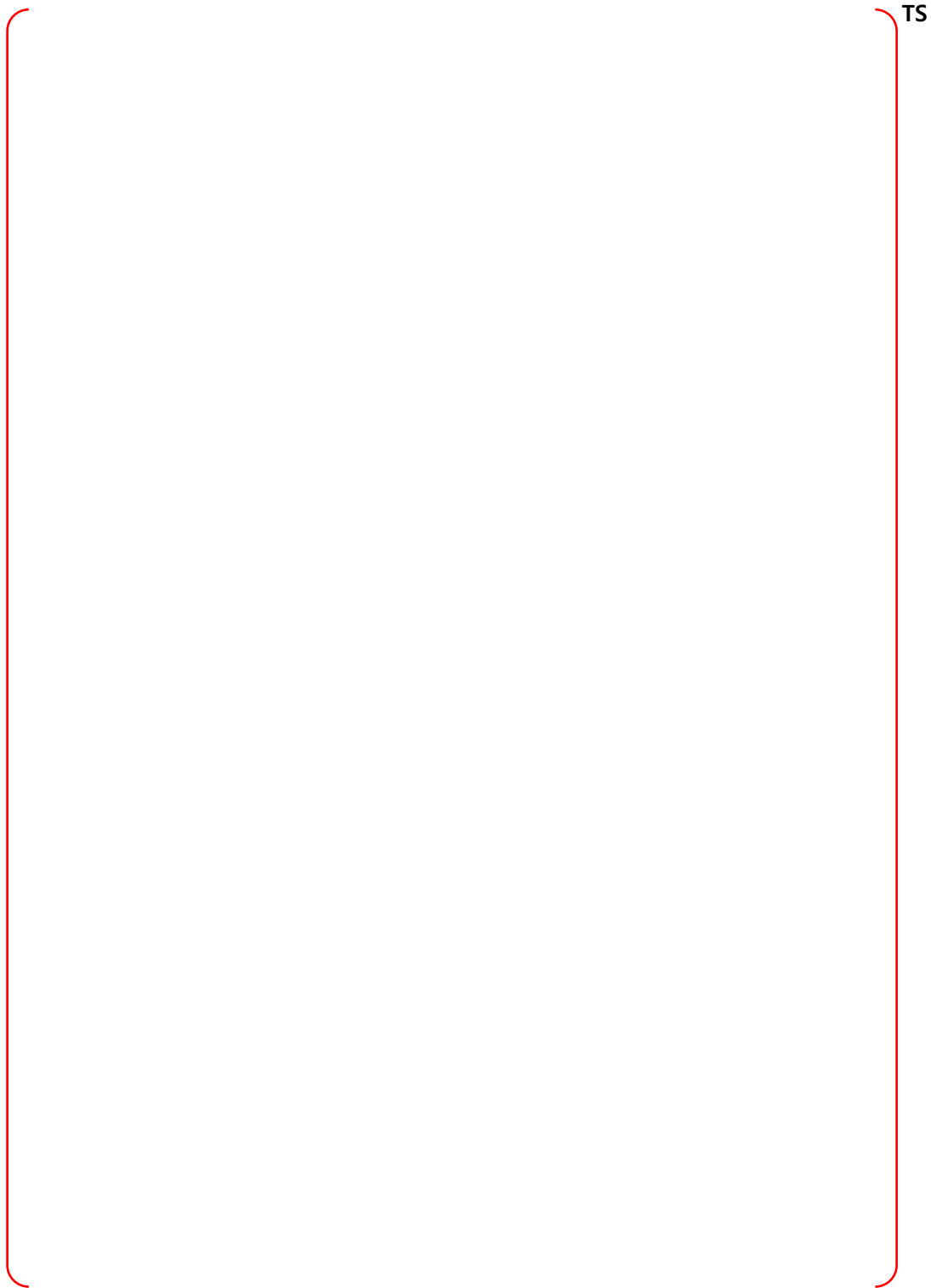


Figure B-136 Node 35, SE Annular Compartment at Elev 136.5' - PRA Sequences

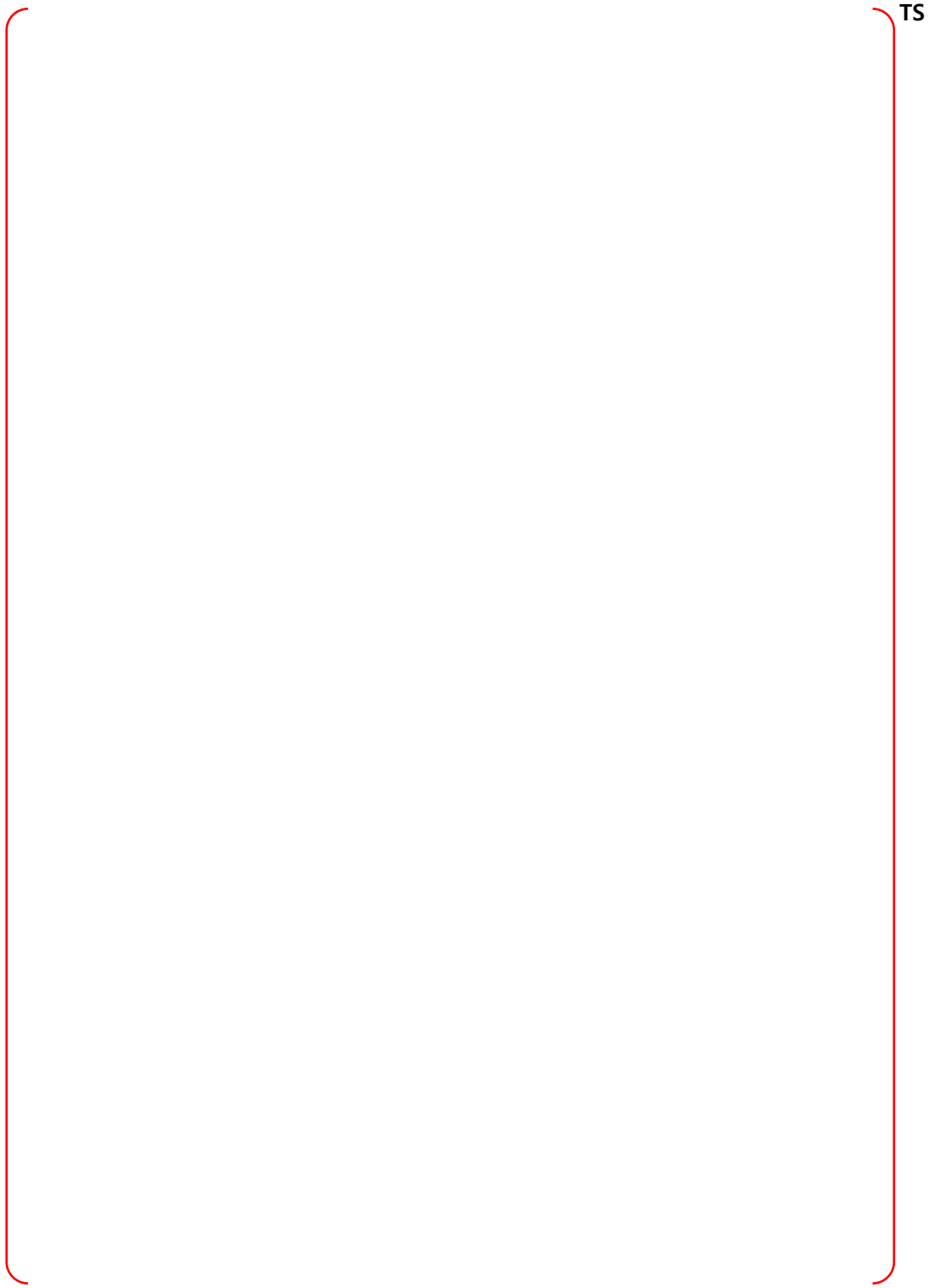


Figure B-137 Node 35, SE Annular Compartment at Elev 136.5' - Bounding Sequences – MCCI

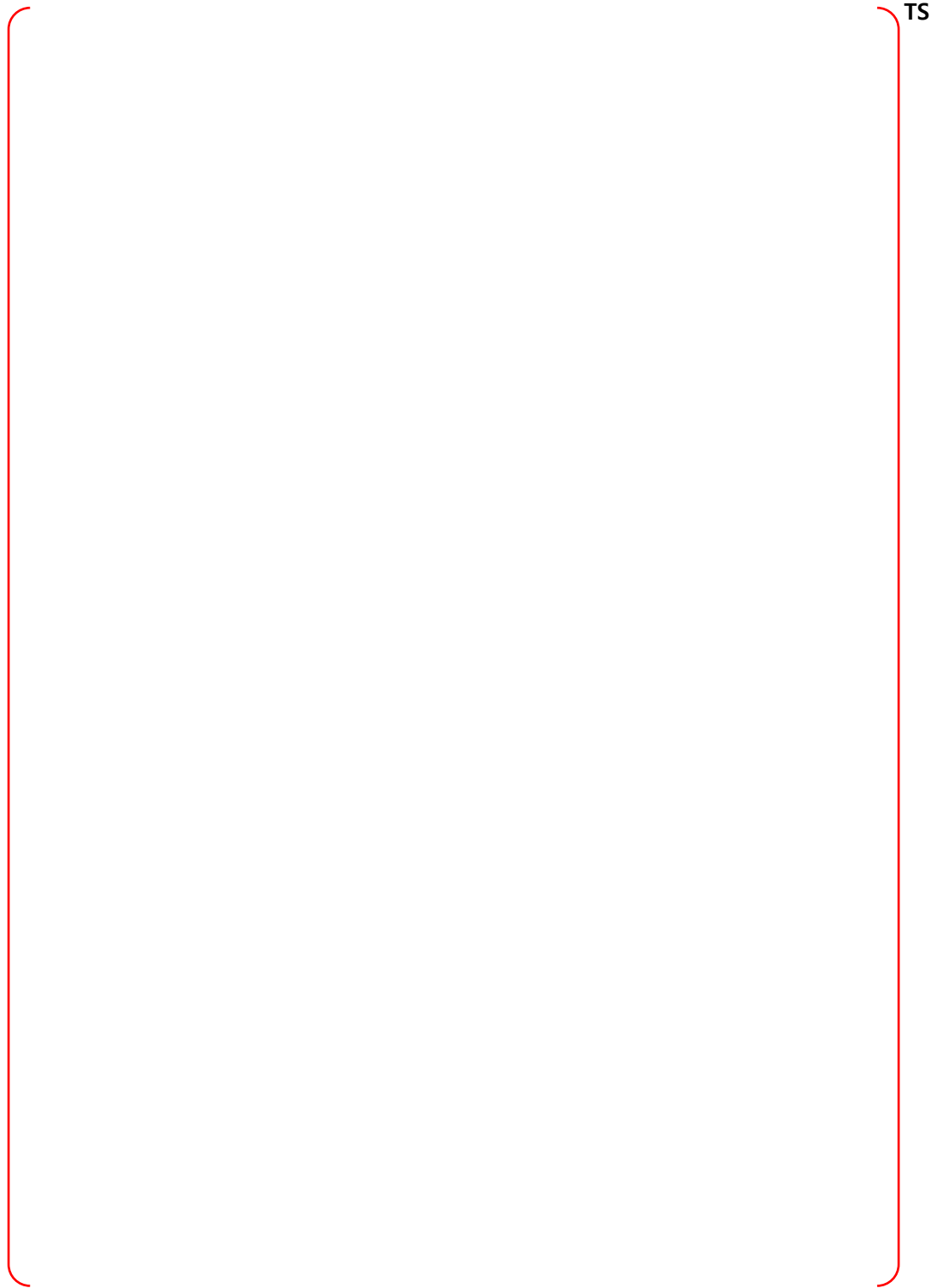


Figure B-138 Node 35, SE Annular Compartment at Elev 136.5' - Bounding Sequences – CP

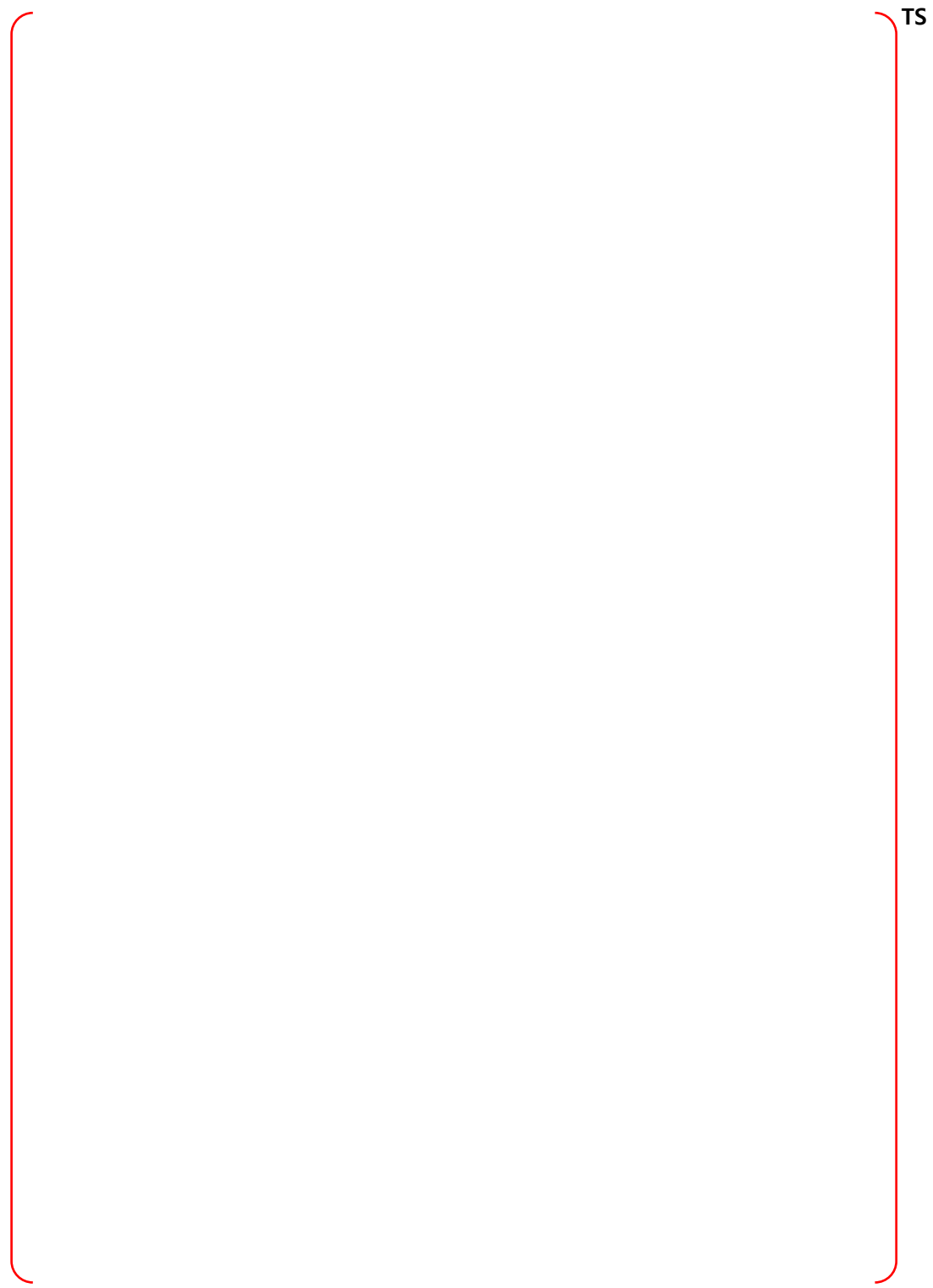


Figure B-139 Node 35, SE Annular Compartment at Elev 136.5' - Bounding Sequences – DF

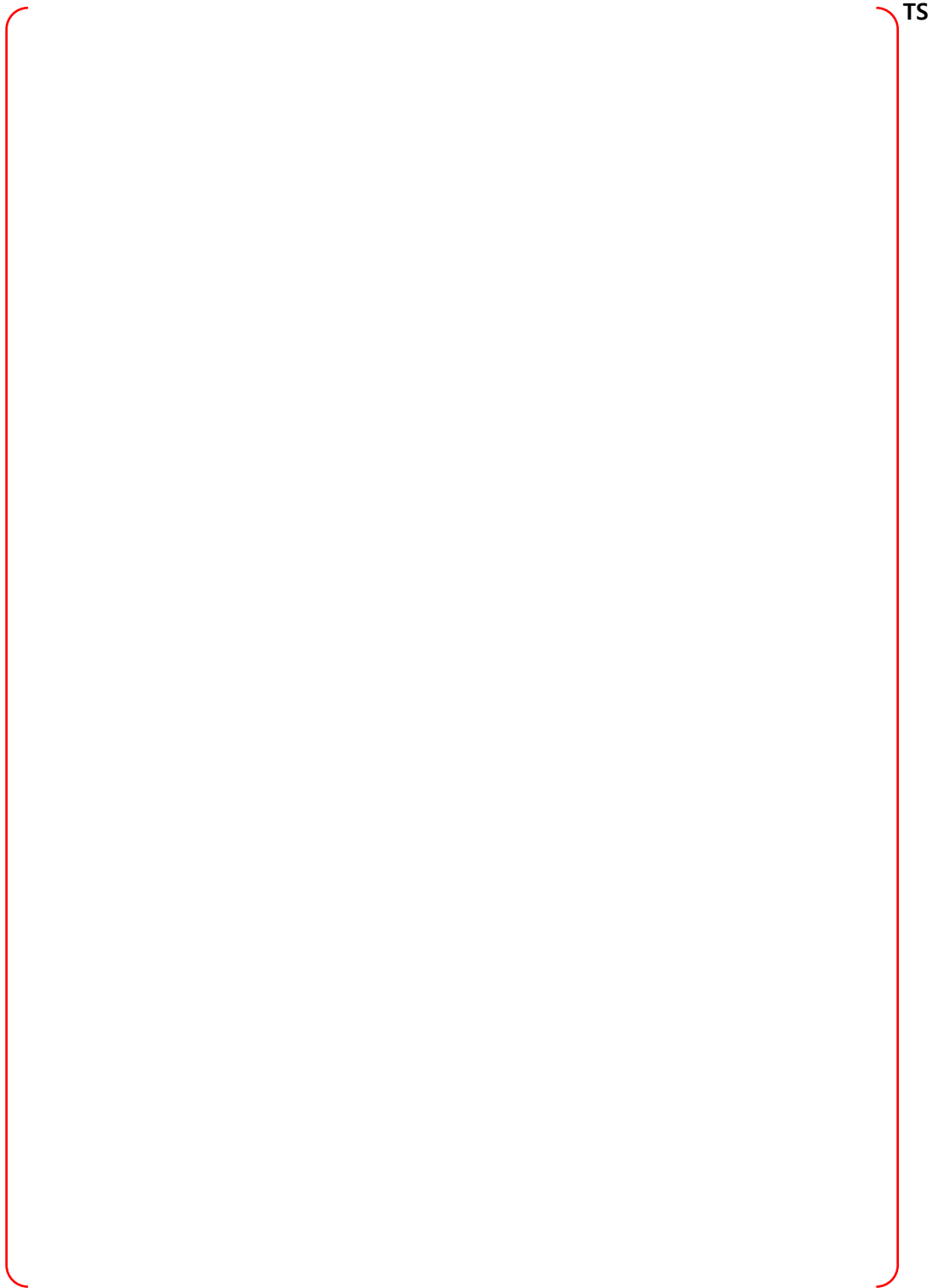


Figure B-140 Node 36, Upper Reactor Vessel Annulus - PRA Sequences

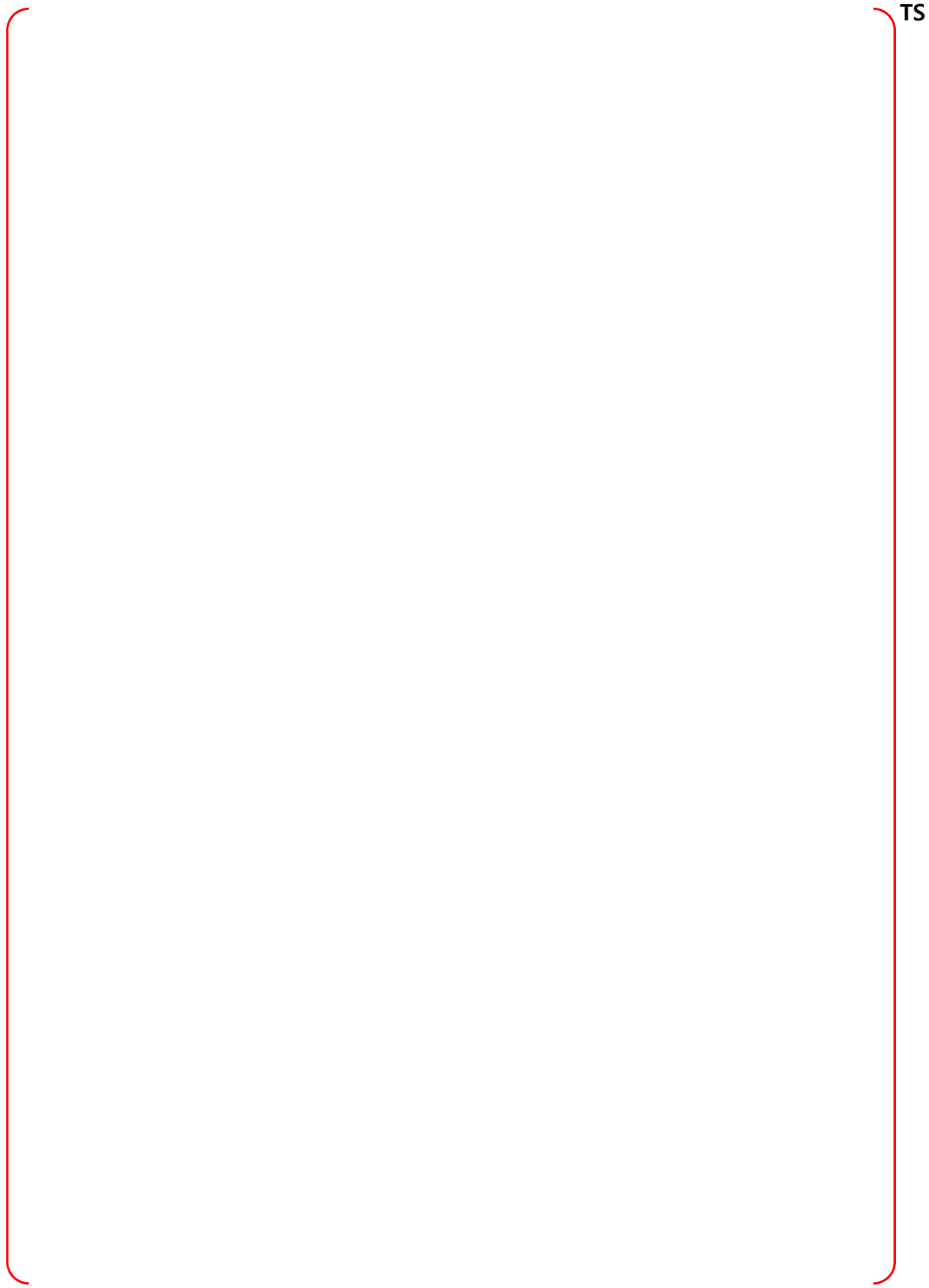


Figure B-141 Node 36, Upper Reactor Vessel Annulus - Bounding Sequences – MCCI

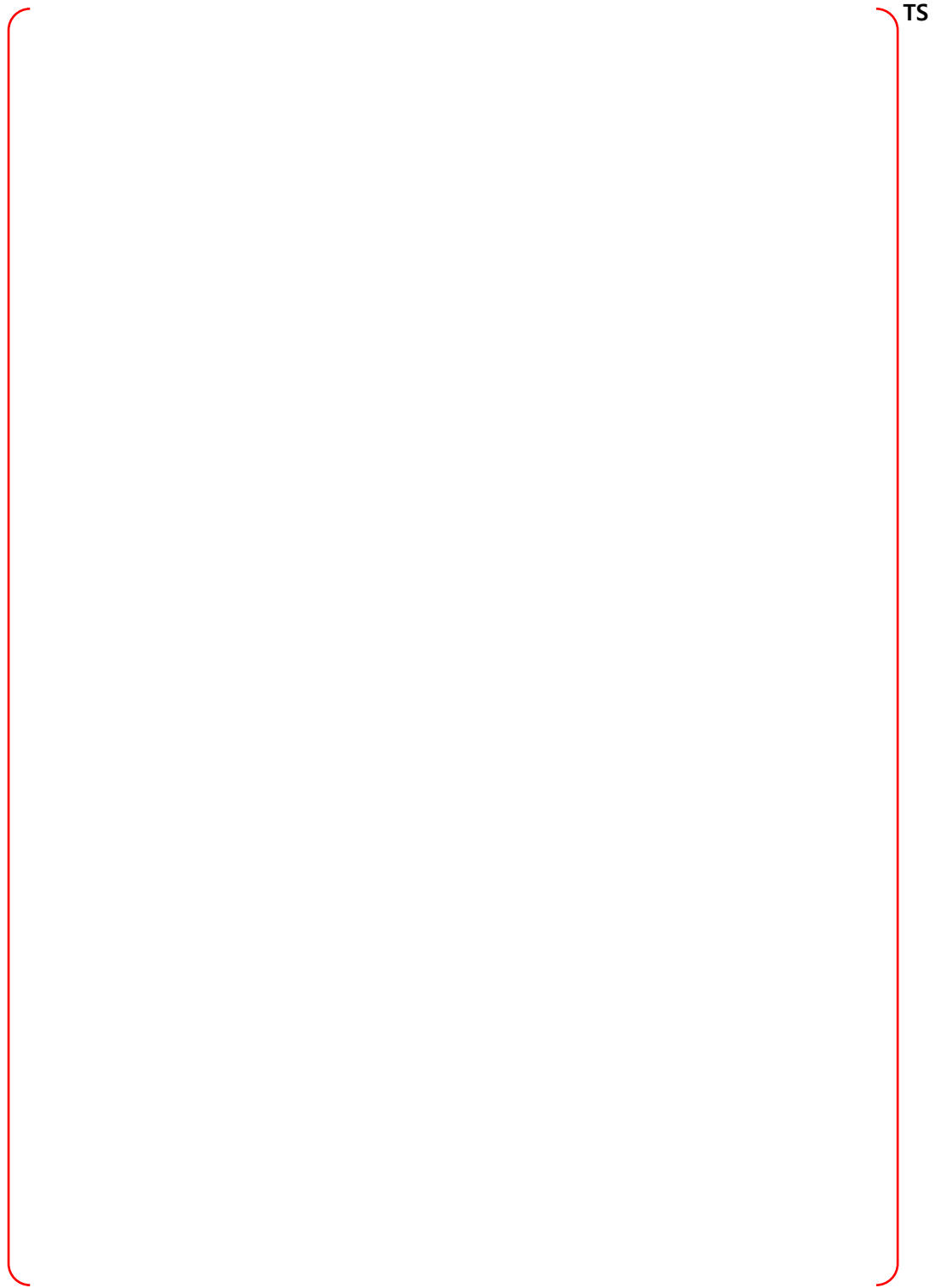


Figure B-142 Node 36, Upper Reactor Vessel Annulus - Bounding Sequences – CP

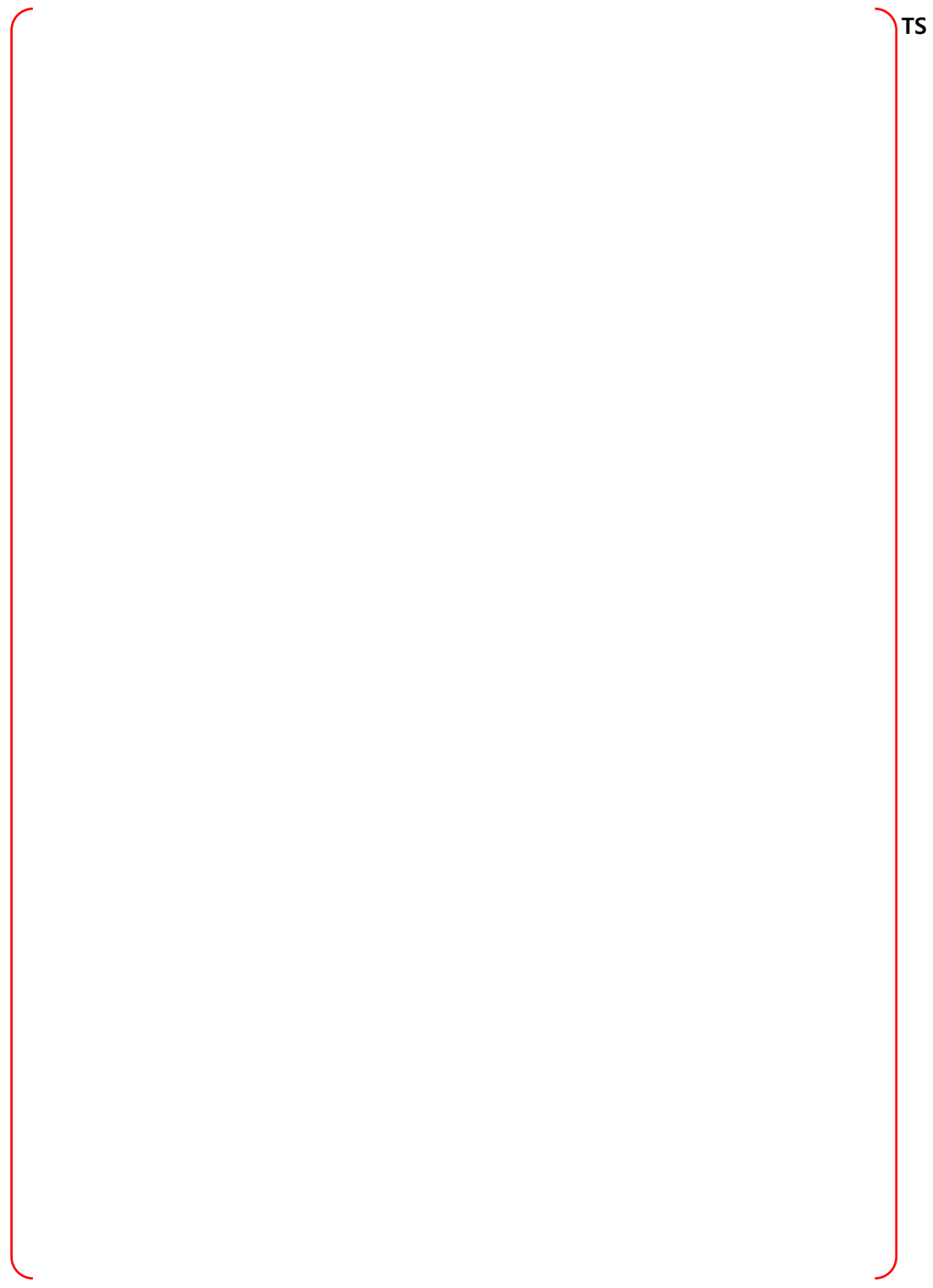


Figure B-143 Node 36, Upper Reactor Vessel Annulus - Bounding Sequences - DF